HIGH-THROUGHPUT PHENOTYPING FOR CROP IMPROVEMENT AND BREEDING

EDITED BY: Ankush Prashar, Lindsey Compton, Martina Stromvik and Helen H. Tai

PUBLISHED IN: Frontiers in Plant Science and Frontiers in Genetics

frontiers Research Topics

frontiers

ISSN 1664-8714
ISBN 978-2-88974-283-7
DOI10.3389/978-2-88974-283-7

About Frontiers

Frontiers is more than just an open-access publisher of scholarly articles: it is a pioneering approach to the world of academia, radically improving the way scholarly research is managed. The grand vision of Frontiers is a world where all people have an equal opportunity to seek, share and generate knowledge. Frontiers provides immediate and permanent online open access to all its publications, but this alone is not enough to realize our grand goals.

Frontiers Journal Series

The Frontiers Journal Series is a multi-tier and interdisciplinary set of open-access, online journals, promising a paradigm shift from the current review, selection and dissemination processes in academic publishing. All Frontiers journals are driven by researchers for researchers; therefore, they constitute a service to the scholarly community. At the same time, the Frontiers Journal Series operates on a revolutionary invention, the tiered publishing system, initially addressing specific communities of scholars, and gradually climbing up to broader public understanding, thus serving the interests of the lay society, too.

Dedication to Quality

Each Frontiers article is a landmark of the highest quality, thanks to genuinely collaborative interactions between authors and review editors, who include some of the world's best academicians. Research must be certified by peers before entering a stream of knowledge that may eventually reach the public - and shape society; therefore, Frontiers only applies the most rigorous and unbiased reviews.
Frontiers revolutionizes research publishing by freely delivering the most outstanding research, evaluated with no bias from both the academic and social point of view. By applying the most advanced information technologies, Frontiers is catapulting scholarly publishing into a new generation.

What are Frontiers Research Topics?

Frontiers Research Topics are very popular trademarks of the Frontiers Journals Series: they are collections of at least ten articles, all centered on a particular subject. With their unique mix of varied contributions from Original Research to Review Articles, Frontiers Research Topics unify the most influential researchers, the latest key findings and historical advances in a hot research area! Find out more on how to host your own Frontiers Research Topic or contribute to one as an author by contacting the Frontiers Editorial Office: frontiersin.org/about/contact

HIGH-THROUGHPUT PHENOTYPING FOR CROP IMPROVEMENT AND BREEDING

Topic Editors:
Ankush Prashar, Newcastle University, United Kingdom
Lindsey Compton, University of Birmingham, United Kingdom
Martina Stromvik, McGill University, Canada
Helen H. Tai, Agriculture and Agri-Food Canada (AAFC), Canada

Citation: Prashar, A., Compton, L., Stromvik, M., Tai, H. H., eds. (2022). High-Throughput Phenotyping for Crop Improvement and Breeding. Lausanne: Frontiers Media SA. doi: 10.3389/978-2-88974-283-7

Table of Contents

05 ***Accelerating Automated Stomata Analysis Through Simplified Sample Collection and Imaging Techniques***
Luke Millstead, Hiranya Jayakody, Harsh Patel, Vihaan Kaura, Paul R. Petrie, Florence Tomasetig and Mark Whitty

19 ***High-Throughput Switchgrass Phenotyping and Biomass Modeling by UAV***
Fei Li, Cristiano Piasecki, Reginald J. Millwood, Benjamin Wolfe, Mitra Mazarei and C. Neal Stewart Jr.

34 ***Improved Accuracy of High-Throughput Phenotyping From Unmanned Aerial Systems by Extracting Traits Directly From Orthorectified Images***
Xu Wang, Paula Silva, Nora M. Bello, Daljit Singh, Byron Evers, Suchismita Mondal, Francisco P. Espinosa, Ravi P. Singh and Jesse Poland

48 ***Comparison of MALDI-TOF-MS and RP-HPLC as Rapid Screening Methods for Wheat Lines With Altered Gliadin Compositions***
You-Ran Jang, Kyoungwon Cho, Sewon Kim, Jae-Ryeong Sim, Su-Bin Lee, Beom-Gi Kim, Yong Q. Gu, Susan B. Altenbach, Sun-Hyung Lim, Tae- Won Goo and Jong-Yeol Lee

59 ***Deep Learning for Predicting Complex Traits in Spring Wheat Breeding Program***
Karansher S. Sandhu, Dennis N. Lozada, Zhiwu Zhang, Michael O. Pumphrey and Arron H. Carter

72 ***Spatial Models With Inter-Tree Competition From Airborne Laser Scanning Improve Estimates of Genetic Variance***
David Pont, Heidi S. Dungey, Mari Suontama and Grahame T. Stovold

81 ***Development and Validation of Methodology for Estimating Potato Canopy Structure for Field Crop Phenotyping and Improved Breeding***
Filipe de Jesus Colwell, Jock Souter, Glenn J. Bryan, Lindsey J. Compton, Neil Boonham and Ankush Prashar Chung-Chi Hu

97 ***High Throughput Field Phenotyping for Plant Height Using UAV-Based RGB Imagery in Wheat Breeding Lines: Feasibility and Validation***
Leonardo Volpato, Francisco Pinto, Lorena González-Pérez, Iyotirindranath Gilberto Thompson, Aluízio Borém, Matthew Reynolds, Bruno Gérard, Gemma Molero and Francelino Augusto Rodrigues Jr

116 ***Identification of the QTL-allele System Underlying Two High-Throughput Physiological Traits in the Chinese Soybean Germplasm Population***
Lei Wang, Fangdong Liu, Xiaoshuai Hao, Wubin Wang, Guangnan Xing, Jingjing Luo, Guodong Zhou, Jianbo He and Junyi Gai

129 ***Remote Sensing Energy Balance Model for the Assessment of Crop Evapotranspiration and Water Status in an Almond Rootstock Collection***
Joaquim Bellvert, Héctor Nieto, Ana Pelechá, Christian Jofre-C ekalovic, Lourdes Zazurca and Xavier Miarnau

147 ***Transpiration Rate of White Clover (*Trifolium repens *L.) Cultivars in Drying Soil***
Lucy Egan, Rainer Hofmann, Shirley Nichols, Jonathan Hadipurnomo and Valerio Hoyos-Villegas

161 ***Heterotic Patterns of Temperate and Tropical Maize by Ear Photometry***
Seth A. Tolley, Amritpal Singh and Mitchell R. Tuinstra

177 ***Robotic Technologies for High-Throughput Plant Phenotyping: Contemporary Reviews and Future Perspectives***
Abbas Atefi, Yufeng Ge, Santosh Pitla and James Schnable

195 ***Raman Spectroscopy as a Robust New Tool for Rapid and Accurate Evaluation of Drought Tolerance Levels in Both Genetically Diverse and Near-Isogenic Maize Lines***
Narangerel Altangerel, Pei-Cheng Huang, Michael V. Kolomiets, Marlan O Scully and Philip R. Hemmer

frontiers in Plant Science

ORIGINAL RESEARCH
published: 25 September 2020
doi: 10.3389/fpls.2020.580389

Accelerating Automated Stomata Analysis Through Simplified Sample Collection and Imaging Techniques

Luke Millstead[1], Hiranya Jayakody[1], Harsh Patel[1], Vihaan Kaura[1], Paul R. Petrie[1,2], Florence Tomasetig[3] and Mark Whitty[1]*

[1] School of Mechanical and Manufacturing Engineering, University of New South Wales, Sydney, NSW, Australia, [2] Crop Sciences Division, South Australian Research and Development Institute, Waite Campus, Urrbrae, SA, Australia, [3] Mark Wainwright Analytical Centre, University of New South Wales, Sydney, NSW, Australia

Digital image processing is commonly used in plant health and growth analysis, aiming to improve research efficiency and repeatability. One focus is analysing the morphology of stomata, with the aim to better understand the regulation of gas exchange, its link to photosynthesis and water use and how they are influenced by climatic conditions. Despite the key role played by these cells, their microscopic analysis is largely manual, requiring intricate sample collection, laborious microscope application and the manual operation of a graphical user interface to identify and measure stomata. This research proposes a simple, end-to-end solution which enables automatic analysis of stomata by introducing key changes to imaging techniques, stomata detection as well as stomatal pore area calculation. An optimal procedure was developed for sample collection and imaging by investigating the suitability of using an automatic microscope slide scanner to image nail polish imprints. The use of the slide scanner allows the rapid collection of high-quality images from entire samples with minimal manual effort. A convolutional neural network was used to automatically detect stomata in the input image, achieving average precision, recall and F-score values of 0.79, 0.85, and 0.82 across four plant species. A novel binary segmentation and stomatal cross section analysis method is developed to estimate the pore boundary and calculate the associated area. The pore estimation algorithm correctly identifies stomata pores 73.72% of the time. Ultimately, this research presents a fast and simplified method of stomatal assay generation requiring minimal human intervention, enhancing the speed of acquiring plant health information.

Keywords: stomata analysis pipeline, stomata sample collection, stomata pore measurement, high-throughput analysis, microscope imagery

OPEN ACCESS

Edited by:
Martina Stromvik, McGill University, Canada

Reviewed by:
Alice Lydia Baillie, University of Bristol, United Kingdom
Matthew Haworth, Italian National Research Council, Italy

***Correspondence:**
Hiranya Jayakody
hiranya.jayakody@unsw.edu.au

Specialty section:
This article was submitted to Technical Advances in Plant Science, a section of the journal Frontiers in Plant Science

Received: *06 July 2020*
Accepted: *10 September 2020*
Published: *25 September 2020*

Citation:
Millstead L, Jayakody H, Patel H, Kaura V, Petrie PR, Tomasetig F and Whitty M (2020) Accelerating Automated Stomata Analysis Through Simplified Sample Collection and Imaging Techniques. Front. Plant Sci. 11:580389. doi: 10.3389/fpls.2020.580389

INTRODUCTION

The size and density of stomata have been studied as important plants traits since the early 19th century (Banks, 1805). Stomata pores, located on the plant leaf epidermis, play a major role in regulating the diffusion for both carbon dioxide and water (Dow et al., 2014) and their distribution provides important information about plant developmental biology (Lau and Bergmann, 2012).

Recent works suggest that stomatal closure under water stress could result in vein embolism, which can cause the plant water transport system to collapse (Brodribb et al., 2016). Hence, stomata shape and behaviour are identified as direct indicators of plant health and the surrounding environmental conditions (Beerling and Chaloner 1993a; Beerling and Chaloner 1993b; Sadras et al., 2012).

Analysis of stomata is also an important aspect of paleoecology; for example, stomatal index (i.e. the ratio between the number of stomata and epidermal cells) of fossil plant cuticles can provide valuable insights into the atmospheric carbon dioxide levels in a given era (Beerling and Chaloner 1993b; Beerling and Royer, 2002). In addition, the undulation index (waviness of stomata cell wall), which is physiologically affected by light, correlates well with growing degree-days (GDD), which provides information on seasonal change (Smith et al., 2010; Wagner-Cremer et al., 2010; Wagner-Cremer and Lotter, 2011) in a given period of time. Thus, microscope analysis of stomata plays a major role in present day agriculture as well as modelling climate change over long periods of time.

Stomatal aperture is often measured using the microscope imaging of leaf samples, epidermal peels, or imprints (Dow et al., 2014; Eisele et al., 2016; Jayakody et al., 2017). These images are analyzed using image processing software such as ImageJ (Rasband, 1997), which enables manual measurements to be made on a computer interface. The manual measurement of stomata is sufficient when it is only necessary to measure a small number; however, this would prove unsuitable when processing an entire leaf surface. For the analysis of larger leaf areas, automated image processing techniques are required.

One of the first papers to implement digital image processing for automating stomatal measurements was Omasa and Onoe's (Omasa and Onoe, 1984) work with stomatal aperture. Here, the authors applied a Hanning Filter, discrete inverse Fourier transform and thresholding to measure individual stomata. In the decades following this paper, numerous advancements have been made in computer vision and microscopy. These advancements have supported improvements in the automation of stomatal analysis. Whether it be through detecting the unique fluorescence emission of stomatal guard cells under UV excitation (Karabourniotis et al., 2001), through rhodamine 6G staining (Eisele et al., 2016), or through template matching (Laga et al., 2014), it has ultimately been the automatic measurement, not detection, of stomatal pores in large samples that has proven most difficult. More recent research (Jayakody et al., 2017; Toda et al., 2018; Fetter et al., 2019; Sakoda et al., 2019) utilizes machine learning and image processing to detect stomata (and sometimes classify the state of the stomata) in microscope images. The accuracy levels achieved in these studies shows promise and enables plant scientists to conduct high-throughput analysis for stomata detection. However, once stomata are detected, correctly measuring the stomatal pores requires additional image processing steps (and sometimes human intervention), which can increase the overall processing time. Thus, it is important to build algorithms which go beyond stomata detection, and reliably measure pore opening under varying image quality.

Although machine learning can enable high-throughput microscope image analysis, the efficiency of the overall pipeline still depends on sample collection and imaging techniques. Hence, for current image processing techniques to have any practical value in the field, microscope samples must be collected and imaged quickly, accurately and in sufficient detail to measure stomatal pore areas. Most current sample collection processes produce images with suitable quality for digital image processing. However, many of these techniques require complex chemicals or intricate leaf manipulations, which are often time consuming and impractical for use in the field by untrained operators (Weyers and Travis, 1981; Celine et al., 2012; Eisele et al., 2016; Monda et al., 2016; Yuan et al., 2020).

There are two common methods that are used to collect samples quickly and simply. The first is the silicon impression method, described by Weyers and Johansen (1985), which uses dental resin to create a negative impression of the leaf surface, and nail varnish to transfer this imprint onto a microscope slide. The second method replaces the dental resin with nail polish, so that a direct impression is made. Upon drying, adhesive tape is used to transfer the imprint to a microscope slide (Rogiers et al., 2011). These methods result in samples of reasonable quality which are suitable for automated stomata detection.

One of the major bottlenecks in this process is the time taken to image the collected samples. As such, techniques used to obtain microscope images from samples must be re-examined to develop a streamlined yet accurate process. Currently, many researchers use simple light-field or other manual stage microscopes to obtain their results (Jayakody et al., 2017; Fetter et al., 2019), which is sufficient to examine small numbers of stomata. However, if a larger portion of the leaf is to be covered, the manual stage movements can take several hours, even with a motorized stage. Additionally, the large proportion of veins create protrusions in the epidermal surface, which requires refocusing the microscope upon every movement of the stage. Consequently, most current research on stomate detection and analysis relies on input images containing up to 40 stomata at most (Li et al., 2019), making it difficult to measure density or observe patterns across a leaf. With these limitations apparent, it is important to investigate fast imaging methods which require minimal manual effort.

We present an accelerated end-to-end process to identify and measure stomata, whilst significantly reducing the manual labour requirements. Two simple approaches for sample collection were assessed, with the aim of producing high quality samples for imaging. Then a microscope slide scanner was utilized to rapidly image the samples, eliminating the need for manual staging and focusing of the sample. A Convolutional Neural Network was implemented to detect stomata from the feature rich images generated by the slide scanner and a novel stomatal pore measurement algorithm is proposed to identify the pore area regardless of the colour intensity of the pore. This is a streamlined solution for efficiently analysing stomatal

morphology, distribution, and patterning across large leaf surfaces.

MATERIALS AND METHODS

Simplified Sample Collection

One of the primary aims of this paper is to determine the most effective sampling technique which is both simple and reliable. The common nail polish imprint method (Miller and Ashby, 1968) meets both these requirements due to its simplicity. The steps involved in the common nail polish imprint method are as follows:

1. A thin layer of nail polish (Revlon Ultra, Revlon Consumer Products Corporation, New York, NY, USA was used in this research) is applied to the abaxial surface of the leaf. The surface covered by the nail polish is set to approximately 30 mm in length and 9 mm in width and is selected such that major veins are avoided.
2. The nail polish is then left to dry for approximately five minutes.
3. One piece of clear adhesive tape is pressed onto the dry nail polish.
4. The tape is removed from the leaf surface and the adhesive side secured to a plastic sleeve for transport to a laboratory environment.

A common issue with the traditional leaf imprint method is the introduction of air bubbles when securing the imprint to the microscope slide using tape. The tape also tends to deform to the shape of the uneven leaf surface, which may create focusing issues during the imaging process. A modified approach is proposed for mounting the imprint on the microscope slide to combat this as follows:

1. In the laboratory, the tape is removed from the plastic sleeve, transferred to a thin glass coverslip and the adhesive side is pressed down to ensure a flat surface.
2. The top (non-adhesive) surface of the tape, including the attached coverslip, is mounted on a microscope slide using transparent sticky tape on the corners of the coverslip as shown in **Figure 1B**. Optionally, a product similar to Vectashield mounting medium (Vector Laboratories, Inc. Burlingame, CA, USA) can be used to mount the coverslip onto the microscope slide. If a mounting medium is used, several glass weights should be placed on the coverslip to distribute the mounting medium evenly.

A diagram of the modified method in comparison to the original technique is shown in **Figure 1**. The coverslip aims to reduce any unevenness of the leaf imprint, allowing shallow depth-of-field sensors to keep larger areas of the sample in focus. With this approach, any artefacts generated on the adhesive side of the tape are no longer obstructing the view of the microscope.

Samples from four plant species, Vitis vinifera L. x V. rupestris Scheele 'Ganzin Glory', Prunus armeniaca 'Moorpark', Citrus sinensis L. Osbeck 'Valencia', and Vinca major L. 'Periwinkle', were collected from Belair, Adelaide. The samples were prepared using both traditional and modified mounting approaches for comparison purposes. A detailed comparison between the proposed sampling method and the common nail polish imprint method is presented in *Simplified Sample Collection*.

Microscope Slide Scanner for Imaging Samples

A manual-stage optical microscope is not capable of capturing a complete 30 mm × 9 mm leaf sample with a single image. Instead, the sample must be moved, and the microscope refocused prior to capturing each image. Once multiple images

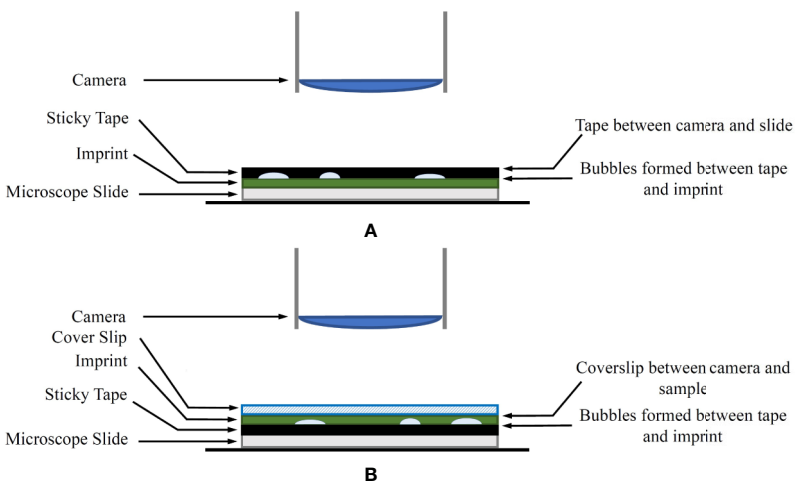

FIGURE 1 | **(A)** The original imprint method. The sticky tape is between the camera and the sample. **(B)** The modified imprint method. The sticky tape and bubbles are no longer between the microscope and the sample. Instead, an appropriate coverslip is covering the sample.

are captured covering the sample, they need to be stitched together to create a single image of the leaf.

These issues are solved by using a microscope slide scanner. Used in the field of cell pathology, slide scanners can rapidly produce high-quality images of the complete sample slide at once. This is achieved by an automated process where the slide is carefully moved under a line-scan camera. The lines are then automatically stitched together to produce a single high-resolution image of the complete sample. Imaging the complete slide at once allows researchers to gain a better understanding on macro level characteristics such as stomata patchiness. In addition to speeding up the image capture process, another major advantage of the slide scanner is its ability to store multiple microscope slides in the device. This feature allows users to load many samples and image them in a single run without adjusting settings for each new sample. In this work, an Aperio® XT (40x) brightfield slide scanner (Wetzlar, Germany) is used. The device uses linescan technology to generate images at a resolution of 0.25 um/pixel and holds up to 120 slides at one time. The performance of the slide scanner is compared with a manual stage optical microscope in *Imaging With Microscope Slide Scanner*.

Stomata Detection With a Convolutional Neural Network

Stomatal pore area measurements require the identification of stomata in a microscope image (Dow et al., 2014); with a small number of stomata, this can be achieved using manual image analysis tools. More recently, higher order image processing and machine learning has been used to automate this process (Laga et al., 2014; Liu et al., 2016; Jayakody et al., 2017; Toda et al., 2018; Fetter et al., 2019; Sakoda et al., 2019). In this work, a CNN (Lecun et al., 1998) based on the MATLAB® implementation of the AlexNet (Krizhevsky et al., 2012) network was used to identify stomata (MathWorks, 2018). AlexNet is pre-trained on more than one million images and can facilitate transfer learning, which takes the pretrained network and utilizes its feature extraction capabilities as a starting point to learn new detection tasks. This requires fewer training images, which reduces the time required to automate the overall process for a new image target. The process of stomate detection using AlexNet is described below. The training data for transfer learning comprised of images collected through both traditional and modified sample collection methods.

1. Using the images extracted for training, a training set was prepared with images assigned to three categories: stomata, vein, and background (as shown in **Figure 2**).
2. Feature vectors are extracted from the training data to train a classifier using AlexNet. Particularly, AlexNet is eight layers deep (MathWorks, 2018) and, when used for feature extraction, the neural network is terminated at one of the fully connected middle layers. This layer outputs the feature vector representing the activations for the input images.
3. Using MATLAB's Classification Learner application (Machine Learning toolbox), a quadratic Support Vector Machine classifier is trained with the feature vector.

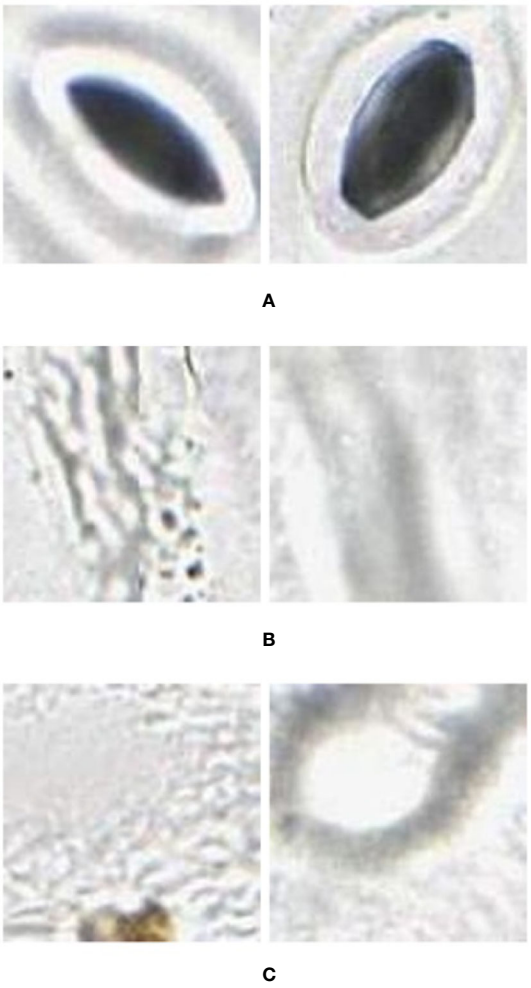

FIGURE 2 | Example **(A)** stomata (positive), and **(B)** veins and **(C)** background (negative) used to train the AlexNet neural network. These were extracted from images (in regions separate to that being classified) collected using the modified imprint method and imaged with the slide slidescanner.

4. The classifier is then applied to the image through a classification window of predefined size, translated across the image by sliding the window. This produces a mask of the image indicating the location of each stomate.
5. To calculate precision, recall, and accuracy, the stomata are manually labelled using a custom GUI. By discretising the manually and automatically labelled images and comparing each grid value (1 if stomate, 0 if background), the number of false positives (FP), true positives (TP), false negatives (FN) and true negatives (TN) were determined.

In order to reduce the processing time involved with applying a sliding window across the entire image, the program first splits the slide scanner image into smaller tiles which are processed individually, and then reassembles the labelled results into a complete image.

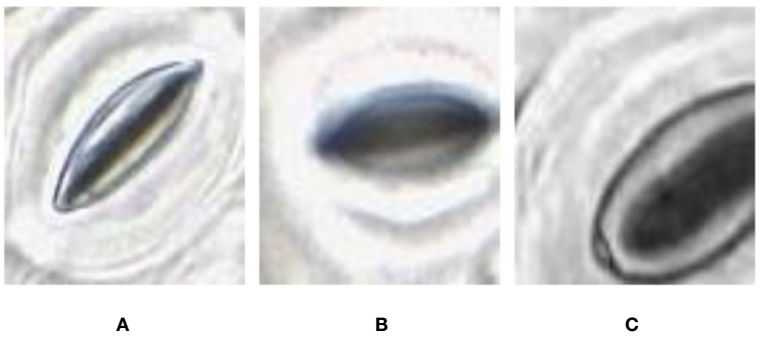

FIGURE 3 | Quality variation of the stomata captured at different parts of the microscope image. **(A)** sharp image. **(B)** blurry image **(C)** partially captured image.

Stomata Pore Area Calculation

With the methods proposed in *Microscope Slide Scanner for Imaging Samples*, the slide scanner is able to produce feature-rich images where stomata can be clearly identified. However, the sharpness of the image can slightly vary along the image due to the uneven nature of the leaf surface, causing variation in focus. This variation directly affects the quality of each individual stomate image based on their location on the leaf. This results in stomata images with different image qualities (**Figure 3**).

In some of the stomata images captured by the slide scanner, the pore area appears darker than the surrounding guard cells whereas in other stomata images the pore area appears lighter than the guard cells (**Figure 4**). These variations depend largely on focus; due to significant variation in height across the sample, and the lens' single plane of focus, regions can appear either in or out of focus. The lighter stomata, for example, are in focus, with the focal plane located in the middle of the pore. When the focal plane is situated slightly above the middle, the reflection of light bouncing off the guard cells results in darker stomata pores. This requires the pore estimation algorithm to be robust against variations in colour space. Existing algorithms require stomata colour space to be consistent and are often tuned to a specific plant species (Karabourniotis et al., 2001; Laga et al., 2014; Jayakody et al., 2017), thus making them unsuitable to analyze images from the slide scanner.

To achieve this goal, a novel approach based on stomata cross section analysis and binary segmentation is proposed. Prior to developing the pore estimation algorithm, the following assumptions were made regarding the stomatal pores.

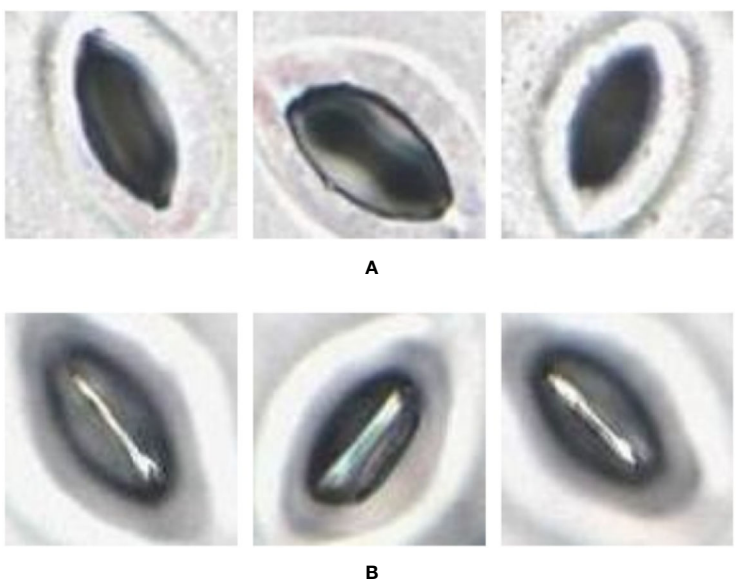

FIGURE 4 | Pore area captured under different lighting conditions. **(A)** Pore area is dark compared to the surroundings. **(B)** Pore area has a lighter colour compared to the surroundings.

1. The centre of the stomatal pore is located reasonably close to the centre of the bounding box containing the stomate. This bounding box is generated by the CNN proposed in *Stomata Detection With a Convolutional Neural Network*. This assumption allows the algorithm to reject stomata-like shapes located at the edges of a bounding box.
2. A stomata area is always larger than a predefined value. In this case, a stomate is assumed to be larger than 50 pixels^2 in area. This allows the algorithm to reject detections resulting from dust particles and air-bubbles.

The pore estimation algorithm consists of the following steps.

1. Contrast Limited Adaptive Histogram Equalisation (CLAHE) is applied to the original input image.
2. The contrast and sharpness of the CLAHE image is improved.
3. The CLAHE image is converted to a grayscale image.
4. The Grayscale image is converted to a binary image via Otsu's thresholding.
5. The binary image contains multiple regions. Regions with areas no larger than a predefined size are removed from the image.
6. The largest region closest to the centre of the image is selected, and all other regions are removed from the image. This region is selected as the mask which represents the stomate.
7. The mask is then applied to the grayscale image in Step 3. Rotate the image using the major axis orientation of the mask. Now the area containing the stomata is aligned horizontally in the image.
8. Now consider the vertical cross-section which goes through the centroid coordinate of the mask as shown in **Figure 5A**. The intensity values of the pixels which lie along this cross-section line can be plotted as shown in **Figure 5B**. The following steps are adopted to find the pore area of the stomate.

    a. Identify all the valleys and peaks on the cross-section plot.
    b. Identify the valley or peak closest to the centroid pixel. This valley or peak is the centre of the stomatal pore (See **Figure 5B**).
    c. If the coordinate corresponding to the stomatal pore centre is a peak, the pore area is lighter than the surrounding region, and if the index corresponding to the stomatal pore centre is a valley, the pore area is darker than the surrounding region.
    d. Once this pore centre is identified, select all pixels of which the intensity values are similar to that of the pore centre, and also connected to the pore centre pixel (dotted box on **Figure 5B**).
    e. This connected set of pixels represent the pore region of the stomate (See **Figure 5C**).

The step-by-step approach of the algorithm is shown in **Figure 6**. The performance of the proposed pore estimation algorithm is discussed in detail in *Pore Area Estimation*.

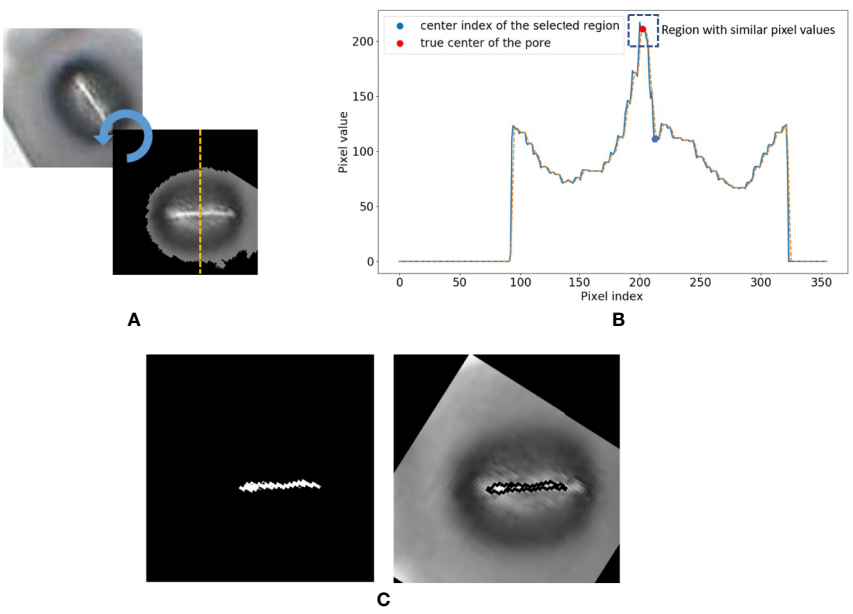

FIGURE 5 | Stomate cross section analysis. **(A)** Horizontal alignment of the stomate. **(B)** Identification of true center of the pore using peak/valley detection. **(C)** Final result.

RESULTS

Simplified Sample Collection

This section focuses on evaluating the performance of the modified nail polish imprint method compared to the traditional method, including their suitability for use with the proposed slide scanner technique. In these comparisons, special attention is given to the time taken in preparing the samples as well as the quality of the resulting images.

Securing the imprint on a plastic sleeve and transporting it to a laboratory environment before mounting onto a slide did not have any discernible negative impact on the sample quality. This approach also reduced contamination and the sample collection time in the field. Additionally, when waiting for the nail polish on one sample to dry, it was efficient to apply the polish to additional leaves in a parallel fashion. Using these methods, it was possible to collect a sample every 2 min.

In the laboratory, the traditional approach of securing the sample directly to a microscope slide took 2.5 min on average. Using the modified nail polish imprint method, the average slide preparation time was measured at 3.5 min. **Figures 7** and **8** indicate that both the traditional and modified sample collection methods produce high quality samples when imaged using the slide scanner technique. For each of the four species, stomatal pores are clearly discernible from background epidermal cells.

Interestingly, no significant difference in quality between the modified and traditional techniques could be observed from our results. This suggests that the quality of the result is dominated more by the sample collection process on-site rather than the mounting technique in the laboratory. Based on the initial assumptions behind the modified mounting method the effect of the modified approach may only become significant if the samples are collected under difficult conditions and contain bubbles or other debris.

Imaging With Microscope Slide Scanner

To measure the performance improvement introduced through the proposed imaging technique, 40 samples were imaged using the Aperio® XT (40×) brightfield slide scanner (Wetzlar, Germany). The imaging time and quality was then compared with the Olympus Olympus® BX53 manual stage microscope. A summary of the processing times of the slide scanner in comparison to the manual stage microscope is presented in **Table 1**.

The slide scanner required 15 min of set-up and 10 min to capture a selected region of the sample. The setup process consists of loading the slides in the device and selecting the focus points. Multiple focus points were selected to ensure the

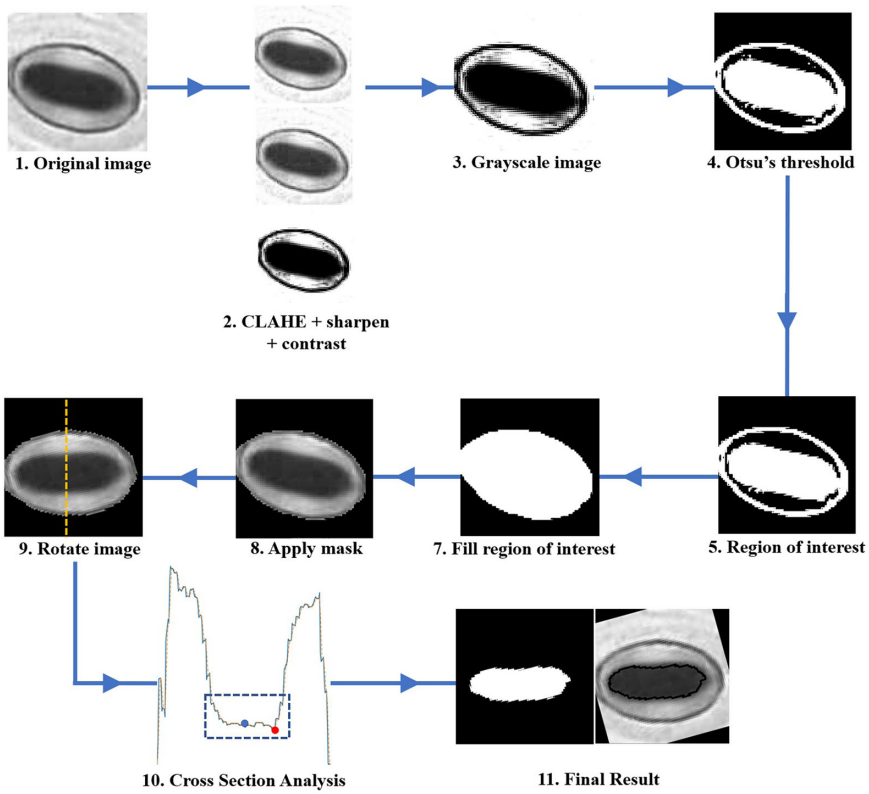

FIGURE 6 | Flowchart describing the step-by-step approach of the pore area calculation algorithm.

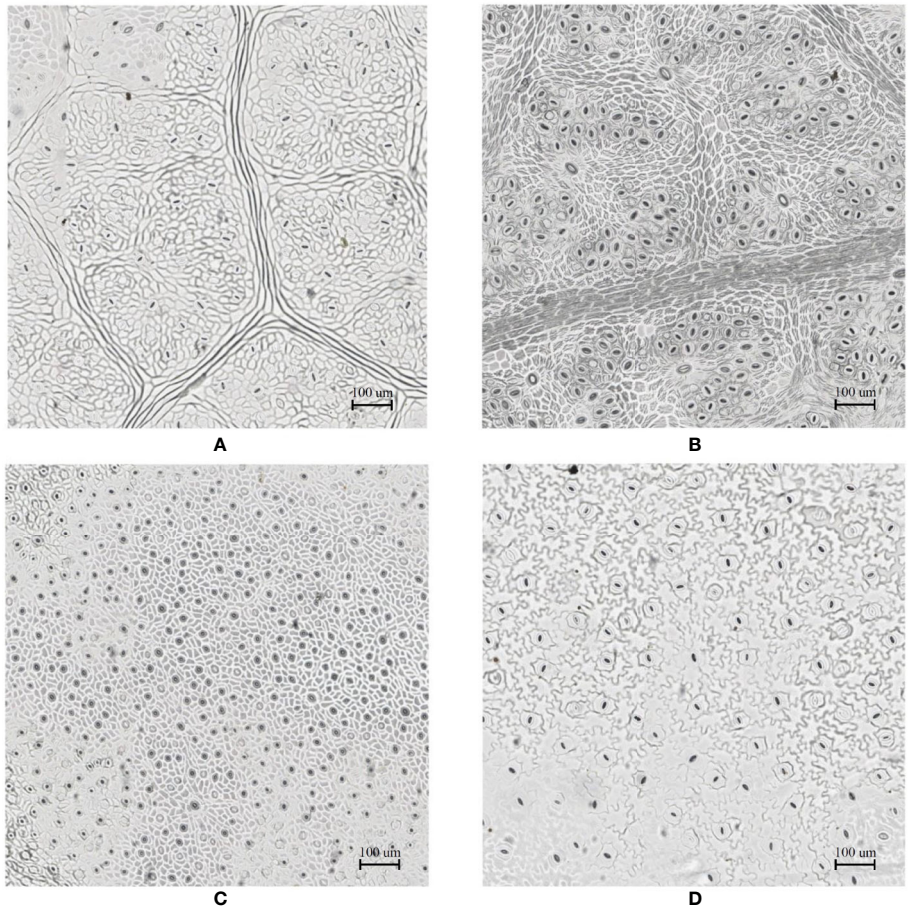

FIGURE 7 | Slide scanner images generated by capturing a section of the samples collected using the modified nail polish imprint method. **(A)** Vitis vinifera L. x V. rupestris Scheele 'Ganzin Glory'. **(B)** Prunus armeniaca 'Moorpark'. **(C)** Citrus sinensis L. Osbeck 'Valencia'. **(D)** Vinca major L. 'Periwinkle'.

stomata remained in focus despite the variation in sample height. The slide scanner allows the coverage of the sample to be scaled up with a minimal increase in processing time. An entire sample of size 30 mm × 9 mm, for example, can be imaged in 30–40 min. Since multiple slides can be loaded on the device (120 glass slides for this model), the device was able to image all 40 samples with a single set-up.

Comparatively, it took two hours to image a 4 mm × 1 mm leaf imprint image using the Olympus® BX53 manual optical microscope. To cover an area the size of 30mm × 9mm, over 70 images are required. If the images need to be stitched together to analyze macro level patterns, images should be captured with some overlap, driving up the number of total images required as a result. Due to the uneven surface of the imprint, each image needed to be focused separately. As the manual-stage microscope is only able to capture a small portion of the leaf surface at a time, special attention was given to ensure overlapping between adjacent images so that the images can be stitched together to form the final leaf surface. The slide scanner approach is clearly the faster approach, with over 100× time improvement over manual processes.

The slide scanner produced feature rich images, suitable for stomata detection and pore measurement. The edges of stomatal guard cells and the presence of background epidermal cells are well defined in the slide scanner images (**Figures 9**, **10**). Whilst blurred sections at various locations across the sample were observed due to the varying distance to the lens from the sample, the image contained plenty of regions with little to no blur containing more than 1,000 stomata, allowing users to observe patterns spanning across large areas of the sample. The optical microscope and the slide scanner produce images of similar quality; but the slide scanner dramatically improves the speed and area that can be imaged.

Stomata Detection Using Convolutional Neural Networks

The neural network created using AlexNet transfer learning was run on slide scanner images of samples collected using the traditional and modified method, for each of the four species; this amounted to

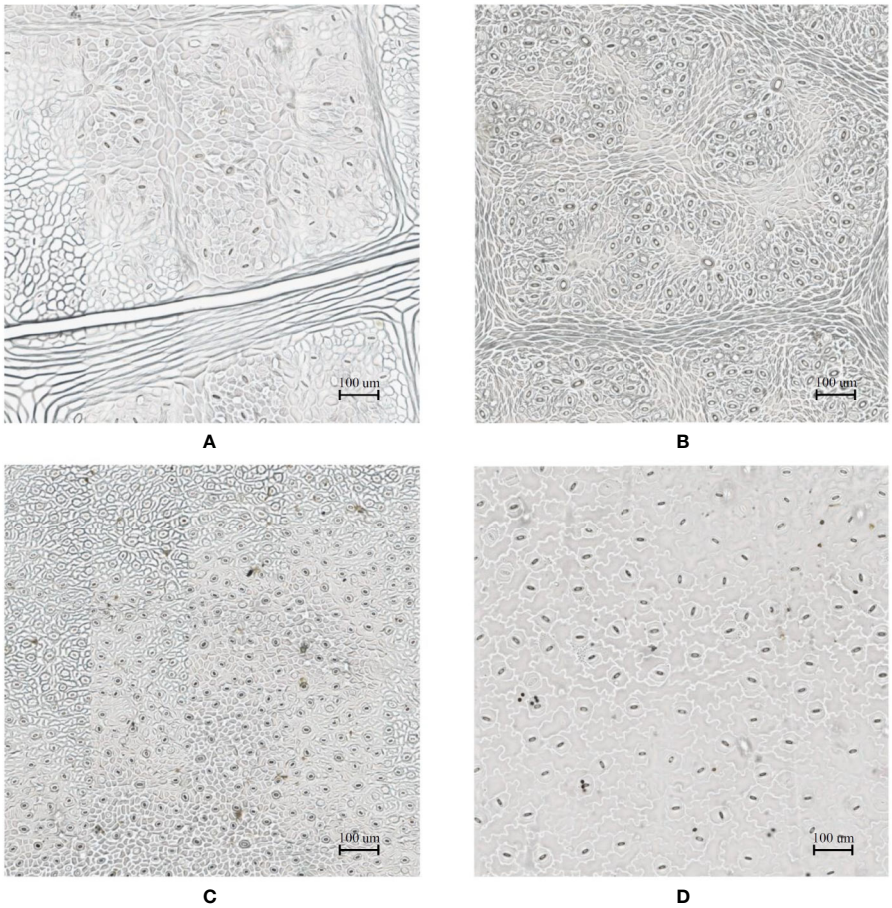

FIGURE 8 | Slide scanner images generated by capturing a section of the samples collected using the traditional nail polish imprint method. **(A)** Vitis vinifera L. x V. rupestris Scheele 'Ganzin Glory'. **(B)** Prunus armeniaca 'Moorpark'. **(C)** Citrus sinensis L. Osbeck 'Valencia'. **(D)** Vinca major L. 'Periwinkle'.

TABLE 1 | Comparison of sample collection, preparation and imaging techniques trialled.

	Original nail polish imprint method with slide scanner	Modified nail polish imprint method with slide scanner	Original nail polish imprint method with manual microscope
Sample collection time	2 min	2 min	2 min
Sample preparation time	2.5 min	3.5 min	2.5 min
Time taken to image section of sample	10 min	10 min	120 min
Time taken to image entire sample	0.5–0.66 h	0.5–0.66 h	120–140 h (estimate)

For sample collection and preparation, the original and modified nail polish methods display similar results for sampling effort, time required and resultant image quality. For imaging, the slide scanner technique offers significant savings in manual effort and imaging time when compared to traditional manual stage microscopes.

eight separate images, including 4,986 stomata in total. Each image included stomata that were both in and out of focus.

The results of running the classifier on each image can be seen in **Table 2**. The overall F-score was 0.817, with the highest of 0.897 recorded for the Citrus sinensis L. Osbeck sample collected using the modified technique; this maximum value was achieved for an image containing 1,168 stomata. The average precision and recall were 0.778 and 0.865, respectively. These results look promising, and provide evidence of the classifier's ability to adequately identify stomata in a background dense with similar features (**Table 2**).

A number of false positives were incorrectly identified as stomata in the images. Some of these features appeared similar to a stomatal pore that is lighter than its surroundings. These may indicate a stomate that has not been reproduced correctly by the imprint or is completely closed, or possibly an elliptical epidermal cell. Similarly, some false positives closely resemble a stomatal pore that is darker than its surroundings. Again, this appears to be a feature of the background reproduced by the sampling technique and slide scanner. Finally, random elliptical features in the background were captured by the high-detail slide scanner. Such false positives can potentially be eliminated with further training samples. In general, it is the precision that constrains the F-score achieved by the classifier, primarily due to the presence of false positives arising from the high level of

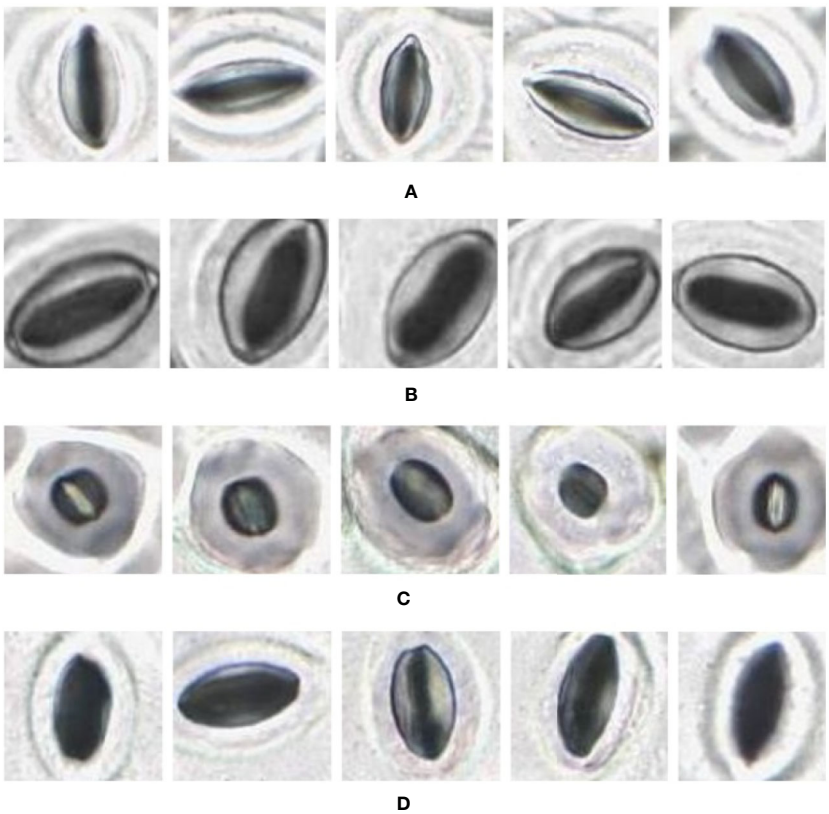

FIGURE 9 | Individual stomata captured from modified samples using the slide scanner. Guard cell boundaries and background epidermal cells are clearly visible. **(A)** Vitis vinifera L. x V. rupestris Scheele 'Ganzin Glory'. **(B)** Prunus armeniaca 'Moorpark'. **(C)** Citrus sinensis L. Osbeck 'Valencia'. **(D)** Vinca major L. 'Periwinkle'.

detail in the slide scanner images. However, these false positives proved to be generally harmless as they were eliminated in the pore identification software, as having no discernible pore to measure.

The false negatives in the results can be attributed to the wide variety of stomata captured by the high level of detail in the slide scanner images. False negatives can be reduced, and the recall can be increased by collecting more training samples and ensuring a standardized method of sample collection. The CNN approach to stomate detection is suitable for the slide scanner images and future investigations are recommended to further optimize this method.

Pore Area Estimation

The pore estimation algorithm was developed using OpenCV 3.4 in Python 3.6. The algorithm was applied to 1,706 individual stomata generated by the CNN classifier over the traditional and modified samples collected from the four plant species. The results generated were analyzed manually for erroneous pore estimations (**Table 3**).

The pore estimation algorithm rejected 182 images where it was unable to make a confident prediction about the pore area (examples in **Figure 11**). The majority of the rejected images contained either false positives from the classifier or stomata where a pore was not visible. Out of the 1,557 images for which stomata pore areas were present, 409 were found to be estimating the pore incorrectly. A result is considered incorrect when the estimation has no overlap with the true pore region, or the pore boundaries of the estimation and the ground truth has a considerable mismatch. This results in an average pore estimation accuracy of 73.72% with a maximum pore estimation accuracy of 90.1%, achieved for Prunus armeniaca samples collected using the modified imprint method. The algorithm works well against stomata from different species, collected using both traditional and modified nail polish methods (**Figure 12**). In a research scenario, the erroneous results generated by the pore estimation algorithm can be easily identified and discarded via manual observation.

DISCUSSION

This research presents a practical pipeline to automatically assess stomatal number and aperture size with minimal human intervention. Key contributions were made in sample imaging and stomatal pore area calculation techniques, whilst existing sample collection and stomata detection methods were adopted and modified to optimize

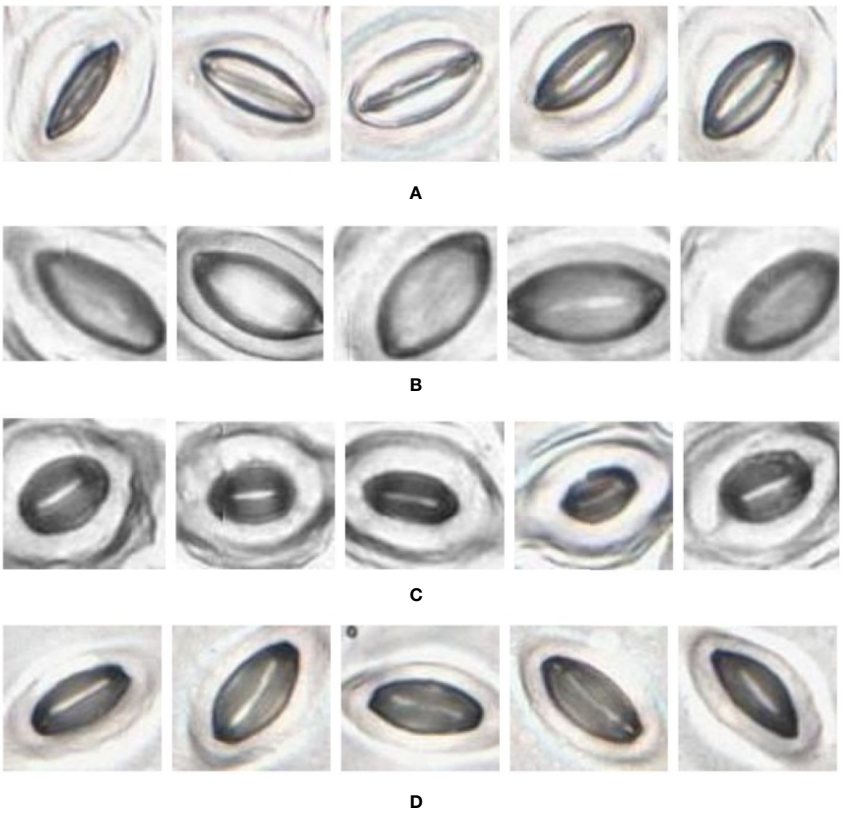

FIGURE 10 | Individual stomata captured from traditional samples using the slide scanner. Guard cell boundaries and background epidermal cells are clearly visible. **(A)** Vitis vinifera L. x V. rupestris Scheele 'Ganzin Glory'. **(B)** Prunus armeniaca 'Moorpark'. **(C)** Citrus sinensis L. Osbeck 'Valencia'. **(D)** Vinca major L. 'Periwinkle'.

TABLE 2 | Results of AlexNet Neural Network classifier applied to 6 images.

Species	Collection technique	Number of stomata	Precision	Recall	F-score
Vitis vinifera L. x V. rupestris Scheele	**Traditional**	248	0.6692	0.9254	0.77672
	Modified	207	0.7825	0.9055	0.83952
Prunus armeniaca	**Traditional**	791	0.7291	0.7388	0.73392
	Modified	917	0.7265	0.7517	0.73889
Citrus sinensis L. Osbeck	**Traditional**	932	0.7290	0.9076	0.80855
	Modified	1168	0.9089	0.8850	0.89679
Vinca major L.	**Traditional**	406	0.8673	0.9095	0.88790
	Modified	317	0.8138	0.8943	0.85215

TABLE 3 | Results of pore area estimation.

Species	Collection technique	Total Images	No detections	Available	Incorrect	Correct	Percentage correct
Vitis vinifera L. x V. rupestris Scheele	**Traditional**	200	21	179	66	113	63.13%
	Modified	200	4	196	43	153	78.06%
Prunus armeniaca	**Traditional**	177	28	149	32	117	78.52%
	Modified	200	29	171	17	154	90.06%
Citrus sinensis L. Osbeck	**Traditional**	200	20	180	40	140	77.77%
	Modified	200	38	162	62	100	61.72%
Vinca major L.	**Traditional**	200	4	196	52	144	73.47%
	Modified	329	5	324	97	227	70.06%

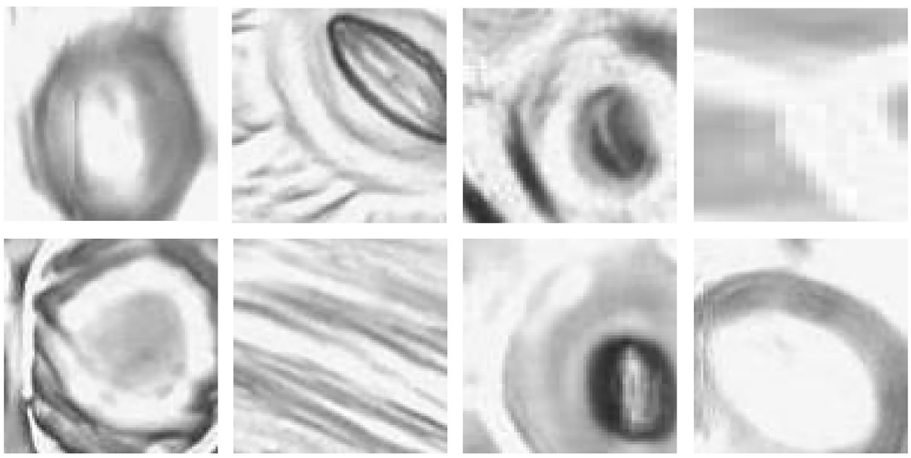

FIGURE 11 | Examples of pores rejected by the pore estimation algorithm.

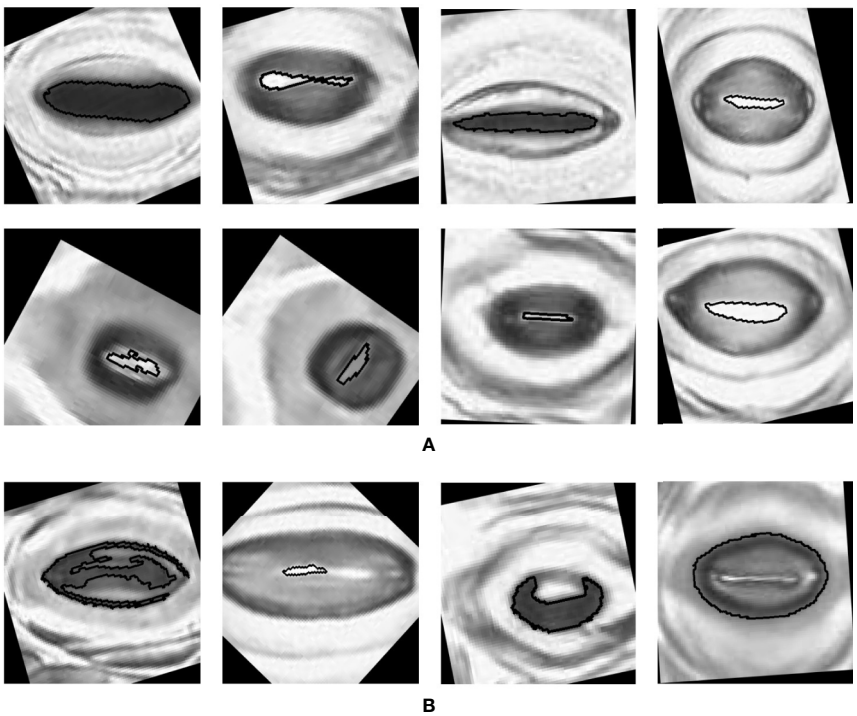

FIGURE 12 | Examples of pores estimated by the algorithm **(A)** Correct estimations. **(B)** Incorrect estimations.

results. The final, end-to-end solution that begins with a plant leaf input, creates a high-quality digital representation, and automatically detects and measures stomata pores.

Currently, with traditional manual stage microscopes, imaging an average sized leaf sample (30 mm by 9 mm) would take multiple days. To alleviate this problem, we took inspiration from the field of cell pathology, where slide scanners are used to produce high-quality images of cell samples rapidly and automatically. This method dramatically reduced the imaging time, covering an entire 30 mm × 9 mm sample in 30–40 min. In addition, using the slide scanner offers great potential to image a large portion of a leaf with minimal human interaction. Unlike most current research, which analyses input images containing up to 40 stomata sampled at random locations on a leaf sample, this technique has shown accuracy on large, continuous sections of a leaf containing over 1,000 stomata. This can offer insights

into the structure of leaves and the morphological properties they entail.

Upon digitization of the leaf samples, a CNN was used to detect stomata in the image, which effectively distinguished stomata from a highly detailed background containing visually similar guard cells. The average precision, recall, and F-score of 0.79, 0.85, and 0.82, respectively, indicate an approach that can be relied upon to accurately assess stomata.

Upon stomata detection, an approach which uses binary image segmentation and stomata cross section analysis was developed to accurately measure stomata pore areas. For the first time, an algorithm is developed, where the pore area can be detected despite the colour of the pore with respect to the surrounding guard cells. The proposed algorithm performed well, with an average pore estimation accuracy of 73.72% across 8 different collections. Although machine learning techniques are widely used for stomata detection, not many research projects tackle the problem of automatic pore measurement. In that context, the pore measurement methodology adds value to the process of fully automating stomata analysis.

The ability to rapidly and consistently assess the number and aperture of stomata over a relatively large portion of a leaf has a number of potential applications in plant science. Plants respond to the changing atmospheric carbon dioxide concentration by altering the ratio between the number of epidermal and stomatal cells (Beerling and Royer, 2002) and can offer a range of responses to increasing temperature; either increasing or decreasing stomatal size and density depending on conditions and species (Wu et al., 2018). Stomatal patchiness (Beyschlag and Eckstein, 2001), or the irregular distribution of stomata across a leaf, has received much attention in recent decades, but is yet to be completely understood. Once again, the slide scanner's ability to rapidly image complete samples offers a valuable method for investigating this phenomenon on a large scale and would offer great benefits for investigators in this field. By investigating the area of open stomata relative to the leaf area, it may be possible to estimate stomatal conductance (Lawson et al., 1998). The pipeline is currently optimized to assess nail polish imprints, but as imaging systems improve; a system based on a field microscope may be developed to assess plant water stress and inform irrigation schedules.

DATA AVAILABILITY STATEMENT

The raw data supporting the conclusions of this article will be made available by the authors, without undue reservation.

AUTHOR CONTRIBUTIONS

LM developed the sample collection and imaging mechanisms, worked on stomata detection, and wrote the paper. HJ developed the stomata pore detection algorithm, worked on sample preparation, and wrote the paper. HP developed the Alexnet neural network. VK worked on stomata detection and image management. FT worked on sample preparation and imaging using the slide scanner. PP collected samples for the study and reviewed the paper. MW managed the overall project and reviewed the paper.

REFERENCES

Banks, J. (1805). "A short account of the causes of the diseases in corn, called by farmers the blight, the mildew, and the rust." in *Practical observations on the British grasses, especially such as are best adapted to the laying down or improving meadows and pasture, likewise an enumeration of the British grasses, 6th edition*, vol. 1824. Ed. L. W. Curtis (London, UK: Sherwood, Jones and Co.), 151–166.

Beerling, D. J., and Chaloner, W. G. (1993a). The Impact of Atmospheric CO2 and Temperature Changes on Stomatal Density: Observation from Quercus Robur Lammas Leaves. *Ann. Bot.* 71 (3), 231–235. doi: 10.1006/anbo.1993.1029

Beerling, D. J., and Chaloner, W. G. (1993b). Evolutionary responses of stomatal density to global CO2 change. *Biol. J. Linn. Soc.* 48, 343–353. doi: 10.1111/j.1095-8312.1993.tb02096.x

Beerling, D. J., and Royer, D. L. (2002). Reading a CO2 Signal from Fossil Stomata. *New Phytol.* 153 (3), 387–397. doi: 10.1046/j.0028-646X.2001.00335.x

Beyschlag, W., and Eckstein, J. (2001). Towards a Causal Analysis of Stomatal Patchiness: The Role of Stomatal Size Variability and Hydrological Heterogeneity. *Acta Oecol.* 22 (3), 161–173. doi: 10.1016/S1146-609X(01)01110-9

Brodribb, T. J., Skelton, R. P., McAdam, S. A. M., Bienaimé, D., Lucani, C. J., and Marmottant, P. (2016). Visual Quantification of Embolism Reveals Leaf Vulnerability to Hydraulic Failure. *New Phytol.* 209 (4), 1403–1409. doi: 10.1111/nph.13846

Celine, Z., Cecile, R., Alain, V., Hubert, B., Rainer, H., and Yves, P. (2012). PHO1 Expression in Guard Cells Mediates the Stomatal Response to Abscisic Acid in Arabidopsis. *Plant J.* 72 (2), 199–211. doi: 10.1111/j.1365-313X.2012.05058.x

Dow, G. J., Bergmann, D. C., and Berry, J. A. (2014). An Integrated Model of Stomatal Development and Leaf Physiology. *New Phytol.* 201 (4), 1218–1226. doi: 10.1111/nph.12608

Eisele, J. F., Fabler, F., Burgel, P. F., and Chaban, C. (2016). A Rapid and Simple Method for Microscopy-Based Stomata Analyses. *PloS One* 11 (10), e0164576. doi: 10.1371/journal.pone.0164576

Fetter, K., Eberhardt, S., Barclay, R., Wing, S., and Keller, S. (2019). StomataCounter: A Neural Network for Automatic Stomata Identification and Counting. *New Phytol.* 223 (3), 1671–1681. doi: 10.1111/nph.15892

Jayakody, H., Liu, S., Whitty, M., and Petrie, P. (2017). Microscope Image Based Fully Automated Stomata Detection and Pore Measurement Method for Grapevines. *Plant Methods* 13 (1), 94. doi: 10.1186/s13007-017-0244-9

Karabourniotis, G., Tzobanoglou, D., Nikolopoulos, D., and Liakopoulos, G. (2001). Epicuticular Phenolics Over Guard Cells: Exploitation for in Situ Stomatal Counting by Fluorescence Microscopy and Combined Image Analysis. *Ann. Bot.* 87 (5), 631–639. doi: 10.1006/anbo.2001.1386

Krizhevsky, A., Sutskever, I., and Hinton, G. E. (2012). ImageNet Classification with Deep Convolutional Neural Networks. *Neural Inf. Process. Syst.* 25 (2), 1097–1105. doi: 10.1145/3065386

Laga, H., Shahinnia, F., and Fleury, D. (2014). "Image-Based Plant Stomata Phenotyping" in *2014 13th International Conference on Control Automation Robotics Vision (ICARCV)*. IEEE, 217–222. doi: 10.1109/ICARCV.2014.7064307

Lau, O. S., and Bergmann, D. C. (2012). Stomatal Development: A Plant's Perspective on Cell Polarity, Cell Fate Transitions and Intercellular Communication. *Development* 139 (20), 3683–3692. doi: 10.1242/dev.080523

Lawson, T., James, W., and Weyers, J. (1998). A Surrogate Measure of Stomatal Aperture. *J. Exp. Bot.* 49 (325), 1397–1403. doi: 10.1093/jxb/49.325.1397

Lecun, Y., Bottou, L., Bengio, Y., and Haffner, P. (1998). Gradient-Based Learning Applied to Document Recognition. *Proc. IEEE* 86 (11), 2278–2324. doi: 10.1109/5.726791

Li, K., Huang, J., Song, W., Wang, J., Lv, S., and Wang, X. (2019). Automatic Segmentation and Measurement Methods of Living Stomata of Plants Based on the CV Model. *Plant Methods* 15 (1), 67. doi: 10.1186/s13007-019-0453-5

Liu, S., Tang, J., Petrie, P., and Whitty, M. (2016). "A Fast Method to Measure Stomatal Aperture by MSER on Smart Mobile Phone," in *Imaging and Applied Optics 2016 (2016), Paper AIW2B.2* (Heidelberg, Germany: Optical Society of America). doi: 10.1364/AIO.2016.AIW2B.2

MathWorks (2018). *Pretrained AlexNet Convolutional Neural Network (version R2018a)* (Massachusetts, USA: MathWorks). Available at: https://au.mathworks.com/help/deeplearning/ref/alexnet.html.

Miller, N. A., and Ashby, W. C. (1968). Studying Stomates with Polish. *Turtox News* 46 (12), 322–324.

Monda, K., Araki, H., Kuhara, S., Ishigaki, G., Akashi, R., Negi, J., et al. (2016). Enhanced Stomatal Conductance by a Spontaneous Arabidopsis Tetraploid, Me-0, Results from Increased Stomatal Size and Greater Stomatal Aperture. *Plant Physiol.* 170 (3), 1435–1444. doi: 10.1104/pp.15.01450

Omasa, K., and Onoe, M. (1984). Measurement of Stomatal Aperture by Digital Image Processing. *Plant Cell Physiol.* 25 (8), 1379–1388. doi: 10.1093/oxfordjournals.pcp.a076848

Rasband, W. S. (1997). *ImageJ* (Maryland, USA: U.S. National Institutes of Health). Available at: https://imagej.nih.gov/ij/.

Rogiers, S. Y., Hardie, W. J., and Smith, J. P. (2011). Stomatal Density of Grapevine Leaves (Vitis Vinifera L.) Responds to Soil Temperature and Atmospheric Carbon Dioxide. *Aust. J. Grape Wine Res.* 17 (2), 147–152. doi: 10.1111/j.1755-0238.2011.00124.x

Sadras, V. O., Montoro, A., Moran, M. A., and Aphalo, P. J. (2012). Elevated Temperature Altered the Reaction Norms of Stomatal Conductance in Field-Grown Grapevine. *Agric. For. Meteorol.* 165 (1), 35–42. doi: 10.1016/j.agrformet.2012.06.005

Sakoda, K., Watanabe, T., Sukemura, S., Kobayashi, S., Nagasaki, Y., Tanaka, Y., et al. (2019). Genetic Diversity in Stomatal Density among Soybeans Elucidated Using High-Throughput Technique Based on an Algorithm for Object Detection. *Sci. Rep.* 9 (1), 7610. doi: 10.1038/s41598-019-44127-0

Smith, R. Y., Greenwood, D. R., and Basinger, J. F. (2010). Estimating paleoatmospheric pCO2 during the Early Eocene Climatic Optimum from stomatal frequency of Ginkgo, Okanagan Highlands, British Columbia, Canada. *Palaeogeogr. Palaeoclimatol. Palaeoecol.* 293, 120–131. doi: 10.1016/j.palaeo.2010.05.006

Toda, Y., Toh, S., Bourdais, G., Robatzek, S., Maclean, D., and Kinoshita, T. (2018). DeepStomata: Facial Recognition Technology for Automated Stomatal Aperture Measurement. *BioRxiv*, 365098. doi: 10.1101/365098

Wagner-Cremer, F., and Lotter, A. (2011). Spring-Season Changes during the Late Pleniglacial and Bølling/Allerød Interstadial. *Quat. Sci. Rev.* 30 (15–16), 1825–1828. doi: 10.1016/j.quascirev.2011.05.003

Wagner-Cremer, F., Finsinger, W., and Moberg, A. (2010). Tracing Growing Degree-Day Changes in the Cuticle Morphology of Betula Nana Leaves: A New Micro-Phenological Palaeo-Proxy. *J. Quat. Sci.* 25 (6), 1008–1017. doi: 10.1002/jqs.1388

Weyers, J. D. B., and Johansen, L. G. (1985). Accurate Estimation of Stomatal Aperture from Silicone-Rubber Impressions. *New Phytol.* 101 (1), 109–115. doi: 10.1111/j.1469-8137.1985.tb02820.x

Weyers, J. D. B., and Travis, A. J. (1981). Selection and Preparation of Leaf Epidermis for Experiments on Stomatal Physiology. *J. Exp. Bot.* 32 (129), 837–850. doi: 10.1093/jxb/32.4.837

Wu, G., Liu, H., Hua, L., Luo, Q., Lin, Y., He, P., et al. (2018). Differential Responses of Stomata and Photosynthesis to Elevated Temperature in Two Co-occurring Subtropical Forest Tree Species. *Front. Plant Sci.* 9, 467. doi: 10.3389/fpls.2018.00467

Yuan, J., Wang, X., Zhou, H., Li, Y., Zhang, J., Yu, S., et al. (2020). Comparison of Sample Preparation Techniques for Inspection of Leaf Epidermises Using Light Microscopy and Scanning Electronic Microscopy. *Front. Plant Sci.* 11 (1), 133. doi: 10.3389/fpls.2020.00133

Conflict of Interest: The authors declare that the research was conducted in the absence of any commercial or financial relationships that could be construed as a potential conflict of interest.

frontiers in Plant Science

ORIGINAL RESEARCH
published: 20 October 2020
doi: 10.3389/fpls.2020.574073

High-Throughput Switchgrass Phenotyping and Biomass Modeling by UAV

Fei Li[1,2†], Cristiano Piasecki[1,2†], Reginald J. Millwood[1,2], Benjamin Wolfe[1,2], Mitra Mazarei[1,2] and C. Neal Stewart Jr.[1,2]*

[1] Department of Plant Sciences, University of Tennessee, Knoxville, Knoxville, TN, United States, [2] Center for Bioenergy Innovation, Oak Ridge National Laboratory, Oak Ridge, TN, United States

Unmanned aerial vehicle (UAV) technology is an emerging powerful approach for high-throughput plant phenotyping field-grown crops. Switchgrass (*Panicum virgatum* L.) is a lignocellulosic bioenergy crop for which studies on yield, sustainability, and biofuel traits are performed. In this study, we exploited UAV-based imagery (LiDAR and multispectral approaches) to measure plant height, perimeter, and biomass yield in field-grown switchgrass in order to make predictions on bioenergy traits. Manual ground truth measurements validated the automated UAV results. We found UAV-based plant height and perimeter measurements were highly correlated and consistent with the manual measurements ($r = 0.93$, $p < 0.001$). Furthermore, we found that phenotyping parameters can significantly improve the natural saturation of the spectral index of the optical image for detecting high-density plantings. Combining plant canopy height (CH) and canopy perimeter (CP) parameters with spectral index (SI), we developed a robust and standardized biomass yield model [biomass = ($m \times$ SI) $\times$ CP $\times$ CH] where the m is an SI-sensitive coefficient linearly varying with the plant phenological changing stage. The biomass yield estimates obtained from this model were strongly correlated with manual measurements ($r = 0.90$, $p < 0.001$). Taking together, our results provide insights into the capacity of UAV-based remote sensing for switchgrass high-throughput phenotyping in the field, which will be useful for breeding and cultivar development.

Keywords: phenotype, LiDAR, spectral index, biomass, Nitrogen

OPEN ACCESS

Edited by:
Ankush Prashar, Newcastle University, United Kingdom

Reviewed by:
Lammert Kooistra, Wageningen University and Research, Netherlands
Francesco Marinello, University of Padua, Italy

****Correspondence:***
C. Neal Stewart Jr.
nealstewart@utk.edu

† These authors have contributed equally to this work

Specialty section:
This article was submitted to Plant Breeding, a section of the journal Frontiers in Plant Science

Received: *18 June 2020*
Accepted: *16 September 2020*
Published: *20 October 2020*

Citation:
Li F, Piasecki C, Millwood RJ, Wolfe B, Mazarei M and Stewart CN Jr (2020) High-Throughput Switchgrass Phenotyping and Biomass Modeling by UAV. Front. Plant Sci. 11:574073. doi: 10.3389/fpls.2020.574073

INTRODUCTION

Switchgrass (*Panicum virgatum* L.) is a native North America prairie grass that has been studied as a potential bioenergy crop in the United States and Europe since the mid-1980s (Lewandowski et al., 2003). It is a perennial grass, with C_4 metabolism, which is adapted to cultivation in much of the eastern United States and similar regions requiring low agronomic inputs (Vogel, 2004; Bouton, 2007; Schmer et al., 2008). It grows as a "clonal modular plant" from tillers (Boe and Casler, 2005). Each plant produces a population of tillers that can grow up to 4 m tall (Bouton, 2007). Switchgrass is highly self-incompatible, and its reproductive structures consist of a diffuse panicle arranged at the end of long branches (Barnes et al., 1995; Vogel, 2004). It produces high aboveground biomass each growing season as well as high lignin and cellulose content in cell walls (Vogel, 2004). The

biomass produced by switchgrass serves as a feedstock for bioenergy production as an effort to create green energy to reduce the consumption of fossil fuels (McLaren, 2005; Naik et al., 2010).

Since the beginning of switchgrass bioenergy feedstock development, breeding programs have utilized germplasm with desirable phenotypes such as high biomass production, nutrient use efficiency and stress tolerance (Barney et al., 2009; Jakob et al., 2009). Despite progress-to-date, there is still a significant frontier to be explored in switchgrass given its high genetic diversity (Lemus et al., 2008; Casler, 2012). Conventional phenotyping studies have been implemented to identify, principally, high biomass phenotypes. However, these trials are performed manually, which is resource-intensive and requires destructive harvests. Also, the results obtained from manual evaluations are prone to assessment errors and are limited in time and space (Vogel et al., 2011).

Reliable and efficient automated high-throughput phenotyping of switchgrass, especially to predict end-of-season biomass, would be a significant advance in the field. Thus, the overriding goal is to rapidly collect high-quality data from a standoff for which current methods are not suited (Walter et al., 2019). One important automated phenotyping tool is light detection and ranging (LiDAR) technology. LiDAR is a laser-based sensor that produces high-throughput and high-density three-dimensional (3D) point clouds by photon-counting (Lim et al., 2003). Another tool that complements LiDAR is multispectral imaging, which collects vegetation spectral indices to be analyzed together with LiDAR data. LiDAR has been widely used for plant architecture measurements such as plant height (Bendig et al., 2015; Jimenez-Berni et al., 2018). While optical imagery models have been made to non-destructively estimate plant biomass (Hansen and Schjoerring, 2003; Bendig et al., 2014), these models have been criticized for the low accuracy and high uncertainties in estimating biomass (Shabanov et al., 2003; Garrigues et al., 2006). One problem inherent to optical imagery techniques is the potential for natural light saturation for detecting the high-density biomass plants (Mutanga and Skidmore, 2004; Li et al., 2014). Integration of LiDAR and spectral index technologies have been used to address these underlying factors determining plant biomass varying with plant type and phenotyping parameters (e.g., plant height and fractional canopy cover) (Tucker et al., 1985; Popescu et al., 2003; Li et al., 2018).

In order to apply current automated phenotyping technologies to estimate switchgrass biomass, our goal was to incorporate plant phenotyping parameters into the spectral index-based biomass models. Our testbed was a common garden in Knoxville, TN, United States growing a diverse collection of switchgrass clones (330 genotypes) under low and moderate nitrogen fertility conditions. The objectives of the present study were to (1) use standoff automation to measure plant height and perimeter for each plant from an over-the-field vertical perspective using unmanned aerial vehicle (UAV)-based LiDAR technology, (2) to improve the capacity of remote sensing to model plant biomass by integrating LiDAR and imagery technologies, and (3) to assess the stability of our biomass model over the growing season. To our knowledge, this is the first study to fully extend UAV technologies into the assessments for high-throughput switchgrass phenotyping and biomass yield estimating under field conditions.

MATERIALS AND METHODS

Switchgrass Field Site and Experimental Design

The 75.2 × 122.5 m common garden was located at the University of Tennessee Plant Sciences Unit of the East Tennessee Research and Education Center (ETREC). The 330-switchgrass natural variant accessions were transplanted from a greenhouse to the field with four tillers per plant on May 28 and 29, 2019 (**Figures 1A,B**). The switchgrass clones used are mostly lowland (tetraploid) accessions provided by Dr. Thomas Juenger, University of Texas – Austin (Lowry et al., 2019). The field experiment is part of a switchgrass domestication project consisting of 330 accessions planted under two nitrogen (N) fertility treatments, one with moderate (135 kg of N ha^{-1}) and another with low (0 kg of N ha^{-1}) supplementation in July 2019. Each accession has four replicates in the field (2 replicates per N treatment), totaling 1,320 switchgrass plants, which were arranged in honeycomb design with ∼2.5 m interplant spacing (**Figure 1C**). The N treatment is part of another long-term study focusing on nitrogen use efficiency (NUE) in switchgrass. This provided the opportunity to determine the impacts of differential growth conditions on automated measurements. The experimental field was surrounded by switchgrass cv "Blackwell" border plants. The N treatment plots were separated by a centralized row of border plants. Water-permeable weed cloth coverage on the soil surface was used to reduce weed interference. Switchgrass was planted in 1 × 1 m holes in the cloth. Any weeds growing adjacent to switchgrass plants were manually removed.

Manual Measurements of Plants

Each plant canopy perimeter and height was manually measured twice during the field season: once in August 2019 (mid-season) and once in December 2019 (end-of-season). The plant canopy height measurement consisted of the distance from ground level to the tip of the tallest central tiller using a tape. The plant canopy perimeter was determined with distance measurement for the outside border of plant canopy from a vertical viewpoint. Measurements were made without touching the plants, and required two people to work 2 days each time. The aboveground plant biomass was determined at the end-of-season after plant senescence (**Table 1**). Dry above ground biomass was determined at the end of the season by harvesting and weighing each plant. Subsequently, the ten tallest tillers were collected from each plant and oven-dried at 45°C for 72 h to determine the ratio of dry-to-fresh weight. Total dry biomass was determined by calculating the percentage of water loss recorded for each subsample and subsequently applying the water loss percentage to the respective total "wet" biomass weight for each plant. Plants with ten or fewer tillers were not subsampled, and whole plants were subjected to the same drying conditions and dry biomass was recorded for each plant. End-of-season biomass measurements required

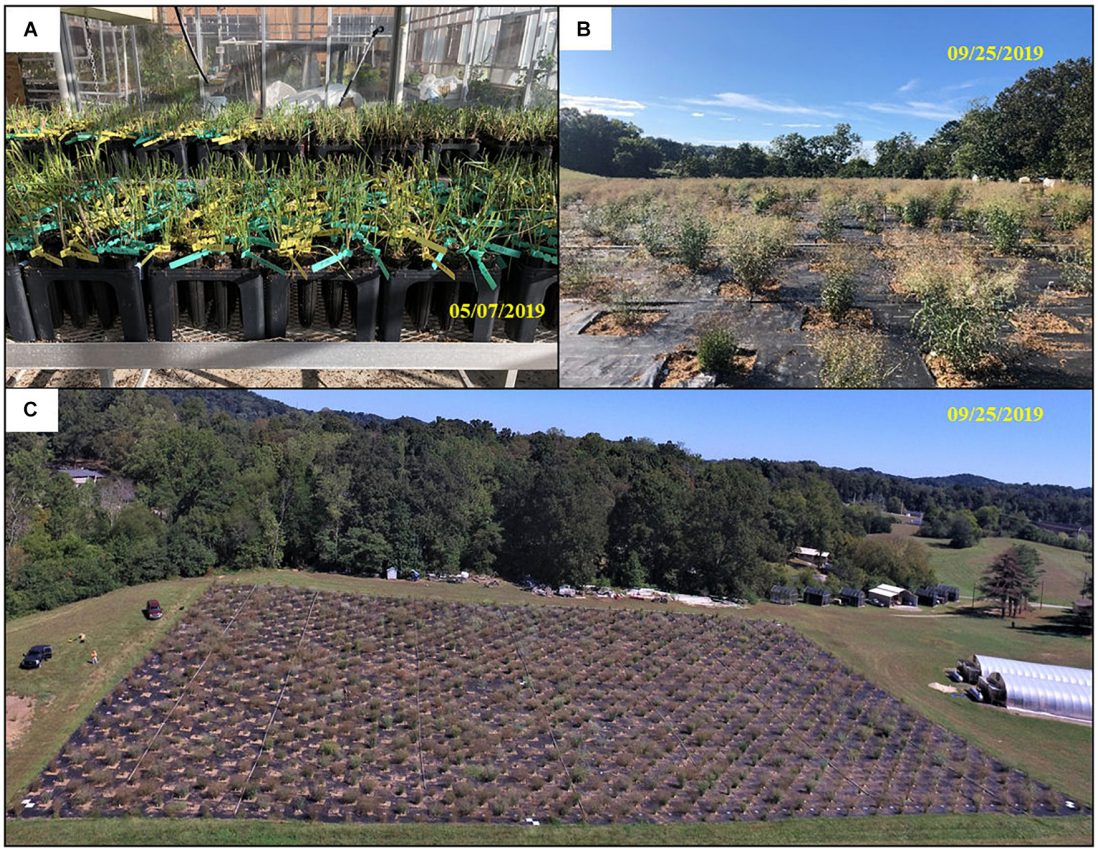

FIGURE 1 | Switchgrass field establishment. **(A)** The 330 switchgrass accessions in pots awaiting transplanting to the field; **(B,C)** status of switchgrass growth nearly 4 months after transplantation into the field site.

two people 2 weeks of work for harvesting, biomass drying, and recording of biomass by plant.

UAV Observations

Over the mid-to-late growing season we made 10 UAV flights to take single observations to estimate each trait by plant (**Table 1**) using a Matrice 600 UAV Pro model (DJI Inc., Shenzhen, China) equipped with multiple sensors including M200 Series Snoopy M8 LiDAR scanner (LiDARUSA Inc., Hartselle, AL, United States), and Red Edge-MX camera (MicaSense, Inc., Seattle, WA, United States) and strict ground control (**Figure 2A**). Flights were performed on cloud-free days between 10:00 am and 12:00 pm with an automatic mode using the drone flight planning mobile app – Pix4Dcapture (Pix4D Inc., Prilly, Switzerland) at 20 m above the ground and speed of approximately 4 km per hour (**Figure 2B**). The settings of image coverage overlapping between UAV-footprint snapshots was 85% in front and 70% on sides. The UAV-footprint shooting images over the field (**Figure 2B**) at a sampling resolution of 1 × 1 cm were mosaicked and transformed into the absolute reflectance images along with the image of the calibrated reflectance panel (CRP) captured prior to implementing flight mission, including blue (475 nm), green (560 nm), red (668 nm), red-edge (717 nm), and near-infrared (842 nm) bands, using Pix4Dmapper (Pix4D Inc., Prilly, Switzerland). Afterward, geometric rectification for the multispectral image was manually performed using the georeferencing tool in ArcGIS software (Esri Inc., Redlands, CA, United States) according to seven ground control points (GCP), which were evenly preassigned over the field and accurately measured using the global positioning system (GPS) base-station

TABLE 1 | UAV data routing observations and manual measurements in the growing season.

Date collection sate	Multispectral image	LiDAR	Manual measurements
08/14/2019	×		Plant perimeter and height
09/09/2019		×	
09/19/2019	×		
09/25/2019	×		
10/03/2019	×		
10/17/2019	×		
11/01/2019		×	
11/18/2019	×		
12/04/2019	×	×	Plant perimeter and height
01/21/2020	×	×	Plant biomass

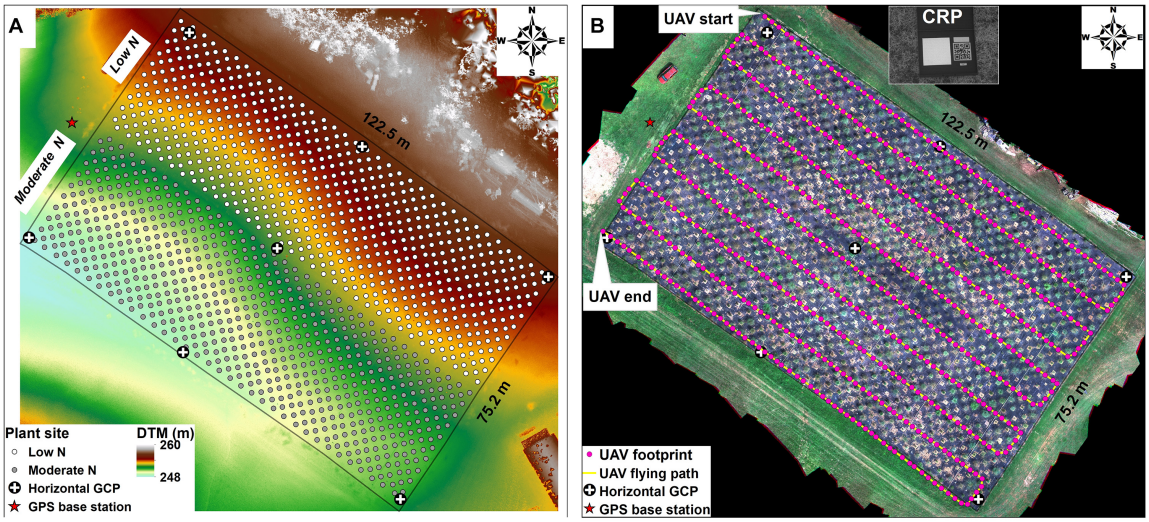

FIGURE 2 | UAV ground control and flight operations. **(A)** Bare ground elevation data (i.e., digital terrestrial models, DTM) obtained after the switchgrass harvest (January 21, 2020) using UAV-based LiDAR scanning technology. The UAV ground control system included a GPS base station used for post-processing differential correction of LiDAR point clouds, horizontal GCP used for geometric rectification of multispectral image. Shown is the planting site for the 1,320 switchgrass plants. **(B)** UAV route over the field, as well as the calibrated reflectance panel (CRP) used to convert raw pixel values from multispectral images to absolute reflectance, where the CRP image was obtained before or after the flight.

with a <4 cm horizontal accuracy. The LiDAR data obtaining was operated by tracking distances and angles through eight individual lasers at a shooting frequency of 440,000 points/s, along with the sensor position (i.e., latitude, longitude, and altitude) through the Global Navigation Satellite Systems (GNSS) and the sensor orientation (i.e., pitch, roll, and yaw) through the inertial measurement unit (IMU), as well as the real-time GPS base-station recording. To achieve a highly precise positioning for both horizontal and vertical (±3 cm), the raw LiDAR data recorded by those devices were repositioned by post-processing differential corrections based on the GPS base-station as well as the IMU data using Inertial Explorer Xpress 8.7 (NovAtel Inc., Calgary, AB, Canada) and were then further converted into the point clouds in the LAS (*.las*) format using ScanLook Point Cloud Creation (LiDARUSA Inc., Hartselle, AL, United States).

Automated Phenotyping Measurements

The 3D plant canopy was delineated by the point clouds that were composed of a high-density mass of point vectors, with each one having its own set of horizontal positioning (latitude and longitude), elevation coordinates, and additional attributes. Individual plant canopy polygons were identified using the MATLAB programming package (Math Works Inc., Natick, MA, United States) through three steps, including plant height calculation, spatial filtering, and boundary identifying (**Figure 3**).

(1) Plant height calculation: Individual.*las* files were combined into LAS datasets (*.lasd*) that were further interpolated into 1 × 1 cm gridded digital surface models (DSM, generated during the growing season and representing the incorporation of the bare ground elevation and plant canopy) in the Tagged Image Format File (*.tiff*) format using ArcGIS software to match the sampling results for the multispectral image. To precisely calculate plant canopy height, the bare ground elevation data, namely the digital terrestrial models (DTM), were generated by UAV-based LiDAR scanning technology after the switchgrass harvest (**Figure 2A**). The plant canopy height models (CHM) were calculated by DSM in the growing season, subtracting the DTM (e.g., **Figure 3A**).

(2) Spatial filtering: Generally, the plant canopy contains gaps between leaves that impact the complete identification of plant canopy. To simplify the process, we applied a spatial filter to the CHM to fill the gaps to unite all the pieces of canopy together. Specifically, the order-statistic filtering function (i.e., *ordfilt2*) with the domain of 5 × 5 pixels and the value of the 25th percentile was used to smooth the CHM (e.g., **Figure 3B**).

(3) Boundary identifying: The CHM was binarized with the threshold of 10 cm, below which was considered as the invalid value resulting from point cloud positioning error as well as ground relative elevation changes. Based on the central coordinates of the plant, the gridded plant canopy was divided from CHM, and the function of *bwboundaries* was used to trace the exterior boundary of the plant canopy. To simplify the boundary, a 2 m line that originated from the center of the plant was used to detect the intersected points between initial plant canopy boundary and scanning line following an interval of 30-degree. Generally, 3–12 points were identified, depending on the overlapping case with the surrounding plants (e.g., **Figure 3C**). The identified points were further converted into the polygon in the Esri shapefile (*.shp*) format using *shapewrite* function.

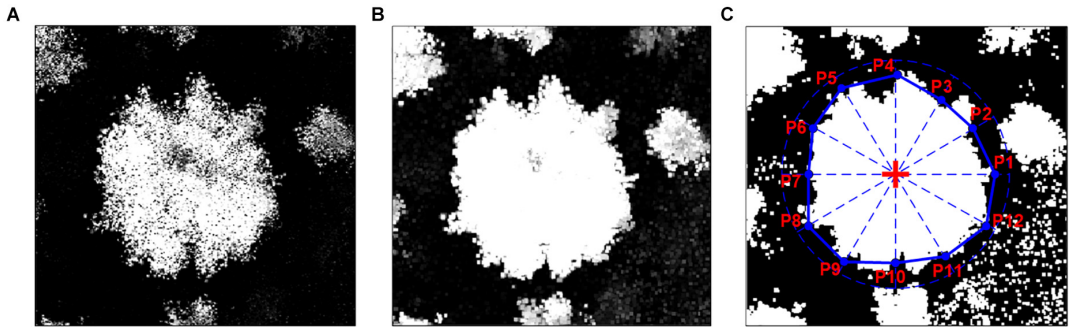

FIGURE 3 | Process of plant phenotyping parameter extraction. **(A)** The gridded plant height. **(B)** The spatially filtered plant height. **(C)** The binarization of plant height for identifying the location of plant canopy based on the central coordinates of plants (red + symbol) and the 2 m scanning line following the 30-degree interval, where the blue points (i.e., P1, P2, . . ., to P12) are the location of intersection between plant canopy boundary and scanning line.

After obtaining the plant canopy polygon for each plant, plant canopy perimeter was measure in a similar way to manual measurements by calculating the distance around the outside plant canopy border as viewed from a vertical perspective. Plant canopy perimeter and area were calculated using the functions of *perimeter* and *polyarea*, respectively. By overlaying each plant canopy polygon to the gridded CHM, the maximum CHM value was identified and used for comparison with manual ground-truth measurements that were implemented referring to the top of the central panicles in the plant, and the mean CHM value over the plant canopy was used for the subsequent driving of the UAV-biomass model. The mean reflectance for each plant and band in the multispectral image was calculated to derive the spectral vegetation index as another driving variable for UAV-biomass modeling.

Plant Biomass Model and Evaluation

The plant canopy perimeter and height, as vital measurements for plant phenotyping structure characteristics, are theoretically related to the magnitude of plant stems (Fernandez et al., 2009). Also, the spectral index was developed based on the fact that leaf chlorophyll electromagnetic spectra measurements are highly correlated with plant leaf density (i.e., leaf area index – LAI) (Broge and Leblanc, 2001). Here, we modeled the plant biomass as a linear combination of phenotyping measurements and spectral index response in the form of (Eq. 1):

$$f_{\text{Biomass}} = (m \times \text{SI}) \times \text{CP} \times \text{CH} \tag{1}$$

where CP and CH refer to the plant canopy perimeter and height, respectively. These phenotyping variables change significantly during the growing stage, but are supposed to approach to a constant status after peak growing season; SI is the spectral index calculated from UAV-based reflectance bands; m is a SI-sensitive coefficient relying on a specific spectral index as well as plant phenological stage. To evaluate biomass yield for the mature plants, all driving variables were obtained during the peak growing season to assure a robust prediction with the UAV-biomass model. This is imperative given plants may "de-green" with plant senescing after peak growing season, and "de-greening" may lower the performance of spectral index (Tillack et al., 2014). Several widely used indices were explored for SI including the spectral index developed in the early period, such as the ratio vegetation index (RVI; Eq. 2) (Pearson and Miller, 1972) and the normalized difference vegetation index (NDVI; Eq. 3) (Rouse et al., 1974), as well as spectral index suggested later for improving sensitivity to vegetation, such as the enhanced vegetation index (EVI; Eq. 4) (Huete et al., 1997) and the normalized difference red edge index (NDRE; Eq. 5) (Hansen and Schjoerring, 2003). These indices were calculated using the following equations:

$$\text{RVI} = \frac{R_{NIR}}{R_{Red}} \tag{2}$$

$$\text{NDVI} = \frac{R_{NIR} - R_{Red}}{R_{NIR} + R_{Red}} \tag{3}$$

$$\text{EVI} = 2.5 \times \frac{R_{NIR} - R_{Red}}{R_{NIR} + 6R_{Red} - 7.5R_{Blue} + 1} \tag{4}$$

$$\text{NDRE} = \frac{R_{NIR} - R_{RE}}{R_{NIR} + R_{RE}} \tag{5}$$

where R_{NIR} is the reflectance at the near-infrared wavelength, R_{Red} is the reflectance at the red wavelength, R_{Blue} is the reflectance at the blue wavelength, and R_{RE} is the reflectance at the red-edge wavelength.

Standard criteria, namely the Pearson coefficient (r), root mean square error ($rmse$), and relative error (re), were used to evaluate how well the assembly of phenotyping measurements and SI-response predicted the biomass compared to manual measurements.

RESULTS

UAV-Based Plant Phenotyping Parameters and Validations

There was a wide range of values from manual measurements of switchgrass perimeter, height, and biomass yield among the 330 genotypes (**Figure 4**). Plant perimeter ranged from 0.36 to 12.37 m with an average (and standard deviation) of 4.15 m

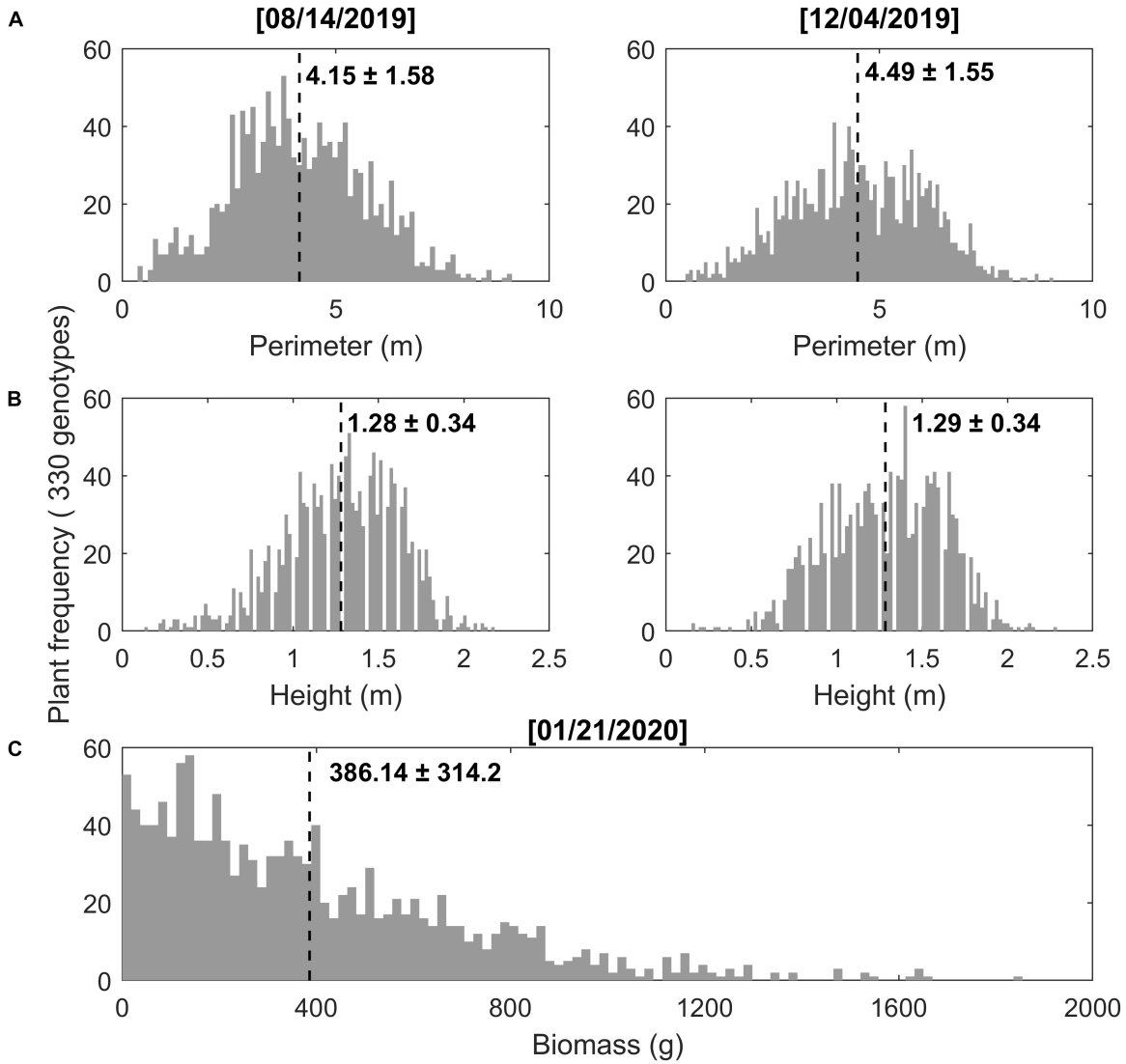

FIGURE 4 | Manual phenotyping measurements for 330 genotypes of switchgrass during mid-season (August 14, 2019) and end-of-season (December 04, 2019), as well as biomass harvest (January 21, 2020). **(A)** Plant perimeter, **(B)** plant height, and **(C)** plant biomass, where the numbers on the figure represent the mean and standard deviation (std) for 1,320 plants with 330 genotypes and four repetitions for each genotype.

(±1.58) and 4.49 m (±1.55) for measurements taken at the mid- and the end-of-season, respectively (**Figure 4A**). In the same way, switchgrass height (i.e., central panicle) ranged from 0.13 to 2.29 m, with an average of 1.28 m (±0.34) and 1.29 (±0.34) (**Figure 4B**). Dry biomass ranged from 2 to 1,855 g per plant, with an average of 386.14 g (±314.2) (**Figure 4C**). Trait variation may be related to genetic diversity among the accessions (Martinez-Reyna and Vogel, 2002; Casler, 2012).

We applied the programming process (involving three steps, i.e., plant height calculation, spatial filtering, and boundary identifying) to the LiDAR point clouds collected from early peak season (**Figure 5A**) to the end-of-season (**Figures 5B,C**) for determining switchgrass phenotyping parameters including plant canopy height and perimeter. Compared to the manual measurements (i.e., from December 4, 2019), we achieved promising results for plant canopy perimeter ($r = 0.95$, $rmse = 0.6$, and $re = 0.11$; **Figure 5D**) as well as canopy height ($r = 0.93$, $rmse = 0.1$, and $re = 0.07$; **Figure 5E**) using LiDAR. The box statistics showed that plant phenotyping parameters for both perimeter and height slightly increased from September 9 to November 1, 2019 (**Figures 5F,G**). Afterward, a notable decrease in height was observed on December 4, 2019. This result might be attributed to plant lodging responses associated with genetic characteristics of each genotype, as well as interactions with environmental effects such as rainfall and snow (Tripathi et al., 2003).

Performance of UAV-Biomass Model

Using the maximum plant phenotyping parameters (i.e., plant perimeter and height on November 1, 2019; **Figure 5**) as a

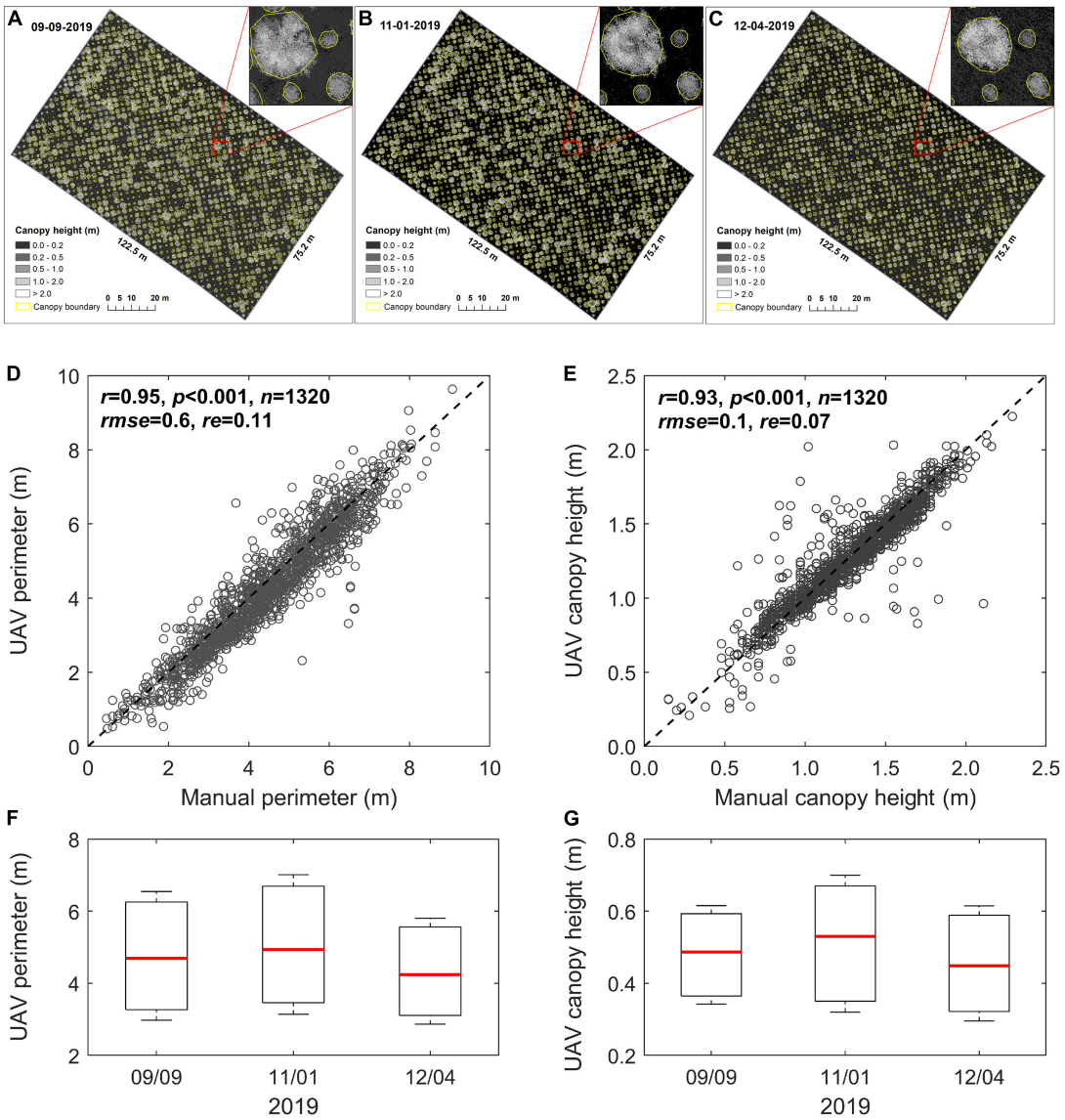

FIGURE 5 | Changes in UAV-based plant phenotyping parameters and validation. **(A–C)** Spatiotemporal changes in plant canopy perimeter and height based on UAV measurements during the growing season; **(D,E)** validation of the UAV-based plant perimeter and height with manual measurements for a total of 1,320 plants, where plant canopy height was compared based on the top of the central panicles. The UAV and manual measurements were collected on December 4, 2019; **(F)** and **(G)** boxplots of the changes in plant perimeter and height, respectively, from peak season to the end of the season, where the red line on the box indicates the median, and the bottom and top edges of the box indicate the 25^{th} and 75^{th} percentiles, respectively.

static forcing variable, we explored the UAV-based biomass models accompanied with changes of varying spectral index and phenological process from early peak season (i.e., August 14, 2019) to the end-of-season (i.e., November 18, 2019) (**Figure 6**). We found that the assembly of phenotyping measurements (plant height and perimeter) and spectral index demonstrated promising performance in predicting the plant biomass ($r \geq 0.74$), but also varied among the spectral indices as well as phenological stages (r = 0.74–0.9). Noticeably, the spectral indices derived from peak season to just prior to the end-of-season (e.g., September 19 to October 17, 2019) demonstrated consistent and robust performance in predicting plant biomass ($r \geq 0.86$). Compared to NDRE, the commonly used spectral indices of RVI, NDVI, and EVI demonstrated a stronger relationship with plant biomass ($r \geq 0.89$). Out of these three spectral indices, EVI demonstrated the lowest estimated bias ($rmse \leq 137.16$). In contrast, using the spectral indices derived from the early peak season (i.e., August 14, 2019) and the end-of-season (i.e., November 18, 2019) were weaker predictions of plant biomass ($r \leq 0.87$).

Plant Responses to N Treatments

Manual and automated measurements of the variables (e.g., plant height, perimeter, area, biomass density, and biomass

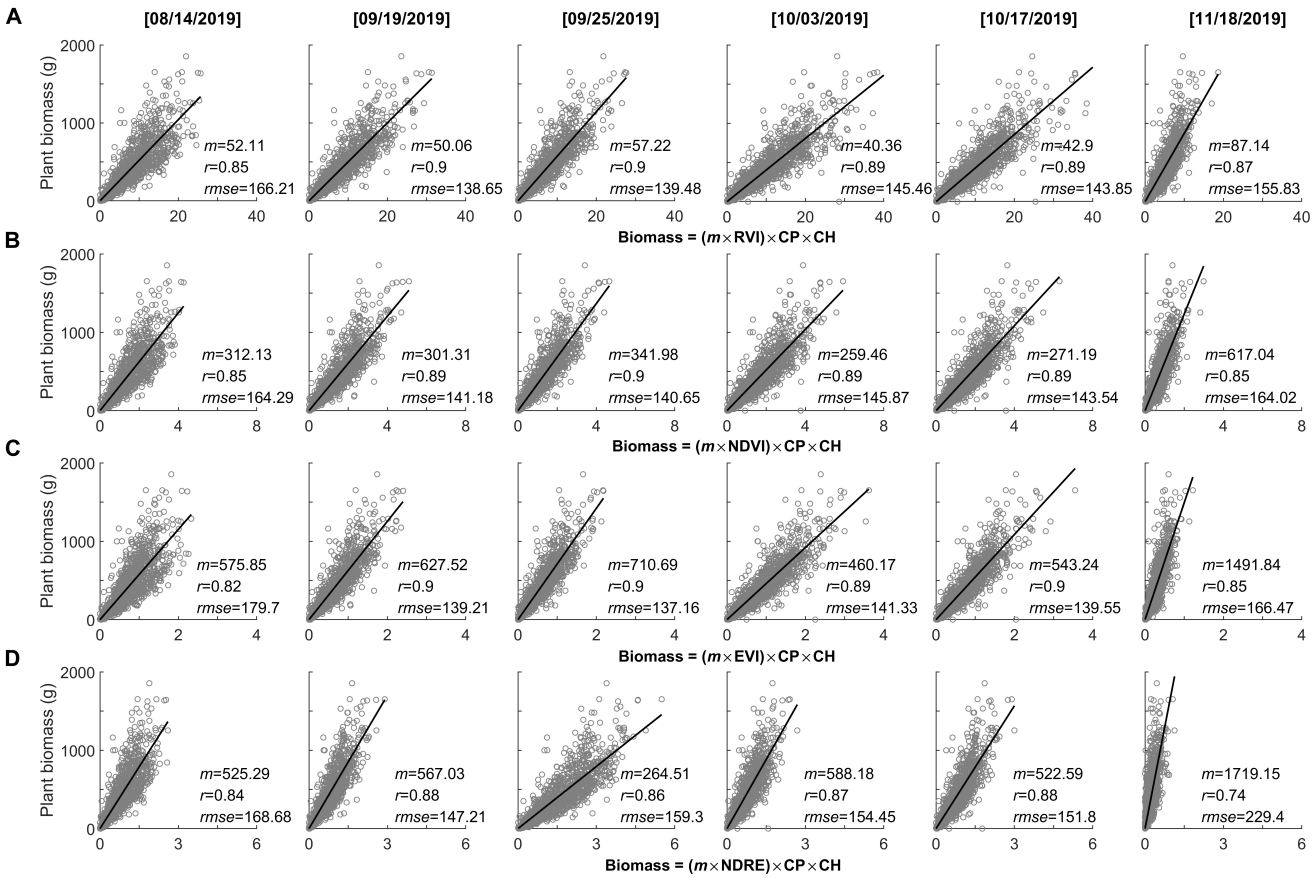

FIGURE 6 | Performance of the assembly of phenotyping measurements (CP, canopy perimeter; CH, canopy height) and spectral index in predicting the plant biomass with changes of the growing season, as well as a different spectral index. **(A)** RVI, **(B)** NDVI, **(C)** EVI, and **(D)** NDRE.

production) demonstrated there were no significant differences in switchgrass growth between the low and moderate N treatments (**Figure 7**). These results were strongly correlated between the automated and manual methods (**Figure 5**), and we found the differential N growth conditions had no effect on automated phenotypic characterization. Based on UAV measurements, we found similar patterns in the distribution of switchgrass plant biomass (**Figure 7A**), as well as biomass density over the field (**Figure 7B**) between the low and moderate N fertilization plots. In contrast, we observed a general positive plant growth response to the N fertilization over the 330 switchgrass genotypes (**Figure 8**). These observations suggested that the high genetic variability of the 330 genotypes is responsible for the large-ranging differences in plant growth factors rather than the N fertilization itself (Cassida et al., 2005). However, there were patterns among genotypic responses to N treatments. We characterized genotype responses as: a) N-positive responsive genotypes, in which growth was positively associated with N (**Figure 8**, representative genotypes above 1:1 line); b) N-neutral genotypes that had congruent growth in both N treatments (**Figure 8**, representative genotypes at 1:1 line); and c) N-negative genotypes that had lower growth with more N (**Figure 8**, representative genotypes below the 1:1 line).

DISCUSSION

LiDAR-Based Plant Phenotyping Measurements

Unmanned aerial vehicle-based LiDAR scanning technology was very useful in measuring switchgrass plant morphological traits over the field. The automated method we are reporting in the present study was validated by the manual measurements with a wide range of phenotypic variabilities. Our assessment demonstrates the reliability of the system for use in different switchgrass growing conditions with high accuracy. It should be noted that the LiDAR sensor used in this study (i.e., M200 Series Snoopy M8 LiDAR scanner) can only record the single echo, implying there may be some uncertainty in accurately calculating plant canopy height (i.e., CHM) relying on single-pass-obtained point cloud data (James and Robson, 2014). To simplify the processing procedure and ensure the measuring accuracy, plant canopy height in the growing season was determined by DSM

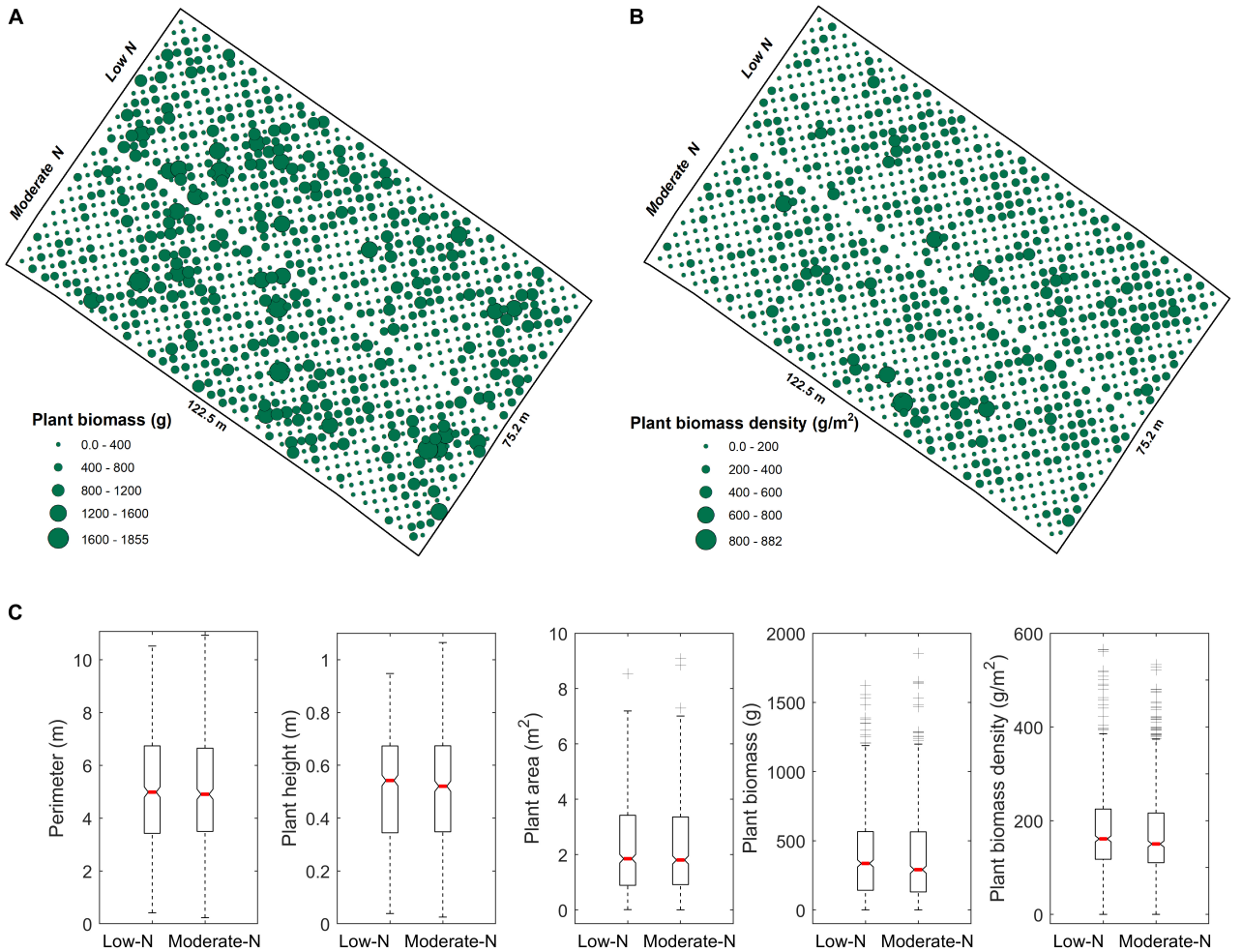

FIGURE 7 | Comparisons of different N treatments for switchgrass. **(A)** Spatial distribution of switchgrass biomass over the experimental field mapped to individual plants. **(B)** Spatial distribution of switchgrass biomass density that is normalized by plant canopy coverage area. **(C)** Boxplots for plant phenotyping parameters (i.e., plant perimeter, height, and plant area), as well as plant yield (single plant biomass and biomass-density) between two levels of N treatments, where the red line on the box indicates the median, and the bottom and top edges of the box indicate the 25^{th} and 75^{th} percentiles, respectively.

generated in the plant growing season by subtracting DTM (**Figure 2A**) generated after all the plants are harvested (i.e., CHM = DSM − DTM). This strategy could be applicable to this study by assuming that the changes in the background surface elevation are negligible. However, most situations require capacities of large-scale detection and timely variable calculation. In these cases, the full waveform or multi-echo LiDAR-scanning technologies can be helpful for producing DTM, DSM, and CHM variables at once through the algorithm of decomposing LiDAR waveforms (Reitberger et al., 2008; Mallet and Bretar, 2009). The value of LiDAR scanning technology is not only characterized by its highly efficient reproducibility and accuracy (Madec et al., 2017) but also due to its irreplaceability. For example, we conducted manual measurements for plant canopy height by sampling representative tillers on each plant. However, because there was a considerable height variation among tillers, the single or multiple tiller height measurements using manual methods, e.g., tape measure will inevitably produce uncertainty in delineation of plant height. Instead, the highly dense LiDAR point clouds have higher repeatability to delineate the height variations for plant tillers, and that consequently can ensure the robust phenotyping measurements, as well as the precise yield prediction with UAV-biomass model. For example, when manual height measurements were made, it took two people 2 days to measure the tallest tiller for each of the 1,320 plants. The single point measurement for each plant may not be an absolute representation of "true plant height," whereas the UAV platform is scalable and able to collect a data cloud for each plant.

We explored the applicability of structure-from-motion (SFM) algorithms using the Pix4Dmapper programming package for the generation of the DSM and DTM based on a large set of overlapping images (Oliensis, 2000). When compared with the LiDAR method, we found that SFM method was suboptimal to capture plant canopy structural details. Lussem et al. (2019) showed that SFM-derived CHM provided a varying

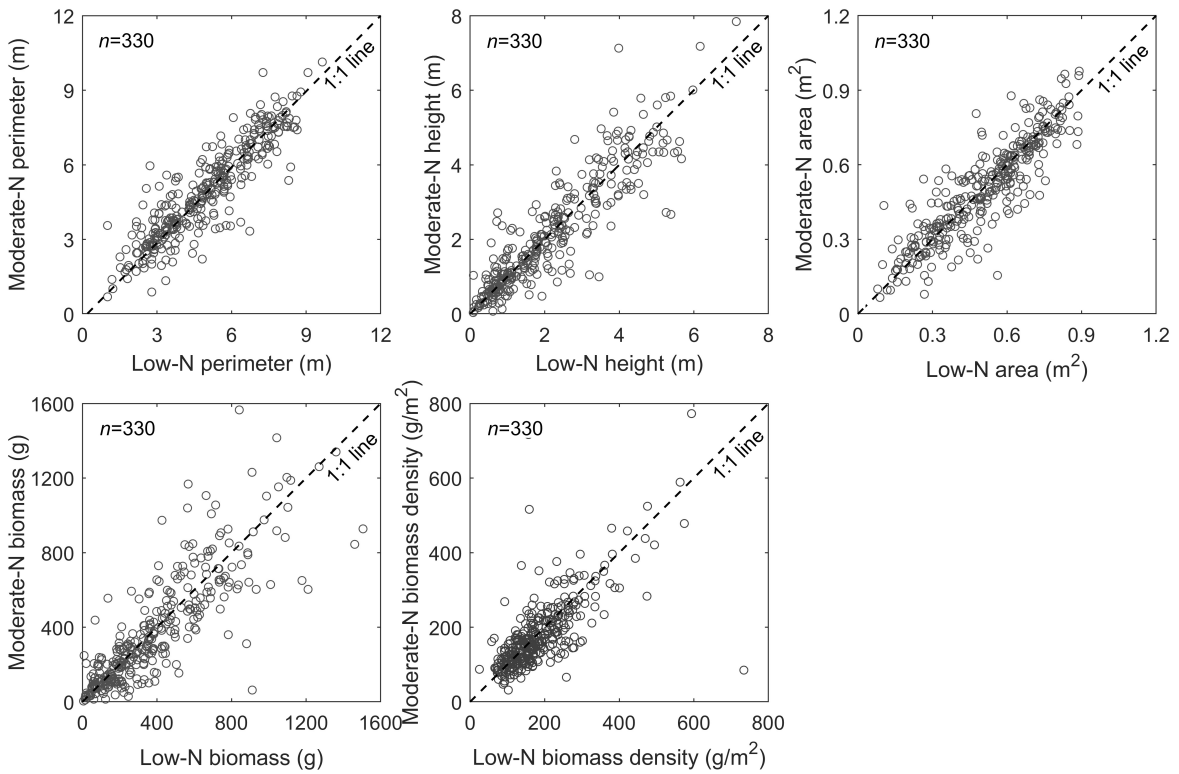

FIGURE 8 | Comparisons of two contrasting N treatments for each genotype with four replicates (2 replicates per N treatment). The comparisons are performed among the plant canopy perimeter, height, and area, as well as single plant biomass and biomass-density, where the data for the plant canopy perimeter, height, and area are derived from peak season of plant growth (i.e., September 25, 2019). Each data point represents an average of two replicates per each N treatment (low and moderate) for a total of 330 switchgrass genotypes.

performance in predicting grassland biomass, indicating this method may not be widely adaptable. The success of SFM depends on several factors, including the complexity of research object, UAV flight control accuracy, image quality, as well as the selection of SFM algorithms (Dandois and Ellis, 2013; Remondino et al., 2014). Based on our study, we suggest that SFM may not be optimal for quantifying small objects with a high degree of accuracy. Rather, SFM may be useful to 3D visualization or structure parameter measurements specific to large objects such as trees and buildings (Bolles et al., 1987). In addition, we experimented with extracting plant canopy perimeters through the spectral index (e.g., NDVI) calculated by the multispectral image. Once a threshold used for segmenting spectral index image is determined, we found this method is applicable for the calculation of plant canopy coverage perimeter and area. However, one substantial problem is determining the appropriate threshold value, which varies with dynamic leaf chlorophyll content during plant development. For example, after switchgrass growth peaks in late summer and senescence ensues, the leaves will be less green. An undistinguished phenotype may be observed along with diverse stresses (e.g., drought, plant pests, and diseases) over the growth season (Anjum et al., 2011; Mahlein et al., 2013). In contrast to the optical image processing method, the LiDAR scanning method appeared to be more robust and applicable for estimating switchgrass phenotypic parameters, such as plant canopy height and perimeter.

Flexibility of UAV-Biomass Model

In recent years, UAV-based biomass models have been developed using UAV platforms equipped with a LiDAR scanner and/or multispectral sensor. When the LiDAR scanning is used, plant biomass is modeled as the function of CHM, such as $[\alpha^{*}e^{(\beta^{*}CHM)}]$ (Bendig et al., 2014). CHM models have high predictive value because the technique precisely delineates plant stem density and height, but suboptimally estimates biomass density in the unit of volume (Asner et al., 2012). Some biomass estimation models largely ignore image spectral index with forms such as $[\alpha^{*}SI + \beta]$ or $[\alpha^{*}SI^{\beta}]$ (Bendig et al., 2015). However, because of the attenuation of electromagnetic wave propagation when passing through a very dense vegetation canopy, namely the saturation of optical remote sensing, these kinds of models may not be appropriate to predict biomass (Shabanov et al., 2003; Mutanga and Skidmore, 2004; Li et al., 2014). Meanwhile, the model coefficients (i.e., α and β vary with choice of spectral index, and its associated phenological stage, as well as taxa. These variations in model forms and coefficients prevent us from cross-analysis among traits, including phenotyping heterogeneity, biomass composition and density, as well as evaluating NUE (Hardin et al., 2013; Li et al., 2018). Taking this a step further, it

will impede our understanding of whether biomass production is largely explained by genotype and canalized phenotypes (Casler, 2012). In the present study, a standardized model is proposed to estimate switchgrass biomass and its coefficients. The model was relatively straightforwardly and applicable to efforts to improve switchgrass cultivation as a bioenergy feedstock across diverse environmental conditions.

UAV-based remote sensing technologies are of value not only for increasing precision of trait measurement (e.g., biomass and LAI) but also for superior performance of mapping large-scale vegetation coverage areas (CAs) (Baret and Guyot, 1991; Jimenez-Berni et al., 2018). Accordingly, when the UAV-based biomass model proposed here is applied to plants grown under agronomic conditions with broad spatial and temporal scales, it is important to validate methods. First, plants grown under agronomic conditions vary in a continuous or undistinguished pattern, along with a certain fractional soil exposure. In this case, instead of using the purely individual plant canopy parameters (i.e., plant phenotyping parameters and spectral index) for modeling biomass, UAV-based remote sensing images for each pixel cell at a certain spatial resolution (e.g., 0.5 × 0.5 m, mostly relying on UAV flying altitude) may be used to build models. To reduce the impacts of bare soil on the spectral index, we suggest using the pure vegetation index (PVI) proposed by Li et al. (2016) for substitution of the spectral index in the UAV-biomass model. Since the soil component is completely excluded from PVI, based on the spectral mixture analysis (SMA) method (Adams et al., 1995), this substitution can be congruent with the role of pure vegetation canopy spectral index used in this study. It will hold a proportional response to changing biomass values. As for plant perimeter, initially, we thought that the assembly of plant canopy area and height could be mathematically used to determine the plant canopy volume magnitude, while adding spectral index can play a role in qualifying the biomass density of the canopy volume. However, we found that this type of assembly suffers a non-proportional response to biomass changes, resulting in a higher bias in predicting biomass yield. The choice of using the different model forms (e.g., exponential or polynomial forms) is possible, but may complicate model applications, given the variations of model form and its coefficients. In addition, we found that plant perimeter plays an important role in the optimization of modeling plant biomass yield. However, plant perimeter used here is only derived from each individual plant. As for biomass modeling based on a pixel cell, we suggest using a highly related function for converting from plant canopy CA in the pixel cell to plant perimeter, which is developed based on UAV phenotyping measurements in the switchgrass field (i.e., $CP = 3.6789 \times CA^{0.4892}$, $r^2 = 0.998$; **Figure 9**). Indeed, in agronomic fields of switchgrass, taking individual plant measurements, e.g., perimeter, will be challenging.

Spectral Index Sensitivity

In some cases, after peak growth season, plants may "de-green," which will alter the performance of spectral index used for plant monitoring (Tillack et al., 2014). However, based on varying spectral indices from peak season to before end-of-season (e.g., September 19 to October 17, 2019) used for the UAV-biomass modeling, we found an insignificant impact of plant phenological changes on its performance in modeling biomass (**Figure 6**). The only changes appear in the coefficient of m in the UAV-biomass model (i.e., Eq. 1), which varies with the choice of the spectral index (i.e., RVI, NDVI, EVI, and NDRE) and its association with the plant-phenological stage changing (**Figure 10**). This finding suggests that we have a broader time window (e.g., during September and October in this study) to reliably estimate the end-of-season plant biomass using UAV-based remote sensing technologies, rather than rushing into the peak growing season for UAV data collection; this stage would have maximum content of chlorophyll in the leaf. The m coefficient, calculated as the ratio between biomass yield and the assembly of plant phenotyping parameters and spectral index, i.e., [m = biomass/(SI × CP × CH)], represents the change in biomass yield per unit change in the integration of plant multi-traits. These traits vary between genotypes and among plant species, as well as phenological stages. Generally, m is determined through *in situ* destructive measurements along with UAV data collecting (Walter et al., 2019). By exploring the time series spectral index, we found that the m magnitude is significantly positively correlated with the spectral index changes that are associated with plant phenological stages (r = 0.994–0.998, $p \leq 0.006$; **Figure 10**). Among the selected spectral indices, the highly sensitive spectral index of EVI demonstrated a more robust performance to determine the m-value for calibration of the UAV-biomass model (i.e., $m = -2289.67 \times EVI + 1092.27$; $r = -0.998$, $p = 0.002$; **Figure 10C**). This finding implies that the coefficient of m in the UAV-biomass model can be determined according to the spectral index of its property, rather than through *in situ* destructive sampling measurement of plant biomass (Li et al., 2018), which is not desirable.

Unmanned aerial vehicle-biomass models varying with diverse forms are primarily attributed to a non-linear response to biomass increasing changes, which is so-called the natural saturation of optical remote sensing detections (Baret and Guyot, 1991; Gitelson, 2004). Based on the experiments from this study, we found that the plant phenotyping variables (e.g., plant canopy height and perimeter) measured by LiDAR technology, and spectral index measured by multispectral image all are subjected to the influence of saturation with varying degrees in response to increasing biomass in the plant canopy of leaves and stems (**Figure 11**). Overall, out of these input variables, plant canopy height is the single best trait to estimate end-of-season aboveground biomass (r = 0.78, $p < 0.001$), followed by plant perimeter (r = 0.76, $p < 0.001$), and then diverse spectral indices (r = 0.54–0.68, $p < 0.001$). Among the spectral indices, a slight difference exists when the individual spectral index is used for biomass modeling, but the insignificant difference is found when assembled with plant canopy perimeter and height.

Effects of N Fertilization on Switchgrass Growth

Nitrogen is an essential nutrient that is important to manage in bioenergy and forage crop production (Monti et al., 2019).

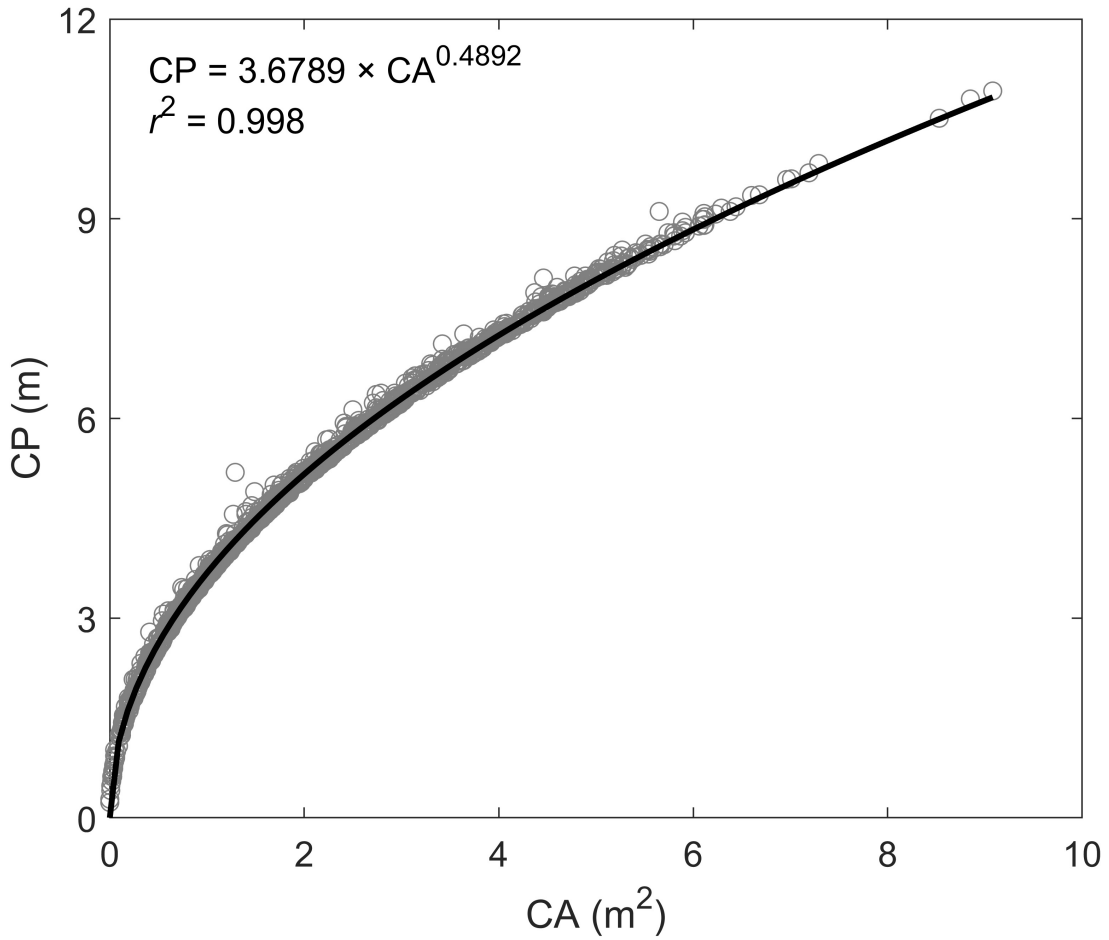

FIGURE 9 | The functional relationship between plant canopy area (CA) and canopy perimeter (CP) according to the UAV-based phenotyping measurements.

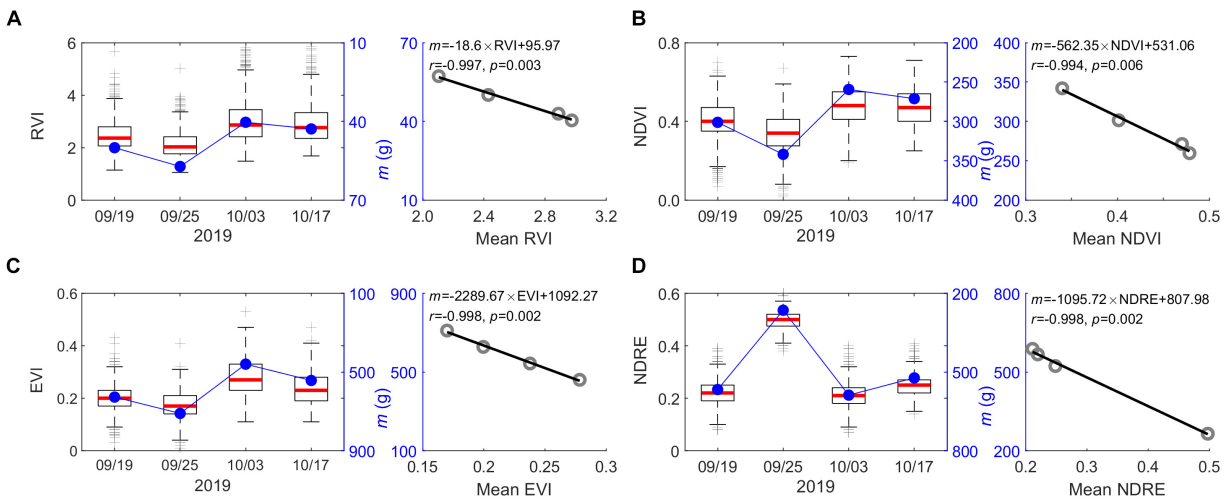

FIGURE 10 | Relationship between the coefficient of *m* in UAV-biomass models and plant phenotype changes qualified by the various spectral indices from the early peak season to the end of the growing season. **(A)** RVI; **(B)** NDVI; **(C)** EVI; and **(D)** NDRE. Time-specific variations of the spectral index for the 1,320 switchgrass plants in the field are reflected by boxplot statistics, where the red line on the box indicates the median, and the bottom and top edges of the box indicate the 25^{th} and 75^{th} percentiles, respectively.

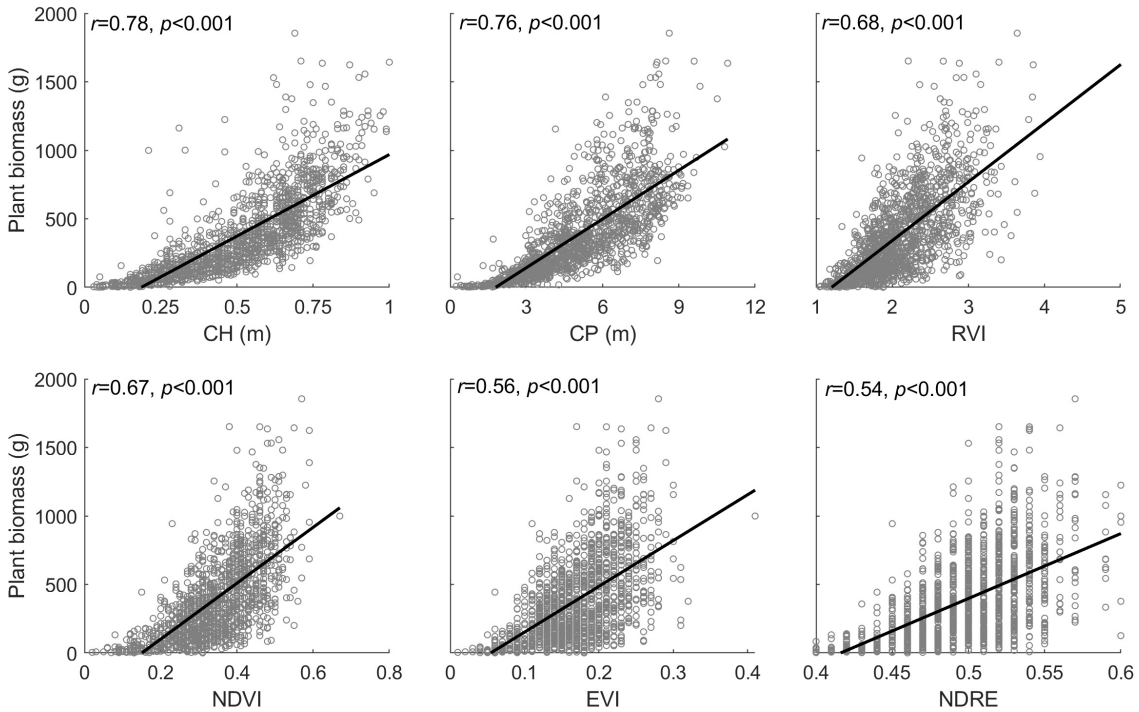

FIGURE 11 | Relationship between the plant phenotyping parameters (CH, canopy height; CP, canopy perimeter), spectral index (i.e., RVI, NDVI, EVI, and NDRE), and plant biomass, where the corresponding data are derived from peak season of plant growth (i.e., September 25, 2019).

We observed that N-supplementation had no significant effects on the global biomass production of the 330 switchgrass genotypes included in this study. This is in contrast to other studies that have shown switchgrass is more productive under N-fertilizer treatments when water is not limited (Schmer et al., 2012; Emery et al., 2020), and when N-supplementation is applied to established fields and during more than one year (Jung and Lal, 2011). However, N-supplementation does not always result in higher biomass production and may have unintended effects on switchgrass growth (Emery et al., 2020). The present study was performed during the establishment year (year one), where switchgrass establishment has been reported to be slow and yield reduction has been observed in the first year (Baxter et al., 2014). This factor may have had a negative influence on biomass production obviating any potential positive effects of N supplementation. However, we emphasize the contribution of N uptake in switchgrass still needs further investigation, especially with the support of UAV-based multi-trait measurements proposed in this study. Meanwhile, to elucidate underlying mechanisms in switchgrass NUE from the perspective of genetic characteristics will be a concern-deserved topic in the follow-on study.

CONCLUSION

Unmanned aerial vehicle (UAV)-based LiDAR and multispectral technologies were assessed for their application of high-throughput phenotyping of switchgrass and biomass estimation in the field. We found that UAV-based LiDAR is a useful tool for the precise qualification of plant phenotypic indicators (i.e., plant canopy perimeter, and height). Furthermore, a relatively simple and standardized model was developed for the estimation of switchgrass biomass yield through combing plant phenotyping characteristics (e.g., plant canopy height and perimeter) measured by LiDAR technology, and plant biomass density, which is detected by a widely used spectral vegetation index. We found that combining these phenotypic indicators significantly improves the performance of the spectral index in modeling and estimating biomass yield in a non-destructive manner. Finally, we found that, globally, N fertilization had non-significant effect on switchgrass phenotyping traits including biomass. In summary, the UAV-based approaches proposed in this study, including plant phenotyping automatic extracting method and biomass predicting model, facilitated high-throughput and precise phenotype mapping, which should have impact on accelerating bioenergy crop breeding as well as practical use in the field to estimate switchgrass biomass prior to destructive harvests at the end of the season.

DATA AVAILABILITY STATEMENT

The raw data supporting the conclusions of this article will be made available by the authors, without undue reservation.

AUTHOR CONTRIBUTIONS

FL and CP designed the study and performed the experiments and the result analysis. BW contributed to the manual measurements and field maintenance. CP, FL, and BW collected UAV and manual data. FL analyzed the UAV-based image data. CP analyzed the manual-based data. RM and MM provided critical insights into the method design and result interpretation. CS organized the study and revised the manuscript. All authors contributed to the text, and approved the final manuscript.

FUNDING

This work was supported by funding from the Center for Bioenergy Innovation. The Center for Bioenergy Innovation is a US Department of Energy Bioenergy Research Center supported by the Office of Biological and Environmental Research in the Department of Energy Office of Science. The research was also supported by the University of Tennessee and a USDA Hatch grant.

ACKNOWLEDGMENTS

We thank Tyler Newton, Nathan Dowdy, Rob Sears, Elijah Worly, Jessica Stockdale, Lana Howe, Ryan Frangoul, Darlene Filomena, and Liam Walker for their help with plant care and field planting. We thank the staff at the East Tennessee Research and Education Center (ETREC) – Plant Sciences Unit for their help with the field experiments.

REFERENCES

Adams, J. B., Sabol, D. E., Kapos, V., Almeida Filho, R., Roberts, D. A., Smith, M. O., et al. (1995). Classification of multispectral images based on fractions of endmembers: application to land-cover change in the Brazilian Amazon. *Remote Sens. Environ.* 52, 137–154. doi: 10.1016/0034-4257(94)00098-8

Anjum, S. A., Xie, X.-Y., Wang, L.-C., Saleem, M. F., Man, C., and Lei, W. (2011). Morphological, physiological and biochemical responses of plants to drought stress. *Afr. J. Agric. Res.* 6, 2026–2032. doi: 10.5897/AJAR10.027

Asner, G. P., Mascaro, J., Muller-Landau, H. C., Vieilledent, G., Vaudry, R., Rasamoelina, M., et al. (2012). A universal airborne LiDAR approach for tropical forest carbon mapping. *Oecologia* 168, 1147–1160. doi: 10.1007/s00442-011-2165-z

Baret, F., and Guyot, G. (1991). Potentials and limits of vegetation indices for LAI and APAR assessment. *Remote Sens. Environ.* 35, 161–173. doi: 10.1016/0034-4257(91)90009-U

Barnes, R. F., Miller, D. F., and Nelson, J. C. (1995). *Forages: An Introduction to Grassland Agriculture*. Ames, IA: Iowa State University Press.

Barney, J. N., Mann, J. J., Kyser, G. B., Blumwald, E., Van Deynze, A., and Ditomaso, J. M. (2009). Tolerance of switchgrass to extreme soil moisture stress: ecological implications. *Plant Sci.* 177, 724–732. doi: 10.1016/j.plantsci.2009.09.003

Baxter, J., Mazarei, M., Labbe, N., Kline, L. M., Cheng, Q., Windham, M. T., et al. (2014). Two-year field analysis of reduced recalcitrance transgenic switchgrass. *Plant Biotechnol. J.* 12, 914–924. doi: 10.1111/pbi.12195

Bendig, J., Bolten, A., Bennertz, S., Broscheit, J., Eichfuss, S., and Bareth, G. (2014). Estimating biomass of barley using crop surface models (CSMs) derived from UAV-based RGB imaging. *Remote Sens.* 6, 10395–10412. doi: 10.3390/rs61110395

Bendig, J., Yu, K., Aasen, H., Bolten, A., Bennertz, S., Broscheit, J., et al. (2015). Combining UAV-based plant height from crop surface models, visible, and near infrared vegetation indices for biomass monitoring in barley. *Int. J. Appl. Earth Obs. Geoinf.* 39, 79–87. doi: 10.1016/j.jag.2015.02.012

Boe, A., and Casler, M. D. (2005). Hierarchical analysis of switchgrass morphology. *Crop Sci.* 45, 2465–2472. doi: 10.2135/cropsci2004.0703

Bolles, R. C., Baker, H. H., and Marimont, D. H. (1987). Epipolar-plane image analysis: an approach to determining structure from motion. *Int. J. Comput. Vis.* 1, 7–55. doi: 10.1007/bf00128525

Bouton, J. H. (2007). Molecular breeding of switchgrass for use as a biofuel crop. *Curr. Opin. Genet. Dev.* 17, 553–558. doi: 10.1016/j.gde.2007.08.012

Broge, N. H., and Leblanc, E. (2001). Comparing prediction power and stability of broadband and hyperspectral vegetation indices for estimation of green leaf area index and canopy chlorophyll density. *Remote Sens. Environ.* 76, 156–172. doi: 10.1016/S0034-4257(00)00197-8

Casler, M. D. (2012). "Switchgrass breeding, genetics, and genomics," in *Switchgrass. Green Energy and Technology*, ed. A. Monti (London: Springer), 29–53. doi: 10.1007/978-1-4471-2903-5_2

Cassida, K., Muir, J., Hussey, M., Read, J., Venuto, B., and Ocumpaugh, W. (2005). Biomass yield and stand characteristics of switchgrass in south central US environments. *Crop Sci.* 45, 673–681. doi: 10.2135/cropsci2005.0673

Dandois, J. P., and Ellis, E. C. (2013). High spatial resolution three-dimensional mapping of vegetation spectral dynamics using computer vision. *Remote Sens. Environ.* 136, 259–276. doi: 10.1016/j.rse.2013.04.005

Emery, S. M., Stahlheber, K. A., and Gross, K. L. (2020). Drought minimized nitrogen fertilization effects on bioenergy feedstock quality. *Biomass Bioenergy* 133:105452. doi: 10.1016/j.biombioe.2019.105452

Fernandez, M. G. S., Becraft, P. W., Yin, Y., and Lübberstedt, T. (2009). From dwarves to giants? Plant height manipulation for biomass yield. *Trends Plant Sci.* 14, 454–461. doi: 10.1016/j.tplants.2009.06.005

Garrigues, S., Allard, D., Baret, F., and Weiss, M. (2006). Influence of landscape spatial heterogeneity on the non-linear estimation of leaf area index from moderate spatial resolution remote sensing data. *Remote Sens. Environ.* 105, 286–298. doi: 10.1016/j.rse.2006.07.013

Gitelson, A. A. (2004). Wide dynamic range vegetation index for remote quantification of biophysical characteristics of vegetation. *J. Plant Physiol.* 161, 165–173. doi: 10.1078/0176-1617-01176

Hansen, P., and Schjoerring, J. (2003). Reflectance measurement of canopy biomass and nitrogen status in wheat crops using normalized difference vegetation indices and partial least squares regression. *Remote Sens. Environ.* 86, 542–553. doi: 10.1016/S0034-4257(03)00131-7

Hardin, C. F., Fu, C., Hisano, H., Xiao, X., Shen, H., Stewart, C. N., et al. (2013). Standardization of switchgrass sample collection for cell wall and biomass trait analysis. *Bioenergy Res.* 6, 755–762. doi: 10.1007/s12155-012-9292-1

Huete, A., Liu, H., Batchily, K., and Van Leeuwen, W. (1997). A comparison of vegetation indices over a global set of TM images for EOS-MODIS. *Remote Sens. Environ.* 59, 440–451. doi: 10.1016/S0034-4257(96)00112-5

Jakob, K., Zhou, F., and Paterson, A. H. (2009). Genetic improvement of C4 grasses as cellulosic biofuel feedstocks. *In Vitro Cell. Dev. Biol. Plant* 45, 291–305. doi: 10.1007/s11627-009-9214-x

James, M. R., and Robson, S. (2014). Mitigating systematic error in topographic models derived from UAV and ground-based image networks. *Earth Surf. Process Landf.* 39, 1413–1420. doi: 10.1002/esp.3609

Jimenez-Berni, J. A., Deery, D. M., Rozas-Larraondo, P., Condon, A. T. G., Rebetzke, G. J., James, R. A., et al. (2018). High throughput determination of plant height, ground cover, and above-ground biomass in wheat with LiDAR. *Front. Plant Sci.* 9:237. doi: 10.3389/fpls.2018.00237

Jung, J. Y., and Lal, R. (2011). Impacts of nitrogen fertilization on biomass production of switchgrass (*Panicum virgatum* L.) and changes in soil organic carbon in Ohio. *Geoderma* 166, 145–152. doi: 10.1016/j.geoderma.2011.07.023

Lemus, R., Brummer, E. C., Burras, C. L., Moore, K. J., Barker, M. F., and Molstad, N. E. (2008). Effects of nitrogen fertilization on biomass yield and quality in large fields of established switchgrass in southern Iowa, USA. *Biomass Bioenergy* 32, 1187–1194. doi: 10.1016/j.biombioe.2008.02.016

Lewandowski, I., Scurlock, J. M., Lindvall, E., and Christou, M. (2003). The development and current status of perennial rhizomatous grasses as energy crops in the US and Europe. *Biomass Bioenergy* 25, 335–361. doi: 10.1016/S0961-9534(03)00030-8

Li, F., Chen, J., Zeng, Y., Wu, B., and Zhang, X. (2018). Renewed estimates of grassland aboveground biomass showing drought impacts. *J. Geophys. Res. Biogeosci.* 123, 138–148. doi: 10.1002/2017JG004255

Li, F., Chen, W., Zeng, Y., Zhao, Q., and Wu, B. (2014). Improving estimates of grassland fractional vegetation cover based on a pixel dichotomy model: a case study in Inner Mongolia, China. *Remote Sens.* 6, 4705–4722. doi: 10.3390/rs6064705

Li, F., Zeng, Y., Luo, J., Ma, R., and Wu, B. (2016). Modeling grassland aboveground biomass using a pure vegetation index. *Ecol. Indic.* 62, 279–288. doi: 10.1016/j.ecolind.2015.11.005

Lim, K., Treitz, P., Wulder, M., St-Onge, B., and Flood, M. (2003). LiDAR remote sensing of forest structure. *Prog. Phys. Geogr.* 27, 88–106. doi: 10.1191/0309133303pp360ra

Lowry, D. B., Lovell, J. T., Zhang, L., Bonnette, J., Fay, P. A., Mitchell, R. B., et al. (2019). QTL× environment interactions underlie adaptive divergence in switchgrass across a large latitudinal gradient. *Proc. Natl. Acad. Sci. U.S.A.* 116, 12933–12941. doi: 10.1073/pnas.1821543116

Lussem, U., Bolten, A., Menne, J., Gnyp, M. L., Schellberg, J., and Bareth, G. (2019). Estimating biomass in temperate grassland with high resolution canopy surface models from UAV-based RGB images and vegetation indices. *J. Appl. Remote Sens.* 13:034525. doi: 10.1117/1.JRS.13.034525

Madec, S., Baret, F., De Solan, B., Thomas, S., Dutartre, D., Jezequel, S., et al. (2017). High-throughput phenotyping of plant height: comparing unmanned aerial vehicles and ground LiDAR estimates. *Front. Plant Sci.* 8:2002. doi: 10.3389/fpls.2017.02002

Mahlein, A.-K., Rumpf, T., Welke, P., Dehne, H.-W., Plümer, L., Steiner, U., et al. (2013). Development of spectral indices for detecting and identifying plant diseases. *Remote Sens. Environ.* 128, 21–30. doi: 10.1016/j.rse.2012.09.019

Mallet, C., and Bretar, F. (2009). Full-waveform topographic lidar: state-of-the-art. *ISPRS J. Photogramm. Remote Sens.* 64, 1–16. doi: 10.1016/j.isprsjprs.2008.09.007

Martinez-Reyna, J., and Vogel, K. P. (2002). Incompatibility systems in switchgrass. *Crop Sci.* 42, 1800–1805. doi: 10.2135/cropsci2002.1800

McLaren, J. S. (2005). Crop biotechnology provides an opportunity to develop a sustainable future. *Trends Biotechnol.* 23, 339–342. doi: 10.1016/j.tibtech.2005.04.004

Monti, A., Zegada-Lizarazu, W., Zanetti, F., and Casler, M. (2019). Nitrogen fertilization management of switchgrass, miscanthus and giant reed: a review. *Adv. Agron.* 153, 87–119. doi: 10.1016/bs.agron.2018.08.001

Mutanga, O., and Skidmore, A. K. (2004). Narrow band vegetation indices overcome the saturation problem in biomass estimation. *Int. J. Remote Sens.* 25, 3999–4014. doi: 10.1080/01431160310001654923

Naik, S. N., Goud, V. V., Rout, P. K., and Dalai, A. K. (2010). Production of first and second generation biofuels: a comprehensive review. *Renew. Sust. Energ. Rev.* 14, 578–597. doi: 10.1016/j.rser.2009.10.003

Oliensis, J. (2000). A critique of structure-from-motion algorithms. *Comput. Vis. Image Underst.* 80, 172–214. doi: 10.1006/cviu.2000.0869

Pearson, R. L., and Miller, L. D. (1972). *Remote Mapping of Standing Crop Biomass for Estimation of the Productivity of the Shortgrass Prairie*. Fort Collins, CO: Colorado State University.

Popescu, S. C., Wynne, R. H., and Nelson, R. F. (2003). Measuring individual tree crown diameter with lidar and assessing its influence on estimating forest volume and biomass. *Can. J. Remote Sens.* 29, 564–577. doi: 10.5589/m03-027

Reitberger, J., Krzystek, P., and Stilla, U. (2008). Analysis of full waveform LIDAR data for the classification of deciduous and coniferous trees. *Int. J. Remote Sens.* 29, 1407–1431. doi: 10.1080/01431160701736448

Remondino, F., Spera, M. G., Nocerino, E., Menna, F., and Nex, F. (2014). State of the art in high density image matching. *Photogramm. Rec.* 29, 144–166. doi: 10.1111/phor.12063

Rouse, J., Haas, R., Schell, J., and Deering, D. (1974). Monitoring vegetation systems in the Great Plains with ERTS. *NASA Spec. Publ.* 351:309.

Schmer, M. R., Vogel, K. P., Mitchell, R., Dien, B., Jung, H., and Casler, M. (2012). Temporal and spatial variation in switchgrass biomass composition and theoretical ethanol yield. *Agron. J.* 104, 54–64. doi: 10.2134/agronj2011.0195

Schmer, M. R., Vogel, K. P., Mitchell, R. B., and Perrin, R. K. (2008). Net energy of cellulosic ethanol from switchgrass. *Proc. Natl. Acad. Sci. U.S.A.* 105, 464–469. doi: 10.1073/pnas.0704767105

Shabanov, N., Wang, Y., Buermann, W., Dong, J., Hoffman, S., Smith, G., et al. (2003). Effect of foliage spatial heterogeneity in the MODIS LAI and FPAR algorithm over broadleaf forests. *Remote Sens. Environ.* 85, 410–423. doi: 10.1016/S0034-4257(03)00017-8

Tillack, A., Clasen, A., Kleinschmit, B., and Förster, M. (2014). Estimation of the seasonal leaf area index in an alluvial forest using high-resolution satellite-based vegetation indices. *Remote Sens. Environ.* 141, 52–63. doi: 10.1016/j.rse.2013.10.018

Tripathi, S. C., Sayre, K., Kaul, J., and Narang, R. (2003). Growth and morphology of spring wheat (*Triticum aestivum* L.) culms and their association with lodging: effects of genotypes, N levels and ethephon. *Field Crops Res.* 84, 271–290. doi: 10.1016/S0378-4290(03)00095-9

Tucker, C., Vanpraet, C. L., Sharman, M., and Van Ittersum, G. (1985). Satellite remote sensing of total herbaceous biomass production in the Senegalese Sahel: 1980-1984. *Remote Sens. Environ.* 17, 233–249. doi: 10.1016/0034-4257(85)90097-5

Vogel, K. P. (2004). "Switchgrass," in *Warm-Season (C4) Grasses ASA-CSSA-SSSA Monograph*, eds L. E. Moser, L. Sollenberger, and B. Burson (Madison, WI: Wiley), 561–588. doi: 10.2134/agronmonogr45.c16

Vogel, K. P., Dien, B. S., Jung, H. G., Casler, M. D., Masterson, S. D., and Mitchell, R. B. (2011). Quantifying actual and theoretical ethanol yields for switchgrass strains using NIRS analyses. *Bioenergy Res.* 4, 96–110. doi: 10.1007/s12155-010-9104-4

Walter, J. D. C., Edwards, J., Mcdonald, G., and Kuchel, H. (2019). Estimating biomass and canopy height with LiDAR for field crop breeding. *Front. Plant Sci.* 10:1145. doi: 10.3389/fpls.2019.01145

Conflict of Interest: The authors declare that the research was conducted in the absence of any commercial or financial relationships that could be construed as a potential conflict of interest.

frontiers in Plant Science

ORIGINAL RESEARCH
published: 21 October 2020
doi: 10.3389/fpls.2020.587093

Improved Accuracy of High-Throughput Phenotyping From Unmanned Aerial Systems by Extracting Traits Directly From Orthorectified Images

Xu Wang[1], Paula Silva[1,2,3], Nora M. Bello[4], Daljit Singh[1,2], Byron Evers[1], Suchismita Mondal[5], Francisco P. Espinosa[5], Ravi P. Singh[5] and Jesse Poland[1]**

[1] Department of Plant Pathology, Kansas State University, Manhattan, KS, United States, [2] Interdepartmental Genetics, Kansas State University, Manhattan, KS, United States, [3] Instituto Nacional de Investigación Agropecuaria (INIA), Programa de Cultivos de Secano, Estación Experimental La Estanzuela, Colonia del Sacramento, Uruguay, [4] Department of Statistics, Kansas State University, Manhattan, KS, United States, [5] Global Wheat Program, International Maize and Wheat Improvement Center, Mexico City, Mexico

OPEN ACCESS

Edited by:
Ankush Prashar, Newcastle University, United Kingdom

Reviewed by:
Lea Hallik, University of Tartu, Estonia
Jianfeng Zhou, University of Missouri, United States

***Correspondence:**
Xu Wang
xuwang@ksu.edu
Jesse Poland
jpoland@ksu.edu

Specialty section:
This article was submitted to Technical Advances in Plant Science, a section of the journal Frontiers in Plant Science

Received: *27 July 2020*
Accepted: *30 September 2020*
Published: *21 October 2020*

Citation:
Wang X, Silva P, Bello NM, Singh D, Evers B, Mondal S, Espinosa FP, Singh RP and Poland J (2020) Improved Accuracy of High-Throughput Phenotyping From Unmanned Aerial Systems by Extracting Traits Directly From Orthorectified Images. Front. Plant Sci. 11:587093. doi: 10.3389/fpls.2020.587093

The development of high-throughput genotyping and phenotyping has provided access to many tools to accelerate plant breeding programs. Unmanned Aerial Systems (UAS)-based remote sensing is being broadly implemented for field-based high-throughput phenotyping due to its low cost and the capacity to rapidly cover large breeding populations. The Structure-from-Motion photogrammetry processes aerial images taken from multiple perspectives over a field to an orthomosaic photo of a complete field experiment, allowing spectral or morphological trait extraction from the canopy surface for each individual field plot. However, some phenotypic information observable in each raw aerial image seems to be lost to the orthomosaic photo, probably due to photogrammetry processes such as pixel merging and blending. To formally assess this, we introduced a set of image processing methods to extract phenotypes from orthorectified raw aerial images and compared them to the negative control of extracting the same traits from processed orthomosaic images. We predict that standard measures of accuracy in terms of the broad-sense heritability of the remote sensing spectral traits will be higher using the orthorectified photos than with the orthomosaic image. Using three case studies, we therefore compared the broad-sense heritability of phenotypes in wheat breeding nurseries including, (1) canopy temperature from thermal imaging, (2) canopy normalized difference vegetation index (NDVI), and (3) early-stage ground cover from multispectral imaging. We evaluated heritability estimates of these phenotypes extracted from multiple orthorectified aerial images via four statistical models and compared the results with heritability estimates of these phenotypes extracted from a single orthomosaic image. Our results indicate that extracting traits directly from multiple orthorectified aerial images yielded increased

estimates of heritability for all three phenotypes through proper modeling, compared to estimation using traits extracted from the orthomosaic image. In summary, the image processing methods demonstrated in this study have the potential to improve the quality of the plant trait extracted from high-throughput imaging. This, in turn, can enable breeders to utilize phenomics technologies more effectively for improved selection.

Keywords: High-throughput phenotyping, unmanned aerial systems, canopy temperature, normalized difference vegetation index, ground cover, wheat

INTRODUCTION

In the past 20 years, spectacular advances in "next-generation" DNA sequencing have rapidly reduced the costs of genotyping and provided almost unlimited access to high-density genetic markers, thus allowing genetic improvement of several economically important crops worldwide (Crossa et al., 2017). Accurate plant trait (i.e., phenotypes) observations have long been the key to enhancing genetic gains through classical plant breeding (Eathington et al., 2007) and also to training prediction models and predict the performance of non-phenotyped individuals from their marker scores (Hayes and Goddard, 2001). Thus, phenotyping plays an essential role in the success of standard phenotypic selection as well as genomic selection models. Reflecting this, the lack of methods for rapid and accurate phenotyping on large sets of germplasm under field conditions remains a bottleneck to genomic selection and plant improvement (Cabrera-Bosquet et al., 2012; Araus and Cairns, 2014). High-throughput phenotyping (HTP) platforms are needed to measure plant traits non-invasively (Reynolds and Langridge, 2016), reduce the labor of manual phenotyping (Cabrera-Bosquet et al., 2012; Cobb et al., 2013), and measure multiple traits, plots, or both efficiently and simultaneously (Barker et al., 2016; Wang et al., 2018).

Unmanned Aerial Systems (UAS)-based remote sensing is being broadly implemented for field-based high-throughput phenotyping due to its low cost and the capacity to cover large field trials with thousands or tens-of-thousands of plots (Shi et al., 2016). Recently, multi-rotor UAS in various sizes have been widely deployed at a low altitude (<50 m) in HTP of plant canopy spectrum features (Haghighattalab et al., 2016; Li et al., 2018), plant growth status (Chu et al., 2017; Singh et al., 2019), and crop water use (Thorp et al., 2018). With the rapid development of low-cost consumer-grade sensors and platforms, UAS phenotyping holds great potential to be an integral part of plant genomics and breeding for precise, quantitative assessment of complex traits on large populations.

Structure-from-Motion (SfM) based photogrammetry is a process widely used to quantify plant phenotypes from aerial images (Shi et al., 2016). In SfM, a large number of aerial images taken from multiple perspectives over a field are used to create an orthomosaic image of a complete field experiment. Then plant traits can be extracted from a defined area (i.e., a shapefile of boundary coordinates for individual plots) within the orthomosaic image. However, during the generation of the orthomosaic image through SfM photogrammetry, pixels within the overlapped area from multiple raw images are blended. For instance, there are multiple optional blending modes such as mosaic and average for orthomosaic image generation in Agisoft Photoscan (Agisoft, 2018). The blending of pixel values has the potential to introduce changes in values intrinsic to the raw images.

Here, we use a complex plant trait – canopy temperature (CT) – as an example of a trait difficult to accurately quantify in the field environment. CT is an indicator of plant water stress and is often correlated with grain yield (Balota et al., 2007). Compared to measuring CT by sensors on the ground (Crain et al., 2016), using the aerial vehicles integrated with thermal imaging sensors can rapidly cover the observation area and potentially reduce diurnal temperature variations. Sagan et al. (2019) compared the performance of measuring CT in soybean and energy sorghum using three commercial thermal cameras on a UAS platform. They demonstrated a high correlation ($R^2 > 0.9$) between temperature extracted from orthomosaic images and ground measurements at noon time assuming minor temperature changes in a short period of UAV-based imaging. By contrast, on much larger field trials with many thousands of entries, longer measurement windows (i.e., hours) often give raise to temperature fluctuations. In such cases, a single CT value extracted from an orthomosaic image may not accurately reflect the actual temperature at each imaging time point. Yet, variation in CT during the measurement window could be thoroughly characterized and accounted for by extracting thermal values directly from the series of raw images, rather than the single orthomosaic image.

An additional confounding factor for thermal imaging is more technical, specifically the flat field correction (FFC) from the thermal camera that may negatively impact the thermal image quality. The FFC consists of a re-calibration of the thermal camera core while the camera is working[1]. FFC is helpful to regulate the thermal data within a defined range of temperature readings but leads to continual recalibration and hence, yields varying values during image acquisition, including temperature differences from the same target in two consecutive images. The error may be compensated using the temperature references on the ground, but the referencing target may not be present in every image. This adds additional complexity to the field operations and image processing. If images with inaccurate thermal measurements are used for mosaicking, the CT values extracted from the orthomosaic image will likely reflect artifacts from both the FFC and the

[1]www.flir-vue-pro.com/news

variability of thermal values from changing ambient conditions during the measurement window. To reduce this effect, Deery et al. (2016) proposed an approach to extract CT from images on a frame-by-frame basis. However, this method requires automation if it is to be used for processing data from large nurseries and for genetic studies with thousands or tens-of-thousands of plots.

Based on the issues described above, measurements of CT using thermal cameras are hypothesized to be substantially influenced by the SfM processing required for mosaicking. Meanwhile, other types of remote sensing datasets are expected to have similar issues from the SfM processing pipeline. For example, the canopy normalized difference vegetation index (NDVI) and the leaf ground cover are widely used remote-sensing traits associated with grain yield and agronomic traits (Rutkoski et al., 2016; Duan et al., 2017). During aerial image acquisition, the reflectance measurements from the canopy changes according to the camera position and the solar angle. This reflectance change can be accurately quantified using a goniometer system and the bidirectional reflectance distribution function (BRDF) under natural illumination conditions on the ground (Sandmeier and Itten, 1999). Also, the leaf area may appear in different densities depending on camera view angles at nadir or off-nadir. Therefore, a single orthomosaic image composed of blended pixels can be expected to have similar problems to reflect variability throughout the measurement window.

According to the theory of SfM processing and the issues previously described, the overall objective of this study is to enhance quality of trait extraction from field-based data collection and measurement using high-throughput phenotyping by UAS remote sensing. For this purpose, we developed a set of image processing methods to extract phenotypes from orthorectified aerial images. We then compared these extracted remote-sensed phenotypes with the same phenotypes extracted from orthomosaic images. In addition to evaluation of CT, we investigated applying this trait extraction method to NDVI and the early-stage ground cover (GC). We fitted four competing linear mixed models to each trait and compared the models using estimates of broad-sense heritability and the Bayesian Information Criterion. Broad-sense heritability is a measure of the proportion of phenotypic variance that is due to all genetic effects relative to unaccounted error variance (Holland et al., 2003). The main purpose of estimating heritability is to understand the level of genetic control of a given phenotype which directly relates to the expected gain from different selection strategies, which is the fundamental concept of plant breeding. A high heritability value is indicative of higher precision and less error and is also connected to higher predictive ability for a given trait (Crain et al., 2017). In comparing methods for analysis of a fixed dataset, a higher heritability reflects that a given method accounts for more variance through decreasing the experimental error. We illustrate the proposed approach using data from three wheat breeding nurseries planted at different locations and in different years as case studies, whereby each nursery provided data on one type of phenotype.

MATERIALS AND METHODS

Plant Material and Field Layout

Spring wheat (*Triticum aestivum* L.) breeding lines used for CT measurements were from the International Maize and Wheat Improvement Center (CIMMYT) wheat breeding program. The trials were planted on November 21, 2017, at Norman E Borlaug Experiment Station (27°22′57.6″N, 109°55′34.7″W) in Ciudad Obregon, Sonora, Mexico during the 2017–18 season. The experiment consisted of 1800 unique spring wheat entries distributed in 60 trials. Each trial was arranged as an alpha lattice design in two blocks. Plots served as experimental units and were 1.7 m × 3.4 m in size, consisting of raised bed planting on two beds spaced 0.8 m apart with paired rows on each bed at 0.15 m spacing for each plot. Details are in the **Supplementary Table 1**.

Winter wheat (*Triticum aestivum*) breeding lines from Kansas State University wheat breeding program were used for canopy NDVI and early-stage ground cover measurements. One trial for canopy NDVI measurements was sown on September 19, 2017 at the KSU Ashland Bottom Agronomy Farm (39°7′54.2″N, 96°37′12.6″W), Manhattan, Kansas, and the other trial for early-stage ground cover measurements was sown on September 17, 2018 at the KSU farm (39°7′56.4″N, 96°37′10.1″W). A total of 146 and 150 winter wheat entries were planted during the 2017–18 and 2018–19 season, respectively. During each season, the entire field experiment was arranged in two blocks. The entries included breeding lines and check varieties. In each block, a breeding line was planted in a single plot, while the checks were planted multiple times. The experimental plot was an individual six-row plot with 20 cm (8″) row spacing with plot dimensions of 1.5 m × 2.4 m. Details of each field experiment are listed in the **Supplementary Table 1**.

To improve the geospatial accuracy of orthomosaic and orthorectified images, ground control points (G) consisting of bright white/reflective square markers were uniformly distributed in the field experiment before image acquisition and surveyed to cm-level resolution. The GCPs in Obregon, Mexico were surveyed using a Trimble R4 RTK (Trimble Inc., Sunnyvale, California, United States) Global Positioning System (GPS). The GCPs in Kansas were surveyed using the Precis BX305 Real-Time Kinematic (RTK) Global Navigation Satellite System (GNSS) unit (Tersus GNSS Inc., Shanghai, China).

UAS, Sensors, and Image Acquisition

The UAS used for image acquisition was a DJI Matrice 100 (DJI, Shenzhen, China). The flight plans were created using Litchi Android App (VC Technology Ltd., United Kingdom) and CSIRO mission planner application[2] for DJI Matrice100. Accordingly, the flight speed, the flight elevation above the ground, and the width between two parallel flight paths were adjusted based on the overlap rate and the camera field of view. Both cameras were automatically triggered with the onboard GNSS unit following a constant interval of distance traveled. A summary of flight settings is listed in the **Supplementary Table 2**.

[2]https://uavmissionplanner.netlify.app/

To collect the thermal image from the spring wheat nurseries, a FLIR VUE Pro R thermal camera (FLIR Systems, United States) was carried by the DJI Matrice 100. Ten 0.25 m × 0.25 m square white metal sheets mounted on 0.50 m posts were used as GCPs. Two data collections were conducted between 11AM and 1PM on March 2 and March 19, 2018, during the grain filling stage. The aerial image overlap rate between two geospatially adjacent images was set to 80% both sequentially and laterally to ensure optimal orthomosaic photo stitching quality. Both flights were set at 60 m above ground level (AGL) at 5 m/s and could cover the 3600 breeding plots in around 16 min. To preserve the image pixel information, the FLIR camera was set to capture Radiometric JPEG (R-JPEG) images.

A MicaSense RedEdge-M multispectral camera (MicaSense Inc., United States) was used to collect winter wheat canopy images in both the 2017–18 and the 2018–19 seasons. White square tiles with a dimension of 0.30 m × 0.30 m were used as GCPs. Nine and four GCPs were placed and surveyed in the field during the 2017–18 and 2018–19 season, respectively. All UAS flights were conducted between 11AM to 2PM. A total of five UAS flights were made during the grain-filling stage in the 2017–18 season, and four UAS flights were made in the early Fall establishment period for 2018–19 season. Detailed flight dates are listed in the **Supplementary Table 2**. The aerial image overlap rate between two geospatially adjacent images was set to 80% both sequentially and laterally to ensure optimal orthomosaic photo stitching quality. All UAS flights were set at 20 m AGL at 2 m/s and could cover 360 (2017–18 season) and 336 (2018–19 season) plots in 14 and 11 min, respectively. To preserve the image pixel intensity, the MicaSense RedEdge-M camera was set to capture uncompressed TIFF images.

Orthomosaic and Orthorectified Images Generation

In this study, models fitted to a trait extracted from the orthomosaic image were used as a benchmark control, against which to compare estimates from models fitted to the same traits extracted from multiple individual orthorectified images. Unlike the approach proposed by Deery et al. (2016), in this study we still needed to generate the orthomosaic image of a complete field as a starting point to calculate the position of each individual image. Through the photogrammetry process, pixels in a raw image were projected to their real geographical location. Following this orthorectification, each individual raw image was converted to an orthorectified image. Therefore, there was no need to manually identify field plots in each orthorectified image because the same shapefile with plot boundaries could be used to identify a plot existing in different orthorectified images. Generating orthomosaic and orthorectified images from raw images consisted of (step 1) image preprocessing (including radiometric calibration), (step 2) GCPs detection, (step 3) photogrammetry process, (step 4) and export of orthomosaic image and orthorectified images (as shown in **Figure 1**), as explained below in detail. The procedure was implemented using Python, and the source code is available online[3].

The image preprocessing procedure for the multispectral images converted the pixel value in each raw spectral image to reflectance before the photogrammetry process. Pixel values in raw thermal images, however, were not converted to temperature values in this step. As each trigger of the MicaSense RedEdge-M camera generated five images of every single spectral band (Blue, Red, Green, Near-infrared, and RedEdge), the completeness check removed images having less than five bands. According to the altitude (i.e., the camera height above the mean sea level) embedded in the image properties, images were divided into two groups – images captured on the ground and images captured in the air. The MicaSense radiometric calibration panels were then automatically detected from images captured on the ground if existing. Following the MicaSense radiometric calibration procedure[4], calibration factors of all five bands were calculated and then applied to images captured in the air, converting raw images to reflectance images for subsequent photogrammetry process.

The GCPs detection procedure automatically identified the GCP in each image captured in the air if existing and matched the GCP with the surveyed position of the closest GCP from the image position. As white square tiles with the pre-known size were used as GCPs in the wheat field, clear patterns of GCPs could be detected through image processing. According to the image position (i.e., the longitude and latitude) embedded in the image properties, the surveyed GCP, whose coordinates were geographically close to the image position, was matched with the detected GCP in the image. Sufficient space (i.e., > 20 m) was left between every two GCPs during placement in the field to avoid having multiple GCPs in a single image and to enable sufficiently accurate geolocation of the UAS to determine which GCP was being imaged. All image file names and detected GCP coordinates were saved in a list for geospatial optimization in the photogrammetry process. Due to the low resolution of the thermal camera and the unclear pattern of GCPs in thermal images, GCPs were manually detected during the photogrammetry process of thermal images.

The photogrammetric processing of aerial images included sparse point cloud generation, geospatial optimization, dense point cloud generation, and 3-dimensional (3D) model generation. The process was implemented using the Agisoft PhotoScan Python API (Version 1.4.0, Agisoft LLC, Russia). An orthomosaic image of a complete field experiment was exported after the process. All images used to generate the orthomosaic image were exported as orthorectified images with the image boundary (i.e., the northwest and southeast corners) coordinates and the original camera position (i.e., longitude, latitude, and altitude) where the image was captured embedded in the image properties.

Plot-Level Traits Extraction

Extraction of plot-level phenotypic values from orthomosaic and orthorectified images consisted of (1) cropping single-plot images from an orthomosaic of the complete field or from multiple orthorectified images, each of which covered a small portion of

[3] github.com/xwangksu/bip

[4] github.com/micasense/imageprocessing

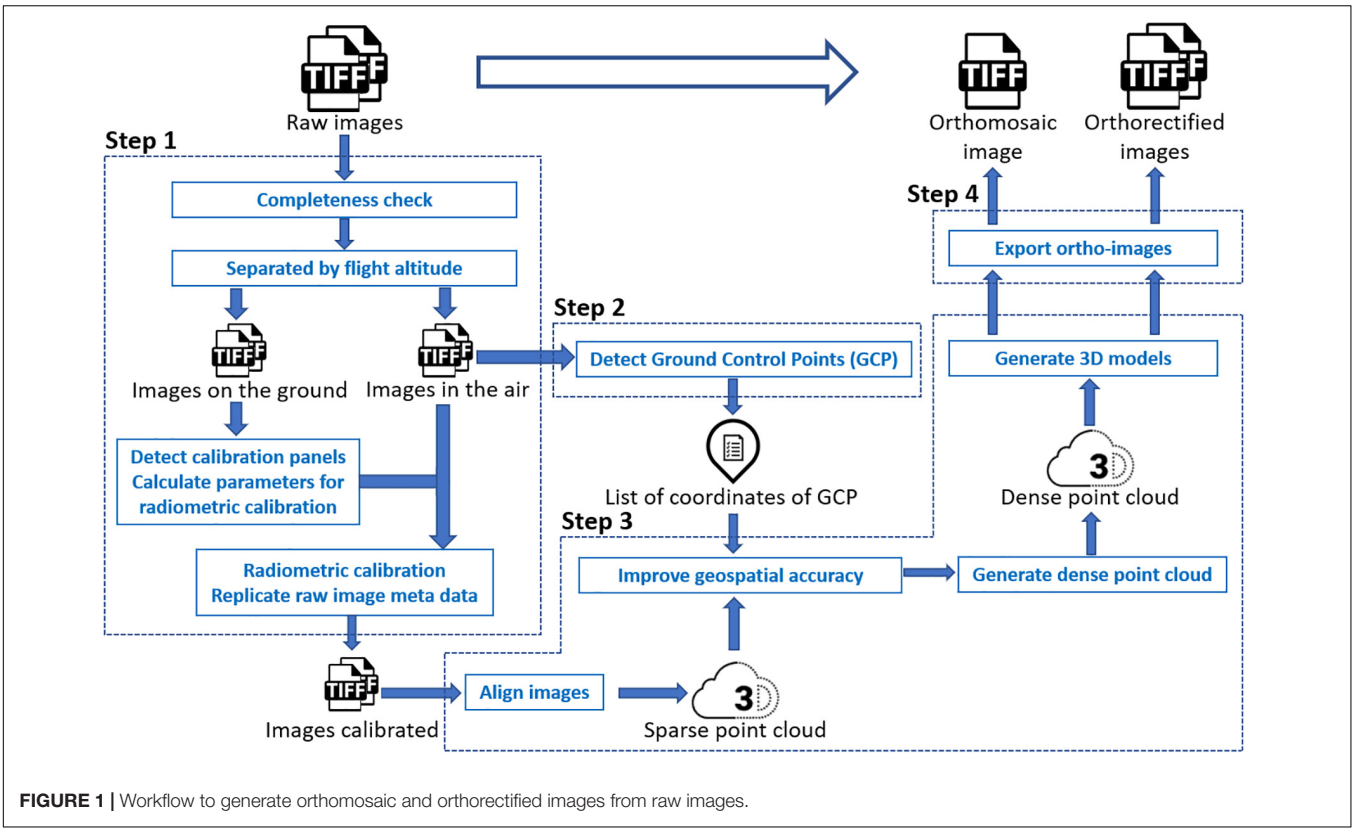

FIGURE 1 | Workflow to generate orthomosaic and orthorectified images from raw images.

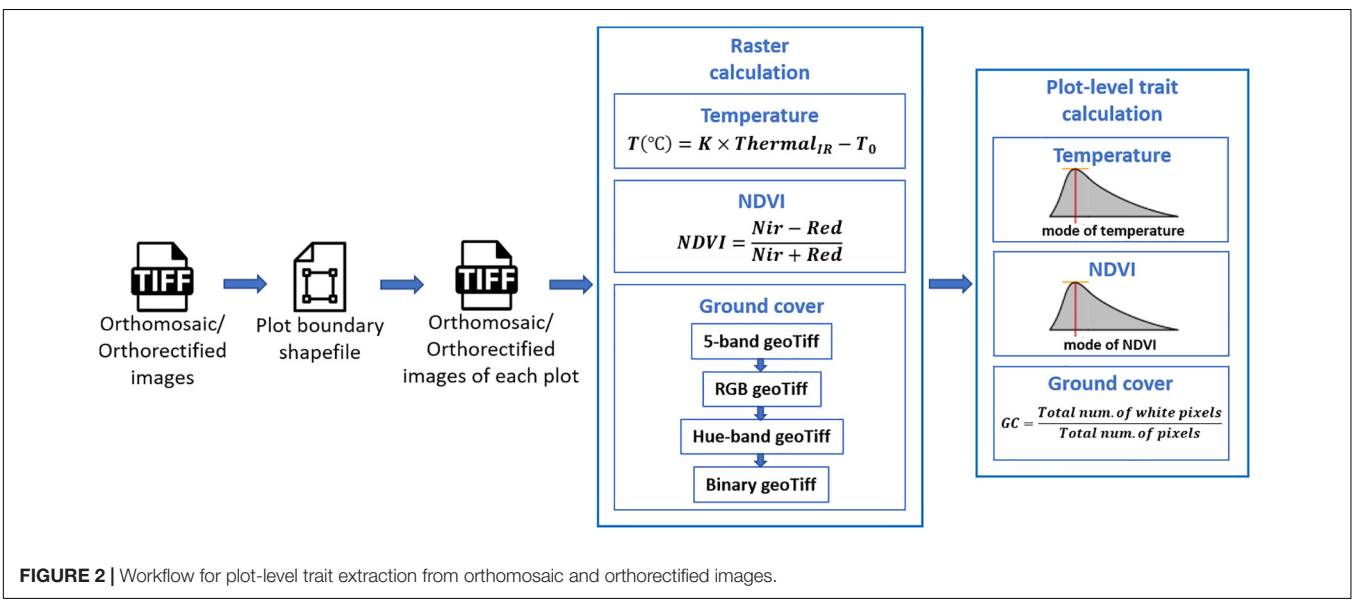

FIGURE 2 | Workflow for plot-level trait extraction from orthomosaic and orthorectified images.

the entire field, (2) converting pixel values to trait values through raster calculation, and (3) summarizing the plot-level trait in each image (as shown in **Figure 2**). The procedure was implemented using Python, and the source code is available online[5].

Following the generation of the orthomosaic image of an entire field, a field map – a shapefile of polygons delineating the four corners of each plot was generated semi-automatically in Quantum Geographic Information System (QGIS, www.qgis.org) with the HTP Geoprocessor plugin (Wang et al., 2016). Specifically, the four corner points of the entire experiment field were first manually defined in QGIS. Then the coordinates of the four corners of the polygon for each plot were automatically calculated with the pre-known plot geometric size (length and width) using a QGIS Python script. Finally, each plot polygon

[5]github.com/xwangksu/traitExtraction

was assigned a plot ID using the HTP Geoprocessor plugin (Wang et al., 2016). According to the field map, an image of each plot could be cropped from the orthomosaic image of the entire field experiment and saved as a GeoTiff image. Unlike the orthomosaic image of the complete field experiment, each orthorectified image only covered a small portion of the entire field. Therefore, only the plots that were completely included in the orthorectified image were cropped and saved as GeoTiff images. As a result, each plot was represented by a single cropped orthomosaic GeoTiff image and multiple orthorectified GeoTiff images.

To extract the CT trait, the pixel values within each GeoTiff image containing the thermal infrared band were directly used as indicators of absolute temperature measurements, as (1) the R-JPEG images have temperature data embedded in each pixel[6] and (2) Sagan et al. (2019) has demonstrated the absolute temperature can be converted from the pixel value following a linear equation:

$$T(^{\circ}\mathrm{C}) = K \times Thermal_{IR} - T_0 \quad (1)$$

where $Thermal_{IR}$ is the pixel value within the thermal infrared band of the GeoTiff image, T is the absolute temperature measurement in Celsius degrees, and K and T_0 are constant parameters. In this study, K and T_0 were set as 0.04 and −273.15 (Flir Systems Inc., 2017; Williamson et al., 2019; Song and Park, 2020).

To generate the NDVI trait from the GeoTiff image from the five-band multispectral GeoTiff image, the following equation was used during raster calculation:

$$NDVI = \frac{NIR - Red}{NIR + Red} \quad (2)$$

where *NIR* and *Red* are the near-infrared and red band of the multispectral GeoTiff images, respectively, and *NDVI* is the output raster layer.

For the canopy GC calculation, the five-band multispectral GeoTiff image was first converted to an RGB GeoTiff image by rendering the Red, Green, and Blue bands. Then the RGB image was converted to a Hue-Saturation-Value (HSV) GeoTiff image. Finally, a binary image was generated from the Hue band of the HSV image by manually selected threshold values leaving white pixels representing the canopy area in the RGB image. In this study, the threshold value was selected from the first image data set (October 3, 2018) and was applied to the subsequent image data sets.

For extraction of CT and NDVI traits, we used the mode of all non-zero values (**Figure 2**) in a plot area as the plot-level CT and NDVI, respectively. This was intended to compensate for noise from the non-vegetative pixels within the plot area, although most of the plots were fully covered by canopies during image acquisition. The plot-level early-stage ground cover (GC in **Figure 2**) was calculated as the overall percentage of white pixels within the binary image. As a result, each type of plot-level trait extracted from the orthomosaic image had only one observation per plot, whereas the same traits extracted from orthorectified images had multiple observations, one per orthorectified image in which that given plot appeared complete.

Orthomosaic and orthorectified images collected on two dates (**Supplementary Table 2**), were used to extract two independent datasets for the CT trait. Similarly, images collected on five and four dates were used to extract five and four independent datasets for the NDVI and the GC traits, respectively (**Supplementary Table 2**).

Statistical Analysis

Four general linear mixed models (models I to IV) were specified and fitted to each of the traits extracted, namely CT, NDVI and GC. For each trait, a null model (Model I) was fitted to observations extracted from the orthomosaic image (one observation per plot; Model I_a) and to the average of the multiple observations per plot, as extracted from the orthorectified images (Model I_b). The remaining three models (II, III, and IV) were fitted to the traits extracted from orthorectified images (i.e., multiple observations per plot) and were intended to recognize different aspects of the data collection process. Model fitting was implemented using the ASReml-R (Ver. 4) package in R (Butler et al., 2009; Gilmour et al., 2015), with variance components estimated by residual maximum likelihood (REML) (Butler et al., 2009; Gilmour et al., 2015). Additional details for each model follow.

Model I

Model I was developed to fit a single observation per plot, with this single observation being either extracted from a single orthomosaic image per plot (y_m, Model I_a) or by averaging multiple plot-level observations ($y_{\bar{r}}$) extracted from orthorectified images (Model I_b). Specifically,

$$\text{Model I}_a : y_{m,ijkl} = \mu^{(\mathrm{I_a})} + G_i^{(\mathrm{I_a})} + B_j^{(\mathrm{I_a})} + R_{k(j)}^{(\mathrm{I_a})} + C_{l(j)}^{(\mathrm{I_a})} + e_{ijkl}^{(\mathrm{I_a})} \quad (3)$$

$$\text{Model I}_b : y_{\bar{r},ijkl} = \mu^{(\mathrm{I_b})} + G_i^{(\mathrm{I_b})} + B_j^{(\mathrm{I_b})} + R_{k(j)}^{(\mathrm{I_b})} + C_{l(j)}^{(\mathrm{I_b})} + e_{ijkl}^{(\mathrm{I_b})} \quad (4)$$

where superscripts (I_a) and (I_b) indicate the model that each parameter corresponds to. Within each model, μ represents the intercept, G_i is the random effect of the i^{th} entry assumed distributed as iid $G_i \sim N(0, \sigma_G^2)$, B_j is the random effect of the j^{th} block assumed distributed as iid $B_j \sim N(0, \sigma_B^2)$, $R_{k(j)}$ is the random effect of the k^{th} row nested within a block and assumed distributed as iid $R_{(j)k} \sim N(0, \sigma_R^2)$, $C_{l(j)}$ is the random effect of the l^{th} column nested within block and distributed as iid $C_{(j)l} \sim N(0, \sigma_C^2)$ Finally, $e_{ijkl}^{(\mathrm{I_a})} \sim N(0, \sigma_{e^{(\mathrm{I_a})}}^2)$ and $e_{ijkl}^{(\mathrm{I_b})} \sim N(0, \sigma_{e^{(\mathrm{I_b})}}^2)$ are model-specific left-over residuals unique to the $\mathrm{ijkl}^{\mathrm{th}}$ plot.

Model II

Given the multiple observations on each plot that were extracted from orthorectified images (y_r), it is possible to assess the

[6]www.flir.com/products/vue-pro-r

variability between observations within a plot (i.e., within-plot variance) by expanding Model I as follows.

$$\text{Model II}: y_{r,ijklm} = \mu^{(\text{II})} + G_i^{(\text{II})} + B_j^{(\text{II})} + R_{k(j)}^{(\text{II})} + C_{l(j)}^{(\text{II})} + (R \times C)(B)_{kl(j)}^{(\text{II})} + \varepsilon_{ijklm}^{(\text{II})} \quad (5)$$

where μ, G_i , B_j , $R_{k(j)}$, and $C_{l(j)}$ are defined as for Model I. Meanwhile, $(R \times C)(B)_{kl(j)}^{(\text{II})}$ is the random effect of an individual plot identified by the combination of the k$^{\text{th}}$ row and the l$^{\text{th}}$ column within the j$^{\text{th}}$ block, assumed iid distributed $(R \times C)(B)_{kl(j)}^{(\text{II})} \sim N(0, \sigma^2_{R\times C(B)^{(\text{II})}})$, and $\varepsilon_{ijklm}^{(\text{II})}$ is the leftover residual noise of the observation collected on the m$^{\text{th}}$ orthorectified image of the ijkl$^{\text{th}}$ plot, and assumed as iid distributed $\varepsilon_{ijklm}^{(\text{II})} \sim N(0, \sigma^2_{\varepsilon^{(\text{II})}})$ Notably, in Model II, left-over residual terms $\varepsilon_{ijklm}^{(\text{II})}$ are unique to each ijklm$^{\text{th}}$ observation within a given plot and thus represent technical replication (i.e., subsampling) of plots in the data collection process.

Model III

Recall that each orthorectified image includes multiple plots in the camera field of view (**Figures 3–5**) and that images were captured by the UAS following a serpentine trajectory (moving along the column direction and turning around at the boundary rows) to cover the entire field. Therefore, for Model III, we consider replacing the specification of spatial effects of row and column with a clustering effect of image, as follows:

$$y_{r,ijn} = \mu^{(\text{III})} + G_i^{(\text{III})} + B_j^{(\text{III})} + I_n^{(\text{III})} + G \times B_{ij}^{(\text{III})} + \varepsilon_{ijn}^{(\text{III})} \quad (6)$$

where μ, G_i, and B_j are defined as for Model II. In turn, $I_n^{(\text{III})}$ is the random effect of the n$^{\text{th}}$ image and is assumed distributed as iid $I_n^{(\text{III})} \sim N(0, \sigma^2_{I^{(\text{III})}})$ Meanwhile, each plot is identified by the combination of the i$^{\text{th}}$ entry in the j$^{\text{th}}$ block, namely $(G \times B)_{ij}^{(\text{III})}$ and assumed iid $(G \times B)_{ij}^{(\text{III})} \sim N(0, \sigma^2_{G\times B^{(\text{III})}})$ Finally, $\varepsilon_{ijn}^{(\text{III})}$ is the left-over residual noise of the observation collected on the n$^{\text{th}}$ orthorectified image of the ij$^{\text{th}}$ plot, assumed distributed as iid $\varepsilon_{ijn}^{(\text{III})} \sim N(0, \sigma^2_{\varepsilon^{(\text{III})}})$ Much like in Model II, residual terms $\varepsilon_{ijn}^{(\text{III})}$ in model III are unique to an observation within a plot and thus represent technical replication (i.e., subsampling) in the data collection process.

Model IV

Model IV extends Model III to recognize that orthorectified images on a given plot are captured from different angles. Thus, Model IV incorporated camera view angle as an explanatory covariate in the linear predictor. This angle is defined from the center of the field plot to the camera's position where the image is captured. As the UAS's altitude could not be held constant during image acquisition, the absolute camera height above the ground level could not be accurately measured. Therefore, only the latitude and longitude (i.e., y and x coordinates) values of both the plot center and the camera were used to calculate the camera azimuth angle (**Figure 3**). Model IV was specified as follows:

$$y_{r,ijn} = \mu^{(\text{IV})} + X_{ijn}\beta^{(\text{IV})} + G_i^{(\text{IV})} + B_j^{(\text{IV})} + I_n^{(\text{IV})} + G \times B_{ij}^{(\text{IV})} + \varepsilon_{ijn}^{(\text{IV})} \quad (7)$$

where X_{ijn} is the camera azimuth angle corresponding to the n$^{\text{th}}$ orthorectified image for the ij$^{\text{th}}$ plot, β is the associated partial regression coefficient, and all remaining terms are defined as in Equation (6).

Model Comparison

Specific model comparisons were targeted to address questions of interest. Specifically, Model I_b was compared to Model I_a to evaluate the effect of an averaged plot-level observation extracted from multiple orthorectified images compared to a single observation extracted from blended pixels in an orthomosaic image. Next, Model II was compared to Model I to investigate the effect of subsampling on estimation of the additive genetic variance (and functions thereof) based on multiple plot-level observations extracted from orthorectified images (II) compared to a single plot-level observation extracted from an orthomosaic image (I_a) or from the average of multiple orthorectified images (I_b). Furthermore, a comparison between Models II and III were intended to consider alternative ways of accounting for spatial variation, namely through rows and columns (II) vs. image clusters (III). Finally, Model IV expanded Model III to adjust for potential technical effects of the UAS with respect to the camera view angle.

Two metrics were selected for model comparisons, specifically the broad-sense heritability (H^2) or repeatability, and the Bayesian Information Criterion (BIC) (Neath and Cavanaugh, 2012).

For all models, variance component estimates were used to compute H^2 as follows. Specifically, to Models I_a and I_b (Equations 3 to 4), H^2 was calculated as,

$$H^2 = \frac{\sigma^2_G}{\sigma^2_G + \frac{\sigma^2_\varepsilon}{r}} \quad (8)$$

Using estimates of the entry-level variance σ^2_ε and the plot-level variance σ^2_e from Models I_a and I_b, and r defined as the number of plots per entry (i.e., number of blocks). For Models II, III, and IV (Equation 5 to 7), the calculation of H^2 included plot-level variance estimates (i.e., $\sigma^2_{R\times C(B)^{(\text{II})}}$, $\sigma^2_{G\times B^{(\text{III})}}$, $\sigma^2_{G\times B^{(\text{IV})}}$), and estimates of σ^2_ε characterizing subsampling, weighted by the number of subsamples (n) per plot, calculated as the harmonic mean number of observations across plots. Specifically, for model II

$$H^2 = \frac{\sigma^2_G}{\sigma^2_G + \frac{\sigma^2_{R\times C(B)}}{r} + \frac{\sigma^2_\varepsilon}{rn}} \quad (9)$$

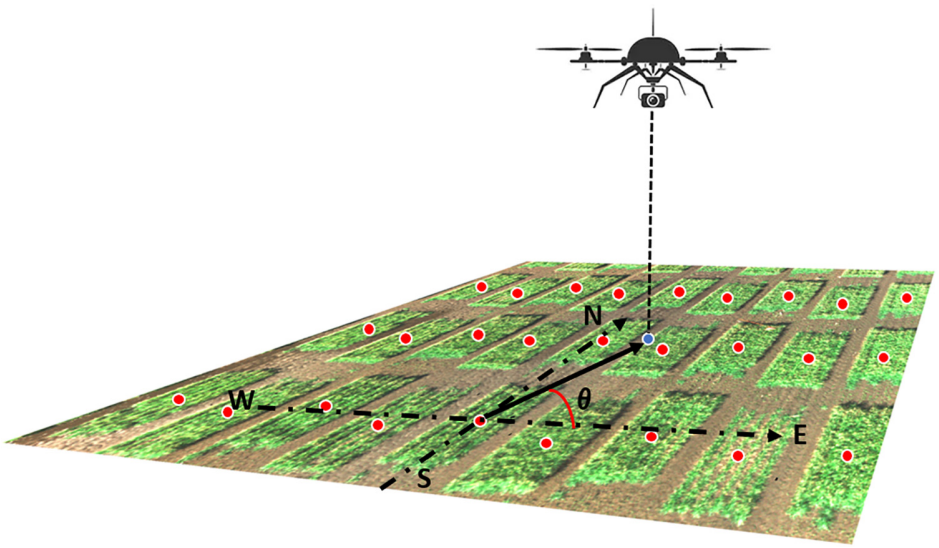

FIGURE 3 | Illustration of the camera azimuth angle. The RGB image was captured by the UAS showing a small part of the field. The blue dot represented the camera projected position on the ground. Red dots represented the center of each plot. The camera azimuth angle (θ) was the angle between the true east (as 0°) and the vector from the plot center to the camera position.

And for each of Models III and IV:

$$H^2 = \frac{\sigma_G^2}{\sigma_G^2 + \frac{\sigma_{G\times B}^2}{r} + \frac{\sigma_\varepsilon^2}{rn}} \quad (10)$$

As Models I_a, I_b, and II have different response variables, and BIC is used for model comparison assuming the same set of observations on the response variable, BIC is only used for Models II, III and IV in this study. Values of BIC were obtained from the ASReml-R (Ver. 4) package output. Smaller values of BIC are considered to indicate better fitting models.

Data Availability

Data associated with these experiments, including the cropped, plot-level orthomosaic images and corresponding orthorectified images, can be accessed at the public repository[7].

RESULTS AND DISCUSSION

Orthomosaic and Orthorectified Image Generation and Gross Description

Using a case-study approach, we illustrate differences in image generation, gross description and corresponding trait extraction from orthomosaic images and orthorectified images. Specifically, for CT we used the March 2, 2018 dataset from spring wheat field (**Figure 4**), for NDVI we used the April 4, 2018 data from the winter wheat field (**Figure 5**), and for GC we used the November 3, 2018 data from the winter wheat field (**Figure 6**).

For the CT trait, gross differences in trait extraction are directly observable in a side-by-side comparison of the orthomosaic image with two of the orthorectified images (**Figures 4A** vs. 4B,C). Notably, all three images in **Figure 3** show ranges in CT from 25°C (blue pixels) to 45°C (red pixels), as shown in the corresponding scales. Consider the individual plot marked with a star; the orthomosaic image seems to indicate a relatively low plot-level CT, based on more yellow pixels for that plot (**Figure 4A**). In contrast, the two orthorectified images show relatively high CT for the said star-marked plot, based on more orange and red pixels (**Figures 4B,C**). As observed, plot-level CT observations extracted from orthorectified images can disagree with the information available from the orthomosaic image, although not all orthorectified images reveal huge difference from the orthomosaic image on a given plot.

Similarly, directly observable differences were apparent between an orthomosaic and two orthorectified images for NDVI in wheat plots (**Figure 5**). Values of NDVI range from 0 (red pixels) to 0.8 (blue pixels) in all three images (**Figure 5**). For instance, consider the subset of six plots inside the yellow dashed rectangle in each of the three images. Although the difference is subtle, it is still visually detectable that more blue pixels in one orthorectified image (**Figure 5C**) than the other (**Figure 5B**). This perceived difference could be due to variation in reflectance over time due to the change of solar angle and different camera view angles. Another possible explanation may be digital artifacts of the camera, as it seemed that plots located at the east and south sides of both orthorectified images (**Figures 5B,C**) showed higher NDVI (i.e., more blue pixels) than plots in the remaining area of each image.

As for visual inspection of images of GC, we could not detect obvious GC differences between the orthomosaic image (**Figure 6A**) and the orthorectified images (**Figures 6B,C**). As GC is sensitive to the view angle from the camera to the plot, this observation supports that both ortho images (either orthomosaic

[7]http://people.beocat.ksu.edu/~xuwang/Data_2019_FPS/

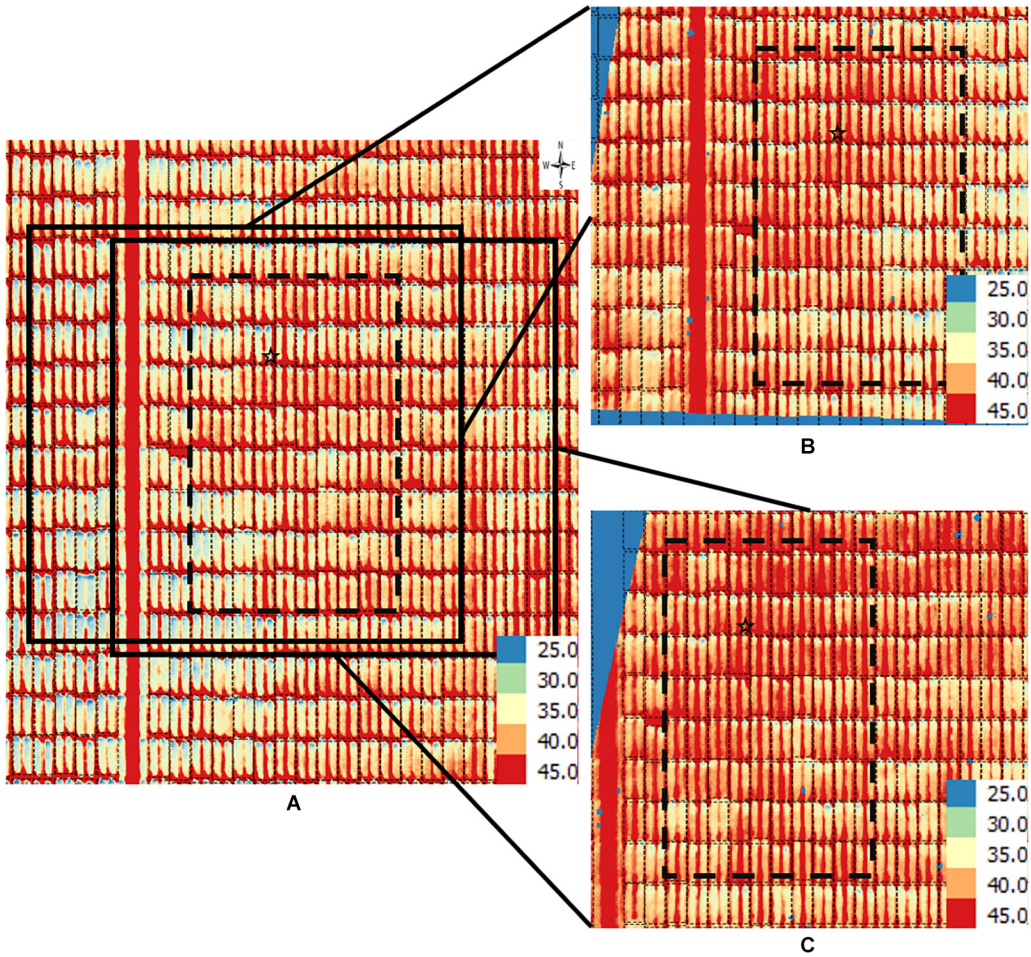

FIGURE 4 | Orthomosaic and orthorectified images of CT. Raw thermal images for CT were captured on March 2, 2018, at 60 m AGL and were processed to generate **(A)** an orthomosaic image of the partial field and multiple orthorectified images of sections of the field, two of which are depicted here **(B,C)**. Black polygons delimited by thin dotted lines within each image delineate plot boundaries. Black polygons in thick dashed lines highlight a field section of interest common to the three images. In each image, a black star marks the same plot. The range of temperature (in Celsius degree) is marked in each image. The continuous blue areas **(B,C)** are non-effective pixels due to orthorectification to the raw images.

or orthorectified) have been processed to apply corrections in the position of ground pixels caused by the perspective of the camera view angle. However, it is still unclear if pixel intensity may vary between orthomosaic and orthorectified images.

Taken together, the case studies presented here support potential variation in traits extracted from orthomosaic and orthorectified images. The main interest of a breeder is to quantify the genetic component of such variation; yet other sources of variation need to be considered and accounted for as well, namely environment factors (e.g., spatial effects) and imaging patterns due to the technology used for data collection (i.e., camera view angles and digital processing artifacts). Specifically, the illustrations presented above raised questions about the information contained in plot-level orthomosaic images generated by the photogrammetry process, as it was perceived to fail to accurately reflect trait variation that was directly apparent on plot-level observations originated from orthorectified images. Our concern is that the blending of pixel information that underlies the photogrammetry generation of orthomosaic images could lead to loss of information, thus undermining the quality of phenotypic data.

Plot-Level Traits Extraction

Plot-level observations on CT, NDVI, and GC traits from two, five, and four datasets, each corresponding to a different data collection date (**Supplementary Table 2**), were extracted from orthomosaic and orthorectified images. For each trait, the total number of observations extracted from orthorectified images and the minimum, maximum, and median number of observations per plot extracted from orthorectified images were summarized (**Supplementary Tables 3–5**). The number of observations per plot extracted from orthorectified images ranged from 3 to 49 across traits. From an experimental design standpoint, each individual plot was assigned to a given genetic line. Thus, the multiple observations per plot extracted from the orthorectified images may be considered subsamples (i.e., technical replication)

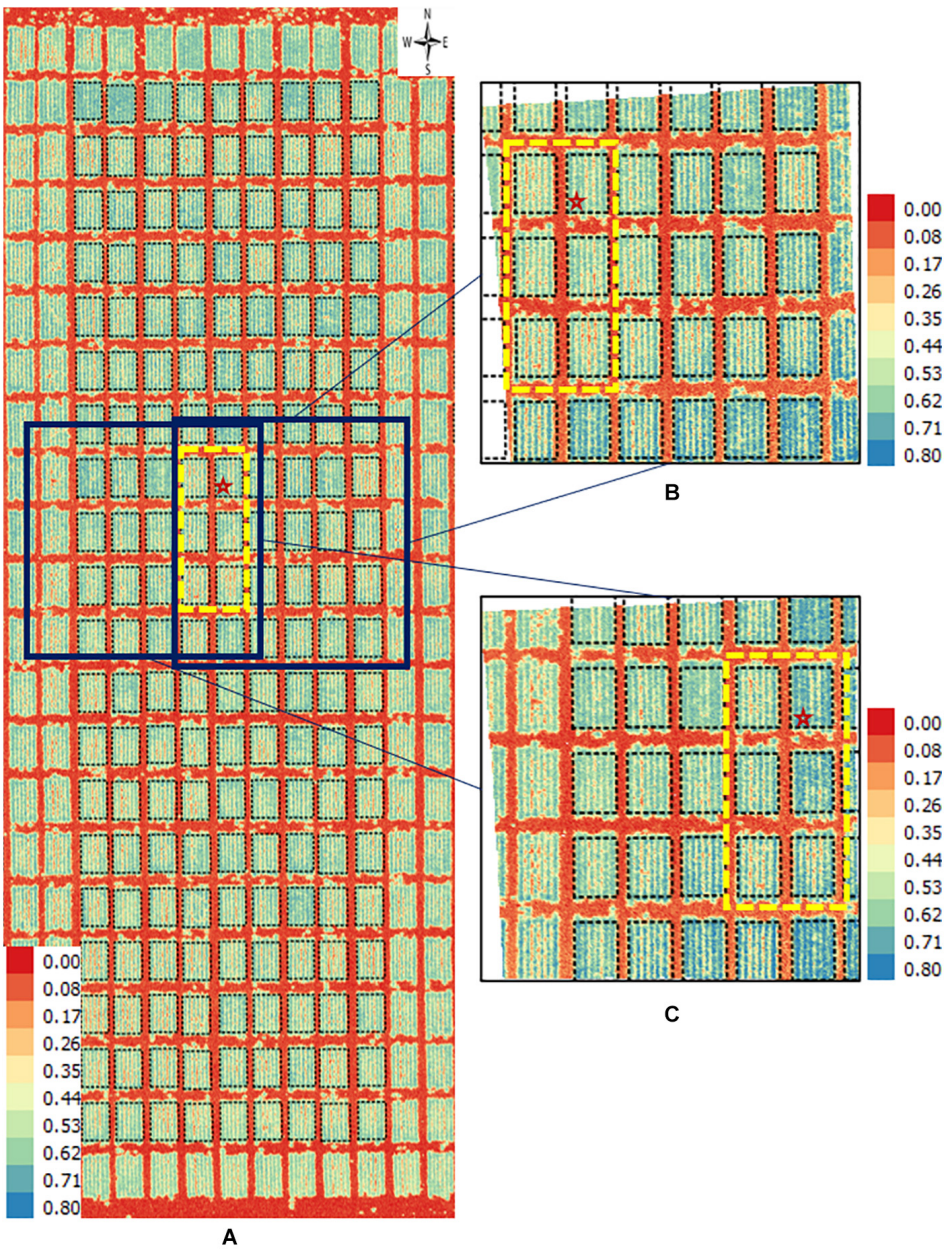

FIGURE 5 | Orthomosaic and orthorectified images of NDVI. Raw images for NDVI were captured on April 4, 2018, at 20 m AGL from the 2017–18 wheat field experiment and were processed to generate **(A)** an orthomosaic image of a block in the field and multiple orthorectified images of sections of such block, two of which are depicted here **(B,C)**. Black polygons delimited by thin dotted lines within each image delineate plot boundaries. Yellow rectangles in dashed lines delimit the same subset of six plots in all three images. The range of NDVI (unitless) is marked in each image. The continuous white areas **(B,C)** are non-effective pixels due to orthorectification to the raw images.

for the entry that plot was assigned to. By contrast, only one observation per plot was obtained for each trait from the orthomosaic image for a given field.

Model Comparison

Table 1 shows estimated H^2 for models I_a, I_b, II, III, and IV fitted to each of the traits extracted, namely CT, NDVI and GC. **Table 2** shows BIC for model comparison between models II, III, and IV fitted to each of the traits extracted, namely CT, NDVI, and GC.

Models I_a, I_b, and II

For both CT and NDVI, the magnitude of H^2 estimates for Model I_b and Model I_a showed an inconsistent pattern across datasets (**Table 1**), though estimates seemed to be numerically greater in magnitude more often under Model I_b. In contrast,

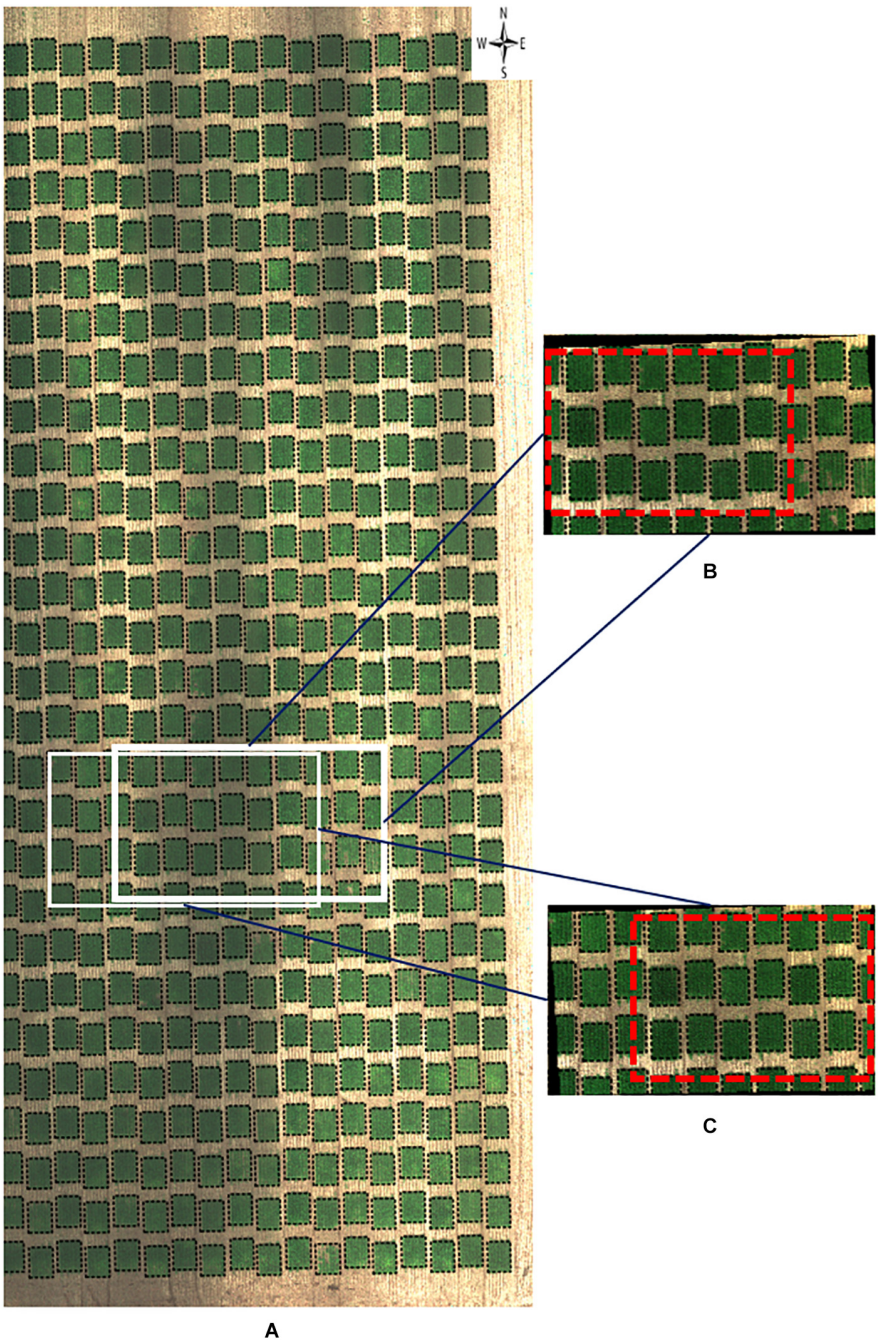

FIGURE 6 | RGB orthomosaic and orthorectified images used for ground cover. Raw images were captured on November 3, 2018, at 20 m AGL from the 2018–19 wheat field experiment and were processed to generate **(A)** an RGB orthomosaic image of two blocks of the entire field, **(B,C)** two orthorectified sample RGB images illustrating different parts of the field. Black polygons in dashed lines within each image delineated plot boundaries. Red rectangles in dashed lines represented overlapped areas between two orthorectified RGB images. The continuous black areas **(B,C)** are non-effective pixels due to orthorectification to the raw images.

for the GC trait, estimates of H^2 were consistently greater in numerical magnitude under Model I_a than I_b based on the four datasets considered.

Comparing H^2 estimates of all three traits between using Model I_a and Model II, we observed that H^2 estimates of the CT trait on both two dates were improved by the latter model, as well as all H^2 estimates of the NDVI trait except the one on the last date (**Table 1**). Taken together, for CT and NDVI traits, fitting multiple observations per plot into a hierarchical model that recognizes subsampling can help recover additive genetic variability in the data, as indicated by greater estimates of broad-sense heritability.

Compared to Model I_b, Model II explicitly accommodated technical replication in phenotypic information, causing beneficial H^2 estimates in all cases; however, the magnitude of gains ranged from moderate to marginal.

In summary, fitting phenotypic values of some crop traits (e.g., CT and NDVI) extracted from orthorectified images could increase estimates of H^2 in some cases, relative to the same phenotypic traits obtained from orthomosaic images (Model I_a). However, the estimation of H^2 through fitting the GC trait could not be improved by simply replacing the single observation from the orthomosaic image with the average observations extracted from multiple orthorectified images. This inconsistent pattern was possibly due to the "mosaic" blending mode selected during photogrammetry processing of the orthomosaic photos. According to the Agisoft User Manual (2018), pixels were not simply blended by averaging pixel values from different photos in this blending mode, but through a pixel frequency related selection – a two-step approach. It was likely to be the reason why Model I_b and II could not always improve the trait estimation compared to Model I_a. Further research is required to characterize the extent of the expected benefit in terms of specific crops traits and circumstances of the growth season and data collection technology.

Model II vs. III

For CT and NDVI traits, H^2 estimates were consistently decreased based on variance component estimates from Model III relative to Model II (**Table 1**), though the magnitude of the difference ranges from 12 to 62%. As for BIC-based model fit comparisons, results proved trait-specific. For CT, Model III showed smaller BIC values, and thus, better fit than Model II. However, for NDVI, most datasets showed better BIC-based fit by Model II compared to Model III (**Table 2**).

As for GC, the H^2 estimates were increased for all datasets using Model III compared to Model II (**Table 1**). However, in all cases, BIC indicated a most prevalent better fit of Model II compared to III (**Table 2**). According to the result, for CT and NDVI traits estimation, considering the image cluster effect introduced in Model III as a factor could improve the phenotypic data quality; however, the row and column effect was still dominate for all the trait estimation in this study.

TABLE 1 | Estimated broad-sense heritability (H^2) for models I_a, I_b, II, III, and IV fitted to plot-level CT, NDVI, and GC observations on the case studies considered.

Date	Model I_a	Model I_b	Model II	Model III	Model IV
	CT				
3/2/2018	0.838	0.815	0.839	0.736	0.717
3/19/2018	0.606	0.825	0.834	0.615	0.619
	NDVI				
4/4/2018	0.432	0.572	0.598	0.348	0.389
4/12/2018	0.529	0.579	0.590	0.492	0.492
4/19/2018	0.262	0.633	0.696	0.311	0.370
4/23/2018	0.489	0.605	0.650	0.250	0.307
5/16/2018	0.489	0.399	0.422	0.370	0.467
	GC				
10/3/2018	0.811	0.794	0.799	0.843	0.877
10/11/2018	0.824	0.808	0.809	0.942	0.942
10/21/2018	0.706	0.700	0.700	0.878	0.882
11/3/2018	0.502	0.417	0.419	0.727	0.731

TABLE 2 | Bayesian Information Criterion (BIC) for models II, III, and IV fitted to plot-level CT, NDVI, and GC observations on the case studies considered.

Date	Model II	Model III	Model IV
	CT		
3/2/2018	739726	620273	597315
3/19/2018	522193	512660	509143
	NDVI		
4/4/2018	−25028	−24832	−25417
4/12/2018	−31071	−30699	−30735
4/19/2018	−20666	−20804	−21751
4/23/2018	−23435	−23156	−24090
5/16/2018	−20888	−19871	−20777
	GC		
10/3/2018	−22314	−23872	−24529
10/11/2018	−19322	−15933	−15939
10/21/2018	−23489	−18529	−18552
11/3/2018	−22831	−20139	−20166

Model III vs. IV

In most cases, H^2 estimates obtained using variance component estimates from Model IV were either increased or tied with those computed based on Model III. The one exception was for the CT trait based on the datasets from March 2, 2018 (**Table 1**). In addition, BIC estimates were smaller for model IV relative to III for all traits and in all cases, thereby indicated consistently improved model fit of Model IV relative to III (**Table 2**). Recall that Model IV included an additional explanatory variable, namely the camera azimuth angle from the plot center to the camera, could be proved to improve model fit. We observed that recent studies have confirmed that the reflectance observed by UAS are affected by multiple solar angles (Assmann et al., 2018) and camera view angles (Cheng et al., 2019). Compared to previous research, the multispectral images were not collected by the UAS at multiple discrete camera view angles intentionally in this study. Instead, the camera azimuth angles in this study were continuously distributed according to the flight route. Therefore, we considered the camera's azimuth angle as an explanatory covariate in a more general way and aimed to improve the trait estimation.

In general, based on broad-sense heritability, the highest H^2 estimates for CT and NDVI traits were most often obtained when Model II was used for estimation, whereas for the GC trait, the highest H^2 estimates were obtained from Model IV (**Table 1**), indicating that the best fitting model may be trait-specific. Specifically, the highest estimates of H^2 for CT and NDVI traits were obtained when row and column effects were recognized in the modeling exercise (i.e., Model II), while for the GC trait, accounting for multiple images and the camera view angle yielded higher H^2 estimates, as shown by Model IV. Other technical aspects or components of experimental design may also be considered for modeling to further explain leftover noise and enhance genetic signal. Moreover, even within a trait,

estimation results were not consistent. For example, for the NDVI trait, the dataset of May 16, 2018 yielded the highest H^2 estimates when fitted with Model I_a. This indicates the need for further research to fine-tune processing of UAS imaging technology for efficient and accurate extraction of phenotypes relevant to crop improvement.

Cost Comparison Between the Two Image Processing Methods

During the Agisoft photogrammetry processing in this study, there is no computing cost difference between generation a single orthomosaic photo or generation of multiple orthorectified images. The export of multiple orthorectified images takes a longer time, though marginal relative to the entire analysis. As the number of orthorectified images per plot has increased compared to only one orthomosaic photo per plot, the trait extraction will take longer time than extracting trait values from the orthomosaic photo. Fortunately, the plot-boundary shapefile only needs to be generated once during trait extraction from the orthomosaic photo and the same shapefile can be used for trait extraction from multiple orthorectified images. Therefore, the analysis pipeline for orthophotos presented here does increase computational time, though a relatively marginal increase compared to overall pipeline computational requirements and the data collection time.

CONCLUSION

In this study, we demonstrated open-source and highly reproducible image processing methods and applied it for processing three crop phenotypes obtained by UAS, namely canopy temperature, canopy NDVI, and early-stage ground coverage, to seek the potential to improve quality of trait extraction from UAS-based remote sensing. We compared plot-level phenotypic traits extracted from the orthomosaic image with those obtained from orthorectified images, and we provided evidence that phenotyping by UAS remote sensing could be improved by extracting observations directly from multiple orthorectified images and through proper statistical models that are used to capture and account for technological sources of variability.

While further research will be needed, this study shows preliminary evidence with important practical implications for plant breeding and genetics. First, we developed image processing pipelines that have the potential to automatically generate the orthomosaic and orthorectified images from aerial images, without any need for manual manipulation. Second, we proposed batch processing pipelines to quantify different types of plot-level phenotypic traits, namely CT, NDVI, and GC. In addition, we illustrate how cropping plot-level images from orthorectified images can highly improve the efficiency to link genotypes to phenotypes. This approach can significantly increase the number of image samples per plot, indicating views of a plot from different angles, and provide huge training datasets for image-based deep learning. Finally, we proposed four statistical linear mixed models to efficiently partition sources of variation in each trait, specifically variation introduced by the UAS technology and accompanying image processing, in addition to experimental design. The models provide breeders multiple options to investigate traits extracted from high-throughput UAS-based imaging. Overall, through this study, it is expected that the future of modern breeding could be further highlighted, where in conjunction with powerful genomics and phenomics tools, UAS remote sensing can accelerate the genetic gains in plant breeding to meet the global demand for food, fiber, and fuel.

DATA AVAILABILITY STATEMENT

The datasets presented in this study can be found in online repositories. The names of the repository/repositories and accession number(s) can be found below: http://people.beocat.ksu.edu/~xuwang/Data_2019_FPS/.

AUTHOR CONTRIBUTIONS

XW and JP conceived and designed the study. XW, DS, and BE conducted UAS flights. XW performed image analysis. PS, NB, XW, JP, and DS contributed to the statistical analysis. RS, SM, and FE provided experimental lines. XW, PS, NB, and JP wrote the manuscript. JP directed the overall project. All authors edited and reviewed the manuscript.

FUNDING

This work was supported by the National Science Foundation (NSF) Plant Genome Research Program (PGRP) (Grant No. IOS-1238187), the Kansas Wheat Commission and Kansas Wheat Alliance, the United States Agency for International Development (USAID) Feed the Future Innovation Lab for Applied Wheat Genomics (Cooperative Agreement No. AID-OAA-A-13-00051), and the International Wheat Yield Partnership (Grant No. 2017-67007-25933/project accession no. 1011391) from the United States Department of Agriculture National Institute of Food and Agriculture (USDA NIFA). The opinions expressed herein are those of the author(s) and do not necessarily reflect the views of the USAID, the NSF, or the USDA.

ACKNOWLEDGMENTS

We thank the assistance of colleagues at Kansas State University, including Mark Lucas, Richard Brown, and Grant Williams and valuable input from Dr. Jose Crossa from CIMMYT, Dr. Atena Haghighattalab from University of Minnesota, and Dr. Scott Chapman from CSIRO, Australia.

SUPPLEMENTARY MATERIAL

The Supplementary Material for this article can be found online at: https://www.frontiersin.org/articles/10.3389/fpls.2020.587093/full#supplementary-material

REFERENCES

Agisoft, L. L. C. (2018). *Agisoft PhotoScan User Manual: Professional Edition, Version 1.4*. St Petersburg: Agisoft LLC.

Araus, J. L., and Cairns, J. E. (2014). Field high-throughput phenotyping: the new crop breeding frontier. *Trends Plant Sci.* 19, 52–61. doi: 10.1016/j.tplants.2013.09.008

Assmann, J. J., Kerby, J. T., Cunliffe, A. M., and Myers-Smith, I. H. (2018). Vegetation monitoring using multispectral sensors—Best practices and lessons learned from high latitudes. *J. Unman. Vehicle Syst.* 7, 54–75. doi: 10.1139/juvs-2018-0018

Balota, M., Payne, W. A., Evett, S. R., and Lazar, M. D. (2007). Canopy temperature depression sampling to assess grain yield and genotypic differentiation in winter wheat. *Crop Sci.* 47, 1518–1529. doi: 10.2135/cropsci2006.06.0383

Barker, J., Zhang, N., Sharon, J., Steeves, R., Wang, X., Wei, Y., et al. (2016). Development of a field-based high-throughput mobile phenotyping platform. *Comput. Electron. Agricult.* 122, 74–85. doi: 10.1016/j.compag.2016.01.017

Butler, D., Cullis, B. R., Gilmour, A., and Gogel, B. (2009). *ASReml-R Reference Manual*. Brisbane: The State of Queensland, Department of Primary Industries and Fisheries.

Cabrera-Bosquet, L., Crossa, J., Von Zitzewitz, J., Serret, M. D., and Luis, A. J. (2012). High-throughput phenotyping and genomic selection: the frontiers of crop breeding converge F. *J. Integrat. Plant Biol.* 54, 312–320. doi: 10.1111/j.1744-7909.2012.01116.x

Cheng, T., Lu, N., Wang, W., Zhang, Q., Li, D., Yao, X., et al. (2019). Estimation of nitrogen nutrition status in winter wheat from unmanned aerial vehicle based multi-angular multispectral imagery. *Front. Plant Sci.* 10:1601. doi: 10.3389/fpls.2019.01601

Chu, T., Starek, M., Brewer, M., Murray, S., and Pruter, L. (2017). Assessing lodging severity over an experimental maize (Zea mays L.) field using UAS images. *Remote Sensing* 9:923. doi: 10.3390/rs9090923

Cobb, J. N., Declerck, G., Greenberg, A., Clark, R., and Mccouch, S. (2013). Next-generation phenotyping: requirements and strategies for enhancing our understanding of genotype–phenotype relationships and its relevance to crop improvement. *Theoret. Appl. Genet.* 126, 867–887. doi: 10.1007/s00122-013-2066-0

Crain, J., Reynolds, M., and Poland, J. (2017). Utilizing high-throughput phenotypic data for improved phenotypic selection of stress-adaptive traits in wheat. *Crop Sci.* 57, 648–659. doi: 10.2135/cropsci2016.02.0135

Crain, J. L., Wei, Y., Barker, J., Thompson, S. M., Alderman, P. D., Reynolds, M., et al. (2016). Development and deployment of a portable field phenotyping platform. *Crop Sci.* 56, 965–975. doi: 10.2135/cropsci2015.05.0290

Crossa, J., Pérez-Rodríguez, P., Cuevas, J., Montesinos-López, O., Jarquín, D., De Los Campos, G., et al. (2017). Genomic selection in plant breeding: methods. models, and perspectives. *Trends Plant Sci.* 22, 961–975. doi: 10.1016/j.tplants.2017.08.011

Deery, D. M., Rebetzke, G. J., Jimenez-Berni, J. A., James, R. A., Condon, A. G., Bovill, W. D., et al. (2016). Methodology for high-throughput field phenotyping of canopy temperature using airborne thermography. *Front. Plant Sci.* 7:1808. doi: 10.3389/fpls.2016.01808

Duan, T., Chapman, S., Guo, Y., and Zheng, B. (2017). Dynamic monitoring of NDVI in wheat agronomy and breeding trials using an unmanned aerial vehicle. *Field Crops Res.* 210, 71–80. doi: 10.1016/j.fcr.2017.05.025

Eathington, S. R., Crosbie, T. M., Edwards, M. D., Reiter, R. S., and Bull, J. K. (2007). Molecular markers in a commercial breeding program. *Crop Sci.* 47, S–154. doi: 10.2135/cropsci2007.04.0015IPBS

Flir Systems Inc. (2017). *FLIR Duo Pro R User Guide*. Wilsonville, OR: FLIR Systems, Inc.

Gilmour, A., Gogel, B., Cullis, B., Welham, S., and Thompson, R. (2015). *ASReml User Guide Release 4.1 Structural Specification*. Hemel Hempstead: VSN international ltd.

Haghighattalab, A., Pérez, L. G., Mondal, S., Singh, D., Schinstock, D., Rutkoski, J., et al. (2016). Application of unmanned aerial systems for high throughput phenotyping of large wheat breeding nurseries. *Plant Methods* 12:35. doi: 10.1186/s13007-016-0134-6

Hayes, B. J., and Goddard, M. E. (2001). Prediction of total genetic value using genome-wide dense marker maps. *Genetics* 157, 1819–1829.

Holland, J. B., Nyquist, W. E., and Cervantes-Martínez, C. T. (2003). Estimating and interpreting heritability for plant breeding: an update. *Plant Breed. Rev.* 22, 9–112. doi: 10.1002/9780470650202.ch2

Li, J., Shi, Y., Veeranampalayam-Sivakumar, A.-N., and Schachtman, D. P. (2018). Elucidating sorghum biomass, nitrogen and chlorophyll contents with spectral and morphological traits derived from unmanned aircraft system. *Front. Plant Sci.* 9:1406. doi: 10.3389/fpls.2018.01406

Neath, A. A., and Cavanaugh, J. E. (2012). The Bayesian information criterion: background, derivation, and applications. *Wiley Interdiscip. Rev.* 4, 199–203. doi: 10.1002/wics.199

Reynolds, M., and Langridge, P. (2016). Physiological breeding. *Curr. Opin. Plant Biol.* 31, 162–171. doi: 10.1016/j.pbi.2016.04.005

Rutkoski, J., Poland, J., Mondal, S., Autrique, E., Pérez, L. G., Crossa, J., et al. (2016). Canopy temperature and vegetation indices from high-throughput phenotyping improve accuracy of pedigree and genomic selection for grain yield in wheat. *G3 Genes Genomes Genetics* 6, 2799–2808. doi: 10.1534/g3.116.032888

Sagan, V., Maimaitijiang, M., Sidike, P., Eblimit, K., Peterson, K. T., Hartling, S., et al. (2019). UAV-based high resolution thermal imaging for vegetation monitoring, and plant phenotyping using ICI 8640 P, FLIR Vue Pro R 640, and thermoMap cameras. *Remote Sensing* 11:330. doi: 10.3390/rs11030330

Sandmeier, S. R., and Itten, K. I. (1999). A field goniometer system (FIGOS) for acquisition of hyperspectral BRDF data. *IEEE Transact. Geosci. Remote Sensing* 37, 978–986. doi: 10.1109/36.752216

Shi, Y., Thomasson, J. A., Murray, S. C., Pugh, N. A., Rooney, W. L., Shafian, S., et al. (2016). Unmanned aerial vehicles for high-throughput phenotyping and agronomic research. *PLoS One* 11:e0159781. doi: 10.1371/journal.pone.0159781

Singh, D., Wang, X., Kumar, U., Gao, L., Noor, M., Imtiaz, M., et al. (2019). High-throughput phenotyping enabled genetic dissection of crop lodging in wheat. *Front. Plant Sci.* 10:394. doi: 10.3389/fpls.2019.00394

Song, B., and Park, K. (2020). Verification of Accuracy of unmanned aerial vehicle (UAV) land surface temperature images using in-situ data. *Remote Sensing* 12:288. doi: 10.3390/rs12020288

Thorp, K., Thompson, A., Harders, S., French, A., and Ward, R. (2018). High-throughput phenotyping of crop water use efficiency via multispectral drone imagery and a daily soil water balance model. *Remote Sensing* 10:1682. doi: 10.3390/rs10111682

Wang, X., Singh, D., Marla, S., Morris, G., and Poland, J. (2018). Field-based high-throughput phenotyping of plant height in sorghum using different sensing technologies. *Plant Methods* 14:53. doi: 10.1186/s13007-018-0324-5

Wang, X., Thorp, K. R., White, J. W., French, A. N., and Poland, J. A. (2016). Approaches for geospatial processing of field-based high-throughput plant phenomics data from ground vehicle platforms. *Transact. ASABE* 59, 1053–1067. doi: 10.13031/trans.59.11502

Williamson, T. N., Dobrowolski, E. G., Meyer, S. M., Frey, J. W., and Allred, B. J. (2019). Delineation of tile-drain networks using thermal and multispectral imagery—Implications for water quantity and quality differences from paired edge-of-field sites. *J. Soil Water Conserv.* 74, 1–11. doi: 10.2489/jswc.74.1.1

Conflict of Interest: The authors declare that the research was conducted in the absence of any commercial or financial relationships that could be construed as a potential conflict of interest.

frontiers in Plant Science

ORIGINAL RESEARCH
published: 04 December 2020
doi: 10.3389/fpls.2020.600489

Comparison of MALDI-TOF-MS and RP-HPLC as Rapid Screening Methods for Wheat Lines With Altered Gliadin Compositions

*You-Ran Jang[1†], Kyoungwon Cho[2†], Sewon Kim[1], Jae-Ryeong Sim[1], Su-Bin Lee[1], Beom-Gi Kim[1], Yong Q. Gu[3], Susan B. Altenbach[3], Sun-Hyung Lim[4], Tae-Won Goo[5] and Jong-Yeol Lee[1]**

[1] National Institute of Agricultural Sciences, RDA, Jeonju, South Korea, [2] Department of Biotechnology, College of Agriculture and Life Sciences, Chonnam National University, Gwangju, South Korea, [3] USDA-ARS, Western Regional Research Center, Albany, CA, United States, [4] Division of Horticultural Biotechnology, Hankyong National University, Anseong, South Korea, [5] Department of Biochemistry, School of Medicine, Dongguk University, Gyeongju, South Korea

OPEN ACCESS

Edited by:
Lindsey Compton,
University of Birmingham,
United Kingdom

Reviewed by:
Shahidul Islam,
Murdoch University, Australia
Carmen Victoria Ozuna,
University of Almería, Spain

***Correspondence:**
Jong-Yeol Lee
jy0820@korea.kr

† These authors have contributed equally to this work

Specialty section:
This article was submitted to Plant Breeding, a section of the journal Frontiers in Plant Science

Received: 30 August 2020
Accepted: 13 November 2020
Published: 04 December 2020

Citation:
Jang Y-R, Cho K, Kim S, Sim J-R, Lee S-B, Kim B-G, Gu YQ, Altenbach SB, Lim S-H, Goo T-W and Lee J-Y (2020) Comparison of MALDI-TOF-MS and RP-HPLC as Rapid Screening Methods for Wheat Lines With Altered Gliadin Compositions. Front. Plant Sci. 11:600489. doi: 10.3389/fpls.2020.600489

The wheat gliadins are a complex group of flour proteins that can trigger celiac disease and serious food allergies. As a result, mutation breeding and biotechnology approaches are being used to develop new wheat lines with reduced immunogenic potential. Key to these efforts is the development of rapid, high-throughput methods that can be used as a first step in selecting lines with altered gliadin contents. In this paper, we optimized matrix-assisted laser desorption/ionization time-of-flight mass spectrometry (MALDI-TOF-MS) and reversed-phase high-performance liquid chromatography (RP-HPLC) methods for the separation of gliadins from *Triticum aestivum* cv. Chinese Spring (CS). We evaluated the quality of the resulting profiles using the complete set of gliadin gene sequences recently obtained from this cultivar as well as a set of aneuploid lines in CS. The gliadins were resolved into 13 peaks by MALDI-TOF-MS. α- or γ-gliadins that contain abundant celiac disease epitopes and are likely targets for efforts to reduce the immunogenicity of flour were found in several peaks. However, other peaks contained multiple α- and γ-gliadins, including one peak with as many as 12 different gliadins. In comparison, separation of proteins by RP-HPLC yielded 28 gliadin peaks, including 13 peaks containing α-gliadins and eight peaks containing γ-gliadins. While the separation of α- and γ-gliadins gliadins achieved by RP-HPLC was better than that achieved by MALDI-TOF-MS, it was not possible to link peaks with individual protein sequences. Both MALDI-TOF-MS and RP-HPLC provided adequate separation of ω-gliadins. While MALDI-TOF-MS is faster and could prove useful in studies that target specific gliadins, RP-HPLC is an effective method that can be applied more broadly to detect changes in gliadin composition.

Keywords: gliadin profiling, chromosomal assignment, aneuploid lines, MALDI-TOF-MS, RP-HPLC, immunogenic potential

INTRODUCTION

Wheat (*Triticum aestivum* L.) is a major staple cereal grain consumed by humans worldwide and a major source of protein in the diet. The gluten proteins comprise about 70% of the total grain protein (Shewry and Halford, 2002). Gluten proteins consist of 70–100 different proteins that play a major role in the dough mixing properties of flours and determine their suitability for bread-making (Shewry et al., 2003). Some gluten proteins also trigger severe diseases in humans, including celiac disease (CD), and food allergies (Biagi et al., 1999; Matsuo et al., 2004, 2005; Battais et al., 2005a; Bittner et al., 2008; Sollid et al., 2012). Gluten proteins are traditionally classified into glutenins and gliadins (Shewry and Tatham, 1990). The polymeric glutenins consist of high-molecular-weight glutenin subunits (HMW-GS) and low-molecular-weight glutenin subunits (LMW-GS) that are linked by disulfide bonds. Gliadins are monomeric proteins that account for approximately 40% of the gluten proteins and are particularly immunogenic (Battais et al., 2005a). Gliadins are generally separated into four complex classes, α-, γ-, δ-, and ω-gliadin, based on their electrophoretic mobility in acid polyacrylamide gel electrophoresis (A-PAGE) (Anderson et al., 2012). The ω-gliadins are further divided into ω-5 gliadins and ω-1,2 gliadins on the basis of both size and repetitive motifs. A number of epitopes that trigger the food allergy wheat-dependent exercise-induced anaphylaxis (WDEIA) have been identified in ω-5 gliadins (Battais et al., 2005b), while α-, γ-, and ω-1,2 gliadins contain clusters of epitopes that are active in celiac disease (Tye-Din et al., 2010; Sollid et al., 2012).

γ-, δ-, and ω-gliadins are encoded at the *Gli-1* loci on the short arms of the group 1 homeologous chromosomes in hexaploid wheat and linked to the LMW-GS, while the α-gliadins are encoded at the *Gli-2* loci on the short arms of the group six chromosomes. Recent genome sequencing efforts in the reference wheat Chinese Spring (CS) revealed the complexity of the gluten protein families and a complete set of gliadin and LMW-GS genes including 47 α-gliadin, 14 γ-gliadin, five δ-gliadin, 19 ω-gliadin, and 17 LMW-GS genes was assembled and annotated [Huo et al., 2018a,b; International Wheat Genome Sequencing Consortium (IWGSC) et al., 2018]. Of these, genes for 26 α-gliadins, 11 γ-gliadins, two δ-gliadins, seven ω-gliadins, and 10 LMW-GS encode full-length proteins. Transcriptomic studies further revealed wide ranges of expression levels for individual genes within the families. Additionally, Altenbach et al. (2020) used two-dimensional gel electrophoresis (2-DE) combined with tandem mass spectrometry (MS/MS) to link individual protein spots in a total protein extract from CS flour to 16 of 26 α-gliadin, 10 of 11 γ-gliadin, one of two δ-gliadin, and six of seven ω-gliadin genes. Most of the genes that were not associated with protein spots encoded proteins that were very similar to other proteins or were expressed at low levels in transcriptomic experiments.

In efforts to reduce the immunogenic potential of wheat flour, many research groups are now using classical breeding methods or biotechnology techniques to eliminate gliadins that contain immunogenic sequences from wheat flour. Mutation breeding using ethyl methanesulfonate (EMS) or γ ray-irradiation, gene silencing by RNA interference (RNAi), and genome editing techniques such as CRISPR/Cas9 can be used to inactivate or delete single genes (EMS, CRISPR, and RNAi), multiple homologous genes (CRISPR, RNAi) or blocks of genes at particular chromosomal locations (γ ray-irradiation). Critical for these efforts is the availability of high-throughput screening methods that can be used as a first step in selecting lines with altered gliadin contents.

In this study, we optimized matrix-assisted laser desorption/ionization time-of-flight mass spectrometry (MALDI-TOF-MS) and reversed-phase high-performance liquid chromatography (RP-HPLC) methods for the analysis of gliadins. By using the reference wheat CS for this study, we were able to take into account the recently published set of gliadin sequences to determine whether the methods have sufficient resolution to reveal the complexity of this group of proteins. In addition, the analysis of aneuploid lines from CS made it possible not only to confirm the chromosomal locations of gliadins found in different peaks of the chromatograms, but also to determine whether lines that are missing regions of chromosomes with multiple gliadin genes could be distinguished. In this paper, we discuss the advantages and limitations of MALDI-TOF-MS and RP-HPLC for use in early screening experiments.

MATERIALS AND METHODS

Plant Materials

Chinese Spring (*Triticum aestivum* L.) and its group 1 and 6 aneuploid lines were kindly provided by National Bioresource Project, Japan. The plants were grown and harvested at National Institute of Agricultural Sciences, Jeonju, South Korea in 2017.

Extraction of Gliadin and Glutenin

For MALDI-TOF-MS analysis, gliadin was prepared as described by Dziuba et al. (2014). Thirty mg of flour was mixed with 150 μl 0.15 M NaCl solution and shaken for 2 h. After centrifugation at 12,000 rpm for 10 min, the supernatant containing albumin/globulin was discarded. The gliadin in the pellet was dissolved and extracted with 150 μl of 60% EtOH for 2 h. After centrifugation at 12,000 rpm for 5 min, 100 μl of the supernatant was moved to a new tube and stored at 4°C.

For RP-HPLC analysis, gliadins were prepared as described by DuPont et al. (2000). One-hundred mg of flour was dissolved in 1 ml of 70% EtOH and shaken for 2 h at room temperature. Gliadin proteins were extracted with 70% EtOH or 70% EtOH containing 0.15% NaCl. After centrifugation at 12,000 rpm for 10 min, 1 ml of the supernatant fraction was transferred to a new 1.5-ml tube and freeze-dried for 3 h. The dried gliadins were stored at −80°C until use.

For detection of contaminated LMW-GS peaks in RP-HPLC analysis of the gliadin fraction, glutenins were prepared as described by Singh et al. (1991). One-hundred mg of flour was extracted with 5 ml of 50% propanol with incubation for 30 min at 65°C, followed by centrifugation for 5 min at 10,000 *g*. The supernatant containing gliadin was removed and the residue containing glutenin was resuspended in 500 μl of extraction buffer (50% propanol, 0.08 M Tris–HCl, pH 8.0) containing 2%

dithiothreitol (DTT). The samples were incubated for 30 min at 65°C. After a 5 min centrifugation, 500 μl of extraction buffer containing 1.4% 4-vinylpyridine for alkylation was added to the supernatant. After incubation for 15 min at 65°C and centrifugation for 5 min, the supernatant was transferred to a new tube and stored at −80°C until use.

All extractions were performed at least two times.

Analysis of Gliadin Using MALDI-TOF-MS

Two matrices were prepared according to the double layer method of instrument maker's manual using sinapic acid (SA). Matrix I consisted of SA saturated in EtOH at a concentration of 10 mg/500 μl and matrix II consisted of SA saturated in 0.3% trifluoroacetic acid (TFA) in 50% acetonitrile (ACN) at a concentration of 200 mg/10 ml. Matrix I (1 μl) was spotted onto a MSP 96 target polished steel (Bruker Daltonics, Bremen, Germany) and allowed to air dry for approximately 5 min at room temperature. Each sample (1 μl) was diluted into 50 μl of matrix II and 1–1.5 μl of the sample/matrix II mixture was deposited onto the top of the matrix thin layer and then dried at room temperature. Gliadins were measured on a MALDI Microflex LT instrument equipped with a 60 Hz nitrogen laser (Bruker Daltonics, Bremen, Germany). Mass spectra were recorded in the linear positive mode and externally calibrated using a mixture of peptide/protein standards. To increase detection sensitivity, the following conditions were used: mass range 22,491–61,376 Da, sample rate 1.00 GS/s, laser shots 100, laser power 85%, laser frequency 60, and detector gain 33X. Each extracted sample was analyzed at least five times.

Analysis of Gliadins Using RP-HPLC

Gliadin fractions were analyzed by RP-HPLC using a Waters Alliance e2695 equipped with an Agilent ZORBAX 300SB-C18 column (5 μm, 4.6 × 250 mm i.d., Agilent Technologies, United States). Water and ACN, both containing 0.1% TFA, were used as the mobile phase A and B. Dried gliadin pellets were mixed completely in 500 μl of 0.1% TFA in 20% ACN and filtered using a PVDF syringe filter (0.45 μm, Whatman, Maidstone, United Kingdom). Ten μl of each sample was injected and a linear gradient of 25–50% of solvent B was applied. The RP-HPLC analysis of gliadin was carried out with a flow rate of 1 ml/min at a column oven temperature of 65°C and monitored at a wavelength of 210 nm. Each extracted sample was analyzed at least five times.

RESULTS

Sample Optimization for MALDI-TOF-MS

To optimize the resolution of the gliadin proteins in MALDI-TOF-MS analysis, we extensively tested three major factors. These included extraction solvents, dilution volumes, and composition of matrix II for protein ionization (**Table 1** and **Figure 1**).

Extraction Solvents

To verify the effects of extraction solvents in mass spectra, we optimized the gliadin protein extraction from whole wheat grains according to the two previously reported methods (Dziuba et al., 2014; Han et al., 2015). The difference between the two methods is the use of 0.15 M NaCl to remove salt-soluble albumins and globulins before extracting gliadins with aqueous alcohol. Four extraction conditions were tested and compared: 60% EtOH, 70% EtOH, 0.15 M NaCl + 60% EtOH, and 0.15 M NaCl + 70% EtOH. Unexpectedly, two ω-5 gliadin peaks in the mass range of about 50–57 kDa were not detected in the gliadin fractions extracted with either 60 or 70% EtOH, but were present in those extracted with 0.15 M NaCl plus EtOH (**Figure 1A**). The best resolution was obtained from the gliadin fraction extracted with 60% EtOH after treatment with 0.15 M NaCl (**Figure 1A**).

Dilution Volume

The effects of different dilution volumes (25, 50, 75, and 100 μl) were investigated to find the optimal volume of sample to dissolve in matrix II. As shown in **Figure 1B**, the mass spectra of the four dilution volumes were almost the same, and the 50 μl dilution volume was selected for MALDI-TOF-MS analysis and for reducing the amount of matrix II (**Figure 1B**).

Matrix II and Optimization of Ratios of the Solvent

For matrix II, we added the ionization solvent SA, which is mainly used to ionize relatively high molecular weight proteins. TFA was added for sharpness of peaks and good resolution at concentrations of 0.1, 0.3, and 0.5%. We also optimized the amount of acetonitrile (ACN) (30% or 50%) in the MALDI-TOF-MS analysis of gliadin proteins. The mass spectra of gliadins with the solvent containing 50% ACN and 0.3% TFA with SA was found to be optimal (**Figure 1C**).

Based on the results described above, we concluded that the optimal method for sample preparation was first to extract gliadins with 60% EtOH containing 0.15 M NaCl. After mixing 1 μl of the gliadin mixture with 50 μl of a solvent of 50% ACN

TABLE 1 | Major factors used in this study to optimize mass spectra of MALDI-TOF-MS in gliadin fraction of Chinese Spring (CS).

Factor	Parameter
Extraction solvents	60% EtOH
	70% EtOH
	0.15 M NaCl + 60% EtOH
	0.15 M NaCl + 70% EtOH
Dilution volume	10 μl
	50 μl
	75 μl
	100 μl
Matrix II components	SA dissolved in 0.1% TFA in 30% ACN
	SA dissolved in 0.1% TFA in 50% ACN
	SA dissolved in 0.3% TFA in 30% ACN
	SA dissolved in 0.3% TFA in 50% ACN
	SA dissolved in 0.5% TFA in 30% ACN
	SA dissolved in 0.5% TFA in 50% ACN

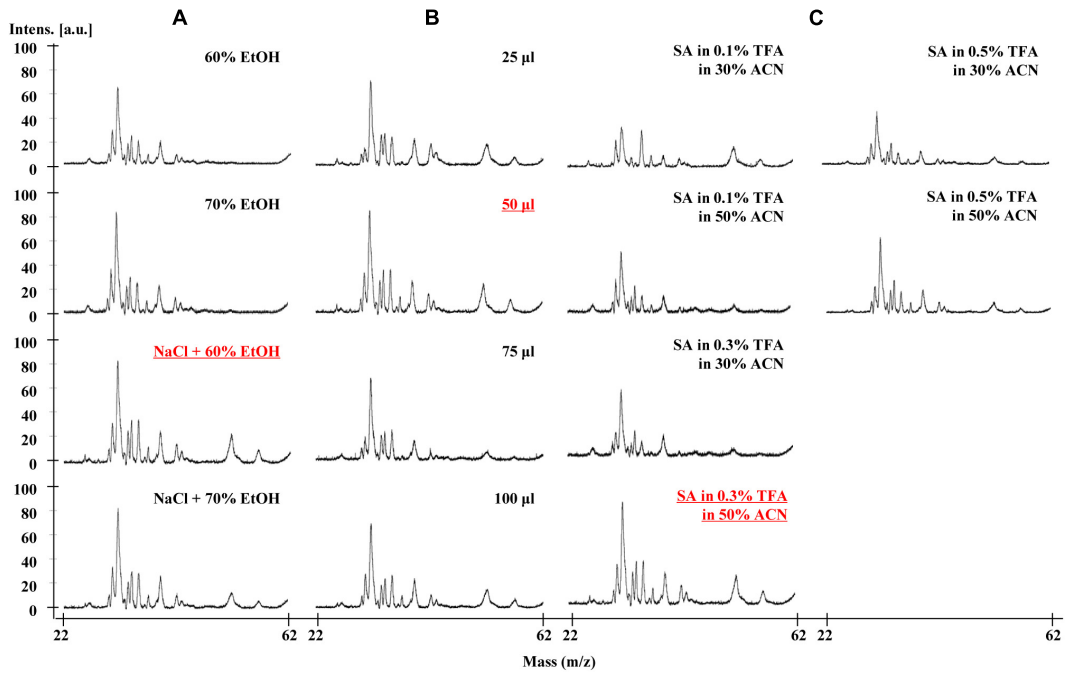

FIGURE 1 | Effects of three major factors on MALDI-TOF-MS resolution of Chinese Spring gliadins. **(A)** gliadin extraction solvents, **(B)** dilution volume, and **(C)** matrix II components. The optimal conditions showing good resolution are underlined.

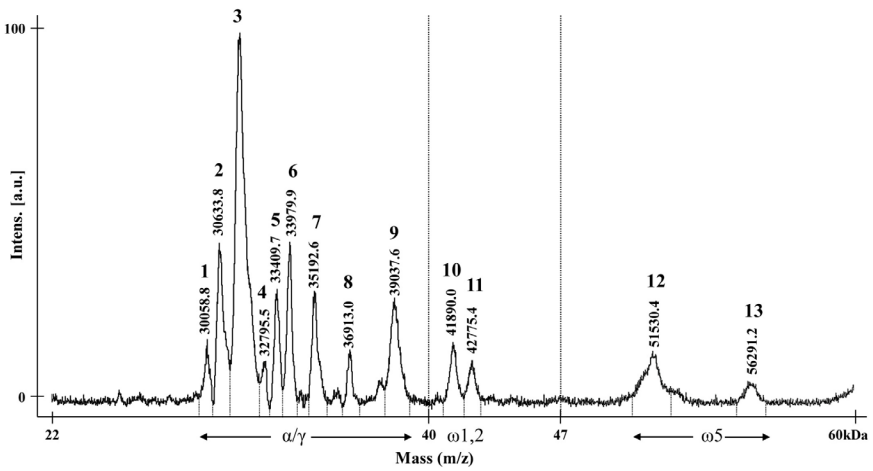

FIGURE 2 | MALDI-TOF mass spectrum of gliadin fraction from Chinese Spring. The numbers for each gliadin peak and their observed molecular weights are indicated. Regions of α-, γ-, and ω-gliadin subgroups are shown with arrows.

and 0.3% TFA with SA, 1 µl of the total mixture was loaded onto the target plate for MALDI-TOF-MS analysis.

Analysis of Gliadin Proteins by MALDI-TOF-MS

The optimized method was used to analyze the gliadin profiles of CS wheat. The mass spectrum of gliadin extracts from CS showed 13 distinct peaks (**Figure 2**). The molecular ion signals of nine peaks at approximately 29–40 kDa, two peaks at approximately 40–44 kDa, and two peaks at approximately 50–57 kDa, likely correspond to α/γ-, ω-1, 2-, and ω-5 gliadins, respectively (Ferranti et al., 2007; Gil-Humanes et al., 2008; Sánchez-León et al., 2018).

Gliadins prepared from 10 nullisomic-tetrasomic (NT) lines for the group 1 or 6 chromosomes and three ditelosomic (DT) lines lacking the short arm of the group 6 chromosomes in the CS background were also analyzed in an attempt to assign proteins in peaks to specific chromosomes (**Figure 3** and **Table 2**). Eight peaks (2, 7, 8, 9, 10, 11, 12, 13) were associated with the

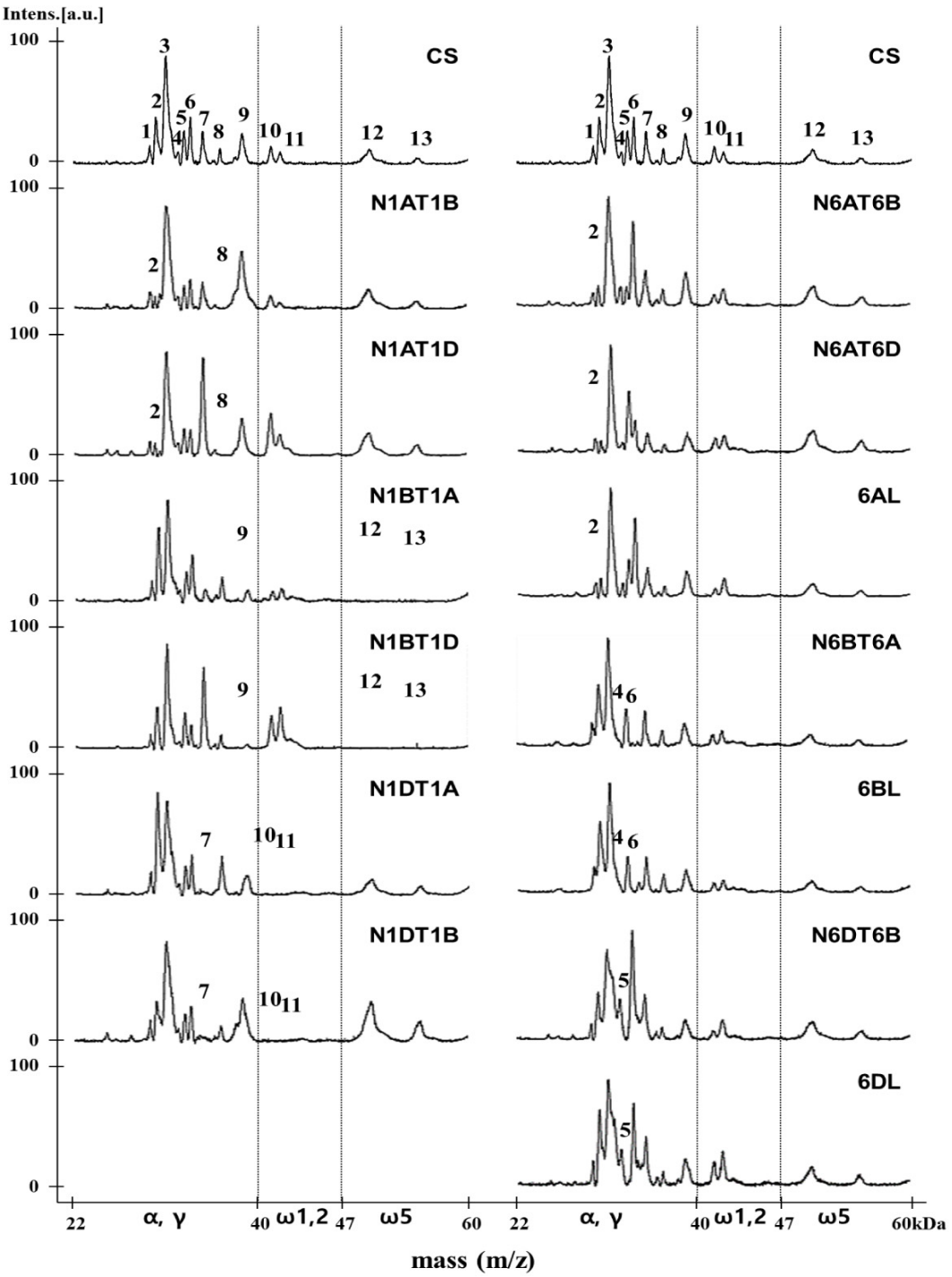

FIGURE 3 | MALDI-TOF-MS profile analysis of gliadin fractions from Chinese Spring and its group 1 and 6 aneuploid lines to assign gliadin peaks to 1A, 1B, 1D, 6A, 6B, and 6D chromosomes. The numbers of distinctly reduced or missing peaks are marked on each mass spectrum of corresponding aneuploid lines of Chinese Spring.

Gli-A1, *Gli-B1*, and *Gli-D1* loci. In the mass spectra of aneuploid lines N1AT1B and N1AT1D (which lack chromosome 1A), Peak 2 was drastically decreased while Peak 8 disappeared. Thus, these two peaks likely correspond to γ-gliadins on chromosome 1A. This assignment was supported by our findings that Peaks 2 and 8 increased in lines N1BT1A and N1DT1A (which lack chromosomes 1B and 1D, respectively, but have an extra copy of chromosome 1A). Peak 9 was significantly reduced

TABLE 2 | Characteristics of 13 gliadin peaks resolved by MALDI-TOF-MS in Chinese Spring and its aneuploid lines, comparison with proteins deduced from full-length gliadin genes by Huo et al. (2018a; 2018b), and with results of quantitative 2-DE analysis reported by Altenbach et al. (2020).

MALDI-TOF-MS				Huo et al., 2018a,b		Altenbach et al., 2020	
Peak	**Range[a]**	**Chromosome[b]**	**Gliadin[c]**	**Gene[d]**	**Predicted MW[e]**	**2-DE Spot#**	**Spot volume[f]**
1	29800–30300	Unknown		α-A10	29,996	117,118	0.8
				α-D12	30,175		
2	30300–31200	1A	γ	α-A4	30,506	119,120	1.8
		6A	α	α-A6	30,621	121,122,123	0.5
				γ-A3[g]	30,655	123, 124,125,126	2.9
				γ-A4[g]	30,655	123,124,125,126	2.9
				α-D1	30,699		
				α-D9	30,810		
				γ-B6	30,982	121,122,123,139	0.8
				α-A8	31,050		
3	31200–32500	Unknown		α-B15	31,284		
				α-B14	31,413	109,112	0.7
				α-D8[h]	31,435	84,85,107,111,113,114	2.1
				α-A1	31,440	111,113,114	1.4
				α-B11	31,535		
				α-D4	31,542	108,109	1.4
				γ-D3	31,619	109	0.3
				α-D6[h]	31,706	102	0.4
				α-B18	31,829		
				γ-B2	31,834	102	0.4
				γ-D4	31,865		
				α-B17	32,039	82	0.2
				α-B16	32,054	113	0.1
				α-A9	32,181		
				γ-B1[h]	32,431	99	0.4
4	32500–33050	6B	α	γ-D1[h]	32,606	99,100,102,107	1.1
5	33050–33600	6D	α	α-D5	33,412	103,106,110,112	1.7
				α-A5	33,479		
6	33600–34300	6B	α	α-B25	33,818		
				α-B7	33,968	85,104	0.5
				α-B9	33,977	105	0.9
NP	34300–34900			α-A2	34,471	81,82,83,84	0.8
				δ-B1	34,558		
				α-B8	34,781	86,91	0.9
7	34900–35900	1D	γ	γ-D2	35,188	86,101	1.7
				δ-D1	35,450	80.81.82	0.9
NP	35900–36600			α-B3	36,206	62	0.3
8	36600–37300	1A	γ	γ-A1	36,892	61.77.78	1.9
9	38600–39900	1B	γ	ω-A4[i]	39,651	37,75,79	1.1
				γ-B4	39,892	74,75,76,78	1.9
10	41550–42400	1D	ω-1,2	c[h,i]	41,831	34,35	0.5
11	42400–43200	1D	ω-1,2	ω-D2[g,i]	42,744	31,32	3.5
				ω-D3[g,i]	42,744	31,32	3.5
NP	43200–50500			ω-D4[j]	44,416	43	0.3
				ω-B3	47,650		
12	50500–52000	1B	ω-5	ω-B6	51,532	25,27,28,29	6.3
13	55600–56800	1B	ω-5				

*[a]Mass range from the beginning to the end of each peak as shown in **Figure 2**. Mass ranges not associated with specific peaks are designated as NP in column 1. [b]Assigned chromosome determined by comparing MALDI-TOF-MS profiles of Chinese Spring and its aneuploid lines. [c]Assigned gliadin protein determined by comparing MALDI-TOF-MS profiles of Chinese Spring and its aneuploid lines, and by mass range. [d]Gliadin genes that encode full-length proteins within the mass range of each peak. [e]Mature protein following removal of signal peptide. [f]% total normalized volume determined by quantitative 2DE analysis. [g]Genes encode identical proteins; the same spot numbers and % total normalized volume are reported for both genes. [h]Genes encode proteins containing an odd number of cysteine residues that are likely to partition in the glutenin fraction. [i]The second predicted MW as a result of processing with an asparingyl protease is not indicated. [j]Considered pseudogenes in Huo et al., 2018a but they contained stop codon near 3′ end resulting in truncated proteins reported by Altenbach et al., 2018, 2020.*

in the α/γ-gliadin region and Peaks 12 and 13 disappeared completely in the ω-5 gliadin region in lines N1BT1A and N1BT1 (missing chromosome 1B). Because these peaks also increased in lines N1AT1B and N1DT1B (containing an extra chromosome 1B), they were assigned to chromosome 1B. Peak 7 in the α/γ-gliadin region and Peaks 10 and 11 in the ω-1,2 gliadin region were assigned to chromosome 1D by comparing the mass spectra of lines N1DT1A and N1DT1B (missing chromosome 1D) and N1AT1D and N1BT1D (containing an extra copy of chromosome 1D).

The comparison of MALDI-TOF mass spectra of the group 6 aneuploid lines missing genes encoding α-gliadins with that of CS allowed the assignment of four peaks (2, 4, 5, 6) to the *Gli-2* loci (**Figure 3** and **Table 2**). In the mass spectra of lines N6AT6B, N6AT6D, and 6AL (which lack chromosome 6A or the short arm of chromosome 6A (6AS), Peak 2 was very small, whereas it was increased in line N6BT6A (containing an extra copy of chromosome 6A), indicating that Peak 2 corresponds to α-gliadins on chromosome 6A. Considering the results in the previous paragraph, gliadins in Peak 2 were assigned to two chromosomes, 1A and 6A. The profiles of lines N6BT6A and 6BL (which are missing chromosome 6B or 6BS), enabled us to assign Peaks 4 and 6 to chromosome 6B. This assignment was also supported by an increase of the two peaks in line N6DT6B (containing an extra chromosome 6B). Peak 5 was assigned to chromosome 6D by analyzing the mass spectra of lines N6DT6B and 6DL (missing chromosomes 6D or 6DS, respectively), and N6AT6D (containing an extra copy of chromosome 6D). Of the 13 peaks in MALDI-TOF mass spectra for CS, 10 peaks were assigned to either chromosomes 1 or 6, one peak (2) was assigned to both chromosomes 1 and 6, and two peaks (1, 3) could not be assigned.

The availability of the sequences for the complete set of full-length gliadin genes from CS (Huo et al., 2018a,b) made it possible to compare the observed molecular weights (MWs) of peaks in the CS gliadin fraction determined by MALDI-TOF-MS to the predicted MWs of the mature proteins. **Table 2** shows the mass ranges corresponding to the beginning and end of peaks observed in MALDI-TOF-MS (**Figure 2**). Gliadin proteins with predicted MWs in the mass range of each peak are also shown along with their accumulation levels in wheat flour measured by quantitative 2-DE analysis combined with MS/MS (Altenbach et al., 2020).

Peak 1 was a minor peak in the MALDI-TOF spectrum that could not be assigned to any chromosome. Two CS gliadins fell in the mass range of this peak, α-A10 and α-D12. However, only α-A10 was also observed by 2-DE. Peak 2 was assigned to chromosomes 1A and 6A. Five α-gliadins (α-A4, α-A6, α-A8, α-D1, and α-D9) and three γ-gliadins (γ-A3, γ-A4, and γ-B6) fell in the mass range of this peak. However, α-gliadins encoded by chromosome 6D were not observed in 2-DE and the gliadins encoded on chromosome 1A and 6A encompassed the bulk of the 2-DE spot volume, consistent with the chromosomal assignment. Fifteen CS gliadins fell within the mass range of peak 3, although three (α-D6, α-D8, and γ-B1) contained an odd number of cysteine residues and likely partition into the glutenin fraction rather than the gliadin fraction. Two, 6 and 2 of the remaining α-gliadins were from the 6A, 6B, and 6D chromosomes, respectively, while 1 and 2 of the remaining γ-gliadins were from the 1B and 1D chromosomes, respectively. Not surprisingly, it was not possible to assign this peak to a particular chromosome using the aneuploid lines. Peak 4 was a very minor peak that was assigned to chromosome 6B. However, the only protein that fell into its mass range was γ-D1 containing an odd number of cysteine residues. Peak 5 was assigned to chromosome 6D and has two gliadin proteins in its mass range, α-A5 and α-D5. However, α-A5 was not observed in the 2-DE analysis. Interestingly, α-D5 is the only α-gliadin in CS that contains the 33-mer toxic peptide, a major trigger for celiac disease (Shan et al., 2002). Gliadins that fell within the mass ranges of peaks 6, 7, 8 were consistent with their chromosomal assignments. Peak 9 was assigned to chromosome 1B, however, both γ-B4 and ω-A4 fell into its mass range. γ-B4 accounted for a greater proportion of the spot volume in quantitative 2-DE. ω-gliadins that fell within the mass ranges of peaks 10, 11 and 12 were consistent with their chromosomal assignments although it should be noted that ω-D1 contains a single cysteine residue. Peak 13 was assigned to chromosome 1B, but there was no gliadin protein corresponding to its mass range. However, it is interesting that one of the four protein spots identified by MS/MS as ω-B6 had a notably slower mobility in 2-DE than the other spots (Altenbach et al., 2020).

Analysis of Gliadin Proteins by RP-HPLC

Gliadin fractions from CS also were extracted and analyzed by RP-HPLC with resolution optimized by adjusting elution time, temperature, flow rate, and solvent conditions as described in the Materials and Methods. As shown in **Figure 4**, **34** peaks from CS were eluted according to their hydrophobicity. To ensure that the gliadins were not contaminated with other proteins, the glutenin fraction of CS was extracted using 50% propanol, and RP-HPLC was conducted under the same analytical conditions. The chromatograms of the gliadin and glutenin fractions were compared. Peaks 15, 16, and 17 were identified as likely LMW-GS (**Supplementary Figure 1**). Similarly, to identify possible contamination of the extract with salt-soluble albumins/globulins, gliadin proteins were extracted with 70% EtOH and 70% EtOH containing 0.15 M NaCl. Comparison of the chromatograms from the two extraction methods showed that Peaks 4, 5, and 6 were likely albumins/globulins (**Supplementary Figure 1**). Thus, ω-5 gliadins eluted in three peaks (1–3) between 5 and 13 min, and ω-1,2 gliadins eluted in four peaks (7–10) between 19 and 25 min. α-gliadins were between 25 and 38.5 min and separated into 13 peaks (11–14, 18–27). γ-gliadins eluted in seven peaks (28–34) between 39 and 60 min (**Figure 4**).

By comparing the chromatogram patterns of RP-HPLC of CS and its aneuploid lines for group 1 and 6 chromosomes, the positions of gliadin peaks encoded by each chromosome were determined (**Figure 5**). To identify gliadin peaks encoded by chromosome 1A, we compared the chromatograms of CS with those of lines N1AT1B and N1AT1D. Peaks 8–10 of ω-1,2 gliadin were reduced, leaving only traces, and peaks 32 and 33 of γ-gliadin disappeared. The conclusion that peaks 8, 9, and 10 of ω-1,2 gliadin are encoded by chromosome 1A

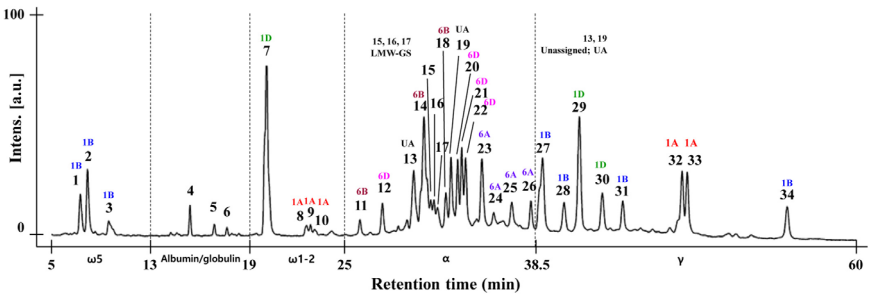

FIGURE 4 | RP-HPLC analysis of gliadin fraction from Chinese Spring. The eluted peak number and the result of chromosomal assignment of individual peaks by comparing the RP-HPLC pattern with group 1 and 6 aneuploid lines are indicated. The position of albumin/globulin proteins (Peaks 4, 5, 6), contaminated LMW-GS (Peaks 15, 16, 17) and unassigned peaks (UA, Peaks 13, 19) are shown as explained in section "Analysis of Gliadin Proteins Using RP-HPLC" of the Results.

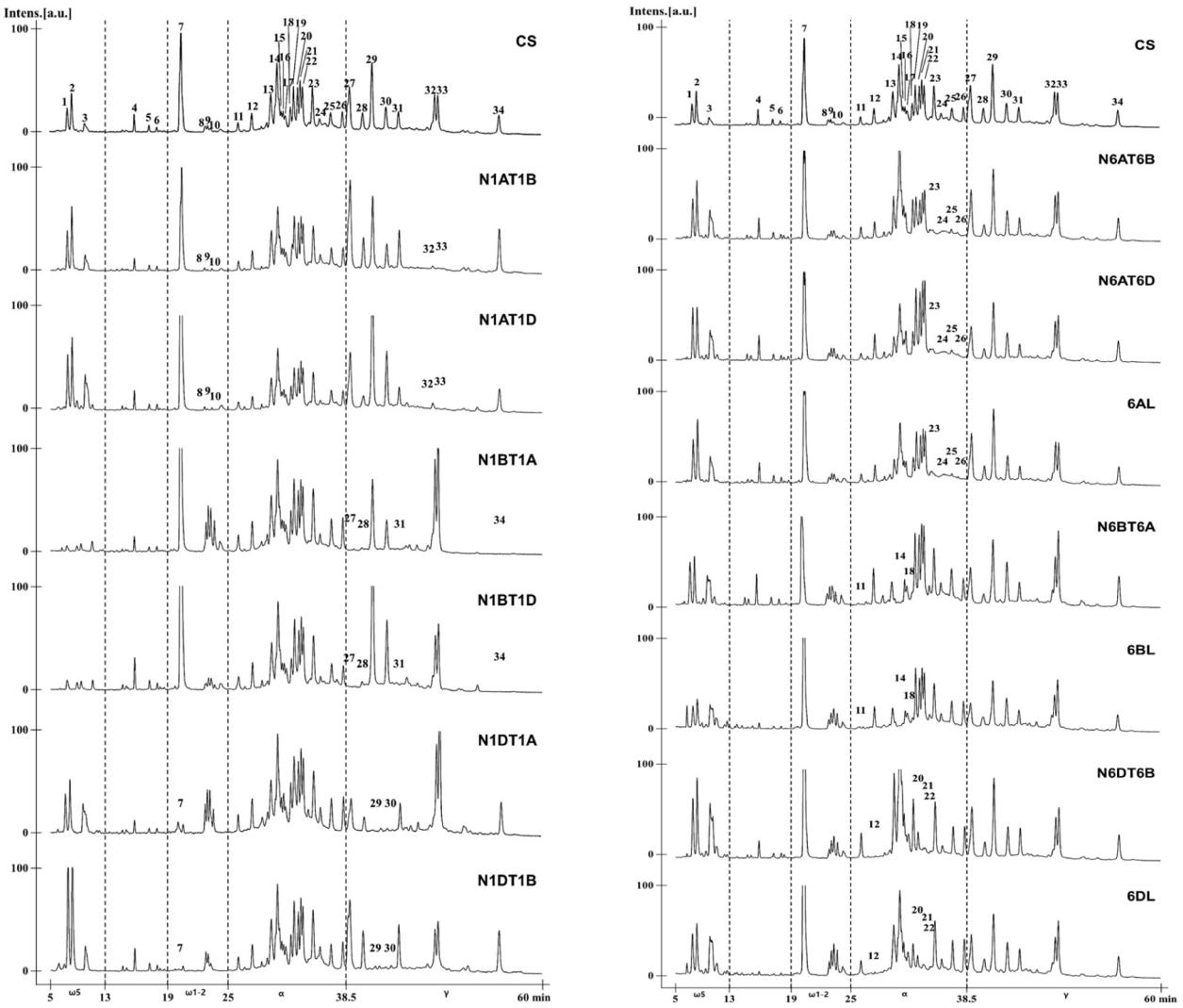

FIGURE 5 | RP-HPLC pattern analysis of gliadin fractions from Chinese Spring and its group 1 and 6 aneuploid lines to assign gliadin peaks to 1A, 1B, 1D, 6A, 6B, and 6D chromosomes. The numbers of distinctly reduced or missing peaks are marked on the chromatogram for the corresponding aneuploid lines of CS.

was also supported by an increase of these three peaks in the 1A tetrasomic lines, N1BT1A and N1DT1A. For detection of gliadin proteins encoded by chromosome 1B, we analyzed the RP-HPLC profiles of CS and the chromosome 1B aneuploid lines, N1BT1A and N1BT1D, and observed that peaks 1, 2, and 3 of ω-5 gliadin were reduced, leaving only traces, and peaks 27, 28, 31, and 34 of γ-gliadin were absent. The traces of peaks 1, 2, and 3 in lines N1BT1A and N1BT1D were assumed to be ω-5 gliadins encoded by ω-D4 on chromosome 1D rather than chromosome 1B, as its expression level is very low (Altenbach et al., 2018, 2020; Huo et al., 2018a). Lines N1DT1A and N1DT1B were used to assign gliadin peaks encoded by chromosome 1D. In these lines, peak 7 of ω-1,2 gliadin and peaks 29 and 30 of γ-gliadin were almost absent. Therefore, among chromosome 1A- and 1D-encoded ω-1,2 gliadins in CS, chromosome 1D encodes the most abundant form.

The NT and DT lines deficient in chromosomes 6A/6AS, 6B/6BS, and 6D/6DS were used to assign gliadin peaks to chromosome 6 (**Figure 5**). Comparison of RP-HPLC profiles of N6AT6B, N6AT6D, and 6AL (null 6A/6AS) lines with that of CS revealed that peaks 23, 24, 25, and 26 of α-gliadin were associated with chromosome 6A. In lines N6BT6A and 6BL (which lack chromosome 6B/6BS), peaks 11, 14, and 18 were absent in the α-gliadin region. In the profiles of lines N6DT6B and 6DL (which lack chromosomes 6D/6DS), peaks 12, 20, 21, and 22 were absent. When combining the comparative analysis of all RP-HPLC profiles, only two peaks (13 and 19) out of 35 peaks could not be assigned to group 1 or 6 chromosomes.

As shown in **Figure 4**, the area of ω- 5-, ω-1, 2-, and γ-gliadin peaks were well separated, but peaks 13–22, mainly assigned to chromosomes 6B and 6D α-gliadin, were difficult to separate. This difficulty can be explained by the grand average of the hydropathicity index (GRAVY) of the 28 full-length gliadin genes of CS with a 2-DE spot volume of 0.4 or higher (**Supplementary Table 1**). The GRAVY is used to represent the hydrophobicity value of a peptide and calculates the sum of the hydropathy values for all the amino acids divided by the sequence length. From these data, it can be seen that the GRAVY was very similar in each of the α-gliadins derived from chromosomes 6A, 6B, and 6D compared to other gliadin subgroups.

DISCUSSION

MALDI-TOF-MS and RP-HPLC procedures were optimized and assessed for use as automatable, high-throughput methods for screening wheat lines with altered gliadin compositions. MALDI-TOF-MS separates proteins on the basis of molecular mass and is attractive because the complete analysis of gliadin proteins in a sample can be completed in about 1 min. RP-HPLC, on the other hand, separates proteins on the basis of hydrophobicity and has been used to analyze gliadin fractions in wheat flours for many years (Brown and Flavell, 1981; Bietz, 1983; Bietz and Burnouf, 1985; Liu et al., 2005; Han et al., 2015; Sánchez-León et al., 2018). However, analysis time per sample is considerably greater than MALDI-TOF-MS, about 70 min per sample.

Both ω-5 and ω-1,2 gliadins were easily resolved by MALDI-TOF-MS. Since ω-5 gliadins contain numerous epitopes that trigger WDEIA and ω-1,2 gliadins contain immunodominant epitopes for CD, both are likely targets for efforts to reduce immunogenic potential of the flour. In comparison, it was difficult to separate individual α- and γ-gliadins because many of the proteins had very similar molecular masses. This represents a fundamental limitation of the MALDI-TOF-MS method. In fact, in one case a single peak in the spectrum likely contained as many as 12 α- and γ-gliadins. Because these gliadins were encoded on chromosomes 6A, 6B, 6D, 1B and 1D, it was also impossible to assign this peak to a single chromosome. This suggests that it would be difficult to detect deletions of multiple α- and γ-gliadin genes on a single chromosome by MALDI-TOF-MS. Nonetheless, three of the nine gamma gliadins that were identified by 2-DE combined with MS/MS in Altenbach et al. (2020) were distinguished by MALDI-TOF-MS. All were relatively abundant proteins encompassing from 1.7 to 1.9% of the total flour protein. Each protein also contained 10 CD epitopes, the most among the CS γ-gliadins. As a result, these γ-gliadins may be the focus of targeted efforts to reduce the immunogenicity of the flour. Only three of 16 α-gliadins identified in 2-DE could be distinguished by MALDI-TOF-MS. It is notable that these included α-D5 in peak 5, and α-B7 and α-B9 in peak 6. Because α-D5 contains the 33-mer toxic peptide, this protein is also a likely candidate for targeted efforts to reduce the immunogenicity of the flour. In comparison, α-B7 and α-B9 do not contain CD epitopes and the presence of this peak in a sample could provide evidence that efforts to selectively eliminate only those proteins containing abundant CD epitopes were effective. Thus, MALDI-TOF-MS could be useful as a rapid screening method, depending on the overall goals of the experiment. Thus far, MALDI-TOF-MS has been used to screen wheat lines in two studies, one that used RNAi (Gil-Humanes et al., 2008) and one that used gene editing to reduce immunogenic potential (Sánchez-León et al., 2018).

Like MALDI-TOF-MS, RP-HPLC effectively separated both ω-5 and ω-1,2 gliadins. Additionally, proteins in the α- and γ-gliadin families were separated by RP-HPLC and a greater number of proteins within each family were resolved. Of the 13 peaks assigned to α-gliadins, four were assigned to chromosome 6A, three to 6B, four to 6D and two were unassigned. Of the 8 peaks assigned to γ-gliadins, two were from chromosome 1A, four from 1B, and two from 1D. In comparison, 16 and 9 protein spots were identified as α- and γ-gliadins, respectively, in quantitative 2-DE experiments of CS (Altenbach et al., 2020). Thus, the RP-HPLC profile of the gliadin fraction generated in this study revealed most of the major gliadin proteins expressed in CS wheat flour. Although most peaks could be assigned to individual chromosomes using the CS aneuploid lines, it was not possible to discern which proteins were found in each peak, a potential drawback of RP-HPLC. Further analysis of peaks by MALDI-TOF-MS or MS/MS is therefore required to identify individual proteins. In the final analysis, it is probably easier to detect overall changes in α- and γ-gliadins by RP-HPLC

than MALDI-TOF-MS, despite the longer analysis time. If chromosomal assignments can be made, it should also be possible to detect deletions of multiple gliadin genes on a single chromosome. However, it is important to keep in mind that aneuploid lines are not available for many cultivars.

Undoubtedly, experiments aimed at reducing the immunogenic potential of flour will be conducted in commercial cultivars grown in various parts of the world rather than in the reference cultivar CS. Because of tremendous allelic variation among cultivars, the complement of gliadins in each cultivar will need to be evaluated. Fortunately, the availability of a reference sequence from CS makes it possible to use gene capture methods to obtain the sequences of gliadins from many different cultivars. Analyses of these sequences will reveal the number of epitopes for CD and food allergies in each protein and highlight the best approaches to reduce the immunogenic potential of the flour. Only then will it be possible to determine whether MALDI-TOF-MS or RP-HPLC is most appropriate for screening altered lines. In any event, it is important to keep in mind that such analyses are only the first screening step and that more robust, time-consuming, and technically challenging methods such as 2-DE combined with MS/MS must ultimately be used to thoroughly characterize the selected lines.

DATA AVAILABILITY STATEMENT

The raw data supporting the conclusions of this article will be made available by the authors, without undue reservation.

AUTHOR CONTRIBUTIONS

J-YL, Y-RJ, and KC designed and conducted the experiments, and wrote the manuscript. YG, SA, T-WG, B-GK, and S-HL contributed to the interpretation of data. SK, J-RS, and S-BL conducted the experiments. All authors contributed to the article and approved the submitted version.

FUNDING

This work was supported by grants from the National Institute of Agricultural Sciences (RDA PJ014838) and the Next-Generation BioGreen 21 Program (RDA PJ013159 and RDA PJ013149), South Korea.

SUPPLEMENTARY MATERIAL

The Supplementary Material for this article can be found online at: https://www.frontiersin.org/articles/10.3389/fpls.2020.600489/full#supplementary-material

Supplementary Figure 1 | RP-HPLC pattern analysis of two gliadin extraction methods (70% EtOH and 0.15 M NaCl + 70% EtOH) and glutenin fraction to confirm salt soluble albumin/globulin (Peaks 4, 5,6) and contaminated LMW-GS (Peaks 15, 16, 17).

Supplementary Table 1 | Grand average of hydropathicity index (GRAVY) for 28 full-length gliadin proteins of Chinese Spring with 2-DE spot volume of 0.4 or higher.

REFERENCES

Altenbach, S. B., Chang, H. C., Simon-Buss, A., Jang, Y. R., Denery-Papini, S., Pineau, F., et al. (2018). Towards reducing the immunogenic potential of wheat flour: omega gliadins encoded by the D genome of hexaploid wheat may also harbor epitopes for the serious food allergy WDEIA. *BMC Plant Biol.* 18:291. doi: 10.1186/s12870-018-1506-z

Altenbach, S. B., Chang, H. C., Simon-Buss, A., Mohr, T., Huo, N., and Gu, Y. Q. (2020). Exploiting the reference genome sequence of hexaploid wheat: a proteomic study of flour proteins from the cultivar Chinese Spring. *Funct. Integr. Genomics* 20, 1–16. doi: 10.1007/s10142-019-00694-z

Anderson, O. D., Dong, L., Huo, N., and Gu, Y. Q. (2012). A new class of wheat gliadin genes and proteins. *PLoS One* 7:e52139. doi: 10.1371/journal.pone.0052139

Battais, F., Courcoux, P., Popineau, Y., Kanny, G., Moneret-Vautrin, D. A., and Denery-Papini, S. (2005a). Food allergy to wheat: differences in immunoglobulin E-binding proteins as a function of age or symptoms. *J. Cereal Sci.* 42, 109–117. doi: 10.1016/j.jcs.2005.01.004

Battais, F., Mothes, T., Moneret-Vautrin, D. A., Pineau, F., Kanny, G., Popineau, Y., et al. (2005b). Identification of IgE-binding epitopes on gliadins of patients with food allergy to wheat. *Allergy* 60, 815–821. doi: 10.1111/j.1398-9995.2005.00795.x

Biagi, F., Zimmer, K. P., Thomas, P. D., Ellis, H. J., and Ciclitira, P. J. (1999). Is gliadin mispresented to the immune system in coeliac disease? A hypothesis. *Q. J. Med.* 92, 119–122. doi: 10.1093/qjmed/92.2.119

Bietz, J. A. (1983). Reversed-phase high-performance liquid chromatography of cereal endosperm proteins. *J. Chromatogr.* 255, 219–238. doi: 10.1016/s0021-9673(01)88286-8

Bietz, J. A., and Burnouf, T. (1985). Chromosomal control of wheat gliadin: analysis by reversed-phase high-performance liquid chromatography. *Theor. Appl. Genet.* 70, 599–609. doi: 10.1007/BF00252285

Bittner, C., Grassau, B., Frenzel, K., and Baur, X. J. (2008). Identification of wheat gliadins as an allergen family related to baker's asthma. *J. Allergy Clin. Immunol.* 121, 744–749. doi: 10.1016/j.jaci.2007.09.051

Brown, J. W. S., and Flavell, R. B. (1981). Fractionation of wheat gliadin and glutenin subunits by two-dimensional electrophoresis and the role of group 6 and group 2 chromosomes in gliadin synthesis. *Theor. Appl. Genet.* 59, 349–359. doi: 10.1007/BF00276448

DuPont, F. M., Vensel, W. H., Chan, R., and Kasarda, D. D. (2000). Characterization of the 1B-type omega gliadins from *Triticum aestivum* 'Butte'. *Cereal Chem.* 77, 607–614. doi: 10.1094/CCHEM.2000.77.5.607

Dziuba, M., Nałęcz, D., Szerszunowicz, I., and Waga, J. (2014). Proteomic analysis of wheat α/A-and β-gliadins. *Czech J. Food Sci.* 32, 437–442. doi: 10.17221/600/2013-CJFS

Ferranti, P., Mamone, G., Picariello, G., and Addeo, F. (2007). Mass spectrometry analysis of gliadins in celiac disease. *J. Mass Spectrom.* 42, 1531–1548. doi: 10.1002/jms.1361

Gil-Humanes, J., Pistón, F., Hernando, A., Alvarez, J. B., Shewry, P. R., and Barro, F. (2008). Silencing of γ-gliadins by RNA interference (RNAi) in bread wheat. *J. Cereal Sci.* 48, 565–568. doi: 10.1016/j.jcs.2008.03.005

Han, C., Lu, X., Yu, Z., Li, X., Ma, W., and Yan, Y. (2015). Rapid separation of seed gliadins by reversed-phase ultraperformance liquid chromatography (RP-UPLC) and its application in wheat cultivar and germplasm identification. *Biosci. Biotechnol. Biochem.* 79, 808–815. doi: 10.1080/09168451.2014.998618

Huo, N., Zhang, S., Zhu, T., Dong, L., Mohr, T., Hu, T., et al. (2018a). Gene duplication and evolution dynamics in the homeologous regions harboring multiple prolamin and resistance gene families in hexaploid wheat. *Front. Plant Sci.* 9:673. doi: 10.3389/fpls.2018.00673

Huo, N., Zhu, T., Altenbach, S., Dong, L., Wang, Y., Mohr, T., et al. (2018b). Dynamic evolution of α-gliadin prolamin gene family in homeologous genomes of hexaploid wheat. *Sci. Rep.* 8:5181. doi: 10.1038/s41598-018-23570-5

International Wheat Genome Sequencing Consortium (IWGSC), Appels, R., Eversole, K., Stein, N., Feuillet, C., Keller, B., et al. (2018). Shifting the limits in wheat research and breeding through a fully annotated and anchored reference genome sequence. *Science* 361:eaar7191. doi: 10.1126/science.aar7191

Liu, F., Pan, C. K., Drumm, P., and Ang, C. Y. W. (2005). Liquid chromatography-mass spectrometry studies of St. John's wort methanol extraction: active constituents and their transformation. *J. Pharm. Biomed. Anal.* 37, 303–312. doi: 10.1016/j.jpba.2004.10.034

Matsuo, H., Kohno, K., and Morita, E. (2005). Molecular cloning, recombinant expression and IgE-binding epitope of ω-5 gliadin, a major allergen in wheat dependent exercise-induced anaphylaxis. *FEBS J.* 272, 4431–4438. doi: 10.1111/j.1742-4658.2005.04858.x

Matsuo, H., Morita, E., Tatham, A. S., Morimoto, K., Horikawa, T., Osuna, H., et al. (2004). Identification of the IgE-binding epitope in ω-5 gliadin, a major allergen in wheat-dependent exercise-induced anaphylaxis. *J. Biol. Chem.* 279, 12135–12140. doi: 10.1074/jbc.M311340200

Shan, L., Molberg, O., Parrot, I., Hausch, F., Filiz, F., Gray, G. M., et al. (2002). Structural basis for gluten intolerance in celiac sprue. Science 297, 2275–2279. doi: 10.1126/science.1074129

Sánchez-León, S., Gil-Humanes, J., Ozuna, C. V., Giménez, M. J., Sousa, C., Voytas, D. F., et al. (2018). Low-gluten, nontransgenic wheat engineered with CRISPR/Cas9. *J. Plant Biotechnol J.* 16, 902–910. doi: 10.1111/pbi.12837

Shewry, P. R., and Halford, N. G. (2002). Cereal seed storage proteins: structures, properties and role in grain utilization. *J. Exp. Bot.* 53, 947–958. doi: 10.1093/jexbot/53.370.947

Shewry, P. R., Halford, N. G., and Lafiandra, D. (2003). Genetics of wheat gluten proteins. *Adv. Genet.* 49, 111–178. doi: 10.1016/S0065-2660(03)01003-4

Shewry, P. R., and Tatham, A. S. (1990). The prolamin storage proteins of cereal seeds: structure and evolution. *Biochem. J.* 267, 1–12. doi: 10.1042/bj2670001

Singh, N. K., Shepherd, K. W., and Cornish, G. B. (1991). A simplified SDS-PAGE procedure for separating LMW subunits of glutenin. *J. Cereal Sci.* 14, 203–208. doi: 10.1016/S0733-5210(09)80039-8

Sollid, L. M., Qiao, S. W., Anderson, R. P., Gianfrani, C., and Koning, F. (2012). Nomenclature and listing of celiac disease relevant gluten T-cell epitopes restricted by HLA-DQ molecules. *Immunogenetics* 64, 455–460. doi: 10.1007/s00251-012-0599-z

Tye-Din, J. A., Stewart, J. A., Dromey, J. A., Beissbarth, T., van Heel, D. A., Tatham, A., et al. (2010). Comprehensive, quantitative mapping of T cell epitopes in gluten in celiac disease. *Sci. Transl. Med.* 2, 41–51. doi: 10.1126/scitranslmed.3001012

Conflict of Interest: The authors declare that the research was conducted in the absence of any commercial or financial relationships that could be construed as a potential conflict of interest.

frontiers in Plant Science

ORIGINAL RESEARCH
published: 05 January 2021
doi: 10.3389/fpls.2020.613325

Deep Learning for Predicting Complex Traits in Spring Wheat Breeding Program

*Karansher S. Sandhu[1], Dennis N. Lozada[2], Zhiwu Zhang[1], Michael O. Pumphrey[1] and Arron H. Carter[1]**

[1]Department of Crop and Soil Sciences, Washington State University, Pullman, WA, United States, [2]Department of Plant and Environmental Sciences, New Mexico State University, Las Cruces, NM, United States

Genomic selection (GS) is transforming the field of plant breeding and implementing models that improve prediction accuracy for complex traits is needed. Analytical methods for complex datasets traditionally used in other disciplines represent an opportunity for improving prediction accuracy in GS. Deep learning (DL) is a branch of machine learning (ML) which focuses on densely connected networks using artificial neural networks for training the models. The objective of this research was to evaluate the potential of DL models in the Washington State University spring wheat breeding program. We compared the performance of two DL algorithms, namely multilayer perceptron (MLP) and convolutional neural network (CNN), with ridge regression best linear unbiased predictor (rrBLUP), a commonly used GS model. The dataset consisted of 650 recombinant inbred lines (RILs) from a spring wheat nested association mapping (NAM) population planted from 2014–2016 growing seasons. We predicted five different quantitative traits with varying genetic architecture using cross-validations (CVs), independent validations, and different sets of SNP markers. Hyperparameters were optimized for DL models by lowering the root mean square in the training set, avoiding model overfitting using dropout and regularization. DL models gave 0 to 5% higher prediction accuracy than rrBLUP model under both cross and independent validations for all five traits used in this study. Furthermore, MLP produces 5% higher prediction accuracy than CNN for grain yield and grain protein content. Altogether, DL approaches obtained better prediction accuracy for each trait, and should be incorporated into a plant breeder's toolkit for use in large scale breeding programs.

Keywords: artificial intelligence, convolutional neural network, deep learning, genomic selection, multilayer perceptron, neural networks, wheat breeding

OPEN ACCESS

Edited by:
Helen H. Tai, Agriculture and Agri-Food Canada (AAFC), Canada

Reviewed by:
Chuang Ma, Northwest A and F University, China
Jedrzej Jakub Szymanski, Leibniz Institute of Plant Genetics and Crop Plant Research (IPK), Germany

***Correspondence:**
Arron H. Carter
ahcarter@wsu.edu

Specialty section:
This article was submitted to Plant Systems and Synthetic Biology, a section of the journal Frontiers in Plant Science

Received: *02 October 2020*
Accepted: *30 November 2020*
Published: *05 January 2021*

Citation:
Sandhu KS, Lozada DN, Zhang Z, Pumphrey MO and Carter AH (2021) Deep Learning for Predicting Complex Traits in Spring Wheat Breeding Program. Front. Plant Sci. 11:613325. doi: 10.3389/fpls.2020.613325

INTRODUCTION

Genomic selection (GS) was first proposed in animal breeding for predicting breeding values of untested individuals (Meuwissen et al., 2001). Recently, this technology has been adopted by plant breeders for predicting genomic estimated breeding values (GEBV) using genome-wide markers in GS models (Lorenzana and Bernardo, 2009; Heffner et al., 2010). GS aids in the selection of parents for use in crossing and in the selection of progenies at an earlier stage, ultimately reducing the time required for completing the breeding cycle (Jonas and De Koning, 2013; Poland, 2015). It offers the potential of increasing the genetic gain per unit time and cost by increasing selection accuracy and shortening the generation of the breeding cycle. GS has been applied in several crop

species, such as barley (*Hordeum vulgare* L.), cassava (*Manihot esculenta*), maize (*Zea mays* L.), wheat (*Triticum aestivum* L.), and rice (*Oryza sativa* L.) (Maenhout et al., 2007; Isidro et al., 2015; Sallam et al., 2015; Okeke et al., 2017; Lozada and Carter, 2019). The fast-growing popularity of GS since the last decade can be attributed to the reduction in genotyping costs, producing thousands of polymorphic markers for most cultivated species (Poland et al., 2012; Wang et al., 2014). This nonetheless has resulted in a problem of so-called "large *p*, small n" when predicting phenotypes using markers.

Several statistical models are used to address this "large *p*, small n" issue by using penalized regression approaches. The most common GS model, ridge regression best linear unbiased predictor (rrBLUP), assumes markers to be random and have common variance and reduces the effect of all markers equally towards zero (Endelman, 2011). Least absolute shrinkage selection operator (LASSO) performs variable selection and continuous shrinkage simultaneously, where some markers are assumed to have an effect while others are set equal to zero (Tishbirani, 1996). Elastic net (EN) is the combination of both rrBLUP and LASSO, which uses average weight penalties from these two models (Zou and Hastie, 2005). Various Bayesian models (Bayes A, Bayes B, Bayes C, Bayes Cpi, and Bayes D) are equally important as they assume a heavy-tailed prior distribution or uses a combination of distributions for marker effects (Pérez et al., 2010; Perez-Rodriguez et al., 2012; Perez and de Los Campos, 2014). These models rely on the use of Markov Chain Monte Carlo (MCMC) for estimating the marker effects and are computationally intensive. Recently, compressed BLUP (cBLUP) and super BLUP (sBLUP) models have been developed which combines the variable selection operator of Bayes models with the computational advantage of mixed models (Wang et al., 2018). All these models are parametric as they assume a relationship between predictors and traits of interest, thus only obtaining the additive variance components, completely ignoring gene-by-gene and higher-order interactions.

Machine learning (ML) is an alternative approach for prediction and classification. ML is a branch of computer science that combines statistic and mathematic techniques for progressively training the models without explicitly programming them. ML builds different algorithms which gradually learn from the sample data and training the model, which ultimately provides predictions (Samuel, 2000). Several studies using non-parametric techniques of ML have been conducted in plants and livestock using support vector machines (SVM), boosting, random forests, and Reproducing Kernel Hilbert Space (RKHS; González-Camacho et al., 2012; González-Recio et al., 2014; Howard et al., 2014). The main advantage of using ML models for GS is that they learn the pattern from the data without being told any prior assumption, in this way they include all the variances, their interactions, and environmental components (Gianola et al., 2006; Campos et al., 2018; Gonzalez-Camacho et al., 2018). Although various studies are using ML for GS, to date, the field of deep learning (DL) has not been widely explored.

Deep learning is a branch of ML focusing on densely connected networks using artificial neural networks for training models (Min et al., 2017). The concept of DL is based on the biological networks of the brain neurons. DL uses a different combination of layers where data is transformed across each layer for obtaining a better fit. Furthermore, DL uses nonlinear activation functions, allowing them to predict the genetic architecture of the trait accurately (Angermueller et al., 2016; Wang et al., 2020). The most prominent advantage of DL is the number of high capacity and flexible trainable parameters. Traditional Bayesian neural networks are not as deep as they do not perform multiple layers of nonlinear transformation to the data (Lecun et al., 2015). DL models are continually being applied for classification and prediction problems (Pérez-Enciso and Zingaretti, 2019; Ramcharan et al., 2019). The performances of the DL algorithm have proved to be higher or similar to that of traditional ML approaches in many fields like image processing, military target recognition, genomics, speed recognition, health care, reconstructing brain circuits, traffic signal classification, and sentiment analysis (Angermueller et al., 2016; Campos et al., 2018; Bresilla et al., 2019; Zou et al., 2019). Also, there are various successful applications of DL for biological sciences, the majority of which are involved in disease classification (Rangarajan et al., 2018; Abdulridha et al., 2020).

Deep learning employs multiple neurons with proposed models such as a convolutional neural network (CNN), recurrent neural networks (RNN), and multilayer perceptron (MLP), and has the potential for application in GS (Alkhudaydi et al., 2019; Crossa et al., 2019; Cuevas et al., 2019). The input layer for these models includes a marker information, whereas the output layer consists of responses, with different number of hidden layers. Implementation of DL algorithms is straightforward, but the optimum model performance depends upon the choice of hyperparameter selection, which is not trivial and computationally intensive (Lecun et al., 2015; Young et al., 2015). Selection of hyperparameters is the most critical step for MLP, as it depends upon its ability to learn from the training data and can be generalized to a new dataset when applied for predictions. The choice of making a right decision of the number of layers, number of epochs, number of neurons, type of activation function, type of regularization penalty, activation rate, stopping criteria, among others, is cumbersome (Pérez-Enciso and Zingaretti, 2019). Optimal selection of these parameters depends upon the expertise in modeling and defining the problem. Often, the selection of parameters from a large number of tuning parameters is difficult because of time constraints and nonlinear interaction between the various parameters (Lecun et al., 2015; Young et al., 2015). There are four commonly used approaches for tuning parameters optimization, namely, random search, grid search, optimization, and Latin hypercube sampling (Koch et al., 2017). The detailed explanations of these approaches are out of the scope of this paper and are referred to in other readings (McKay, 1992; Koch et al., 2017; Montesinos-López et al., 2018a).

Several studies have focused on the use of DL models in wheat. Ma et al. (2018) have reported that CNN performs better for predicting grain length in wheat compared to traditional genomic best linear unbiased predictor (GBLUP). Similarly, Montesinos-López et al. (2018b) observed that DL models were

better than GBLUP when genotype-by-environment interactions were ignored in predicting grain yield in maize and wheat. Mcdowell (2016) reported that DL models perform similarly to several linear regression and Bayesian techniques employed for GS. Although previous studies have not demonstrated a consistent advantage of DL over conventional penalized regression approaches, more efforts are required to explore the potential and constraints of DL for GS scenarios (Bellot et al., 2018; Li et al., 2018; Montesinos-López et al., 2019a; Abdollahi-Arpanahi et al., 2020). It would, therefore, be necessary to assess different DL models in the context of GS in plant breeding programs. In this study, we evaluated the performance of two different DL algorithms, namely MLP and CNN, for predicting yield, yield components, and agronomic traits having a different genetic architecture. The objectives of this study are to (1) optimize DL models for predicting complex traits in spring wheat; (2) compare the accuracy of GS for DL models with rrBLUP, one of the most commonly used GS models in plant breeding; and (3) evaluate the effect of marker number on the accuracy of the models. This study will allow us to explore the potential of DL for predicting quantitative traits in breeding programs.

MATERIALS AND METHODS

Plant Material and Field Data

The spring wheat dataset used in this study consists of a nested association mapping (NAM) population containing 32 founder parents each crossed to common cultivar "Berkut" (Jordan et al., 2018; Blake et al., 2019). Due to space constraint, 650 Recombinant inbred lines (RILs) from 26 NAM families which have genotyping data provided by Kansas State University were planted between the 2014 and 2016 growing seasons at the Spillman Agronomy Farm near Pullman, WA, United States. A modified augmented field design was used in each trial with three replicated check cultivars ["Berkut," "McNeal" (Lanning et al., 1994), and "Thatcher"] in each block. Five agronomic traits with varying heritability and genetic architecture, including grain yield, grain protein content, heading date, plant height, and test weight were evaluated. Grain yield (t/ha) was calculated using a Wintersteiger Nursery Master combine (Ried im Innkreis, Austria) from grain weight per plot by harvesting whole plots. A Perten DA 7000 NIR analyzer (Perkin Elmer, Sweden) was used to determine the percentage of protein content in the grain. Days to heading was recorded as the number of days from planting to full exposure of spikes in 50% of the plot. Plant height (cm) was measured as length between the base of the plant to the tip of the fully emerged spike, excluding the awn when present. Test weight (kg hL^{-1}) was measured postharvest (Perkin Elmer, Sweden).

Statistical Analysis

Adjusted means were calculated for the unreplicated genotypes using the residuals derived separately for the individual environment using "lme4" function implemented in the R program using the model:

$$Y_{ij} = Block_i + Check_j + residuals_{ij}$$

where Y_{ij} is the trait of interest, $Block_i$ is the fixed effect of the ith block, and $Check_j$ corresponds to the effect of replicated check cultivar (Bates et al., 2015; R Core Team, 2017).

Broad-sense heritability for all phenotypic data points were calculated for each environment separately using the formula:

$$H^2 = \sigma^2{}_g / \left(\sigma^2{}_g + \sigma^2{}_e\right)$$

where H^2 is the broad-sense heritability, σ^2_g and σ^2_e are the genotypic and error variance components, respectively, obtained from the augmented randomized complete block design model treating genotype effects as random using the model equation:

$$Y_{ij} = \propto + Block_i + Check_j + Gen_{j(i)} + e_{ij}$$

where Y_{ij} is the trait of interest, $Block_i$ is the fixed effect of the ith block, Gen_j is the random effect of unreplicated genotypes j nested within ith block and distributed as independent and identically distributed, $Gen_j \sim N(0, \sigma^2_g)$, $Check_j$ corresponds to effect of replicated check cultivar, and e_{ij} is the standard normal errors distributed as $e_{ij} \sim N(0, \sigma^2_e)$ (Federer, 1961; Aravind et al., 2020).

Genotyping

The NAM population was genotyped using the Illumina 90 K SNP array (Wang et al., 2014) and genotyping-by-sequencing (GBS; Poland et al., 2012). Information on genotyping, map construction, and marker calling has been previously reported (Jordan et al., 2018). The initial genotypic information consisted of 73,345 polymorphic markers anchored to the Chinese Spring RefSeqv1 map (International Wheat Genome Sequencing Consortium, 2014; Jordan et al., 2018). RILs with missing phenotypic information in one environment were removed before filtering the genotypic data. SNP markers with more than 20% missing data, minor allele frequency of <0.10, and RIL missing >10% genotypic data were also discarded, resulting in a total of 635 RILs with 40,000 SNP markers used for analyses. Principal component analysis (PCA) was performed for assessing the population structure among the 26 NAM families using 40,000 SNP markers and 635 RILs. The whole data set and filtering pipeline used is provided on GitHub.[1]

Genomic Selection Models

Penalized Regression Models

Ridge regression best linear unbiased predictor is one of the most used GS models in plant breeding and was included here for comparison with the DL algorithms. Genome-wide marker effects were estimated using rrBLUP model for all traits (Endelman, 2011). GEBVs were calculated with mixed solve function implemented in R package "rrBLUP," according to the model:

$$y = \mu + Zu + e$$

where y is an $N \times 1$ vector of adjusted means for all unreplicated genotypes, μ is the overall mean, Z is an $N \times M$

[1]https://github.com/Sandhu-WSU/DL_Wheat.git

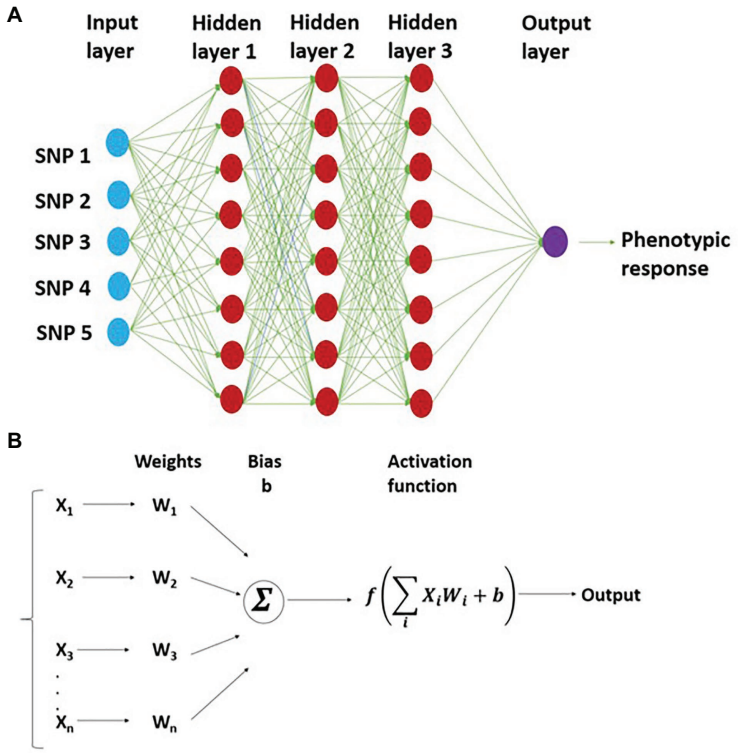

FIGURE 1 | Representation of multilayer perceptron (MLP) with three hidden layers and five SNP markers in the input layer. This shows the network structure for working of MLP, where the connection between different neurons is depicted **(A)**; bottom half represents weight assigned to each neuron and prediction of output using nonlinear activation function **(B)**.

matrix assigning markers to genotypes, u is a vector with normally distributed random marker effects as $u \sim N(0, I\sigma^2_u)$, and e is the residual error with $e \sim N(0, I\sigma^2_e)$. The solution for mixed equation can be written as

$$u = Z^T\left(ZZ^T + \lambda I\right)^{-1} y$$

where λ is the ridge regression parameter represented as $\lambda = \sigma^2_e/\sigma^2_u$ is the ratio of residual and marker variances. rrBLUP has the potential for dealing with "large p and small n" with penalized regression and has high numerical stability with highly correlated markers (Hoerl and Kennard, 2000). Codes and data set used for implementing the rrBLUP GS model is uploaded at GitHub.[1]

Multilayer Perceptron

Multilayer perceptron is a densely connected network, which is a typical feedforward neural network and does not assume a particular structure in the input features (Gulli and Pal, 2017). The basic structure of MLP consists of a densely connected network of the input layer, output layer, and multiple hidden layers (**Figure 1**). All these layers are connected by a dense network of neurons, where each neuron has its characteristic weight (Angermueller et al., 2016). In the case of GS, the input layer consists of a certain fixed number of neurons where each neuron represents an SNP marker in the training set. There are multiple hidden layers with a different number of neurons. Different layers are connected by neurons with a strength called "weight." The weight coefficient of neurons between the input and output layers is obtained from the training dataset using non-linear transformations. The number of output layer neurons is equal to the number of response variables in the GS model.

During the GS model training, the output of hidden layer one is a weighted average nonlinear transformation function of each input plus a bias (b; **Figure 1**). The output of the first layer (hidden layer 1) is represented as

$$Z_1 = b_0 + W_0 f_0(x)$$

where Z_1 is the output of the first layer, b_0 is the bias for the first layer estimated from the rest of the weights (W_0), x represents the genotypes of each individual, and f is a nonlinear activation function. This model is trained successively, where the output of neurons from the previous layer act as input for the next layer. The general expression for the model is

$$Z_k = b_{k-1} + W_{k-1} f_{k-1}(x)$$

where Z_k is the output vector for the GEBVs, and other terms of this equation are defined previously.

Convolutional Neural Network

Convolutional neural network is proposed to accommodate inputs that are associated with each other such as linkage disequilibrium between nearby SNP markers. A CNN is a special case of artificial neural networks where hidden layers typically consist of convolutional layers, pooling layers, flatten layers, and fully connected dense layers. In each convolutional layer, CNN automatically performs the convolution operation along with an input of predefined width and strides through the application of kernels and filters where the weights are the same for all SNP marker windows. The filter moves for the same window size across the input SNP markers, and CNN obtains the local weighted sum. The learned filters move across the input SNP marker data until the entire genotypic data are transverse. Each of these convolutional operations learns the coefficient of the so-called "kernel" or filter, which is equivalent to neurons of MLP. The output of the convolutional function can be defined as an integral transformation and is represented as

$$s(t) = (f * k)(t) = \sum_x k(t-x) f(x)$$

where k represents the kernel, convolution is the transformation of f into $s(t)$, and this operation is performed over an infinite number of copies f shifting over the kernel along each chromosome and filters take into account the linkage disequilibrium along the chromosome. A max-pooling layer is added after each convolutional layer to account for dimensionality reduction and making filters invariant to the small changes in the input. The pooling layer smoothed out the results by merging the output of the previous convolutional layer by taking the minimum, mean, and maximum. Activation function and dropout is employed after the convolutional and dense layer (**Figure 2**).

The greatest advantage of CNN over MLP is their capability to reduce the estimation of the number of hyperparameters required for training the model. Successive output layers are produced by the action of the activation function over the previous convolution layer. Finally, the pooling operation is performed resulting in dimension reduction, smoother representation, and merging of kernel output by computing their mean, maximum, or minimum.

Hyperparameter Optimization

A grid search cross-validation (CV), which selects the parameters that provide minimum mean square error (MSE; Pedregosa et al., 2011; Cho and Hegde, 2019) was implemented to optimize the hyperparameters on the whole population and for all traits evaluated in this study. Based upon available literature, we selected hyperparameters for training, and based on those parameters, a grid search CV with the full factorial design was implemented. The different hyperparameters which were tried for optimizing includes learning rate (constant and adaptive), activation function (relu, linear, tanh, identity, and logistic), solver (lbfgs, sgd, and adam), number of hidden layers (1, 4, 6, 8, and 10), number of neurons in completely dense network (10, 19, 38, 50, 62, 98, 112, and 150), drop out (0, 0.01, 0.1, and 0.2), number of filters (16, 32, 64, and 128), and regularizations (L1 and L2). Grid search CV used the inner CV where the outer training data set was split to 80% for inner training and the remaining 20% for inner testing. The inner training data set was used for hyperparameter optimization using the Keras validation split function and internal capabilities. The best hyperparameters were selected that give the least MSE on the inner testing population, and hence those parameters were used for the individual traits (Gulli and Pal, 2017).

Overfitting, which is related to poor model performance on the validated set, is one of the biggest constraints in implementing DL strategies in plant breeding. With this, approaches such as regularization, dropout, and early stopping were applied to minimize overfitting in the models. Dropout includes randomly assigning a subset of training neuron's weight

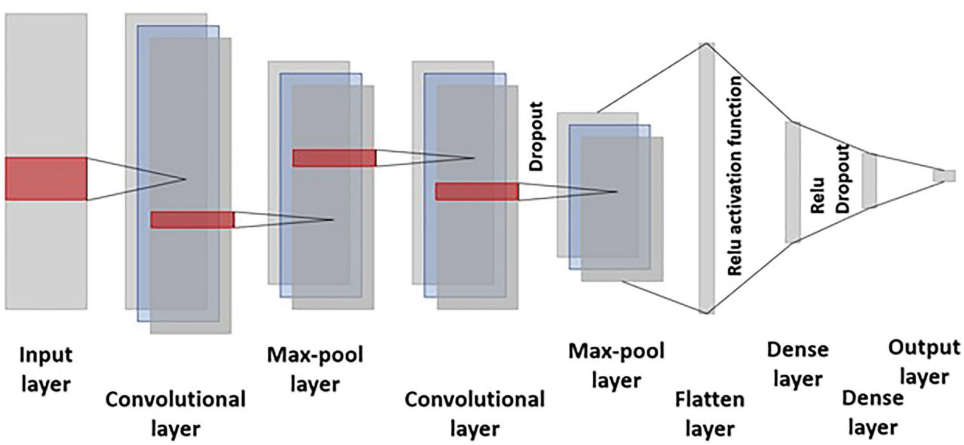

FIGURE 2 | Representation of the convolutional neural network (CNN) employed in this study. The input layer consists of 40,000 markers with a kernel size of three in the convolutional layer. Dropout is employed after the second convolutional and first dense layer. Relu activation function was used for training the model and hyperparameters were selected by lowering the mean squared error.

to zero to reduce complexity and overfitting. Herein, we used a 0.2 fixed dropout rate during hyperparameter optimization based on Srivastava et al. (2014) and Early stopping involves terminating the training process depending on the validation performance. As soon as the validation error reaches a minimum, training is halted. Keras provides an API (Callbacks) to incorporate the feature of early stopping. We used the EarlyStopping callback to create our MLP and CNN model. The other regularization techniques, L1 and L2, penalize weight values of the neural network. This technique involves making values close to zero and negative equal to 0 as they do not affect the model's performance. L1 penalizes the sum of the absolute values of weights, whereas L2 penalizes the weight's sum of the square. Our analysis made use of the parameter alpha of MLP and added L1_L2 regularizer in the first convolutional layer of CNN model. The DL algorithms were implemented in Scikit learn and Keras in Spyder (Python 3.7; Pilgrim and Willison, 2009; Pedregosa et al., 2011; Gulli and Pal, 2017). Codes and data set used for implementing the DL models is uploaded at GitHub.[1]

Cross-Validation and Independent Prediction

Prediction accuracy for the GS models (rrBLUP, MLP, and CNN) was evaluated by implementing a five-fold CV where 80% of the data was included in the training population, and 20% of the remaining data was used as a testing set within each environment. Two hundred replications were performed for each model to assess model performance. Each replication consisted of five iterations, where the dataset was split into five groups, and a different testing set was used for each iteration. Instant accuracy was calculated where correlation for each testing set was obtained and an average of five iterations was reported. Accuracy of the GS model was defined as the Pearson correlation coefficient between GEBVs and true (observed) phenotypes. A total of nine random sets of markers were used for training models and comparing the effect of marker number on the model's performance, including 1,000 ($M_{1,000}$), 5,000 ($M_{5,000}$), 10,000 ($M_{10,000}$), 15,000 ($M_{15,000}$), 20,000 ($M_{20,000}$), 25,000 ($M_{25,000}$), 30,000 ($M_{30,000}$), 35,000 ($M_{35,000}$), and 40,000 ($M_{40,000}$) SNP markers, and these models were also implemented using 200 replications with five-fold CV.

Independent validation was performed by training the GS model on the previous growing season, and predictions were made for future years. Briefly, the GS model was trained on the 2014 environment, and the prediction was made for the 2015 and 2016 environments. Similarly, the GS model trained on 2015 environment was used for predicting the 2016 environment. This type of validation represents the scenario of predicting the performance of a line before planting them in the field for the next growing season. Due to the computational burden of DL models, the whole analysis was completed on the WSU's high computing cluster.[2] When implemented on a single system, MLP and CNN were 40- and 55-fold more time-consuming. We solved this issue by executing the iterations in parallel on the cluster computers.

RESULTS

Heritability and Population Structure

Broad-sense heritability for all the five traits was obtained for each environment (**Table 1**). Each trait had different heritability values, depicting different genetic makeup, and varying environmental effects. Plant height and heading date were highly heritable, grain protein content, and test weight were moderately heritable, and grain yield was the least heritable among the traits. The heritability of each trait was lowest for the 2015 environment suggesting a more non-genetic variance effect for that environment. PCA showed the presence of two subgroups in population where PC1 and PC2 explained 5 and 4% of total genetic variation, respectively (**Supplementary Figure 1**). Furthermore, PC1 and PC2 for five different phenotypic traits evaluated in this study explained 31.8 and 21.4% of the variation (**Supplementary Figure 2**). In PC1, grain protein content and days to heading were clustered together and were opposite from test weight and grain yield.

Optimization of Hyperparameters for Each Trait

Different hyperparameters for each trait were selected using a grid search CV for 200 iterations by lowering the MSE. The combinations of hyperparameters were selected for each trait that had the lowest MSE during 200 iterations of grid search CV. These selected hyperparameters were used for predicting the traits for each environment separately. All the hyperparameters chosen in this study are provided for MLP (**Table 2**) and CNN (**Table 3**). The number of filters was the most important factor for lowering MSE in the case of CNN. In the case of MLP, activation function and number of neurons in layers were the main parameters controlling model performance. Different dropout and regularization values were selected to reduce overfitting in the model by looking at training accuracy, and these values were used for the testing set (**Tables 2** and **3**). We provided the information about the hyperparameters required for tuning each trait separately because of the different genetic architecture of the five traits used in

[2]https://hpc.wsu.edu/

TABLE 1 | Broad-sense heritability of five different traits for each environment (2014–2016) evaluated in this study.

Environment	Grain yield	Grain protein content	Test weight	Plant height	Heading date
2014	0.38	0.57	0.68	0.81	0.84
2015	0.24	0.35	0.59	0.59	0.80
2016	0.40	0.63	0.57	0.89	0.91

TABLE 2 | Hyperparameters selected for each trait using a random grid search CV for MLP.

Hyperparameter	Grain yield	Grain protein content	Test weight	Plant height	Heading date
Activation function	relu	relu	relu	tanh	tanh
Solver	adam	adam	sgd	sgd	sgd
Learning rate	Adaptive	Adaptive	Constant	Constant	Constant
No. of hidden layers	4	4	4	3	3
No. of neurons	(38, 38, 38, 19)	(19, 19, 19)	(50, 38, 38)	(120, 90, 90)	(90, 90, 90)
Dropout	0.2	0.2	0.2	0.2	0.2
Epochs	200	200	200	150	150
Regularization	0.1	0.1	0.05	0.05	0.05

These hyperparameters were later used for training the models.

TABLE 3 | Hyperparameters selected for each trait using a random grid search CV for CNN.

Hyperparameter	Grain yield	Grain protein content	Test weight	Plant height	Heading date
Activation function	relu	relu	relu	relu	relu
Solver	adam	adam	adam	adam	adam
Learning rate	adaptive	adaptive	constant	constant	constant
Number of filters	64	64	64	64	64
Dropout	0.2	0.2	0.2	0.2	0.2
Epochs	200	200	200	200	200
Regularization	0.05	0.05	0.05	0.05	0.05

These hyperparameters were later used for training the models.

this study. These results were consistent with other studies which also showed that different hyperparameters are required for various traits in plant breeding (Cuevas et al., 2019; Montesinos-López et al., 2019b).

Comparison of Model Performances for Cross-Validations

We compared the performances of two DL models with rrBLUP for each of the environments using the whole marker dataset ($M_{40,000}$) for GS. **Figure 3** shows the prediction accuracy for each of the five traits with three models, namely rrBLUP, MLP, and CNN under each environment. Furthermore, average prediction accuracy over the environment for each model is provided for all five traits (**Table 4**). Average prediction accuracy was highest with MLP for all the five traits. MLP improves the prediction accuracy from 3 to 5% for all the traits compared to rrBLUP, which is the most often used model in wheat breeding for predicting quantitative traits (Rutkoski et al., 2011; Sun et al., 2019). Even CNN gave 0 to 3% higher prediction accuracy than rrBLUP (**Table 4**). These results suggest that DL models should be included to obtain slightly higher prediction accuracies, as even minor increases in prediction accuracy could improve the selection efficiency in a breeding program. The improvement in prediction accuracy with DL models compared to the linear rrBLUP model is attributed to the use of nonlinear activation functions relu and tanh, which model the nonlinear relationship and ignore the restrictive assumptions of rrBLUP.

Multilayer perceptron gave 5% higher prediction accuracy than CNN for grain protein content and grain yield (**Table 4**). Among the five tested traits, grain yield and grain protein content are controlled by a large number of QTL, and high prediction accuracy with MLP is due to use of more hidden layers and less number of neurons which more efficiently capture the complex relationship between the SNP markers and response (**Table 2**; Sukumaran et al., 2015; Arora et al., 2017). Furthermore, both MLP and CNN performed similarly for predicting test weight, plant height, and days to heading. This suggests that either of these models could be used for predicting those traits in spring wheat. Furthermore, some hyperparameters are specific for particular traits (**Tables 2** and **3**). Grain yield and grain protein content requires a greater number of hidden layers compared to the other three traits, demonstrating that complex DL networks are required for highly quantitative traits (Bellot et al., 2018).

Complete details about prediction accuracy for each model on each environment is provided in full detail in **Figure 3**. There was a difference in prediction accuracy for each trait with all the models under different environmental conditions. This is because of the different heritability of each trait across the environments and the varying amounts of genetic variances captured by each model. Furthermore, DL models were able to capture the different amount of environmental variance as shown in **Figure 3A**, where the rrBLUP and DL models performed similarly for the 2016 environment, whereas for 2014, MLP had an 8% higher prediction accuracy than rrBLUP, suggesting that more environmental effect was captured. Similar trends can be explained for all the other traits predicted in this study (**Figure 3**).

Marker Set Optimization

The number of predictors (markers) has been reported to have a significant effect on the GS model performance (Heffner et al., 2011; Ma et al., 2018; Lozada and Carter, 2019). Therefore, we assessed the effect of the number of SNP markers on the

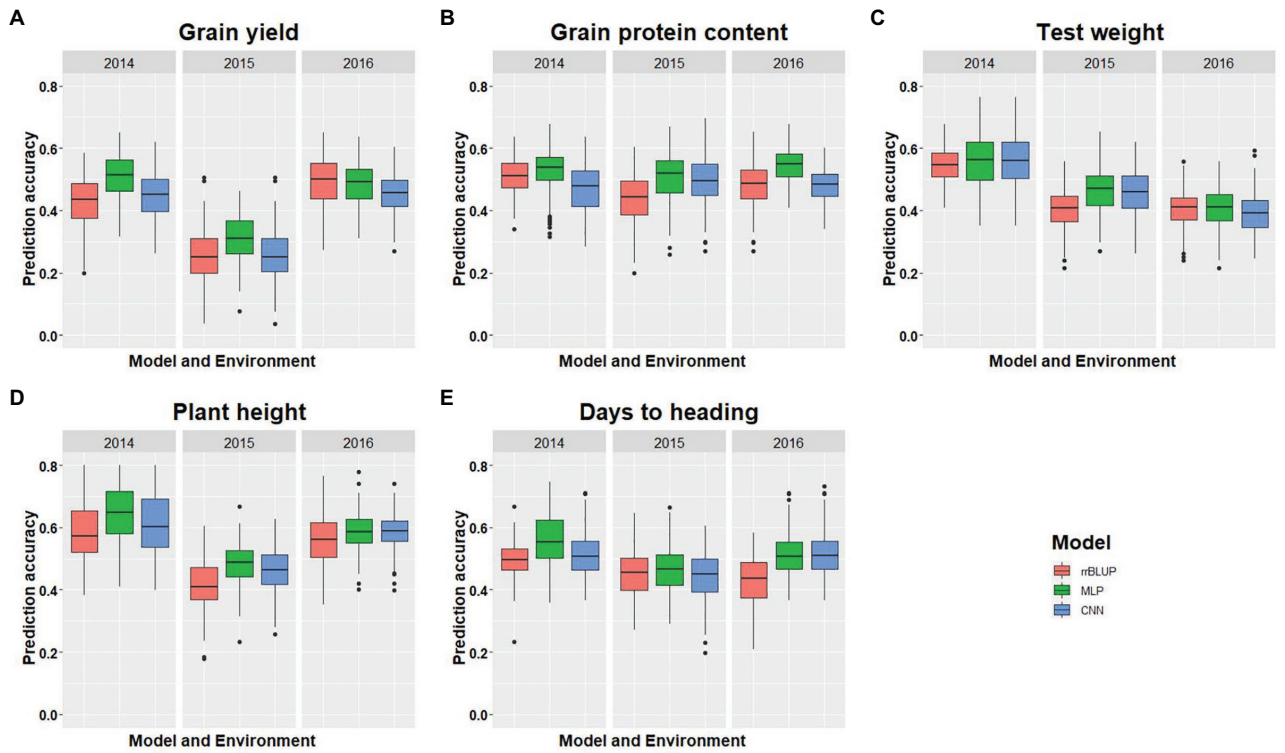

FIGURE 3 | Comparison of model performance for five different traits used in this study. **(A-E)** represent the model's performance for grain yield, grain protein content, test weight, plant height, and days to heading, for each trait under each environment using five-fold cross-validation (CV) and 40,000 SNP markers. The *x*-axis represents the environment, and the *y*-axis represents the prediction accuracy for the model.

TABLE 4 | Comparison of average prediction accuracy with three models (rrBLUP, MLP, and CNN) for five traits evaluated in this study and predicted separately for each environment for spring wheat.

Model	Grain yield	Grain protein content	Test weight	Plant height	Heading date
rrBLUP	0.39	0.48	0.45	0.52	0.46
MLP	**0.44**	**0.53**	**0.48**	**0.57**	**0.51**
CNN	0.39	0.48	0.47	0.55	0.49

The highest prediction accuracy is bolded for each trait under each model scenario.

performance of GS models evaluated in this study. Across all models, an increased marker number was related to improved prediction accuracy. The lowest prediction accuracy was obtained using $M_{1,000}$ for all the evaluated traits (**Figure 4**). Non-significant differences in model performances were observed when the marker number was increased from $M_{5,000}$ to $M_{40,000}$ for rrBLUP (**Figure 4**). MLP and CNN models rendered consistent improvement in prediction accuracy as the number of markers were increased in the model (**Figure 4**); nevertheless, trends vary across traits. Accuracy for plant height and days to heading reached a stable value when $M_{5,000}$ or more markers were used for MLP and $M_{10,000}$ or more markers were included in CNN model (**Figures 4D,E**). This can be attributed to a small number of QTLs which are controlling these traits; hence, this number of markers is able to capture all of them efficiently. In the case of test weight, there was a consistent increase in prediction accuracy for MLP and CNN until marker numbers reached above $M_{15,000}$, where no further significant increase in accuracy was observed (**Figure 4C**). Prediction accuracy for grain protein content and grain yield continuously increased as markers were increased to $M_{30,000}$ for MLP and $M_{25,000}$ for CNN (**Figures 4A,B**). These results suggest that with the reduction in genotyping cost, which produces a plethora of genotyping information, DL models should be used to obtain an increased prediction accuracy by efficiently using a large number of predictors in the GS models.

Prediction Accuracy Across Environments

In addition to looking at prediction accuracy within environments, model performance in an across-environment prediction scenario was also assessed. GS models were trained on data from the previous year, and predictions were made for next year phenotypic data. Average prediction accuracy for the independent validations for all five traits is provided (**Table 5**). **Figure 5** shows the prediction accuracy for each of the five traits with three tested models under each environmental condition when the model was trained on the previous year dataset. There was a significant decrease in prediction accuracy under independent validation compared to CV for each trait (**Tables 4** and **5**). This is because of using different populations for training and testing the model, which results in a different amount of non-genetic variances.

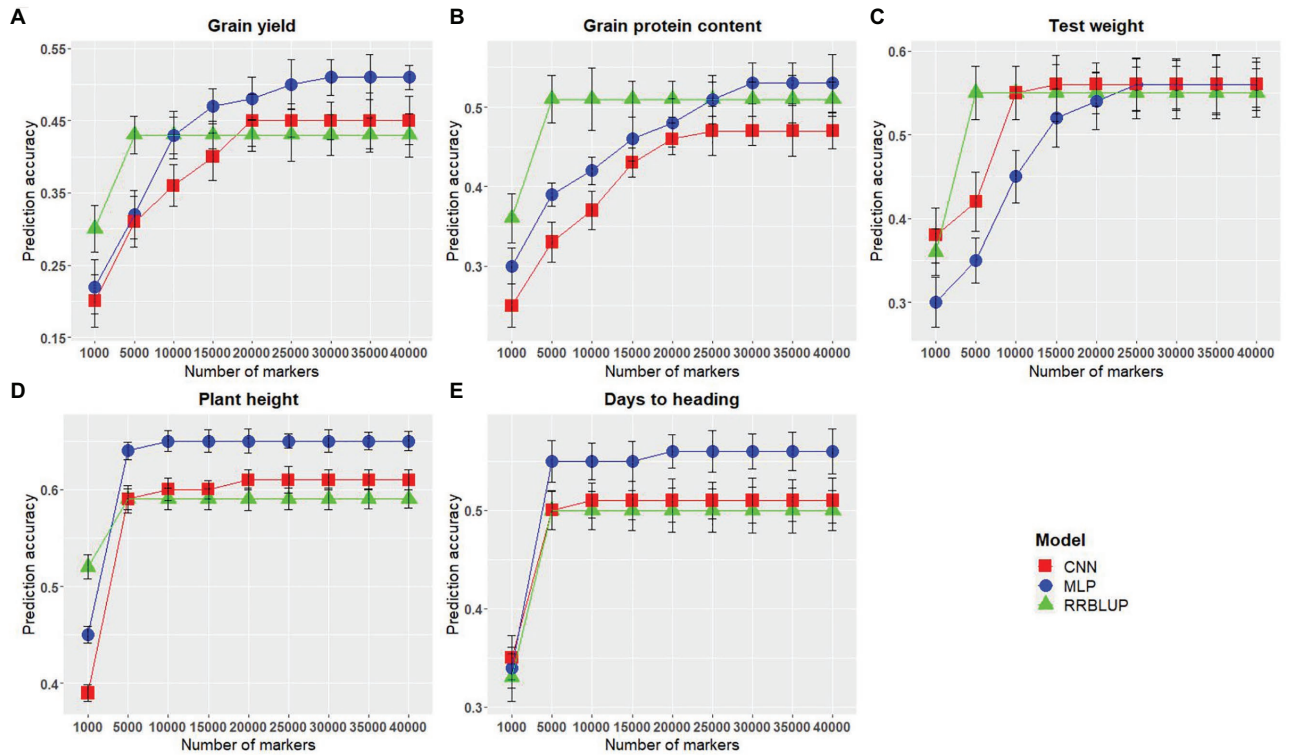

FIGURE 4 | Comparison of markers numbers for each of the genomic selection (GS) models for predicting five different traits in wheat. **(A-E)** represent the model performances for grain yield, grain protein content, test weight, plant height, and days to heading, respectively. The *x*-axis represents the number of markers in the model, and the *y*-axis represents prediction accuracy.

TABLE 5 | Comparison of average prediction accuracy under the independent validation scenario with three models (rrBLUP, MLP, and CNN) for five traits evaluated in this study for spring wheat.

Model	Grain yield	Grain protein content	Test weight	Plant height	Heading date
rrBLUP	0.20	0.34	0.25	0.33	0.25
MLP	**0.24**	**0.37**	**0.29**	**0.39**	**0.27**
CNN	0.23	0.35	0.28	**0.39**	**0.27**

The highest prediction accuracy is bolded for each trait under each model scenario.

Independent validations could be potentially improved by inclusion of genotype by environmental interactions in the model or by inclusion of more phenotypic data in the training models (Heffner et al., 2010; Lorenz et al., 2011). Furthermore, DL models performed equal or slightly better than rrBLUP for all the traits and strengthens the findings from the CV analysis (**Table 5**).

DISCUSSION

Genomic selection is transforming the field of plant breeding, and therefore using models with increased predictive power is relevant. DL is a new ML-based technique which explores the complex relationships hidden in the data for making predictions. In this study, we investigated the application of DL-based GS models for predicting complex traits in spring wheat. DL approaches were successfully applied for predictions and optimization of hyperparameters for each trait. Higher prediction accuracy (0–5%) with DL models compared to rrBLUP were observed for predicting five traits. Using a different number of markers in the model influenced the accuracy of GS for the evaluated traits, where an improved accuracy was related to increased marker number.

The optimization of hyperparameters for DL models is critical and challenging because of the high computational costs in this study, nevertheless, this optimization issue was solved using grid search CV (Young et al., 2015). First, we observed that each trait requires various combinations of hyperparameters, as prediction accuracy is dependent upon the interaction of these factors (Bellot et al., 2018; Montesinos-López et al., 2018b). The different tuning parameters for each trait depend on the genetic architecture of the trait. We observed that the "relu" activation function was the most important for predicting all traits in CNN and most of the traits in MLP, suggesting that "relu" function is critical for training GS models in wheat. Several studies have validated this function as a universal function for regression-based prediction models (Lecun et al., 2015; Pérez-Enciso and Zingaretti, 2019). Furthermore, different layers in CNN (convolutional, max-pooling, dense and fully connected) require a different set of hyperparameters, thus creating challenges

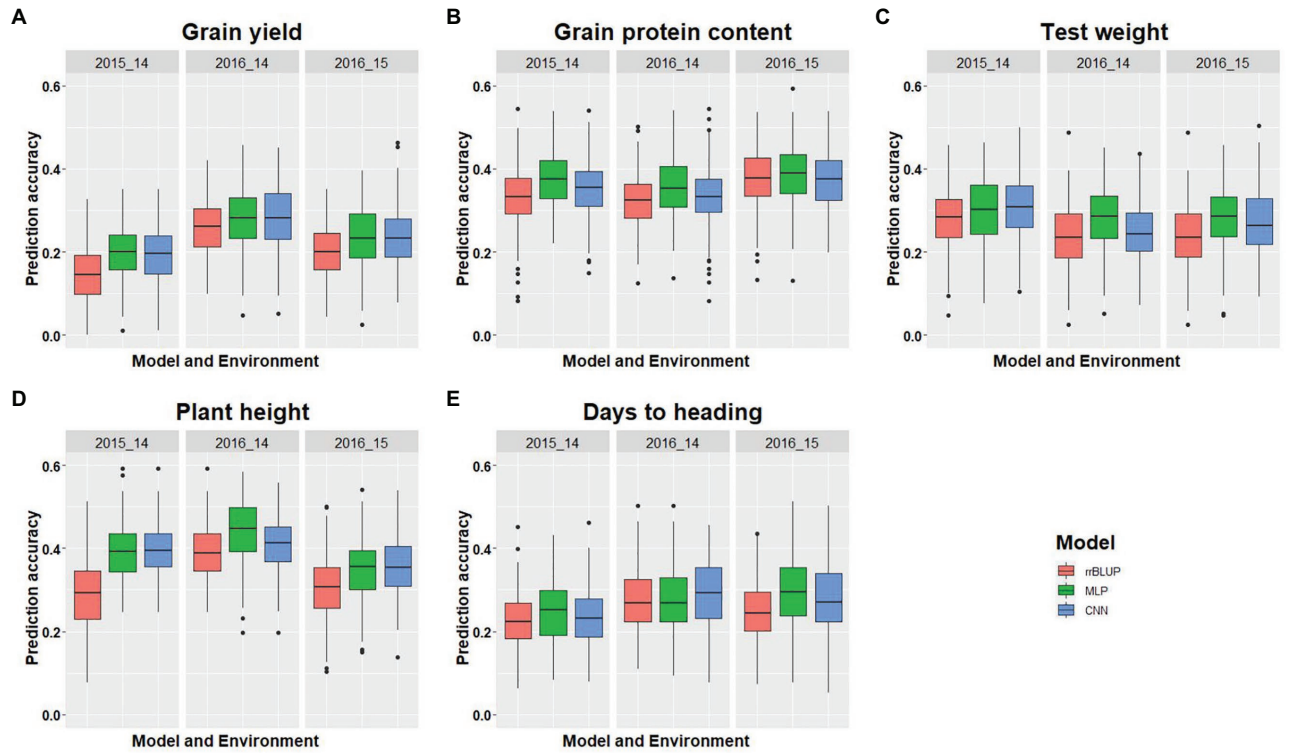

FIGURE 5 | GS model performance for independent validation using all three models for predicting five different traits in wheat **(A-E)**. The *x*-axis represents the environments where predictions were implemented. The first year indicates the testing, whereas the second year is the training environment.

in understanding the complex biological connection (Min et al., 2017). We obtained a higher prediction accuracy with DL, but those results are only valid for the hyperparameters used in this study (Montesinos-López et al., 2018b).

The high prediction accuracy of DL models compared to rrBLUP under both cross- and independent-validation scenarios can be attributed to the presence of hidden layers which automatically captures the complex hidden interaction without prior specification (Lecun et al., 2015). This means that unlike rrBLUP, which only models first-order interactions, DL models can capture interactions of large orders without specifying so in the model. DL could therefore explore data in such a way that humans cannot see and extract conclusions which otherwise are not possible to catch (Goodfellow et al., 2016). Higher or equal prediction accuracy of DL with rrBLUP for all the traits suggest that these models should be further explored in wheat, to further improve the prediction accuracy with inclusion of secondary correlated traits and genotype-by-environment interaction effects (Cuevas et al., 2019; Montesinos-López et al., 2019b).

It should be noted that rrBLUP was competitive with the DL models in terms of the accuracy of GS in the current study. The rrBLUP model's interpretability, transparency, and absence of the time-consuming task of hyperparameter tuning still makes it an attractive approach for GS, though the potential of improving prediction accuracy using DL approaches could not be discounted. Ma et al. (2018) reported that DL-based methods performed better than rrBLUP for predicting grain length, grain hardness, plant height, grain protein, and thousand kernel weight in wheat. They further suggested that both DL and rrBLUP models should be used for selecting the "best" individuals. Our results were consistent with their observations that DL approaches give slightly better prediction accuracy than rrBLUP, but with some computational costs associated with the DL models. Montesinos-López et al. (2018b) on the other hand observed DL models to be superior compared to GBLUP in six out of the nine traits evaluated in wheat and maize. Liu et al. (2019) also demonstrated the superiority of single and dual CNN models over the rrBLUP for predicting yield, protein, oil, moisture, and height in soybean (*Glycine max* L.). Similarly, Zingaretti et al. (2020) showed that DL models perform better than conventional linear statistical models for predicting traits having epistatic variances in the allopolyploid species of strawberries (*Fragaria x ananassa*) and blueberries (*Cyanococcus* spp.). These and our results open the field of DL in plant breeding and suggest that there is a great potential to increase predictive power for complex traits using DL approaches.

The performance of DL models improves when a large dataset is used for training the model (Min et al., 2017). Our current results and some related works, nonetheless, support that DL based models can reach an equivalent or superior accuracy than traditional linear models for GS even with the smaller dataset for training (Ma et al., 2018; Montesinos-López et al., 2018a). Furthermore, a previous study using the largest dataset analyzed so far (100 k individuals) for training the DL

model does not provide the superiority over the linear models (Bellot et al., 2018). These results altogether suggest that training population size is less important compared to the trait used for the prediction; this does not however undermine the use of large population sizes in the GS model. The biggest issue with a small dataset for DL is overfitting, which results from the failure of the model to learn general patterns present in the data. We tried to avoid overfitting in our models using dropout and regularization, which involves the removal of some fixed number of neurons during model training (Lecun et al., 2015; Bellot et al., 2018).

One drawback of DL models is that different hyperparameters handle different parts of the data, resulting in a problem for interpreting biological significance and importance of each feature (marker) in the model (Bellot et al., 2018; Cuevas et al., 2019). DL models, consequently, might not be useful for providing insights into the genetic architecture of the trait; instead, genome-wide association studies might be more appropriate for this purpose. Furthermore, the computational cost is a significant hindrance for training DL models, as multiple hyperparameters are required to be optimized for each trait separately (Gulli and Pal, 2017; Cho and Hegde, 2019). Plant scientists are often interested in understanding the biological meaning of prediction models, which is difficult in DL-based models because of the "black-box" nature of neural networks, and a large number of layers and neurons involved in training the model. Finally, DL based models require a background in computer science and statistics, which might require additional expertise or collaborations. Nevertheless, despite these limitations, DL approaches could still be used in the context of GS in plant breeding programs. Overall, this study opens a new avenue of DL for the prediction of complex traits in plant breeding.

CONCLUSION

In this study, we compared the performance of two DL models, namely MLP and CNN, with rrBLUP for predicting five different traits in spring wheat. Our results suggest that DL based models are superior for predicting all five traits used in this study. We optimized the hyperparameters required for training different traits and validated that each trait requires a specific set of hyperparameters for best performance. We observed that prediction accuracy for DL models was trait dependent and improved as the number of predictors (markers) in the models increased. Although training the DL models is computationally intensive and challenging, we found that the application of DL-based approaches is feasible and promising in terms of improving the prediction accuracy for complex traits in spring wheat. For these reasons, DL models should be incorporated into a plant breeder's toolkit for use in large scale breeding programs to improve genetic gain for quantitative traits.

DATA AVAILABILITY STATEMENT

The source codes and datasets used are made available on the GitHub account, and a link is provided in the manuscript.

AUTHOR CONTRIBUTIONS

KS analyzed data, conceptualized the idea, and drafted the manuscript. DL edited the manuscript. ZZ assisted in data analysis and edited the manuscript. MP and AC edited the manuscript, conducted field trials, and obtained the funding for the project. All authors contributed to the article and approved the submitted version.

FUNDING

This project was supported by the Agriculture and Food Research Initiative Competitive Grant 2017-67007-25939 (WheatCAP) and 2016-68004-24770 from the USDA National Institute of Food and Agriculture and Hatch project 1014919.

SUPPLEMENTARY MATERIAL

The Supplementary Material for this article can be found online at: https://www.frontiersin.org/articles/10.3389/fpls.2020.613325/full#supplementary-material

REFERENCES

Abdollahi-Arpanahi, R., Gianola, D., and Peñagaricano, F. (2020). Deep learning versus parametric and ensemble methods for genomic prediction of complex phenotypes. *Genet. Sel. Evol.* 52:12. doi: 10.1186/s12711-020-00531-z

Abdulridha, J., Ampatzidis, Y., Roberts, P., and Kakarla, S. C. (2020). Detecting powdery mildew disease in squash at different stages using UAV-based hyperspectral imaging and artificial intelligence. *Biosyst. Eng.* 197, 135–148. doi: 10.1016/j.biosystemseng.2020.07.001

Alkhudaydi, T., Reynolds, D., Zhou, J., Iglesia, B., and Griffiths, S. (2019). An exploration of deep-learning based phenotypic analysis to detect spike regions in field conditions for UK bread wheat. *Plant Phenom.* 2019:7368761. doi: 10.34133/2019/7368761

Angermueller, C., Pärnamaa, T., Parts, L., and Stegle, O. (2016). Deep learning for computational biology. *Mol. Syst. Biol.* 12:878. doi: 10.15252/msb.20156651

Aravind, J., Mukesh, S. S., and Wankhede, D. P. (2020). AugmentedRCBD: Analysis of augmented randomised complete block designs. R package version 0.1.3.

Arora, S., Singh, N., Kaur, S., Bains, N. S., Uauy, C., Poland, J., et al. (2017). Genome-wide association study of grain architecture in wild wheat *Aegilops tauschii*. *Front. Plant Sci.* 8:886. doi: 10.3389/fpls.2017.00886

Bates, D., Mächler, M., Bolker, B., and Walker, S. (2015). Fitting linear mixed-effects models using lme4. *J. Stat. Softw.* 67, 1–48. doi: 10.18637/jss.v067.i01

Bellot, P., de los Campos, G., and Pérez-Enciso, M. (2018). Can deep learning improve genomic prediction of complex human traits? *Genetics* 210, 809–819. doi: 10.1534/genetics.118.301298

Blake, N. K., Pumphrey, M., Glover, K., Chao, S., Jordan, K., Jannick, J. L., et al. (2019). Registration of the triticeae-cap spring wheat nested association mapping population. *J. Plant Regist.* 13, 294–297. doi: 10.3198/jpr2018.07.0052crmp

Bresilla, K., Perulli, G. D., Boini, A., Morandi, B., Corelli Grappadelli, L., and Manfrini, L. (2019). Single-shot convolution neural networks for real-time fruit detection within the tree. *Front. Plant Sci.* 10:611. doi: 10.3389/fpls.2019.00611

Cho, M., and Hegde, C. (2019). "Reducing the search space for hyperparameter optimization using group sparsity" in *ICASSP, IEEE International Conference on Acoustics, Speech and Signal Processing - Proceedings*, May 12–17, 2019 (Institute of Electrical and Electronics Engineers Inc.), 3627–3631.

Crossa, J., Martini, J. W. R., Gianola, D., Pérez-rodríguez, P., Jarquin, D., Juliana, P., et al. (2019). Deep kernel and deep learning for genome-based prediction of single traits in multienvironment breeding trials. *Front. Genet.* 10:1168. doi: 10.3389/fgene.2019.01168

Cuevas, J., Montesinos-lópez, O., Juliana, P., Guzmán, C., Pérez-rodríguez, P., González-bucio, J., et al. (2019). Deep kernel for genomic and near infrared predictions in multi-environment breeding trials. *G3 (Bethesda)* 9, 2913–2924. doi: 10.1534/g3.119.400493

de los Campos, G., Vazquez, A. I., Hsu, S., and Lello, L. (2018). Complex-trait prediction in the era of big data. *Trends Genet.* 34, 746–754. doi: 10.1016/j.tig.2018.07.004

Endelman, J. B. (2011). Ridge regression and other kernels for genomic selection with R package rrBLUP. *Plant Genome* 4, 250–255. doi: 10.3835/plantgenome2011.08.0024

Federer, W. T. (1961). Augmented designs with one-way elimination of heterogeneity. *Int. Biom. Soc.* 17, 447–473.

Gianola, D., Fernando, R. L., and Stella, A. (2006). Genomic-assisted prediction of genetic value with semiparametric procedures. *Genetics* 173, 1761–1776. doi: 10.1534/genetics.105.049510

González-Camacho, J. M., de los Campos, G., Pérez, P., Gianola, D., Cairns, J. E., Mahuku, G., et al. (2012). Genome-enabled prediction of genetic values using radial basis function neural networks. *Theor. Appl. Genet.* 125, 759–771. doi: 10.1007/s00122-012-1868-9

González-Camacho, J. M., Ornella, L., Pérez-Rodríguez, P., Gianola, D., Dreisigacker, S., and Crossa, J. (2018). Applications of machine learning methods to genomic selection in breeding wheat for rust resistance. *Plant Genome* 11:170104. doi: 10.3835/plantgenome2017.11.0104

González-Recio, O., Rosa, G. J. M., and Gianola, D. (2014). Machine learning methods and predictive ability metrics for genome-wide prediction of complex traits. *Livest. Sci.* 166, 217–231. doi: 10.1016/j.livsci.2014.05.036

Goodfellow, I. J., Bengio, Y., and Courville, A. C. (2016). *Deep learning. Adaptive computation and machine learning*. Cambridge: MIT Press.

Gulli, A., and Pal, S. (2017). *Deep learning with Keras*. Birmingham: Packt Publishing Ltd.

Heffner, E. L., Jannink, J. L., and Sorrells, M. E. (2011). Genomic selection accuracy using multifamily prediction models in a wheat breeding program. *Plant Genome* 4, 65–75. doi: 10.3835/plantgenome2010.12.0029

Heffner, E. L., Lorenz, A. J., Jannink, J. L., and Sorrells, M. E. (2010). Plant breeding with genomic selection: gain per unit time and cost. *Crop Sci.* 50, 1681–1690. doi: 10.2135/cropsci2009.11.0662

Hoerl, A. E., and Kennard, R. W. (2000). Ridge regression: biased problems nonorthogonal estimation for nonorthogonal problems. *Technometrics* 42, 80–86.

Howard, R., Carriquiry, A. L., and Beavis, W. D. (2014). Parametric and nonparametric statistical methods for genomic selection of traits with additive and epistatic genetic architectures. *G3 (Bethesda)* 4, 1027–1046. doi: 10.1534/g3.114.010298

International Wheat Genome Sequencing Consortium (2014). A chromosome-based draft sequence of the hexaploid bread wheat (*Triticum aestivum*) genome. *Science* 345:1251788. doi: 10.1126/science.1251788

Isidro, J., Jannink, J. L., Akdemir, D., Poland, J., Heslot, N., and Sorrells, M. E. (2015). Training set optimization under population structure in genomic selection. *Theor. Appl. Genet.* 128, 145–158. doi: 10.1007/s00122-014-2418-4

Jonas, E., and De Koning, D. J. (2013). Does genomic selection have a future in plant breeding? *Trends Biotechnol.* 31, 497–504. doi: 10.1016/j.tibtech.2013.06.003

Jordan, K. W., Wang, S., He, F., Chao, S., Lun, Y., Paux, E., et al. (2018). The genetic architecture of genome-wide recombination rate variation in allopolyploid wheat revealed by nested association mapping. *Plant J.* 95, 1039–1054. doi: 10.1111/tpj.14009

Koch, P., Wujek, B., Golovidov, O., and Gardner, S. (2017). "Automated hyperparameter tuning for effective machine learning" *in proceedings of the SAS Global Forum 2017 Conference*. Carry, NC, 1–23.

Lanning, S. P., Talbert, L. E., McGuire, C. F., Bowman, H. F., Carlson, G. R., Jackson, G. D., et al. (1994). Registration of 'McNeal' wheat. *Crop Sci.* 34, 1126-1127. doi: 10.2135/cropsci1994.0011183x003400040060x

Lecun, Y., Bengio, Y., and Hinton, G. (2015). Deep learning. *Nature* 521, 436–444. doi: 10.1038/nature14539

Li, B., Zhang, N., Wang, Y. G., George, A. W., Reverter, A., and Li, Y. (2018). Genomic prediction of breeding values using a subset of SNPs identified by three machine learning methods. *Front. Genet.* 9:237. doi: 10.3389/fgene.2018.00237

Liu, Y., Wang, D., He, F., Wang, J., Joshi, T., and Xu, D. (2019). Phenotype prediction and genome-wide association study using deep convolutional neural network of soybean. *Front. Genet.* 10:1091. doi: 10.3389/fgene.2019.01091

Lorenz, A. J., Chao, S., Asoro, F. G., Heffner, E. L., Hayashi, T., Iwata, H., et al. (2011). "Genomic selection in plant breeding: knowledge and prospects" in *Advances in agronomy*. *1st Edn. Vol. 110.* ed. D. L. Sparks (Cambridge: Academic Press), 77–123.

Lorenzana, R. E., and Bernardo, R. (2009). Accuracy of genotypic value predictions for marker-based selection in biparental plant populations. *Theor. Appl. Genet.* 120, 151–161. doi: 10.1007/s00122-009-1166-3

Lozada, D. N., and Carter, A. H. (2019). Accuracy of single and multi-trait genomic prediction models for grain yield in US Pacific northwest winter wheat. *Crop Breed Genet. Genom.* 1:e190012. doi: 10.20900/cbgg20190012

Ma, W., Qiu, Z., Song, J., Li, J., Cheng, Q., Zhai, J., et al. (2018). A deep convolutional neural network approach for predicting phenotypes from genotypes. *Planta* 248, 1307–1318. doi: 10.1007/s00425-018-2976-9

Maenhout, S., De Baets, B., Haesaert, G., and Van Bockstaele, E. (2007). Support vector machine regression for the prediction of maize hybrid performance. *Theor. Appl. Genet.* 115, 1003–1013. doi: 10.1007/s00122-007-0627-9

Mcdowell, R. M. (2016). Genomic selection with deep neural networks. [graduate theses and dissertations], 50.

McKay, M. D. (1992). "Latin hypercube sampling as a tool in uncertainty analysis of computer models" in *Proceedings of the 24th Conference on Winter Simulation*; December 1992; 557–564.

Meuwissen, T. H. E., Hayes, B. J., and Goddard, M. E. (2001). Prediction of total genetic value using genome-wide dense marker maps. *Genetics* 157, 1819–1829.

Min, S., Lee, B., and Yoon, S. (2017). Deep learning in bioinformatics. *Brief. Bioinform.* 18, 851–869. doi: 10.1093/bib/bbw068

Montesinos-López, O. A., Martín-Vallejo, J., Crossa, J., Gianola, D., Hernández-Suárez, C. M., Montesinos-López, A., et al. (2019a). A benchmarking between deep learning, support vector machine and Bayesian threshold best linear unbiased prediction for predicting ordinal traits in plant breeding. *G3 (Bethesda)* 9, 601–618. doi: 10.1534/g3.118.200998

Montesinos-López, O. A., Martín-Vallejo, J., Crossa, J., Gianola, D., Hernández-Suárez, C. M., Montesinos-López, A., et al. (2019b). New deep learning genomic-based prediction model for multiple traits with binary, ordinal, and continuous phenotypes. *G3 (Bethesda)* 9, 1545–1556. doi: 10.1534/g3.119.300585

Montesinos-López, O. A., Montesinos-López, A., Crossa, J., Gianola, D., Hernández-Suárez, C. M., and Martín-Vallejo, J. (2018b). Multi-trait, multi-environment deep learning modeling for genomic-enabled prediction of plant traits. *G3 (Bethesda)* 8, 3829–3840. doi: 10.1534/g3.118.200728

Montesinos-López, A., Montesinos-López, O. A., Gianola, D., Crossa, J., and Hernández-Suárez, C. M. (2018a). Multi-environment genomic prediction of plant traits using deep learners with dense architecture. *G3 (Bethesda)* 8, 3813–3828. doi: 10.1534/g3.118.200740

Okeke, U. G., Akdemir, D., Rabbi, I., Kulakow, P., and Jannink, J. L. (2017). Accuracies of univariate and multivariate genomic prediction models in African cassava. *Genet. Sel. Evol.* 49:88. doi: 10.1186/s12711-017-0361-y

Pedregosa, F., Michel, V., Grisel, O., Blondel, M., Prettenhofer, P., Weiss, R., et al. (2011). Scikit-learn: machine learning in python. *J. Mach. Learn. Res.* 12, 2825–2830.

Pérez, P., and de Los Campos, G. (2014). Genome-wide regression and prediction with the BGLR statistical package. *Genetics* 198, 483–495. doi: 10.1534/genetics.114.164442

Pérez, P., de los Campos, G., Crossa, J., and Gianola, D. (2010). Genomic-enabled prediction based on molecular markers and pedigree using the bayesian linear regression package in R. *Plant Genome* 3:106. doi: 10.3835/plantgenome2010.04.0005

Pérez-Enciso, M., and Zingaretti, L. M. (2019). A guide for using deep learning for complex trait genomic prediction. *Genes* 10:553. doi: 10.3390/genes10070553

Pérez-Rodríguez, P., Gianola, D., González-Camacho, J. M., Crossa, J., Manès, Y., and Dreisigacker, S. (2012). Comparison between linear and non-parametric regression models for genome-enabled prediction in wheat. *G3 (Bethesda)* 2, 1595–1605. doi: 10.1534/g3.112.003665

Pilgrim, M., and Willison, S. (2009). *Dive into python 3. Vol.* 2. New York: Apress.

Poland, J. (2015). Breeding-assisted genomics. *Curr. Opin. Plant Biol.* 24, 119–124. doi: 10.1016/j.pbi.2015.02.009

Poland, J., Endelman, J., Dawson, J., Rutkoski, J., Wu, S., Manes, Y., et al. (2012). Genomic selection in wheat breeding using genotyping-by-sequencing. *Plant Genome* 5, 103–113. doi: 10.3835/plantgenome2012.06.0006

Ramcharan, A., McCloskey, P., Baranowski, K., Mbilinyi, N., Mrisho, L., Ndalahwa, M., et al. (2019). A mobile-based deep learning model for cassava disease diagnosis. *Front. Plant Sci.* 10:272. doi: 10.3389/fpls.2019.00272

Rangarajan, A. K., Purushothaman, R., and Ramesh, A. (2018). "Tomato crop disease classification using pre-trained deep learning algorithm" in *Procedia Comput. Sci.* 133, 1040–1047. doi: 10.1016/j.procs.2018.07.070

R Core Team (2017). *A language and environment for statistical computing*. Vienna, Austria: R Foundation for Statistical Computing.

Rutkoski, J. E., Heffner, E. L., and Sorrells, M. E. (2011). Genomic selection for durable stem rust resistance in wheat. *Euphytica* 179, 161–173. doi: 10.1007/s10681-010-0301-1

Sallam, A. H., Endelman, J. B., Jannink, J. L., and Smith, K. P. (2015). Assessing genomic selection prediction accuracy in a dynamic barley breeding population. *Plant Genome* 8:eplantgenome2014.05.0020. doi: 10.3835/plantgenome2014.05.0020

Samuel, A. L. (2000). Some studies in machine learning. *IBM J. Res. Dev.* 44, 206–226. doi: 10.1147/rd.441.0206

Srivastava, N., Hinton, G., Krizhevsky, A., Sutskever, I., and Salakhutdinov, R. (2014). Dropout: a simple way to prevent neural networks from overfitting. *J. Mach. Learn. Res.* 15, 1929–1958.

Sukumaran, S., Dreisigacker, S., Lopes, M., Chavez, P., and Reynolds, M. P. (2015). Genome-wide association study for grain yield and related traits in an elite spring wheat population grown in temperate irrigated environments. *Theor. Appl. Genet.* 128, 353–363. doi: 10.1007/s00122-014-2435-3

Sun, J., Poland, J. A., Mondal, S., Crossa, J., Juliana, P., Singh, R. P., et al. (2019). High-throughput phenotyping platforms enhance genomic selection for wheat grain yield across populations and cycles in early stage. *Theor. Appl. Genet.* 132, 1705–1720. doi: 10.1007/s00122-019-03309-0

Tishbirani, R. (1996). Regression shrinkage and selection *via* the Lasso. *J. R. Stat. Soc. Series B Stat. Methodol.* 58, 267–288. doi: 10.1111/j.2517-6161.1996.tb02080.x

Wang, H., Cimen, E., Singh, N., and Buckler, E. (2020). Deep learning for plant genomics and crop improvement. *Curr. Opin. Plant Biol.* 54, 34–41. doi: 10.1016/j.pbi.2019.12.010

Wang, S., Wong, D., Forrest, K., Allen, A., Chao, S., Huang, B. E., et al. (2014). Characterization of polyploid wheat genomic diversity using a high-density 90 000 single nucleotide polymorphism array. *Plant Biotechnol. J.* 12, 787–796. doi: 10.1111/pbi.12183

Wang, J., Zhou, Z., Zhang, Z., Li, H., Liu, D., Zhang, Q., et al. (2018). Expanding the BLUP alphabet for genomic prediction adaptable to the genetic architectures of complex traits. *Heredity* 121, 648–662. doi: 10.1038/s41437-018-0075-0

Young, S. R., Rose, D. C., Karnowski, T. P., Lim, S. H., and Patton, R. M. (2015). "Optimizing deep learning hyper-parameters through an evolutionary algorithm" in *Proceedings of the Workshop on Machine Learning in High-Performance Computing Environments*; November 2015; 1–5.

Zingaretti, L. M., Gezan, S. A., Ferrão, L. F. V., Osorio, L. F., Monfort, A., Muñoz, P. R., et al. (2020). Exploring deep learning for complex trait genomic prediction in polyploid outcrossing species. *Front. Plant Sci.* 11:25. doi: 10.3389/fpls.2020.00025

Zou, H., and Hastie, T. (2005). Addendum: regularization and variable slection *via* the elastic net. *J. R. Stat. Soc. Series B Stat. Methodol.* 67:768. doi: 10.1111/j.1467-9868.2005.00527.x

Zou, J., Huss, M., Abid, A., Mohammadi, P., Torkamani, A., and Telenti, A. (2019). A primer on deep learning in genomics. *Nat. Genet.* 51, 12–18. doi: 10.1038/s41588-018-0295-5

Conflict of Interest: The authors declare that the research was conducted in the absence of any commercial or financial relationships that could be construed as a potential conflict of interest.

frontiers in Plant Science

ORIGINAL RESEARCH
published: 07 January 2021
doi: 10.3389/fpls.2020.596315

Spatial Models With Inter-Tree Competition From Airborne Laser Scanning Improve Estimates of Genetic Variance

David Pont[1], Heidi S. Dungey[2], Mari Suontama[2,3] and Grahame T. Stovold[2]*

[1] Forest Informatics, Scion, Rotorua, New Zealand, [2] Forest Genetics, Scion, Rotorua, New Zealand, [3] Tree Breeding, Skogforsk, Umeå, Sweden

Phenotyping individual trees to quantify interactions among genotype, environment, and management practices is critical to the development of precision forestry and to maximize the opportunity of improved tree breeds. In this study we utilized airborne laser scanning (ALS) data to detect and characterize individual trees in order to generate tree-level phenotypes and tree-to-tree competition metrics. To examine our ability to account for environmental variation and its relative importance on individual-tree traits, we investigated the use of spatial models using ALS-derived competition metrics and conventional autoregressive spatial techniques. Models utilizing competition covariate terms were found to quantify previously unexplained phenotypic variation compared with standard models, substantially reducing residual variance and improving estimates of heritabilities for a set of operationally relevant traits. Models including terms for spatial autocorrelation and competition performed the best and were labelled ACE (autocorrelation-competition-error) models. The best ACE models provided statistically significant reductions in residuals ranging from −65.48% for tree height (*H*) to −21.03% for wood stiffness (*A*), and improvements in narrow sense heritabilities from 38.64% for *H* to 14.01% for *A*. Individual tree phenotyping using an ACE approach is therefore recommended for analyses of research trials where traits are susceptible to spatial effects.

Keywords: spatial analysis, tree competition, environment, tree phenotyping, airborne laser scanning, heritability, field trial

OPEN ACCESS

Edited by:
Helen H. Tai, Agriculture and Agri-Food Canada (AAFC), Canada

Reviewed by:
Francois Du Toit, The University of British Columbia, Canada
Jean-François Côté, Canadian Wood Fibre Centre, Canada

****Correspondence:***
David Pont
david.pont@scionresearch.com

Specialty section:
This article was submitted to Technical Advances in Plant Science, a section of the journal Frontiers in Plant Science

Received: *19 August 2020*
Accepted: *08 December 2020*
Published: *07 January 2021*

Citation:
Pont D, Dungey HS, Suontama M and Stovold GT (2021) Spatial Models With Inter-Tree Competition From Airborne Laser Scanning Improve Estimates of Genetic Variance. Front. Plant Sci. 11:596315. doi: 10.3389/fpls.2020.596315

INTRODUCTION

The development of a precision approach to forestry can improve the efficiency and sustainability of managed forests. The aspiration is to utilize improved tree breeds, planted on the most suitable sites, and managed to optimize production, while minimizing costs and environmental impacts by targeted applications of inputs such as fertilizers (Dungey et al., 2018). A critical requirement for precision forestry is accurate and cost-effective methods to characterize individual trees (Tsaftaris et al., 2016; D'odorico et al., 2020). This capability could not only be utilized in trials to support research into improved breeds for tree growth and quality, but also in assessment of trees for inventory of forest stands at different stages of the production cycle. Traditional forest inventory and trial measurement rely on ground-based measurement of traits such as tree diameter, height,

and volume. Such measurements are time consuming and error-prone. Remote sensing offers the potential for high throughput, accurate, and spatially explicit phenotyping, providing an essential foundation for precision management (Fahlgren et al., 2015). At this stage, airborne laser scanning has been most successfully adopted for forest inventory internationally, typically using area-based methods to characterize patches of the order of 0.04 ha in size (White et al., 2013; Maltamo et al., 2014). Alternative methods, identifying and delineating individual trees using ALS, have been developed and evaluated on New Zealand radiata pine stands (Pont, 2016).

Radiata pine (*Pinus radiata D. Don*) is the dominant tree species in the New Zealand forest estate comprising 90% of the planted area (Forest Owners Association, 2019). The New Zealand radiata pine forest estate comprises a monospecific, even aged, intensively managed forest crop. Considerable levels of variation in tree attributes remain, due to genetics, environment, and silviculture (Dungey et al., 2006). Forest tree breeding requires the evaluation of large numbers of trees and sufficient replication due to genetic variability, resulting in trials containing thousands of trees, and occupying several hectares (Dungey et al., 2009).

A standard approach to mitigate the effects of environmental variation in genetics trials is the use of spatial terms in analytical models (Dutkowski et al., 2006). A useful method is the separable first-order autoregressive model (AR1) in two dimensions (Cullis et al., 1998), utilizing inverse distance-weighted correlations across rows and columns in the trial, allowing for differing spatial correlations in the row and column directions. This successfully accounts for various forms of environmental effects in trial analyses (Cullis et al., 2014). Competition is a form of negative autocorrelation, where neighbors of a larger tree are more likely to be smaller, and vice versa (Griffith and Arbia, 2010). Autocorrelative methods such as AR1 models do not distinguish positive and negative autocorrelation and as a result the two effects are confounded (Griffith and Arbia, 2010). In order to accurately account for environmental variation, methods to quantify both positive (site) and negative (competition) autocorrelation are needed (Cappa and Cantet, 2008; Costa et al., 2013; Dong et al., 2020).

Tree traits of primary importance to breeders and forest managers include size, wood quality and disease susceptibility. Height, diameter at breast height (DBH) and total stem volume are widely used fundamental measures of tree size and productivity, able to be estimated from tree-based analyses of ALS (Lindberg et al., 2013; Dalponte et al., 2018). Dothistroma needle blight (*Dothistroma septosporum* (Dorog.) M. Morelet) is a foliar disease causing considerable productivity losses (Watt et al., 2011), and wood stiffness is an wood quality characteristic important for structural uses of timber (Carson et al., 2014). Individual tree crown metrics derived from the ALS were shown to correlate with these aforementioned tree size, disease, and wood quality traits, and to provide accurate estimates of genetic parameters such as heritabilities (Pont, 2016).

Competition metrics express the growth potential of a tree relative to nearby trees, generally considering the size and proximity of those trees (Pretzsch, 2010; Burkhart and Tomé, 2012). The inclusion of such competition metrics in analytical models was of interest to partition competition effects from general environmental effects. Spatially registered crown metrics from tree-based analysis of ALS quantifying tree size and locations are suitable for derivation of individual tree competition metrics. In a review of competition metrics for use with individual tree analysis of ALS (Suárez, 2010), distance weighted size ratios were utilized. Such ratios, initially used by Hegyi (1974), were expressed in terms of tree diameters:

$$CI = \sum_{j-1}^{n} \left(\frac{d_j / d_i}{L_{ij}} \right)$$

where, d_i = DBH of reference tree i, d_j = DBH of competitor tree j, L_{ij} = distance between reference tree i and competitor j.

It is hypothesized that spatial models including autoregressive and competition terms reduce unexplained variation compared to conventional models lacking spatial terms. The ability to more accurately quantify spatial effects reduces model residuals and thereby improves heritability estimates. The study was carried out in a genetics trial, providing the unique opportunity to work within an experimental design of known spacing and documented genetics. Environmental effects due to competition and site related variation were evident in the selected trial, providing the opportunity to examine models accounting for these effects in a controlled setting.

MATERIALS AND METHODS

Genetics Trial Site

The genetics trial BC 35-3 was established in 2007 by the Radiata Pine Breeding Company Ltd., in compartment 76 at Kaingaroa forest (38.53° S, 176.66° E) in the central North Island of New Zealand. The trial was designed to evaluate Dothistroma needle blight resistance for families in a breeding program and used an incomplete block design with single tree plots (Dungey et al., 2009). The trial site covered a total area of 2.8 ha and sloped gently (<5 degrees) to the southeast. The trial comprised 75 blocks, with 25 replicates and 3 incomplete blocks per replicate (**Figure 1**). Each block measured 19.2 × 19.2 m, with tree spacing on a uniform grid of 3.2 × 3.2 m. Blocks were established with 36 trees from different families in a 6 × 6 grid. Six control families were present in every block and the remaining 90 families were assigned across the three incomplete blocks for each replicate, with randomized spatial locations within the blocks and replicates. The surrounding stand was also established with radiata pine in 2007 at a density of 1000 stems ha^{-1} and thinned to 786 stems ha^{-1} in 2012.

Initial inspection of the trial data showed evidence of spatial autocorrelation, with reduced height and diameter growth and increased levels of Dothistroma infection associated with small gullies within the trial (**Figures 2**, **3**). Favorable conditions for Dothistroma are known to occur in gullies, where moist conditions persist, indicating the possibility of reduced tree growth associated with Dothistroma infection (Bulman et al., 2004). In addition to observable site effects, the trial had missing

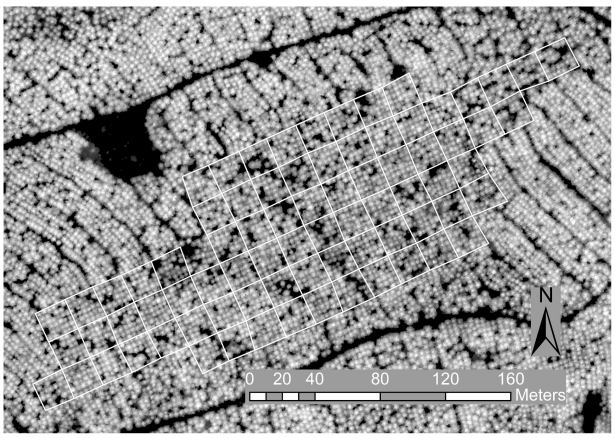

FIGURE 1 | Trial layout with blocks outlined in white on the canopy height model image derived from the ALS data at 0.25 m resolution and used for tree detection.

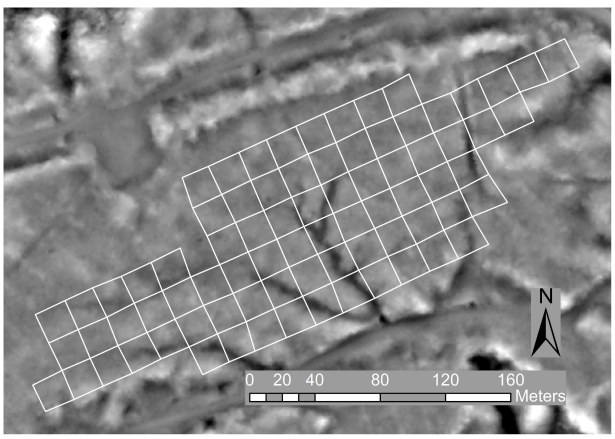

FIGURE 2 | Trial layout with blocks outlined in white on an image of a digital terrain model (derived from the ALS data at 0.8 m resolution) shaded to indicate relative elevation and reveal a number of gullies evident as dark areas.

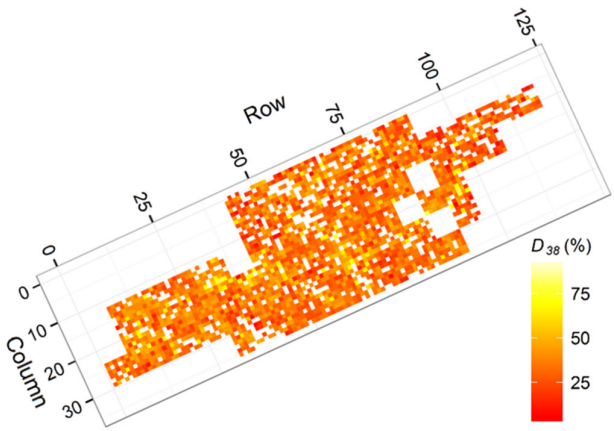

FIGURE 3 | Heatmap presenting ground measured degree of Dothistroma infection (D_{38}) for each tree (white indicates no data). Areas with elevated infection coincided with the gullies identified within the trial.

trees. Missing trees typically occur due to mortality, and in this trial dead, unhealthy, and highly malformed trees were also removed during the 2012 operational thinning of the surrounding stand. The resulting gaps in the trial grid created potential for competition effects (Fins et al., 1992).

Field Measurement of Tree Traits

A ground-based assessment of a number of tree traits was carried out in July 2014 when the trial was aged 7 years, following standard tree breeding measurement methodologies (Jayawickrama, 2001). Measurements of tree diameter at breast height (*DBH*), height (*H*), and outerwood stress wave velocity (*A*), and degree of needle loss caused by Dothistroma needle blight (D_{38}), were carried out. Tree *DBH* was measured using a fiberglass girth tape with diameter gradations at millimeter intervals (Friedrich Richter Messwerkzeuge GmbH & Co., Speichersdorf, Germany). Tree *H* was measured using a Vertex IV (Haglof, Sweden). Total stem volume (*V*) was estimated for each tree using the standard volume equation V182 (Goulding, 1995):

$$V = DBH^a \left(\frac{H^2}{H-1.4}\right)^b e^c$$

where $a = 1.79068$, $b = 1.07473$, $c = -10.03201$, and e is Euler's number.

Outerwood stress wave velocity (*A*) was measured using a HITMAN ST300 (Fibre-gen Ltd., Christchurch, New Zealand) with the probes placed 1 m apart, avoiding knots and defects that could affect readings. The measure *A* is correlated with wood stiffness, an important engineering property for structural uses of timber (Carson et al., 2014). Degree of needle loss (D_{38}) was assessed at age 38 months as a percentage of needles infected or lost, estimated visually in 5 percent increments (Van Der Pas et al., 1984). Individual tree D_{38} measurements are presented in **Figure 3** where indication of increased infection in association with gullies crossing the trial (see **Figure 2**) was evident.

Airborne Laser Scanning Data

The discrete return ALS data were acquired in early 2014 using an Optech Pegasus scanner with a pulse rate of 100 kHz, a maximum scan angle of ± 12°, a 25% swath overlap, and a 0.25 m footprint size. The data were georeferenced to the NZGD2000 NZTM coordinate system and all returns were classified as ground and above ground (using Terrascan TerraSolid software). The average point density of the point cloud over the trial area was 17 total returns per m^2 and 7 last returns per m^2.

Crown Metrics

A canopy height model (CHM) with 0.25 m resolution was extracted from ALS data collected over the trial and image defects referred to as pits were removed using the standard image processing method *closing* (Ronse and Heijmans, 1991; Andersen et al., 2006). Individual trees were detected and crown boundaries determined on the CHM image using the calibrated

TABLE 1 | Individual tree crown metrics used in candidate competition metrics with most highly correlated tree size trait and Pearson's *r*.

Abbreviation	Description	Units	Trait *r*
$CR = \sqrt{\frac{CA_P}{\pi}}$	Crown radius derived from crown area (CA_P).	m	*DBH* 0.679
CL	Crown length, difference between crown highest point and average height of crown boundary points.	m	*H* 0.476
GA_P	Two-dimensional ground area of crown growing space from watershed segmentation polygon.	m^2	*DBH* 0.518
CA_P	Two-dimensional ground area of crown determined from crown boundary polygon.	m^2	*V* 0.574
A_{CG}	Ratio of crown and growing space areas (CA_P/GA_P).	–	*H* 0.297
		m^2	*V* 0.598
CS_T	Surface area of triangulated crown CHM heights.	m^2	*V* 0.574
CV_F	The volume between the crown upper surface and the ground (Chen et al., 2007).	m^3	*V* 0.844
CV_P	The volume between the crown upper surface and the base of the crown.	m^3	*DBH* 0.541

ITC method (Pont et al., 2015). The method uses watershed segmentation with operator calibration to determine the level of image smoothing and has been shown to provide tree detection accuracy of 95% for New Zealand radiata pine across a range of stand densities and crown sizes. Detected trees were matched to ground trees with an automated least squares approach (Hauglin et al., 2014) and unmatched trees used to identify and manually correct segmentation errors.

Watershed segmentation resulted in growing space polygons, one per detected tree, which completely tiled the image, each including a tree crown and a portion of any adjacent gap between trees. Tree crown boundaries were then delineated within each growing space polygon to exclude any gap area. For tree crowns with no adjacent gaps, growing space and crown polygons were identical. The CHM image gray values within each crown represent heights above ground. Growing space boundaries, crown boundaries, and crown elevation values were used to derive a total of nine crown size metrics (**Table 1**) correlated with the traits of interest (Pont, 2016). Crown volumes (CV_F and CV_P) quantified three-dimensional crown size, while surface areas from projected polygon outlines (GA_P and CA_P) and from surface areas of three-dimensional crown surfaces (CS_C and CS_T) provided two-dimensional measures of crown sizes. Crown length and radius (*CL* and *CR*) provided one-dimensional measures and the ratio of crown and growing space areas (A_{GC}) provided a dimensionless measure of crown size. These crown size metrics were then used in competition metrics described subsequently.

Competition Metrics

Rouvinen and Kuuluvainen (1997) presented a set of competition metrics, *CI*10, *CI*11, and *CI*12, derived from the original by Hegyi (1974). Those competition metrics were evaluated by Suárez (2010) using ground measured *DBH* and using *DBH* estimated from LiDAR CHM crown metrics. Those competition models were generalized in our study to utilize the crown metrics (see **Table 1**) derived from the ALS CHM as:

$$\mathrm{CIA} = \sum_{j-1}^{n}\left(\frac{c_j/c_i}{L_{ij}}\right)$$

$$\mathrm{CIB} = \sum_{j-1}^{n}\left(\frac{c_j/{c_i}^2}{L_{ij}}\right)$$

$$\mathrm{CIC} = \sum_{j-1}^{n}\left(\frac{(c_j/c_i)^2}{L_{ij}}\right)$$

where c_i = crown metric for reference tree i, c_j = crown metric for competitor tree j, L_{ij} = distance between reference tree i and competitor j.

Two methods were used for determining the neighboring trees included in the calculation of the competition metrics described above. In the area method (N_A), all trees within a fixed radius were included, an approach used in a number of previous studies (Hegyi, 1974; Pukkala et al., 1994; Rouvinen and Kuuluvainen, 1997; Suárez, 2010). The grid spacing in the trial was used to estimate a radius of 8.273 m to include an average of twenty trees surrounding the central tree. In the boundary method (N_B), only trees sharing a segment boundary (as delineated on the CHM) with the target tree were included (Suárez, 2010). Processing of the CHM included a 50 m buffer around the trial and competition metrics using both neighborhood methods included trees surrounding the trial, a distinction with competition metrics which often only account for trees measured within plots or trials (Dutkowski et al., 2006). The use of 9 crown metrics (**Table 1**) and 3 model formulations (CIA, CIB, CIC) gave 27 competition metrics. Use of the two neighborhood methods (N_A and N_B) with the 27 metrics gave a total of 54 competition metrics for evaluation.

Spatial Models

The following general individual tree linear mixed model was used as the basis of all spatial models:

$$y = Xb + Zu + e$$

where $\boldsymbol{y}$ is a vector of individual tree observations of a specific trait (*H*, *DBH*, *V*, D_{38} or *A*), $\boldsymbol{b}$ is a vector of fixed effects, $\boldsymbol{u}$ is a vector of random effects, and $\boldsymbol{e}$ is a vector of random residuals. The terms $\boldsymbol{X}$ and $\boldsymbol{Z}$ correspond to design matrices relating the observations in $\boldsymbol{y}$ to the fixed and random effects in $\boldsymbol{b}$ and $\boldsymbol{u}$, respectively (Dungey et al., 2012).

We fitted a model without spatial terms, as routinely used in estimating variance components and genetic parameters including narrow sense heritabilities, referred to as Base model (B) (Dutkowski et al., 2006). Fixed effects in vector $\boldsymbol{b}$ included the overall mean and a factor with two levels to account for the effects of control versus non-control material. Random terms in vector $\boldsymbol{u}$ included the additive genetic effects of individual

TABLE 2 | Models fitted for each trait to compare improvements from random terms to account for spatial autocorrelation (AR1) and addition of competition covariates derived from analyses of the ALS tree crown metrics.

Model	Abbreviation	Fixed terms	Random terms
Base	B	control	replicate + iblock:rep + pedigree
Base + AR1	BA	control	pedigree + units + AR1
Base + Competition	BC	control	replicate + iblock:rep + pedigree + competition
Base + AR1 + Competition	BAC	control	pedigree + units + AR1 + competition

genotypes for pedigreed material, the effects of replicates and the effects of incomplete blocks within replicates. We also fitted a standard spatial model using an auto-regressive order 1 random term, commonly referred to as AR1xAR1, and abbreviated to AR1 hereafter (Dutkowski et al., 2006). We referred to this standard spatial model as Base plus AR1 (BA). In this model vector $\boldsymbol{e}$ was partitioned into spatially correlated (ξ) and uncorrelated (η) residuals and replicate was removed as a fixed effect. The spatially correlated error ξ, was modeled by using a first-order separable autoregressive process in the row and column directions (Gilmour et al., 1997; Costa et al., 2001; and Dutkowski et al., 2002).

Competition metrics were then introduced as covariates to those models, referred to as Base plus Competition (BC) and Base plus AR1 plus Competition (BAC). Covariate values were standardized by subtracting the mean and dividing by the standard deviation (Butler et al., 2009). Control and the overall mean appeared as the only fixed terms, and the additive genetic effects of individual trees appeared as a random term, in all models. Trees were assigned to grid rows and columns, and missing values added to ensure a complete grid for AR1 models. A nugget effect (referred to as units) was added to models having an AR1 spatial term, as this has been shown to be significant in several studies (Suontama et al., 2015). Incomplete block by replicate was tried as a random term in all models, but it became non-significant when an AR1 spatial term was added, so it was dropped from those models (Dungey et al., 2012). The set of models evaluated are summarized in **Table 2**.

The B and BA models were fitted to each of the 5 traits (H, DBH, V, D_{38}, A), requiring 10 model runs. The BC and BAC models were fitted for the 5 traits by 54 competition metrics, requiring 270 model runs. The total number of model runs being 280.

Model Evaluation

Models can be compared with log-likelihood (LL) ratio tests if they have the same fixed effects, and if one model has a subset of the random effects in the other model (nested models) (Isik et al., 2017). Models with the same fixed effects that are not nested can be compared with information criteria, Akaike's (AIC) or Schwarz's Bayesian Information Criteria (BIC). In our study we evaluated four nested models with the same fixed effects (control only), presented in **Table 2**. We evaluated models under the premise that all models including some spatial component were alternative approaches to accounting for spatial variation compared to the base model. If LL_M and LL_B are the REML log-likelihoods for a test and base models, respectively, the test statistic (D) is given by:

$$D = 2\left(LL_M - LL_B\right)$$

where Akaike Information Criteria (AIC) and Bayesian Information Criteria (BIC) used to rank models (Dutkowski et al., 2006) are derived as follows:

$$AIC = -2LL_{Ri} + 2t_i$$

$$BIC = -2LL_{Ri} + 2t_i log\ \nu$$

where LL is the log-likelihood of the model, t_i is the number of variance parameters in model i, and $\nu = n - p$ is the residual degrees of freedom.

Narrow sense heritabilities (h^2) were estimated for each model fit, using the additive genetic variance as a ratio of the phenotypic variance, expressed as the sum of the additive and residual variances:

$$h^2 = \frac{Var_A}{Var_A + Var_E}$$

where Var_A is the additive genetic variance and Var_E is the residual variance.

In the case of models with an AR1 term, the residual is represented by the units component (Dutkowski et al., 2002). Models where competition covariates terms were fitted for each trait (BC, and BAC) were ranked by LL and the best model selected. All models tested were ranked by LL (higher being better), and then associated h^2 and residual variance components were examined. Two metrics were derived to express the improvements of spatial models compared to the base model, the change in h^2, and in residual (ϵ), compared to the standard (base) model, multiplied by 100 to be expressed as percentages:

$$\Delta h^2 = \frac{h^2_M - h^2_B}{h^2_B}$$

$$\Delta \epsilon = \frac{\epsilon_M - \epsilon_B}{\epsilon_B}$$

where the subscripts M and B represent the spatial and base models, respectively.

RESULTS

Spatial models provided statistically significant improvements in LL over a base model for all traits (H, D, V, D_{38}, and A),

TABLE 3 | ASReml model fit statistics Log-likelihood (LL) and test statistic (*D*) and results heritability (h^2) with its standard error (SE), by trait and model, ordered by decreasing Log-likelihood (LL) within trait and traits are ordered by decreasing improvement in residual ($\Delta\varepsilon\%$) from the best model, improvement in heritability ($\Delta h^2\%$) is also shown.

Trait	Model	LL	*D*	h^2	SE	$\Delta h^2\%$	$\Delta\varepsilon\%$
H	BAC	−1291	<0.001	0.4117	0.0950	38.64	−65.48
	BC	−1381	<0.001	0.3011	0.0679	1.39	−32.90
	BA	−1758	<0.001	0.3425	0.0770	15.34	−24.87
	B	−1800	<0.001	0.2969	0.0660	–	–
DBH	BAC	−8406	<0.001	0.3753	0.0899	33.55	−63.65
	BC	−8440	<0.001	0.2954	0.0657	5.13	−38.90
	BA	−8930	<0.001	0.2950	0.0671	4.99	−8.58
	B	−8948	<0.001	0.2810	0.0636	–	–
V	BAC	5757	<0.001	0.3642	0.0856	22.47	−56.26
	BC	5742	<0.001	0.2980	0.0649	0.21	−31.89
	BA	5347	<0.001	0.3140	0.0678	5.60	−8.87
	B	5334	<0.001	0.2973	0.0640	–	–
D_{38}	BAC	−6024	<0.001	0.4912	0.0931	34.88	−50.31
	BC	−6096	<0.001	0.3546	0.0705	−2.63	−14.43
	BA	−6210	<0.001	0.4926	0.0922	35.28	−40.18
	B	−6276	<0.001	0.3642	0.0713	–	–
A	BAC	1052	<0.001	0.4862	0.1101	14.10	−21.03
	BC	1047	<0.001	0.4221	0.0764	−0.93	−0.30
	BA	1038	0.002	0.4531	0.0819	6.34	−9.63
	B	1033	<0.001	0.4261	0.0772	–	–

the ranking order in **Table 3** was BAC, BC, BA. Spatial BAC models resulted in reductions in residual ranging from −65.48% for *H* to −21.03% for *A*, and improvements in h^2 from 38.64% for *H* to 14.10% for *A*. Results confirmed prior research that auto-regressive order 1 (AR1) models are able to account for spatial effects from a wide variety of sources (Isik et al., 2017). Results also showed the utilization of a competition covariate in combination with an AR1 term explained additional variation, substantially reducing the residual and improving h^2 for all traits except D_{38}. The tree size traits *DBH*, *H*, and *V* benefited the most from competition covariates, and the greatest improvements in residual and h^2 relative to a BA model were −55% and 29%, respectively from a BAC model for *DBH*.

The use of competition covariates in spatial models without an AR1 term (BC models) resulted in statistically significant improvements in LL, and reductions in residuals. However, the BC models did not generally result in increased h^2, the best improvements being 5.13% and −2.63% for *D* and D_{38}, respectively. The sign and strength of Pearson's correlation coefficients (*r*) were examined to elucidate the relationships between crown metrics and traits (see **Table 4**).

The crown metric CV_F (see **Table 1**) appeared in the competition metric for the top performing BAC models for all traits except *A*. Models with competition metrics based on the CV_F crown metric were consistently ranked highest, but only marginally higher than models with the *CR* and CA_P crown metrics (results not shown). Those three metrics represented crown size in terms of volume, radius, and projected area, respectively. Moderate to strong correlations were observed for

TABLE 4 | Best performing (least Log-Likelihood) crown metrics in BAC models compared to the BA model by trait.

Trait	Model	Crown metric	N/CI	*r*
H	BAC	CV_F	N_B *CIA*	−0.5436
	BA			
DBH	BAC	CV_F	N_B *CIA*	−0.5990
	BA			
V	BAC	CV_F	N_B *CIA*	−0.5423
	BA			
D_{38}	BAC	CV_F	N_A *CIA*	0.3971
	BA			
A	BAC	A_{CG}	N_A *CIA*	0.1328
	BA			

The competition crown metric, neighborhood definition (N) and competition index (CI) used are shown along with Pearson's correlation coefficient (r) for the trait and crown metric.

competition metrics with tree size traits (*H*, *DBH*, and *V*, with *r* from −0.54 to −0.60) and with disease expression (D_{38}, $r = 0.40$). Results associated higher competition metrics with reduced tree size, and increased disease levels.

Competition metrics based on distance-weighted crown size metrics (*CIA*, *CIB*, *CIC*) were derived using area (N_A) and boundary (N_B) neighborhoods. The *CIA* formulation, representing a linear distance weighting of crown sizes, appeared in the best BAC models for all traits (**Table 4**) and the boundary neighbourhood definition (N_B) performed best for the tree size traits (*H*, *DBH*, and *V)*. The exponentially weighted derivations of competition index (*CIB* and *CIC*) were inferior.

DISCUSSION

The Autocorrelation-Competition-Error Approach

Results from our study have confirmed the recognized general utility of AR1 spatial models with a spatially independent units term to take account of spatial environmental variation (Costa et al., 2001; Dutkowski et al., 2006). However, spatial autocorrelation can be positive, representing various site effects such as temperature and aspect, and negative, representing competition effects. Competition effects can result in the mutual masking of these forms of autocorrelation (Griffith and Arbia, 2010). Where negative autocorrelation is left unaccounted for, it can even result in insignificant spatial autocorrelation test statistics. The inclusion of competition effects to reduce residual variation was described in a theoretical approach, focused on competition of genetic origin, and showed failure to account for competition resulted in biased model estimates and increased residual variation (Costa et al., 2013). Our study was a practical demonstration of the presence of both positive (site) and negative (competition) autocorrelation, and the best models combined AR1 and competition terms to explain these respective environmental sources of variation. Models having an explicit competition term and a generic term to account for

positive autocorrelation are referred to as ACE (autocorrelation-competition-error) models. Results confirmed our hypothesis that models including autoregressive and competition terms reduce residuals and improve estimates of heritabilities compared to conventional models without spatial terms.

The success of ACE models was attributed to three key features. Firstly, it was critical to separate negative and positive autocorrelation, representing variation due to competition and other environmental effects, respectively, which were otherwise confounded. Secondly, the inverse-distance weighted competition metrics employed successfully accounted for competition. Thirdly, we observed there are potentially numerous positively auto-correlated environmental effects on tree growth besides competition, which were robustly accounted for by an autoregressive model component. We suggest ACE models as a useful approach to analyses of tree and plant growth due to the ubiquity of both competition and site effects. Thus, we propose that it will be beneficial for modelers to test for, and quantify, those effects with ACE models, when possible, as a useful evolution of the currently recommended practice of applying AR1 models.

The competition and crown metrics utilized were parsimonious, easy to derive, and to interpret, which will aid application of ACE models. The competition metrics were of a widely recognized and applied form, utilizing positions and relative sizes of neighboring trees (Maleki et al., 2015). The crown metrics represented fundamental crown morphological features, and were derived from analysis of the CHM, a model of the upper surface of the canopy derived from the three-dimensional point cloud created by laser scanning (Pont et al., 2013). This is referred to as a raster-based approach, and is contrasted with point- and voxel-based methods which derive numerous measures from the three-dimensional point cloud, a majority of which are statistical measures of point dispersion (Zhen et al., 2016). The latter methods can yield large numbers of metrics, but we note that studies evaluating such metrics have typically found that a more limited set of crown morphological metrics, representing crown features such as diameter, length, area, and volume, were typically among the most useful variables in models estimating tree attributes (Vauhkonen et al., 2016). Raster based metrics derived using the methods described in this study permit the use of widely available point cloud data, either from ALS or photogrammetric methods (Krause et al., 2019), making the methods flexible and amenable to operational uses in forestry. Future research could compare the efficacy of ALS and photogrammetric data sources with ACE models.

Generality of ACE Models

An autoregressive model relates a characteristic of a target tree to the same characteristic of its neighbors, reflecting Tobler's first law of geography (Tobler, 1970). Autoregressive models make no attempt to explain effects or cause, and therein lies their power. We postulate that an AR1 term can effectively account for spatial effects from multiple sources and scales, particularly once a separate term for competition is included. As a hypothetical example of scale independence, consider a group of neighboring trees where height growth is being positively affected by soil fertility at a short scale, and negatively affected by temperature at a much larger scale. There could also be additional unknown influences on growth, all operating at different scales. An autoregressive model is agnostic to the factors or scales at play and utilizes the integrated result of all such effects on neighboring trees as a robust proxy for the effects on the target tree. The ACE approach could therefore robustly account for environmental variation of unknown sources and scales with an AR1 term, and is also amenable to the addition of terms representing explicit environmental effects as they are elucidated in future research.

Traits Have Distinct Environmental Responses

The ACE approach was shown to be beneficial for a range of traits, but it was also apparent that the relative amounts of variation due to genotype, competition, and site were distinct by trait. Tree *DBH* and *V* apparently had strong overall spatial variation, predominantly due to competition, while *H* also exhibited strong spatial variation due to nearly equal amounts of competition and site effects. The weaker competition effect noted for Dothistroma infection agreed with a predominant site effect due to the localized spread of the disease, reliant on a water-borne transmission, and re-infection of trees from fallen needles (Bulman et al., 2013) and the known tendency for the disease to occur in gullies due to increased moisture and reduced air movement (Bulman et al., 2004). The smaller, but evident, competition effect for D_{38} could reflect reduced tree growth resulting from the disease, or increased infection of smaller trees.

Applications

There are several important operational applications for tree level phenotyping which could be supported by the ACE modeling approach, ranging from trial, stand, and forest levels, for breeding, research, and management objectives. The use of ALS data provides accurate tree locations and sizes for use in competition metrics. It should be noted the modeling approach is even applicable to conventional ground measurement of trials, where remote sensed crown metrics are not available. In that case competition metrics could be derived from ground measured tree size, or other traits. The use of ACE models including known genetics in analysis of a genetics trial was shown to substantially reduce model residuals and improve heritabilities, potentially improving breeding values, tree selection, and future breeds. The benefits of improved tree breed selection for forest sites are accentuated in the context of climate change (Dungey et al., 2018; D'odorico et al., 2020; De Los Campos et al., 2020). The ACE method is also advocated for use in general research trial analyses to improve accuracy and precision of results by accounting for environmental variation. In this study ACE models were applied to tree size (*H*, *DBH*, *V*), disease expression (D_{38}) and wood quality (*A*), representing a set of traits of primary importance to tree breeders and forest managers.

CONCLUSION

Crown metrics utilized in competition metrics substantially reduced residual variation and improved heritabilities for a range of operationally relevant traits. Tree height, DBH,

volume, Dothistroma infection and stiffness exhibited significant variation attributable to spatial environmental effects. Analyses showed that traits exhibited distinct combinations of genotypic, competition, and site related variation, which needs be considered when modeling. The crown metrics and competition metrics identified in this study were parsimonious, effective, and warrant further investigation.

Analyses of results lead to the proposal of ACE models as a robust and effective approach to account for environmental variation in tree traits. Those models comprise an explicit competition term accounting for negative autocorrelation and a generic spatial term to account for positively autocorrelated site effects. Inclusion of a competition term, which we derived from individual tree crown metrics, was observed to be critical to improving the effectiveness of spatial modeling for environmental effects, avoiding the confounding of negative and positive autocorrelation.

The ACE approach is recommended for wider evaluation in tree and plant growth analyses, particularly for size and disease attributes. The analysis of remotely sensed data using ACE models will be developed and evaluated in future studies to determine utility in improving accuracy of trial analyses, identification of superior trees, tree growth research, and precision forest management.

DATA AVAILABILITY STATEMENT

The raw data supporting the conclusions of this article will be made available by the authors, without undue reservation.

AUTHOR CONTRIBUTIONS

DP developed the crown and competition metrics, carried out model fitting, and wrote the core of the manuscript. DP, HD, and MS contributed to development of modeling approach. GS carried out field ground truth data collection. All authors participated in the writing and review of the manuscript, contributed to the article, and approved the submitted version.

FUNDING

This research was supported by the 'Growing Confidence in Forestry's Future' program which is jointly funded by the New Zealand Ministry of Business, Innovation and Employment (contract CO4X1306) and the New Zealand Forest Growers Levy Trust.

ACKNOWLEDGMENTS

We are grateful to Timberlands Ltd., for supplying the LiDAR dataset and to the Radiata Pine Breeding Company Ltd., for making available trial measurement data. We would like to acknowledge useful discussions and support from Jaroslav Klapste on ASReml model specification and evaluation. We also gratefully acknowledge Rod Brownlie, Rodrigo Osorio, Toby Stovold, Mark Miller, Kane Fleet, and Jody Wharekura for collection of the ground measurements at the genetics trial used in this study.

REFERENCES

Andersen, H. E., Reutebuch, S. E., and Mcgaughey, R. J. (2006). A rigorous assessment of tree height measurements obtained using airborne LiDAR and conventional field methods. *Can. J. Remote Sens.* 32, 355–366. doi: 10.5589/m06-030

Bulman, L. S., Dick, M. A., Ganley, R. J., Mcdougal, R. L., Schwelm, A., and Bradshaw, R. E. (2013). "Dothistroma needle blight," in *Infectious Forest Diseases*, eds P. Gonthier and G. Nicolotti (Wallingford: CAB International).

Bulman, L. S., Gadgil, P. D., Kershaw, D. J., and Ray, J. W. (2004). *Assessment and control of Dothistroma needle blight Forest Research Bulletin*, (New Zealand: Forest Research).

Burkhart, H. E., and Tomé, M. (2012). "Indices of individual-tree competition," in *Modeling Forest Trees and Stands*, eds H. E. Burkhart and M. Tomé (Dordrecht: Springer Netherlands), 201–232. doi: 10.1007/978-90-481-3170-9_9

Butler, D. G., Cullis, B. R., Gilmour, A. R., and Gogel, B. J. (2009). *ASReml-R reference manual*. The State of Queensland: The Department of Primary Industries and Fisheries.

Cappa, E. P., and Cantet, R. J. C. (2008). Direct and competition additive effects in tree breeding: Bayesian estimation from an individual tree mixed model. *Silvae Genetica* 57, 45–56. doi: 10.1515/sg-2008-0008

Carson, S. D., Cown, D. J., Mckinley, R. B., and Moore, J. R. (2014). Effects of site, silviculture and seedlot on wood density and estimated wood stiffness in radiata pine at mid-rotation. *N. Zealand J. Forestry Sci.* 44, 1–12. doi: 10.1186/s40490-014-0026-3

Chen, Q., Gong, P., Baldocchi, D., and Tian, Y. Q. (2007). Estimating basal area and stem volume for individual trees from LiDAR data. *Photogram. Eng. Remote Sens.* 73, 1355–1365. doi: 10.14358/PERS.73.12.1355

Costa, E., Silva, J., and Kerr, R. J. (2013). Accounting for competition in genetic analysis, with particular emphasis on forest genetic trials. *Tree Genet. Genom.* 9, 1–17. doi: 10.1007/s11295-012-0521-8

Costa, E., Silva, J., Dutkowski, G. W., and Gilmour, A. R. (2001). Analysis of early tree height in forest genetic trials is enhanced by including a spatially correlated residual. *Can. J. Forest Res.* 31, 1887–1893. doi: 10.1139/x01-123

Cullis, B. R., Jefferson, P., Thompson, R., and Smith, A. B. (2014). Factor analytic and reduced animal models for the investigation of additive genotype-by-environment interaction in outcrossing plant species with application to a *Pinus radiata* breeding programme. *Theor. Appl. Genet.* 127, 2193–2210. doi: 10.1007/s00122-014-2373-0

Cullis, B., Gogel, B., Verbyla, A., and Thompson, R. (1998). Spatial analysis of multi-environment early generation variety trials. *Biometrics* 54, 1–18. doi: 10.2307/2533991

Dalponte, M., Frizzera, L., Ørka, H. O., Gobakken, T., Næsset, E., and Gianelle, D. (2018). Predicting stem diameters and aboveground biomass of individual trees using remote sensing data. *Ecol. Indicat.* 85, 367–376. doi: 10.1016/j.ecolind.2017.10.066

De Los Campos, G., Perez-Rodriguez, P., Bogard, M., Gouache, D., and Crossa, J. (2020). A data-driven simulation platform to predict cultivars' performances under uncertain weather conditions. *Nat. Commun.* 11:4876. doi: 10.1038/s41467-020-18480-y

D'odorico, P., Besik, A., Wong, C. Y. S., Isabel, N., and Ensminger, I. (2020). High-throughput drone-based remote sensing reliably tracks phenology in thousands of conifer seedlings. *N. Phytolog.* 226, 1667–1681. doi: 10.1111/nph.16488

Dong, L., Xie, Y., Wu, H. X., and Sun, X. (2020). *Spatial and competition models increase the progeny testing efficiency of Japanese larch**. doi: 10.1139/cjfr-2020-0007

Dungey, H. S., Brawner, J. T., Burger, F., Carson, M., Henson, M., Jefferson, P., et al. (2009). A new breeding strategy for *Pinus radiata* in New Zealand and New South Wales. *Silvae Genetica* 58, 28–38. doi: 10.1515/sg-2009-0004

Dungey, H. S., Dash, J. P., Pont, D., Clinton, P. W., Watt, M. S., and Telfer, E. J. (2018). Phenotyping Whole Forests Will Help to Track Genetic Performance. *Trends Plant Sci.* 23, 854–864. doi: 10.1016/j.tplants.2018.08.005

Dungey, H. S., Matheson, A. C., Kain, D., and Evans, R. (2006). Genetics of wood stiffness and its component traits in *Pinus radiata*. *Can. J. Forest Res.* 36, 1165–1178. doi: 10.1139/x06-014

Dungey, H. S., Russell, J. H., Costa, E., Silva, J., Low, C. B., Miller, M. A., et al. (2012). The effectiveness of cloning for the genetic improvement of Mexican white cypress *Cupressus lusitanica (Mill.)*. *Tree Genet. Genom.* 9, 443–453. doi: 10.1007/s11295-012-0565-9

Dutkowski, G. W., Costa, E., Silva, J., Gilmour, A. R., Wellendorf, H., and Aguiar, A. (2006). Spatial analysis enhances modelling of a wide variety of traits in forest genetic trials. *Can. J. Forest Res.* 36, 1851–1870. doi: 10.1139/x06-059

Dutkowski, G. W., Silva, J. C. E., Gilmour, A. R., and Lopez, G. A. (2002). Spatial analysis methods for forest genetic trials. *Can. J. Forest Res.* 32, 2201–2214. doi: 10.1139/x02-111

Fahlgren, N., Gehan, M. A., and Baxter, I. (2015). Lights, camera, action: High-throughput plant phenotyping is ready for a close-up. *Curr. Opinion Plant Biol.* 24, 93–99. doi: 10.1016/j.pbi.2015.02.006

Fins, L., Friedman, S. T., and Brotschol, J. V. eds (1992). *Handbook of quantitative forest genetics*. Dordrecht: Springer Science & Business Media. doi: 10.1007/978-94-015-7987-2

Forest Owners Association. (2019). *New Zealand Plantation Forest Industry Facts and figures*. New Zealand: Forest Owners Association.

Gilmour, A. R., Cullis, B .R., and Verbyla, A. P. (1997). Accounting for natural and extraneous variation in the analysis of field experiments. *J. Agr. Biol. Environ. Stat.* 2, 269–293. doi: 10.2307/1400446

Goulding, C. J. (1995). "Individual tree volume, taper, bark, and breakage equations," in *Forestry handbook*, ed Edn, ed. D. Hammond (New Zealand: New Zealand Institute of Foresters (Inc.)), 115–116.

Griffith, D. A., and Arbia, G. (2010). Detecting negative spatial autocorrelation in georeferenced random variables. *Int. J. Geograp. Inform. Sci.* 24, 417–437. doi: 10.1080/13658810902832591

Hauglin, M., Gobakken, T., Astrup, R., Ene, L., and Næsset, E. (2014). Estimating single-tree crown biomass of norway spruce by airborne laser scanning: A comparison of methods with and without the use of terrestrial laser scanning to obtain the ground reference data. *Forests* 5, 384–403. doi: 10.3390/f5030384

Hegyi, F. (1974). "A simulation model for managing jackpine stands Growth models for tree and stand simulation," in *Proceedings of the IUFRO Meeting*, Sweden: Royal College of Forestry. 74–90.

Isik, F., Holland, J., Maltecca, C., and Whetten, R. (2017). *Genetic data analysis for plant and animal breeding*. New York,NY: Springer International Publishing. doi: 10.1007/978-3-319-55177-7

Jayawickrama, K. J. S. (2001). Genetic parameter estimates for radiata pine in New Zealand and New South Wales: A synthesis of results. *Silvae Genetica* 50, 45–53.

Krause, S., Sanders, T. G. M., Mund, J.-P., and Greve, K. (2019). UAV-Based Photogrammetric Tree Height Measurement for Intensive Forest Monitoring. *Remote Sens.* 11:758. doi: 10.3390/rs11070758

Lindberg, E., Holmgren, J., Olofsson, K., Wallerman, J., and Olsson, H. (2013). Estimation of tree lists from airborne laser scanning using tree model clustering and k-MSN imputation. *Remote Sens.* 5, 1932–1955. doi: 10.3390/rs5041932

Maleki, K., Kiviste, A., and Korjus, H. (2015). Analysis of individual tree competition on diameter growth of Silver Birch in Estonia. *Forest Syst.* 24:e023. doi: 10.5424/fs/2015242-05742

Maltamo, M., Naesset, E., and Vauhkonen, J. (2014). *Forestry applications of airborne laser scanning*. Netherlands: Springer.

Pont, D. (2016). *Assessment of individual trees using aerial laser scanning in New Zealand Radiata Pine forests*. Ph.D thesis, University of Canterbury.

Pont, D., Kimberley, M. O., Brownlie, R. K., Sabatia, C. O., and Watt, M. S. (2015). Calibrated tree counting on remotely sensed images of planted forests. *Int. J. Remote Sens.* 36, 3819–3836. doi: 10.1080/01431161.2015.1054048

Pont, D., Morgenroth, J., and Watt, M. S. (2013). "Tree-based analysis of ALS to estimate tree size and quality," in *proceeding of the MeMoWood – Measurement Methods and Modelling Approaches for Predicting Desirable Future Wood Properties*, Nancy.

Pretzsch, H. (2010). *Forest dynamics, growth and yield: From measurement to model*. Berlin Heidelberg: Springer-Verlag.

Pukkala, T., Vettenranta, J., Kolström, T., and Miina, J. (1994). Productivity of mixed stands of *pinus sylvestris* and *picea abies*. *Scandinavian J. Forest Res.* 9, 143–153. doi: 10.1080/02827589409382824

Ronse, C., and Heijmans, H. J. A. M. (1991). The algebraic basis of mathematical morphology: II. Openings and closings. *CVGIP: Image Understanding* 54. 74–97. doi: 10.1016/1049-9660(91)90076-2

Rouvinen, S., and Kuuluvainen, T. (1997). Structure and asymmetry of tree crowns in relation to local competition in a natural mature scots pine forest. *Can. J. Forest Res.* 27, 890–902. doi: 10.1139/x97-012

Suárez, J. C. (2010). *An analysis of the consequences of stand variability in sitka spruce plantations in Britain using a combination of airborne LiDAR analysis and models*. Ph.D thesis, University of Sheffield.

Suontama, M., Low, C. B., Stovold, G. T., Miller, M. A., Fleet, K. R., Li, Y., et al. (2015). Genetic parameters and genetic gains across three breeding cycles for growth and form traits of *Eucalyptus regnans* in New Zealand. *Tree Genet. Genom.* 11:133. doi: 10.1007/s11295-015-0957-8

Tobler, W. (1970). A computer movie simulating urban growth in the Detroit region. *Econom. Geograp.* 1970, 234–240. doi: 10.2307/143141

Tsaftaris, S. A., Minervini, M., and Scharr, H. (2016). Machine learning for plant phenotyping needs image processing. *Trends Plant Sci.* 21, 989–991. doi: 10.1016/j.tplants.2016.10.002

Van Der Pas, J. B., Bulman, L., and Slater-Hayes, J. D. (1984). Evaluation of the assessment of Dothistroma needle blight in stands of *Pinus radiata*. *N. Zealand J. Forestry Sci.* 14, 3–13.

Vauhkonen, J., Holopainen, M., Kankare, V., Vastaranta, M., and Viitala, R. (2016). Geometrically explicit description of forest canopy based on 3D triangulations of airborne laser scanning data. *Remote Sens. Environ.* 173, 248–257. doi: 10.1016/j.rse.2015.05.009

Watt, M., Bulman, L., and Palmer, D. (2011). The economic cost of Dothistroma needle blight to the New Zealand forest industry. *N. Zealand J. Forestry* 56, 20–22.

White, J. C., Wulder, M. A., Varhola, A., Vastaranta, M., Coops, N. C., Cook, B. D., et al. (2013). *A best practices guide for generating forest inventory attributes from airborne laser scanning data using an area-based approach (Version 2.0)*. Victoria: Canadian Wood Fibre Centre.

Zhen, Z., Quackenbush, L., and Zhang, L. (2016). Trends in automatic individual tree crown detection and delineation – Evolution of LiDAR data. *Remote Sens.* 8:333. doi: 10.3390/rs8040333

Conflict of Interest: The authors declare that the research was conducted in the absence of any commercial or financial relationships that could be construed as a potential conflict of interest.

frontiers in Plant Science

ORIGINAL RESEARCH
published: 10 February 2021
doi: 10.3389/fpls.2021.612843

Development and Validation of Methodology for Estimating Potato Canopy Structure for Field Crop Phenotyping and Improved Breeding

*Filipe de Jesus Colwell[1], Jock Souter[2], Glenn J. Bryan[3], Lindsey J. Compton[4], Neil Boonham[1] and Ankush Prashar[1]**

[1] School of Natural Environmental Sciences, Newcastle University, Newcastle upon Tyne, United Kingdom, [2] Survey Solutions Scotland, Edinburgh, United Kingdom, [3] The James Hutton Institute, Dundee, United Kingdom, [4] School of Biosciences, University of Birmingham, Birmingham, United Kingdom

Traditional phenotyping techniques have long been a bottleneck in breeding programs and genotype- phenotype association studies in potato, as these methods are labor-intensive and time consuming. In addition, depending on the trait measured and metric adopted, they suffer from varying degrees of user bias and inaccuracy, and hence these challenges have effectively prevented the execution of large-scale population-based field studies. This is true not only for commercial traits (e.g., yield, tuber size, and shape), but also for traits strongly associated with plant performance (e.g., canopy development, canopy architecture, and growth rates). This study demonstrates how the use of point cloud data obtained from low-cost UAV imaging can be used to create 3D surface models of the plant canopy, from which detailed and accurate data on plant height and its distribution, canopy ground cover and canopy volume can be obtained over the growing season. Comparison of the canopy datasets at different temporal points enabled the identification of distinct patterns of canopy development, including different patterns of growth, plant lodging, maturity and senescence. Three varieties are presented as exemplars. Variety Nadine presented the growth pattern of an early maturing variety, showing rapid initial growth followed by rapid onset of senescence and plant death. Varieties Bonnie and Bounty presented the pattern of intermediate to late maturing varieties, with Bonnie also showing early canopy lodging. The methodological approach used in this study may alleviate one of the current bottlenecks in the study of plant development, paving the way for an expansion in the scale of future genotype-phenotype association studies.

Keywords: high throughput phenotyping, plant breeding, unmanned aerial vehicles, canopy structure, potato, crop growth and development, crop surface models

OPEN ACCESS

Edited by:
Shawn Carlisle Kefauver, University of Barcelona, Spain

Reviewed by:
Wei Guo, The University of Tokyo, Japan
Omar Vergara-Diaz, University of Barcelona, Spain

***Correspondence:**
Ankush Prashar
ankush.prashar@newcastle.ac.uk

Specialty section:
This article was submitted to Technical Advances in Plant Science, a section of the journal Frontiers in Plant Science

Received: *08 October 2020*
Accepted: *19 January 2021*
Published: *10 February 2021*

Citation:
de Jesus Colwell F, Souter J, Bryan GJ, Compton LJ, Boonham N and Prashar A (2021) Development and Validation of Methodology for Estimating Potato Canopy Structure for Field Crop Phenotyping and Improved Breeding. Front. Plant Sci. 12:612843. doi: 10.3389/fpls.2021.612843

INTRODUCTION

Potato (*Solanum tuberosum* L.) is the fourth most important food crop in the world and is regarded as one of the highest yielding crops amongst the staple foods (Birch et al., 2012). In order to feed a growing population under changing climatic conditions, the demand for high yielding and stress tolerant varieties is expected to increase (Birch et al., 2012). While on one hand breeders

and biotechnologists have focussed on engineering and breeding crop plants for achieving higher yields and quality, on the other the aim is to maintain agricultural productivity under changing environmental conditions by combating abiotic and biotic stresses.

Breeding programs have traditionally focused on commercially important traits, the major one being yield. Plant performance, along with economic yield, has been shown to be strongly associated with traits related to plant growth and development. These include plant architecture, leaf structure and vascular architecture as some of the major traits that determine overall crop performance (Mathan et al., 2016). Thus, in order to meet the increase in demand for high yielding and stress tolerant crops, it is necessary to expand breeding programs to encompass traits linked to plant growth and development (Prashar et al., 2013; Yang et al., 2017). Engineering developmental and growth traits with the aim of improving plant performance and yield requires a thorough understanding of the underlying genetics, which can be linked with quantitative phenotypic assessments. In the last few decades there has been major developments in genomic and genotyping technologies allowing faster and cheaper creation of complete genetic profiles (Wang et al., 2018), but despite these advances there are few genomics-assisted breeding programs.

One of the major current limiting factors in modern breeding programs is the acquisition of large-scale phenotypic assessment under natural conditions in the field for performance traits. Most of these evaluations have been conducted in controlled environments until very recently (Anithakumari et al., 2011; Khan et al., 2015). However, results from such environments may poorly predict what happens under field conditions (Prashar and Jones, 2014; Williams et al., 2017; Yang et al., 2017). Furthermore, such studies frequently use only a small number of genotypes, and thus may fail to detect Quantitative Trait Loci (QTL) with small effect sizes. In addition, greater precision in phenotypic data collection allows the increase in selection accuracy in breeding, which is a function of heritability, which increases with increased repeatability and thus rate of genetic gain also increases (Araus et al., 2018). Phenotypic evaluation for the genetic study of performance related traits therefore requires large-scale field studies (Prashar et al., 2013; Prashar and Jones, 2014) involving large genetic populations (Furbank and Tester, 2011; Lopes and Reynolds, 2012). However, the requirement for phenotypic assessment is currently one of the major bottlenecks in both genotype-phenotype association studies and large-scale breeding programs.

Current phenotyping methodologies are very laborious and time consuming and therefore impractical for large-scale field studies. In addition, depending on the trait being measured, they can be inaccurate, inconsistent and susceptible to user assessment bias (Friedli et al., 2016; Jimenez-Berni et al., 2018; Wang et al., 2018). For example, leaf area index (LAI) and ground cover (GC) are two traits frequently used in monitoring plant growth (Khurana and McLaren, 1982; Boyd et al., 2002), with most potato yield prediction models requiring at least one of these (Haverkort et al., 2015; Raymundo et al., 2017). Traditional methods such as the use of grids to estimate GC, or light interception based techniques to estimate LAI, are labor-intensive and time consuming (Khurana and McLaren, 1982; Boyd et al., 2002). These challenges limit monitoring to small sample plots, which may not accurately represent the heterogeneity in agricultural fields. This seriously limits the high accuracy and precision that is required in modern agriculture, not only to achieve lower resource inputs and hence environmental impact, but also to accelerate genetic gain through increasing heritability, and hence selection accuracy (Araus et al., 2018). Remote sensing techniques for quantitative assessments and stress detection have been suggested as a possible solution to these limitations (Prashar et al., 2013; Friedli et al., 2016; Yang et al., 2017; Jimenez-Berni et al., 2018; Wang et al., 2018).

Sensing approaches used for crop trait phenotyping and crop monitoring include satellite-based systems, manned aircraft or unmanned aerial vehicle (UAV) linked systems and tractor mounted sensing tools. Satellite remote sensing is capable of monitoring large areas at the same time and has undergone significant improvements in recent years, especially with regards to spatial resolution and increased coverage due to the addition of low orbit satellites. Nevertheless, it still frequently lacks the spatial resolution necessary for precise and detailed canopy phenotyping of relatively small plots. Satellites are also limited to data collection or observations at fixed times, which may not match the phenotyping needs, and by cloud coverage, which may impede data collection during those times (Berni et al., 2009; Matese et al., 2015). In recent decades, UAV technology has become more accurate, and importantly, more affordable. It is capable of monitoring agricultural fields with greater flexibility and higher spatial resolution, in a short time period (Matese et al., 2015; Yang et al., 2017). The nature and extent of the data to be collected with UAVs depends on the type of sensor used (Yang et al., 2017). RGB sensors allow not only visual assessment of the sampled areas, but also the assessment of traits influencing plant development from the point cloud data, such as leaf color, plant height, canopy cover and 3D plant structure. Near-Infrared (NIR) sensors allow estimation of various vegetation indices that can be used to estimate biomass, nitrogen content and disease detection, while thermal sensors are useful for understanding stress and assessing water status (Yang et al., 2017; Zheng et al., 2018; Roitsch et al., 2019). Through the combined use of different types of sensor, numerous traits can be evaluated more efficiently and objectively, with the potential for temporal studies with more frequent data collection points, enabling accurate growth and development models to be created (Prashar et al., 2013; Friedli et al., 2016; Yang et al., 2017; Jimenez-Berni et al., 2018; Wang et al., 2018).

With the images acquired by UAV equipment using various sensors (RGB, multispectral and/or hyperspectral), Structure from Motion (SfM) point cloud data has been used to understand plant growth and development. Early applications of this method include artificial monocultures (e.g., orchards) and diverse biomes (e.g., forestry), which share many of the same challenges, including resource intensive monitoring of large areas and understanding tree crown heterogeneity. For example, a combination of RGB and NIR sensors have been used to develop an object-based image analysis technique for

automatically calculating tree height, canopy cover and volume of individual olive trees (Torres-Sánchez et al., 2015), as well as to assess the effect of different pruning methods on olive tree growth (Jiménez-Brenes et al., 2017). UAV based systems have also shown potential for estimating flower biodiversity (Getzin et al., 2012) and for the creation of a rapid and accurate forest census (Mohan et al., 2017). However, applications in agriculture have mostly been limited to cereals (Bendig et al., 2013, 2014, 2015; Holman et al., 2016; Jin et al., 2017) and cotton (Xu et al., 2019). In potato, UAV acquired images have been used to estimate plant emergence (Sankaran et al., 2017; Li et al., 2019) and assess disease severity (Sugiura et al., 2016; Franceschini et al., 2017). However, there have been no published studies related to plant structure, including canopy architecture and development, under field conditions.

This article evaluates the use of a low-cost UAV system, mainly in the form of RGB imaging resources and obtained datasets, for understanding plant growth and development in potato under natural field conditions. The image datasets from this system are used to develop new methodology for quantifying canopy growth parameters and assessing canopy variability through developing crop growth and development models, with validation using ground truth datasets. This methodology enables quantitative trait assessment and modeling of growth and development parameters in potato, which can allow high-throughput phenotyping of canopy traits for integration with large-scale genetic datasets and hence the improvement of future potato breeding programs.

MATERIALS AND METHODS

Plant Material and Field Layout

The data used in this paper forms part of a large study that was performed at Nafferton Farm, Newcastle University, United Kingdom, with field trials at 54°59′12.0″N 1°53′33.9″W/54.986655, −1.892751 and 54°58′51.3″N 1°53′56.5″W/54.980924, −1.899018, in 2017 and 2018 respectively. A total of 297 varieties of potato (*Solanum tuberosum* L.), which form a large part of a tetraploid variety association panel available at The James Hutton Institute (Sharma et al., 2018), were planted in April 2017 and May 2018. The experimental design consisted of two replicate blocks for each of two management systems (organic and conventional), making a total of 4 blocks. Each block consisted of 6 rows spaced 90 cm apart and comprising 50 plots per row. Each plot contained 3 plants of a given variety planted 35 cm apart. Spacing of 90 cm was maintained between plots within each row. To minimize edge effects, a row of guard plants was planted surrounding each block. Both conventional and organic trials were conducted using their respective standard management practices.

UAV Flight Parameters

UAV flights were performed in collaboration with Survey Solutions Scotland using a fixed wing UX5 HP UAV (Trimble, Sunnyvale, California, United States). The UX5 HP uses Global Navigation Satellite System (GNSS) post-processed kinematic techniques to determine the UAV trajectory. Images were taken using a Sony α7R 36MP full frame 35 mm RGB camera with a custom made Voigtlander 35 mm lens. The 35 mm lens was selected to deliver a 1.0 cm Ground Sample Distance (GSD) at 75 m Above Ground Level (AGL), while also offering pixel sizes down to 4.9 μm, to maximize the signal to noise ratio and dynamic range, while maintaining affordability. Given the importance of the canopy volume in this research, a UAV sensor with a global rather than a sliding shutter was selected for the imagery as this greatly reduces noise in the images, which leads to a much cleaner and more precise deliverable. The data was collected at 75 m altitude with overlaps of 85% (both front and side) between neighboring images. The speed of flight was nominally 85 km/h, therefore flying height was restricted to 75 m AGL to minimize image distortion due to motion blur. Details of flight dates and their relation to canopy development in days after planting are given in **Table 1**.

Image and Data Analysis

The images acquired using UAV were processed and analyzed using the Trimble Business Center (TBC) software version 4.1 and 5.0, for the 2017 and 2018 datasets, respectively (Trimble, Sunnyvale, California, United States). This includes the subsequent use of GCP referencing, point cloud data generation, creation of digital surface models, manual plot demarcation, computation of difference models and canopy data acquisition e.g., canopy cover and volume (further details in the following sections). Plant height data clean up, subsequent statistical analysis (regression and correlation) and other data processing was carried out in R (R: Project for Statistical Computing, The R foundation) using the following packages: dplyr, ggplot2, gridExtra, Hmisc, plotrix, plyr, SDMtools, tidyr, tidyverse (Lemon, 2006; Wickham, 2011, 2016; Vanderwal et al., 2014; Wickham et al., 2015, 2019; Baptiste, 2017; Wickham and Henry, 2019; Harrell, 2020).

UAV DATA PRE-PROCESSING

UAV Trajectory Processing

Raw GNSS data was recorded in the UX5 HP UAV by the on-board 336-channel multi constellation GNSS receiver, which is downloaded at the end of the flight and processed against a local base station situated within our flight area. The local base position

TABLE 1 | Planting and UAV flight schedule for assessing potato canopy characteristics.

Year	Planting	Flight date	Days after planting
2017	28-04-2017	07-07-2017	70
		24-07-2017	87
		08-08-2017	102
2018	03-05-2018	05-06-2018	33
		04-07-2018	62
		06-08-2018	95
		28-08-2018	117

was established by processing the local base against Ordnance Survey CORS (Continuously Operating Reference Stations), sourcing 1 hourly RINEX data, which provide GNSS data at reference stations coordinated in ETRS89 (ETRF2009.756). Processing the local base station relative to known Ordnance Survey CORS (OSNet) helps in establishing the position of the local base for each UAV flight and its repeatability is assured. Processing multi constellation GNSS data relative to fixed OS CORS typically gave estimated precisions of ≈5 mm in plan and ≈20 mm in height (at 95% confidence) over 30 km baselines. OSTN15 CORS stations, relative to each other, are considered error free. The processed base stations used the OSTN15 transformation model and OSGM15 geoid correction surface to convert the ETRS89 global WGS84 coordinates into Ordnance Survey (OS) grid coordinates. The local base was processed (using the final local base station coordinate) against the 20 Hz UAV data to produce a continuous flight trajectory of the UAV. This estimated *a posteriori* trajectory accuracy of 97.20% @ 0–5 cm and 2.60% @ 5–15 cm, and the remaining values were considered outliers.

PPK (Post-processed Kinematic) was used to create the trajectory as it is more robust than alternative methods, which may rely on radio or other communications. In addition, precise ephemerides can be incorporated into the processing later, to enhance the baseline processing algorithms if needed. Although we used a processed UAV trajectory, we still used and placed Ground Control Points (GCPs) as required, but the number of these can be greatly reduced in comparison to non-PPK methods.

Photogrammetric Processing

The UAV trajectory was processed in TBC software, with feedback events recorded at better than millisecond accuracy. This helps to precisely establish the location of the photo center of each image at the time of exposure. Having image positions at the cm level negates the need for dense pixel matching, a process which is required in non-PPK aerial photogrammetric processing. It also greatly reduces the need for intensive, time consuming and expensive GCP placement, which would be impractical given the expected development of the canopy in this research.

Around 6 GCPs were placed in the periphery of the trial and were used in all flights to ensure repeatable and accurate deliverables and to generate an accurate camera calibration. In addition to being measured as vectors from the local base, the GCPs were also georeferenced using Network RTK (Real-time Kinematic), which provides an independent check on the GCP coordinates. These GCP coordinates were fixed for the duration of the project, thus providing a common datum for all flights in a given year.

Image Processing

The images were imported into TBC software at the same time as the Raw GNSS data, so that when the trajectory is processed and the event markers created, each image will be positioned in the correct 3D position. To resolve the orientation of each image, i.e., the omega, phi and kappa rotations, a precise Interior Orientation (IO) is computed using the GNSS positions, i.e., a tie point adjustment, highlighting how well the images tie together. In non-PPK processing, this is a computer intensive and time-consuming process. However, a PPK trajectory resolves for the image location, thus only the orientation needs to be resolved, resulting in a more rapid and robust solution.

The IO was followed by an exterior orientation (EO) with camera calibration. For the EO, visible GCPs in each image were "picked" so that the real-world coordinates are allocated to the GCP image coordinates (as produced by RTK observations and verified by Network RTK). As mentioned above, GCPs allow camera calibration and computation of distortion parameters for the lens. The combination of GNSS and GCPs also allows computation of the focal length. Both of these parameters are a necessity for creating "noiseless" deliverables. After the EO is performed, the flight report is analyzed for errors and accuracy. The low errors and high confidence accuracy confirms the validity of the flight and ensures observation repeatability over the duration of the experiment (data not presented).

UAV DATA PROCESSING

Deliverable Creation

The next step after measuring accuracy and acceptance of the EO results is to create deliverables (e.g., point cloud, orthophoto, etc.). Both point cloud and true orthophotos require well-orientated images. Different types of surfaces can be generated from orthomosaic images. Surface generation is the creation of a point cloud and it requires at least two, and preferably more, overlapping images. Insufficient overlap produces noise, or worse, gaps in the data. A surface was generated using the maximum resolution available (appropriate to the flight parameters) using a Cost-based Matching algorithm. Briefly, the algorithm uses pixel-by-pixel matching, rather than an area based or feature based technique, though a detailed discussion of the algorithm is beyond the scope of this work.

The orthophoto (i.e., geometrically corrected or orthorectified) was created after processing of the point cloud surface, to give an image where the scale is uniform and true. A "True" orthophoto rather than "Classic orthophoto" was selected because it uses the surface model to calculate occlusions and fill them in from other images, which is essential when the canopy is not uniform. A "Classic" orthophoto, on the other hand, would require bare Earth.

Preliminary Data Clean Up

Raw data and the generated point clouds typically include errors due to several factors. These include vegetation movement due to wind, UAV crabbing in flight, which lessens the expected image overlap and bad reflection points (i.e., noise due to inadequate overlap and image uncertainty). These erroneous points need to be removed from the point cloud (**Figure 1A**). This was accomplished by the manual removal of points that would be considered impossible, as determined by their height based on proximity to other points, position in the field, and visual inspection of the point cloud. We used a manual removal process because the outlier points

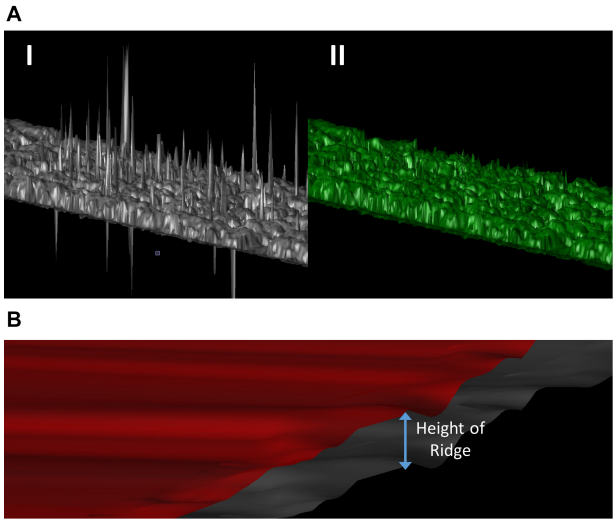

FIGURE 1 | (A) 3D representation of the point cloud before (I) and after (II) the manual removal of erroneous points. **(B)** Generation of a soil reference surface (red surface) by increasing every point of the topographical surface (gray surface) by the average height of all the ridges in the block.

in our data were sparse and inconsistent in local point density. Automatic outlier removal methods are available if needed, such as the discontinuous operators-based method (Ning et al., 2018).

Surface Model Creation

Following clean up, the point cloud data was used to generate two surfaces (where surface is referred here as 3D models generated from point cloud data), including one for the soil reference and another for the canopy. Surfaces created in the TBC software are a 3D digital representation of topography (in this case, canopy), formed by a mesh of contiguous triangles, and sometimes referred to as a Triangulated Irregular Network (TIN). The triangles are connected at their vertices, which are defined by points with horizontal positions (X and Y–values) and elevations (Z-values), i.e., points in a point cloud forming three sided planar faces. The surface model from a point cloud is a simple set of triangles, but can be enhanced by the inclusion (or omission) of boundaries, break lines, and points, etc. that make up the surface model and that are used to define its shape.

Canopy surfaces in our case used the totality of the point cloud within each experimental block. Ideally, the creation of a soil reference surface would use point cloud data from below the canopy, but Structure from Motion imagery does not permit this, especially when plants are growing. Therefore, to overcome this limitation a surface was created to estimate the soil topography. Since potatoes are grown on ridges, a topographical surface was first created using the bare soil surrounding the plants, hence excluding the ridges and any potential vegetation. Second, the height of every point on this surface was increased by the average height of all the ridges in the block to construct a raised surface (**Figure 1B**).

Difference Model Creation and Plot Demarcation

As a next step after generating surfaces, difference models were created for the entirety of each experimental block. Difference models are a 3D representation of a model, where each point in the model has the elevation difference between two surfaces on the same point. Once generated, this difference model was then used in combination with the orthomosaic image to accurately demarcate individual plots. The demarcation of individual plots made it possible to create difference models for each and every plot in each block, using the same surfaces that were created previously, from which we are able to extract canopy volume, ground cover and canopy height datasets for further analysis. Details of the workflow are shown in **Figure 2**.

Difference Model Computation Methods

Two difference model computation methods were compared (**Figure 3**). The "trace all triangles" method (**Figure 3B**) creates a new vertex at each point of the point cloud where soil surface and canopy surface triangles either overlap or intersect, while taking into account any existing breaklines created during demarcation. These vertices serve as new points for the creation of the difference model; therefore, the resulting difference model has a denser mesh of vertices than the original surfaces. The "do not track breaklines" method (**Figure 3C**) uses only existing points of the point cloud to create a difference model, ignoring breaklines and not creating new vertices, with the generated difference model having the same density of vertexes as the original surfaces. For comparison, 300 field plots were selected and both methods were applied to generate the triangular mesh. Subsequent calculations of plot volume were compared using Spearman's rank correlation coefficient.

Plant Height Calculation

The difference model helps us build up the height data at any point within the plot area, at a resolution of 1 cm. This allows us not only to determine the highest point within the demarcated area (representing the maximum height of the 3 plants within the plot), but also allows the construction of a frequency table of the height distribution that provides information on the canopy structure and allows calculation of the average height of the plants.

Plant Height Data Clean Up

Preliminary point cloud clean-up removes the more noticeable errors, which tend to be the impossible or unrealistic values. However, smaller errors tend to remain in the point cloud. These smaller errors have a negligible effect on the average height, but maximum height is more susceptible to influence. Weeds are also a probable source of errors when it is not possible to manually remove them from the potato plants. An integrated approach using different imaging sensors (not illustrated here) is more valid in this scenario but falls outside the scope of this work. Small weeds will provide a small, potentially negligible, effect on the histograms and the average height. However, maximum height can easily be overestimated because of a single

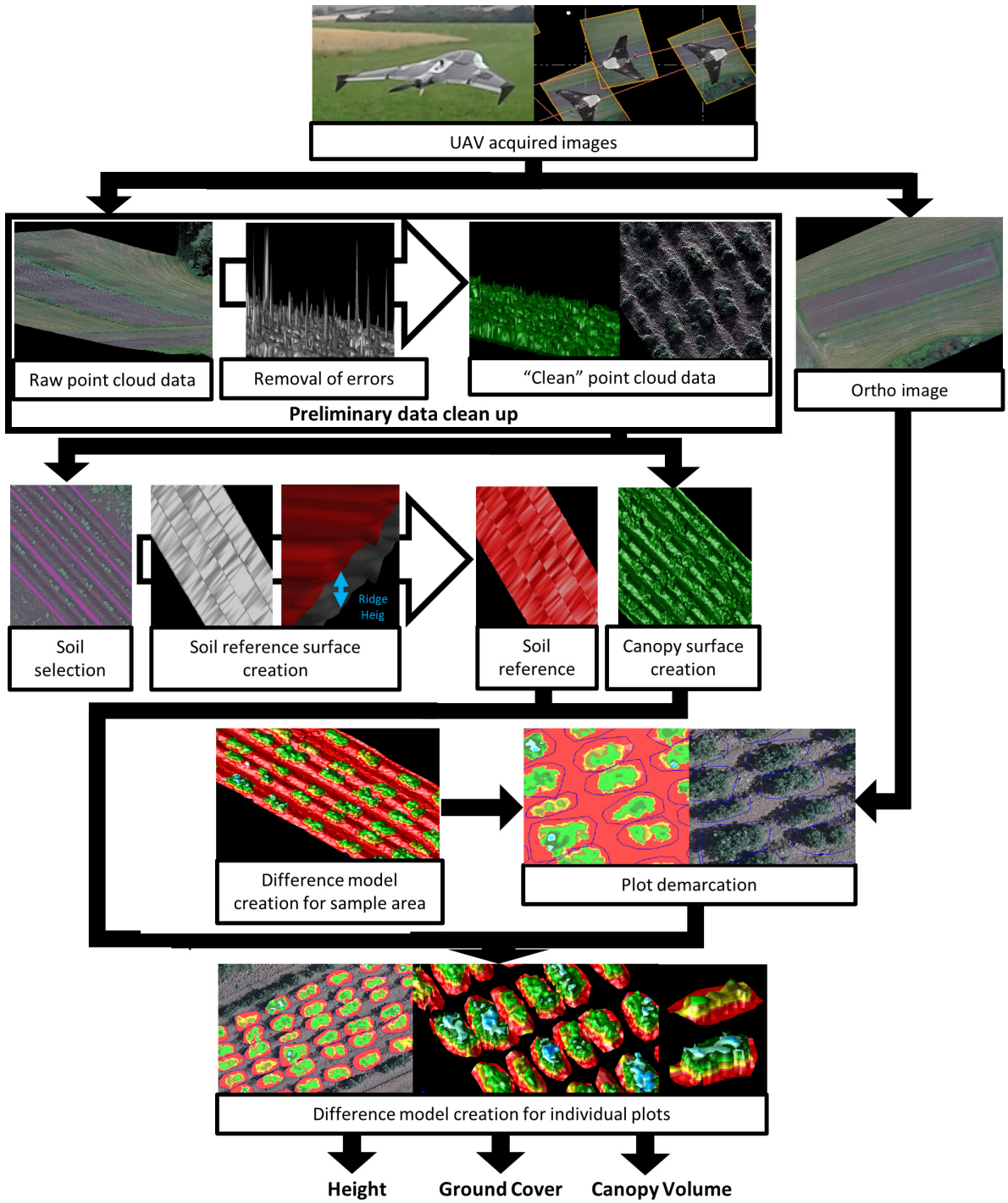

FIGURE 2 | Methodological flowchart showing the acquisition of quantitative data on potato plant canopy structure (e.g., canopy volume, canopy ground cover, and plant height) using a Structure from Motion algorithm from UAV acquired images.

weed plant that outgrows the potato plants, thus necessitating a more precise clean up. First, all points above 1.2 m were removed, as potato plants do not reach this height. Second, further clean-up was achieved by using the standard deviation (SD) of the plot canopy height distribution as a cut-off for the maximum height. Cut-offs of 2, 2.5, and 3 SDs above the mean were evaluated by comparing post cut-off data with field/proximal data using regression analysis and other graphical visualizations including histograms to observe the effects on individual plots.

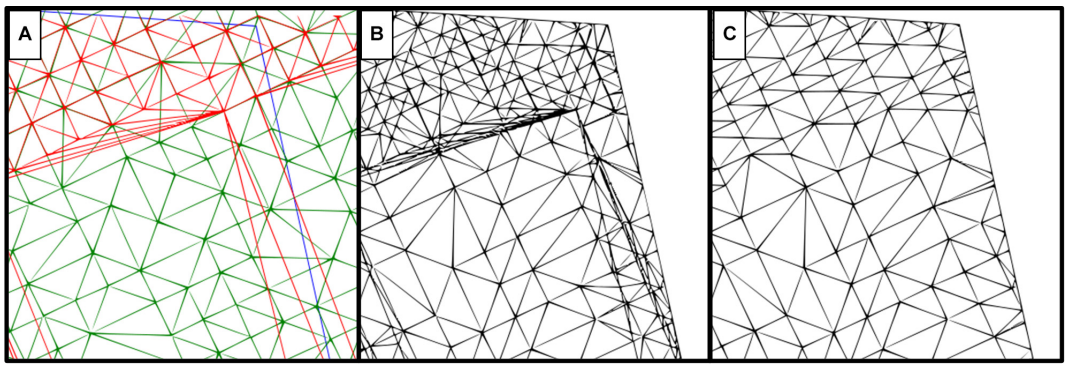

FIGURE 3 | Comparison of two difference model computation methods using the same reference surfaces. **(A)** Surfaces used for computation, where red represents the soil reference, green is the canopy surface generated from the point cloud, and a blue line demarcates the plot border. **(B)** Difference model using the "trace all triangles" method. **(C)** Difference model using the "do not track breaklines" method.

Canopy Ground Cover and Canopy Volume

Canopy ground cover and canopy volume are defined as the sum planimetric area and total canopy volume, respectively, that is above the level of the soil reference surface in the difference model for each plot.

PROXIMAL DATA ACQUISITION

Ground truth data was collected for comparison with measurements obtained from the UAV point cloud data approach.

Plant height was measured proximally using a ruler in randomly selected plots on the same day as UAV data collection. The highest contact point of the plant for each of the 3 plants in each plot was recorded. The maximum height from the 3 plants per plot was compared to the maximum height determined from the UAV data.

Leaf Area Index (LAI) data was obtained using a ceptometer (ACCUPAR LP-80, METER ENVIRONMENT, part of METER Group, Inc. United States). The ratio of the length of the horizontal to the vertical axis of the spheroid described by the leaf angle distribution of a canopy was assumed to be 2 for the leaf distribution parameter in potato plants. The sensor was angled so that the angle to the ridge was kept the same and would cover all plants within a plot (**Supplementary Figure S1**). All LAI measurements were taken in tandem with the field height measurements in 2018.

RESULTS

Ground Truth Versus Image Based Plant Height Measurements

Plant height measurements from field collected proximal data were compared with measurements based on UAV imaging. A two-step data cleaning procedure for the UAV image data involved manual removal of obvious outliers to produce "pre clean up" data, followed by a second round of cleaning using various standard deviation cut-offs based on the plot height dataset (see section "Materials and Methods"). Data cleaning significantly increased the concordance between field and UAV data (**Figure 4**). The pre clean up data showed a relatively low R^2 of 0.39 ($p < 0.01$), and this value increased to moderate levels for cut-offs of 3 SD, 2.5 SD and 2 SD (R^2 of 0.48, 0.50, and 0.52, respectively, all $p < 0.01$). Observations from **Figure 4** highlight that the different cut-off levels are not significantly different (data not presented). To determine the most appropriate cut-off level, we visually evaluated the risk of removing real canopy data in three selected exemplar plots (representing relatively common height distribution profiles) (**Figure 5**). The first example plot in **Figure 5Ai** presents an ideal situation in which all cut-offs remove only the elongated tail that is caused by computational errors and weeds integrated within the canopy structure of the plot, thus affecting the maximum height measurements. In the other two exemplar plots shown in **Figures 5Aii,iii**, the 2 SD cut-off point clearly removes part of the canopy, while the 2.5 SD cut-off removes part of the canopy in **Figure 5Aii**, but not in **Figure 5Aiii**. This increase in percentage of points removed is also exhibited in **Figure 5B**. The combined analysis from **Figures 4**, **5** suggested that the 3 SD cut-off was the most appropriate as it deterred the removal of the canopy data while also removing most of the noise.

To gain a clearer understanding of how the observations made in **Figure 5** were reflected in the rest of the field, **Figure 6A** presents the overall effects of the same standard deviation cut-offs on all experimental plots (individual histograms are not shown). In accordance with **Figure 5**, the 2 SD cut-off removed the highest percentage of data points. A large number of plots had relatively high percentages of data removed, with an overall average of more than 1%, indicating that canopy data is removed from most plots. The 2.5 SD cut-off performed better, but still removed the canopy data from a significant portion of the experimental plots. As expected, the 3 SD cut-off removed the lowest percentage of data points, but still preserved the canopy profile of all the

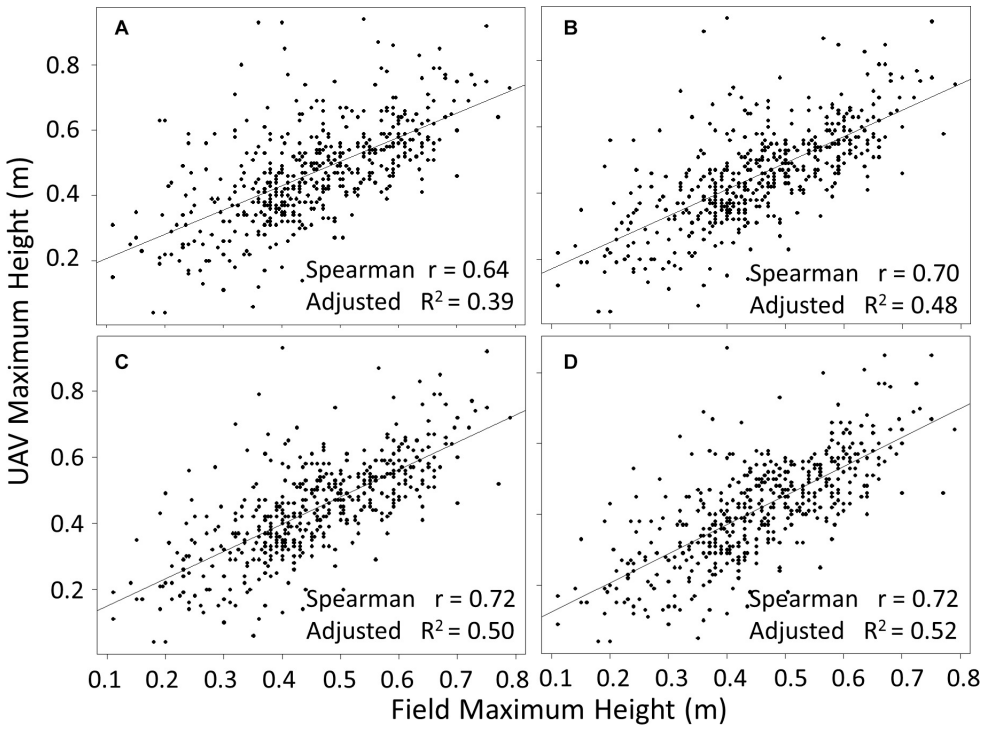

FIGURE 4 | Comparison of maximum height computed from UAV flights with proximal ground truth measurements at plot level, for pre clean up UAV data **(A)**, and data cleaned using cut-offs of 3 **(B)**, 2.5 **(C)**, and 2 **(D)** standard deviations above the mean. $p < 0.01$ in all cases and $n = 488$.

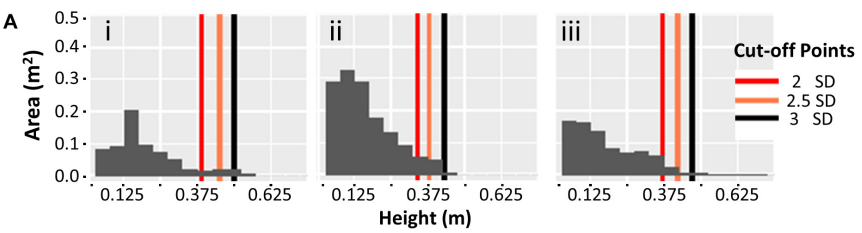

B

Cut-off	Removed points (%)		
	i	ii	iii
2 SD	6.09	4.68	2.76
2.5 SD	3.39	2.26	0.58
3 SD	1.03	0.14	0.25

FIGURE 5 | (A) Effect of 3 different standard deviation (SD) cut-offs on plot canopy datasets. Histograms represent the canopy area coverage at different height levels using pre clean up canopy height data. **(i–iii)** Demonstrate 3 exemplar canopy plots. **(B)** Percentage of points removed from the point cloud at each SD cut-off for the corresponding histograms in **(A)**.

plots in the experiment (a similar scenario to the one shown in **Figure 5Ai**, where over 1% of points are removed from a particularly pronounced elongated tail).

Independent of the nature of the data points (i.e. canopy data versus errors), their removal will always reduce the measured average and maximum canopy heights (**Figures 6Bi,ii**, respectively). As expected, the estimated maximum canopy height based on the 2 SD cut-off showed the most divergence from the estimate based on pre clean up data, while the 2.5 and 3 SD cut-offs led to a stronger correlation (**Figure 6Bii**). In contrast, for the average canopy height, the three different standard deviation cut-offs have no effect (**Figure 6Bi**). This indicated that the average height was not significantly affected by the existence of elongated tails caused by computational errors and weeds integrated within the canopy structure. Similarly, comparing average height with proximally measured field maximum height, there was no discernible difference between using pre clean up data or data cleaned using different SD cut-offs, with all comparisons showing an adjusted R^2 of 0.46 and all $p < 0.01$. Thus, the point cloud generated average height

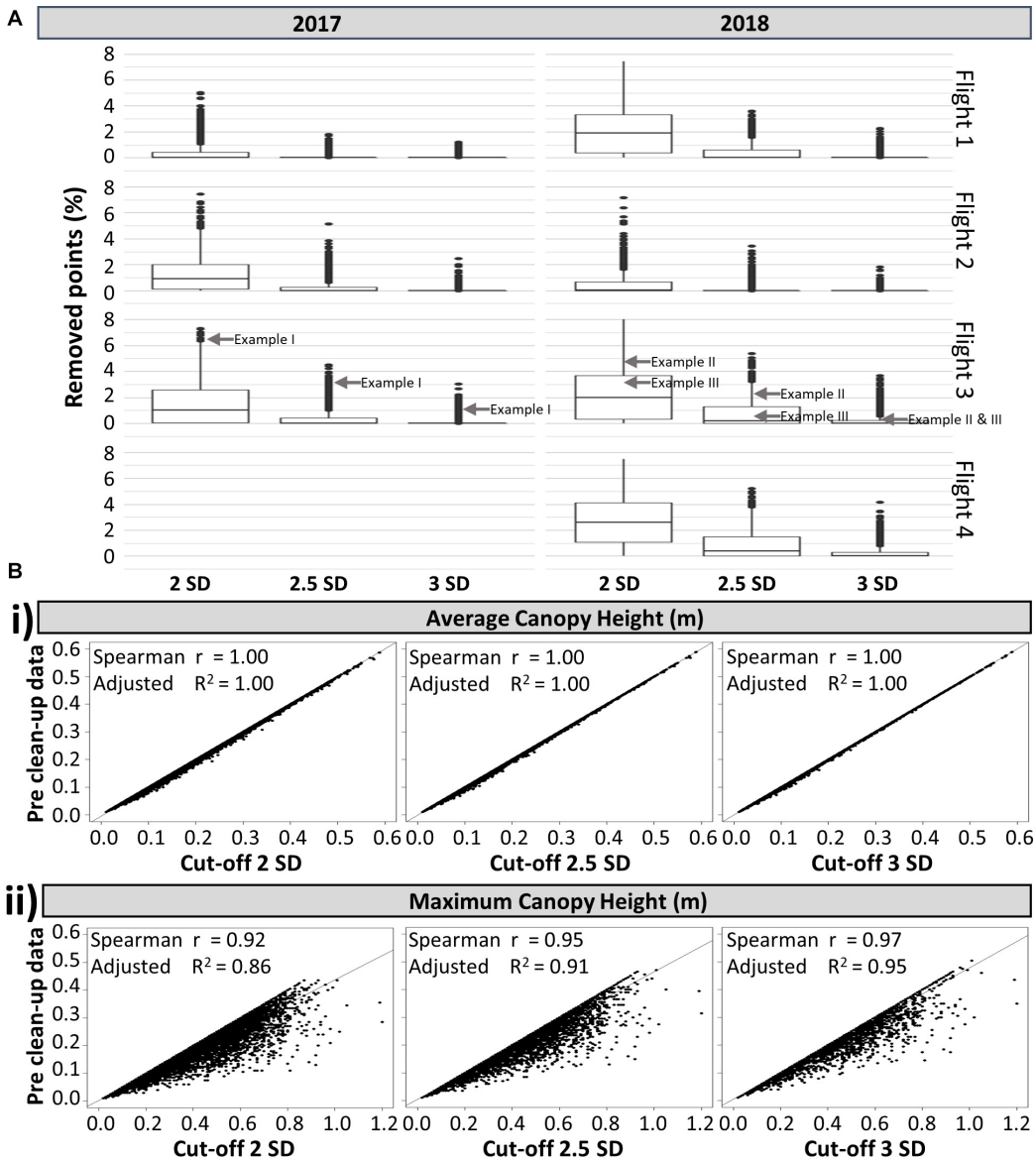

FIGURE 6 | (A) Box-plot of the percentage of points removed from the point cloud of individual plots based on 3 different standard deviation (SD) cut-offs, shown by flight and by year (n = 8,264). The locations of the exemplar plots shown in **Figure 5** are indicated with gray arrows. **(B)** Relationship between the pre clean up dataset and post clean up dataset using three SD cut-offs, for the: **(i)** average canopy height and **(ii)** maximum canopy height. All analyses have a $p < 0.01$, n = 8,264.

provided a more consistent measure than the maximum height for evaluating canopy height in potato.

Comparison of Difference Model Computation Methods

There are various methods for constructing difference models in the TBC software. These differ according to feature usage, including breaklines and newly extrapolated points where surfaces intersect, in addition to existing points in the surfaces. We compared the "trace all triangles" method with the "do not track breaklines" method and evaluated the pros and cons of each.

The "trace all triangles" method (**Figure 3B**) had a much denser mesh generation compared with the "do not track breaklines" method (**Figure 3C**), especially where the canopy and soil references overlapped. To assess any potential impact on our results, 300 plots were analyzed using both computational methods. There was no significant difference between the two methods for the canopy volume generated (Spearman's rank correlation r = 1.00, adjusted R^2 = 1.00, $p < 0.01$, n = 300; **Supplementary Figure S2**). However, the "trace all triangles" method was computationally demanding and took significantly longer (48 h) than the "do not track breaklines" method (25 min) to compute all 300 plots. Though it was not based on a

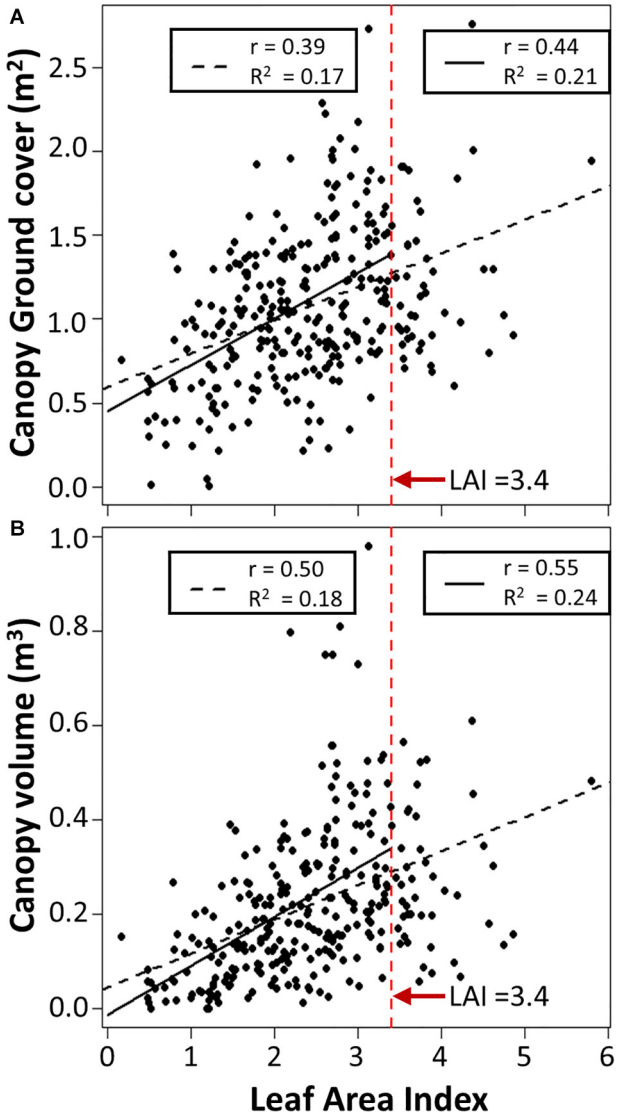

FIGURE 7 | Relationship between Leaf Area Index and computed **(A)** Canopy ground cover and **(B)** Canopy volume for all observations (dashed black line, $n = 291$) or when observations with LAI above 3.4 are discarded (solid black line, $n = 251$). r is the Spearman's rank correlation, R^2 is the adjusted R^2. All statistical tests have a $p < 0.01$.

quantitative in-depth analysis when compared to the "trace all triangles" method, the "do not track breaklines" method therefore seemed the most appropriate based on the required computational resources.

Relationship of Canopy Traits With LAI

Previous potato studies (Haverkort et al., 1991; Boyd et al., 2002) indicated that when leaf area index (LAI) is higher than 3, there is no longer a relationship between LAI and ground cover, because the canopy has grown to the point of achieving full ground cover. We found LAI correlated significantly ($p < 0.01$) with both canopy volume and canopy ground cover, with correlation coefficients of 0.50 and 0.39, respectively (**Figure 7**). The strongest relationships with canopy volume ($r = 0.55$, $p < 0.01$) and ground cover ($r = 0.44$, $p < 0.01$) were identified when observations with LAI above 3.4 were discarded, as those discarded observations showed no relationship with either canopy trait.

Temporal Variation of Canopy Characteristics

The combination of canopy height, ground cover and volume can provide comprehensive canopy size information. Though average height is a more robust parameter than maximum height for canopy height measurement, it does not provide quantitative information on canopy shape or structure. Therefore, height distribution data is important for characterizing the canopy profile. The combined information on the canopy size and shape from sequential flights helps to better understand the pattern of canopy growth and development and the current stage of plant growth.

Figure 8 presents a simplified version of the more complex real-world plant growth pattern data. It provides a general guide for the interpretation of growth patterns over time and illustrates how UAV data can be used to infer canopy development and size distribution. This guide can be a useful tool not only for monitoring individual plant/canopy development, but also to understand varietal variation. The canopy exemplars in **Figure 8** show several growth patterns, canopy shapes and their corresponding height distribution histograms. In the simulated growth pattern, we mimic the increase in area/ground cover (e.g., "sideways growth"), the increase in height (e.g., "vertical pyramid growth," "vertical even growth with higher starting point"), and present examples of plant lodging and plant senescence.

We chose three varieties to provide an illustration of not only how the interpretation of canopy data can be used to infer canopy development, but also how data gathered over the entire growing season allows the determination of maturity (**Figure 9**). In variety Nadine (**Figure 9A**), we observed that from 33 days after planting (DAP) to 62 DAP the change in height distribution showed an almost perfect example of the "Vertical even growth" pattern (**Figure 8**), with the canopy changing from a pyramid like shape to a more bulky rectangular shape. This growth was associated with an increase in canopy volume, ground cover and height. By 95 DAP, senescence had begun, with the accompanying decrease in canopy volume, ground cover and height, as expected. The height distribution also resembled the "senescence" pattern (**Figure 8**), and by 117 DAP the canopy had already senesced completely. A quick early growth followed by rapid senescence indicated that Nadine was an early maturing variety.

In variety Bonnie (**Figure 9B**), we observed that from 33 DAP to 62 DAP there was an expected increase in canopy height, ground cover and volume. However, unlike Nadine, the height distribution pattern was not perfectly matched to the one shown in the guide (**Figure 8**). At both 33 and 62 DAP, the canopy growth seemed to be occurring more like "vertical even growth," but the height in the middle part of the canopy increased more rapidly than the remaining area, i.e., the height of the main

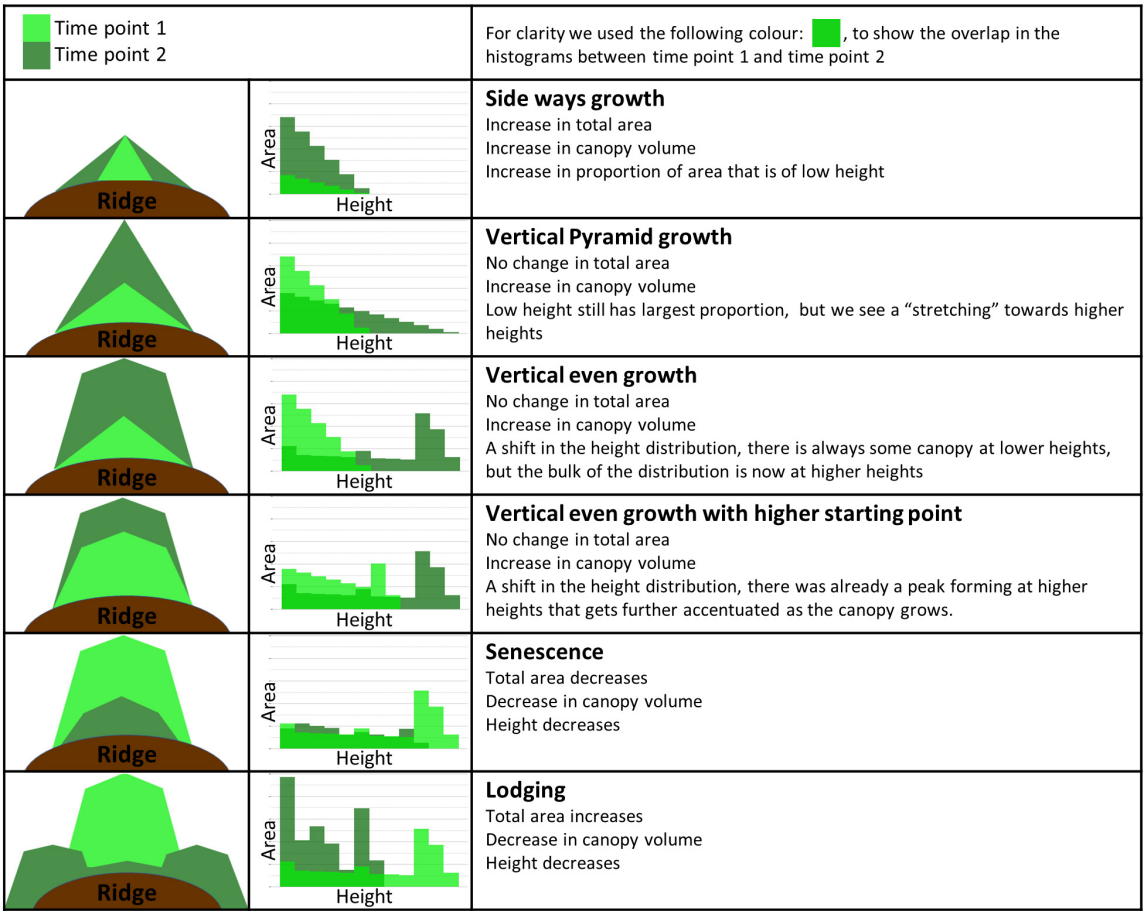

FIGURE 8 | Guide to interpretation of canopy development data at two time points. Column 1 shows a diagrammatic representation of the canopy side profile with the corresponding height distribution histograms located in column 2 (simulated data). Time points 1 and 2 are shown in light green and dark green, respectively. Column 3 defines the name given to each growth pattern, followed by a brief description of the most relevant changes between the two time points.

stem seemed to be increasing more quickly relative to the side stems. At 95 DAP, we observed a good example of plant lodging, with the bulk of the canopy shifting toward lower height, and canopy ground cover continuing to increase despite the decrease in canopy volume and height. This variety also serves as an example of continued growth after lodging, as we observed an increase in canopy volume, ground cover and height at 117 DAP, which was also evident in the corresponding 3D model, with the growth of new stems at the center of the canopy (**Figure 9B**). The continuous growth until 117 DAP indicated that this variety was an intermediate to late maturing variety, but that lodging probably hinders its full growth potential.

Variety Bounty (**Figure 9C**) had a small canopy at 33 DAP due to late emergence. By 62 DAP it presented a similar height distribution pattern to Nadine but was clearly smaller. At 95 DAP the canopy size continued to increase. When looking at the height distribution pattern, there was a noticeable increase in area in the low to medium height range, with little increase in the maximum height. Combined with the consistent increase in the ground cover growth from 33 to 95 DAP, this suggested that either there was a chance of small partial lodging, which allowed the plant to increase its ground cover, or that this variety invested more in lateral growth than vertical growth (for more photosynthetic capacity). Only at 117 DAP was the start of senescence observed. This pattern of continuous growth until nearly the end of the season indicated that this variety was either intermediate leaning toward late maturing, or a late maturing variety.

DISCUSSION

Approaches for Determining Soil Topography

One of the major difficulties in using Structure from Motion to generate point clouds is the inability to determine the topography of the soil below the plant canopy. To overcome this hurdle, a soil surface was created using soil surrounding the plots and then a compensation was made for the average ridge height. This is the first study to implement and evaluate this new method in ridged crops, which is an extrapolation of the method commonly used in height assessment studies (Bendig et al., 2015;

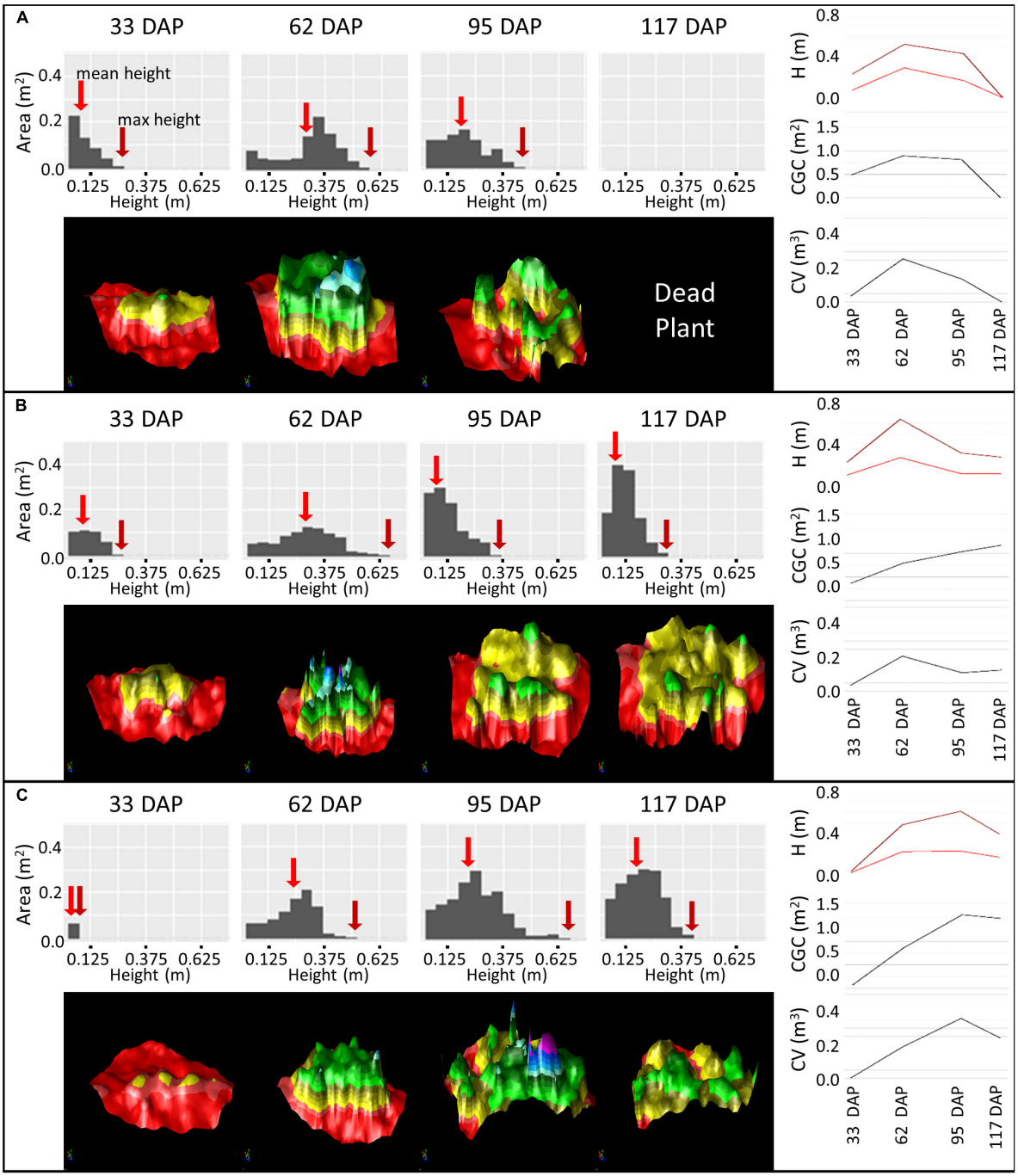

FIGURE 9 | Monitoring Canopy Volume (CV), Canopy Ground Cover (CGC) and Plant Height (H) over the growing season using difference models of three varieties: Nadine **(A)**, Bonnie **(B)** and Bounty **(C)** from 33 to 117 days after planting (DAP). Histograms represent the height distribution of the corresponding difference model. Maximum height is indicated with a dark red arrow and mean height with a medium red arrow. The difference model is color coded based on height, with red (<0 cm, soil), yellow (0–20 cm), green (20–40 cm), blue (40–60 cm), and purple (>60 cm).

Holman et al., 2016; Mohan et al., 2017; Hassan et al., 2019). This method depends on the existence of easily identifiable bare soil in close proximity to the crops, which is easy at the beginning of the season (also evident from Holman et al., 2016; Mohan et al., 2017), but may become impossible when the plant canopy achieves total ground coverage, depending on canopy structure.

An alternative method would be to perform a UAV flight before plant emergence begins and use the soil topography as a reference for all subsequent data collection points. This method has the dual advantage of capturing the true ridge height and allowing plant growth to be monitored below the ridge height, which is particularly relevant later in the season when lodging and plant senescence significantly alter

the canopy structure. However, in some potato planting cases (e.g., in organic systems), re-ridging is important, which further motivated the evaluation of the new technique in this work. Both methods share the assumption that soil topography remains relatively constant throughout the growing season. However, changes in soil topography during the season could be a significant factor during data collection for crop phenotyping and growth monitoring studies. Such effects are expected to be more significant when plots are used for scientific research, and hence subject to higher intervention rates, but may be much less in large commercial agricultural fields. Simultaneous use of both methods may be beneficial, as the measurement of canopy proportion that is above or below the ridge height may be of use in monitoring senescence and plant lodging.

Consistency Between Proximal and UAV Based Measurements

Previous studies in various crops including rice, wheat and maize, have demonstrated high correlations ($r > 0.90$) between remote and proximal measurements of plant height (Bendig et al., 2015; Holman et al., 2016; Li et al., 2016). Here, we observed correlations between 0.64 and 0.7 ($p < 0.01$) between plant height measured proximally using a ruler in the field and height measured using point cloud UAV data after clean up. The comparatively low level of correlation we observed may be attributed to several factors. One important difference between potato and the crops in previous studies is the canopy architecture. Potato plants are usually grown from tuber seeds, which result in a potato plant canopy composed of several main stems (Struik, 2007) in the form of a shrub, while the previously studied crops (mostly cereals) either have only one main stem or tend to have mostly vertical growth. This increases user bias error in the field measurement of potato plant height, as the user may erroneously measure a stem that is not the same as the one selected with point cloud data. This error may be removed by using a GPS based height measurement tool to ensure that the same point of proximal measurement in the field is compared with its UAV cloud dataset counterpart. The potato canopy is also shorter than some previous crops analyzed, and hence the relatively fixed error associated with Structure from Motion point clouds can have a slightly greater proportional impact on measurement. The spatial resolution or flight conditions also play an important role in the calculation of height, as lower flight altitudes generate more accurate height estimates (Holman et al., 2016). This may well have played a role in our datasets as we used fixed wing aircraft with most flight data collected at around 75 m with over 85% overlap in data collection. A multi-copter would allow more freedom regarding control over the spatial resolution, with similar image overlaps.

Height Measurements

Maximum height is commonly used to represent plant growth characteristics in shrub plants including potato, cotton, and fruit trees, and in cereals where data is collected from large plots and maximum height based on a small number of point clouds is used. We have shown that compared with the maximum height, the average height provides a more consistent measure of plant height, which is both more robust to the data cleaning strategy, and better representative of the entire canopy height distribution, as demonstrated using temporal data on the canopy structure of three varieties (**Figure 9**). In addition, the use of maximum height data has higher potential for user bias during in-field measurements, and for computational error effects while analyzing the UAV point cloud data. Thus, though it is almost impossible to verify using traditional in-field measurements, we recommend the use of average height as it gives a much better representation of plant growth, which is of utmost importance when attempting to understand the genotype-phenotype relationship in plant breeding. The improved precision in phenotype datasets allow us to decrease the error values and hence provides the opportunity to improve the heritability of traits (Cobb et al., 2013). Thus, the accuracy and precision in phenotyping provide the necessary tools to empower the next generation of linkage mapping and association studies and further improve the results of genomic selection (Cobb et al., 2013; Prashar and Jones, 2014; Bhat et al., 2016; Melandri et al., 2019).

Canopy Traits and LAI

Previous studies have reported correlations between leaf area index and ground cover ranging from 0.52 to 0.92 based on analyses of one or two potato varieties (Haverkort et al., 1991; Boyd et al., 2002). These studies also highlight high correlation with canopy cover for LAI values below 3, but no relationship for LAI above 3, due to complete ground cover. Here, we observed a lower correlation of $r = 0.44$ ($p < 0.01$) and a similar cut-off point of LAI 3.4 was established. The reduced correlation within our dataset is likely due to the high levels of varietal variation in canopy architecture compared to previous studies where analysis was carried out on one or two varieties. Canopy volume exhibits a higher correlation with LAI ($r = 0.55$, $p < 0.01$) in our data, because even though UAV measured canopy volume does not consider canopy leaf density, larger canopies are more likely to have a higher leaf density and hence higher LAI. Further developments for UAV determined canopy volume, ground cover and LAI would have to take into consideration varietal data to enable integration into potato yield prediction models in the future.

Plant Growth and Development Monitoring

Crop monitoring for growth and performance during development is an important aspect of agricultural management, and not only allows creation of yield prediction models, but also enables implementation of timely interventions to ensure optimal yields. Therefore, while individual flights provide useful point information on the size and the general canopy health of the plants, it is the continuous data integration of the potato

plants over the growing season that gives the greatest potential for a predictive modeling approach. In our study, data collection from just 4 flights over the growing season allowed us not only to identify the maturity of the different varieties, but also to better understand the canopy development of those varieties. Canopy architecture impacts light interception, water uptake and transpiration, important factors for carbon acquisition and allocation (Haverkort et al., 1991; Burgess et al., 2017; Tang et al., 2019). These represent some of the most valuable traits that breeders need to focus on for breeding improved crop varieties that are well adapted for meeting the challenges posed by climate change. Hence, use of the crop canopy assessment techniques described here will help to determine optimal plant architecture or ideotypes for different breeding purposes (Da Silva et al., 2014; Obidiegwu et al., 2015; Burgess et al., 2017).

Opportunities and Challenges

Many studies have explored the potential of structure from motion techniques in life sciences. In the field of agriculture, the focus has been on monocot crops, specifically wheat, whose development is usually assessed via height measurements (Bendig et al., 2013, 2014, 2015; Holman et al., 2016; Jin et al., 2017; Hassan et al., 2019). Wheat, like most cereals, has a relatively homogeneous height distribution of the canopy when compared to potato. Potatoes are also grown on ridges or ridged rows where soil background is distinguishable in most scenarios and are a bush like crop in which ground cover is recognized as one of the main methods to evaluate growth. The pipeline developed in this work combines vertical growth with canopy cover data, as potato grows in a great variety of canopy shapes and structures that will be hard to capture with only a 2-dimensional parameter such as height or ground cover. This pipeline and the difference model creation allows us to capture the entire canopy distribution at ∼1 cm resolution and determine canopy cover and volume at different height levels during crop growth and development. That said, we want to highlight that structure from motion is one of the available techniques which can be used for obtaining surface information of crop canopies non-destructively. There are other approaches such as terrestrial laser scanning, laser triangulation, time of flight etc., which allow higher point cloud resolution (depending upon sensor and platform) and hence 3D sensing for plant phenotyping (Paulus, 2019).

CONCLUSION

The paper highlights the application of existing tools for processing point cloud data obtained from UAV imaging for practical and accurate phenotyping of canopy architecture traits (plant height, canopy cover and volume) in potato which can be replicated in other bush type crops. In particular, the approach allows the consistent monitoring of canopy traits, which will facilitate the creation of accurate individual growth profiles for new and existing varieties. These profiles will enhance all future studies that assess not only varietal variability, but also its interaction with environmental factors (e.g., drought, temperature stress) and agriculture management practices (e.g., fertilization, tillage and crop rotation), thus supplying valuable environmental interaction data to help alleviate one of the current bottlenecks in genotype-phenotype association studies (Elias et al., 2016).

Using the newly developed and low-cost techniques, farmers could use the information from temporal monitoring of canopy size characteristics to identify key indicators of canopy age, health and development. For example, identification of early senescence (a potential indicator of stress), drooping due to stress or disease, or canopy lodging due to inadequate stem strength or maturity, thus facilitating the prediction of disease occurrence and spread. Identification of the current stage of the crop life cycle based on the detailed crop and variety profiles, in combination with other datasets, would allow farmers to determine the optimal time for harvesting based on varietal variation. These examples illustrate how a better understanding of the time course of crop development can inform important decisions and hence improve agricultural management practices.

DATA AVAILABILITY STATEMENT

The raw data supporting the conclusions of this article will be made available by the authors, without undue reservation, to any qualified researcher.

AUTHOR CONTRIBUTIONS

NB and AP conceived the project and designed the study. FdJ, JS, and AP performed the experiments, data collection, performed image data analysis, and drafted the manuscript. FdJ, NB, GB, LC, and AP participated in the experiments and statistical data analysis. NB, GB, and LC contributed with editing and revisions. All authors contributed to the article and approved the submitted version.

FUNDING

The research was funded by IAFRI, Institute of Agri-Food Research and Innovation and ISCF Agri-Food Technology Seeding Catalyst, BB/SCA/Newcastle/17.

ACKNOWLEDGMENTS

We thank Survey Solutions Scotland for their UAV survey support and Trimble for providing us with TBC software under the University Partnership Program. We also want to thank technical help from farm staff at Newcastle University farms.

SUPPLEMENTARY MATERIAL

The Supplementary Material for this article can be found online at: https://www.frontiersin.org/articles/10.3389/fpls.2021.612843/full#supplementary-material

REFERENCES

Anithakumari, A. M., Dolstra, O., Vosman, B., Visser, R. G. F., and Van Der Linden, C. G. (2011). In vitro screening and QTL analysis for drought tolerance in diploid potato. *Euphytica* 181, 357–369. doi: 10.1007/s10681-011-0446-6

Araus, J. L., Kefauver, S. C., Zaman-Allah, M., Olsen, M. S., and Cairns, J. E. (2018). Translating high-throughput phenotyping into genetic gain. *Trends Plant Sci.* 23, 451–466. doi: 10.1016/j.tplants.2018.02.001

Baptiste, A. (2017). *gridExtra: Miscellaneous Functions for "Grid" Graphics. R Package Version* 2.

Bendig, J., Bolten, A., Bennertz, S., Broscheit, J., Eichfuss, S., and Bareth, G. (2014). Estimating biomass of barley using crop surface models (CSMs) derived from UAV-based RGB imaging. *Remote Sens.* 6, 10395–10412. doi: 10.3390/rs61110395

Bendig, J., Willkomm, M., Tilly, N., Gnyp, M. L., Bennertz, S., Qiang, C., et al. (2013). Very high resolution crop surface models (CSMs) from UAV-based stereo images for rice growth monitoring In Northeast China. *Int. Arch. Photogramm. Remote Sens. Spatial Inf. Sci.* XL-1/W2, 45–50. doi: 10.5194/isprsarchives-XL-1-W2-45-2013

Bendig, J., Yu, K., Aasen, H., Bolten, A., Bennertz, S., Broscheit, J., et al. (2015). Combining UAV-based plant height from crop surface models, visible, and near infrared vegetation indices for biomass monitoring in barley. *Int. J. Appl. Earth Obs. Geoinf.* 39, 79–87. doi: 10.1016/j.jag.2015.02.012

Berni, J. A. J., Zarco-Tejada, P. J., Suárez, L., and Fereres, E. (2009). Thermal and narrowband multispectral remote sensing for vegetation monitoring from an unmanned aerial vehicle. *IEEE Trans. Geosci. Remote Sens.* 47, 722–738. doi: 10.1109/tgrs.2008.2010457

Bhat, J. A., Ali, S., Salgotra, R. K., Mir, Z. A., Dutta, S., Jadon, V., et al. (2016). Genomic selection in the era of next generation sequencing for complex traits in plant breeding. *Front. Genet.* 7:221. doi: 10.3389/fgene.2016.00221

Birch, P. R. J., Bryan, G., Fenton, B., Gilroy, E. M., Hein, I., Jones, J. T., et al. (2012). Crops that feed the world 8: Potato: are the trends of increased global production sustainable? *Food Secur.* 4, 477–508. doi: 10.1007/s12571-012-0220-1

Boyd, N. S., Gordon, R., and Martin, R. C. (2002). Relationship between leaf area index and ground cover in potato under different management conditions. *Potato Res.* 45, 117–129. doi: 10.1007/bf02736107

Burgess, A. J., Retkute, R., Herman, T., and Murchie, E. H. (2017). Exploring relationships between canopy architecture, light distribution, and photosynthesis in contrasting rice genotypes using 3D canopy reconstruction. *Front. Plant Sci.* 8:734. doi: 10.3389/fpls.2017.00734

Cobb, J. N., Declerck, G., Greenberg, A., Clark, R., and Mccouch, S. (2013). Next-generation phenotyping: requirements and strategies for enhancing our understanding of genotype-phenotype relationships and its relevance to crop improvement. *Theor. Appl. Genet.* 126, 867–887. doi: 10.1007/s00122-013-2066-0

Da Silva, D., Han, L., Faivre, R., and Costes, E. (2014). Influence of the variation of geometrical and topological traits on light interception efficiency of apple trees: sensitivity analysis and metamodelling for ideotype definition. *Ann. Bot.* 114, 739–752. doi: 10.1093/aob/mcu034

Elias, A. A., Robbins, K. R., Doerge, R. W., and Tuinstra, M. R. (2016). Half a century of studying genotype × environment interactions in plant breeding experiments. *Crop Sci.* 56, 2090–2105. doi: 10.2135/cropsci2015.01.0061

Franceschini, M. H. D., Bartholomeus, H., Van Apeldoorn, D., Suomalainen, J., and Kooistra, L. (2017). Assessing changes in potato canopy caused by late blight in organic production systems through UAV-based pushbroom imaging spectrometer. *Int. Arch. Photogramm. Remote Sens. Spat. Inf. Sci. ISPRS Arch.* 42, 109–112. doi: 10.5194/isprs-archives-xlii-2-w6-109-2017

Friedli, M., Kirchgessner, N., Grieder, C., Liebisch, F., Mannale, M., and Walter, A. (2016). Terrestrial 3D laser scanning to track the increase in canopy height of both monocot and dicot crop species under field conditions. *Plant Methods* 12, 1–15.

Furbank, R. T., and Tester, M. (2011). Phenomics – technologies to relieve the phenotyping bottleneck. *Trend Plant Sci.* 16, 635–644. doi: 10.1016/j.tplants.2011.09.005

Getzin, S., Wiegand, K., and Schöning, I. (2012). Assessing biodiversity in forests using very high-resolution images and unmanned aerial vehicles. *Methods Ecol. Evol.* 3, 397–404. doi: 10.1111/j.2041-210x.2011.00158.x

Harrell, F. E. (2020). *"With Contributions from Charles Dupont and Many Others (2017). Hmisc: Harrell Miscellaneous". R package version 4.0-1.*

Hassan, M. A., Yang, M., Fu, L., Rasheed, A., Zheng, B., Xia, X., et al. (2019). Accuracy assessment of plant height using an unmanned aerial vehicle for quantitative genomic analysis in bread wheat. *Plant Methods* 15:37.

Haverkort, A. J., Franke, A. C., Steyn, J. M., Pronk, A. A., Caldiz, D. O., and Kooman, P. L. (2015). A robust potato model: LINTUL-POTATO-DSS. *Potato Res.* 58, 313–327. doi: 10.1007/s11540-015-9303-7

Haverkort, A. J., Uenk, D., Veroude, H., and Vandewaart, M. (1991). Relationships between ground cover, intercepted solar-radiation, leaf-area index and infrared reflectance of potato crops. *Potato Res.* 34, 113–121. doi: 10.1007/bf02358105

Holman, F. H., Riche, A. B., Michalski, A., Castle, M., Wooster, M. J., and Hawkesford, M. J. (2016). High throughput field phenotyping of wheat plant height and growth rate in field plot trials using UAV based remote sensing. *Remote Sens.* 8:1031. doi: 10.3390/rs8121031

Jimenez-Berni, J. A., Deery, D. M., Rozas-Larraondo, P., Condon, A. T. G., Rebetzke, G. J., James, R. A., et al. (2018). High throughput determination of plant height, ground cover, and above-ground biomass in wheat with LiDAR. *Front. Plant Sci.* 9:237. doi: 10.3389/fpls.2018.00237

Jiménez-Brenes, F. M., López-Granados, F., Castro, A. I., Torres-Sánchez, J., Serrano, N., and Peña, J. M. (2017). Quantifying pruning impacts on olive tree architecture and annual canopy growth by using UAV-based 3D modelling. *Plant Methods* 13, 1–15.

Jin, X., Liu, S., Baret, F., Hemerlé, M., and Comar, A. (2017). Estimates of plant density of wheat crops at emergence from very low altitude UAV imagery. *Remote Sens. Environ.* 198, 105–114. doi: 10.1016/j.rse.2017.06.007

Khan, M. A., Saravia, D., Munive, S., Lozano, F., Farfan, E., Eyzaguirre, R., et al. (2015). Multiple QTLs linked to agro-morphological and physiological traits related to drought tolerance in potato. *Plant Mol. Biol. Report.* 33, 1286–1298. doi: 10.1007/s11105-014-0824-z

Khurana, S. C., and McLaren, J. S. (1982). The influence of leaf area, light interception and season on potato growth and yield. *Potato Res.* 25, 329–342. doi: 10.1007/bf02357290

Lemon, J. (2006). Plotrix: a package in the red light district of R. *R News* 6, 8–12.

Li, B., Xu, X., Han, J., Zhang, L., Bian, C., Jin, L., et al. (2019). The estimation of crop emergence in potatoes by UAV RGB imagery. *Plant Methods* 15:15.

Li, W., Niu, Z., Chen, H., Li, D., Wu, M., and Zhao, W. (2016). Remote estimation of canopy height and aboveground biomass of maize using high-resolution stereo images from a low-cost unmanned aerial vehicle system. *Ecol. Indic.* 67, 637–648. doi: 10.1016/j.ecolind.2016.03.036

Lopes, M. S., and Reynolds, M. P. (2012). Stay-green in spring wheat can be determined by spectral reflectance measurements (normalized difference vegetation index) independently from phenology. *J. Exp. Bot.* 63, 3789–3798. doi: 10.1093/jxb/ers071

Matese, A., Toscano, P., Di Gennaro, S. F., Genesio, L., Vaccari, F. P., Primicerio, J., et al. (2015). Intercomparison of UAV, aircraft and satellite remote sensing platforms for precision viticulture. *Remote Sens.* 7, 2971–2990. doi: 10.3390/rs70302971

Mathan, J., Bhattacharya, J., and Ranjan, A. (2016). Enhancing crop yield by optimizing plant developmental features. *Development* 143, 3283–3294. doi: 10.1242/dev.134072

Melandri, G., Prashar, A., Mccouch, S. R., Linden, G. V. D., Jones, H. G., Kadam, N. N., et al. (2019). Association mapping and genetic dissection of drought-induced canopy temperature differences in rice. *J. Exp. Bot.* 71, 1614–1627. doi: 10.1093/jxb/erz527

Mohan, M., Silva, C. A., Klauberg, C., Jat, P., Catts, G., Cardil, A., et al. (2017). Individual tree detection from unmanned aerial vehicle (UAV) derived canopy height model in an open canopy mixed conifer forest. *Forests* 8, 1–17.

Ning, X., Li, F., Tian, G., and Wang, Y. (2018). An efficient outlier removal method for scattered point cloud data. *PLoS One* 13:e0201280.doi: 10.1371/journal.pone.0201280

Obidiegwu, J. E., Bryan, G. J., Hamlyn, J. G., and Prashar, A. (2015). Coping with drought: stress and adaptive responses in potato and perspectives for improvement. *Front. Plant Sci.* 6:542. doi: 10.3389/fpls.2015.00542

Paulus, S. (2019). Measuring crops in 3D: using geometry for plant phenotyping. *Plant Methods* 15:103.

Prashar, A., and Jones, H. G. (2014). Infra-red thermography as a high-throughput tool for field phenotyping. *Agronomy* 4, 397–417. doi: 10.3390/agronomy4030397

Prashar, A., Yildiz, J., Mcnicol, J. W., Bryan, G. J., and Jones, H. G. (2013). Infra-red thermography for high throughput field phenotyping in *Solanum* tuberosum. *PLoS One* 8:e65816.doi: 10.1371/journal.pone.0065816

Raymundo, R., Asseng, S., Prassad, R., Kleinwechter, U., Concha, J., Condori, B., et al. (2017). Performance of the SUBSTOR-potato model across contrasting growing conditions. *Field Crops Res.* 202, 57–76. doi: 10.1016/j.fcr.2016.04.012

Roitsch, T., Cabrera-Bosquet, L., Fournier, A., Ghamkhar, K., Jiménez-Berni, J., Pinto, F., et al. (2019). Review: new sensors and data-driven approaches-a path to next generation phenomics. *Plant Sci.* 282, 2–10. doi: 10.1016/j.plantsci.2019.01.011

Sankaran, S., Quirós, J. J., Knowles, N. R., and Knowles, L. O. (2017). High-resolution aerial imaging based estimation of crop emergence in potatoes. *Am. J. Potato Res.* 94, 658–663. doi: 10.1007/s12230-017-9604-2

Sharma, S. K., Mackenzie, K., Mclean, K., Dale, F., Daniels, S., and Bryan, G. J. (2018). Linkage disequilibrium and evaluation of genome-wide association mapping models in tetraploid potato. *G3 Genes Genomes Genet.* 8, 3185–3202. doi: 10.1534/g3.118.200377

Struik, P. C. (2007). "Above-ground and below-ground plant development," in *Potato Biology and Biotechnology*, 1st Edn, ed. D. Vreugenhil (Amsterdam: Elsevier).

Sugiura, R., Tsuda, S., Tamiya, S., Itoh, A., Nishiwaki, K., Murakami, N., et al. (2016). Field phenotyping system for the assessment of potato late blight resistance using RGB imagery from an unmanned aerial vehicle. *Biosyst. Eng.* 148, 1–10. doi: 10.1016/j.biosystemseng.2016.04.010

Tang, L., Yin, D., Chen, C., Yu, D., and Han, W. (2019). Optimal design of plant canopy based on light interception: a case study with loquat. *Front. Plant Sci.* 10:364. doi: 10.3389/fpls.2019.00364

Torres-Sánchez, J., López-Granados, F., Serrano, N., Arquero, O., and Peña, J. M. (2015). High-throughput 3-D monitoring of agricultural-tree plantations with unmanned aerial vehicle (UAV) technology. *PLoS One* 10:e0130479.doi: 10.1371/journal.pone.0130479

Vanderwal, J., Falconi, L., Januchowski, S., Shoo, L., and Storlie, C. (2014). *SDMTools: Species Distribution Modelling Tools: Tools for Processing Data Associated with Species Distribution Modelling Exercises. R Package Version* 1.1-221.

Wang, X., Singh, D., Marla, S., Morris, G., and Poland, J. (2018). Field-based high-throughput phenotyping of plant height in sorghum using different sensing technologies. *Plant Methods* 14, 1–16. doi: 10.1109/lgrs.2020.3039179

Wickham, H. (2011). The split-apply-combine strategy for data analysis. *J. Stat. Softw.* 40, 1–29.

Wickham, H. (2016). *ggplot2: Elegant Graphics for Data Analysis*. New York, NY: Springer.

Wickham, H., and Henry, L. (2019). *Tidyr: Tidy Messy Data. R Package Version 1.0*.

Wickham, H., Averick, M., Bryan, J., Chang, W., Mcgowan, L. D. A., François, R., et al. (2019). Welcome to the Tidyverse. *J. Open Source Softw.* 4:1686. doi: 10.21105/joss.01686

Wickham, H., Francois, R., Henry, L., and Müller, K. (2015). *dplyr: A Grammar of Data Manipulation.* R Package Version 0.4. 3. Vienna: R Foundation Statistical Computing.

Williams, D., Britten, A., Mccallum, S., Jones, H., Aitkenhead, M., Karley, A., et al. (2017). A method for automatic segmentation and splitting of hyperspectral images of raspberry plants collected in field conditions. *Plant Methods* 13, 1–12.

Xu, R., Li, C., and Paterson, A. H. (2019). Multispectral imaging and unmanned aerial systems for cotton plant phenotyping. *PLoS One* 14:e0205083.doi: 10.1371/journal.pone.0205083

Yang, G., Yang, X., Zhang, X., Li, Z., Liu, J., Zhu, D., et al. (2017). Unmanned aerial vehicle remote sensing for field-based crop phenotyping: current status and perspectives. *Front. Plant Sci.* 8:1111. doi: 10.3389/fpls.2017.01111

Zheng, H., Cheng, T., Li, D., Zhou, X., Yao, X., Tian, Y., et al. (2018). Evaluation of RGB, color-infrared and multispectral images acquired from unmanned aerial systems for the estimation of nitrogen accumulation in rice. *Remote Sens.* 10:824. doi: 10.3390/rs10060824

Conflict of Interest: JS was employed by company Survey Solutions Scotland.

The remaining authors declare that the research was conducted in the absence of any commercial or financial relationships that could be construed as a potential conflict of interest.

frontiers in Plant Science

ORIGINAL RESEARCH
published: 16 February 2021
doi: 10.3389/fpls.2021.591587

High Throughput Field Phenotyping for Plant Height Using UAV-Based RGB Imagery in Wheat Breeding Lines: Feasibility and Validation

*Leonardo Volpato[1], Francisco Pinto[2], Lorena González-Pérez[2], Iyotirindranath Gilberto Thompson[2], Aluízio Borém[1], Matthew Reynolds[2], Bruno Gérard[2], Gemma Molero[2,3] and Francelino Augusto Rodrigues Jr.[2]**

[1] Department of Agronomy, Federal University of Viçosa, Viçosa, Brazil, [2] International Maize and Wheat Improvement Center (CIMMYT), Texcoco, Mexico, [3] KWS Momont Recherche, Mons-en-Pevele, France

Plant height (PH) is an essential trait in the screening of most crops. While in crops such as wheat, medium stature helps reduce lodging, tall plants are preferred to increase total above-ground biomass. PH is an easy trait to measure manually, although it can be labor-intense depending on the number of plots. There is an increasing demand for alternative approaches to estimate PH in a higher throughput mode. Crop surface models (CSMs) derived from dense point clouds generated via aerial imagery could be used to estimate PH. This study evaluates PH estimation at different phenological stages using plot-level information from aerial imaging-derived 3D CSM in wheat inbred lines during two consecutive years. Multi-temporal and high spatial resolution images were collected by fixed-wing ($Plat_{FW}$) and multi-rotor ($Plat_{MR}$) unmanned aerial vehicle (UAV) platforms over two wheat populations (50 and 150 lines). The PH was measured and compared at four growth stages (GS) using ground-truth measurements (PHground) and UAV-based estimates (PHaerial). The CSMs generated from the aerial imagery were validated using ground control points (GCPs) as fixed reference targets at different heights. The results show that PH estimations using $Plat_{FW}$ were consistent with those obtained from $Plat_{MR}$, showing some slight differences due to image processing settings. The GCPs heights derived from CSM showed a high correlation and low error compared to their actual heights ($R^2 \geq 0.90$, $RMSE \leq 4$ cm). The coefficient of determination (R^2) between PHground and PHaerial at different GS ranged from 0.35 to 0.88, and the root mean square error ($RMSE$) from 0.39 to 4.02 cm for both platforms. In general, similar and higher heritability was obtained using PHaerial across different GS and years and ranged according to the variability, and environmental error of the PHground observed (0.06–0.97). Finally, we also observed high Spearman rank correlations (0.47–0.91) and R^2 (0.63–0.95) of PHaerial adjusted and predicted values against PHground values. This study provides an example of the use of UAV-based high-resolution RGB imagery to obtain time-series estimates of PH, scalable to tens-of-thousands of plots, and thus suitable to be applied in plant wheat breeding trials.

Keywords: multi-temporal crop surface model, structure from motion, RGB camera, dense point cloud, drones, post-processed kinematic, wheat breeding, adjusted and predicted genotypic values

OPEN ACCESS

Edited by:
Ankush Prashar, Newcastle University, United Kingdom

Reviewed by:
Weixing Cao, Nanjing Agricultural University, China
Robert John French, Department of Primary Industries and Regional Development of Western Australia (DPIRD), Australia

***Correspondence:**
Francelino Augusto Rodrigues Jr.
f.a.rodrigues@cgiar.org

Specialty section:
This article was submitted to Plant Breeding, a section of the journal Frontiers in Plant Science

Received: *04 August 2020*
Accepted: *25 January 2021*
Published: *16 February 2021*

Citation:
Volpato L, Pinto F, González-Pérez L, Thompson IG, Borém A, Reynolds M, Gérard B, Molero G and Rodrigues FA Jr (2021) High Throughput Field Phenotyping for Plant Height Using UAV-Based RGB Imagery in Wheat Breeding Lines: Feasibility and Validation. Front. Plant Sci. 12:591587. doi: 10.3389/fpls.2021.591587

INTRODUCTION

Wheat (*Triticum* sp.) is among the leading food crops, and it is grown in a range of environments and geographical areas. It is highly relevant to the human diet, given its protein quantity, quality, and variety of derived products (Shewry et al., 2016). Lately, wheat has become the most important source of dietary protein and the second most important source of calories (carbohydrates) for humans (Shewry et al., 2016). During the 2017/2018 season, wheat was sown in 11.7% of the world's arable land, corresponding to around 30% of world grain production (USDA, 2018). Wheat is vital for food security, supplying an affordable source of nutrition to a large portion of the global population, particularly millions of people with low-middle incomes, and is an essential crop for the composition of sustainable agricultural production systems (Walters et al., 2016; Hickey et al., 2019).

Wheat breeding for plant height (PH) has been historically used to reduce lodging and improve grain yield and quality (Reynolds et al., 2020). The identification and introduction of major dwarfing or semi-dwarfing genes were significant advancements in the wheat breeding work led by Norman Borlaug that enabled grain yield increase in most environments and contributed to the "Green Revolution" (Reynolds and Borlaug, 2006; Würschum et al., 2015). To date, PH continues to be one of the most critical and heritable traits in wheat breeding, also used to select suitable parental lines for hybrid breeding (Würschum et al., 2015; Barmeier et al., 2016). In addition, PH contributes to biomass production, as it is associated with increased photosynthesis due to a better light interception and distribution through the canopy in taller plants (Song et al., 2013).

PH is commonly calculated by measuring the distance between the upper boundary of the main photosynthetic tissues (excluding the awns) and the ground level using a simple metric ruler or a graduated stick (Torres and Pietragalla, 2012). Although simple, such assessment is costly, laborious, and prone to subjectivity, especially in extensive field trials (Holman et al., 2016; Hu et al., 2018). Manual ground measurements in the field are only feasible on a few plants per plot and can be biased by the lack of standardized criteria (Wilke et al., 2019). The temporal characterization of PH, that is, PH estimations at the various plant growth stages, could provide a better understanding of the mechanism of plant growth and its underlying genetic effects by providing insight into the environmental variables of this trait (Torres-Sánchez et al., 2013; Hassan et al., 2019a). Phenotyping under environmental field conditions is often considered a bottleneck in plant breeding programs (Yang et al., 2017; Rebetzke et al., 2019). Consequently, there is a need for faster, more accurate, and continuous measurements of PH.

HTP (high-throughput phenotyping) could be applied to accurately and efficiently conduct temporal PH characterization. The introduction of HTP approaches into breeding schemes can significantly improve the phenotyping standards for agronomic traits, contributing to better understanding of their genetic basis and diversity, as well as the environmental influences throughout the crop's development cycle (Reynolds et al., 2020). Non-destructive data collected via ground-based and aerial HTP techniques are highly desirable for application in plant breeding since they can be used to assess different traits in large-scale field trials (Rodrigues et al., 2018; Loladze et al., 2019). In particular, aerial HTP platforms have become favored overground platforms, as they are suitable for use in large breeding trials and show a good trade-off between time, data accuracy, and resolution (Yang et al., 2017; Gracia-Romero et al., 2019; Zhao et al., 2019). The rapid development of sensors and unmanned aerial vehicles (UAVs), as well as that of image and data analyses algorithms and improved computer capacities observed in recent years, have enabled a broad range of possibilities for aerial HTP to measure plant traits such as PH, stand count, and vegetation indices, among others (Maes and Steppe, 2019; Matias et al., 2020; Morales et al., 2020). These aerial images are used as a proxy for the characterization of quantitative plant traits. Recent advances in remote sensing using UAV with sensors measuring the visible (RGB—red, green, and blue bands) and/or near-infrared (NIR) wavelengths have made it possible to create high-throughput, cost-effective, and accurate quantitative phenotyping datasets in wheat breeding programs (Singh et al., 2019; Reynolds et al., 2020).

Digital color images (i.e., RGB) collected from UAVs have been used for estimating PH in wheat through different settings and capabilities (**Table 1**). Feature matching and structure from motion (SfM) techniques applied to such imagery enable the generation of three-dimensional (3D) point clouds that can be used to reconstruct multi-temporal crop surface models (CSMs) from which PH can be estimated plot-wise (Singh et al., 2016; Hassan et al., 2019b). SfM photogrammetry is a method that uses a set of overlapped images to generate high-resolution topographic 3D-reconstructions. Through automatic extraction of corresponding feature points, this method optimizes the 3D location based on images taken from multiple perspectives, enabling a simple workflow (James and Robson, 2014; Nex and Remondino, 2014).

Despite the advances of this method for estimating PH using UAV imagery (PHaerial), there are several factors that should be taken into account, such as image ground sampling distance (GSD) or weather conditions, that can potentially affect its performance and accuracy (Han et al., 2018; Lu et al., 2019). Willkomm et al. (2016) also found that plant movement during image acquisition and the lack of protocol for field hand measurements can lead to PH underestimations. In view of these limitations, an effective and low-cost workflow using RGB camera can be deployed considering an adequate GSD and statistical aerial analysis under field conditions.

To the best of our knowledge, the image and data quality of ground-truth measurements (PHground) have not been adequately evaluated to assess their impact on PHaerial at individual plot growth stages (GS) in wheat breeding programs. Therefore, this study aims to validate PH derived from RGB imagery data and to understand the effect of data quality from different UAV platforms and PHground. The study's specific objectives are: (i) to develop a semi-automated low-cost workflow for extraction, analysis, and evaluation of PHaerial at multiple GS; (ii) to compare different UAV platforms used for PH estimations,

TABLE 1 | Summary of published studies on the estimation of plant height (PH) for wheat from RGB imagery acquired using unmanned aerial vehicles (UAVs).

References	GS	Platform—UAV	Camera/sensor	GSD cm/p	Total number of plots	Plot size (m)	Pixel extraction method	R^2 for PHground vs. PHaerial[‡]	RMSE for PHground vs. PHaerial (cm)[¶]
Holman et al. (2016)	GS30 to GS61	Cinestar octocopter	Sony NEX 7 24.4 mgpx	1	300	9 × 3	99th percentile	0.52–0.99	1.5–9.9
Madec et al. (2017)	GS20 to GS69	Hexacopter	Sony ILCE-6,000 digital[$]	1	1,173	10 × 1.9	99.5th percentile	0.95–0.99	2.9–9.8
Hassan et al. (2019a)	GS41 and GS85	DJI inspires 1 model T600	Sequoia 4.0 16 mgpx	2.5	600	1.3 × 1.3	90th and 99th percentile	0.8–0.96	5.75
Li et al. (2019)	GS21 to GS87	DJI matrice 600 Pro	Zenmuse X5R RGB camera	0.5	170	3 × 0.23	Mean, median, 95th percentile, and standard deviation	–	–
Lu et al. (2019)	GS30 to GS69	DJI phantom series	High-resolution digital RGB camera	1.66	36	6 × 5	Mean, median, standard deviation, coefficient of variation, and 25th, 50th, 75th, and 95th percentiles	0.89	6
Schirrmann et al. (2016)	GS41 to GS83	P-Y6, hexapilots, dresden (hexacopter)	Sony NEX 7 24 mgpx	1.2	20	1 x 1	90th percentile	0.76–0.92	6.0–15.0
Song and Wang (2019)	GS31, GS65 and GS83	DJI phantom 3	High-resolution digital RGB camera	1.5	15	2 × 2	Cuboid filter 3D classification	–	4.5–7.7
Yuan et al. (2018)	GS30 to GS87	Matrice 600 pro (M600) and DJI phantom 3 Pro	High-resolution digital RGB camera	0.47–0.67	100	1.5 x 1.524	89th and 100th percentiles	0.91	9
Yue et al. (2017)	GS30 and GS65	DJI S1000	UHD 185 firefly—hyperspectral sensor[#]	1	48	6 × 8	Average of pixel values	0.69	19

GS, Growth stage; UAV, unmanned aerial vehicles; GSD, ground sampling distances (cm/pixel). [#]*Adapted sensor capturing 450–950 nm wavelengths.* [$]*30 and 19 mm focal length was used to equip the camera.* [‡]*Coefficient of determination (R^2).* [¶]*Root mean square error (RMSE) between PHground and PHaerial, where the single numbers are the joining values obtained across GS by the respective authors.*

and; (iii) to assess the potential environmental issues associated between PHground and PHaerial. Finally, we investigate PHaerial and PHground predictions using the genotypic values.

MATERIALS AND METHODS

Plant Material, Site Description, and Data Collection

The experiments were conducted over two spring wheat (*Triticum aestivum* L.) growing breeding cycles: 2016–2017 and 2017–2018 at the CIMMYT experimental station Campo Experimental Norman E. Borlaug in Ciudad Obregon, northwestern Mexico (27°20'N; 109°54'W; and 38 masl). Environmental and management details of this site are given in Sayre et al. (1997). Two spring wheat panels were studied under potential yield conditions: the high biomass association panel (HiBAP)-I and the HiBAP-II. Fifty inbred lines were used for the validation in HiBAP-I during the 2016–2017 (Y17) and 2017–2018 (Y18) crop cycle, while the whole population of 150 lines was measured in HiBAP-II during the 2017–2018 (Y18). Both panels include representative lines derived from breeding and pre-breeding programs with a restricted range of maturity and height (Molero et al., 2019). The experimental design in both HiBAP panels consisted of an alpha-lattice design with two replicates and 30 incomplete blocks per replicate. The plots consisted of two beds in HiBAP-I Y17 and one bed in HiBAP I Y18 with two plant rows on the top of the beds for both trials. In HiBAP-II Y18, three replicates were evaluated in two beds plots. The beds in all three trials were 0.8 m wide, while the inter-row spacing within the bed and the space between beds were 0.24 and 0.36 m, respectively. Plot length was 4 m for HiBAP I Y17 and HiBAP II Y18 and 2 m for HiBAP I Y18.

Aerial (PHaerial, using UAV platforms) and ground-truth (PHground) plant height (PH) phenotyping were performed in the experiments during the following GSs: 40 days after emergence (E+40), at booting (B), 7 days after anthesis (A+7) and at physiological maturity (M). PHground was measured using a ruler when 50% of the plot reached a particular GS, as described by Torres and Pietragalla (2012). Similarly, the two UAVs were flown on the same day or 1 day apart, depending on the logistics in the field and the weather conditions. The optimal time and weather conditions for UAV data collection were defined as: around solar noon, under clear sky, and a low wind speed. A summary of solar radiation and wind speed conditions during the entire flight campaigns for each platform used is given in **Supplementary Table S1**. The average height was obtained from four random individual culms inside each plot (two in each bed), measuring the distance from the soil surface to the tip of the spike, excluding the awns, and avoiding any mounds or cracks in the soil.

Flight Campaign and Imagery Quality Parameters

The flight campaigns were performed with a high-resolution digital RGB camera mounted in two different types of UAVs across the growing cycles: the fixed-wing ($Plat_{FW}$) eBee (SenseFly Ltd., Cheseaux-Lausanne, Switzerland) employed in Y17 and Y18, the multi-rotor ($Plat_{MR}$) AscTec Falcon 8 (Ascending Technologies, Krailling, Germany) in Y17 and the Matrice 100 (DJI, Nanshan, Shenzhen, China) in Y18.

The flights were planned at the time of PHground phenotyping for assessing trials according to the predominant GS of interest in this study (E+40, B, A+7, and M). **Table 2** summarizes the number of flights and main specifications for each GS assessment at the time of PHaerial estimation, including the number of flights. The ground control points (GCPs) or post-processed kinematic (PPK; see below for details) were used for georeferencing corrections. A set of black and white squared GCPs were uniformly distributed over the entire field area in all trials. These GCPs, distributed for each panel according to **Table 2**, were surveyed with a Global Navigation Satellite System (GNSS) receiver using a real-time kinematic (RTK) correction (Trimble R4 GNSS system, Trimble, Sunnyvale, CA, United States). Additionally, 11 checkpoints (CP), surveyed using RTK correction, were placed across the site during the crop cycle Y18 for georeferenced accuracy assessment of the orthomosaics.

The flights of the $Plat_{FW}$ followed the technical recommendations in Loladze et al. (2019) and are described in **Table 3**. The flight plan was designed for north/south and east/west flights to achieve both a lateral and longitudinal overlap of 80%. The flights covered an area larger than the experiment to cover the entire experimental field and obtain accurate orthomosaics. High-accuracy corrections of the geolocation data measured with the $Plat_{FW}$ global navigation satellite system (GNSS) were calculated in the post-processing stage using the position of a fixed base station as a reference and the PPK correction while imagery geotagging (Benassi et al., 2017; Forlani et al., 2018).

The flight plans for both multi-rotor platforms were designed to achieve lateral and longitudinal overlaps of 80%, flying north/south. The flight operations of these multi-rotor UAVs are shown in **Table 3**, and further details can be checked in Tattaris et al. (2016) for the AscTec Falcon 8, and in Horton and Ranganathan (2018) for the Matrice 100. The flight plans of both types of platforms, $Plat_{FW}$ and $Plat_{MR}$, were designed to acquire images with different ground sampling distances (GSD in **Table 3**).

Three-Dimensional Crop Reconstruction and Plant Height Accuracy Assessment

The aerial data collected by both types of platforms were geotagged for orthomosaic processing using Pix4D Mapper software (v4.4.10; Pix4D, Lausanne, Switzerland). Images were imported into Pix4D software. GCPs were manually located to improve the accuracy of the three-dimensional (3D) point cloud georeferencing for $Plat_{FW}$ flights that did not use PPK corrections, as well as for the flight campaign using $Plat_{MR}$ (**Figure 1A**). The georeference accuracy was checked by rather than in the bundle adjustment of the orthomosaic product. The digital terrain model (DTM, i.e., the topography of the site without any plant) was generated for each trial from images

TABLE 2 | Crop phenology information across the measurements presented as days after emergence (DAE), the predominant development crop stage expressed by Zadoks growth scale, corresponding phenological stage and identification nomenclature in this investigation, as well as the number of flights for each platform using ground control points (GCPs) or post-processed kinematic (PPK) corrections for fixed-wing ($Plat_{FW}$) and multi-rotor ($Plat_{MR}$) platforms.

Trial	Pred. phenological stage	Ident. stage[a]	Zadoks scale[b]	DAE[c]	Number of flights ($Plat_{FW}$)		Number of flights ($Plat_{MR}$)
					PPK	GCP	Only GCP
HiBAP-I Y17 (30/Nov/2016[d])	Stem elongation	E+40	37–39	40	1	0	1
	Flowering	A+7	61–65	73–87	5	0	5
	Maturity	M	91–92	100	1	0	1
HiBAP-II Y18 (03/Dec/2017)	Stem elongation	E+40	37–39	40	1	0	0
	Booting	B	41–47	55–72	6	0	7
	Flowering	A+7	61–69	76–98	6	2	8
	Maturity	M	91–92	105–118	2	0	3
HiBAP-I Y18 (18/Dec/2017)	Stem elongation	E+40	37–39	40	1	0	1
	Booting	B	41–45	55–69	2	1	3
	Flowering	A+7	61–69	74–91	1	1	2
	Maturity	M	91–92	106–111	1	0	1

[a]Specific identification of the GS estimated/predominant: at 40 days after emergence (E+40), booting (B), 7 days after anthesis (A+7) and at physiological maturity (M). [b]The decimal (or Zadoks Scale according to Zadoks et al., 1974) growth stage code estimated according to the genetic variability. [c]Days after emergence represented by 50% of the plants with the first leaf through coleoptile (GS10). [d]Emergence date in each crop season.

TABLE 3 | Parameters of flight specifications details for fixed-wind ($Plat_{FW}$) and multi-rotor ($Plat_{MR}$) platforms.

	HiBAP-I Y17		HiBAP-II Y18		HiBAP-I Y18	
	$Plat_{FW}$	$Plat_{MR}$	$Plat_{FW}$	$Plat_{MR}$	$Plat_{FW}$	$Plat_{MR}$
Sensor	Canon PowerShot 110 camera of 16.2 MegaPixels	Sony NEX 5	SODA	ZenMuse X5	SODA	ZenMuse X5
Resolution (image pixels)	4,608 × 3,456	4,592 × 3,056	5,472 × 3,648	4,608 × 3,456	5,472 × 3,648	4,608 × 3,456
GSD[a] resolution (cm/Pixel)	1.7	0.7	1.7	0.7	1.7	0.7
GCPs[b] numbers for internal processing	7	7	9	9	7	7
Flight altitude	65	30	85	30	85	30

[a]GSD, ground sampling distance.
[b]GCPs: ground control points used for internal processing for$Plat_{MR}$ and$Plat_{FW}$ without PPK corrections.

collected by a single flight of each UAV platform prior to the vegetation emergence. The digital surface model (DSM; i.e., the topography of the site accounting for the plants) was obtained along with vegetation development at each GS.

The DSM and DTM rasters were computed following the workflow recommended by Pix4D for high-resolution RGB imagery (Pix4D, 2019b). This workflow uses a structure from motion (SfM) algorithm (Ullman, 1979; Snavely et al., 2008) to obtain a 3D point cloud. The point cloud was later meshed via an algorithm based on Delauney triangulation (Matthew et al., 2009; Susanto et al., 2016) computed on multiple image scales with noise filtering and a "sharp" surface smoothing filter. Afterward, the DTM was subtracted from the DSM to estimate the crop surface model (CSM, i.e., the height of individual plot surfaces) using R software version 3.6.1 (R Core Team, 2018). The PHaerial scripts used to perform the image analyses and trait extract are available at https://github.com/volpatoo/HTP-via-drone-imagery/tree/master/UAV-HTP_PlantHeight.

Figure 1 represents the major steps of the data acquisition and processing, as well as the software, packages, and tools used in this workflow.

Before computing the CSM for all flight campaigns, we conducted a preliminary test to define the best parametrization of the Pix4D workflow. Different settings in Pix4D were combined and tested to obtain the best high-density point clouds and DSM (for details, see **Supplementary Table S1**). The test results (not shown) were compared based on the accuracy of PHaerial against the PHground for each platform. This exercise used the data from the Y17 growing cycle at E+40, A+7, and M GS and the best performing processing scheme parameters to generate the 3D point clouds of all the flight campaigns (**Supplementary Table S1**).

The PH from the CSM raster was assessed using ArcGIS (version 10.6, Esri Inc., Redlands, United States). The buffer tool was used to create regions of interest (ROI_{PH}) to extract PH values from each plot (**Figure 1C**). Plant breeding trials usually consist of small plots within 0.5–1 m of each other in the interests of trial uniformity. Under these conditions, the canopies of

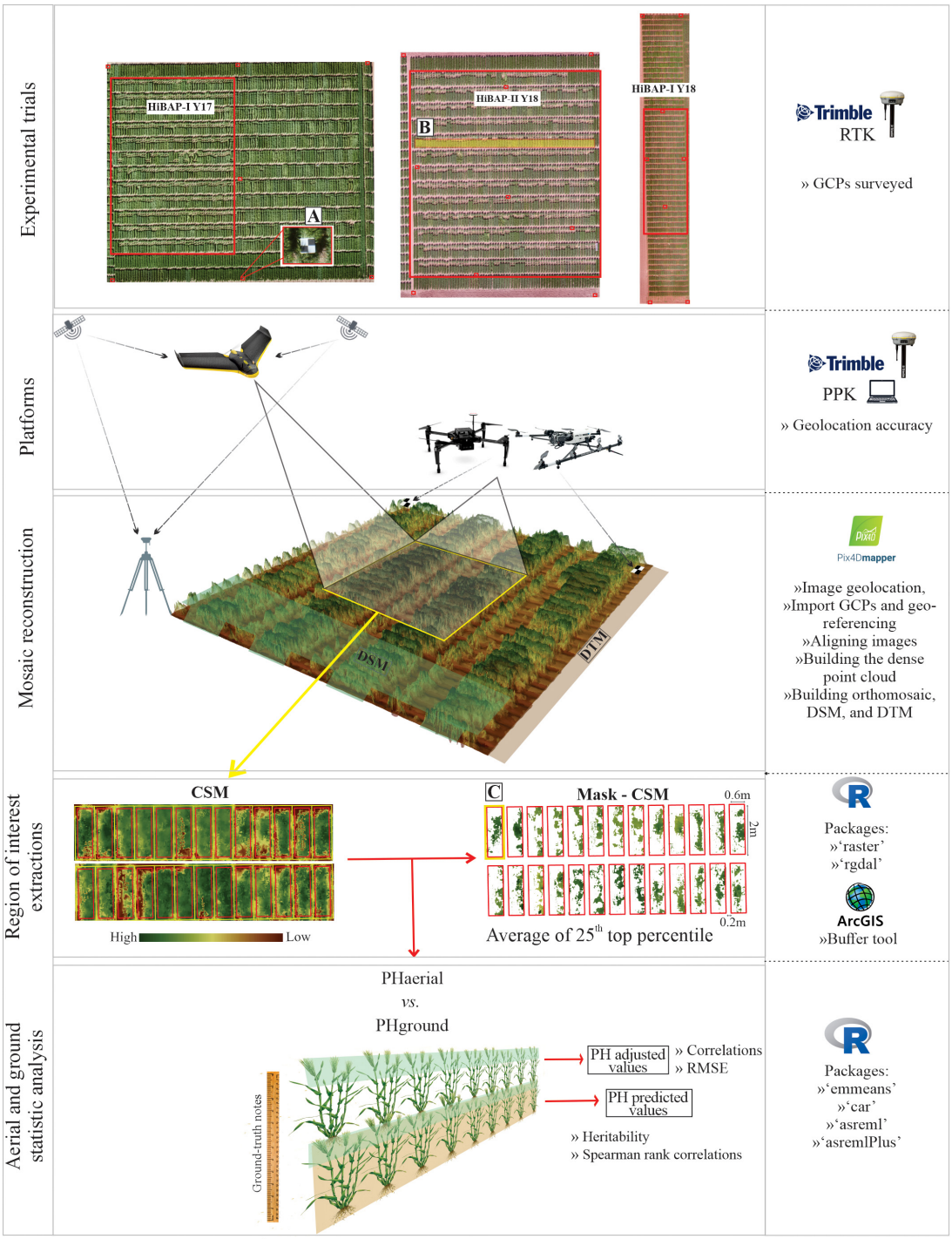

FIGURE 1 | Phenotyping workflow for estimation of plant height (PH) using $Plat_{FW}$ and $Plat_{MR}$ (UAVs) platforms (PHaerial) used in north-west Mexico during the 2017 and 2018 growing cycles. PHground, ground-truth measurements; DTM, digital terrain model; DSM, digital surface model; CSM, crop surface model. **(A–C)** are GCPs design, locality of the profile selected, and cropped area with the mask of CSM as the top 25th percentile pixels value, respectively.

adjacent plots can interfere with one another by shading, lodging, or wind load. The small plots can easily cause noise in the PH estimation, especially after flowering. To ensure the extraction of pure pixel values (i.e., pixels containing only information from the plot of interest), we built the regions of interest with a buffer zone of 0.1 m from the plot edges aligned at the center of the

two-bed rows. ROI_{PH} were exported as polygons into a shapefile for the data extraction.

We extracted data from the regions of interest by overlapping the CSM and the shapefile containing the ROI_{PH} using the R packages "raster" and "rgdal." Average PHaerial was calculated for each plot using pixel values greater than the 75th percentile for that plot. We tested different criteria for selecting pixels within the ROI_{PH} but this proved to be the optimum indicator for PHaerial based on comparison with the PHground values.

Accuracy Assessment of Orthomosaics Georeferencing

The automation of data extraction per plot requires a high accuracy in the orthomosaics and DTM georeferencing. To ensure this, we performed a preliminary study using two techniques: GCPs and PPK correction. PPK correction was used to obtain accurately geotagged $Plat_{FW}$ imagery. The table in **Figure 2** shows the comparison between the absolute accuracy of longitude and latitude coordinates estimated by the two methods. The accuracy is expressed as the difference between the XY geocoordinates from the CPs (which were not used in the bundle adjustment process) by comparing the coordinates of the CPs obtained at the CSM with the in-site geocoordinates obtained by an RTK GNSS system (i.e., delta-X and delta-Y, being X latitude and Y longitude). The delta-X and delta-Y were calculated for both platforms using the set of 11 CPs placed in the field during the crop cycle Y18. Additionally, the root mean square error (RMSE) of the differences between X and Y coordinates, the mean values and the standard deviations (SD) were computed. These parameters showed that the PPK achieved similar results than those obtained with GCPs for horizontal XY coordinates (RMSE $\sim$ 1 cm and SD $<$ 3.62 cm; **Figure 2**). The average accuracy measured as SD on the CPs coordinates was in agreement with the accepted limits mentioned by Vautherin et al. (2016): one to two times the GSD in X and Y directions either to GCP or PPK corrections.

We also evaluated the accuracy for altitude estimations (i.e., *Z*-axis) by contrasting calculated and ground-truth GCP height values using one flight in each breeding cycle for $Plat_{FW}$ and $Plat_{MR}$ (**Figure 3**). The height accuracy measured on the GCPs was acceptable in all flight dates, with the $Plat_{MR}$ showing slightly better results (RMSE = 1.77–1.85; and SD = 1.63–1.76) than $Plat_{FW}$ (RMSE = 2.81–3.84; and SD = 1.62–2.88). The R^2 was greater than 0.95 for all cases. The accuracy measured as SD also followed the criterion adopted by Vautherin et al. (2016): two to three times the GSD in the Z direction for both platforms. Overall, the accuracy obtained in the CSMs using PPK and GCP approaches reached similar results.

Statistical Models and Genetic Selection Evaluation

Since we conducted few flights at each GS, we first built a linear model to fit a single PH value per plot. In this model, the PHaerial from each platform at each GS was used as a dependent variable against plot and number of flights as explanatory variables. The adjusted means per plot for PHaerial and PHground values were then used to calculate best linear unbiased estimates (BLUEs) within each crop cycle, using the following model:

$$y_{ijk} = \mu + g_i + r_j + b_{k(j)} + \varepsilon_{ijk}$$

where y_{ijk} is the trait value for genotype i, replicate j, and block k; μ is the overall mean; g_i is the fixed effect for genotype i; r_j is the random effect for replicate j, which are assumed to be independently and identically distributed according to a normal distribution with mean zero and variance σ_r^2; that is, $r_j \sim iid\ N(0, \sigma_r^2)$; $b_{k(j)} \sim iid\ N(0, \sigma_b^2)$ is the random effect for block k within replicated j; and $\varepsilon_{ijk} \sim iid\ N(0, \sigma_\varepsilon^2)$ is the residual effect.

For each growing cycle, Pearson's correlations, R^2, and RMSE for PHs between PHground and PHaerial were calculated using the BLUEs derived from the above model at each GS after removing the outliers. Outliers were flagged using studentized residual from PHground values, and the significance of their correlation with PHaerial was determined by the Bonferroni test at $P < 0.01$ (Fox and Weisberg, 2019). The identified outliers were removed from both PHground and PHaerial to perform the analysis. Finally, the $RMSE_{dev}$ was computed to measure the deviation between the estimated values (PHaerial) and the measured values (PHground) across GS in each trial, according to Zhou et al. (2020).

The validation of the prediction model used best linear unbiased predictions (BLUPs) and heritability for PHground and PHaerial. The genotypic variance components (σ_g^2 and σ_ε^2) were derived by the fitted model described above for both PHground and PHaerial to calculate the broad-sense heritability (H_g^2, sometimes termed "repeatability") with the genotype g_i treated as a random effect in which $g_i \sim iid\ N(0, \sigma_g^2)$. Thus, H_g^2 quantifying the repeatability of the plant height trait estimation was computed as the ratio between the genotypic to the total variances (Holland et al., 2002). The significance (Ripley, 2019) of the Spearman rank correlation coefficient (ρ) (Spearman, 1904) was calculated using the BLUPs from both UAV-platforms against PHground for assessing the accuracy of genotypic rank selection.

Additionally, we measured 50 coincident genotypes in Y17 and Y18 (HiBAP-I) crop cycles (considering $g_i \sim iid\ N(0, A\sigma_g^2)$ where $\boldsymbol{A}$ is the associated additive relationship matrix) to obtain the narrow-sense heritability (h_a^2) for both UAV-platforms and to assess the accuracy under a G $\times$ E interaction model design, including the genotype $\times$ year interaction effect (t_{ge}) also as random with $t_{ge} \sim N(0, \sigma_{ge}^2)$. The data collected during booting in HiBAP-I Y18 was removed from the statistic-genetic model for G $\times$ E interaction in order to match better the GSs and calculate the BLUPs. For this analysis, R^2 represents the accuracy of predicted values from the correlations between the PHground and PHaerial. The standard errors (SE) of the heritability parameters in both validation models were obtained through mixed model output (Wolak, 2018).

We used the R software to run the statistical analyses, including linear models (Gilmour et al., 2015), multiple comparison procedures (Lenth, 2016), mixed and prediction models (Brien, 2018), and testing of model terms (Fox et al., 2019). The coefficients of parentage for the pedigree relationship matrices (A) were estimated as twice the coefficient of parentage

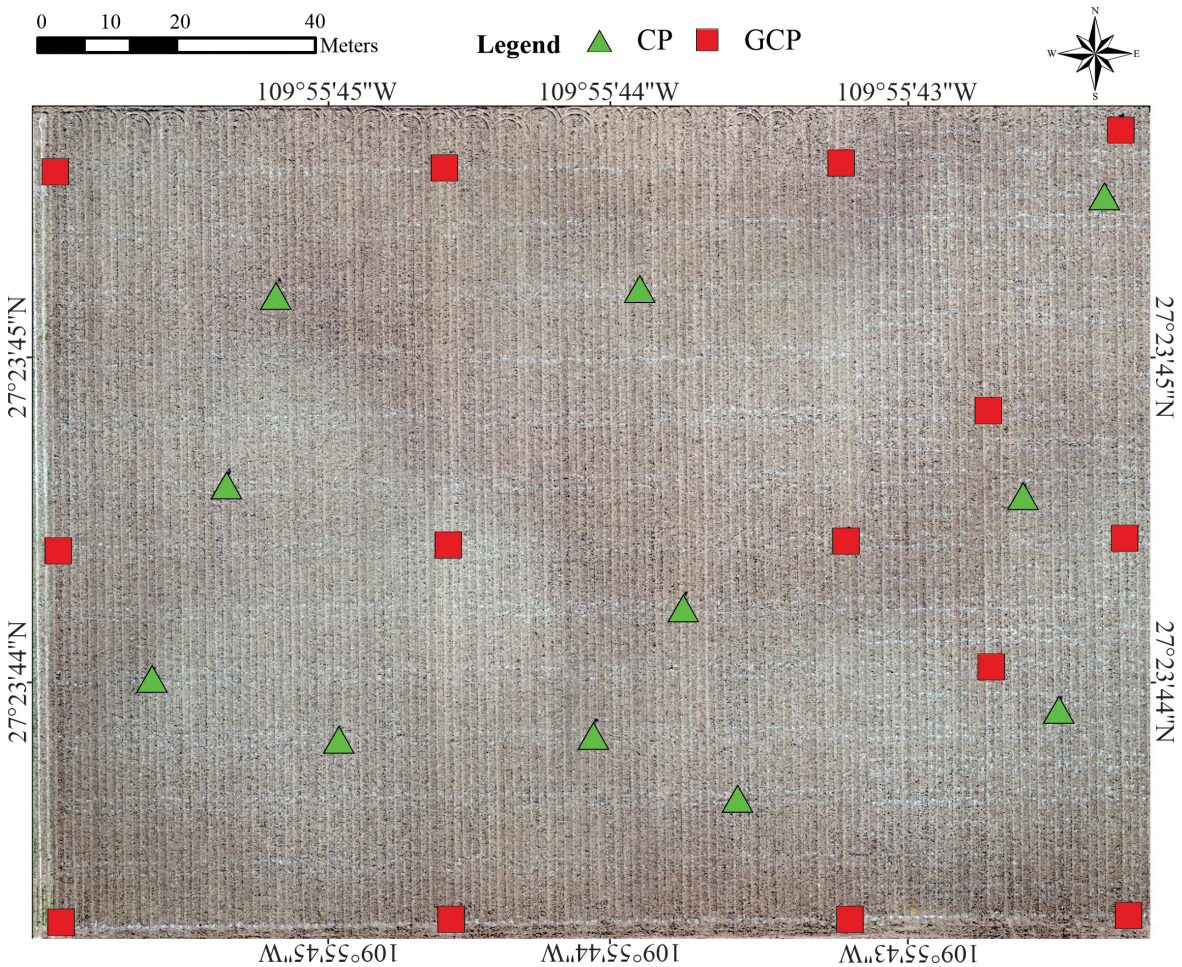

	GCP		PPK	
	X(cm)	Y(cm)	X(cm)	Y(cm)
Mean[1]	-0.8184	0.6810	-0.3274	1.7980
SD	3.0794	2.5758	3.2832	3.6209
RMSE	0.9285	0.7766	0.9899	1.0917

FIGURE 2 | The mean delta-X and delta-Y from all geocoordinates obtained from 11 checkpoints (CP) vs. the geocoordinates obtained from the orthomosaic (CSM) resulted from 14 GCP and PPK corrections. Standard deviation (SD) and Root Mean Square Error (RMSE) for X and Y coordinates. The base image corresponds to the bare soil flight using $Plat_{FW}$ in the HiBAP-II trial during November 2018. [1]Mean difference between measured coordinates to GCP and PPK.

using the "Browse" application within the International Crop Information System software package (McLaren et al., 2000).

RESULTS

Descriptive Statistics Across Growth Stages

PHground values were similar across crop cycles at the same evaluated GS (**Figure 4**). The heterogeneity within each trial remained relatively stable at B, A+7, and M (*SD* = 4.13–4.97 in HiBAP-I Y17, *SD* = 6.02–7.04 in HiBAP-I Y18, and *SD* = 4.62–5.65 in HiBAP-II Y18). The median value and SD for ground-truth PH measured at E+40 showed some discrepancies across cycles and trials, possibly attributable to the different genotypes used in each HiBAP panel, the year effect and differences in emergence dates.

UAV Plant Height Assessment and Validation

The PHaerial estimates were, in general, similar to PHground values. This matching can be visualized in **Figure 5**, where

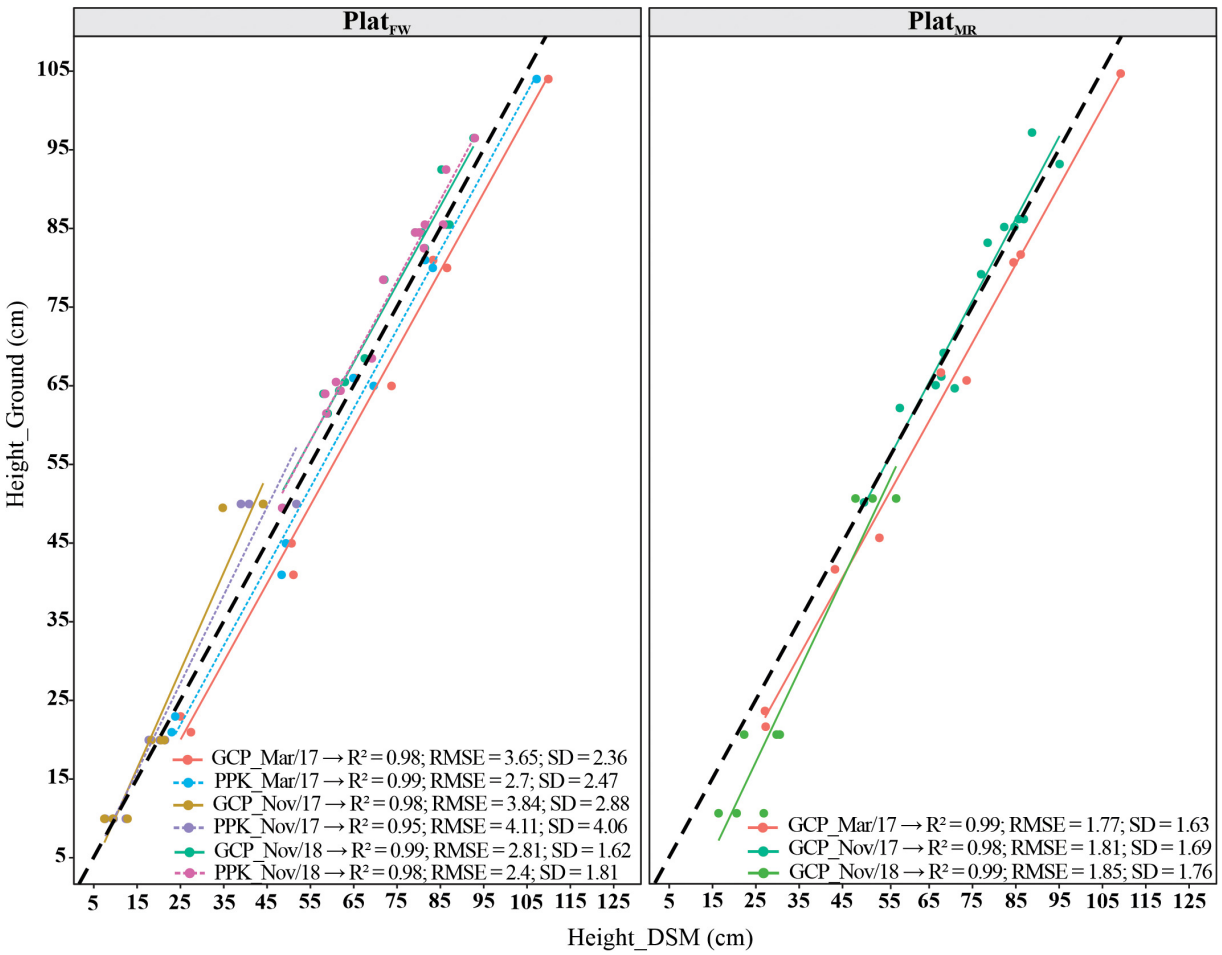

FIGURE 3 | Coefficient of determination (R^2), root mean square deviation (RMSE), and standard deviation (SD) of the errors, between ground control points (GCPs) height estimate from the digital surface model (DSM), and ground-truth measurements for three different dates of flights using PPK for fixed-wind platform ($Plat_{FW}$) and only GCP corrections for $Plat_{FW}$ and multi-rotor ($Plat_{MR}$). The dark black dashed diagonals represent the 1:1 line, and the colored solid (GCP) and dashed (PPK) lines represent the regression lines.

transects of PHground and PHaerial data from HiBAP-II are compared (refer to **Figure 1B** for the location of this transect within the HiBAP-II trial). Considerable mismatching between PHground and PHaerial values was detected at booting (B), whereas the best agreement was observed during maturity (M).

The agreement between PHground and PHaerial data was further confirmed by the strong correlations observed during most of the growing cycle for both platforms (**Figure 6**). The coefficient of determination at the different GS ranged from non-significant to $R^2 = 0.88$, and from non-significant to $R^2 = 0.81$, for $Plat_{FW}$ and $Plat_{MR}$, respectively. The measurements at maturity showed the highest and most consistent correlations across the different trials and platforms, with R^2 values ranging between 0.7 and 0.88. The lowest correlations were obtained at booting, observing even non-significance in HiBAP-II Y18 for both $Plat_{FW}$ and $Plat_{MR}$ ($p \geq 0.78$). The $Plat_{FW}$ platform performed better than $Plat_{MR}$ in HiBAP-I, except at E+40 during Y17, where $Plat_{MR}$ showed a coefficient of determination of 0.66 against 0.41 in $Plat_{FW}$. Conversely, $Plat_{MR}$ performed slightly better than $Plat_{FW}$ in HiBAP-II (**Figure 6**), particularly at A+7 (R^2 = 0.47 in $Plat_{MR}$ vs. R^2 = 0.37 in $Plat_{FW}$) and M (R^2 = 0.74 in $Plat_{MR}$ vs. R^2 = 0.7 in $Plat_{FW}$). Overall, the RMSE of the predicted model for individual GS did not exceeded 4.02 cm. However, the $RMSE_{dev}$ obtained across GS for each platform in HiBAP-I Y17 and HiBAP-I Y18 were around 15 cm ($RMSE_{dev}$ = 15.06 and 14.95 cm in HiBAP-I Y17; $RMSE_{dev}$ = 14.44 and 15.42 in HiBAP-I Y 18). The best performance for $RMSE_{dev}$ was in HiBAP-II Y18 in both platforms. Nevertheless, the $Plat_{FW}$ provided better results than $Plat_{MR}$ ($RMSE_{dev}$ = 8.19 for $Plat_{FW}$ *vs.* 12.14 = $Plat_{MR}$).

HTP for Genotypic Prediction of Plant Height From Wheat Breeding Trials

The evaluation strategy using H_g^2 shows strong potential for PHaerial implementation in a wheat breeding program, as PHaerial reached similar or higher values H_g^2 than those from PHground for each GS and across locations (**Figure 7**).

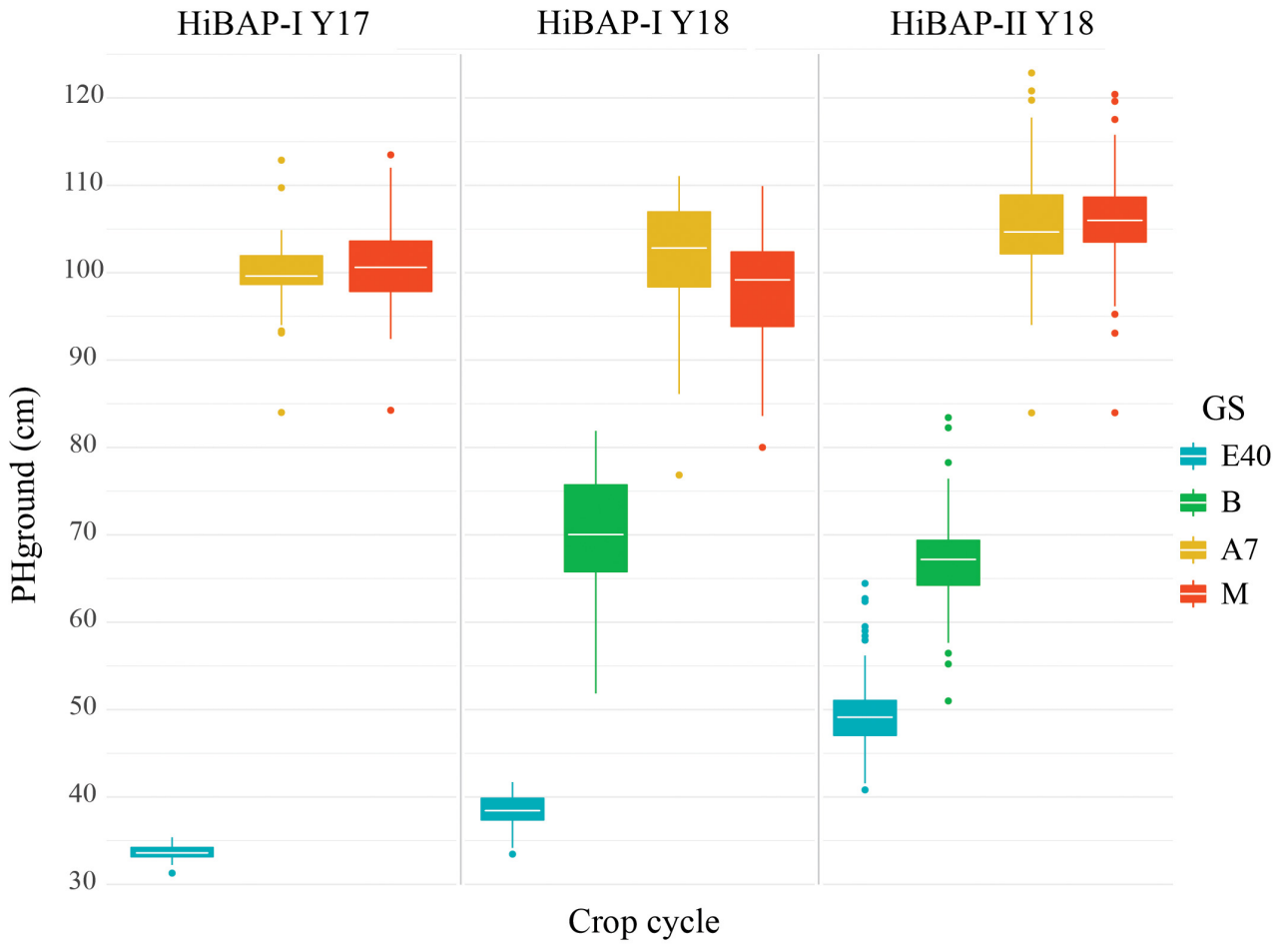

FIGURE 4 | Boxplot of BLUEs for wheat plant height (PH, cm) in each of the observed crop cycles at the following growth stages (GS): 40 days after emergence (E+40), booting (B), 7 days after flowering (A+7) and at physiological maturity (M).

The $Plat_{MR}$ provided better H_g^2 estimations than $Plat_{FW}$ and PHground for all GS at HiBAP-I Y17, except for maturity from PHground, ranging from 0.71 to 0.97 for $Plat_{MR}$ vs. 0.46–0.93 for $Plat_{FW}$, and vs. 0.62–0.96 for PHground. On the other hand, the $Plat_{FW}$ obtained greater H_g^2 values than $Plat_{MR}$ and PHground at HiBAP-I Y18 in all GS analyzed, except for A+7 from PHground (H_g^2 = 0.80, 0.96, 0.95, and 0.90 for $Plat_{FW}$ vs. H_g^2 = 0.37, 0.56, 0.90, and 0.85 for $Plat_{MR}$, and vs. H_g^2 = 0.71, 0.96, 0.97, and 0.92 for PHground, for E+40, B, A+7 and M, respectively). On HiBAP-II Y18, both platforms obtained similar results, but H_g^2 PHaerial estimations were significantly better than PHground at booting and $Plat_{FW}$ at A+7 was better estimations than $Plat_{MR}$ and PHground. Furthermore, $Plat_{FW}$ and PHground in HiBAP-I Y18 provided more accurate estimations of H_g^2 in comparison with $Plat_{MR}$ at booting.

Overall, the H_g^2 responses were in agreement with the results from the correlations (R^2) between PHground and PHaerial data. For HiBAP-I trials the H_g^2 degraded at E+40, and increased at later GS. Additionally, the UAV platforms showed better H_g^2 estimations than PHground across GS for each crop cycle (H_g^2 0.78, 0.92 and 0.94 for $Plat_{FW}$, and H_g^2 0.88, 0.67 and 0.93 for $Plat_{MR}$ vs. H_g^2 0.82, 0.89 and 0.78 for PHground, within HiBAP-I Y17, HiBAP-I Y18, and HiBAP-II Y18 trials, respectively).

The Spearman rank correlations (ρ) between predicted values for PHaerial and PHground were significant ($P < 0.001$) at all GS in all trials except at booting in HiBAP-II Y18. The highest ρ for HiBAP-I Y17 was observed at maturity for both platforms, and at HiBAP-I Y18, except at booting using the $Plat_{FW}$ (ρ = 0.91). Moreover, the greatest ρ in HiBAP-II Y18 was achieved at E+40 via $Plat_{FW}$ (ρ = 0.83). Lower, but still significant correlations using both platforms were observed at A+7 in HiBAP-II Y18 (ρ = 0.45 for $Plat_{FW}$, and ρ = 0.46 for $Plat_{FW}$) (**Figure 7**).

When genotype-environment interaction (G × E) effects were considered in the prediction of the genotypic PH values, the narrow-sense heritability (h_a^2) for $Plat_{FW}$ was greater than for $Plat_{MR}$ for all GS analyzed (h_a^2 0.29, 0.65, and 0.62 in $Plat_{FW}$, vs. h_a^2 0.06, 0.42, and 0.41 in $Plat_{MR}$, for E+40, A+7, and maturity growth stages, respectively). However, the h_a^2 from PHground was

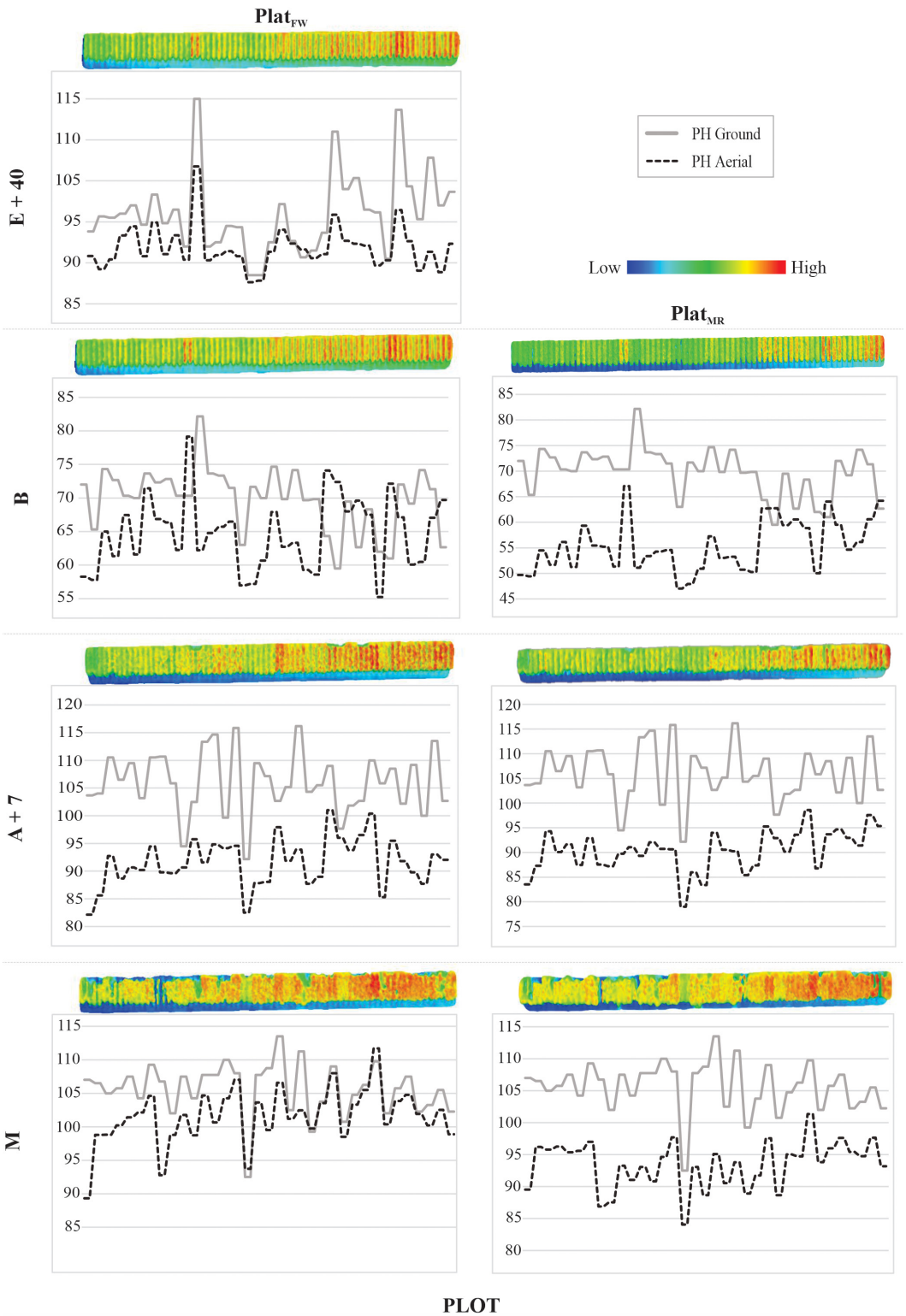

FIGURE 5 | Profile of 70 plots from HiBAP-II for *Plat*$_{FW}$ and *Plat*$_{MR}$ at the following growth stages (GS): 40 days after emergence (E+40), booting (B), 7 days after flowering (A+7), and at physiological maturity (M). Plant height (PH, cm) via ground-truth (ground) and unmanned aerial vehicle (UAV) data (aerial) are represented in the solid and dotted lines, respectively, matching with low (blueish) and high (reddish) color scale to PH. The 2D plots profiles image were generated using the textured mesh feature via the densified point cloud of Pix4D processing.

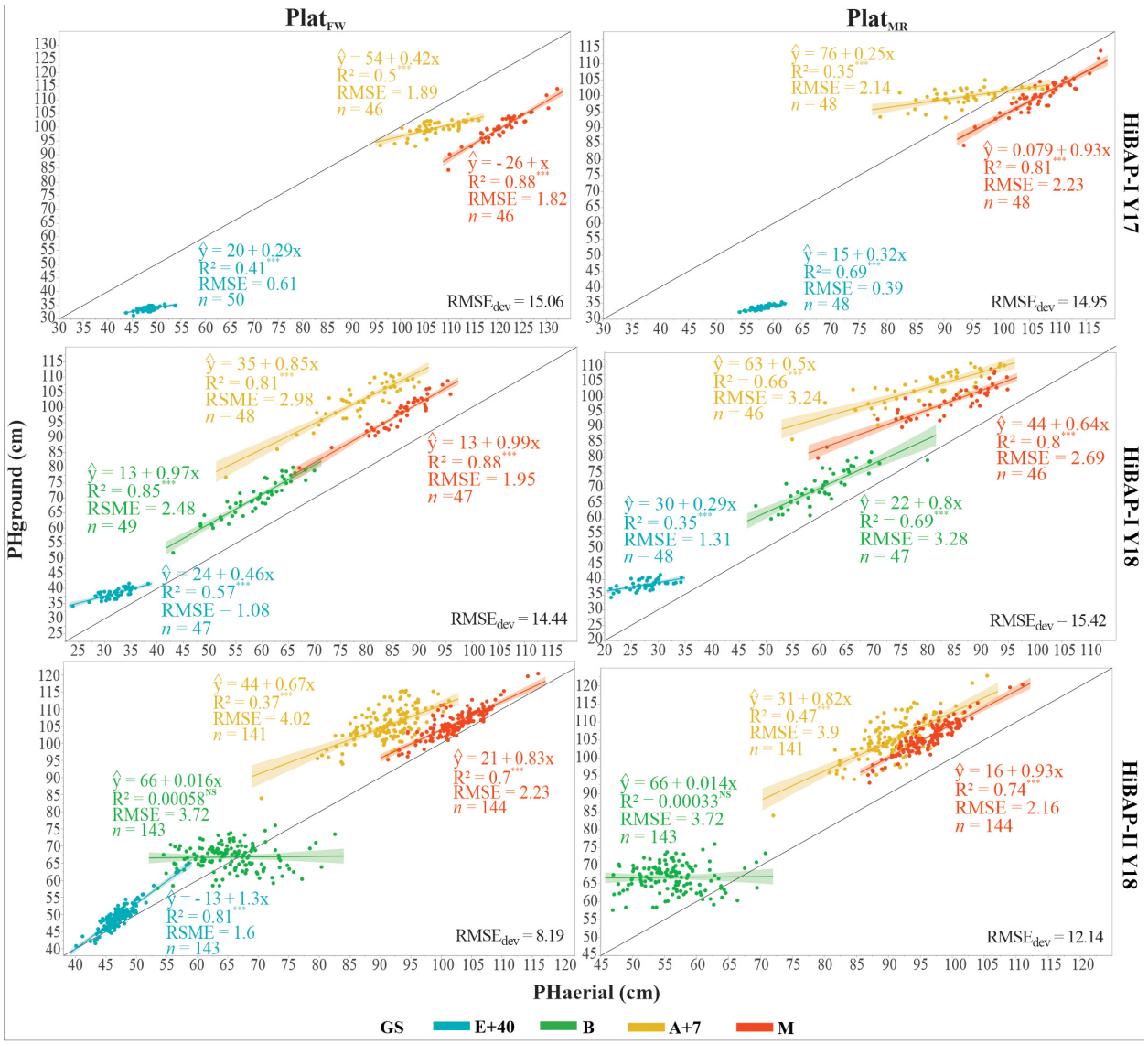

FIGURE 6 | Linear relationship between plant height (PH, cm) estimated from the unmanned aerial vehicle (UAV-based) data (PHaerial) and that ground-truth measured manually (PHground), as well as RMSE, and the number (*n*) of genotypes considered at four growth stages (GS): 40 days after emergence (E+40), booting (B), 7 days after flowering (A+7), and at physiological maturity (M) for $Plat_{FW}$ and $Plat_{MR}$ considering all locations in this study. Black solid line shows the 1:1 lines; light shadow color represents a 99% confidence interval. The $RMSE_{dev}$ in the bottom right represents the deviation between the PHaerial and the PHground across GS. *** indicate *p*-value of the coefficient of determination (R^2), with ***$P < 0.001$; NS, non-significative value.

higher than PHaerial at A+7 (h_a^2 0.71) and M (h_a^2 0.71). The accuracy (or R^2) remains constant across GS ranging from 0.75 to 0.96 in $Plat_{FW}$ vs. 0.64–0.92 in $Plat_{MR}$, but with lower values at E+40 for both UAV platforms (**Figure 8**).

DISCUSSION

The present study aimed to prove the applicability of aerial photogrammetry (i.e., using UAVs) to estimate PH in the wheat breeding context. Throughout the growing season, aerial HTP approaches were conducted on two different wheat panels (HiBAP-I and II) with two UAV platform classes (multi-rotor and fixed-wing) equipped with RGB cameras using PPK or GCP corrections. Our findings showed that for most of the growing stages, the UAV-based data (PHaerial) could be used for reliable estimations of PH and that genotype selection based on this data was equivalent to that obtained by manual ground measurements (PHground) (R^2 = 0.35–0.88). We attribute the good results obtained for a large number of experimental wheat plots (100 for HiBAP-I and 450 for HiBAP-II) partly to the strategy used in the pixel PH values extraction within each plot. The selection of pixels from the top 25th percentile within each plot region of interest of the imagery was intended to increase

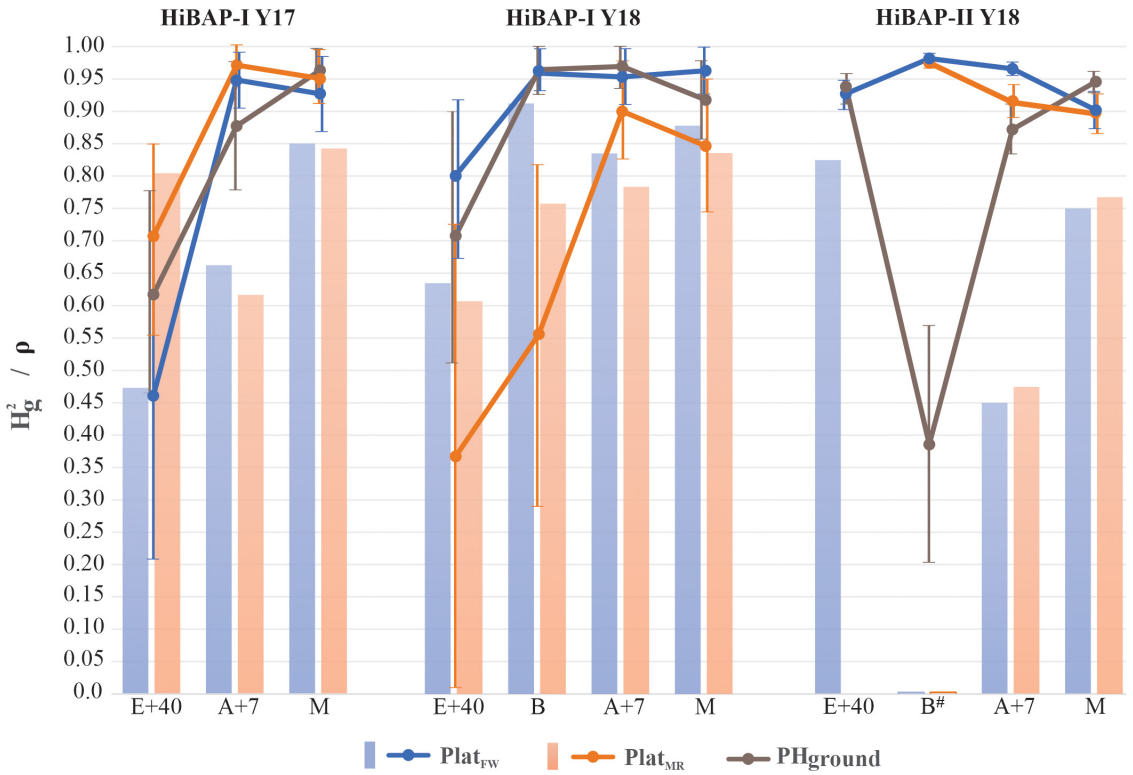

FIGURE 7 | The solid color lines represent the broad-sense heritability (H_g^2) across crop cycles (2016–2017 and 2017–2018) for $Plat_{FW}$, $Plat_{MR}$ and PHground in the growth stages: 40 days after emergence (E+40), booting (B), 7 days after flowering (A+7), and at physiological maturity (M) and its 95% confidence interval based on standard errors. The color bars show the Spearman Rank Correlation (ρ) from the predicted values between PHground and PHaerial. All ρ significant at $P < 0.0001$ except to B (non-significant) in HiBAP-II Y18.

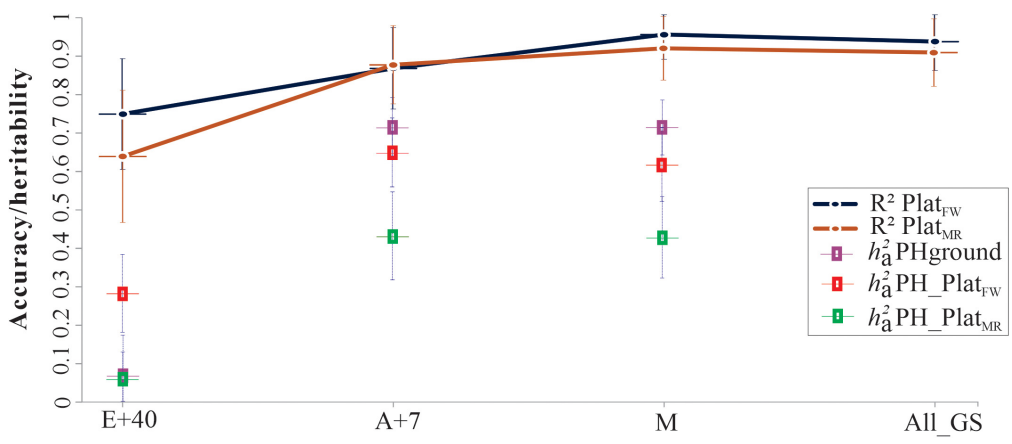

FIGURE 8 | Narrow-sense heritability (h_a^2) and coefficient of determination (R^2) from genotype-by-environment interaction (G × E) model using HiBAP-I genotypes measured in 2016–2017 and 2017–2018 growing cycles via $Plat_{FW}$ and $Plat_{MR}$, and across growth stages (GS): 40 days after emergence (E+40), 7 days after flowering (A+7), and at physiological maturity (M). The solid color lines represent the accuracy (R^2) for predict values between PHground and PHaerial, plus the confidence interval (CI) by the error bar. The colored squared represents the h_a^2 and the error bars indicate standard error. All growth stages (All_GS) were also considered to confirm the accuracy of genetic correlations. The cross lines give the upper and lower bounds of the 95% CI of the correlations computed using $\widehat{\rho} = 1.96\sqrt{(1-\widehat{\rho})/(n-2)}$, where $\widehat{\rho}$ is the estimated correlation, and n is the number of records used to compute the correlation.

the proportion of observations from the upper canopy in further analyses (**Figure 1C**). This strategy showed the best results in our study, differing from other studies, as shown in **Table 1**, which used either the average or very restricted statistical methods such as the 99th or 99.5th percentiles. These restricted models may be "too selective"—going against field hand measurement protocols

where randomization within the plot and a minimum number of measurements should be respected.

Assessing the Data Quality of UAV-Based Plant Height Estimations

A number of factors can have an impact on PHaerial estimations. In this section, we outline major potential sources of error discussed in previous studies, including UAV imagery parameters, choice of platform, and environmental factors, and their potential relevance to our study.

Ground sampling distance (GSD) is important in creating high-quality orthomosaics via orthorectification to obtain the DSM from the dense image matching as an additional source of data to enhance the PH model accuracy (Madec et al., 2017; Lu et al., 2019; Wilke et al., 2019). This orthomosaic generation method confers more accurate 3D points due to the extraction of common characteristic points (keypoints) in different images and by removing perspective distortion from the images using the DSM (Pix4D, 2019a). In our study, the differences observed in the performance of the two aerial platforms suggest that UAV imagery parameters such as GSD, altitude, and point cloud density may have influenced the PHaerial estimation accuracy. Our results indicate the $Plat_{FW}$ produced slightly more accurate PH estimations using a higher GSD (GSD = 2 cm/pixel) and a lower point cloud density (see **Supplementary Table S1**) compared to $Plat_{MR}$. Therefore, our results suggest there is no need to work with sub-centimeter resolution for DSM reconstruction when targeting PH estimation. This is in alignment with results obtained by Lu et al. (2019).

Even though in the case of our study $Plat_{FW}$ produced the best correlations and RMSE results overall, the choice between the two classes of platforms that have been evaluated in this study depends on the processing pipeline used, plant breeding target, and several other technical factors such as area extension, pilot expertise, total flight time, and intended GSD (Puri et al., 2017; Park et al., 2019). Each of these decisions can affect the quality of the PH data.

Other authors have noted several sources of error in aerial estimation of PH in wheat crops, including inefficient image pre- and post-processing due to suboptimal flying altitude, inaccurate DTM construction and errors in height extraction strategy from images (Hassan et al., 2019a). Chu et al. (2017) demonstrated that under unfavorable weather conditions, the quality of a dense point could affect the 3D-pixel constructions. For example, wheat PH data bias can occur due to wind conditions when using high spatial resolution images similar to those recorded from $Plat_{MR}$ (GSD = 0.7 cm/pixel). In our study, the high-resolution images recorded from the $Plat_{MR}$ captured a higher variability within the vegetation, probably making the CSM reconstruction more susceptible to slight plant movements and changes in illumination conditions within the canopy. Future studies or applications should consider these factors when planning to use high resolution imagery for 3D surface reconstruction. Otherwise, our study shows that a GSD of (GSD = 2 cm/pixel) may be sufficient for an efficient plant height estimation.

Environmental conditions during data acquisition can also lead to noisy point clouds that hinder PH estimations. These factors could result in lower 3D point accuracy during the orthorectification processing, affecting the point cloud densification step (Tirado et al., 2019). Indeed, our results for HiBAP-I Y17 show evidence that the PHaerial accuracy increased as the wind speed decreased, in contrast with the solar radiation that only slightly influenced the correlations (with no significant differences across GS) in HiBAP-I Y18 (**Supplementary Figure S1**). Other environmental factors that can potentially have an impact on the PHaerial are shadows (Jin et al., 2017; Brocks and Bareth, 2018), radiometric calibration (Mafanya et al., 2018), brightness levels (López-Granados et al., 2019), and cloudy weather (Niedzielski and Jurecka, 2018).

The UAV/PPK results in our study showed a high agreement with those obtained from CPs and GCPs. This demonstrates that PHaerial using PPK corrections could be an affordable method to increase image georeference accuracy by reducing human interference such as surveying GCPs, importing and manually marking them into the software (**Figures 2**, **3**). As we elaborated in our study, correct calibration of the camera also depends on proper image georeferencing based on the distribution of a sufficient number of GCPs across the field and extensive overlapping between images (Madec et al., 2017; Sanz-Ablanedo et al., 2018). In other studies, RTK/PPK has been used to correct the location of drone mapping imagery and improve the accuracy of GNSS data or geotags as they are captured either during flights (RTK) or after flight (PPK) (Forlani et al., 2018; Padró et al., 2019). However, these previous studies haven't concluded whether direct georeferencing using RTK/PPK will supersede GCPs to become the standard referencing technique for UAV imagery. The challenges of surveying the GCPs and keeping them in place throughout the life of the crop makes the PPK method cost-effective. It is also time-consuming to check all GCPs on the photogrammetry software to compute the keypoints on the images. To avoid this issue in a practical field situation, we recommend the use of a UAV/PPK system as implemented for $Plat_{FW}$, since the results were comparable to those orthomosaics georeferenced with GCPs.

Finally, the settings used in the software for orthomosaics and the DSM generation could also impact the accuracy of PH estimation using UAVs. As discussed by Holman et al. (2016), the software settings should be carefully selected and accurately reported for future improvements in UAV-based SfM methods. Our study achieved reliable outputs after testing different combinations of the settings in Pix4D. The optimal settings can be replicated according to **Supplementary Table S1**. Additionally, we provide a user-friendly script to perform the pixel values extractions using an open-source software (R software) to support future user.

Accuracy and Phenotypic Variations in UAV-Based Plant Height

The strong correlations and CI observed between PHground, and PHaerial values indicate that this approach can be used for growth rate analysis and wheat selection in a breeding pipeline.

The UAV data processing chain used in this study demonstrated itself to be quick, cost-effective, and accurate for the target trait. Moreover, our results showed accuracy levels similar to previous studies (**Table 1**) for PH estimation at individual GS, with higher correlations at late GS, matching findings of other studies (Hassan et al., 2019a). Nevertheless, it is essential to note that in some studies, the authors report correlations across stages along the growth cycle (Madec et al., 2017; Yue et al., 2017; Yuan et al., 2018; Harkel et al., 2019; Lu et al., 2019), masking the actual assessment power of PHaerial by stretching the response variable (i.e., ground PHs).

Efforts using high-throughput to estimate PH have also achieved reliable results using other platforms in several crops (Harkel et al., 2019; Reynolds et al., 2020). In particular, ground-based light detection and ranging (LiDAR) has been reported to provide more accurate PH estimations than UAV photogrammetry in wheat (Holman et al., 2016; Jimenez-Berni et al., 2018; Deery et al., 2020). However, the implementation of such a platform is limited and can be expensive (Nex and Remondino, 2014; Guo et al., 2018) compared to high-resolution RGB cameras. In addition, cutting-edge technologies in remote sensing have triggered the rapid development of affordable high-performance sensors (i.e., RGB, multispectral and hyperspectral cameras) and UAVs with higher autonomy and payload capacity, increasing the possibilities for field phenotyping applications (Sankaran et al., 2015). Our workflow using UAV-based imagery may be comparatively cheap and more efficient than ground platforms for phenotyping large and multi-location trials, targeting quick data acquisition and reducing computer resources; concepts that are supported by the literature via SfM approaches (Wang et al., 2018; Reynolds et al., 2019).

Despite the high correlations and acceptable RSME of the fitted model, in early stages (i.e., E+40 in **Figure 6**), the limited range of variation of PH can limit the correlations as demonstrated in HiBAP-I trials (**Figure 4**), which was also found by Madec et al. (2017). The deviation between PHground and PHaerial obtained in this study corroborates with errors in the literature in wheat PH estimations using UAV platforms (**Table 1**). In this study, we assessed the $RMSE_{dev}$ by the agreement between PHground and PHaerial as a measure of accuracy. Studies suggest that bias in crop height estimations by UAV platforms is due to the inability of SfM to reconstruct the top of the canopy accurately (Madec et al., 2017), the influence of neighboring plants (Khanna et al., 2015; Watanabe et al., 2017), and an inaccurate DTM strategy for pixel value extraction (Hu et al., 2018). However, the performance of SfM reconstruction could be improved by increasing the image overlapping (Seifert et al., 2019), and possibly by using better quality camera lenses and shortening flight time to avoid different sky conditions during flight timing. In our study, using fixed-ground targets at different heights proved to be an essential validation step in the current data processing workflow for PH estimations. The very accurate height estimations of the ground targets achieved using $Plat_{MR}$ and $Plat_{FW}$ ($R^2 >$ 0.95 and RMSE $<$ 4.11 cm; **Figure 3**), show the real potential of this method, and suggest that differences in plot-level estimations of PH between the PHaerial and PHground may be partly related to inaccuracies in manual scouting over very extensive field trials and wind movement.

In our study, the lack of correlations in HiBAP-II at booting highlighted some issues with PHground that are easily detectable when drawing a transect to compare trend lines (**Figure 5**). Accurate phenotyping is fundamental for the calibration or validation of novel HTP approaches (Araus and Cairns, 2014), as reported in studies on high-throughput genotyping (Ma et al., 2014). Reynolds et al. (2019) discuss the cost-benefit for phenotyping, showing that UAV-based photogrammetry is relatively affordable when flights operate under favorable conditions, i.e., with no rain, sunny days, and light to moderate wind speed. However, during the flights performed at booting in HiBAP-II Y18, the weather conditions for wind speed and solar radiation were reasonable compared with the other GS in the same trial. The weak correlations in this case could be attributed to heterogeneity within and between plots and canopy architecture issues in detecting the booting during the vegetative stage in experimental wheat plots (Torres and Pietragalla, 2012; Rosyara et al., 2019).

The accuracy of the DTM is paramount for accurate estimations of PH, especially in highly dense canopies such as those observed at A+7 and M (Bendig et al., 2014; Iqbal et al., 2017; Yang et al., 2019). The DTM can be obtained from measurements over the bare soil before the vegetation grows, as performed in this study. Additionally, the DTM can also be generated when vegetation is present by means of point cloud classification (Pix4D, 2018). However, the main challenge of this latter method is that generally at late GS, the bare soil is rarely exposed close to the region of interest during flights to capture in-field pixels. Furthermore, as the detection of bare soil pixels is usually done by image classification methods, this can be affected by rugged relief (Hassan et al., 2019a). Despite these limitations, some authors prefer the estimation of DTM from vegetation DSM, arguing that there are advantages in terms of processing time (Zhang et al., 2018; Hassan et al., 2019a). In our study, we use as a baseline a DTM generated from bare soil images acquired before plant emergence. The advantage of this approach is that it does not rely on image classification algorithms. A drawback of using such DTM is that an extra flight is demanded and more reference points for the SfM algorithm are needed.

UAV-Based Plant Height as a Reliable Trait for Wheat Phenotyping

The satisfactory correlations (R^2) between PHground and PHaerial observed in this study indicate the applicability of our study's UAV-based workflow. However, this may not serve all the needs of plant breeders, who often use heritability as a measure of the precision of trials and/or to compute the response to selection (Piepho and Möhring, 2007; Schmidt et al., 2019). Therefore our study also used heritability (H_g^2 andh_a^2) to confirm the UAV-based approach's ability to infer the predicted genetic values. Additionally, we used the genotypic correlation to compare the similarity between PHground and PHaerial rankings using the predicted values.

We found that the highest H_g^2 values across GS for PHaerial may indicate more reliable phenotyping measurements. In this case, the selection ranking of the best genotypes could be done using PHaerial assessments. This finding was also confirmed by the Spearman rank correlation (**Figure 7**). Therefore, our workflow for phenotyping PH combined with reliable H_g^2 can be an affordable and efficient method to offer breeders more accurate genotype selection criteria. Other studies have also supported a link between higher heritability (or repeatability, in some cases) and PH in later GS (Hassan et al., 2019a; Deery et al., 2020). However, some issues may appear in the temporal image when the target traits depend on the geometric structure, as described by Madec et al. (2017), who observed poor H_g^2 at the end of the growth cycle due to plant lodging. These circumstances were not evident in our study.

Medium to low levels of h_a^2 observed in the GS suggest a meaningful environmental influence, indicating that G × E interactions affect PH predictions (**Figure 8**). These results were supported by the random effect significance (Wilks, 1938) of G × E interaction at most of the GS analyzed, except in E+40 for $Plat_{MR}$ and PHground (data not shown). The non-significance, in these cases, can be attributed in part to the limited range of variability for PH. Furthermore, lower h_a^2 are expected when compared with H_g^2 due to pedigree information, in which the h_a^2 uses the proportion of genetic variation due to additive genetic effects only (Piepho and Möhring, 2007). The results confirmed that PH is a critical trait responsive by G × E interaction, as expected in quantitative traits (Tian et al., 2017; Tshikunde et al., 2019). The high correlations between predicted values for PHaerial and PHground across and within GS indicate that each platform measured similar underlying genetic traits. This means PHaerial can reliably predict genotypic values and rank genotypes as reliably as PHground.

CONCLUSION

The present study implemented and validated an efficient and scalable approach to acquire PH measurements under extensive wheat breeding trials at different growth stages. The remote sensing techniques applied in this study allowed the estimation of PH using high-resolution RGB imagery recorded from two UAV platforms and processed through a semi-automatic pipeline. The results for all trials in two growing cycles prove that the study workflow was able to estimate PH from UAV platforms comparable in accuracy to those measured by ground-truth notes. Our findings also indicate that using PHaerial for genotype selection could be a cost-effective way to predict PH values using temporal data from drone imagery taken in multiple environments, mainly in late GS. Due to the reliable results achieved by $Plat_{FW}$ to compute PH, it is reasonable to conclude that a lower density point cloud does not confer PH noise or underestimation in comparison to $Plat_{MR}$.The accuracy was responsive to image quality (i.e., GSD, weather conditions, etc.) and the settings in the processing steps of the surface model generation. A proper georeferencing of the orthomosaic is an essential step for data extraction, and the UAV-PPK approach was demonstrated to be a suitable method to replace laborious conventional methods using GCPs.

As evidenced by wheat PH studies in **Table 1**, different pixel extraction approaches can be made by choosing different thresholds for capturing the genotype variability within and among experimental plots. In this study, the reliably results obtained using PH estimations at multiple GSs and environments was also endorsed by the authors in **Table 1**. Finally, this study demonstrates that it is feasible to process high-volume field-based phenotypic data using UAV-based imagery.

DATA AVAILABILITY STATEMENT

The raw data supporting the conclusions of this article will be made available by the authors, without undue reservation.

AUTHOR CONTRIBUTIONS

FR conceived and designed the study and supervised the project. LV, LG-P, and IT collected and analyzed UAS data as supervised by FP and FR. LV performed the imagery quality analysis and conducted the literature survey. LV and LG-P performed image analysis, analyzed the data, and developed the statistical code of the study. LV, FP, LG-P, IT, and FR conducted the Remote Sensing component of the study. LV, FP, and FR drafted the manuscript. AB, MR, BG, and GM provided critical insights into the manuscript writing. All authors listed have made a substantial, direct, and intellectual contribution to writing and revision of the manuscript and approved it for publication.

ACKNOWLEDGMENTS

This work was supported by the CGIAR Research Program on Wheat (www.wheat.org), the International Wheat Yield Partnership (IWYP), by the UK Space Agency's International Partnership Programme (IPP), funded from the Department for Business, Energy and Industrial Strategy's (BEIS) Global Challenges Research Fund (GCRF), and the Sustainable Modernization of Traditional Agriculture (MasAgro)—an initiative from the Secretariat of Agriculture and Rural Development (SADER) and CIMMYT. We are very thankful to CIMMYT's Biometrics and Statistics Unit (BSU) for their support on statistical programming; for the whole Crop Nutrition and Wheat Physiology teams for their assistance with field measurements, flight campaign, and image processing. LV's scholarship was provided by the Coordenação de Aperfeiçoamento de Pessoal de Nível Superior—Brazil (CAPES)—Finance Code 001.

SUPPLEMENTARY MATERIAL

The Supplementary Material for this article can be found online at: https://www.frontiersin.org/articles/10.3389/fpls.2021.591587/full#supplementary-material

REFERENCES

Araus, J., and Cairns, J. (2014). Field high-throughput phenotyping: the new crop breeding frontier. *Trends Plant Sci.* 19, 52–61.

Barmeier, G., Mistele, B., and Schmidhalter, U. (2016). Referencing laser and ultrasonic height measurements of barleycultivars by using a herbometre as standard. *Crop Pasture Sci.* 67:1215. doi: 10.1071/cp16238

Benassi, F., Dall'Asta, E., Diotri, F., Forlani, G., Cella, U. M. D., Roncella, R., et al. (2017). Testing accuracy and repeatability of UAV blocks oriented with gnss-supported aerial triangulation. *Remote Sens.* 9:172. doi: 10.3390/rs9020172

Bendig, J., Bolten, A., Bennertz, S., Broscheit, J., Eichfuss, S., and Bareth, G. (2014). Estimating biomass of barley using crop surface models (CSMs) derived from UAV-based RGB imaging. *Remote Sens.* 6, 10395–10412. doi: 10.3390/rs61110395

Brien, C. (2018). *asremlPlus: Augments the Use of "ASReml-R" and "ASReml4-R" in Fitting Mixed Models. R Packag V*. Available online at: https://cran.r-project.org/web/packages/asremlPlus/asremlPlus.pdf (accessed October 22, 2020).

Brocks, S., and Bareth, G. (2018). Estimating barley biomass with crop surface models from oblique RGB imagery. *Remote Sens.* 10:268. doi: 10.3390/rs10020268

Chu, T., Starek, M. J., Brewer, M. J., Murray, S. C., and Pruter, L. S. (2017). Assessing lodging severity over an experimental maize (*Zea mays* L.) field using UAS images. *Remote Sens.* 9, 1–24. doi: 10.3390/rs9090923

Deery, D. M., Rebetzke, G. J., Jimenez-berni, J. A., Condon, A. G., Smith, D. J., Bechaz, K. M., et al. (2020). Ground-based LiDAR improves phenotypic repeatability of above-ground biomass and crop growth rate in wheat. *Plant Phenomics* 2020, 1–11. doi: 10.34133/2020/8329798

Forlani, G., Dall'Asta, E., Diotri, F., di Cella, U. M., Roncella, R., and Santise, M. (2018). Quality assessment of DSMs produced from UAV flights georeferenced with on-board RTK positioning. *Remote Sens.* 10:311. doi: 10.3390/rs10020311

Fox, J., and Weisberg, S. (2019). *An R Companion to Applied Regression*, 3rd Edn. Thousand Oaks, CA: Sage.

Fox, J., Weisberg, S., and Price, B. (2019). *Package' car.' 608*. Available online at: https://cran.r-project.org/web/packages/car/index.html (accessed December 25, 2019).

Gilmour, A. R., Gogel, B. J., Cullis, B. R., Welham, S. J., and Thompson, R. (2015). *ASReml User Guide Release 4.1 Functional Specification*. United Kingdom: VSN International Ltd.

Gracia-Romero, A., Kefauver, S. C., Fernandez-Gallego, J. A., Vergara-Díaz, O., Nieto-Taladriz, M. T., and Araus, J. L. (2019). UAV and ground image-based phenotyping: a proof of concept with durum wheat. *Remote Sens.* 11:1244. doi: 10.3390/rs11101244

Guo, Q., Wu, F., Pang, S., Zhao, X., Chen, L., Liu, J., et al. (2018). Crop 3D—a LiDAR based platform for 3D high-throughput crop phenotyping. *Sci. China Life Sci.* 61, 328–339. doi: 10.1007/s11427-017-9056-0

Han, L., Yang, G., Yang, H., Xu, B., Li, Z., and Yang, X. (2018). Clustering field-based maize phenotyping of plant-height growth and canopy spectral dynamics using a UAV remote-sensing approach. *Front. Plant Sci.* 9:1638. doi: 10.3389/fpls.2018.01638

Harkel, J. T., Bartholomeus, H., and Kooistra, L. (2019). Biomass and crop height estimation of different crops using UAV-based LiDAR. *Remote Sens.* 12:17. doi: 10.3390/rs12010017

Hassan, M. A., Yang, M., Fu, L., Rasheed, A., Zheng, B., Xia, X., et al. (2019a). Accuracy assessment of plant height using an unmanned aerial vehicle for quantitative genomic analysis in bread wheat. *Plant Methods* 15:37. doi: 10.1186/s13007-019-0419-7

Hassan, M. A., Yang, M., Rasheed, A., Yang, G., Reynolds, M., Xia, X., et al. (2019b). A rapid monitoring of NDVI across the wheat growth cycle for grain yield prediction using a multispectral UAV platform. *Plant Sci.* 282, 95–103. doi: 10.1016/j.plantsci.2018.10.022

Hickey, L. T., Hafeez, A. N., Robinson, H., Jackson, S. A., Leal-Bertioli, S. C. M., Tester, M., et al. (2019). Breeding crops to feed 10 billion. *Nat. Biotechnol.* 37, 744–754. doi: 10.1038/s41587-019-0152-9

Holland, J. B., Nyquist, W. E., and Cervantes-Martínez, C. T. (2002). "Estimating and interpreting heritability for plant breeding: an update," in *Plant Breeding Reviews*, ed. J. Janick (New York, NY: John Wiley & Sons Ltd), 9–112. doi: 10.1002/9780470650202.ch2

Holman, F. H., Riche, A. B., Michalski, A., Castle, M., Wooster, M. J., and Hawkesford, M. J. (2016). High throughput field phenotyping of wheat plant height and growth rate in field plot trials using UAV based remote sensing. *Remote Sens.* 8:1031. doi: 10.3390/rs8121031

Horton, E., and Ranganathan, P. (2018). Development of a GPS spoofing apparatus to attack a DJI Matrice 100 Quadcopter. *J. Glob. Position. Syst.* 16:9. doi: 10.1186/s41445-018-0018-3

Hu, P., Chapman, S. C., Wang, X., Potgieter, A., Duan, T., Jordan, D., et al. (2018). Estimation of plant height using a high throughput phenotyping platform based on unmanned aerial vehicle and self-calibration: example for *Sorghum* breeding. *Eur. J. Agron.* 95, 24–32. doi: 10.1016/j.eja.2018.02.004

Iqbal, F., Lucieer, A., Barry, K., and Wells, R. (2017). Poppy crop height and capsule volume estimation from a single UAS flight. *Remote Sens.* 9, 24–27. doi: 10.3390/rs9070647

James, M. R., and Robson, S. (2014). Mitigating systematic error in topographic models derived from UAV and ground-based image networks. *Earth Surf. Process. Landforms* 39, 1413–1420. doi: 10.1002/esp.3609

Jimenez-Berni, J. A., Deery, D. M., Rozas-Larraondo, P., Condon, A. T. G., Rebetzke, G. J., James, R. A., et al. (2018). High throughput determination of plant height, ground cover, and above-ground biomass in wheat with LiDAR. *Front. Plant Sci.* 9:237. doi: 10.3389/fpls.2018.00237

Jin, X., Liu, S., Baret, F., Hemerlé, M., and Comar, A. (2017). Estimates of plant density of wheat crops at emergence from very low altitude UAV imagery. *Remote Sens. Environ.* 198, 105–114. doi: 10.1016/j.rse.2017.06.007

Khanna, R., Martin, M., Pfeifer, J., Liebisch, F., Walter, A., and Siegwart, R. (2015). "Beyond point clouds – 3D mapping and field parameter measurements using UAVs," in *Proceedings of the 2015 IEEE 20th Conference on Emerging Technologies & Factory Automation (ETFA)*, Luxembourg. doi: 10.1109/ETFA.2015.7301583

Lenth, R. V. (2016). Least-squares means: the r package lsmeans. *J. Stat. Softw.* 69:12695. doi: 10.18637/jss.v069.i01

Li, J., Veeranampalayam-Sivakumar, A. N., Bhatta, M., Garst, N. D., Stoll, H., Stephen Baenziger, P., et al. (2019). Principal variable selection to explain grain yield variation in winter wheat from features extracted from UAV imagery. *Plant Methods* 15, 1–13. doi: 10.1186/s13007-019-0508-7

Loladze, A., Rodrigues, F. A., Toledo, F., San Vicente, F., Gérard, B., and Boddupalli, M. P. (2019). Application of remote sensing for phenotyping tar spot complex resistance in maize. *Front. Plant Sci.* 10:552. doi: 10.3389/fpls.2019.00552

López-Granados, F., Torres-Sánchez, J., Jiménez-Brenes, F. M., Arquero, O., Lovera, M., and De Castro, A. I. (2019). An efficient RGB-UAV-based platform for field almond tree phenotyping: 3-D architecture and flowering traits. *Plant Methods* 15, 1–16. doi: 10.1186/s13007-019-0547-0

Lu, N., Zhou, J., Han, Z., Li, D., Cao, Q., Yao, X., et al. (2019). Improved estimation of above-ground biomass in wheat from RGB imagery and point cloud data acquired with a low-cost unmanned aerial vehicle system. *Plant Methods* 15:17. doi: 10.1186/s13007-019-0402-3

Ma, C., Zhang, H. H., and Wang, X. (2014). Machine learning for Big Data analytics in plants. *Trends Plant Sci.* 19, 798–808. doi: 10.1016/j.tplants.2014.08.004

Madec, S., Baret, F., de Solan, B., Thomas, S., Dutartre, D., Jezequel, S., et al. (2017). High-throughput phenotyping of plant height: comparing unmanned aerial vehicles and ground LiDAR estimates. *Front. Plant Sci.* 8:2002. doi: 10.3389/fpls.2017.02002

Maes, W. H., and Steppe, K. (2019). Perspectives for remote sensing with unmanned aerial vehicles in precision agriculture. *Trends Plant Sci.* 24, 152–164. doi: 10.1016/j.tplants.2018.11.007

Mafanya, M., Tsele, P., Botai, J. O., Manyama, P., Chirima, G. J., and Monate, T. (2018). Radiometric calibration framework for ultra-high-resolution UAV-derived orthomosaics for large-scale mapping of invasive alien plants in semi-arid woodlands: *Harrisia pomanensis* as a case study. *Int. J. Remote Sens.* 39, 5119–5140. doi: 10.1080/01431161.2018.1490503

Matias, F. I., Caraza-harter, M. V., and Endelman, J. B. (2020). FIELDimageR: an R package to analyze orthomosaic images from agricultural field trials. *Plant Phenome J.* 3, 1–6. doi: 10.1002/ppj2.20005

Matthew, B., Michael, K., Randal, B., and Hugues, H. (2009). "Parallel poisson surface reconstruction," in *Proceedings of the Advances in Visual Computing. ISVC2009.* (Berlin: Springer).

McLaren, C. G., Ramos, L., Lopez, C., and Eusebio, W. (2000). "Applications of the genealogy management system," in *International Crop Information System. Technical Development Manual*, eds C. G. McLaren, J. W. White, and P. N. Fox (Mexico: CIMMYT and IRRI), 5.8–5.13. doi: 10.1534/g3.118.200856

Molero, G., Joynson, R., Pinera-Chavez, F. J., Gardiner, L. J., Rivera-Amado, C., Hall, A., et al. (2019). Elucidating the genetic basis of biomass accumulation and radiation use efficiency in spring wheat and its role in yield potential. *Plant Biotechnol. J.* 17, 1276–1288. doi: 10.1111/pbi.13052

Morales, N., Mueller, L. A., Kaczmar, N. S., Robbins, K. R., Santantonio, N., and Gore, M. A. (2020). ImageBreed: open-access plant breeding web – database for image-based phenotyping field experiments. *Plant Phenome J.* 3:e20004. doi: 10.1002/ppj2.20004

Nex, F., and Remondino, F. (2014). UAV for 3D mapping applications: a review. *Appl. Geomatics* 6, 1–15. doi: 10.1007/s12518-013-0120-x

Niedzielski, T., and Jurecka, M. (2018). Can clouds improve the performance of automated human detection in aerial images? *Pure Appl. Geophys.* 175, 3343–3355. doi: 10.1007/s00024-018-1931-9

Padró, J. C., Muñoz, F. J., Planas, J., and Pons, X. (2019). Comparison of four UAV georeferencing methods for environmental monitoring purposes focusing on the combined use with airborne and satellite remote sensing platforms. *Int. J. Appl. Earth Obs. Geoinf.* 75, 130–140. doi: 10.1016/j.jag.2018.10.018

Park, S., Lee, H., and Chon, J. (2019). Sustainable monitoring coverage of unmanned aerial vehicle photogrammetry according to wing type and image resolution. *Environ. Pollut.* 247, 340–348. doi: 10.1016/j.envpol.2018.08.050

Piepho, H. P., and Möhring, J. (2007). Computing heritability and selection response from unbalanced plant breeding trials. *Genetics* 177, 1881–1888. doi: 10.1534/genetics.107.074229

Pix4D (2018). *How to Automatically Generate a Digital Terrain Model (DTM) – Support*. Available online at: https://support.pix4d.com/hc/en-us/articles/202560579-How-to-automatically-generate-a-Digital-Terrain-Model-DTM#gsctab=0 (accessed on October 20, 2020).

Pix4D (2019a). *Getting GCPs on the Field or Through Other Sources*. Available online at: https://support.pix4d.com/hc/en-us/articles/202557489-Step-1-Before-Starting-a-Project-4-Getting-GCPs-on-the-field-or-through-other-sources-optional-but-recommended (accessed on December 20, 2019).

Pix4D (2019b). *How to Improve the Outputs of Dense Vegetation Areas? – Support*. Available online at: https://support.pix4d.com/hc/en-us/articles/202560159-How-to-improve-the-outputs-of-dense-vegetation-areas (accessed July 26, 2019).

Puri, V., Nayyar, A., and Raja, L. (2017). Agriculture drones: a modern breakthrough in precision agriculture. *J. Stat. Manag. Syst.* 20, 507–518. doi: 10.1080/09720510.2017.1395171

R Core Team (2018). *R: A Language and Environment for Statistical Computing*. Vienna: R Foundation for Statistical Computing.

Rebetzke, G. J., Jimenez-Berni, J., Fischer, R. A., Deery, D. M., and Smith, D. J. (2019). Review: high-throughput phenotyping to enhance the use of crop genetic resources. *Plant Sci.* 282, 40–48. doi: 10.1016/j.plantsci.2018.06.017

Reynolds, D., Baret, F., Welcker, C., Bostrom, A., Ball, J., Cellini, F., et al. (2019). What is cost-efficient phenotyping? Optimizing costs for different scenarios. *Plant Sci.* 282, 14–22. doi: 10.1016/j.plantsci.2018.06.015

Reynolds, M., Chapman, S., Crespo-Herrera, L., Molero, G., Mondal, S., Pequeno, D. N. L., et al. (2020). Breeder friendly phenotyping. *Plant Sci.* 295:110396. doi: 10.1016/j.plantsci.2019.110396

Reynolds, M. P., and Borlaug, N. E. (2006). Impacts of breeding on international collaborative wheat improvement. *J. Agric. Sci.* 144, 3–17. doi: 10.1017/S0021859606005867

Ripley, B. (2019). *boot:Bootstrap Functions. 1.3-23*. Available online at: https://cran.r-project.org/web/packages/boot/index.html (accessed April 15, 2020).

Rodrigues, F. A., Blasch, G., Defourny, P., Ortiz-Monasterio, J. I., Schulthess, U., Zarco-Tejada, P. J., et al. (2018). Multi-temporal and spectral analysis of high-resolution hyperspectral airborne imagery for precision agriculture: assessment of wheat grain yield and grain protein content. *Remote Sens.* 10:930. doi: 10.3390/rs10060930

Rosyara, U., Kishii, M., Payne, T., Sansaloni, C. P., Singh, R. P., Braun, H. J., et al. (2019). Genetic contribution of synthetic hexaploid wheat to CIMMYT's spring bread wheat breeding germplasm. *Sci. Rep.* 9:12355. doi: 10.1038/s41598-019-47936-5

Sankaran, S., Khot, L. R., and Carter, A. H. (2015). Field-based crop phenotyping: multispectral aerial imaging for evaluation of winter wheat emergence and spring stand. *Comput. Electron. Agric.* 118, 372–379. doi: 10.1016/j.compag.2015.09.001

Sanz-Ablanedo, E., Chandler, J. H., Rodríguez-Pérez, J. R., and Ordóñez, C. (2018). Accuracy of Unmanned Aerial Vehicle (UAV) and SfM photogrammetry survey as a function of the number and location of ground control points used. *Remote Sens.* 10:1606. doi: 10.3390/rs10101606

Sayre, K. D., Rajaram, S., and Fischer, R. A. (1997). Yield potential progress in short bread wheats in northwest Mexico. *Crop Sci.* 37, 36–42. doi: 10.2135/cropsci1997.0011183X003700010006x

Schirrmann, M., Hamdorf, A., Garz, A., Ustyuzhanin, A., and Dammer, K. H. (2016). Estimating wheat biomass by combining image clustering with crop height. *Comput. Electron. Agric.* 121, 374–384. doi: 10.1016/j.compag.2016.01.007

Schmidt, P., Hartung, J., Bennewitz, J., and Hans-Peter, P. (2019). Heritability in plant breeding on a genotype-difference basis. *Genetics* 212, 991–1008. doi: 10.1534/genetics.119.302134

Shewry, P. R., Pellny, T. K., and Lovegrove, A. (2016). Is modern wheat bad for health? *Nat. Plants* 2:16097. doi: 10.1038/nplants.2016.97

Seifert, E., Seifert, S., Vogt, H., Drew, D., van Aardt, J., Kunneke, A., et al. (2019). Influence of drone altitude, image overlap, and optical sensor resolution on multi-view reconstruction of forest images. *Remote Sens.* 11:1252. doi: 10.3390/rs11101252

Singh, A., Ganapathysubramanian, B., Singh, A. K., and Sarkar, S. (2016). Machine learning for high-throughput stress phenotyping in plants. *Trends Plant Sci.* 21, 110–124. doi: 10.1016/j.tplants.2015.10.015

Singh, D., Wang, X., Kumar, U., Gao, L., Noor, M., Imtiaz, M., et al. (2019). High-throughput phenotyping enabled genetic dissection of crop lodging in wheat. *Front. Plant Sci.* 10:394. doi: 10.3389/fpls.2019.00394

Snavely, N., Seitz, S. M., and Szeliski, R. (2008). Modeling the world from Internet photo collections. *Int. J. Comput. Vis.* 80, 189–210. doi: 10.1007/s11263-007-0107-3

Song, Q., Zhang, G., and Zhu, X. G. (2013). Optimal crop canopy architecture to maximise canopy photosynthetic CO 2 uptake under elevated CO2-A theoretical study using a mechanistic model of canopy photosynthesis. *Funct. Plant Biol.* 40, 109–124. doi: 10.1071/FP12056

Song, Y., and Wang, J. (2019). Winter wheat canopy height extraction from UAV-based point cloud data with a moving cuboid filter. *Remote Sens.* 11, 10–14. doi: 10.3390/rs11101239

Spearman, C. (1904). The proof and measurement of association between two things. *Psychol. Bull.* 1, 363–363. doi: 10.1037/h0065390

Susanto, F., de Souza, P., and He, J. (2016). Spatiotemporal interpolation for environmental modelling. *Sensors (Basel)* 16, 1–20. doi: 10.3390/s16081245

Tattaris, M., Reynolds, M. P., and Chapman, S. C. (2016). A direct comparison of remote sensing approaches for high-throughput phenotyping in plant breeding. *Front. Plant Sci.* 7:1131. doi: 10.3389/fpls.2016.01131

Tian, X., Wen, W., Xie, L., Fu, L., Xu, D., Fu, C., et al. (2017). Molecular mapping of reduced plant height gene Rht24 in bread wheat. *Front. Plant Sci.* 8:1379. doi: 10.3389/fpls.2017.01379

Tirado, S. B., Hirsch, C. N., and Springer, N. M. (2019). UAV based imaging platform for monitoring maize growth throughout development. *bioRxiv* [Preprint]. doi: 10.1101/794057

Torres-Sánchez, J., López-Granados, F., De Castro, A. I., and Peña-Barragán, J. M. (2013). Configuration and specifications of an Unmanned Aerial Vehicle (UAV) for early site specific weed management. *PLoS One* 8:e58210. doi: 10.1371/journal.pone.0058210

Torres, A., and Pietragalla, J. (2012). "Crop morphological traits," in *Physiological Breeding II: A Field Guide to Wheat Phenotyping*, eds A. J. D. Pask, J. Pietragalla, D. M. Mullan, and M. P. Reynolds (Mexico: CIMMYT), 1–30. doi: 10.1017/CBO9781107415324.004

Tshikunde, N. M., Mashilo, J., Shimelis, H., and Odindo, A. (2019). Agronomic and physiological traits, and associated quantitative trait loci (QTL) affecting yield response in wheat (*Triticum aestivum* L.): a review. *Front. Plant Sci.* 10:1428. doi: 10.3389/fpls.2019.01428

Ullman, S. (1979). The interpretation of structure from motion. *Proc. R. Soc. Lond. B Biol. Sci.* 203, 405–426. doi: 10.1098/rspb.1979.0006

USDA (2018). *World Agricultural Outlook Board*. Washington, DC: USDA.

Vautherin, J., Rutishauser, S., Schneider-Zapp, K., Choi, H. F., Chovancova, V., Glass, A., et al. (2016). "Photogrammetric accuracy and modeling of rolling shutter cameras," in *ISPRS Annals of the Photogrammetry, Remote Sensing and Spatial Information Sciences*, (Göttingen: Copernicus), 139–146. doi: 10.5194/isprs-annals-III-3-139-2016

Walters, J. P., Archer, D. W., Sassenrath, G. F., Hendrickson, J. R., Hanson, J. D., Halloran, J. M., et al. (2016). Exploring agricultural production systems and their fundamental components with system dynamics modelling. *Ecol. Modell.* 333, 51–65. doi: 10.1016/j.ecolmodel.2016.04.015

Wang, X., Singh, D., Marla, S., Morris, G., and Poland, J. (2018). Field-based high-throughput phenotyping of plant height in *Sorghum* using different sensing technologies. *Plant Methods* 14, 1–16. doi: 10.1186/s13007-018-0324-5

Watanabe, K., Guo, W., Arai, K., Takanashi, H., Kajiya-Kanegae, H., Kobayashi, M., et al. (2017). High-throughput phenotyping of *Sorghum* plant height using an unmanned aerial vehicle and its application to genomic prediction modeling. *Front. Plant Sci.* 8:421. doi: 10.3389/fpls.2017.00421

Wilke, N., Siegmann, B., Klingbeil, L., Burkart, A., Kraska, T., Muller, O., et al. (2019). Quantifying lodging percentage and lodging severity using a UAV-based canopy height model combined with an objective threshold approach. *Remote Sens.* 11:515. doi: 10.3390/rs11050515

Wilks, S. S. (1938). The large-sample distribution of the likelihood ratio for testing composite hypotheses. *Ann. Math. Stat.* 9, 60–62. doi: 10.1214/aoms/1177732360

Willkomm, M., Bolten, A., and Bareth, G. (2016). Non-destructive monitoring of rice by hyperspectral in-field spectrometry and UAV-based remote sensing: case study of field-grown rice in North Rhine-Westphalia, Germany. *Int. Arch. Photogramm. Remote Sens. Spat. Inf. Sci. ISPRS Arch.* 2016, 1071–1077. doi: 10.5194/isprsarchives-XLI-B1-1071-2016

Wolak, M. (2018). *nadiv:(Non)Additive Genetic Relatedness Matrices. 2.16.0.0*.

Würschum, T., Langer, S. M., and Longin, C. F. H. (2015). Genetic control of plant height in European winter wheat cultivars. *Theor. Appl. Genet.* 128, 865–874. doi: 10.1007/s00122-015-2476-2

Yang, B., Wang, M., Sha, Z., Wang, B., Chen, J., Yao, X., et al. (2019). Evaluation of above-ground nitrogen content of winter wheat using digital imagery of unmanned aerial vehicles. *Sensors (Switzerland)* 19, 1–18. doi: 10.3390/s19204416

Yang, G., Liu, J., Zhao, C., Li, Z. Z., Huang, Y., Yu, H., et al. (2017). Unmanned aerial vehicle remote sensing for field-based crop phenotyping: current status and perspectives. *Front. Plant Sci.* 8:1111. doi: 10.3389/fpls.2017.01111

Yuan, W., Li, J., Bhatta, M., Shi, Y., Baenziger, P. S., and Ge, Y. (2018). Wheat height estimation using LiDAR in comparison to ultrasonic sensor and UAS. *Sensors (Switzerland)* 18:3731. doi: 10.3390/s18113731

Yue, J., Yang, G., Li, C., Li, Z., Wang, Y., Feng, H., et al. (2017). Estimation of winter wheat above-ground biomass using unmanned aerial vehicle-based snapshot hyperspectral sensor and crop height improved models. *Remote Sens.* 9:708. doi: 10.3390/rs9070708

Zadoks, J. C., Chang, T. T., and Konzak, C. F. (1974). A decimal code for the growth stages of cereals. *Weed Res.* 14, 415–421.

Zhang, H., Sun, Y., Chang, L., Qin, Y., Chen, J., Qin, Y., et al. (2018). Estimation of grassland canopy height and above-ground biomass at the quadrat scale using unmanned aerial vehicle. *Remote Sens.* 10:851. doi: 10.3390/rs10060851

Zhao, C., Zhang, Y., Du, J., Guo, X., Wen, W., Gu, S., et al. (2019). Crop phenomics: current status and perspectives. *Front. Plant Sci.* 10:714. doi: 10.3389/fpls.2019.00714

Zhou, L., Gu, X., Cheng, S., Yang, G., Shu, M., and Sun, Q. (2020). Analysis of plant height changes of lodged maize using UAV-LiDAR data. *Agriculture* 10:146. doi: 10.3390/agriculture10050146

Conflict of Interest: GM was not employed by company KWS Momont Recherche during the execution of this research.

The remaining authors declare that the research was conducted in the absence of any commercial or financial relationships that could be construed as a potential conflict of interest.

frontiers in Genetics

ORIGINAL RESEARCH
published: 25 February 2021
doi: 10.3389/fgene.2021.600444

Identification of the QTL-allele System Underlying Two High-Throughput Physiological Traits in the Chinese Soybean Germplasm Population

Lei Wang[1†], Fangdong Liu[1†], Xiaoshuai Hao[1], Wubin Wang[1,3,4,5], Guangnan Xing[1,3,4,5], Jingjing Luo[2], Guodong Zhou[2], Jianbo He[1,3,4,5] and Junyi Gai[1,3,4,5,6*]*

[1] Soybean Research Institute, Nanjing Agricultural University, Nanjing, China, [2] Plant Phenomics Research Center, Nanjing Agricultural University, Nanjing, China, [3] MARA National Center for Soybean Improvement, Nanjing Agricultural University, Nanjing, China, [4] MARA Key Laboratory of Biology and Genetic Improvement of Soybean (General), Nanjing Agricultural University, Nanjing, China, [5] State Key Laboratory for Crop Genetics and Germplasm Enhancement, Nanjing Agricultural University, Nanjing, China, [6] Jiangsu Collaborative Innovation Center for Modern Crop Production, Nanjing Agricultural University, Nanjing, China

OPEN ACCESS

Edited by:
Ankush Prashar, Newcastle University, United Kingdom

Reviewed by:
Anna Maria Mastrangelo, Research Centre for Cereal and Industrial Crops (CREA), Italy
Naeem Hasan Syed, Canterbury Christ Church University, United Kingdom

***Correspondence:**
Jianbo He
hjbxyz@gmail.com
Junyi Gai
sri@njau.edu.cn

[†] These authors have contributed equally to this work

Specialty section:
This article was submitted to Systems Biology, a section of the journal Frontiers in Genetics

Received: *30 August 2020*
Accepted: *01 February 2021*
Published: *25 February 2021*

Citation:
Wang L, Liu F, Hao X, Wang W, Xing G, Luo J, Zhou G, He J and Gai J (2021) Identification of the QTL-allele System Underlying Two High-Throughput Physiological Traits in the Chinese Soybean Germplasm Population. Front. Genet. 12:600444. doi: 10.3389/fgene.2021.600444

The QTL-allele system underlying two spectral reflectance physiological traits, NDVI (normalized difference vegetation index) and CHL (chlorophyll index), related to plant growth and yield was studied in the Chinese soybean germplasm population (CSGP), which consisted of 341 wild accessions (WA), farmer landraces (LR), and released cultivars (RC). Samples were evaluated in the Photosynthetic System II imaging platform at Nanjing Agricultural University. The NDVI and CHL data were obtained from hyperspectral reflectance images in a randomized incomplete block design experiment with two replicates. The NDVI and CHL ranged from 0.05–0.18 and 1.20–4.78, had averages of 0.11 and 3.57, and had heritabilities of 78.3% and 69.2%, respectively; the values of NDVI and CHL were both significantly higher in LR and RC than in WA. Using the RTM-GWAS (restricted two-stage multi-locus genome-wide association study) method, 38 and 32 QTLs with 89 and 82 alleles and 2–4 and 2–6 alleles per locus were identified for NDVI and CHL, respectively, which explained 48.36% and 51.35% of the phenotypic variation for NDVI and CHL, respectively. The QTL-allele matrices were established and separated into WA, LR, and RC submatrices. From WA to LR + RC, 4 alleles and 2 new loci emerged, and 1 allele was excluded for NDVI, whereas 6 alleles emerged, and no alleles were excluded, in LR + RC for CHL. Recombination was the major motivation of evolutionary differences. For NDVI and CHL, 39 and 32 candidate genes were annotated and assigned to GO groups, respectively, indicating a complex gene network. The NDVI and CHL were upstream traits that were relatively conservative in their genetic changes compared with those of downstream agronomic traits. High-throughput phenotyping integrated with RTM-GWAS provides an efficient procedure for studying the population genetics of traits.

Keywords: annual wild soybean (G. soja Sieb. & Zucc.), cultivated soybean (G. max (L.) Merr.), chlorophyll index (CHL), high-throughput phenotyping, normalized difference vegetation index (NDVI), QTL-allele matrix, restricted two-stage multi-locus genome-wide association study (RTM-GWAS), spectral reflectance image

INTRODUCTION

With the rapid development of high-throughput genome sequencing technology, high-quality genotype data can be obtained quickly and cheaply, enabling the detection of quantitative trait loci (QTL) at a high level of resolution through genome-wide association studies (GWAS) (Shendure and Ji, 2008; Visscher et al., 2017). Previous QTL studies have primarily focused on the collection of phenotype data (phenotyping) for agronomic traits to achieve various breeding objectives. As upstream biological traits often underlie breeding target traits, there is much interest in identifying upstream traits for the control of downstream agronomic traits. These upstream traits generally consist of some physiological or biochemical traits that are time-consuming and difficult to identify without the appropriate tools. Both high-quality genotype and phenotype data are required for accurate and powerful QTL detection. Because of improvements in the reliability of current genotyping technologies, obtaining high-quality phenotype data in QTL studies has become a major challenge (Cobb et al., 2013). Recently, spectral reflectance has been developed as a high-throughput phenotyping technique (Rebetzke et al., 2019; Watt et al., 2020). Remote-sensing images have been widely used to measure crop traits, such as plant height, biomass, chlorophyll content, disease susceptibility, drought stress sensitivity, nitrogen content, and yield (Gitelson et al., 2003; Estrada et al., 2015; Nigon et al., 2015, Holman et al., 2016; Jay et al., 2017, Salas Fernandez et al., 2017; Pérez-Bueno et al., 2019). Specifically, the approach is based on quantifying differences in canopy spectral reflectance among varieties for the aforementioned traits (Yang et al., 2017). The high-throughput phenotyping platform usually consists of several sensors and automatic systems and provides an efficient method for characterizing plant phenotypes (Furbank and Tester, 2011).

Multispectral and hyperspectral reflectance images have been widely used in high-throughput phenotyping platforms; the spectral index has been found to be closely related to the growth and development of crops (Duan et al., 2017). In studies of hyperspectral remote-sensing technology, vegetation indices are typically used to maximize the relationship between certain reflectance wavelengths and plant function when the effect of background noise is controlled (Huete et al., 2002; Hatfield and Prueger, 2010). Most of the vegetation indices are correlated with plant parameters, such as pigment status, grain yield, NDVI (normalized difference vegetation index), RVI (ration vegetation index), and GNDVI (green and near-infrared difference vegetation index) (Wiegand et al., 1991; Peñuelas et al., 1997; Lewis et al., 1998; Rutkoski et al., 2016). NDVI is calculated based on the near-infrared spectrum and red-light spectrum (Tucker, 1979), which has been extensively used to evaluate crop growth and estimate nitrogen content, nitrogen uptake, and nitrogen efficiency in crops (Erdle et al., 2011; Samborski et al., 2015; Foster et al., 2017). Studies of crop diseases have also shown that NDVI can be used for crop disease assessment (Kumar et al., 2016). More recently, studies have shown that NDVI is closely related to crop yield (Hassan et al., 2019). Zhang et al. (2019) used hyperspectral remote sensing to establish plot-yield prediction models for field selection in large-scale soybean breeding programs. Specifically, they found that NDVI and RVI were the best combination of vegetation indices for plot-yield prediction in their models.

Chlorophyll is the primary component involved in plant photosynthesis and is closely related to biomass accumulation and yield formation, making it critically important for crop improvement. The rapid and non-destructive estimation of chlorophyll content facilitates genetic studies of chlorophyll. Chlorophyll content can be predicted using different wavelength spectra; for example, there is a strong correlation between the reflectance ratio of the near-infrared band to the 700-nm band and chlorophyll content (Gitelson et al., 2003). The hyperspectral sensor in the high-throughput phenotyping platform is often used to estimate the chlorophyll index (CHL), and this index has been widely used to evaluate chlorophyll content, crop biotic stress, and abiotic stress (Estrada et al., 2015; Awlia et al., 2016; Pérez-Bueno et al., 2019).

NDVI and CHL are both spectral reflectance physiological traits related to plant growth and yield. To evaluate the usefulness of these traits in breeding programs, knowledge of their variability and genetic basis in germplasms is essential. Previously, the measurement of these two physiological traits was tedious and often not possible using traditional instruments. Now, multispectral and hyperspectral images have greatly facilitated the measurement of these traits. The greenhouse high-throughput phenotyping platform (GHTPP) in the Plant Phenomics Research Center (PPRC) at Nanjing Agricultural University (NJAU) has been used by several studies. Phenotype data from the high-throughput phenotyping platforms of previous studies have primarily been used for the prediction of agronomic traits, such as plant yield (Maimaitijiang et al., 2020). However, there is a need for more studies to assess the genetic basis of high-throughput spectral reflectance phenotypes.

The aims of this study were the following: (i) characterize variation in two spectral reflectance physiological traits, NDVI and CHL, in the Chinese soybean germplasm population (CSGP), including wild accessions (WA), cultivated farmer landraces (LR), and released modern cultivars (RC), using the facilities and equipment of the GHTPP at the PPRC, NJAU, to compare wild and cultivated soybeans; (ii) explore genetic variation in QTL-alleles through association mapping using the novel RTM-GWAS procedure and evolutionary changes from WA to LR and RC; (iii) predict the genetic potentials of the germplasm population through recombination among the accessions; and (iv) predict the candidate genes as well as the gene constitutions of NDVI and CHL in the CSGP based on information in SoyBase[1].

MATERIALS AND METHODS

Plant Materials and Experimental Design

A total of 341 soybean accessions of the CSGP, including 76 WAs, 83 LRs, and 182 RCs, were sampled in this study.

[1]http://soybase.org

A randomized incomplete block design experiment with two replicates was conducted for high-throughput phenotyping. Because of the space limitations of the high-throughput phenotyping platform, the accessions were randomly divided into two groups. Two replicates of the phenotyping experiment were performed for the first group of 172 accessions on September 9, 2019 and October 13, 2019, and for the second group of 169 accessions on November 20, 2019 and May 1, 2020. For each test, approximately 4∼5 viable seeds were selected from each accession and were planted in a plastic pot (Φ23 × H17 cm). The experimental soil was a 3:1 mixture of vermiculite and nutrient soil; one best soybean seedling remained in each pot on the seventh day after sowing. The temperature in the greenhouse was maintained between 25–33°C, and light was provided for 16 hours (06:00 to 22:00).

High-Throughput Phenotyping

The greenhouse high-throughput phenotyping platform at the PPRC, NJAU, was used for phenotyping. The platform consisted of a planting area, irrigation area, and PSII (Photosynthetic System II) imaging room. An automatic and high-throughput transfer system was used to transfer plants from the planting/growing area to the imaging room. The PSII imaging room was equipped with a camera system (CropReporter, Phenovation B.V., Netherlands, https://www.phenovation.com/) with a CCD (charge-coupled device) camera, spectral LEDs (light-emitting diodes) for actinic treatment, an illuminated area of 70 cm × 70 cm, and a spectral range of 350–1000 nm. The spectral reflectance images were captured at six different wavelengths. From these images, the NDVI and CHL of the plant canopy for individual pots were estimated. According to CropReporter, the NDVI was calculated as $(R_{\mathrm{NIR}} - R_{\mathrm{red}})/(R_{\mathrm{NIR}} + R_{\mathrm{red}})$, and the CHL was calculated as $R_{700}^{-1} - R_{\mathrm{NIR}}^{-1}$, where R_{NIR}, R_{red}, and R_{700} are the spectral reflectance in the near-infrared band, the visible red band, and the 700-nm wavelength band, respectively.

The platform was also equipped with the automatic experiment management software IS Agriware Logistics (Version2018.06.99, Indigo Logistics, Netherlands) to control system operation, CropReporter (Version 4.4.2, Phenovation B.V., Netherlands) to control the camera system, and the image analysis software Data Analysis (Version 5.4.8-64b, Phenovation B.V, Netherlands) to process the data. The two traits were unitless, as they represent relative values of reflectance. All of the NDVI and CHL values were obtained directly from the platform system.

The automatic phenotype measurements began on the sixth day after sowing (DAS6). Each pot with a plant was transferred from the planting area into the PSII imaging room to measure NDVI and CHL. Each pot was then returned to the planting/growing area. This phenotyping process was automatically executed every 3 days, and a total of nine measurements (DAS6, DAS9, DAS12, DAS15, DAS18, DAS21, DAS24, DAS27, and DAS30, which means the 6th, 9th,. . ., and 30th day counting from sowing, respectively) were taken throughout the experimental period for each accession type.

SNP Genotyping and SNPLDB Assembly

The 341 soybean accessions were genotyped with RAD-seq (restriction site-associated DNA sequencing) in previous studies (He et al., 2017; Fu et al., 2020; Liu et al., 2020). A total of 145,558, 82,966, and 98,482 SNPs were recovered in these three studies, respectively, and the intersection of SNP data from different studies was taken and filtered with a minor allele frequency > 2% (each allele is present in at least six individuals). A total of 44,931 SNPs were obtained and used in the present study.

The RTM-GWAS (restricted two-stage multi-locus genome-wide association study) procedure (He et al., 2017) was used for QTL-allele detection in this study. With RTM-GWAS, a total of 11,716 multi-allelic SNPLDB markers were assembled based on the 44,931 genome-wide SNPs. The number of alleles of the SNPLDB markers ranged from 2 to 11 with an average of 3.1, enabling the detection of QTLs with up to 11 alleles per locus.

Statistical Analysis

The experiment consisted of an incomplete block design. The plot values were adjusted using the block means according to the equal block mean assumption because the material set in each block was randomly selected; therefore, the entire experiment was treated as a completely randomized design with two replicates. The linear model for the adjusted dataset was $y_i = \mu + g_i + \varepsilon_i$, where y_i is the observed corrected phenotype of the i-th accession, μ is the population mean, g_i is the genotypic effect of the i-th accession, and ε_i is the random error following a normal distribution with a mean of zero and variance of σ^2. The analysis of variance of the corrected phenotype data was performed using the PROC GLM in SAS/STAT 9.4 (SAS Institute, Cary, NC), and variance components were estimated using PROC VARCOMP with the REML method. The trait heritability estimate was calculated as $h^2 = \sigma_g^2/(\sigma_g^2 + \sigma^2/r)$, where σ_g^2 is the genetic variance, and r is the number of replicates. This h^2 is heritability in narrow sense because σ_g^2 contains only additive and additive by additive genetic variance in selfpollinated soybean germplasm population.

Phenotype Data Selection

There were nine measurements (DAS6, DAS9, DAS12, DAS15, DAS18, DAS21, DAS24, DAS27, and DAS30) for each trait (NDVI or CHL) each accession. The trait heritability value was used to assess the goodness of the trait expression, and the measurement with a highest heritability value was chosen to represent the trait. Therefore, the variance components and heritability values were estimated based on analysis of variance for all the nine measurements, and the measurement with the highest trait heritability value was used for genome-wide association study.

Restricted Two-Stage Multi-Locus Genome-Wide Association Study (RTM-GWAS)

The RTM-GWAS method was used for QTL-allele detection (He et al., 2017). Briefly, RTM-GWAS first involved the construction of multi-allelic SNPLDB (SNP linkage disequilibrium block) markers by grouping multiple adjacent and tightly linked SNPs through the LD-block partition. Second, the genetic similarity

coefficient matrix based on SNPLDB markers was used to correct for population structure bias by incorporating its eigenvectors as model covariates. Finally, two-stage association analysis was conducted to detect QTLs and their corresponding multiple alleles based on a multi-locus multi-allele model. The linear model of RTM-GWAS in matrix form is $\mathbf{y} = \mathbf{1}\mu + \mathbf{Wa} + \mathbf{Xb} + \mathbf{e}$, where **y** is the phenotype, μ is the population mean, **W** is the eigenvector matrix representing the population structure, **X** is the design matrix of locus genotype, **a** and **b** are vectors of corresponding effects. At the first stage, **X** includes only a single SNPLDB marker for pre-selection. At the second stage, **X** includes multiple SNPLDB markers for multi-locus modeling. In the present study, at the first stage under the single locus model, 1,296 and 2,147 SNPLDBs were pre-selected from the 11,716 SNPLDBs for the second stage of stepwise regression association analysis under the multi-locus model for NDVI and CHL, respectively. As the RTM-GWAS was based on the multi-locus model having built-in control for the experiment-wise error rate, a normal significance level of 0.05 was used for QTL detection in this study.

Prediction of the Genetic Potential of NDVI and CHL in the CSGP

To predict the recombination potential of the population, all possible single crosses among entire accessions, among subpopulation accessions, and between subpopulation accessions were simulated *in silico* (He et al., 2017). For each cross, 2,000 inbred lines were derived, and the phenotypes were predicted for each line according to the QTL-allele matrix. Finally, the recombination potential of each cross was assessed using the 99th percentiles of the predicted phenotype data.

Annotation of Candidate Genes and GO Analysis of NDVI and CHL

According to SoyBase(see footnote 1), the candidate genes for NDVI and CHL were annotated from the identified QTLs. Next, the annotated candidate genes were subjected to gene ontology (GO) analysis using the Williams 82 genome version 1 (Wm82.a1.v1.1) as the reference genome. The candidate genes were searched within the interval (with a 50-kb flanking expansion) of the associated loci. In order to have a preliminary validation of the annotated candidate genes, the RNA Seq-Atlas project data set in SoyBase (see footnote 1) was downloaded and analyzed to assess the expression level of the annotated genes for NDVI and CHL.

RESULTS

Phenotypic Variation of NDVI and CHL in the CSGP

Phenotype measurements for each accession were taken nine times on different days during growth (DAS6, DAS9, DAS12, and DAS30); the trait heritability at each measurement ranged between 16.0–78.3% and 25.4–69.2% for NDVI and CHL, respectively. The NDVI at DAS21 and CHL at DAS24 had the highest heritabilities and were thus examined in subsequent analyses.

The frequency distribution showed that the NDVI ranged from 0.05 to 0.18 with an average of 0.11 (**Table 1**). The entire population was separated into WA, LR, and RC subpopulations; the mean NDVI of the WA was relatively small (0.07) with values ranging from 0.05–0.13. The mean NDVI of LR and RC was 0.11 and 0.12, respectively, with values ranging from 0.06–0.18 and 0.06–0.17, respectively. The CHL frequency distribution of the entire population ranged from 1.20 to 4.78, with an average of 3.57. The CHL mean of WA was 3.08 and ranged from 1.20–4.49; the CHL mean of LR and RC was 3.68 and 3.72, respectively, and ranged from 2.73–4.78 and 2.67–4.50, respectively (**Table 1**).

Both NDVI and CHL, two physiological traits related to photosynthesis and growth, significantly differed between wild (0.07, 3.08) and cultivated (0.11–0.12, 3.68–3.72) soybeans, suggesting that cultivated soybeans have experienced significant improvements in photosynthesis- and growth-related traits following their domestication (**Table 1**). Thus, these basic shortcomings of wild soybean should not be neglected when wild soybeans are used to improve cultivated soybeans.

The analysis of variance revealed significant differences among accessions for both NDVI and CHL, indicating that there was significant genetic variation for the two spectral reflectance traits (**Supplementary Table 1**). The trait heritability was estimated to be 78.3% for NDVI and 69.2% for CHL (**Table 1**). These findings indicate that phenotypic variation (PV) was primarily driven by genetic factors, and the underlying QTLs or genes could be traced through further genetic analysis.

Identification of the QTL-allele System Determining NDVI and CHL in the CSGP

According to the RTM-GWAS procedure involving the use of 1,296 and 2,147 multi-allelic SNPLDB markers preselected at the first stage for the second stage multi-locus multi-allele association analysis, a total of 38 and 32 SNPLDBs, each with 2–4 and 2–6 alleles were determined to be significantly associated with NDVI and CHL, respectively (**Table 2**, **Supplementary Tables 2**, **4**).

The 38 NDVI-associated loci explained 48.39% of the phenotypic variation (PV), among which 17 large-contribution loci ($R^2 \geq 1\%$) explained 34.77% of the PV and 21 small-contribution loci ($R^2 < 1\%$) explained 13.62% of the PV (**Table 2**). The phenotypic contribution of each associated locus to PV ranged between 0.37–3.84%. These loci were distributed on 15 chromosomes with 1 to 5 loci on each chromosome; chromosome 1 had the most loci (**Figures 1A–C**). In NDVI, the total genetic variation (heritability) was 78.3%, and the genetic contribution of the detected 38 QTLs was 48.39%; consequently, 29.91% of the genetic variation was not detected, which can be attributed to a collection of unmapped QTLs that needs to be further explored under controlled conditions where experimental error is minimized.

The CHL-associated loci had a similar pattern to those of NDVI (**Table 2**). The PV explained by the CHL-associated loci was 51.35%, among which 19 large-contribution loci explained 42.95% of the PV and 13 small-contribution loci explained

TABLE 1 | Frequency distribution of NDVI and CHL in the Chinese soybean germplasm population.

Trait	Pop.	Midpoint and frequency											*N*	Mean	Range	h^2 (%)
NDVI		0.06	0.07	0.08	0.09	0.10	0.11	0.12	0.13	0.14	0.15	≥0.16				
	Entire	22	34	35	26	34	27	53	48	26	22	14	341	0.11	0.05–0.18	78.3
	WA	19	26	18	7	2	1	2	1	0	0	0	76	0.07[a]	0.05–0.13	
	LR	2	3	8	6	8	8	17	13	6	6	6	83	0.11[b]	0.06–0.18	
	RC	1	5	9	13	24	18	34	34	20	16	8	182	0.12[b]	0.06–0.17	
CHL		≤2.50	2.70	2.90	3.10	3.30	3.50	3.70	3.90	4.10	4.30	≥4.50				
	Entire	4	16	22	22	46	50	69	60	30	13	5	337	3.57	1.20–4.78	69.2
	WA	4	13	19	11	13	6	5	1	0	1	1	74	3.08[a]	1.20–4.49	
	LR	0	1	2	4	13	16	20	13	6	5	3	83	3.68[b]	2.73–4.78	
	RC	0	2	1	7	20	28	44	46	24	7	1	180	3.72[b]	2.67–4.50	

Pop.: Population. N: the number of accessions.
NDVI: normalized difference vegetation index, measured on the 21st day after sowing; CHL: chlorophyll index, measured on the 24th day after sowing. h^2, trait heritability. WA, wild accessions; LR, cultivated farmer landraces; RC, released modern cultivars.
[a,b]different letters indicate significant differences between subpopulations based on t-tests at a significance level of 0.01.

8.40% of the PV; the number of large-contribution loci was greater than the number of small-contribution loci. The PV of each associated locus ranged from 0.38 to 5.38%. These loci were distributed on 18 chromosomes with 1–6 loci on each chromosome; chromosome 5 had the most loci (**Figures 1D–F**). In CHL, the total genetic variation (trait heritability) was 69.2%, and the genetic contribution of the detected 32 QTLs was 51.35%; therefore, 27.85% of the genetic variation was not detected and will require further study to elucidate.

For other agronomic traits, such as 100-seed weight, days to flowering, and drought tolerance, the number of alleles per locus detected have been reported to range from 2–10 (He et al., 2017), 2–10 (Fu et al., 2020), and 2–12 (Wang et al., 2020), respectively. By comparison, the alleles per locus of NDVI and CHL in the present study were only 2–4 and 2–6, respectively, and the per-marker number of alleles was 2–11. The differences observed in these two spectral reflectance physiological traits potentially indicate that genetic differentiation at single loci is less likely for these two traits compared with other agronomic traits.

QTL-allele Matrices of NDVI and CHL and Their Evolution From WA to LR and RC

The RTM-GWAS method provides a powerfull approach for the detection of genome-wide QTLs and their multiple allele effects. In this study, the effects of the 2–4 alleles per locus for a total of 89 alleles on 38 loci were obtained for NDVI. These QTL-alleles of the 341 accessions can be organized into a 38 × 341 (locus × accession) matrix (**Figure 1G**), which represents a compact form of the genetic structure of the population and was designated as the QTL-allele matrix of NDVI. Similarly, the effects of the 2–6 alleles per locus for a total of 82 alleles on 32 loci and the 32 × 341 (locus × accession) matrix were obtained for CHL (**Figure 1I**). The QTL-allele matrix detected from the RTM-GWAS contained all of the genetic constitutions of a trait in a population and can thus be used for the study of population genetic differentiation. The cultivated soybean is generally thought to have been domesticated from annual wild soybean, with released cultivars developed from farmer landraces (Liu et al., 2020). The QTL-allele matrix can be separated into its component matrices to facilitate the tracing of evolutionary genetic changes from WA to LR and RC. For NDVI, there were 85 alleles on 38 loci in WA; 82 wild alleles on 38 loci were passed to LR, with the emergence of 2 new alleles on 2 loci and the exclusion of 3 alleles on 3 loci for a total of 84 alleles on 38 loci (**Table 3**). From LR, 82 alleles on 38 loci were passed to RC, with the emergence of 2 new alleles on 2 loci, the recovery of 2 wild alleles on 2 loci, and the exclusion of 2 alleles on 2 loci for a total of 86 alleles on 38 loci. In LR + RC, 84 alleles on 38 loci were inherited from WA, including the emergence of 4 new alleles on 4 loci and the exclusion of 1 allele on 1 locus for a total of 88 alleles on 38 loci. Among the 4 newly emerged alleles on 4 loci in the cultivated LR + RC, 2 new loci with 2 new alleles emerged in LR + RC. In LR vs. WA, 1 of the 2 newly emerged alleles was in the newly formed QTL *qNdvi-01-5* in LR, which was not polymorphic in WA; in RC vs. LR, 1 of the 2 emerged alleles was in the newly formed QTL *qNdvi-03-1* in RC and was not polymorphic in WA and LR (**Figures 2**, **3**; **Table 3**).

Similar results were obtained for CHL. There were 76 alleles on 32 loci in WA; 76 wild alleles on 32 loci were passed to LR, with the emergence of 4 new alleles on 4 loci for a total of 80 alleles on 32 loci; no alleles were excluded (**Table 3**). From LR, 80 alleles on 32 loci were passed to RC, with the emergence of 2 new alleles on 2 loci and the exclusion of 1 allele on 1 locus for a total of 81 alleles on 32 loci; no wild alleles were recovered. In LR + RC, 76 alleles on 32 loci were inherited from WA, with the emergence of 6 new alleles on 5 loci for a total of 82 alleles on 32 loci; no wild alleles were excluded.

All of the emerged and excluded alleles and their associated QTLs are listed in **Table 4**. For NDVI, there were 4 newly emerged alleles on 4 loci (*qNdvi-01-5*, *qNdvi-02-1*, *qNdvi-03-1*, and *qNdvi-15-2*); *qNdvi-01-5* and *qNdvi-03-1* were also newly formed in LR and RC, respectively. One allele in *qNdvi-05-4* was excluded in LR, and 1 allele in *qNdvi-05-3* was excluded in RC. For CHL, there were 6 newly emerged alleles on 5 loci (*qChl-06-2, qChl-08-3, qChl-18-2, qChl-19-1*, *and qChl-20-1*), and 1 allele on *qChl-01-1* was excluded in RC. The allele frequencies of the newly emerged

TABLE 2 | The detected QTLs associated with NDVI and CHL in the CSGP.

QTL	No. alleles	−lg*P*	R^2 (%)	QTL	No. alleles	−lg*P*	R^2 (%)
qNdvi-01-1	2	3.80	1.28	*qChl-01-1*	3	7.32	2.97
qNdvi-01-2	2	1.82	0.53	*qChl-02-1*	2	8.17	2.96
qNdvi-01-3	3	4.06	1.69	*qChl-03-1*	2	3.66	1.18
qNdvi-01-4	2	8.42	3.18	*qChl-05-1*	2	2.98	0.93
qNdvi-01-5	2	1.72	0.49	*qChl-05-2*	2	1.96	0.56
qNdvi-02-1	4	8.33	3.84	*qChl-06-1*	2	2.37	0.70
qNdvi-03-1	2	2.85	0.92	*qChl-06-2*	3	6.74	2.73
qNdvi-05-1	2	1.96	0.58	*qChl-07-1*	3	3.01	1.20
qNdvi-05-2	2	1.46	0.40	*qChl-07-2*	3	6.35	2.57
qNdvi-05-3	4	7.73	3.57	*qChl-08-1*	2	1.84	0.51
qNdvi-05-4	4	3.80	1.82	*qChl-08-2*	3	12.97	5.38
qNdvi-05-5	2	1.74	0.50	*qChl-08-3*	3	3.74	1.50
qNdvi-05-6	2	1.55	0.43	*qChl-08-4*	2	1.46	0.38
qNdvi-06-1	2	6.24	2.27	*qChl-09-1*	2	2.41	0.72
qNdvi-06-2	2	2.44	0.76	*qChl-10-1*	3	12.42	5.14
qNdvi-06-3	2	2.58	0.81	*qChl-11-1*	3	5.90	2.38
qNdvi-08-1	2	2.73	0.87	*qChl-13-1*	2	2.59	0.78
qNdvi-08-2	2	3.96	1.35	*qChl-13-2*	2	3.93	1.29
qNdvi-08-3	2	3.36	1.11	*qChl-14-1*	2	1.91	0.54
qNdvi-10-1	3	1.78	0.74	*qChl-14-2*	2	2.77	0.85
qNdvi-10-2	2	5.58	2.00	*qChl-15-1*	2	1.68	0.46
qNdvi-11-1	2	2.58	0.81	*qChl-15-2*	2	2.50	0.75
qNdvi-11-2	2	5.16	1.83	*qChl-15-3*	2	1.98	0.56
qNdvi-11-3	3	2.18	0.90	*qChl-16-1*	2	4.24	1.40
qNdvi-13-1	3	2.57	1.06	*qChl-16-2*	2	3.66	1.18
qNdvi-13-2	2	1.98	0.59	*qChl-16-3*	2	3.78	1.23
qNdvi-13-3	2	1.37	0.37	*qChl-17-1*	2	2.24	0.66
qNdvi-14-1	2	1.63	0.46	*qChl-17-2*	2	5.88	2.04
qNdvi-14-2	3	7.06	2.97	*qChl-18-1*	4	2.65	1.26
qNdvi-15-1	3	1.89	0.78	*qChl-18-2*	4	3.58	1.66
qNdvi-15-2	3	6.27	2.63	*qChl-19-1*	6	4.25	2.36
qNdvi-15-3	2	3.88	1.32	*qChl-20-1*	4	5.59	2.52
qNdvi-15-4	2	2.06	0.62	**Total**	**82**	**32**	**51.35**
qNdvi-16-1	2	1.93	0.57				
qNdvi-17-1	2	2.63	0.83				
qNdvi-18-1	2	4.76	1.67				
qNdvi-19-1	2	3.53	1.18				
qNdvi-19-2	2	2.17	0.66				
Total	**89**	**38**	**48.36**				

NDVI, normalized difference vegetation index, measured on the 21st day counting from sowing; CHL, chlorophyll index, measured on the 24th day counting from sowing; CSGP, Chinese soybean germplasm population. h^2, trait heritability. R^2, genetic contribution of a QTL; A QTL is designated as qNdvi-01-1, where -01 represents chromosome 1, and -1 represents its order on the chromosome; No. alleles: number of alleles in a SNPLDB; -lgP, P-value in the log10 scale of the association test in the RTM-GWAS. The corresponding SNPLDB of a QTL and its position are shown in ***Supplementary Table 2****.*

alleles in LR + RC ranged between 3.40–13.58%, and the new alleles were not dominant over older alleles.

Thus, genetic changes were limited during the evolution from WA to LR and RC, as the three subpopulations shared a large number of common alleles. Among the 89 wild alleles of 38 NDVI-associated loci, 80 alleles were shared among the three subpopulations and among the 76 wild alleles of 32 CHL-associated loci, and 75 wild alleles were shared among the three subpopulations (**Figure 3**). Here, the total change (emerged plus excluded) in alleles (5 alleles (5.7%) on 5 loci (13.2%) for NDVI and 6 alleles (7.3%) on 5 loci (15.6%) for CHL) was much lower relative to the changes in alleles observed for other agronomic traits. For example, there were a total of 261 alleles on 75 loci in Chinese cultivated soybeans for drought tolerance, and 46 alleles (17.6%) on 27 loci (36.0%) were changed in RC relative to LR (Wang et al., 2020). In addition, there were a total of 342 alleles on 81 loci in Northeast China soybeans for earliness, and 143 alleles (41.8%) on 67 loci (82.7%) were changed in the early group relative to the late group (Fu et al., 2020).

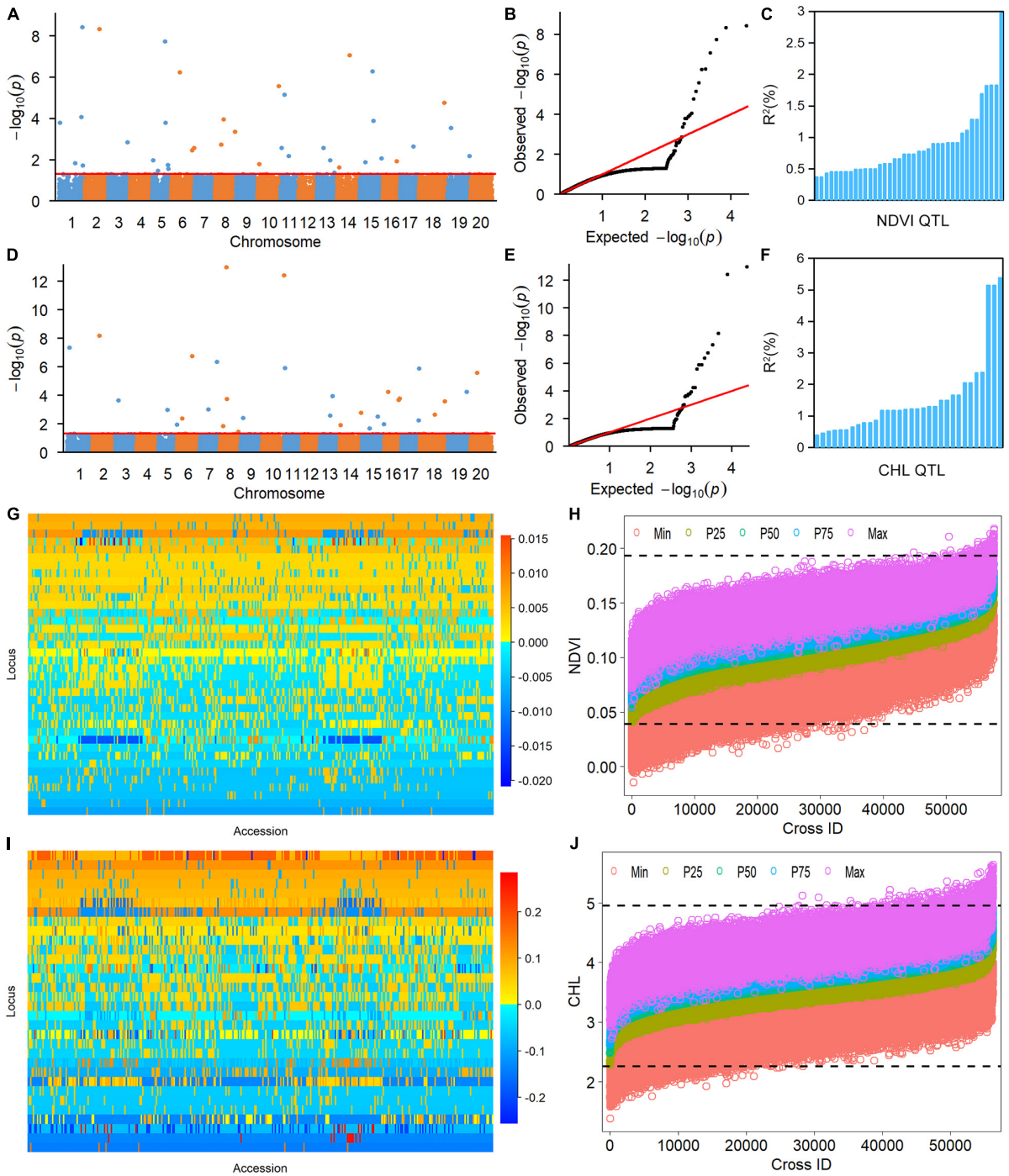

FIGURE 1 | Genetic analysis of NDVI and CHL phenotypic variation in the soybean population using the restricted two-stage multi-locus genome-wide association study (RTM-GWAS) method. **(A)** Manhattan plot of the RTM-GWAS results for NDVI. **(B)** QQ plot of the RTM-GWAS results for NDVI. **(C)** The phenotypic contribution of the detected 38 NDVI QTLs. The vertical and horizontal axes indicate the genetic contribution R^2 (%) and the order of QTLs according to their genetic contribution. **(D)** Manhattan plot of RTM-GWAS results for CHL. **(E)** QQ plot of the RTM-GWAS results for CHL. **(F)** The phenotypic contribution of the detected 32 CHL SNPLDBs. The vertical and horizontal axes indicate the genetic contribution R^2 (%) and the order of QTLs according to their genetic contribution. **(G)** The NDVI QTL–allele matrix. **(H)** The predicted NDVI of progenies in the optimal crosses among the 341 lines based on the linkage model. On the horizontal axis, the crosses are arranged in increasing order of the predicted 50th percentile (P50) NDVI from left to right. The black dotted horizontal lines are the minimum and maximum values in the entire population, which were 0.039 and 0.193, respectively. The vertical axis is the predicted NDVI value of the crosses. **(I)** The CHL QTL–allele matrix. **(J)** The predicted CHL of the progenies in the optimal crosses among the 341 lines based on the linkage model. On the horizontal axis, the crosses are arranged in increasing order of the predicted 50th percentile (P50) NDVI from the left to right. The black dotted horizontal lines are the minimum and maximum values in the entire population, which were 2.26 and 4.95, respectively. The vertical axis is the predicted CHL value of the crosses.

TABLE 3 | The QTL-alleles changes from WA to LR and RC.

	WA		LR vs. WA		RC vs. LR		LR + RC vs. WA	
	Locus	Allele	Locus	Allele	Locus	Allele	Locus	Allele
NDVI								
Total	38	85	38	84	38	86	38	88
Inherited			38	82	38	82	38	84
Emerged			2	2	2	2	4	4
Recovery			–	–	2	2	–	–
Excluded			3	3	2	2	1	1
Changed			4	5	5	6	5	5
CHL								
Total	32	76	32	80	32	81	32	82
Inherited			32	76	32	80	32	76
Emerged			4	4	2	2	5	6
Recovery			–	–	–	–	–	–
Excluded			–	–	1	1	–	–
Changed			4	4	3	3	5	6

WA, wild accession; LR, cultivated farmer landraces; RC, released modern cultivars. LR vs. WA means the number of changed alleles or changed loci of LR compared with WA. Inherited: the inherited allele/locus between populations. Emerged: the emerged allele/locus between populations. Excluded: the excluded allele/locus between populations. Changed: the changed allele/locus between populations (the emerged plus excluded alleles). Recovery: the alleles that were excluded from WA to LR but were recovered in RC. In LR vs. WA of NDVI, 1 of the 2 emerged alleles was in the newly formed QTL qNdvi-01-5 in LR, which was not polymorphic in WA, while in RC vs. LR of NDVI, 1 of the 2 emerged alleles was in the newly formed. QTL qNdvi-03-1 in RC, which was not polymorphic in WA and LR.

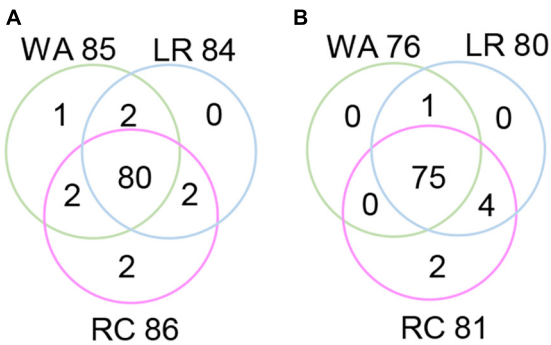

FIGURE 2 | Venn diagram of QTL-allele changes among populations. **(A)** Venn diagram of the NDVI allele distribution in populations. **(B)** Venn diagram of the CHL allele distribution in populations. WA, wild accessions; LR, cultivated farmer landraces; RC, released modern cultivars.

In summary, these two spectral reflectance physiological traits (NDVI and CHL) were genetically conservative. Inheritance played a major role in determining the genetic motivation, For NDVI, 4 alleles on 4 loci emerged; for CHL, 6 alleles on 5 loci emerged. Two new loci emerged for NDVI, but none emerged for CHL. For NDVI, only 1 allele on 1 locus was excluded, whereas no alleles were excluded for CHL. The transition from WA to LR and from LR to RC took approximately 5,000 and 100 years, respectively; despite this long history, large genetic changes have not occurred, especially during the transition from WA to LR. This genetic stability indicates that the two physiological traits NDVI and CHL are highly conservative compared with other agronomic traits. However, the same number of genetic changes occurred during the transition from WA to LR (5,000 years) and the transition from LR to RC (100 years), indicating that the enhanced artificial breeding in the transition from LR to RC accelerated the rate of genetic change.

Prediction of the Recombination Potential of NDVI and CHL in the CSGP

To assess the recombination potential for NDVI and CHL in the CSGP, a total of 57,970 possible single crosses among the 341 accessions were simulated based on the QTL-allele matrix; possible crosses between the accessions for each subpopulation were also simulated. The 99th percentile of 2,000 progenies of each cross was used to represent the recombination potential (**Table 5**). For NDVI, the recombination potential within the WA, LR, and RC was not large (0.15 vs. 0.13 of the extreme phenotype, 0.20 vs. 0.18 of the extreme phenotype, and 0.20 vs. 0.17 of the extreme phenotype, respectively), but the predicted value was larger in LR and RC (the superior subpopulations) than in WA. Among the three between-subpopulation crosses, the highest recombination potential was observed for LR × RC (0.21 vs. 0.19 in WA × LR and WA × RC); for the crosses at the entire population level, the NDVI was 0.21, which was the same as that observed for LR × RC (**Table 5**, **Figure 1H**).

For CHL, the recombination potentials within WA, LR, and RC were also not large (4.93 vs. 4.49 of the extreme phenotype, 5.31 vs. 4.78 of the extreme phenotype, and 5.06 vs. 4.50 of the extreme phenotype, respectively), but the predicted value was larger in LR and RC (the superior populations) than in WA. Among the three between-subpopulation crosses, the highest recombination potential was observed for WA × LR (5.41 vs. 5.38 and 5.21 in WA × RC and LR × RC, respectively); for the crosses at the entire population level, the CHL was 5.41, which was the same as that observed for WA × LR (**Table 5**, **Figure 1J**). Thus,

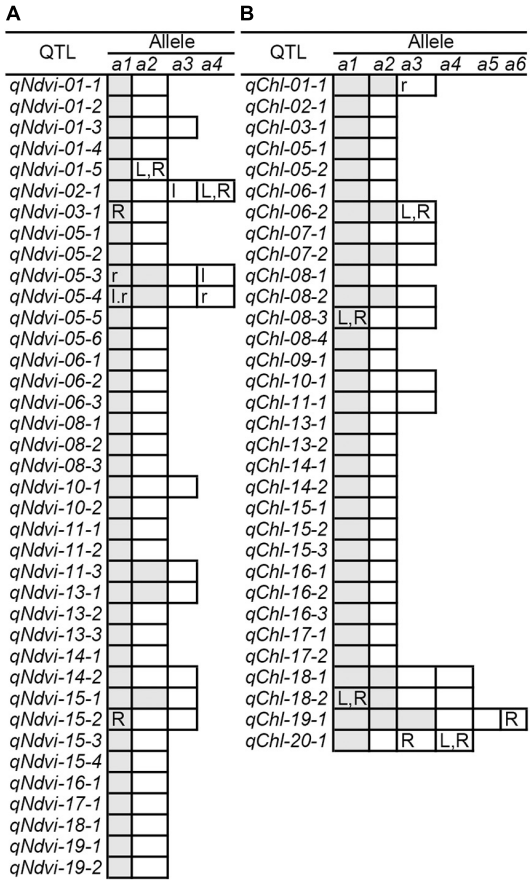

FIGURE 3 | QTL-allele changes among populations. **(A)** NDVI QTL-allele changes among populations. **(B)** CHL QTL-allele changes among populations. *a1 –a6* are the alleles of each QTL, arranged in descending order according to their allele effect values. The cells marked with white (positive effect) and gray (negative effect) are all alleles in WA. The cells with lowercase letters l and r are alleles excluded in LR and RC (vs. WA), respectively. The uppercase letters L and R in cells are alleles that emerged in LR and RC (vs. WA), respectively. In addition, the QTL *qNdvi-01-5* emerged in LR and was not polymorphic in WA. The QTL *qNdvi-03-1* emerged in RC and was not polymorphic in WA and LR.

crosses with the WA had a greater recombination potential for CHL, which was opposite to the pattern observed for NDVI.

Annotation of Candidate Genes and GO Analysis of NDVI and CHL in the CSGP

From the detected QTLs, a total of 39 candidate genes were annotated on 20 NDVI-associated loci, and 32 candidate genes on 22 CHL-associated loci (**Supplementary Table 3**). Only 9 candidate genes were annotated on 7 large-contribution loci of NDVI, but most (21 out of 32) of the CHL-related candidate genes were annotated on 13 large-contribution loci of CHL. Gene ontology (GO) analysis revealed that these candidate genes for both NDVI and CHL can be classified into three categories: biological process, molecular function, and cellular component (**Table 6**, **Supplementary Figure 1**). In biological process, NDVI involved 14 of 15 function groups, and CHL involved 11 of 15 function groups with five group differences. In molecular function, NDVI and CHL both involved 4 of 5 groups with two group differences. In cellular component, both NDVI and CHL involved all of the 5 function groups (**Table 5**, **Supplementary Figure 1**). The candidate gene systems of NDVI and CHL both involved a similar set of genes, although their frequency distributions differed. The two genetic systems consisted of a series of genes involved in a complex gene network.

The validation of these candidate genes are left for further studies, however, a preliminary verification was carried out using the transcriptome data set of RNA Seq-Atlas project in SoyBase (see footnote 1). The gene expression results (**Supplementary Figure 2**) showed that 31 out of the 39 annotated genes for NDVI were expressed in 14 soybean tissues, among which *Glyma05g23230* and *Glyma14g06630* showed especially high expression level. For CHL, there were 28 out of 32 annotated genes were expressed in 14 soybean tissues, and *Glyma08g10960* showed high expression level in young leaf and pod shell, indicating these identified candidate genes are possibly functional.

DISCUSSION

Efficiency of High-Throughput Phenotyping Integrated With RTM-GWAS in Identifying NDVI and CHL QTL-allele Systems

This study presented a genetic analysis of two spectral reflectance traits, NDVI and CHL, using a high-throughput phenotyping platform. Both NDVI and CHL showed significant genetic variation in CSGP, indicating that the spectral reflectance phenotyping data can not only be used for predicting agronomic traits but also for dissecting their underlying genetic basis. In this study, 89 alleles on 38 loci for NDVI and 82 alleles on 32 loci for CHL were detected, and the RTM-GWAS method was used to characterize their allele effects. High-throughput phenotyping integrated with RTM-GWAS was an efficient method for identifying the QTL-allele systems for NDVI and CHL. However, only 48.36% and 51.35% of the PV for NDVI and CHL were explained by the detected loci, which is low compared with other agronomic traits, such as 100-seed weight (139 QTLs explained 98.2% of the PV with a heritability of 98.9%, He et al., 2017). Although the large-contribution QTLs have been identified, many small-contribution QTLs consisting of unmapped minor QTLs have yet to be identified according to the RTM-GWAS. This observation might stem from experimental error given that the heritability values were only 78.3% and 69.2% for NDVI and CHL, respectively. Such error might have decreased the sensitivity of our analysis to detect QTLs, leaving 29.91% and 27.85% of the genetic variation (presumably unmapped minor QTLs) undetected. In the present study, an incomplete block design was conducted to separate all accessions into two sets for two respective tests to circumvent the space limitations associated with the high-throughput phenotyping platform. Although we

TABLE 4 | Emerged and excluded alleles conferring NDVI and CHL from WA to LR and then to RC.

QTL	R^2 (%)	Allele	Effect	Frequency (%)				
				Entire	WA	LR	RC	LR + RC
qNdvi-01-5	0.49	*a1*	−0.0049	96.48	100.00	98.78	93.99	95.47
		a2	0.0049	3.52	0.00	1.22	6.01	4.53
qNdvi-02-1	3.84	*a1*	−0.0138	24.34	90.79	14.63	1.09	5.28
		a2	0.0000	54.84	7.89	76.83	64.48	68.30
		a3	0.0051	5.28	1.32	0.00	9.29	6.42
		a4	0.0087	15.54	0.00	8.54	25.14	20.00
qNdvi-03-1	0.92	*a1*	−0.0068	4.11	0.00	0.00	7.65	5.28
		a2	0.0068	95.89	100.00	100.00	92.35	94.72
qNdvi-05-3	3.57	*a1*	−0.0208	2.05	5.26	3.66	0.00	1.13
		a2	−0.0002	28.74	44.74	29.27	21.86	24.15
		a3	0.0056	63.64	26.32	67.07	77.60	74.34
		a4	0.0154	5.57	23.68	0.00	0.55	0.38
qNdvi-05-4	1.82	*a1*	−0.0081	2.64	11.84	0.00	0.00	0.00
		a2	−0.0016	15.54	19.74	26.83	8.74	14.34
		a3	0.0003	76.83	47.37	71.95	91.26	85.28
		a4	0.0093	4.99	21.05	1.22	0.00	0.38
qNdvi-15-2	2.63	*a1*	−0.0063	7.33	0.00	0.00	13.66	9.43
		a2	0.0029	78.30	90.79	75.61	74.32	74.72
		a3	0.0034	14.37	9.21	24.39	12.02	15.85
qChl-01-1	2.97	*a1*	−0.2100	22.29	9.21	21.95	27.87	26.04
		a2	−0.0740	73.31	75.00	74.39	72.13	72.83
		a3	0.2840	4.40	15.79	3.66	0.00	1.13
qChl-06-2	2.73	*a1*	−0.0927	15.25	57.89	87.80	74.86	78.87
		a2	−0.0070	74.19	42.11	8.54	7.10	7.55
		a3	0.0997	10.56	0.00	3.66	18.03	13.58
qChl-08-3	1.5	*a1*	−0.2560	2.64	0.00	3.66	3.28	3.40
		a2	0.0771	39.59	98.68	45.12	12.57	22.64
		a3	0.1789	57.77	1.32	51.22	84.15	73.96
qChl-18-2	1.66	*a1*	−0.1740	6.45	0.00	6.10	9.29	8.30
		a2	−0.0214	58.36	39.47	54.88	67.76	63.77
		a3	0.0585	22.58	35.53	30.49	13.66	18.87
		a4	0.1369	12.61	25.00	8.54	9.29	9.06
qChl-19-1	2.36	*a1*	−0.1815	7.62	25.00	4.88	1.64	2.64
		a2	−0.0625	10.56	36.84	1.22	3.83	3.02
		a3	−0.0619	29.62	1.32	31.71	40.44	37.74
		a4	0.0009	41.64	13.16	58.54	45.90	49.81
		a5	0.0899	7.33	23.68	3.66	2.19	2.64
		a6	0.2152	3.23	0.00	0.00	6.01	4.15
qChl-20-1	2.52	*a1*	−0.1325	72.73	92.11	81.71	60.66	67.17
		a2	0.0005	14.37	7.89	13.41	17.49	16.23
		a3	0.0358	2.93	0.00	0.00	5.46	3.77
		a4	0.0963	9.97	0.00	4.88	16.39	12.83

WA, wild accession; LR, cultivated farmer landraces; RC, released modern cultivars. Boldface QTLs are newly emerged QTLs. Heavy shaded alleles are emerged ones, while light-shaded alleles are excluded ones; the number of changed alleles is consistent with that shown in ***Figure 2****.*

employed a method to make the environment uniform between the different tests, much room for improvement remains.

In the present study, the PV explained by individual QTL ranged between 0.37-3.84% for NDVI, and 0.38-5.38% for CHL. There were 17 and 19 large-contribution (R2 $\geq$ 1%) and 21 and 13 small-contribution (R2 $<$ 1%) QTLs for NDVI and CHL, respectively. The PV in RTM-GWAS is relatively lower than that in single-locus model such as the mixed linear model method (Yu et al., 2006). In single-locus model, association test is performed for each locus individually, and the estimated contribution of a locus may be inflated obviously due to the correlations among neighboring loci (He et al., 2017). But in RTM-GWAS, multiple QTLs are jointly fitted in a multi-locus model and the estimated PV for each QTL is unbiased and the total PV is controlled within

TABLE 5 | The predicted optimal crosses for NDVI and CHL in the different material groups.

Trait	Population	Extreme phenotype phenotype	No. crosses	Predicted phenotype	
				Mean	Max
NDVI	WA	0.05–0.13	2,851	0.10	0.15
	LR	0.06–0.18	3,322	0.14	0.20
	RC	0.06–0.17	16,427	0.14	0.20
	WA × LR	–	6,234	0.13	0.19
	WA × RC	–	13,834	0.14	0.19
	LR × RC	–	14,926	0.14	0.21
	Entire	0.05–0.18	57,594	0.14	0.21
CHL	WA	1.20–4.49	2,702	3.66	4.93
	LR	2.63–4.78	3,322	4.18	5.31
	RC	2.67–4.50	16,111	4.20	5.06
	WA × LR	–	6,070	3.97	5.41
	WA × RC	–	13,322	4.01	5.38
	LR × RC	–	14,762	4.21	5.21
	Entire	1.20–4.78	56,289	4.11	5.41

WA, wild accession; LR, cultivated farmer landraces; RC, released modern cultivars. The extreme phenotype is the observed minimum and maximum phenotype in the population. The predicted phenotype is the 99th percentile of a cross in the group of crosses.

TABLE 6 | The number of candidate genes enriched in different GO annotations for NDVI and CHL.

GO category	GO group	NDVI	CHL
Biological process	Biological regulation	11	10
	Cellular component biogenesis	13	3
	Cellular process	20	18
	Developmental process	12	4
	Localization	4	3
	Metabolic process	18	19
	Multicellular organismal process	11	4
	Multi-organism process	7	–
	Response to stimulus	–	10
	Regulation of biological process	11	–
	Reproduction	9	–
	Response to stimulus	14	–
	Others	5	4
Molecular function	Binding	20	15
	Catalytic activity	12	9
	Structural molecule activity	3	–
	Transcription regulator activity	–	3
	Others	2	2
Cellular component	Cell	34	6
	Membrane	8	21
	Organelle	27	7
	Protein-containing complex	5	3
	Others	5	3
Total candidate genes		39	32

heritability value, therefore, the individual QTL in RTM-GWAS may look smaller than those from single locus model procedure.

The fact of many QTLs each with a smaller PV is a characteristic of a quantitative trait controlled by a large number of QTLs. Or as we understand, the total PV of a quantitative trait in fact is a projection of a large number of genes/QTLs with different but interrelated biological functions onto the trait plane in a specific population. The statistically estimated genetic effect or PV of a QTL is relative to and largely depends on the genetic background of the population. A same QTL may exhibit varying effects in different populations with different genetic background. For example, the PV of a QTL in a simple genetic background such as near-isogenic lines is much greater than that in a germplasm population. Therefore, the small-contribution QTL in a study may exhibit large effects in other populations with simple genetic background. In fact, the purpose of the RTM-GWAS method is to achieve a relatively thorough detection of whole-genome QTLs and their multiple alleles or the QTL-allele system rather than a few individual large PV QTLs. Thus for the genetic improvement of quantitative traits in plant breeding, background control and foreground control are both important. It is likely that breakthroughs can be achieved through increase of positive alleles and decrease of negative alleles among multiple loci, rather than through recombination between/among a few loci like in the qualitative trait situation.

Genetic Conservativeness of NDVI and CHL, Their Improvement Potential and Implications to Breeding for Seed-Yield of Soybeans

Both phenotypic and genotypic analysis showed that the two spectral reflectance traits were genetically conservative in comparison to the agronomic traits, such as seed yield, 100 seed weight, days to flowering (He et al., 2017; Zhang et al., 2019; Fu et al., 2020). Because in the present results, (i) no significant phenotypic improvements were observed in RC, and trait values were low in LR and RC; (ii) there was a limited number of alleles per locus; (iii) there was a large number of shared wild alleles among WA, LR, and RC, few new alleles, and little exclusion

of wild alleles; and (iv) the recombination potential was low. In other words, the two spectral reflectance traits, NDVI and CHL, were more conservative than other agronomic traits in their genetic changes. We suspect that these spectral reflectance traits are upstream traits, whereas the other agronomic traits are downstream traits, the upstream traits may be more conservative than the downstream traits due to more factors may influence the downstream traits. For example, NDVI and CHL are traits related to the biological process of photosynthesis or organic synthesis while the agronomic traits such as seed yield may relate to the biological processes of transportation and storage of organics in addition to organic synthesis. The fact that breeding generally acts on downstream traits more readily compared to upstream traits may explain why the latter was more conservative and with less phenotypic improvements. Thus, additional effort is needed to improve upstream traits, such as NDVI and CHL, which are involved in light interception, light function and therefore, in photosynthesis and organics production.

However, some potential for improvement in NDVI and CHL was observed from WA to LR + RC, although the improvement was small (**Table 1**). The genetic mechanism underlying the observed evolutionary improvements might be recombination among loci-alleles given that all of the wild alleles passed to LR + RC except one negative wild allele excluded; furthermore, new alleles did not make up a large proportion of the alleles, given that few new alleles emerged (**Tables 3**, **4**). This point is supported by the optimal cross prediction that the recombination among the loci/accessions might result in transgressive progenies, i.e., approximately 13–16% of genetic progress for NDVI and CHL might be achieved through hybridization in the CSGP (**Table 5**).

The previous studies on high-throughput phenotypes in crops usually focused on predicting yield-related agronomic traits, such as plant height, biomass and seed yield (Holman et al., 2016; Salas Fernandez et al., 2017, Maimaitijiang et al., 2020). For example, our previous results showed that NDVI was selected as the best vegetation indices in the establishment of plot-yield prediction models in breeding programs of soybeans (Zhang et al., 2019). Here in the present study, genetic dissection of the two high-throughput physiological traits, NDVI and CHL, was performed based on the high-throughput phenotyping technique. As NDVI and CHL are upstream traits and agronomic traits are breeding-acted target traits, identifying the genetic system of upstream traits may help to understand the genetic mechanism of downstream targets and also may provide additional control of downstream targets. For example, it was reported that NDVI was also a proxy for drought-adaptive traits in durum wheat, and high-throughput data collection of NDVI with capable precision can facilitate the genetic dissection of drought-adaptive traits (Condorelli et al., 2018). Thus, in breeding programs, breeders can combine the selection for upstream traits using high-throughput phenotyping data and the selection for downstream traits using agronomic data to have both selected and improved, which might benefit the enhanced selection of the downstream traits. This explains the reason that we suggested in yield breeding programs to combine the selection before harvest using NDVI prediction models established from hyperspectral reflectance data and the selection of harvested yield to achieve an enhanced selection for genotypic yield (Zhang et al., 2019).

DATA AVAILABILITY STATEMENT

The datasets presented in this study can be found in online repositories. The names of the repository/repositories and accession number(s) can be found below: https://github.com/njau-sri/leiwang2020ndvichl.

AUTHOR CONTRIBUTIONS

JG designed the study. LW and FL performed the experiments. JH, LW, and FL performed data analysis. XH, WW, GX, JL, and GZ participated in the experiments and data collection. JH, LW, and JG drafted the manuscript. All authors reviewed and approved the manuscript.

FUNDING

This research was supported by the China National Key R&D Program for Crop Breeding (2017YFD0101500), the Natural Science Foundation of China (31701447), the MOE 111 Project (B08025), the MOE Program for Changjiang Scholars and Innovative Research Team in University (PCSIRT_17R55), the Fundamental Research Funds for the Central Universities (KYZZ201901), and the MARA CARS-04 program and the Jiangsu JCIC-MCP. This research was also supported by the Bioinformatics Center of Nanjing Agricultural University.

SUPPLEMENTARY MATERIAL

The Supplementary Material for this article can be found online at: https://www.frontiersin.org/articles/10.3389/fgene.2021.600444/full#supplementary-material

REFERENCES

Awlia, M., Nigro, A., Fajkus, J., Schmoeckel, S. M., Negrão, S., Santelia, D., et al. (2016). High-throughput non-destructive phenotyping of traits that contribute to salinity tolerance in *Arabidopsis thaliana*. *Front. Plant Sci.* 7:1414. doi: 10.3389/fpls.2016.01414

Cobb, J. N., Declerck, G., Greenberg, A., Clark, R., and McCouch, S. (2013). Next-generation phenotyping: requirements and strategies for enhancing our understanding of genotype-phenotype relationships and its relevance to crop improvement. *Theor. Appl. Genet.* 126, 867–887. doi: 10.1007/s00122-013-2066-0

Condorelli, G. E., Maccaferri, M., Newcomb, M., Andrade-Sanchez, P., White, J. W., French, A. N., et al. (2018). Comparative aerial and ground based high throughput phenotyping for the genetic dissection of NDVI as a proxy for drought adaptive traits in durum wheat. *Front. Plant Sci.* 9:893. doi: 10.3389/fpls.2018.00893

Duan, T., Chapman, S. C., Guo, Y., and Zheng, B. (2017). Dynamic monitoring of NDVI in wheat agronomy and breeding trials using an unmanned aerial vehicle. *Field Crops Res*. 210, 71–80. doi: 10.1016/j.fcr.2017.05.025

Erdle, K., Mistele, B., and Schmidhalter, U. (2011). Comparison of active and passive spectral sensors in discriminating biomass parameters and nitrogen status in wheat cultivars. *Field Crops Res*. 124, 74–84. doi: 10.1016/j.fcr.2011.06.007

Estrada, F., Escobar, A., Romero-Bravo, S., González-Talice, J., Poblete-Echeverría, C., Caligari, P. D. S., et al. (2015). Fluorescence phenotyping in blueberry breeding for genotype selection under drought conditions, with or without heat stress. *Sci. Hortic*. 181, 147–161. doi: 10.1016/j.scienta.2014.11.004

Foster, A. J., Kakani, V. G., and Mosali, J. (2017). Estimation of bioenergy crop yield and N status by hyperspectral canopy reflectance and partial least square regression. *Precis. Agric*. 18, 192–209. doi: 10.1007/s11119-016-9455-8

Fu, M., Wang, Y., Ren, H., Du, W., Wang, D., Bao, R., et al. (2020). Genetic dynamics of earlier maturity group emergence in south-to-north extension of Northeast China soybeans. *Theor. Appl. Genet*. 133, 1839–1857.

Furbank, R. T., and Tester, M. (2011). Phenomics—technologies to relieve the phenotyping bottleneck. *Trends Plant Sci*. 16, 635–644. doi: 10.1016/j.tplants.2011.09.005

Gitelson, A. A., Gritz, Y., and Merzlyak, M. N. (2003). Relationships between leaf chlorophyll content and spectral reflectance and algorithms for non-destructive chlorophyll assessment in higher plant leaves. *J. Plant Physiol*. 160, 271–282. doi: 10.1078/0176-1617-00887

Hassan, M. A., Yang, M., Rasheed, A., Yang, G., Reynolds, M., Xia, X., et al. (2019). A rapid monitoring of NDVI across the wheat growth cycle for grain yield prediction using a multi-spectral UAV platform. *Plant Sci*. 282, 95–103. doi: 10.1016/j.plantsci.2018.10.022

Hatfield, J., and Prueger, J. (2010). Value of using different vegetative indices to quantify agricultural crop characteristics at different growth stages under varying management practices. *Remote Sens*. 2, 562–578. doi: 10.3390/rs2020562

He, J., Meng, S., Zhao, T., Xing, G., Yang, S., Li, Y., et al. (2017). An innovative procedure of genome-wide association analysis fits studies on germplasm population and plant breeding. *Theor. Appl. Genet*. 130, 2327–2343. doi: 10.1007/s00122-017-2962-9

Holman, F., Riche, A., Michalski, A., Castle, M., Wooster, M., and Hawkesford, M. (2016). High throughput field phenotyping of wheat plant height and growth rate in field plot trials using UAV based remote sensing. *Remote Sens*. 8:1031. doi: 10.3390/rs8121031

Huete, A., Didan, K., Miura, T., Rodriguez, E., Gao, X., and Ferreira, L. (2002). Overview of the radiometric and biophysical performance of the MODIS vegetation indices. *Remote Sens. Environ*. 83, 195–213. doi: 10.1016/s0034-4257(02)00096-2

Jay, S., Maupas, F., Bendoula, R., and Gorretta, N. (2017). Retrieving LAI, chlorophyll and nitrogen contents in sugar beet crops from multi-angular optical remote sensing: comparison of vegetation indices and PROSAIL inversion for field phenotyping. *Field Crops Res*. 210, 33–46. doi: 10.1016/j.fcr.2017.05.005

Kumar, S., Röder, M. S., Singh, R. P., Kumar, S., Chand, R., Joshi, A. K., et al. (2016). Mapping of spot blotch disease resistance using NDVI as a substitute to visual observation in wheat (*Triticum aestivum* L.). *Mol. Breed*. 36:95. doi: 10.1007/s11032-016-0515-6

Lewis, J., Rowland, J., and Nadeau, A. (1998). Estimating maize production in Kenya using NDVI: some statistical considerations. *Int. J. Remote Sens*. 19, 2609–2617. doi: 10.1080/014311698214677

Liu, F., He, J., Wang, W., Xing, G., and Gai, J. (2020). Bi-phenotypic trait may be conferred by multiple alleles in a germplasm population. *Front. Genet*. 11:559. doi: 10.3389/fgene.2020.00559

Maimaitijiang, M., Sagan, V., Sidike, P., Hartling, S., Esposito, F., and Fritschi, F. B. (2020). Soybean yield prediction from UAV using multimodal data fusion and deep learning. *Remote Sens. Environ*. 237:111599. doi: 10.1016/j.rse.2019.111599

Nigon, T., Mulla, D., Rosen, C., Cohen, Y., Alchanatis, V., Knight, J., et al. (2015). Hyperspectral aerial imagery for detecting nitrogen stress in two potato cultivars. *Comput. Electron. Agric*. 112, 36–46. doi: 10.1016/j.compag.2014.12.018

Peñuelas, J., Isla, R., Filella, I., and Araus, J. (1997). Visible and near infrared reflectance assessment of salinity effects on barley. *Crop Sci*. 37, 198–202. doi: 10.2135/cropsci1997.0011183X003700010033x

Pérez-Bueno, M. L., Pineda, M., and Barón, M. (2019). Phenotyping plant responses to biotic stress by chlorophyll fluorescence imaging. *Front. Plant Sci*. 10:1135. doi: 10.3389/fpls.2019.01135

Rebetzke, G. J., Jimenez-Berni, J., Fischer, R. A., Deery, D. M., and Smith, D. J. (2019). Review: High-throughput phenotyping to enhance the use of crop genetic resources. *Plant Sci*. 282, 40–48. doi: 10.1016/j.plantsci.2018.06.017

Rutkoski, J., Poland, J., Mondal, S., Autrique, E., Pérez, L. G., Crossa, J., et al. (2016). Canopy temperature and vegetation indices from high-throughput phenotyping improve accuracy of pedigree and genomic selection for grain yield in wheat. *G3 (Bethesda)* 6, 2799–2808. doi: 10.1534/g3.116.032888

Salas Fernandez, M. G., Bao, Y., Tang, L., and Schnable, P. S. (2017). A high-throughput, field-based phenotyping technology for tall biomass crops. *Plant Physiol*. 174, 2008–2022. doi: 10.1104/pp.17.00707

Samborski, S. M., Gozdowski, D., Walsh, O. S., Lamb, D. W., Stępień, M., Gacek, E. S., et al. (2015). Winter wheat genotype effect on canopy reflectance: implications for using NDVI for in-season nitrogen topdressing recommendations. *Agron. J*. 107, 2097–2106. doi: 10.2134/agronj14.0323

Shendure, J., and Ji, H. (2008). Next-generation DNA sequencing. *Nat. Biotechnol*. 26, 1135–1145. doi: 10.1038/nbt1486

Tucker, C. J. (1979). Red and photographic infrared linear combinations for monitoring vegetation. *Remote Sens. Environ*. 8, 127–150. doi: 10.1016/0034-4257(79)90013-0

Visscher, P. M., Wray, N. R., Zhang, Q., Sklar, P., McCarthy, M. I., Brown, M. A., et al. (2017). 10 years of gwas discovery: biology, function, and translation. *Am. J. Hum. Genet*. 101, 5–22. doi: 10.1016/j.ajhg.2017.06.005

Wang, W., Zhou, B., He, J., Zhao, J., Liu, C., Chen, X., et al. (2020). Comprehensive identification of drought tolerance QTL-allele and candidate gene systems in Chinese cultivated soybean population. *Int. J. Mol. Sci*. 21:4830. doi: 10.3390/ijms21144830

Watt, M., Fiorani, F., Usadel, B., Rascher, U., Muller, O., and Schurr, U. (2020). Phenotyping: new windows into the plant for breeders. *Annu. Rev. Plant Biol*. 71, 689–712. doi: 10.1146/annurev-arplant-042916-041124

Wiegand, C., Richardson, A., Escobar, D., and Gerbermann, A. (1991). Vegetation indexes in crop assessment. *Remote Sens. Environ*. 35, 105–119.

Yang, G., Liu, J., and Zhao, C. (2017). Unmanned aerial vehicle remote sensing for field-based crop phenotyping: current status and perspectives. *Front. Plant Sci*. 8:1111. doi: 10.3389/fpls.2017.01111

Yu, J., Pressoir, G., Briggs, W. H., Vroh Bi, I., Yamasaki, M., Doebley, J. F., et al. (2006). A unified mixed-model method for association mapping that accounts for multiple levels of relatedness. *Nat. Genet*. 38, 203–208. doi: 10.1038/ng1702

Zhang, X., Zhao, J., Yang, G., Liu, J., Cao, J., Li, C., et al. (2019). Establishment of plot-yield prediction models in soybean breeding programs using UAV-based hyperspectral remote sensing. *Remote Sens*. 11:2752. doi: 10.3390/rs11232752

Conflict of Interest: The authors declare that the research was conducted in the absence of any commercial or financial relationships that could be construed as a potential conflict of interest.

frontiers in Plant Science

ORIGINAL RESEARCH
published: 10 March 2021
doi: 10.3389/fpls.2021.608967

Remote Sensing Energy Balance Model for the Assessment of Crop Evapotranspiration and Water Status in an Almond Rootstock Collection

Joaquim Bellvert[1], Héctor Nieto[2], Ana Pelechá[1], Christian Jofre-Čekalović[1], Lourdes Zazurca[3] and Xavier Miarnau[3]*

[1] Efficient Use of Water in Agriculture Program, Institute of Agrifood Research and Technology, Fruitcentre, Parc Científic i Tecnològic Agroalimentari de Lleida, Lleida, Spain, [2] Complutum Tecnologías de la Información Geográfica, Madrid, Spain, [3] Fruit Production Program, Institute of Agrifood Research and Technology, Fruitcentre, Parc Científic i Tecnològic Agroalimentari de Lleida, Lleida, Spain

One of the objectives of many studies conducted by breeding programs is to characterize and select rootstocks well-adapted to drought conditions. In recent years, field high-throughput phenotyping methods have been developed to characterize plant traits and to identify the most water use efficient varieties and rootstocks. However, none of these studies have been able to quantify the behavior of crop evapotranspiration in almond rootstocks under different water regimes. In this study, remote sensing phenotyping methods were used to assess the evapotranspiration of almond cv. "Marinada" grafted onto a rootstock collection. In particular, the two-source energy balance and Shuttleworth and Wallace models were used to, respectively, estimate the actual and potential evapotranspiration of almonds grafted onto 10 rootstock under three different irrigation treatments. For this purpose, three flights were conducted during the 2018 and 2019 growing seasons with an aircraft equipped with a thermal and multispectral camera. Stem water potential (Ψ_{stem}) was also measured concomitant to image acquisition. Biophysical traits of the vegetation were firstly assessed through photogrammetry techniques, spectral vegetation indices and the radiative transfer model PROSAIL. The estimates of canopy height, leaf area index and daily fraction of intercepted radiation had root mean square errors of 0.57 m, 0.24 m m^{-1} and 0.07%, respectively. Findings of this study showed significant differences between rootstocks in all of the evaluated parameters. Cadaman® and Garnem® had the highest canopy vigor traits, evapotranspiration, Ψ_{stem} and kernel yield. In contrast, Rootpac® 20 and Rootpac® R had the lowest values of the same parameters, suggesting that this was due to an incompatibility between plum-almond species or to a lower water absorption capability of the rooting system. Among the rootstocks with medium canopy vigor, Adesoto and IRTA 1 had a lower evapotranspiration than Rootpac® 40 and Ishtara®. Water productivity (WP) (kg kernel/mm water evapotranspired) tended to decrease with Ψ_{stem}, mainly in 2018. Cadaman® and Garnem® had the highest WP, followed by INRA GF-677, IRTA 1, IRTA 2, and Rootpac® 40. Despite the low Ψ_{stem} of Rootpac® R, the WP of this rootstock was also high.

Keywords: thermal, field phenotyping, water productivity, TSEB model, stem water potential, crown area, yield

OPEN ACCESS

Edited by:
Helen H. Tai, Agriculture and Agri-Food Canada (AAFC), Canada

Reviewed by:
Iván Francisco García-Tejero, Ifapa Centro Las Torres Tomejil, Spain
Arturo Reyes, Forestales y Pecuarias, Mexico

****Correspondence:***
Joaquim Bellvert
joaquim.bellvert@irta.cat

Specialty section:
This article was submitted to Technical Advances in Plant Science, a section of the journal Frontiers in Plant Science

Received: *22 September 2020*
Accepted: *08 February 2021*
Published: *10 March 2021*

Citation:
Bellvert J, Nieto H, Pelechá A, Jofre-Čekalović C, Zazurca L and Miarnau X (2021) Remote Sensing Energy Balance Model for the Assessment of Crop Evapotranspiration and Water Status in an Almond Rootstock Collection. Front. Plant Sci. 12:608967. doi: 10.3389/fpls.2021.608967

INTRODUCTION

The study of the behavior of *Prunus* cultivars grafted on different rootstocks in fruit production serves to adapt cultivars to different edaphic and environmental conditions and to enhance sustainable crop production. The selection of a suitable scion-rootstock combination is the first step to monitor the vegetative growth, yield and fruit composition parameters of the scion (Caruso et al., 1996; Mestre et al., 2017; Font i Forcada et al., 2020; Reig et al., 2020). There is growing interest in selecting and breeding new rootstocks and cultivars with a higher water use efficiency (WUE) in order to improve water productivity and better adapt fruit production to future climate changes (Solari et al., 2006; Xiloyannis et al., 2007; Díez-Palet et al., 2019). In almonds [*Prunus dulcis* (Mill.) DA Webb], with the recent introduction of high-density planting systems, particular attention has been paid to using dwarf rootstocks in order to control canopy vigor and facilitate mechanical harvesting (Pinochet, 2009; Casanova-Gascón et al., 2019). In addition, with the introduction of new dwarfing rootstocks and hybrids coming mainly from the peach sector, the paradigm has changed since information about their response to drought or a limited water supply is scant.

For many years, breeding programs for fruit crop rootstocks, as well as for obtaining scion cultivars, have used similar evaluation methods based on both agronomic and molecular traits. Some of the commonly measured agronomic traits are trunk cross-sectional area (TCSA), plant height, tree canopy vigor, phenology, yield parameters, and fruit quality attributes (Reighard et al., 2011; Font i Forcada et al., 2012; Legua et al., 2012; Lordan et al., 2019). However, most of these agronomic traits are a consequence of differences in the root system architecture or the hydraulic properties of a rootstock, which contribute in influencing the transpiration rate through their effects on the stem water potential (Ψ_{stem}) and the control of stomatal conductance (Hernandez-Santana et al., 2016). On the other hand, the development of markers to help select individuals with traits that are complex to evaluate should speed up the development of new rootstocks that are resistant or tolerant to multiple biotic or abiotic stresses (Cantini et al., 2001; Arismendi et al., 2012; Jiménez et al., 2013; Guajardo et al., 2015). However, the types of methodology required for this remain fairly time-consuming, costly and, in some cases, are still scarce.

In recent years, proximal and remote sensing (RS) technologies have increasingly been used to assess vegetation in the context of field-based phenotyping (FBP) (Deery et al., 2014; Araus and Kefauver, 2018). These technologies have shown the potential to reduce labor requirements in the assessment of "breeder-preferred" traits and, in some cases, can deliver more detailed information about the biophysical crop parameters. Usually, most efforts in this field are focused on using low-cost RGB (visible), multispectral/hyperspectral, light detection and ranging (LIDAR) or thermal infrared imaging sensors. Detailed information can be found in the literature about different applications for field phenotyping using these sensors (Araus and Cairns, 2014; Deery et al., 2014; Araus et al., 2018). For example, applications of digital RGB sensors in FBP include visible imaging to estimate leaf color, crop ear counting, canopy cover, or canopy height (Kefauver et al., 2015; Holman et al., 2016; Fernandez-Gallego et al., 2019). Spectral imaging sensors are normally used to derive the spectral response of the vegetation and their biophysical traits such as leaf water content, chlorophyll and xanthophyll levels, biomass or the leaf area index (LAI) (Li et al., 2014; Mazis et al., 2020). Thermal imaging has been used to estimate plant water status (Romano et al., 2011; Prashar and Jones, 2014), and LIDAR point clouds to estimate vegetation structural parameters (Madec et al., 2017; Jimenez-Berni et al., 2018). However, most of the breeding programs focused on these targets have tended to use RS technologies to phenotype annual crops. Such studies are rarely performed in woody crops. To the best of our knowledge, only Virlet et al. (2014); Ampatzidis et al. (2019); Coupel-Ledru et al. (2019); Gutiérrez-Gordillo et al. (2020), and López-Granados et al. (2019) have used RS imagery for FBP in woody crops such as apple, citrus and almond.

As previously mentioned, there is an urgent need to identify rootstocks with improved WUE, which, for instance, could be planted in drylands or to cope with scarce water supplies. For this purpose, it is critical to develop tools capable of determining actual transpiration rates at canopy level which can be widely used in breeding programs. Until now, the field phenotyping response of woody crops to water use constraints has constituted a bottleneck for breeding programs due to the complexity of measuring actual transpiration or water status in a large number of trees (Virlet et al., 2014). The few studies that have been published were conducted using high-throughput phenotyping platforms deployed in greenhouses and under controlled conditions, which have the advantage that plants in pots can be weighed and biomass estimated from imagery (Pereyra-Irujo et al., 2012; Lopez et al., 2015).

In recent years, improvements in computational performance, open-source programming languages, lower data requirements, and the simplification of different complex approaches used to estimate actual crop evapotranspiration (ET_a) through RS have contributed, at least in part, to reducing the existing gap between RS physical modeling methods and agricultural applications. Among the different methods, the surface energy balance (SEB) models are probably the most complex to run, but at the same time provide high accuracy and robustness in estimating ET_a in different environments (Norman et al., 1995; Bastiaanssen et al., 1998; Mecikalski et al., 1999; Allen et al., 2007; Boulet et al., 2015). These models have mostly been used for assessing the spatial and temporal variability of ET_a at regional and field scale using satellite imagery (Semmens et al., 2016; He et al., 2017; Knipper et al., 2019), although some of them have also been used with very high-resolution aircraft imagery (Hoffman et al., 2016; Xia et al., 2016; Nieto et al., 2019). Among the different SEB models, the two-source energy balance (TSEB) modeling scheme allows the possibility to estimate transpiration and evaporation separately (Norman et al., 1995), by using the Priestley-Taylor approach (Priestley and Taylor, 1972) when radiometric temperature (T_{rad}) is obtained from satellite imagery (e.g., Knipper et al., 2019), or through a contextual approach if high-resolution thermal imagery is available, in which case it is possible to directly obtain soil (T_s) and canopy (T_c) surface temperatures (Nieto et al., 2019).

The TSEB is a two-source model built on the Shuttleworth-Wallace (S-W) energy combination model which can be used to estimate potential evapotranspiration (ET_p) and its partition components separately (Shuttleworth and Wallace, 1985).

Based on the hypothesis that the ratio between ET_a and ET_p can be used as a crop water stress indicator, this paper aims to demonstrate the potential of the TSEB and S-W models for phenotyping and breeding purposes in woody crops. Differences in the amount of evapotranspired water and water status will be explored in the almond cultivar "Marinada" grafted onto a collection of 10 rootstocks irrigated under different water regimes. Different RS approaches to determine certain biophysical traits of the vegetation are also explored and the values obtained are used as inputs of the TSEB and S-W models.

MATERIALS AND METHODS

Study Site and Experimental Design

The study was carried out in an experimental almond orchard located at the experimental station of IRTA (Institute of Research and Technology, Food and Agriculture) in Les Borges Blanques, Spain (41°30′31.89″N; 0°51′10.70″E, 323 m elevation) during the 2018 and 2019 growing seasons (**Figure 1**). The climate in the area is Mediterranean, with annual rainfall of 535 and 377 mm for 2018 and 2019, respectively. The orchard is the result of a rootstock trial planted in 2010 which used cv. "Marinada" as the scion cultivar (Vargas et al., 2008) and the following rootstocks: Adesoto, Cadaman®, Garnem®, INRA GF-677, IRTA 1, IRTA 2, Ishtara®, Rootpac® R, Rootpac® 40, and Rootpac® 20 (**Table 1**). Trees were planted at a spacing distance of 4.5 m with 5.0 m between rows, and trained to an open vase system.

The study followed a split-plot design, where irrigation treatment is the main plot and the rootstocks are the sub-plots. The trial consisted of three irrigation treatments: (i) conventional irrigation (I_{100}), receiving 100% of ET_c during the whole irrigation season; (ii) half irrigation (I_{50}), receiving 50% of ET_c during the whole irrigation season, and (iii) deficit irrigation (I_0), which received 100% of ET_c during the whole irrigation season except for ∼30 days before the airborne campaign when irrigation was halted. The total amount of water applied in I_{100} throughout the growing season (from April to October) was 652 mm and 618 mm in 2018 and 2019, respectively. Each treatment had three repetitions, each in a row, with the 10 different rootstocks in each row. Rootstock distribution within each row followed a randomized design. One additional row was included between treatments for protection.

Trees were irrigated on a daily basis calculating water requirements through a water balance method for replacing crop evapotranspiration (ET_c) as follows: ET_c = (ET_o x Kc)–effective rainfall. The ET_o was collected from the public network of weather stations closest to the study site (Xarxa Agrometeorològica de Catalunya (XAC), and Servei Meteorològic de Catalunya., 2020), which uses the Penman-Monteith method (Allen et al., 1998) to calculate it. Annual ET_o was 1061 and 1133 mm in 2018 and 2019, respectively. The Kc used were derived from Goldhamer (2012): Kc_1 = 0.70 (April), Kc_2 = 0.95 (May), Kc_3 = 1.09 (June), Kc_4 = 1.15 (July), Kc_5 = 1.17 (August), and Kc_6 = 1.12 (September). Effective rainfall was estimated as half of the rainfall for a single event-day with more than 10 mm of precipitation; otherwise was considered to be zero. The irrigation system consisted of two drip lines, with fifteen drippers per tree (3.5 L h^{-1} per dripper). Soil texture was clay-loam and the effective soil depth was ∼150 cm. Tree management for pruning, diseases and pests control, soil management and fertilization was based on Spanish integrated production management practices (BOE, 2002).

Image Collection

The airborne campaign was conducted on 24th July and 28th of August 2018, and on 24th July 2019. Air temperature (T_a)

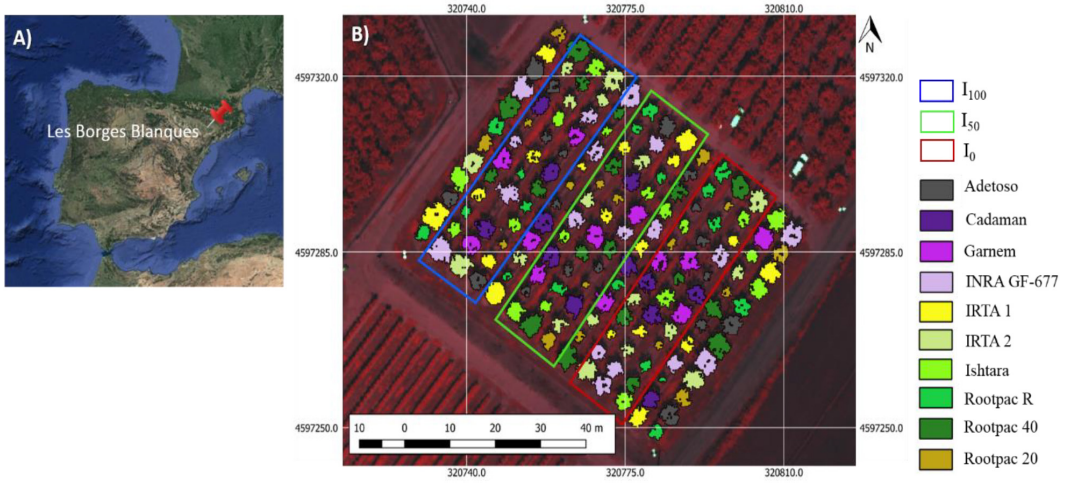

FIGURE 1 | Location of the field experiment, observing in **(A)** the study site located at the IRTA experimental station in Les Borges Blanques (Lleida, Spain), and **(B)** design of the almond rootstock trial with three irrigation treatments (I_{100}, I_{50}, and I_0).

TABLE 1 | List of evaluated rootstock, parentage, origin and tested cultivar.

Rootstock	Parentage	Origin
Adesoto	Clonal selection of *Prunus insititia*	CSIC-Aula Dei (Spain)
Cadaman®	*Prunus persica* × *Prunus davidiana*	IFGO (Hungary) and INRA
Garnem®	*Prunus dulcis* × *Prunus persica*	CITA (Spain)
INRA GF-677	*Prunus dulcis* × *Prunus persica*	INRA (France)
IRTA-1	*Prunus dulcis* × *Prunus persica*	IRTA (Spain)
IRTA-2	*Prunus cerasifera* × *Prunus dulcis*	IRTA (Spain)
Ishtara®	*(Prunus cerasifera* × *Prunus salicina)* × *(Prunus cerasifera* × *Prunus persica)*	INRA (France)
Rootpac® R	*Prunus cerasifera* × *Prunus dulcis*	Agromillora Iberia (Spain)
Rootpac® 40	(*Prunus dulcis* × *Prunus persica*) × (*Prunus dulcis* × *Prunus persica*	Agromillora Iberia (Spain)
Rootpac® 20	*Prunus besseyi* × *Prunus cerasifera*	Agromillora Iberia (Spain)

and vapor pressure deficit (VPD) at the moment of image acquisition were, respectively, 33.4°C and 2.9 kPa for 24th July 2018, 31.3°C and 2.2 kPa for 28th August 2018, and 34.4°C and 3.6 kPa for 24th July 2019. Flights were conducted at 12:00 solar time (14:00 local time) with a thermal (FLIR SC655, FLIR Systems, Wilsonville, OR, United States) and multispectral sensor (MACAW, Tetracam, Chatsworth, CA, United States) on board a manned aircraft. Flight altitude was ∼200 m above ground level, providing thermal and multispectral images at ∼0.25 and 0.03 m pixel^{-1} average resolution, respectively. The thermal sensor has a spectral response in the range of 7.5–13 μm and an image resolution of 640 × 480 pixels. The optical focal length is 13.1 mm, yielding an angular field of view of 45°. The sensor has a focal plane array based on uncooled microbolometers. The MACAW sensor has 1.4 mega-pixel complementary metal-oxide semiconductor (CMOS) sensors with a 9.6 mm fixed lens. These provide images of 1,280 × 1,024 pixels. The sensor contains six user-selectable narrow band filters at 10 nm full width at half maximum (FWHM), with center wavelengths at 515.3, 570.9, 682.2, 710.5, 781.1, and 871.8 nm. The thermal sensor was connected to a laptop via ethernet, and the multispectral camera via USB 3.0 protocol. All thermal and multispectral images were radiometrically, atmospherically and geometrically corrected. The radiometric calibration of the thermal sensor was assessed in the laboratory using a blackbody (model P80P, Land Instruments, Dronfield, United Kingdom). The radiometric calibration of the multispectral sensor was conducted through an external incident light sensor which measured the irradiance levels of light at the same bands as the MACAW multispectral sensor. In addition, *in situ* spectral measurements in ground calibration targets were performed using a Jaz spectrometer (Ocean Optics, Inc., Dunedin, FL, United States). The Jaz has a wavelength response from 200 to 1,100 nm and an optical resolution of ∼0.3–10.0 nm. During spectral collection, spectrometer calibration measurements were taken with a reference panel (white color Spectralon) and dark current before and after taking readings from radiometric calibration targets. In addition, a range of field calibrations were conducted through *in situ* surface temperature measurements in ground calibration targets using a portable IR gun (Fluke 62 mini IR thermometer, Everett, WA, United States). Geometric correction was conducted using ground control points (GCP), and measuring the position in each with a handheld GPS (Global Positioning System) (Geo7×, Trimble GeoExplorer series, Sunnyvale, CA, United States) with a precision of ∼0.20 cm. All images were mosaicked using the Agisoft Metashape Professional software (Agisoft LLC., St. Petersburg, Russia) and geometrically and radiometrically terrain corrected with QGIS 3.4 (QGIS 3.4.15). **Figure 2** shows the flowchart of the procedures used to process the images and obtain the information of the different parameters.

Field Measurements

The fraction of photosynthetically active radiation (PAR) intercepted by the canopy (*fiPAR*) was measured on the same clear days as image acquisition from 11:00 to 14:00 h (local time) using a portable linear ceptometer (AccuPAR model LP-80, Decagon Devices Inc., Pullman, WA, United States). Incident PAR above and below the canopy was measured for each tree. Twenty PAR readings were recorded below each tree canopy covering the tree spacing. The ceptometer was placed in a horizontal position at ground level perpendicular to the row. The *fiPAR* was calculated by dividing the averaged PAR below the canopy by the incident PAR taken in full sunlight at an open site with no interference from the canopy. The LAI was derived by means of *fiPAR*, using the Norman-Jarvis model (Norman and Jarvis, 1974) and assuming a leaf absorptivity for light at 0.9. Daily *fiPAR* ($fiPAR_d$) was estimated using an hourly model of light interception (Oyarzun et al., 2007). In the model, the porosity parameter was estimated so that the simulated hourly intercepted value at noon equalled the instantaneous value measured in the field. Then, $fiPAR_d$ was calculated by integrating the diurnal course of the simulated *fiPAR*. Tree architectural parameters such as canopy height, crown width perpendicular to and along rows, and branch insertion height were also measured.

Concomitant to image acquisition, one midday Ψ_{stem} was measured in each tree. Shaded leaves were selected and kept in a plastic bag covered by aluminum foil for 2 h before the measurement in order to equilibrate the water potential between leaf, stem and branches. All measurements were acquired in less than 2 h with a pressure chamber (Plant Water Status Console, Model 3500; Soil Moisture Equipment Corp., Santa Barbara, CA) and following the protocol established by Shackel et al. (1997).

Biophysical Traits of the Vegetation

Three different approaches were tested to estimate LAI and $fiPAR_d$: (i) estimates of canopy height and volume through photogrammetry, (ii) spectral vegetation indices (VIs), and (iii) the PROSAIL radiative transfer model.

The three-dimensional (3D) tree canopy volume was obtained following the protocol described by Caruso et al. (2019). The digital surface model (DSM) was generated from

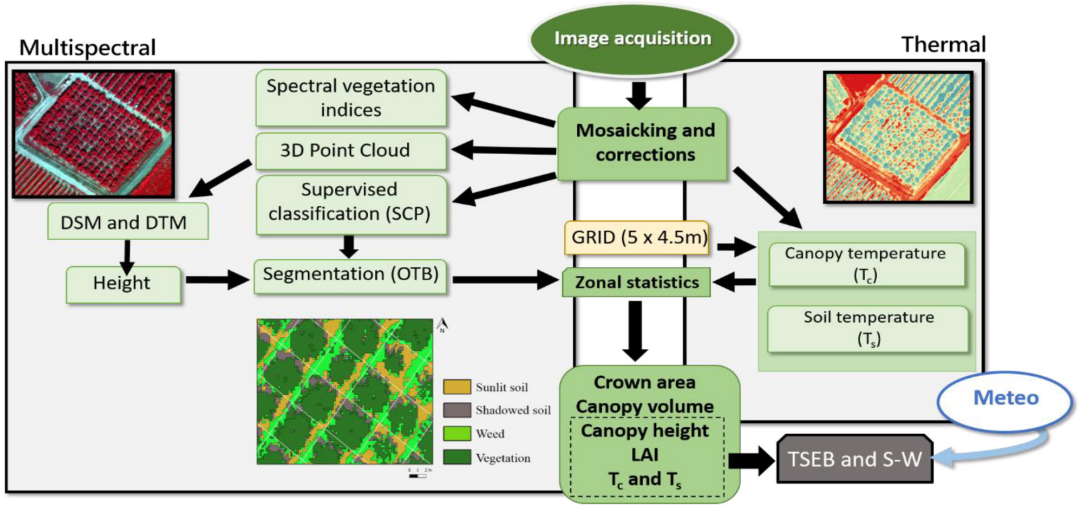

FIGURE 2 | Flowchart of the procedures used for processing the multispectral and thermal images in order to obtain the different biophysical variables of the vegetation and some of the inputs for the two-source energy balance (TSEB) and Shuttleworth and Wallace (S-W) models.

the photogrammetric point cloud of multispectral images. A classification of bare ground pixels located between tree rows were used to obtain the digital terrain model (DTM) of the orchard. Then, a raster corresponding to heights (from the ground to maximum height of the canopy) was obtained by subtracting the DTM from the DSM using the raster calculator tool of the QGIS software.

The semi-automatic OS v.6 classification plugin of the QGIS software (Congelo, 2016) was used to classify vegetation, sunlit and shadowed bare soil and weeds (**Figure 2**). Then, the vegetation mask was used to delineate each crown area through the watershed object-based segmentation algorithm included in the Orfeo Toolbox, and to obtain the average height and crown area of each individual tree. Canopy volume of each pixel was obtained by multiplying the pixel area by its corresponding height value (from the ground to the maximum height within the pixel) (Caruso et al., 2019). The total volume of each tree was obtained by adding all the canopy pixels. Finally, the net canopy volume was calculated by subtracting the volume comprised between the ground and the branch insertion of the canopy from the total volume of each tree.

Several spectral VIs were obtained from multispectral images (**Table 2**). These indices have been shown to be closely related to certain specific features of plant structure and have demonstrated a great potential to estimate the LAI (Haboudane et al., 2004). Besides the extensively used normalized difference vegetation index (NDVI), this study tested different indices within the red-edge spectral region. The red-edge region is characterized by a sharp change in vegetation reflectance due to chlorophyll absorption, and it has been demonstrated that this is strongly influenced by the LAI (Delegido et al., 2013; Xie et al., 2018).

The LAI and *fiPAR* were also estimated following the protocol described by Weiss and Baret (2016), which retrieves these parameters from Sentinel-2 bands. Instead, this study used the six very-high resolution spectral bands of the multispectral sensor. The method consists of generating a large comprehensive dataset of vegetation characteristics, covering all possible ranges in the vegetation parameters described in **Table 3**, after which simulated reflectance factors are obtained by running the PROSAIL model (Jacquemoud et al., 2009) in forward mode. With these two arrays of values (vegetation parameters and simulated spectra), a neural network was built per each parameter (many-to-one relation). Finally, the trained neural network was applied to the multispectral images for each tree, computing the average reflectance of a rectangular grid with tree spacing distance (4.5 × 5.0 m), in order to predict the biophysical parameters from the reflectances acquired by the multispectral camera.

Evapotranspiration and Crop Water Stress Index

The TSEB model was used to estimate ET_a and its partition between soil and vegetation. One of the main advantages of TSEB is that it estimates evaporation (E) and transpiration (T) separately using information from T_{rad} and biophysical parameters of the vegetation, which are available from RS. The TSEB was originally formulated by Norman et al. (1995) and further improved by Kustas and Anderson (2009). The energy

TABLE 2 | List of spectral vegetation indices (VI), their formulation and reference.

Index	Formula	References
NDVI	$(R_{870}-R_{680})/(R_{870}+R_{680})$	Rouse et al., 1973
GNDVI	$(R_{870}-R_{570})/(R_{870}+R_{570})$	Gitelson et al., 1996
MCARI	$[(R_{710}-R_{680})-0.2\,(R_{710}-R_{570})]\,R_{710}/R_{680}$	Daughtry et al., 2000
NDRE	$(R_{870}-R_{710})/(R_{870}+R_{710})$	Barnes et al., 2000
MSRRE	$(R_{870}/R_{710})-1/\sqrt{R_{870}+R_{710}+1}$	Wu et al., 2008

R is defined as reflectance.

balance is based on the principle of conservation of energy, which calculates latent heat flux as a residual of the surface energy equation (Eq. 1):

$$LE \approx R_n - H - G \quad (1a)$$

$$LE_S \approx R_{n,S} - H_S - G \quad (1b)$$

$$LE_C \approx R_{n,C} - H_C \quad (1c)$$

where LE is the latent heat flux (W m^{-2}), R_n is the net radiation flux (W m^{-2}), G is the soil heat flux (W m^{-2}), and H is the sensible heat flux (W m^{-2}). The subscripts *c* and *s* refer to canopy and soil, respectively. Surface soil heat flux around solar noon (G) is often calculated in TSEB as a constant fraction of $R_{n,S}$.

Sensible heat flux (H) is partitioned into soil (H_s) and canopy (H_c) fluxes, in which heat flux transport between soil and canopy are connected in series following an analogy of Ohm's law for electric transport:

$$H_s = \rho C_p \frac{T_s - T_{ac}}{r_s} \quad (2a)$$

$$H_c = \rho C_p \frac{T_c - T_{ac}}{r_x} \quad (2b)$$

$$H_s + H_c = H = \rho C_p \frac{T_{ac} - T_a}{r_{ah}} \quad (2c)$$

where ρ is the air density (kg m^{-3}), C_p is the specific heat of air (J kg K^{-1}), T_s is the soil temperature (K), T_a is the air temperature (K), T_{ac} is the air temperature in the canopy layer (K), r_s is the resistance to heat flow in the boundary layer immediately above the soil surface (s m^{-1}), r_x is the total boundary layer resistance of the complete canopy leaves (s m^{-1}), and r_{ah} is the aerodynamic resistance (s m^{-1}) to turbulent heat transport between the air-canopy layer and the overlying air layer.

When TSEB runs with coarse resolution satellite-derived images, soil and canopy temperature cannot be directly retrieved. In such cases, T_c and T_s are estimated in an iterative process in which it is first assumed that green canopy transpires at a potential rate based on the Priesley-Taylor equation (Priestley and Taylor, 1972). In this study, however, the high spatial resolution imagery allowed direct retrieval of T_s and T_c without the need to compute an initial canopy transpiration (Nieto et al., 2019). That is, T_c and T_s were individually obtained for each tree and for the bare soil pixels within the 5 × 4.5 m square grid, respectively. For this purpose, the previously mentioned supervised classification was used, and T_s corresponded to the averaged sunlit and shadowed bare soil pixels within each grid.

As in other TSEB models, this methodology also requires LAI to calculate radiation partitioning as well as wind attenuation through the canopy toward the soil surface. Ground measurements of LAI were used in the TSEB. Ancillary variables that were needed, such as meteorological data, were obtained from the closest weather station to the study site (XAC, Les Borges Blanques: 41°30′40.85″N; 0°51′22.21″E). Given T_c and T_s, the heat fluxes from the soil and canopy can be derived directly using Eqs. (2a,b) and the sensible heat flux from Eq. (2c). Actual evapotranspiration at the instant of aircraft image acquisition (ET_{inst}) was calculated as:

$$ET_{inst} = 3600 \frac{LE}{I \rho_w} \quad (3)$$

where ET_{inst} is the instantaneous ET (mm h^{-1}), ρ_w represents the density of water (1,000 kg m^{-3}), and λ is the latent heat of vaporization (J kg^{-1}). Then, ET_{inst} was upscaled to daily water fluxes, in units of mm/day, by multiplying the instantaneous ratio between latent heat flux and solar irradiance by average daily solar irradiance (Cammalleri et al., 2014).

The ET_p was retrieved from the S-W model (Shuttleworth and Wallace, 1985). This model also considers two coupled sources in a resistance network: the transpiration from vegetation and the evaporation from substrate soil. The theoretical basis of the S-W model is the Penman-Monteith energy combination equation, and includes two parts, one for the soil surface and the other for the plant surface. The potential evapotranspiration and transpiration computed by the S-W model, setting a minimum stomatal resistance value of 100 sm^{-1}, are then used as the basis for estimating the theoretical metrics of the crop water stress index (CWSI). In this study, the CWSI was calculated as:

$$CWSI = 1 - \frac{ET_a}{ET_p} \quad (4)$$

where ET_a and ET_p correspond to actual and potential evapotranspiration, estimated, respectively, from the TSEB and S-W models.

TABLE 3 | List of parameters and their ranges used in PROSAIL reflectance modeling.

Image acquisition	24th July 2018	28th August 2018	24th July 2019
DOY	205	240	205
Time image acquisition	12.50	12.25	12.25
Solar irradiance (W.m^{-2})	924	778	910
Solar zenith angle (°)	21.81	32.04	21.38
Solar azimuth angle (°)	193.43	184.53	183.91
Spectral bands (nm)	515.3, 570.9, 682.2, 710.5, 781.1, 871.8		
Soil reflectance	0.121, 0.163, 0.192, 0.319, 0.373, 0.363		
Number of simulations	100,000		
Latitude	41.5		
Longitude	0.85		
N_{leaf}	1.2–2.2		
C_{ab} (μg.cm^{-2})	0–90		
C_{ar} (μg.cm^{-2})	0–40		
C_{brown}	0.0–1.0		
C_w (g.cm^{-2})	0.003–0.011		
C_{dm} (g.cm^{-2})	0.003–0.011		
LAI	0.0–6.0		
Average leaf angle (°)	30–80		
Hotspot (m.m^{-1})	0.1–0.5		

N_{leaf}, Leaf mesophyll structure parameter; C_{ab}, Leaf chlorophyll content; C_{ar}, Carotenoids content; C_{brown}, Leaf brown pigments content; C_w, Leaf water content; C_{dm}, Leaf dry matter content.

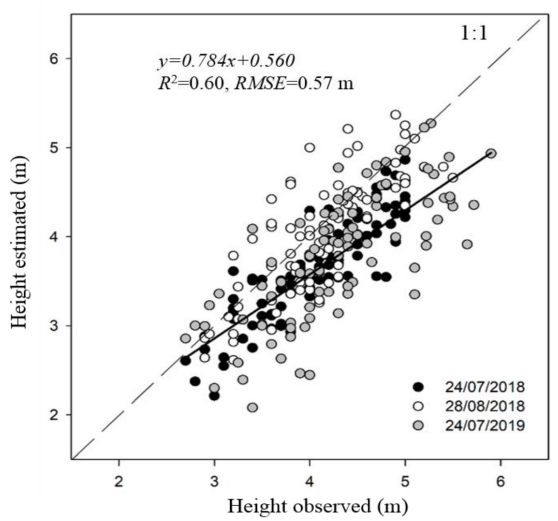

FIGURE 3 | Comparison between ground measured and airborne-estimated maximum canopy height of almond trees on 24th July and 28th August 2018 and 24th July 2019. Linear regression corresponds to aggregated data of the three dates.

Statistical Analysis

Data was analyzed using the JMP® statistical software (SAS Institute Inc., SAS Campus Drive, Cary, NC, United States). Estimates of LAI and $fiPAR_d$ were also derived using a stepwise multiple regression analysis which included the VIs and canopy volume estimates as dependent variables. All the variables were evaluated with a three-way analysis of variance (three-way ANOVA). Statistical significance was established for $P < 0.05$. Tukey's HSD test was applied to separate least square means that differed significantly.

RESULTS

Estimates of the Biophysical Variables of the Vegetation

The one-to-one relationship between observed and estimated canopy height was significant for the three dates of image acquisition, with R^2-values ranging from 0.54 to 0.77 and RMSE values from 0.43 to 0.65 m. The R^2 and RMSE were, respectively, 0.60 and 0.57 m when aggregating data from the three dates (**Figure 3**). Values of measured canopy height and LAI ranged between 2.7–5.9 m and 0.3–2.0 m m^{-1}, respectively. Estimates of crown area and canopy volume through photogrammetry were linearly related with $fiPAR_d$ and LAI, with R^2 ranging from 0.38 to 0.72 (**Table 4**), and being slightly higher for LAI. Non-significant differences were found when estimating these parameters either through crown area or canopy volume, in part because canopy height (used to estimate canopy volume) was quadratically correlated with crown area ($R^2 = 0.60$, $p < 0.001$). All the tested spectral VIs were significant and linearly correlated with LAI and $fiPAR_d$ when the data was analyzed for individual dates, but most of the regressions were not significant when the data from the three dates was aggregated. The modified chlorophyll absorption in reflectance index (MCARI) showed the lowest R^2 in all cases. The NDVI and normalized difference red-edge (NDRE) index had the highest R^2 with LAI on 28th August 2018 and 24th July 2019. In addition, NDRE had the highest R^2 on 24th July 2018. On that day, estimates of LAI through NDVI, MCARI and the green normalized difference vegetation index (GNDVI) showed the lowest R^2. The VIs with the highest R^2 with $fiPAR_d$ were similar to those reported for LAI. The use of the radiative transfer model PROSAIL significantly improved the estimates of LAI and $fiPAR_d$ in comparison to the use of simple VIs. The R^2 and RMSE for LAI ranged from 0.46 to 0.67 and from 0.24 to 0.39 m m^{-1}, respectively, and for $fiPAR_d$ from 0.45 to 0.64 and from 0.07 to 0.14%, respectively. In addition, when the data from the three dates were analyzed together, the R^2 and RMSE were, respectively 0.40 and 0.34 m m^{-1} for LAI and 0.29 and 0.12% for $fiPAR_d$.

The multiple regression analysis using the empirical variables slightly increased the predictions of LAI and $fiPAR_d$ in all cases. Results indicated that the best predictions were obtained when canopy volume was combined with other VIs, which varied between dates. Overall, the best predictions of LAI and $fiPAR_d$ using the three dates of data together were observed with the multiple regression analysis. The R^2 and RMSE were, respectively, 0.60 and 0.22 m m^{-1} for LAI and 0.56 and 0.07% for $fiPAR_d$ (**Table 4** and **Figure 4**).

Comparison Between Rootstocks

The analysis of variance showed that the rootstock source was significant for all the evaluated variables ($p < 0.0001$) and that the *treatment x rootstock* interactions were not significant, except for Ψ_{stem} (**Table 5**). Significant differences between treatments and for the *date x treatment* interaction were also observed for Ψ_{stem} ($p < 0.0001$). The remotely sensed estimates of crown area, canopy volume, LAI and $fiPAR_d$ were significant for the interaction *date x rootstock*. The date source was also significant for ET_a, $ET_a/fiPAR_d$, and kernel yield.

Overall, Cadaman® and Garnem® had the highest crown area, canopy volume, LAI and $fiPAR_d$, followed by INRA GF-677 (**Table 6**). On the other hand, Rootpac® 20 had the lowest values for all the evaluated variables. Non-significant differences were detected between IRTA 1, IRTA 2, Ishtara®, Rootpac® R, Rootpac® 40, and Adesoto. **Figure 5** shows the significant differences in Ψ_{stem} between rootstock and irrigation treatments. The results show that Rootpac® R and Rootpac® 20 were the two rootstocks with the lowest Ψ_{stem} for the three measured dates. However, the latter had slightly lower values, mostly during 2018. On the other hand, Garnem®, Cadaman®, Adesoto, INRA GF-677, IRTA 1, IRTA 2, and Rootpac® 40 displayed similar behavior for the three dates, showing the highest Ψ_{stem} values. Measurements conducted on 24th July 2018 showed significant differences between treatments in Adesoto, IRTA 1, Ishtara® and Rootpac® 20. Significant differences in Ψ_{stem} for 28th August 2018 were only observed in INRA GF-677 and Rootpac® 40. On 24th July 2019, all rootstocks except Garnem®, IRTA 2 and Rootpac® R had significant differences in Ψ_{stem} between

TABLE 4 | Coefficients of determination (R^2) of the regressions between leaf area index (LAI) and daily fraction of intercepted radiation ($fiPAR_d$) with spectral vegetation indices (VIs), crown area and canopy volume, PROSAIL radiative transfer model, and multiple regression analysis with empirical variables.

Parameters	NDVI	GNDVI	MCARI	NDRE	MSRre	Crown area (m^2)	Canopy volume (m^3)	Predicted LAI and *fiPAR* (PROSAIL)	Multiple regression analysis
LAI $_{24/7/2018}$	0.24	0.25	0.30	0.56	0.54	0.72	0.72	y = 0.45x+0.60, R^2 = 0.67, RMSE = 0.24	y = −0.74+3.31NDRE+0.03Volume, R^2 = 0.74, RMSE = 0.19
LAI $_{28/8/2018}$	0.57	0.50	0.49	0.51	0.48	0.65	0.64	y = 0.57x+0.20, R^2 = 0.46, RMSE = 0.38	y = −1.81+6.93GNDVI-1.98MSRre+ 0.02Volume, R^2 = 0.70, RMSE = 0.17
LAI $_{24/7/2019}$	0.41	0.41	0.36	0.42	0.41	0.44	0.49	y = 1.00x+0.05, R^2 = 0.56, RMSE = 0.39	y = −1.22+3.50NDRE+ 0.02Volume, R^2 = 0.54, RMSE = 0.30
LAI $_{all}$	ns	ns	ns	0.15	ns	0.59	0.58	y = 0.59x+0.49, R^2 = 0.40, RMSE = 0.34	y = 0.49+1.98NDRE-1.06NDVI+0.03Volume, R^2 = 0.60, RMSE = 0.24
$fiPAR_{d\ 24/7/2018}$	0.37	0.39	0.15	0.49	0.46	0.53	0.50	y = 0.54x+0.28, R^2 = 0.64, RMSE = 0.07	y = −0.91+0.05MSRre+ 2.22NDVI+0.01Volume, R^2 = 0.64, RMSE = 0.06
$fiPAR_{d\ 28/8/2018}$	0.45	0.49	0.38	0.47	0.46	0.49	0.45	y = 0.80x+0.09, R^2 = 0.45, RMSE = 0.14	y = 0.03+0.83GNDVI+0.01Volume, R^2 = 0.56, RMSE = 0.05
$fiPAR_{d\ 24/7/2019}$	0.38	0.40	0.32	0.41	0.39	0.38	0.43	y = 1.15x−0.15, R^2 = 0.51, RMSE = 0.14	y = −2.93–3.21MSRre+12.75NDRE, R^2 = 0.53, RMSE = 0.10
$fiPAR_{d\ all}$	ns	0.18	ns	0.16	ns	0.49	0.48	y = 0.44x+0.34, R^2 = 0.29, RMSE = 0.12	y = −0.24+0.62GNDVI+6.95MCARI+ 1.19NDRE-0.65NDVI+0.01Volume, R^2 = 0.56, RMSE = 0.07

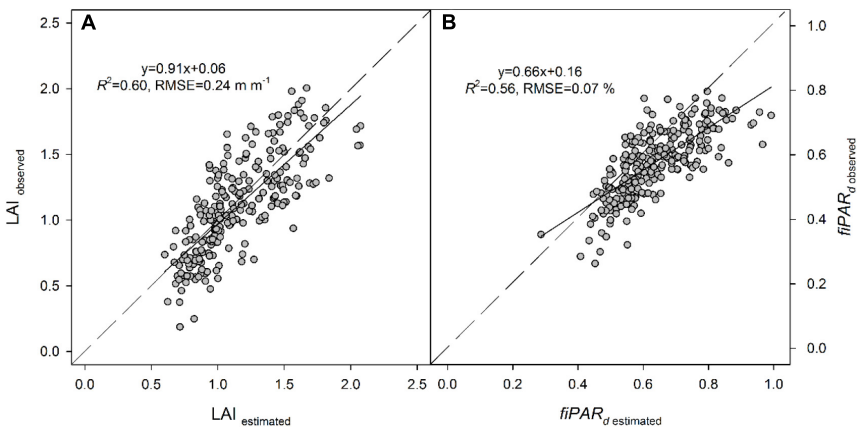

FIGURE 4 | Relationships between observed and estimated **(A)** LAI and **(B)** $fiPAR_d$ in almond trees, calculated from the equations obtained in the multiple regression analysis for the three dates together (LAI = 0.49+1.98NDRE-1.06NDVI+0.03Volume; $fiPAR_d$ = −0.24+0.62GNDVI+6.95MCARI+1.19NDRE-0.65NDVI+0.01Volume).

irrigation treatments. In all cases, the I_0 treatment tended to have the lowest Ψ_{stem} values.

Among other parameters, LAI and T_c are inputs required by the TSEB model to estimate the ET_a of a crop. In this study, differences in canopy to air temperature (T_c-T_a) between rootstocks were also significant and agreed with Ψ_{stem} measurements. More specifically, the relationships between T_c-T_a and Ψ_{stem} had R^2 values of 0.57, 0.60, and 0.53 for 24th July 2018, 28th August 2018 and 24th July 2019, respectively (graphs not shown). The relationships between ET_a with T_c-T_a and LAI gave respective R^2-values of 0.57 and 0.87 for 24th July 2018, 0.66 and 0.87 for 28th August 2018, and 0.63 and 0.68 for 24th July 2019 (graphs not shown). These results suggest that ET_a had a stronger relationship with LAI than with T_c-T_a, probably due to the lack of range in T_c-T_a values. In fact, both ET_a and ET_p were also positive and linearly correlated with the canopy crown area (**Figures 6A,B**). Values of ET_a ranged from 1.8 to 8 mm day^{-1}, depending on date and rootstock. For a given crown area, ET_a values varied between dates, with ET_a rates corresponding to 28th August 2018 lower than those of 24th July 2018 and 24th

TABLE 5 | Results of an analysis of variance (three-way ANOVA) testing the factor effects (date, treatment and rootstock) on the different variables estimated through remote sensing.

Variables/Source	Area	Volume	LAI	$fiPAR_d$	Ψ_{stem}	T_c-T_a	ET_a	$ET_a/fiPAR_d$	CWSI	Kernel yield
Date	ns	ns	ns	ns	ns	ns	<.0001*	<.0001*	ns	<.0001*
Treatment	ns	ns	Ns	ns	<.0001*	ns	Ns	ns	ns	ns
Rootstock	<.0001*	<.0001*	<.0001*	<.0001*	<.0001*	<.0001*	<.0001*	<.0001*	<.0001*	<.0001*
Date*Rootstock	0.0242*	0.0001*	<.0001*	0.0076*	ns	ns	ns	ns	ns	<.0001*
Date*Treatment	ns	ns	Ns	ns	0.0084*	ns	ns	ns	ns	ns
Rootstock*Treatment	ns	ns	Ns	ns	0.033*	ns	ns	ns	ns	ns
Date*Rootstock*Treatment	ns	ns	Ns	ns	ns	ns	ns	ns	ns	ns

Corresponds to significant differences at $p \leq 0.05$; ns, not significant.

TABLE 6 | Comparison of crown area, canopy volume, leaf area index (LAI) and daily fraction of intercepted radiation ($fiPAR_d$) between almond rootstocks for each image acquisition date.

Date	Rootstock/ Variable	Adesoto	Cadaman®	Garnem®	INRA GF-677	IRTA 1	IRTA 2	Ishtara®	Rootpac® R	Rootpac® 40	Rootpac® 20
24th July 2018	Area	3.29 ef	10.97 a	11.30 a	8.72 b	5.31 cde	6.02 cd	6.09 cd	4.36 cde	6.97 bc	2.58 f
28th August 2018		8.34 cde	14.12 a	11.03 abc	9.51 bcd	9.02 bcd	7.21 de	7.09 de	8.62 cd	4.98 e	5.18 e
24th July 2019		4.58 fg	12.15 ab	12.62 a	10.02 bc	6.37 def	7.24 de	6.98 def	5.48 efg	8.21 cd	2.96 g
Mean		6.52 c	12.41 a	11.65 a	9.41 b	6.90 c	6.82 c	6.74 c	6.15 c	6.79 c	3.74 d
24th July 2018	Volume	4.81 ef	23.58 a	26.29 a	17.58 b	8.46 cde	10.87 cd	10.81 cd	6.77 def	12.81 c	3.04 f
28th August 2018		20.98 bc	36.32 a	28.52 ab	18.85 bc	19.55 bc	13.20 cd	14.24 cd	19.77 bc	7.39 d	8.11 d
24th July 2019		6.87 fg	29.86 ab	33.08 a	23.66 bc	11.87 ef	16.65 de	12.24 ef	8.46 fg	19.31 cd	2.87 g
Mean		10.57 c	29.92 a	29.21 a	20.03 b	13.29 c	13.57 c	12.49 c	11.67 c	13.39 c	5.07 d
24th July 2018	LAI	0.66 d	1.46 a	1.51 a	1.33 ab	0.84 cd	0.93 cd	0.96 cd	0.73 d	1.09 bc	0.60 d
28th August 2018		1.22 bcd	1.57 a	1.34 abc	1.27 abcd	1.19 bcd	0.98 def	1.05 cde	1.17 bcd	0.81 f	0.90 ef
24th July 2019		0.79 ef	1.25 abcd	1.69 a	1.60 ab	1.08 cde	1.08 cde	1.32 abc	0.81 def	1.23 bcd	0.46 f
Mean		0.92 bc	1.44 a	1.51 a	1.39 a	1.04 b	0.99 b	1.08 b	0.91 bc	1.05 b	0.67 c
24th July 2018	$fiPAR_d$	0.47	0.63 ab	0.65 a	0.60 abc	0.50 cde	0.51 bcd	0.54 abcd	0.46 de	0.55 abcd	0.41 e
28th August 2018		0.68 ab	0.70 a	0.67 abc	0.64 abcd	0.61 abcd	0.57 cde	0.59 bcde	0.61 bcd	0.51 e	0.54 de
24th July 2019		0.49 de	0.61 abcd	0.68 ab	0.69 a	0.56 cd	0.56 bcd	0.65 abc	0.53 d	0.60 abcd	0.39 e
Mean		0.54 b	0.65 a	0.66 a	0.64 a	0.55 b	0.55 b	0.59 ab	0.53 b	0.55 b	0.45 c

Different letters mean significant differences between rootstocks at $p \leq 0.05$ using Tukey's honest significant difference test.

July 2019 (**Figure 6A**). These differences in ET_a between dates were more pronounced as crown area increased. The highest ET_a and ET_p were observed in Cadaman® and Garnem® in the three dates, followed by INRA GF-677. On the other hand, Rootpac® 20 was the rootstock with the lowest ET_a and ET_p. Adesoto and Rootpac® R also had low ET_a and ET_p values. When differences between dates were atmospherically normalized through the CWSI, all the data followed the same polynomial regression, indicating that rootstocks with a low crown area (Rootpac® 20) also seemed to be more stressed than those with higher crown areas (Cadaman® and Garnem®) (**Figure 6C**). Maximum CWSI values reached ∼0.6 for trees with a crown area of ∼2.5 m^{-2}. The relationship between averaged ET_a and Ψ_{stem} was significant (**Figure 7A**), as was the regression between CWSI and Ψ_{stem} (**Figure 7B**). These regressions indicate that trees grafted on the least vigorous rootstocks (Rootpac® 20 and Rootpac® R) were also those with the lowest Ψ_{stem} values. Accordingly, these two rootstocks also had the highest CWSI and lowest ET_a rates, with values ranging from 1.4 to 5.3 mm day^{-1}. Of these two rootstocks, Rootpac® 20 had the lowest Ψ_{stem} and ET_a.

It can be seen in **Figure 8A** that kernel yield was positively linearly related to ET_a in both years, although the R^2 varied between them. It can also be seen that kernel yield tended to decrease as CWSI increased, reaching minimum yields at CWSI values of around 0.5–0.7 (**Figure 8B**).

DISCUSSION

The effect of rootstock on tree canopy vigor has been widely reported through *in situ* measurements of TSCA, canopy volume or LAI (Russo et al., 2007; Gullo et al., 2014; Mestre et al., 2015; Yahmed et al., 2016; Lordan et al., 2019). However, this study demonstrates the feasibility of using very high-resolution multispectral airborne imagery to estimate the architectural traits of the vegetation in an almond rootstock trial and to use them to estimate ET_a.

The results confirm that the best fit to estimate LAI and $fiPAR_d$ was through the combination of information derived from photogrammetry and VIs (**Table 4**). The highest R^2 values

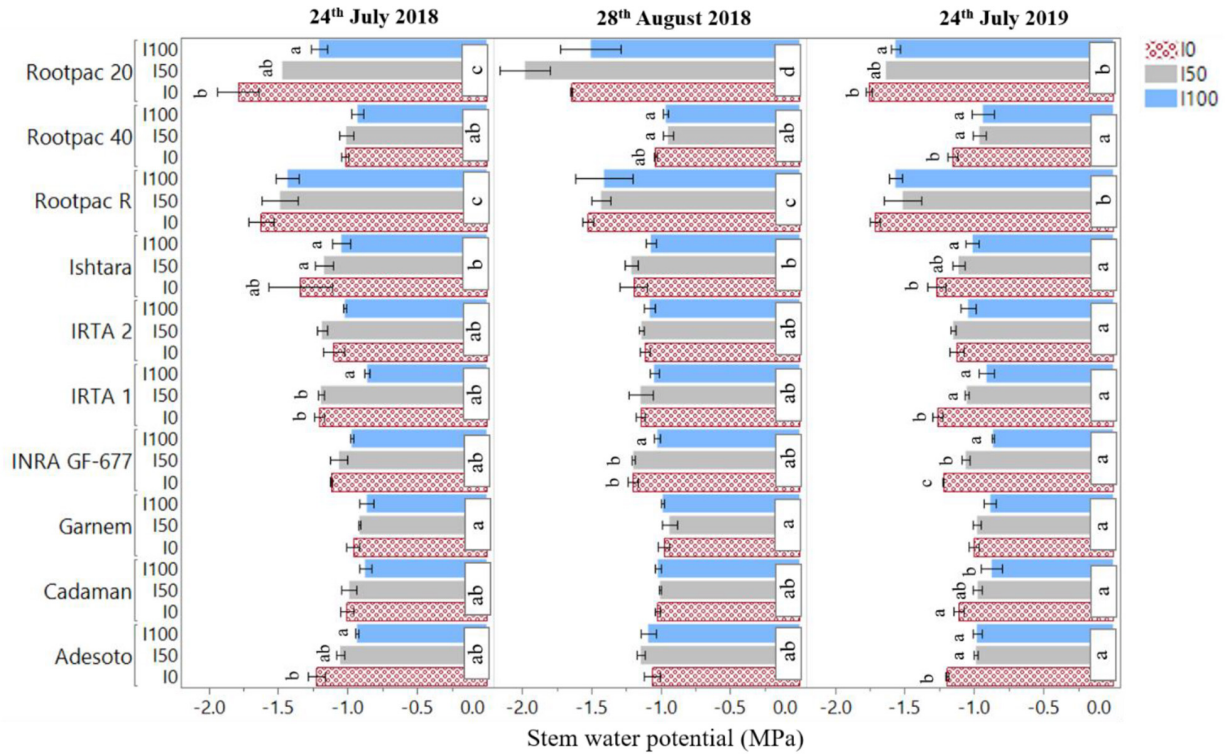

FIGURE 5 | Differences in stem water potential (Ψ_{stem}) between rootstock and irrigation treatments (I_{100}, I_{50}, I_0) for the three dates of image acquisition (24th July and 28th August 2018 and 24th July 2019). Letters indicate statistically significant differences between rootstock ($P < 0.05$, Tukey's HSD test).

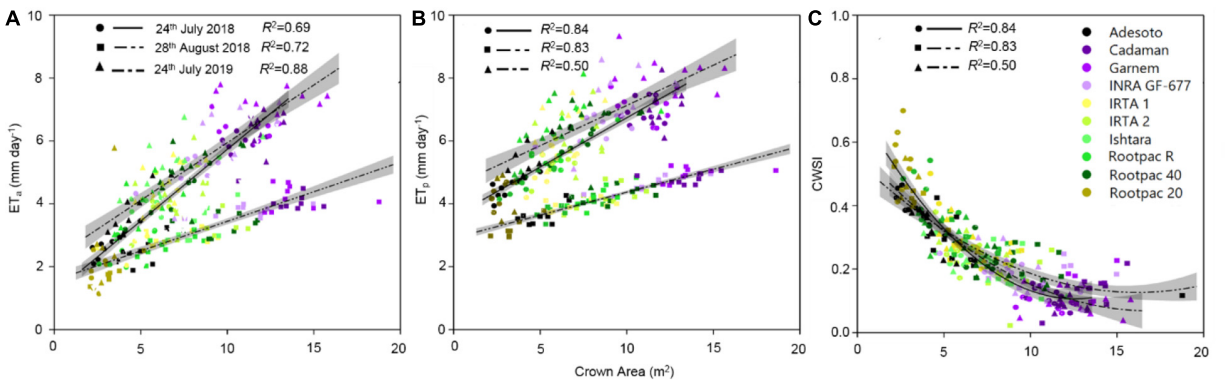

FIGURE 6 | Relationships between estimated canopy crown area and **(A)** actual evapotranspiration (ET_a), **(B)** potential evapotranspiration (ET_p) and **(C)** CWSI, calculated as 1-ET_a/ET_0, for the three dates of image acquisition (24th July 2018 and 2019 and 28th August 2018). Shadowed lines indicate the 95% confidence intervals of the regression models.

with both LAI and $fiPAR_d$ were obtained when photogrammetric techniques were used to estimate crown area and canopy volume. Since the latter depends on canopy height, which showed an RMSE of 0.57 m (**Figure 3**), it is possible that any advance in accuracy when estimating canopy height could also contribute to improving estimates of LAI and $fiPAR_d$. Increasing the number of images acquired from different viewing angles, higher overlap, or lower flying altitude in order to describe the full 3D scene and avoid occlusion effects are some of the ways that could help to improve canopy height estimates. Other authors have been able to estimate canopy height with greater accuracy. For instance, Zarco-Tejada et al. (2014) and Caruso et al. (2019) obtained RMSE values of 0.22 and 0.35 m, respectively, in olive trees. However, the difference between these two studies and ours was flight altitude (∼130 m of difference) and the trajectories taken by the unmanned aerial vehicle platform which ensured larger image overlaps and point cloud densities.

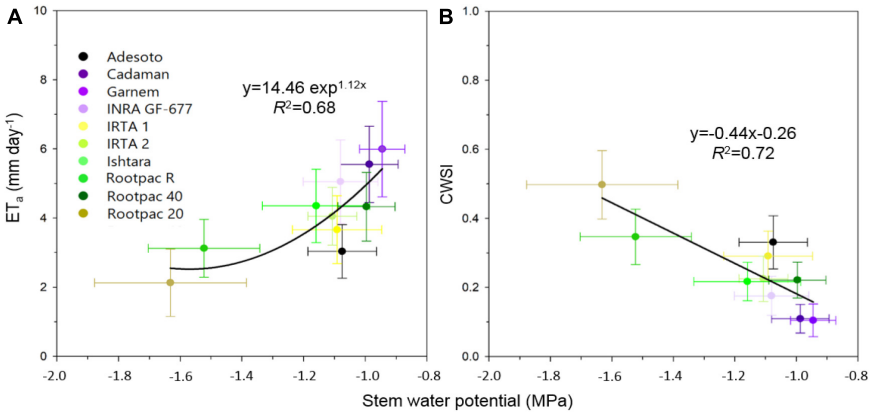

FIGURE 7 | Relationships between stem water potential (Ψ_{stem}) and **(A)** actual evapotranspiration (ET_a), and **(B)** crop water stress index (CWSI) calculated as $1\text{-}ET_a/ET_p$.

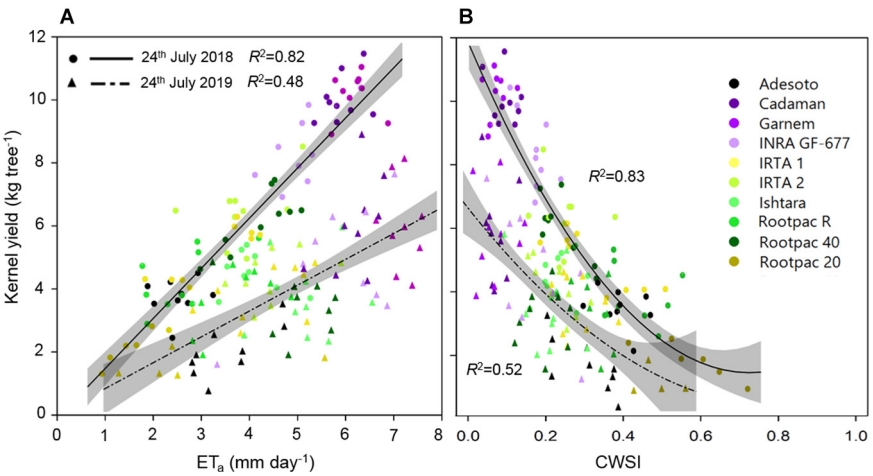

FIGURE 8 | Relationships between kernel yield (kg $tree^{-1}$) and **(A)** actual evapotranspiration (ET_a) and **(B)** CWSI of the different rootstocks estimated on 24th July 2018 and 2019. Shadowed lines indicate the 95% confidence intervals of the regression models.

The use of the PROSAIL model did not improve the estimates of LAI and $fiPAR_d$ in comparison to the multiple regression analysis, probably because this model was not designed for sparse canopies with multiple layers, as is the case of almond orchards (Berger et al., 2018). Until now, PROSAIL has been mostly used to estimate LAI and *fiPAR* with multispectral satellite imagery in non-woody vegetation canopies such as croplands (Duan et al., 2014; Li et al., 2015) and grasslands (Darvishzadeh et al., 2008; Casas et al., 2014), as PROSAIL assumes a homogeneous canopy of randomly placed leaves. However, the model has barely been used in woody crops in combination with very high resolution airborne multispectral imagery. This study also showed that PROSAIL tends to overestimate LAI (**Table 4**).

On the other hand, it is well-established that VIs are strongly influenced by canopy architecture, optical properties, sun illumination angle, viewing properties and soil background (Huete, 1988; Guillen-Climent et al., 2012; Xie et al., 2018; Prudnikova et al., 2019). In addition, saturations at moderate-to-dense canopies, leaf area distribution, and clumping effect are three of the most important issues influencing the accuracy of optical LAI estimates in row crops (Delalieux et al., 2008; Shafian et al., 2018; Yan et al., 2019). For instance, our study showed that NDVI, GNDVI and MCARI had low R^2 with LAI and $fiPAR_d$ on 24th July 2018, probably caused by a soil background effect. The previous week, and up to 3 days before the flight, a series of rainfall events occurred at the study site amounting to a total precipitation value of 20.2 mm. These events resulted in the moist soil (i.e., "darker") absorbing more light than other days, mostly in the visible and NIR bands, and therefore affecting the values provided by the indices that used these bands. On the other hand, since most of these parameters are taken into consideration in the PROSAIL model, estimates of LAI and $fiPAR_d$ tended to be better and more consistent over time, although with a systematic overestimation. The methodology used in this study to obtain the biophysical variables of the vegetation was the same as that

developed for the Sentinel-2 toolbox (Weiss and Baret, 2016). In that case, a database containing the input radiative transfer model variables was generated first. Then, the corresponding top-of-canopy reflectance for the eight Sentinel-2 bands were simulated with the PROSAIL model. In contrast, in our study we used the six bands derived from the MACAW multispectral sensor. It is also possible that the use of different and a lower number of bands slightly affected the estimates of the biophysical variables.

In this study, all the estimates of the structural parameters of the vegetation indicated that the most dwarfing rootstock was Rootpac® 20, followed by Rootpac® R, Rootpac® 40, Adesoto, Ishtara, IRTA 1, and IRTA 2. Garnem®, Cadaman®, and INRA GF-677 provided the highest values for the same structural traits. These results are in agreement with, for instance, those reported by Lordan et al. (2019), who evaluated tree canopy vigor in the same rootstock trial for a longer period and also identified Garnem®, Cadaman® and INRA GF-677 as those with the greatest tree volume, and Rootpac® 20 as the most dwarfing rootstock in the trial. In agreement, Yahmed et al. (2016) also observed that Garnem® and Rootpac® 40 were, respectively the most and medium vigorous rootstocks and that scions grafted on Rootpac® 20 were the most dwarfing.

The observed differences in ET_a between dates could be attributable to changes in atmospheric water demand, plant response (stomatal closure) due to water stress, or some phenological effect. In this case study, water stress can be discarded because Ψ_{stem} values of the date with the lowest ET_a (28th August 2018) were slightly less negative in comparison to the other two dates, and because the same behavior was observed with the estimates of ET_p with the S-W model (**Figure 6B**). Our hypothesis for the lower ET_a values observed for 28th August 2018 is that these are associated with a lower atmospheric demand of water, since the midday VPD and daily solar irradiance (R_s) for that day were slightly lower (VPD = 2.2 KPa and $R_s = 195$ W m^{-2}) than the other 2 days (respectively, 2.9 KPa and 319 W m^{-2} for 24th July 2018 and 3.6 KPa and 294 W m^{-2} for 24th July 2019). Accordingly, T_c-T_a values for that day were also higher. Several studies have published non-water-stressed baselines (NWSB)for different crops, which consist in relating T_c-T_a with VPD at midday for well-watered trees (Bellvert et al., 2016; García-Tejero et al., 2018; Gonzalez-Dugo et al., 2019; Gutiérrez-Gordillo et al., 2020). These regressions indicate that T_c-T_a tended to decrease as VPD increased. In addition, Bellvert et al. (2018) showed that the regression between T_c-T_a and VPD in California almonds was sensitive to the phenology, indicating that for a given increase in VPD, early growth stages, which correspond to vegetative growth (shell expansion and hardening), have more transpiration cooling than the kernel and post-kernel filling stages.

Although the amount of water applied in the different irrigation treatments was the same for all rootstocks, the response of most of the evaluated parameters varied between rootstocks, particularly for Ψ_{stem} where the *rootstock x treatment* and *date x treatment* interactions were significant (**Table 5**). As seen in **Figure 7**, the least vigorous rootstocks (Rootpac® 20, Rootpac® R) had the lowest Ψ_{stem} and ET_a values. However, Rootpac® 20 had slightly lowest Ψ_{stem} than Rootpac® R. These rootstocks are characterized by having *Prunus cerasifera* (myrobolan) as one of the parents, which may lead to a slight and delayed "localized" incompatibility between plum-almond species, as has previously been described in cherry and peach/plum (Treutter and Feucht, 1991) or almond/plum (Bernhard and Grasselly, 1959) combinations. This type of incompatibility is characterized by anatomical irregularities at the rootstock/scion union interface with breaks in vascular connections, which, in turn, prevent quick resumption of the growth of both root and canopy (Errea et al., 2001; Leonardi and Romano, 2004). It has also been demonstrated that trees grafted on dwarfing rootstocks such as Rootpac® 20 and Rootpac® R tend to have lower Ψ_{stem} values, and that this is likely related to the lower water absorption capability of the root system to satisfy the transpiration demand of the canopy (Yahmed et al., 2016). In our case, defoliation and yellowing problems were also observed in some trees of the I_0 treatment. The lower Ψ_{stem} observed in Rootpac® 20 could be explained because this rootstock was obtained by crossing two plum species (*Prunus besseyi*× *Prunus cerasifera*), and therefore probably displaying a smaller root system, while Rootpac® R had a higher compatibility with the scion because at least has a *Prunus dulcis* as one of the parents.

In terms of WUE or drought tolerance, several studies have related canopy vigor and root system with the level of tolerance (Serra et al., 2014; Zhang et al., 2016). The hypothesis is that vigorous plants are usually more tolerant due to a bigger root system, and vice versa. However, a comparison between rootstocks with statistical differences in canopy vigor is not always the most appropriate method because both plant water demand and the amount of water available in the soil per unit of canopy vigor will differ depending on canopy size and may therefore lead to inappropriate interpretations of the results. In this study, in order to explain the differences between rootstocks, we grouped them according to canopy vigor (mean of canopy volume) (**Table 7**), and then analyzed the statistical differences in the relations between Ψ_{stem} and ET_a within each group by using data of the three flights. A first group, which contained Garnem®, Cadaman® and INRA GF-677, was characterized by having the highest ET_a rates due to high canopy volume and probably a longer root system which permitted a higher water absorption capacity. Concurring with this finding, Black et al. (2010) described Cadaman® as a rootstock with a high root biomass. The ANCOVA analysis showed no significant differences between rootstocks in the ET_a vs. Ψ_{stem} regressions of the group 1 ($p = 0.721$) (**Table 8**). Despite of this, it seems that INRA GF-677 had slightly lower Ψ_{stem} and ET_a values and a higher CWSI. A second group with medium canopy vigor rootstocks was composed of Rootpac® 40, Adesoto, IRTA 1, IRTA 2, Ishtara®, and Rootpac® R. Rootpac® R had by some way the lowest Ψ_{stem} values, which together with Adesoto and IRTA 1 corresponded with the lowest ET_a rates, without significant differences among them. However, the low Ψ_{stem} of Rootpac® R suggests that this rootstock was acting as if it had a lower hydraulic conductivity or root biomass in comparison to the others which caused a fall in Ψ_{stem}. The ANCOVA analysis of group 2 only showed significant differences between rootstock

TABLE 7 | Mean of the variables Ψ_{stem}, ET_a, and CWSI, and slope and intercept of the regression ET_a vs. Ψ_{stem} for each rootstock grouped on the basis of the analysis of variance of canopy volume.

Rootstock	Group by canopy volume	Ψ_{stem}	ET_a	CWSI	Slope	Intercept
Garnem®	1	−0.95 ± 0.07a	5.99*a*	0.10*b*	10.13	15.46
Cadaman®	1	−0.99 ± 0.07a	5.55*ab*	0.11*b*	5.59	11.07
INRA GF-677	1	−1.08 ± 0.12 b	5.05*b*	0.18*a*	2.66	7.92
Rootpac® 40	2	−0.99 ± 0.09 a	4.32*a*	0.22*c*	−0.01	4.43
Adetoso	2	−1.07 ± 0.11 ab	3.07*b*	0.33*ab*	3.91	7.12
IRTA 1	2	−1.09 ± 0.15 ab	3.66*ab*	0.29*b*	2.99	6.93
IRTA 2	2	−1.11 ± 0.07 b	4.04*a*	0.22*c*	0.34	4.35
Ishtara®	2	−1.16 ± 0.17 b	4.35*a*	0.22*c*	0.84	5.33
Rootpac® R	2	−1.52 ± 0.18 c	3.12*b*−	0.34*a*	0.67	4.29
Rootpac® 20	3	−1.63 ± 0.24 −	2.12 −	0.49 −	0.66	3.14

*Different letters mean significant differences within each group at $p \leq 0.05$ using Tukey's honest significant difference test. – means that no statistical analysis was performed. *Corresponds to significant differences at $p \leq 0.05$*

TABLE 8 | Analysis of covariance (ANCOVA) of the relationships between ET_a and Ψ_{stem} shown in **Table 7** for rootstocks of groups 1 and 2.

	Source	g.l	Sum squares	Mean square	F	Prob > F	HSD Tukey	
Group 1	Model	5	28.71	5.74	4.13	0.003*	Garnem®	5.56 a
	Error	68	94.57	1.39			Cadaman®	5.37 a
	Total	73	123.28				INRA GF-677	5.22 a
	Ψ_{stem}	1	15.99		11.49	0.001*		
	Rootstock	2	0.91		0.32	0.721		
	Rootstock * Ψ_{stem}	2	3.84		1.38	0.257		
Group 2	Model	11	42.52	3.86	5.46	<.0001*	Rootpac® 40	3.99 ab
	Error	129	91.39	0.71			Adesoto	2.87 c
	Total	140	133.92				IRTA 1	3.49 bc
	Ψ_{stem}	1	3.26		4.61	0.034*	IRTA 2	3.97 ab
	Rootstock	5	21.73		6.13	<.0001*	Ishtara®	4.22 a
	Rootstock * Ψ_{stem}	5	3.18		0.89	0.495	Rootpac® R	3.62 bc

Different letters mean significant differences between rootstocks at $p \leq 0.05$ using Tukey's honest significant difference test.

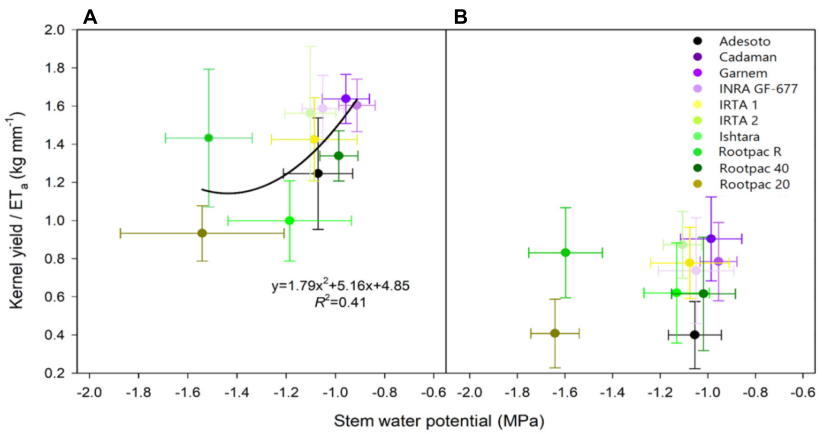

FIGURE 9 | Relationships between kernel yield/ET_a (kg tree^{-1} / mm of water evapotranspired) and stem water potential (Ψ_{stem}) for **(A)** 24th July 2018, and **(B)** 24th July 2019.

in the intercept ($p = 0.034$) (**Table 8**). Therefore, as there were not significant differences between slopes, we cannot affirm that these rootstocks have differences in the root hydraulic resistance (R_{root}). In order to improve our understanding of the response of rootstocks to water stress, future studies should be able to determine the hydraulic resistances of different

rootstocks through measurements of water potential gradients and transpiration (López-Bernal et al., 2015). Differences in the intercept could be explained either due to still small differences in the canopy volume between rootstocks of group 2 or due to a physiological response related with an anisohydric or isohydric behavior. In fact, the rootstock with the significantly lower intercept (Adesoto) was the one with the lowest crown area (**Figure 6**). The last group consisted solely of Rootpac® 20, which had the lowest Ψ_{stem} and ET_a values. Opazo et al. (2020) compared Rootpac® 20 and Rootpac® 40 and reported that plants grafted on the former had lower transpiration rates, less root biomass and proved to be less tolerant to drought than the latter. Results obtained in our study reinforce these observations (**Table 7**).

The establishment of the relationship between crop yield and the consumptive use of water (the so-called production function) in row crops is of particular interest, but at the same time is not easy to obtain due to the need for long-term studies and the difficulty in assessing consumptive use (Goldhamer and Fereres, 2017). Although many studies have demonstrated that almonds are one of the species able to maintain high kernel yield under deficit irrigation conditions (Torrecillas et al., 1989; Girona et al., 2005; Egea et al., 2010), other studies have reported that yield is dependent on canopy PAR light interception, and therefore this will increase with $fiPAR_d$ (Jin et al., 2020). In our study, the rootstocks with the highest canopy volumes and $fiPAR_d$ (Cadaman® and Garnem®) had the highest ET_a and yields, while the lowest yields were observed in those which had the lowest ET_a (Rootpac® 20, followed by Rootpac® 40 and Rootpac® R) (**Figure 8A**). It should also be noted that the R^2 of both the yield-ET_a and yield-CWSI regressions were higher in 2018 than in 2019, because the former had higher yield while the latter coincided with an alternate bearing year.

This study also shows the daily water production function as yield per unit of water evapotranspired, using data from 24th July 2018 to 24th July 2019. **Figure 9** shows that water productivity (kernel yield/mm water evapotranspired) differed between rootstocks and that the regression with Ψ_{stem} tended to decrease as water stress increased. This regression was significant for 2018 (**Figure 9A**) but not for 2019 (**Figure 9B**). The rootstocks in the previously mentioned first group (Garnem® and Cadaman®) showed the highest water productivity in both years, together with INRA GF-677, IRTA 1, IRTA 2, and Rootpac® 40. Although Adesoto and Ishtara® had similar high Ψ_{stem} values, water productivity was slightly lower. Interestingly, despite the negative Ψ_{stem} of Rootpac® R, water productivity values were similar to those obtained in the rootstocks in group 1. This is attributable to the significantly higher yield of Rootpac® R, despite having Ψ_{stem} and ET_a values similar to Rootpac® 20.

CONCLUSION

This study has demonstrated, for the first time, the feasibility of using a surface energy balance model for high-throughput phenotyping of crop evapotranspiration in an almond rootstock collection. The analysis allowed the quantification of the following almond traits that are of paramount importance in rootstock phenotyping: canopy tree height, crown area, canopy volume, LAI, $fiPAR_d$, actual and potential crop evapotranspiration, and the crop water stress index. The LAI and $fiPAR_d$ were, respectively, estimated with an R^2 of 0.60 and 0.56 through a multiple linear regression equation, which included estimates of both parameters obtained from spectral vegetation indices and estimates of crown area and canopy volume through photogrammetry techniques. Cadaman® and Garnem® were identified as the rootstocks with the highest canopy vigor as well as the highest ET_a. These two rootstocks were characterized by maintaining high Ψ_{stem} values despite reducing the amount of irrigation water applied. In contrast, Rootpac® 20 and Rootpac® R had the lowest canopy vigor and ET_a, and also the lowest Ψ_{stem} in the I_{100} treatment suggesting that this was due to a localized incompatibility between plum-almond species, differences in the root system and/or low hydraulic conductivity. Other rootstocks had medium canopy vigor. Of these, Adesoto and IRTA 1 had the lowest ET_a values and Rootpac® 40 and Ishtara the highest. Yield was linearly related with ET_a. Cadaman® and Garnem® also had the highest water productivity, and Rootpac® 20 and Rootpac® R the lowest. However, the water productivity of Rootpac® R was significantly higher than that of Rootpac® 20.

The use of energy balance models such as the TSEB using very high-resolution imagery opens the possibility to efficiently evaluate the WUE of a crop in many other different rootstock collections or varieties located in different environments. This will improve the manner in which field phenotyping has been applied until now and will help crop breeders to better understand and identify the rootstocks/varieties best adapted to drought. In addition, since the TSEB allows the partitioning of plant transpiration and surface evaporation components, future studies will focus on using transpiration instead of ET_a, and together with measurements of water potential gradients, to determine differences in root hydraulic resistances.

DATA AVAILABILITY STATEMENT

Publicly available datasets were analyzed in this study. This data can be found here: https://github.com/hectornieto.

AUTHOR CONTRIBUTIONS

JB wrote the manuscript and analyzed the remote sensing and field data. HN was the developer of the pyTSEB code used in this study. AP processed all the images and did the preliminary analysis. CJ-Č conducted the radiometric calibration of images and the analysis with the PROSAIL model. LZ conducted field measurements during the airborne campaign. XM designed the experimental design, collaborated in the field measurements campaign and provided critical insights into the manuscript

writing. All authors contributed to the article and approved the submitted version.

FUNDING

This study was partially supported by the PRIMA ALTOS project (No. PCI2019-103649) of the Ministry of Science, Innovation and Universities of the Spanish government and the Horizon 2020 Programme for Research and Innovation (H2020) of the European Commission, in the context of the Marie Skłodowska-Curie Research and Innovation Staff Exchange (RISE) action through the ACCWA project: grant agreement no. 823965.

ACKNOWLEDGMENTS

We would like to thank Mercè Mata and Marta Maldonado for, respectively, conducting stem water potential measurements and for scheduling irrigation during the growing season.

REFERENCES

Allen, R. G., Pereira, L. S., Raes, D., Smith, M., and Ab, W. (1998). *Irrigation and Drainage Paper*; No. 56. Rome: FAO. doi: 10.1016/j.eja.2010.12.001

Allen, R. G., Tasumi, M., and Trezza, R. (2007). Satellite-based energy balance for mapping evapotranspiration with internalized calibration (METRIC)–Model. *J. Irrig. Drain. Eng.* 133, 380–394. doi: 10.1061/(ASCE)0733-94372007133:4(380)

Ampatzidis, Y., Partel, V., Meyering, B., and Albrecht, U. (2019). Citrus rootstock evaluation utilizing UAV-based remote sensing and artificial intelligence. *Comp. Electronics Agric.* 164:104900. doi: 10.1016/j.compag.2019.104900

Araus, J. L., and Cairns, J. E. (2014). Field high-throughput phenotyping: the new crop breeding frontier. *Trends Plant Sci.* 19:1. doi: 10.1007/978-1-4939-2493-6_1036-1

Araus, J. L., and Kefauver, S. C. (2018). Breeding to adapt agriculture to climate change: affordable phenotyping solutions. *Curr. Opin. Plant Biol.* 45, 237–247. doi: 10.1016/j.pbi.2018.05.003

Araus, J. L., Kefauver, S. C., Zaman-Allah, M., Olsen, M. S., and Cairns, J. E. (2018). Translating high-throughput phenotyping into genetic gain. *Trends Plant Sci.* 23, 451–466. doi: 10.1016/j.tplants.2018.02.001

Arismendi, M. J., Hinrichsen, P., Almada, R., Pimentel, P., Pinto, M., and Sagredo, B. (2012). Characterization of genetic diversity of stone fruit rootstocks used in Chile by means of microsatellite markers. *J. Am. Soc. Horticult. Sci.* 137, 302–310. doi: 10.21273/jashs.137.5.302

Barnes, E. M., Clarke, T. R., Richards, S. E., Colaizzi, P. D., Haberland, J., Kostrzewski, M., et al. (2000). "Coincident detection of crop water stress, nitrogen status and canopy density using ground based multispectral data," in *Proceedings of the Fifth International Conference on Precision Agriculture*, ed. P. C. Robert (Madison, WI: ASA).

Bastiaanssen, W. G. M., Pelgrum, H., Wang, J., Ma, Y., Moreno, J. F., Roerink, G. J., et al. (1998). Remote sensing surface energy balance algorithm for land (SEBAL): 2. Validation. *J. Hydrol.* 212–213, 213–229. doi: 10.1016/S0022-1694(98)00254-6

Bellvert, J., Adeline, K., Baram, S., Pierce, L., Sanden, B. L., and Smart, D. (2018). Monitoring crop evapotranspiration and crop coefficients over an almond and pistachio orchard throughout remote sensing. *Remote Sensing* 10:2001. doi: 10.3390/rs10122001

Bellvert, J., Marsal, J., Girona, J., Gonzalez-Dugo, V., Fereres, E., Ustin, S. L., et al. (2016). Airborne thermal imagery to detect the seasonal evolution of crop water status in peach, nectarine and saturn peach orchards. *Remote Sensing* 8:39. doi: 10.3390/rs8010039

Berger, K., Atzberger, C., danner, M., D'Urso, G., Mauser, W., Vuelo, F., et al. (2018). Evaluation of the PROSAIL model capabilities for future model environments: a review study. *Remote Sensing* 10:85. doi: 10.3390/rs10010085

Bernhard, R., and Grasselly, C. H. (1959). Les pruniers portegreffes du pêcher. *Arboric. Fruit.* 62, 27–28.

Black, B. L., Drost, D., Lindstrom, T., Reeve, J., Gunnell, J. D., and Reighard, G. L. (2010). A comparison of root distribution patterns among Prunus rootstock. *J. Am. Pomol. Soc.* 64, 52–62. doi: 10.1016/j.envexpbot.2016.01.009

BOE (2002). *Real decreto 1201/2002, de 20 de Noviembre, por el que se Regula la Producción Integrada de Productos Agrícolas*. Madrid: Boletin Oficial del Estado.

Boulet, G., Mougenot, B., Lhomme, J. P., Fanise, P., Lili-Chabaane, Z., Olioso, A., et al. (2015). The SPARSE model for the prediction of water stress and evapotranspiration components from thermal infra-red data and its evaluation over irrigated and rainfed wheat. *Hydrol. Earth Syst. Sci.* 19, 4653–4672. doi: 10.5194/hess-19-4653-2015

Cammalleri, C., Anderson, M. C., Gao, F., Hain, C. R., and Kustas, W. P. (2014). Mapping daily evapotranspiration at field scales over rainfed and irrigated agricultural areas using remote sensing data fusion. *Agric. For. Meteorol.* 186, 1–11. doi: 10.1016/j.agrformet.2013.11.001

Cantini, C., Iezzoni, A. F., Lamboy, W. F., Boritzki, M., and Struss, D. (2001). DNA fingerprinting of tetraploid cherry germplasm using simple sequence repeats. *J. Am. Soc. Horticult. Sci.* 126, 205–209. doi: 10.21273/jashs.126.2.205

Caruso, G., Zarco-Tejada, P. J., González-Dugo, V., Moriondo, M., Tozzini, L., Palai, G., et al. (2019). High-resolution imagery acquired from an unmanned platform to estimate biophysical and geometrical parameters of olive trees under different irrigation regimes. *PLoS One* 14:e0210804. doi: 10.1371/journal.pone.0210804

Caruso, T., Giovanni, D., and Liverani, A. (1996). Rootstock influences the fruit mineral, sugar and organic acid content of a very early ripening peach cultivar. *J. Horticult. Sci.* 71, 931–937. doi: 10.1080/14620316.1996.11515477

Casanova-Gascón, J., Figueras-Panillo, M., Iglesias-Castellarnau, I., and Martín-Ramos, P. (2019). Comparison of SHD and open-center training systems in almond tree orchards cv.'Soleta'. *Agronomy* 9:874.

Casas, A., Riaño, D., Ustin, S. L., Dennison, P., and Salas, J. (2014). Estimation of water-related biochemical and biophysical vegetation properties using multitemporal airborne hyperspectral data and its comparison to MODIS spectral response. *Remote Sens. Environ.* 148, 28–41. doi: 10.1016/j.rse.2014.03.011

Congelo, L. (2016). *Semi-Automatic Classification Plugin Documentation. Release 6.0.1.1*. Rome. doi: 10.13140/RG.2.2.29474.02242/1

Coupel-Ledru, A., Pallas, B., Delande, M., Boudon, F., Carrié, E., Martinez, S., et al. (2019). Multi-scale high-throughput phenotyping of apple architectural and functional traits in orchard reveals genotypic variability under contrasted watering regimes. *Horticult. Res.* 6:52.

Darvishzadeh, R., Skidmore, A., Schlerf, M., and Atzberger, C. (2008). Inversion of a radiative transfer model for estimating vegetation LAI and chlorophyll in a heterogeneous grassland. *Remote Sens. Environ.* 112, 2592–2604. doi: 10.1016/j.rse.2007.12.003

Daughtry, C. S., Walthall, C. L., Kim, M. S., Brown de Colstoun, E., and McMurtrey, J. E. (2000). Estimating corn leaf chlorophyll concentration from leaf and canopy reflectance. *Remote Sens. Environ.* 74, 229–239. doi: 10.1016/S0034-4257(00)00113-9

Delalieux, S., Somers, B., Hereijgers, S., Verstraeten, W. W., Keulemand, W., and Coppin, P. (2008). A near-infrared narrow-waveband ratio to determine Leaf Area Index in orchards. *Remote Sensing Environ.* 112, 3762–3772. doi: 10.1016/j.rse.2008.05.003

Delegido, J., Verrelst, J., Meza, C. M., Rivera, J. P., Alonso, L., and Moreno, J. (2013). A red-edge spectral index for remote sensing estimation of Green LAI over agroecosystems. *Eur. J. Agron.* 46, 42–52. doi: 10.1016/j.eja.2012.12.001

Deery, D., Jimenez-Berni, J., Jones, H., Sirault, X., and Furbank, R. (2014). Proximal remote sensing buggies and potential applications for field-based phenotyping. *Agronomy* 4, 349–379. doi: 10.3390/agronomy4030349

Díez-Palet, I., Funes, I., Savé, R., Biel, C., de Herralde, F., Miarnau, X., et al. (2019). Blooming under mediterranean climate: estimating cultivar-specific chill and

heat requirements of almond and Apple trees using a statistical approach. *Agronomy* 9:760. doi: 10.3390/agronomy9110760

Duan, S.-B., Li, Z.-L., Wu, H., Tang, B.-H., Ma, L., Zhao, E., et al. (2014). Inversion of the PROSAIL model to estimate leaf area index of maize potato, and sunflower fields from unmanned aerial vehicle hyperspectral data. *Int. J. Appl. Earth Observation Geoinform.* 26, 12–20. doi: 10.1016/j.jag.2013.05.007

Egea, G., Nortes, P. A., González-Real, M. M., Baille, A., and Domingo, R. (2010). Agronomic response and water productivity of almond trees under contrasted deficit irrigation regimes. *Agricult. Water Manage.* 97, 171–181. doi: 10.1016/j.agwat.2009.09.006

Errea, P., Garay, L., and Marin, J. A. (2001). Early detection of graft incompatibility in apricot (*Prunus armeniaca*) using *in vitro* techniques. *Physiol. Plant.* 112, 135–141. doi: 10.1034/j.1399-3054.2001.1120118.x

Fernandez-Gallego, J. A., Kefauver, S. C., Vatter, T., Aparicio-Gutiérrez, N., Nieto-Taladriz, M. T., and Araus, J. L. (2019). Low-cost assessment of grain yield in durum wheat using RGB images. *Eur. J. Agron.* 105, 146–156. doi: 10.1016/j.eja.2019.02.007

Font i Forcada, C., Gogorcena, Y., and Moreno, M. A. (2012). Effect of almond × peach hybrid rootstocks on fruit quality parameters and yield characteristics of peach cultivars. *Acta Hort.* 962, 599–604. doi: 10.17660/actahortic.2012.962.81

Font i Forcada, C., Reig, G., Mestre, L., Mignard, P., Betrán, J. A., and Moreno, M. A. (2020). Scion x rootstock response on production, mineral composition and fruit quality under heavy-calcareous soil and hot climate. *Agronomy* 10:1159. doi: 10.3390/agronomy10081159

García-Tejero, I. F., Gutiérrez-Gordillo, S., Ortega-Arévalo, C., Iglesias-Contreras, M., Moreno, J. M., Souza-Ferreira, L., et al. (2018). Thermal imaging to monitor the crop-water status in almonds by using the non-water stress baselines. *Sci. Hortic.* 238, 91–97. doi: 10.1016/j.scienta.2018.04.045

Girona, J., Mata, M., and Marsal, J. (2005). Regulated deficit irrigation during kernel-filling period and optimal irrigation rates in almond. *Agricult. Water Manage.* 75, 152–167. doi: 10.1016/j.agwat.2004.12.008

Gitelson, A. A., Kaufman, Y. J., and Merzlyak, M. N. (1996). Use of a green channel in remote sensing of global vegetation from EOS-MODIS. *Remote Sens. Environ.* 58, 289–298. doi: 10.1016/S0034-4257(96)00072-7

Goldhamer, D. A. (2012). in *Almond in Grop Yield Response to Water. FAO Irrigation and Drainage Paper No. 66*, Vol. 246, eds P. Steduto, T. C. Hsiao, E. Fereres, and D. Raes (Rome: Food and Agriculture Organization of the United Nations), 296.

Goldhamer, D. A., and Fereres, E. (2017). Establishing an almond water production function for California using long-term yield response to variable irrigation. *Irrig. Sci.* 35, 169–179. doi: 10.1007/s00271-016-0528-2

Gonzalez-Dugo, V., Lopez-Lopez, M., Espadafor, M., Orgaz, F., Testi, L., Zarco-Tejada, P. J., et al. (2019). Transpiration from canopy temperature: Implications for the assessment of crop yield in almond orchards. *Eur. J. Agron.* 105, 78–85. doi: 10.1016/j.eja.2019.01.010

Guajardo, V., Hinrichsen, P., and Muñoz, C. (2015). Breeding rootsock for Prunus species: advances in genetic and genomics of peach and cherry as a model. *Chilenean J. Agricult. Res.* 75 (Suppl. 1), 17–27. doi: 10.4067/s0718-58392015000300003

Guillen-Climent, M. L., Zarco-Tejada, P. J., Berni, J. A. J., North, P. R. J., and Villalobos, F. J. (2012). Mapping radiation interception in row-structured orchards using 3D simulation and high-resolution airborne imagery acquired from a UAV. *Precision Agricult.* 13, 473–500. doi: 10.1007/s11119-012-9263-8

Gullo, G., Motisi, A., Zappia, R., Dattola, A., Diamanti, J., and Mezzetti, B. (2014). Rootstock and fruit canopy position affect peach [*Prunus persica* (L.) Batsch] (cv. Rich May) plant productivity and fruit sensorial and nutritional quality. *Food Chem.* 153, 234–242. doi: 10.1016/j.foodchem.2013.12.056

Gutiérrez-Gordillo, S., García-Tejero, I. F., Durán Zuazo, V. H., García Escalera, A., Ferrera Gil, F., Amores-Agüera, J. J., et al. (2020). Assessing the water-stress baselines by thermal imaging for irrigation management in almond plantations under water scarcity conditions. *Water* 12:1298. doi: 10.3390/w12051298

Haboudane, D., Miller, J. R., Pattey, E., Zarco-Tejada, P. J., and Strachan, I. S. (2004). Hyperspectral vegetation indices and novel algorithms for predicting green LAI of crop canopies: modeling and validation in the context of precision agriculture. *Remote Sensing Environ.* 90, 337–352. doi: 10.1016/j.rse.2003.12.013

He, R., Jin, Y., Kandelous, M. M., Zaccaria, D., Sanden, B. L., Snyder, R. L., et al. (2017). Evapotranspiration estimate over an almond orchard using Landsat satellite observations. *Remote Sens.* 9:436. doi: 10.3390/rs9050436

Hernandez-Santana, V., Rodriguez-Dominguez, C. M., Fernández, J. E., and Diaz-Espejo, A. (2016). Role of leaf hydraulic conductance in the regulation of stomatal conductance in almond and olive in response to water stress. *Tree Physiol.* 36, 725–735. doi: 10.1093/treephys/tpv146

Hoffman, H., Nieto, H., Jensen, R., Guzinski, R., Zarco-Tejada, P., and Friborg, T. (2016). Estimating evaporation with UAV data and two-source energy balance models. *Hydrol. Earth Syst. Sci.* 20, 697–713. doi: 10.5194/hess-20-697-2016

Holman, F. H., Riche, A. B., Michalski, A., Castle, M., Wooster, M. J., and Hawkesford, M. J. (2016). High throughput field phenotyping of wheat plant height and growth rate in field plot trials using UAV based remote sensing. *Remote Sensing* 8:1031. doi: 10.3390/rs8121031

Huete, A. R. (1988). A soil-adjusted vegetation index (SAVI). *Remote Sens. Environ.* 25, 295–309. doi: 10.1016/0034-4257(88)90106-x

Jacquemoud, S., Verhoef, W., Baret, F., Bacour, C., Zarco-Tejada, P. J., Asner, G. P., et al. (2009). PROSPECT + SAIL models: a review of use for vegetation characterization. *Remote Sens. Environ.* 113, S56–S66.

Jiménez, S., Dridi, J., Gutiérrez, D., Moret, D., Irigoyen, J. J., Moreo, M. A., et al. (2013). Physiological, biochemical and molecular responses in four Prunus rootstock submitted to drought stress. *Tree Physiol.* 33, 1061–1075. doi: 10.1093/treephys/tpt074

Jimenez-Berni, J. A., Deery, D. M., Rozas-Larraondo, P., Condon, A. G., Rebetzke, G. J., James, R. A., et al. (2018). High throughput determination of plant height, ground cover, and above-ground biomass in wheat with LiDAR. *Front. Plant. Sci.* 9:237. doi: 10.3389/fpls.2018.00237

Jin, Y., Chen, B., Lampinen, B. D., and Brown, P. H. (2020). Advancing agricultural production with machine learning analytics: yield determinants for California's almond orchards. *Front. Plant Sci.* 11:290. doi: 10.3389/fpls.2020.00290

Kefauver, S. C., El-Haddad, G., Vergara-Diaz, O., and Araus, J. L. (2015). "RGB picture vegetation indexes for high-throughput phenotyping platforms (HTPPs)," in *Proceedings of the SPIE Remote Sensing for Agriculture*. Ecosystems, and Hydrology XVII, Vol. 9637, eds M. U. Christopher and N. A. Maltese (Toulousse), 96370J.

Knipper, K. R., Kustas, W. P., Anderson, M. C., Alfieri, J. G., Prueger, J. H., Hain, C. R., et al. (2019). Evapotranspiration estimates derived using thermal-based satellite remote sensing and data fusion for irrigation management in California vineyards. *Irrig. Sci.* 37, 431–449. doi: 10.1007/s00271-018-0591-y

Kustas, W., and Anderson, M. (2009). Advances in thermal infrared remote sensing for land surface modeling. *Agric. For. Meteorol.* 149, 2071–2081. doi: 10.1016/j.agrformet.2009.05.016

Legua, P., Pinochet, J., Moreno, M. A., Martinez, J. J., and Hernández, F. (2012). Prunus hibrids rootstocks for flat peach. *Sci. Agricola* 69, 13–18. doi: 10.1590/s0103-90162012000100003

Leonardi, C., and Romano, D. (2004). Recent issues on vegetable grafting. *Acta Horticult.* 631, 163–174. doi: 10.17660/actahortic.2004.631.21

Li, X., Zhang, Y., Bao, Y., Luo, J., Jin, X., Xu, X., et al. (2014). Exploring the best hyperspectral features for LAI estimation using partial least squares regression. *Remote Sensing* 6, 6221–6241. doi: 10.3390/rs6076221

Li, Z., Jin, X., Wang, J., Yang, G., Nie, C., Xu, X., et al. (2015). Estimating winter wheat (*Triticum aestivum*) LAI and leaf chlorophyll content from canopy reflectance data by integrating agronomic prior knowledge with the PROSAIL model. *Int. J. Remote Sens.* 36, 2634–2653. doi: 10.1080/01431161.2015.1041176

Lopez, G., Pallas, B., Martinez, S., Lauri, P. E., Regnard, J. L., Durel, C. -É, et al. (2015). Genetic variation of morphological traits and transpiration in an apple core collection under well-watered conditions: towards the identification of morphotypes with high water use efficiency. *PLoS One* 10:e0145540. doi: 10.1371/journal.pone.0145540

López-Bernal, A., García-Tejera, O., Testi, L., and Orgaz, F. (2015). Low winter temperatures induce a disturbance of water relations in field olivet rees. *Trees* 29, 1247–1257. doi: 10.1007/s00468-015-1204-5

López-Granados, F., Torres-Sánchez, J., Jiménez-Brenes, F. M., Arquero, O., Lovera, M., and de Castro, A. I. (2019). An eficient RGB-UAV-based platform for field almond tree phenotyping: 3-D architecture and flowering traits. *Plant Methods* 15:160.

Lordan, J., Zazurca, L., Maldonado, M., Torguet, L., Alegre, S., and Miarnau, X. (2019). Horticultural performance of 'Marinada' and 'Vairo' almond cultivars grown on a genetically diverse set of rootstocks. *Sci. Horticult.* 256:108558. doi: 10.1016/j.scienta.2019.108558

Madec, S., Baret, F., de Solan, B., Thomas, S., Dutartre, D., Jezequel, S., et al. (2017). High-throughput phenotyping of plant height: comparing unmanned aerial vehicles and ground LiDAR estimates. *Front. Plant. Sci.* 8:2002. doi: 10.3389/fpls.2017.02002

Mazis, A., Chroudhury, S. D., Morgan, P. B., Stoerger, V., Hiller, J., Ge, Y., et al. (2020). Application of high-throughput plant phenotyping for assessing biophysical traits and drought response in two oak species under controlled environment. *Forest Ecol. Manage.* 465:118101. doi: 10.1016/j.foreco.2020.118101

Mecikalski, J. R., Diak, G. R., Anderson, M. C., and Norman, J. M. (1999). Estimating fluxes on continental scales using remotely sensed data in an atmospheric-land exchange model. (1999). *J. Appl. Meteorol.* 38, 1352–1369. doi: 10.1175/1520-0450

Mestre, L., Reig, G., Betrán, J. A., and Moreno, M. A. (2017). Influence of plum rootstocks on agronomic performance, leaf mineral nutrition and fruit quality of 'Catherina' peach cultivar in heavy-calcareous soil conditions. *Spanish J. Agric. Res.* 15:e0901. doi: 10.5424/sjar/2017151-9950

Mestre, L., Reig, G., Betrán, J. A., Pinochet, J., and Moreno, M. A. (2015). Influence of peach-almond hybrids and plum-based rootstocks on mineral nutrition and yield characteristics of 'Big Top' nectarine in replant and heavy-calcareous soil conditions. *Sci. Hortic.* 192, 475–481. doi: 10.1016/j.scienta.2015.05.020

Nieto, H., Kustas, W. P., Torres-Rúa, A., Alfieri, J. G., Gao, F., Anderson, M. C., et al. (2019). Evaluation of TSEB turbulent fluxes using different methods for the retrieval of soil and canopy component temperatures from UAV thermal and multispectral imagery. *Irrig. Sci.* 37, 389–406. doi: 10.1007/s00271-018-0585-9

Norman, J. M., and Jarvis, P. G. (1974). Photosynthesis in Sitka spruce (Picea sitchensis (Bong.) Carr.). III. Measurements of canopy structure and interception of radiation. *J. Appl. Ecol.* 81, e375–e398.

Norman, J. M., Kustas, W. P., and Humes, K. S. (1995). Source approach for estimating soil and vegetation energy fluxes in observations of directional radiometric surface temperature. *Agric. For. Meteorol.* 77, 263–293. doi: 10.1016/0168-1923(95)02265-y

Opazo, I., Toro, G., Salvatierra, A., Pastenes, C., and Pimentel, P. (2020). Rootstocks modulate the physiology and growth responses to water deficit and long-term recovery in grafted Stone fruit trees. *Agric. Water Manag.* 228:105897. doi: 10.1016/j.agwat.2019.105897

Oyarzun, R. A., Stöckle, C. O., and Whiting, M. D. (2007). A simple approach to modeling radiation interception by fruit-tree orchards. *Agric. For. Meteorol.* 142, 12–24. doi: 10.1016/j.agrformet.2006.10.004

Pereyra-Irujo, G., Gasco, E. D., Peirone, L. S., and Aguirrezábal, L. A. N. (2012). GlyPh: a low-cost platform for phenotyping plant growth and water use. *Funct. Plant Biol.* 39, 905–913. doi: 10.1071/fp12052

Pinochet, J. (2009). 'Greenpac', a new peach hybrid rootstock adapted to Mediterranean 459 conditions. *HortScience* 44, 1456–1457. doi: 10.21273/hortsci.44.5.1456

Prashar, A., and Jones, H. (2014). Infra-red thermography as a high-throughput tool for field phenotyping. *Agronomy* 4, 397–417. doi: 10.3390/agronomy4030397

Priestley, C. H. B., and Taylor, R. J. (1972). On the assessment of surface heat flux and evaporation using large-scale parameters. *Mon. Weather Rev.* 100, 81–92. doi: 10.1175/1520-0493

Prudnikova, E., Savin, I., Vindeker, G., Grubina, P., Shishkonakova, E., and Sharychev, D. (2019). Influence of soil background on spectral reflectance of winter wheat crop canopy. *Remote Sensing* 11:1932. doi: 10.3390/rs11161932

Reig, G., Garanto, X., Mas, N., and Iglesias, I. (2020). Long-term agronomical performance and iron chloosis susceptibility of several Prunus rootstock grown under loamy and calcareous soil conditions. *Sci. Hortic.* 262:109035. doi: 10.1016/j.scienta.2019.109035

Reighard, G. L., Beckman, T., Belding, R., Black, B., Byers, P., Cline, J., et al. (2011). Six-year performance of 14 prunus rootstocks at 11 sites in the 2001 NC-140 peach trial. *J. Am. Pomol. Soc.* 65, 26–41.

Romano, G., Zia, S., Spreer, W., Sanchez, C., Cairns, J., Araus, J. L., et al. (2011). Use of thermography for high throughput phenotyping of tropical maize adaptation in water stress. *Comp. Electronics Agric.* 79, 67–74. doi: 10.1016/j.compag.2011.08.011

Rouse, J. W., Haas, R. H., Schell, J. A., and Deering, D. W. (1973). "Monitoring vegetation systems in the great plains with ERTS," In *Third ERTS Symposium* (Washington, DC: NASA SP 351 I), 309–317.

Russo, N., Robinson, T., Fazio, G., and Aldwinckle, H. (2007). Field evaluation of 64 apple rootstocks for orchard performance and fire blight resistance. *HortScience* 42, 1517–1525. doi: 10.21273/hortsci.42.7.1517

Semmens, K. A., Anderson, M. C., Kustas, W. P., Gao, F., Alfieri, J. G., McKee, L., et al. (2016). Monitoring daily evapotranspiration over two California vineyards using Landsat 8 in a multi-sensor data fusion approach. *Remote Sens. Environ.* 185, 155–170. doi: 10.1016/j.rse.2015.10.025

Serra, I., Strever, A., Myburgh, P. A., and Deloire, A. (2014). Review: the interaction between rootstocks and cultivars (*Vitis vinifera* L.) to enhance drought tolerance in grapevine. *Aust. J. Grape Wine Res.* 20, 1–14. doi: 10.1111/ajgw.12054

Shackel, K., Ahmadi, H., Biasi, W., Buchner, R., Godhamer, D., Gurusinghe, S., et al. (1997). Plant water status as an index of irrigation need in deciduous fruit trees. *HorTechnology* 7, 23–29. doi: 10.21273/horttech.7.1.23

Shafian, S., Rajan, N., Schnell, R., Bagavathiannan, M., Valasek, J., Shi, Y., et al. (2018). Unmanned aerial systems-based remote sensing for monitoring sorghum growth and development. *PLoS One* 13:e0196605. doi: 10.1371/journal.pone.0196605

Shuttleworth, W. J., and Wallace, J. S. (1985). Evaporation from sparse crops-an energy combination theory. *Q. J. R. Meteorol. Soc.* 111, 839–855. doi: 10.1002/qj.49711146510

Solari, L. I., Johnson, S., and DeJong, T. M. (2006). Relationship of water status to vegetative growth and leaf gas exchange of peach (*Prunus persica*) trees on different rootstocks. *Tree Physiol.* 26, 1333–1341. doi: 10.1093/treephys/26.10.1333

Torrecillas, A., Ruiz-Sanchez, M. C., Leon, A., and del Amor, F. (1989). The response of Young almond tres to different drip-irrigated conditions. Development and yield. *J. Horticult. Sci.* 64, 1–7. doi: 10.1080/14620316.1989.11515920

Treutter, D., and Feucht, W. (1991). Accumulation of phenolic compounds above the graft union of cherry trees. *Gartenbauwissenschaft* 56, 134–137.

Vargas, F., Romero, M., Clavé, J., Vergés, J., Santos, J., and Batlle, I. (2008). 'Vayro', 'Marinada', 'Constantí', and 'Tarraco' Almonds. *HortScience* 43, 535–537. doi: 10.21273/HORTSCI.43.2.535

Virlet, N., Lebourgeois, V., Martinez, S., Costes, E., Labbé, S., and Regnard, J. L. (2014). Stress indicators based on airborne thermal imagery for field phenotyping a heterogeneous tree population for response to water constraints. *J. Exp. Bot.* 65, 5429–5442. doi: 10.1093/jxb/eru309

Weiss, M., and Baret, F. (2016). *S2ToolBox Level 2 products: LAI, FAPAR, FCOVER—Version 1.1. Sentin. ToolBox Level2 Products*. 53. Available online at: https://step.esa.int/docs/extra/ATBD_S2ToolBox_L2B_V1.1.pdf (accessed July 20, 2020).

Wu, C., Niu, Z., Tang, Q., and Huang, W. (2008). Estimating chlorophyll content from hyperspectral vegetation indices: modeling and validation. *Agric. For. Meteorol.* 148, 1230–1241. doi: 10.1016/j.agrformet.2008.03.005

Xarxa Agrometeorològica de Catalunya (XAC), and Servei Meteorològic de Catalunya. (2020). Available online at: https://www.ruralcat.net/web/guest/agrometeo.estacions (accessed March 10, 2020).

Xia, T., Kustas, W. P., Anderson, M. C., Alfieri, J. G., Gao, F., McKee, L., et al. (2016). Mapping evapotranspiration with high-resolution aircraft imagery over vineyards using one-and two-source modeling schemes. *Hydrol. Earth Syst. Sci.* 20, 1523–1545. doi: 10.5194/hess-20-1523-2016

Xie, Q., Dash, J., Huang, W., Peng, D., Qin, Q., Mortimer, H., et al. (2018). "Vegetation indices combining the red and red-edge spectral information for leaf area index retrieval," in *IEEE Journal of selected topics in applied earth observations and remote sensing*, (New York, NY: IEEE), 1939–1404.

Xiloyannis, C., Dichio, B., Tuzio, A. C., Kleinhentz, M., Salesses, G., Gomez-Aparisi, J., et al. (2007). Characterization and selection of prunus rootstocks resistant to abiotic stresses: waterlogging, drought and Iron chlorosis. *Acta Hortic.* 732, 247–251. doi: 10.17660/actahortic.2007.732.35

Yahmed, J. B., Ghrab, M., and Mimoun, M. B. (2016). Eco-physiological evaluation of different scion-rootstock combinations of almond grown in Mediterranean conditions. *Fruits* 71, 185–193. doi: 10.1051/fruits/2016003

Yan, G., Hu, R., Luo, J., Weiss, M., Jiang, H., Mu, X., et al. (2019). Review of indirect optical measurements of leaf area index: recent advances, challenges, and perspectives. *Agricult. Forest Meteorol.* 265, 390–411. doi: 10.1016/j.agrformet.2018.11.033

Zarco-Tejada, P. J., Diaz-Varela, R., Angilera, V., and Loudjani, P. (2014). Tree height quantification using very high resolution imagery acquired from an unmanned aerial vehicle (UAV) and automatic 3D photo-reconstruction methods. *Eur. J. Agron.* 55, 89–99. doi: 10.1016/j.eja.2014.01.004

Zhang, L., Marguerit, E., Rossdeutsch, L., Ollat, N., and Gambetta, G. (2016). The influence of grapevine rootstock on scion and drought resistance. *Theor. Exp. Plant Physiol.* 28, 143–157. doi: 10.1007/s40626-016-0070-x

Conflict of Interest: The authors declare that the research was conducted in the absence of any commercial or financial relationships that could be construed as a potential conflict of interest.

frontiers in Plant Science

ORIGINAL RESEARCH
published: 17 March 2021
doi: 10.3389/fpls.2021.595030

Transpiration Rate of White Clover (*Trifolium repens* L.) Cultivars in Drying Soil

*Lucy Egan[1,2], Rainer Hofmann[2], Shirley Nichols[3], Jonathan Hadipurnomo[2] and Valerio Hoyos-Villegas[4]**

[1] AgResearch Lincoln Research Centre, Christchurch, New Zealand, [2] Faculty of Agriculture and Life Sciences, Lincoln University, Lincoln, New Zealand, [3] AgResearch Ruakura Research Centre, Hamilton, New Zealand, [4] Faculty of Agricultural and Environmental Sciences, McGill University, Montreal, QC, Canada

Determining the performance of white clover cultivars under drought conditions is critical in dry climates. However, comparing the differences in cultivar performance requires equivalent soil water content for all plants, to reduce the water deficit threshold eliciting stomatal closure. In this study, the objective was to compare the rate of stomatal closure in eighty white clover cultivars in response to soil drying. Two glasshouse experiments were conducted, and the daily transpiration rate was measured by weighing each pot. The transpiration rate of the drought-stressed plants were normalized against the control plants to minimize effects from transpiration fluctuations and was recorded as the normalized transpiration rate (NTR). The daily soil water content was expressed as the fraction of transpirable soil water (FTSW). The FTSW threshold (FTSWc) was estimated after which the NTR decreases linearly. The FTSWc marks the critical point where the stomata start to close, and transpiration decreases linearly. The significant difference ($p < 0.05$) between the 10 cultivars with the highest and lowest FTSWc demonstrates the cultivars would perform better in short- or long-term droughts.

Keywords: transpiration, normalized transpiration rate, fraction of transpirable soil water, white clover, drought tolerance, abiotic stress tolerance

OPEN ACCESS

Edited by:
Ankush Prashar, Newcastle University, United Kingdom

Reviewed by:
Dimitrios Fanourakis, Technological Educational Institute of Crete, Greece
Xinquan Zhang, Sichuan Agricultural University, China

***Correspondence:**
Valerio Hoyos-Villegas
valerio.hoyos-villegas@mcgill.ca

Specialty section:
This article was submitted to Plant Breeding, a section of the journal Frontiers in Plant Science

Received: *14 August 2020*
Accepted: *17 February 2021*
Published: *17 March 2021*

Citation:
Egan L, Hofmann R, Nichols S, Hadipurnomo J and Hoyos-Villegas V (2021) Transpiration Rate of White Clover (Trifolium repens L.) Cultivars in Drying Soil. Front. Plant Sci. 12:595030. doi: 10.3389/fpls.2021.595030

INTRODUCTION

White clover is the most important pastoral legume in temperate regions of the world and is usually grown in companion with ryegrass (Caradus et al., 1989). The pasture mix of ryegrass and white clover is common in a variety of grazing systems, including sheep and beef, deer, and dairy. Globally, white clover is an attractive plant to have in pastoral systems due to the nitrogen fixation ability and the resulting role in sustainable farming systems. White clover is economically important to New Zealand and fixes approximately 1.57 million tons of nitrogen annually (Caradus et al., 1996). New Zealand has the highest export share of white clover globally (57.5%), exporting approximately 4500 tons of white clover seed annually (Rattray, 2005). In a more recent report by Nixon (2016), the estimated direct and dependent industry GDP total contribution from white and red clover was ∼$2.3billion. The domestic impact was ∼$1.5million and the export impact was

Abbreviations: NTR, Normalized transpiration rate; FTSW, Fraction of transpirable soil water; VPD, Vapor pressure deficit; ISH, Interspecific hybrid.

∼$6.3million. Pyke et al. (2004) used data from Nas (2003) and estimated that in 2002, New Zealand had a 38% share of the global white clover seed production market. Hampton et al. (2012) stated in 2010 and 2011, 3108, and 3745 tons of white clover seed were produced in New Zealand.

Globally, drought stress is one of the major limiting factors in white clover performance in pastoral systems. Climate change predictions show that there will be a global increase in temperature of 4.5–18°C over the next century; increasing drought periods globally (Fischlin et al., 2007; IPCC, 2013). With the expansion of farming into arid geographic areas, climate change and increased water restrictions, there has been more urgency to breed and utilize cultivars that can perform under drought stress (Jahufer et al., 2013).

There have been several studies investigating the response of white clover to drought conditions (Thomas, 1984; Annicchiarico and Piano, 2004; Bermejo et al., 2006; Li et al., 2013). Thomas (1984) showed that the competitiveness of white clover in a sward is reduced significantly in drought-stressed environments which impacts severely on farm production.

Recurring droughts in New Zealand have increased farm management challenges for farmers. There have been many studies aimed at increasing performance in drought through agronomic practices (van den Bosch et al., 1993; Widdup and Barrett, 2011). Although there has been little success in breeding drought tolerance white clover cultivars, differing grazing management schemes can aid in protecting the plants under drought conditions (Brock, 1988).

White clover cultivars need to be exposed to the same drought condition to make accurate assumptions on differences of phenotypic performance in drought (Tuberosa, 2012). In a field trial environment, phenotypic differences in performance can be due to differences in water regimes. Other measures of drought tolerance are needed to accurately determine the performance of plants in drought conditions (Sinclair and Ludlow, 1986; Weisz et al., 1994; Ray and Sinclair, 1997, 1998).

Selecting genotypes that are conservative in water use is a selection strategy to increase drought tolerance (Ray and Sinclair, 1997, 1998; Giday et al., 2013; Fanourakis et al., 2015). Traits such as normalized transpiration rate (NTR) and fraction of transpirable soil water (FTSW) can be used to determine cultivars or families that perform better in drought-like conditions (Lecoeur and Sinclair, 1996; Ray and Sinclair, 1997, 1998; Miller, 2000). Short-term drought is defined as being less than 6 months, while long-term drought is defined as longer than 6 months (Dziegielewski, 2003). Transpiration rate is controlled by stomatal closure (Ray and Sinclair, 1997, 1998). Genotypes that are more sensitive to drought will close their stomata earlier to preserve soil water content and may perform better in long-period drought conditions as water-conserving efforts occur earlier. Genotypes that have late stomatal closure may be better suited for short-period drought conditions.

Currently, there is limited published literature on calculating the NTR and FTSW critical threshold (FTSWc) of white clover cultivars in drying soil. This study aims to build on previous reports of FTSWc in plant species (Sinclair and Ludlow, 1986; Weisz et al., 1994; Lecoeur and Sinclair, 1996; Ray and Sinclair, 1998; Gholipoor et al., 2013). We used a panel of 80 white clover cultivars to determine the FTSWc, marking permanent stomatal closure and the start of senescence.

METHODOLOGY

Germplasm

The 80 cultivars used in this study were the same as in Hoyos-Villegas et al. (2019) and were released from 1920 to 2010 by both public and private breeding programs. The cultivars were from across New Zealand, Australia, United Kingdom, and the United States of America. The cultivars ranged in leaf size from small (N = 1), to medium (N = 53), and to large (N = 26) (**Table 1**).

NTR and FTSW Trial Design

Two glasshouse experiments were conducted at AgResearch, Lincoln, New Zealand in the summer months (December–February). The data was from both trials were combined and analyzed together. The first experiment ran for 14 days (09/12/2016–22/12/2016) after planting. Weather and glasshouse data for that period showed that the average temperature was 22.39°C, the average relative humidity was 57.00% and the average total daily solar radiation was 24.39MJ/m^2. The second experiment ran for 19 days (02/02/2017–20/02/2017) after planting. The average temperature was 22.79°C, the average relative humidity was 56.51% and the average total daily solar radiation was 19.82 MJ/m^2. The average vapor pressure deficits for each experiment are reported in **Figures 1A,B**. The weather station was not equipped to measure sunshine hours.

The 80 cultivars were exposed to two treatments, irrigated (control) and drought, and replicated twice (technical replicates) in a randomized complete block design. Four stolons (biological replicates) were potted individually in potting mix in 4L pots and grown in a glasshouse with the optimum temperature of 20–25°C maintained. The pots were arranged in a 4 × 80 pot arrangement across 8 glasshouse tables. The plant stolons were cut and transplanted from trays and were young plants. Stolons from mother plants were cut after 3 weeks of growth. Vegetative growth is the primary way that white clover survives under natural conditions after it loses its taproot in the first year. We utilized stolons to emulate growth after the second year of growth under field conditions. The irrigated pots were watered with the exact amount of water that had transpired. Ten bare pots were used to measure water loss through evaporation. The pots were watered to container capacity and then left to drain and sealed on the bottom with duct tape. The saturated weight of each pot was recorded. Daily measurements of soil water content, measured as the weight of each pot, and the amount of water transpired, measured as the difference in pot weight, were recorded. The drought treatment ceased once the cultivars had died.

Dry weight was measured by the harvesting the roots and shoots together and weighed as total plant weight. The samples were dried at 80°C for 12 h and weighed (g) until a constant weight was reached. The leaf size used was the commercially stated leaf size associated with the cultivar.

TABLE 1 | The cultivar names, the decade of release, countries of release, registered leaf sizes, dry weights of the drought and irrigated treatments and the critical fraction of transpirable soil water (FTSWc) threshold of eighty white clover cultivars.

Cultivar	Decade of release	Country of origin	Leaf size	Dry weight drought	Dry weight irrigated	FTSWc
$LSD_{(0.05)}$				1.99	1.99	2.02
Dutch white	1920	Netherlands	Medium	13.58	17.75	0.23
Irrigation	1930	Australia	Medium	18.63	20.78	/
Kent White	1930	UK	Small	16.85	26.28	0.17
Louisiana	1930	USA	Medium	17.78	29.08	0.25
S 100	1930	UK	Medium	18.73	20.70	0.35
Kersey	1940	UK	Medium	21.55	28.68	/
S 184	1940	UK	Medium	17.18	23.05	0.28
California Ladino	1950	USA	Large	15.65	23.18	/
Grasslands Huia	1950	NZ	Medium	17.45	25.95	0.36
Ladino Gitante Lodigiano	1950	USA	Large	23.33	27.40	/
Louisiana S1	1950	USA	Medium	20.53	26.25	/
Pilgrim	1950	USA	Medium	17.35	29.25	0.28
Sonja	1950	Sweden	Large	18.70	23.30	0.33
Tribla	1950	Belgium	Medium	13.70	21.38	0.42
Clarence	1960	Australia	Medium	15.88	19.83	0.22
Crau	1960	France	Medium	16.43	22.38	/
Haifa	1960	Israel	Medium	14.95	22.35	0.38
Regal	1960	USA	Large	13.80	20.23	/
Donna	1970	UK	Medium	13.75	19.78	0.37
Lune de mai	1970	France	Large	17.28	24.23	0.21
Milkanova	1970	Denmark	Medium	17.18	24.13	0.26
Olwen	1970	UK	Large	15.08	21.88	/
Pitau	1970	NZ	Medium	14.00	19.20	0.48
Radi	1970	Poland	Large	15.85	24.23	0.23
Sacramento	1970	Poland	Large	15.85	21.48	0.49
Siral	1970	Australia	Medium	15.25	18.35	/
Alice	1980	UK	Medium	14.18	19.38	0.36
Aran	1980	Ireland	Large	13.30	22.78	/
Kopu	1980	NZ	Large	17.05	21.93	/
Lirepa	1980	Germany	Medium	17.65	22.83	0.34
Menna	1980	UK	Medium	12.23	21.90	0.39
Merwi	1980	Belgium	Medium	15.35	22.33	0.37
Osceola	1980	USA	Medium	12.93	17.20	0.42
Ross	1980	Ireland	Large	16.75	24.95	0.40
AberHerald	1990	UK	Medium	14.13	22.25	0.12
Challenge	1990	NZ	Medium	14.40	21.40	0.27
Crescendo Ladino	1990	USA	Large	12.88	19.75	0.32
Dacia	1990	Romania	Large	16.53	26.03	0.28
Jumbo	1990	USA	Medium	18.80	24.00	0.20
Kopu II	1990	NZ	Large	14.33	20.80	0.34
Le Bons	1990	NZ	Medium	16.10	18.80	0.24
Prop	1990	NZ	Medium	14.20	23.00	0.34
Regal Graze	1990	USA	Large	18.15	28.40	/
Reisling	1990	Netherlands	Medium	15.75	22.75	0.30
Sustain	1990	NZ	Medium	16.05	17.50	0.32
Triffid	1990	France	Large	16.23	24.30	0.30
Waverley	1990	Australia	Large	12.93	22.53	/
AberConcord	2000	UK	Medium	15.95	23.13	0.20
AberDance	2000	UK	Medium	17.88	22.65	0.35
AberNormous	2000	UK	Large	16.78	21.58	0.26

(Continued)

TABLE 1 | Continued

Cultivar	Decade of release	Country of origin	Leaf size	Dry weight drought	Dry weight irrigated	FTSWc
Aquiles	2000	Uruguay	Medium	20.50	24.40	0.13
Artigas	2000	Uruguay	Large	16.10	22.90	/
Barblanca	2000	France	Medium	15.75	25.08	0.27
Bounty	2000	NZ	Medium	12.53	20.43	0.47
Chieftain	2000	Ireland	Medium	17.25	21.40	0.17
Crusader	2000	France	Medium	15.60	16.40	/
Emerald	2000	NZ	Medium	15.98	20.78	0.33
Goliath	2000	Uruguay	Large	17.95	26.58	0.17
Klondike	2000	Denmark	Medium	13.95	25.33	/
Kotare	2000	NZ	Large	14.65	19.45	0.42
Quest	2000	NZ	Medium	13.95	20.95	0.33
Saracen	2000	Australia	Medium	15.28	24.20	0.27
Super Haifa	2000	Australia	Medium	15.93	21.75	0.24
Super Ladino	2000	Australia	Large	17.10	22.98	0.18
Tasman	2000	NE	Medium	13.48	21.80	0.30
Tillman II	2000	USA	Large	16.80	23.15	0.28
Tribute	2000	NZ	Medium	16.48	21.05	0.52
Trophy	2000	Australia	Medium	10.65	11.23	/
Vysocan	2000	Czech	Large	15.33	21.93	/
ABM21252	2010	NZ	Large	17.33	24.25	0.18
Calimero	2010	USA	Medium	17.93	22.50	/
Dairy B GC276	2010	Australia	Medium	16.18	21.58	/
Dairy D	2010	NZ	Medium	21.53	26.08	0.18
Elite Breeding A	2010	Australia	Medium	18.05	24.73	0.24
Kakariki	2010	NZ	Large	18.08	25.93	/
Katy	2010	USA	Medium	18.70	21.28	0.24
Legacy	2010	NZ	Large	18.15	27.98	0.29
Mainstay	2010	NZ	Medium	18.40	26.95	0.29
Quartz	2010	NZ	Medium	16.53	23.58	0.24
Weka	2010	NZ	Medium	18.75	25.98	0.18

$LSD_{0.05}$ is presented for the dry weights of the irrigated and drought cultivars and the FTSWc. The "/" denotes that the FTSW threshold was unable to be calculated for the cultivar because of the irregularities in the data for curve generation. Abbreviations: NZ, New Zealand; UK, United Kingdom; USA, United States of America.

Calculations

Vapor pressure deficit (VPD) was calculated using the formula in Conaty et al. (2014):

$$VPD = e_s - e_a$$

where VPD is the difference between ambient water vapor (e_a) and the saturated vapor pressure (e_s) at the same temperature. The air temperature (T_a in °C) and relative humidity (RH in %) where:

$$e_s = 0.6108e\left(\frac{17.27T_a}{T_a + 237.3}\right)$$

$$e_a = \left(\frac{RH}{100}\right)e_s$$

The transpiration data were analyzed by the methodology described in Ray and Sinclair (1997).

The transpiration rate (TR) was calculated using the formula:

$$TR = \frac{Weight\ of\ drought\ pot}{Weight\ of\ control\ pot}$$

where the soil water content and amount of water transpired were normalized against the control pots.

The NTR was calculated using the formula:

$$NTR = \frac{TR}{Day\ 3\ and\ 5\ average\ TR}$$

The transpiration values were normalized against the days 3 and 5 average TR to minimize the effects of fluctuations in transpiration. The TR on days 3 and 5 are considered to be under well-watered conditions (Sinclair and Ludlow, 1986), allowing the plants to have an average NTR near-equal to one when sufficient soil water was available.

FTSW was calculated using the formula:

$$Daily\ FTSW = \frac{(Daily\ pot\ weight - Final\ pot\ weight)}{(Initial\ pot\ weight - Final\ pot\ weight)}$$

where the initial and final pot weights were the first and last day of the trials.

The relationship between the transpiration value and FTSW of each cultivar was explained by using non-linear regression to fit

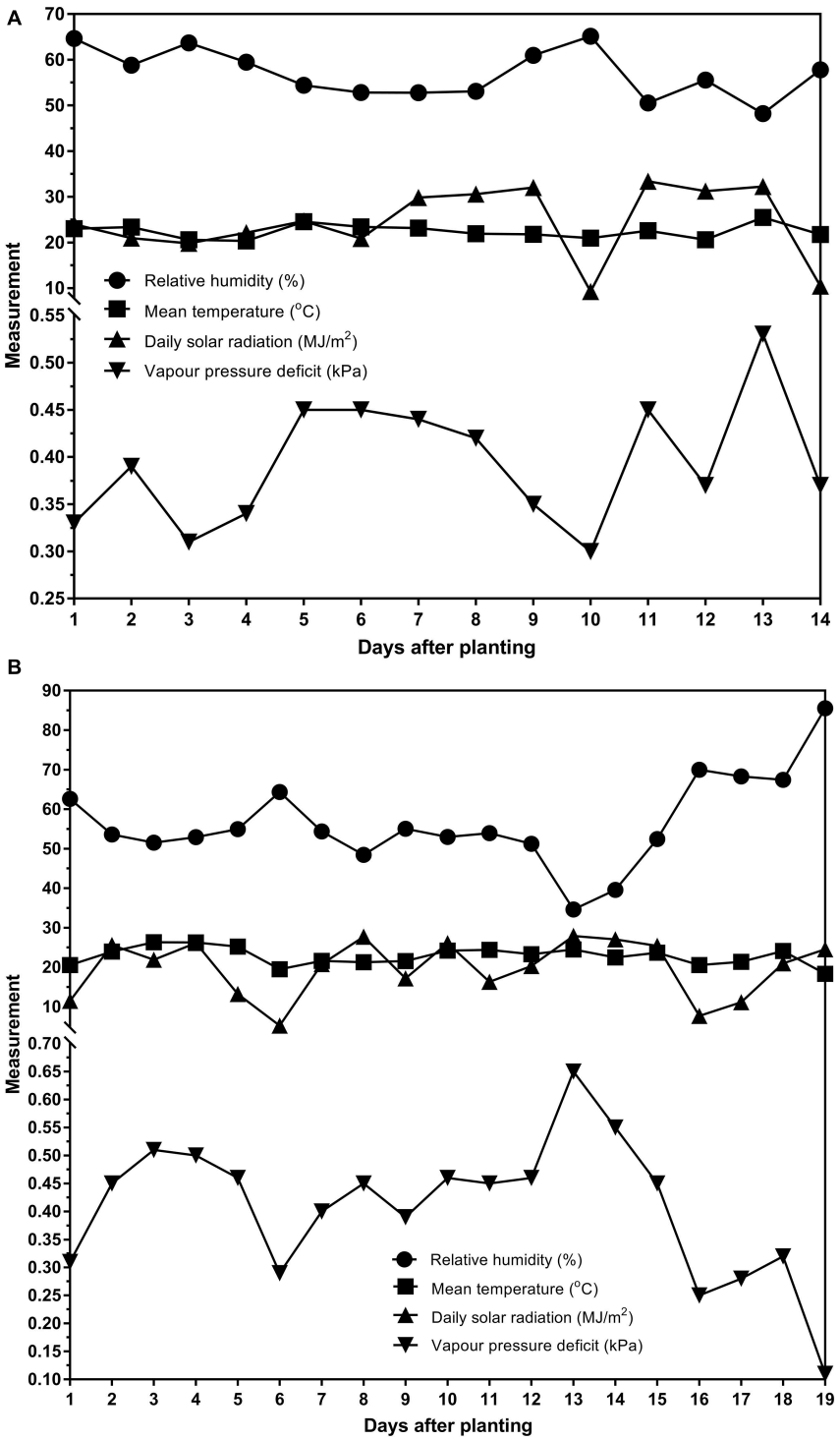

FIGURE 1 | The relative humidity (%), mean temperature (°C), daily solar radiation (MJ/m^2) and vapor pressure deficit (kPa) for the **(A)** 14 days of the first experiment (09/12/2016–22/12/2016) and **(B)** 19 days of the second experiment (02/02/2017–20/02/2017).

the equation:

$$NTR = \frac{1}{[1 + A \times exp(B \times FTSW)]}$$

Comparisons of the curve generated for each cultivar were based on 95% confidence intervals of coefficients *A* and *B*. *A* and *B* were empiric parameters generated through curve fitting. Plateau regression was used to determine the FTSWc. The curve predicts

that NTR will remain near 1 up until a critical point, after which NTR decreases. The FTSWc is estimated, where NTR decreases linearly after that. The FTSWc marks the critical point where the stomata start to close, and transpiration decreases linearly.

Statistical Analysis

ANOVA in GenStat (VSN-International, 2019) examined the main effects of water and cultivar, as well as their interaction. Before ANOVA, data were tested for homogeneity of variances and no transformation of the data was required.

A linear spline model was used to analyze the trend of the FTSWc over decades. Since the average trend showed a linear increase from 1920 up to 1960, then, changed into a decrease after 1960, the trend pattern was modeled as a linear spline model with a single knot at 1965. The linear spline trend model was estimated in regression by the formula:

$$Inflection\ point\ =\ a + b\ \times\ Time + c\ x\ Time\_2$$

where *Time* is a variable representing the decades in order, *Time_2* is a variable also representing decades in non-sequential order, and *a*, *b* and *c* are parameters to be estimated. In this formula, the increasing trend up to 1960 was estimated as a positive *b* value—i.e., *b* = increasing rate per decade till 1960, while the decreasing trend after 1960 was estimated as the sum of $b + c$, which should be a negative value—i.e., the absolute value of $b + c$ = decreasing rate per decade after 1960. In addition, since the value of *c* indicated the difference of two trend slopes (one till 1960 and the other after 1960), the significance level (*p*-value) associated with *c* indicated if the change of the trend from the increase to the decrease was statistically significant.

Duncans lettering was used to indicate groups that are significantly different at the 5% significance level (Duncan, 1955).

RESULTS

Dry Weights

The average total plant dry weight for drought and irrigated plants was 16.27 and 22.70 g, respectively. The plant total dry matter weights ranged from 11.23 to 29.25 g for control plants and 10.65 g and 23.32 for drought plants (**Table 1**). There was a significant overall difference ($p < 0.01$) in the dry weights of the cultivars when averaged across the two water treatments (**Figures 2A,B**; Duncan, 1955). The average dry weight of medium-leaved cultivars was highest between 1930 and 1950. The medium-leaved cultivars released in the 1920s were significantly different from all other groups for drought and irrigated plant dry weight (**Supplementary Tables 1**, **2**). The large-leaved cultivars released in the 1950s and 1960s were significantly different from all other groups for drought plant dry weight (**Supplementary Table 1**). The cultivar and drought interaction was not significant.

Shoot to root ratio was unable to be calculated as only total plant weight was recorded. However, in future experiments the effect of drought on shoot to root ratio would be beneficial.

Transpiration Rate, NTR, and FTSW

No significant difference ($P > 0.05$) in the average transpiration rate data between leaf size was found. There was a significant difference ($P < 0.05$) in the average transpiration rate data between the decade of cultivar release. Over the decades, the average NTR decreased from 1920 (0.84) to 1940 (0.78) before increasing to the peak in the 1960s (0.92) (**Figure 3A**). There was a decrease to 1980 (0.82), followed by a slight increase in the 1990s (0.84). The average NTR decreased in 2000 (0.81) before an increase in 2010 (0.83).

A consistent relationship was found between NTR and FTSW values for each cultivar, as illustrated in **Figure 4** by the cultivars Tribute and Chieftain (**Figures 4A,B**). On average among all cultivars, the NTR value was equivalent to well-watered plants until the FTSWc reached 0.29. The NTR value decreased linearly to 0 below an FTSW value of 0.29. Generally, there was no decrease in NTR until FTSW reached 0.7. The average number of days until the end of transpiration for the NTR was 9.95 and 14.48 for the FTSW. The FTSW values ranged from 0.11 to 0.50, with an average of 0.29.

Stomatal Closure

Plateau regression was used to determine the FTSW value where the stomata permanently closed. The average FTSWc across the decades had an increasing trend from 1920 (0.23) to 1960 (0.38) (**Figure 2B**). There was a slight decrease in the 1970s (0.34) before it increased back to 0.38 in the 1980s. From the 1980s to 2010, there is a general decreasing trend until 2010 (0.23). The trend in the decade of release and FTSWc had an r^2-value of 0.81. The *P*-value of 0.016 associated with parameter *b* indicated that the FTSWc value statistically significantly increased on average at a rate of 0.0329 (with a standard error of 0.013) per decade until 1960 (**Supplementary Table 3**). Then, the *P*-value of 0.002 associated with parameter *c* indicated that the increasing trend changed statistically significantly downwards after 1960. The *P*-value of 0.001 associated with the sum of parameters $b + c$, indicated that the FTSWc value statistically significantly decreased on average at a rate of 0.0307 (with standard error of 0.0089) per decade after 1960.

There was a significant ($P < 0.001$) difference between the 10 cultivars with the highest and lowest FTSWc (**Figure 5**). The five cultivars with the lowest FTSW were AberHerald (0.12), Aquiles (0.13), Kent White (0.17), Goliath (0.17), and Chieftain (0.17). The five cultivars with the highest FTSW were Kotare (0.44), Bounty (0.47), Pitau (0.48), Sacramento (0.49), and Tribute (0.52).

DISCUSSION

FTSW Threshold

The objective of this study was to evaluate the response of 80 white cultivars to drying soil. The results of this experiment are similar to previous reports (Muchow and Sinclair, 1991). The transpiration rate in plant species has shown to be unaffected by drying soil until the FTSWc decreases to between approximately 0.25 and 0.35 (Ritchie, 1973;

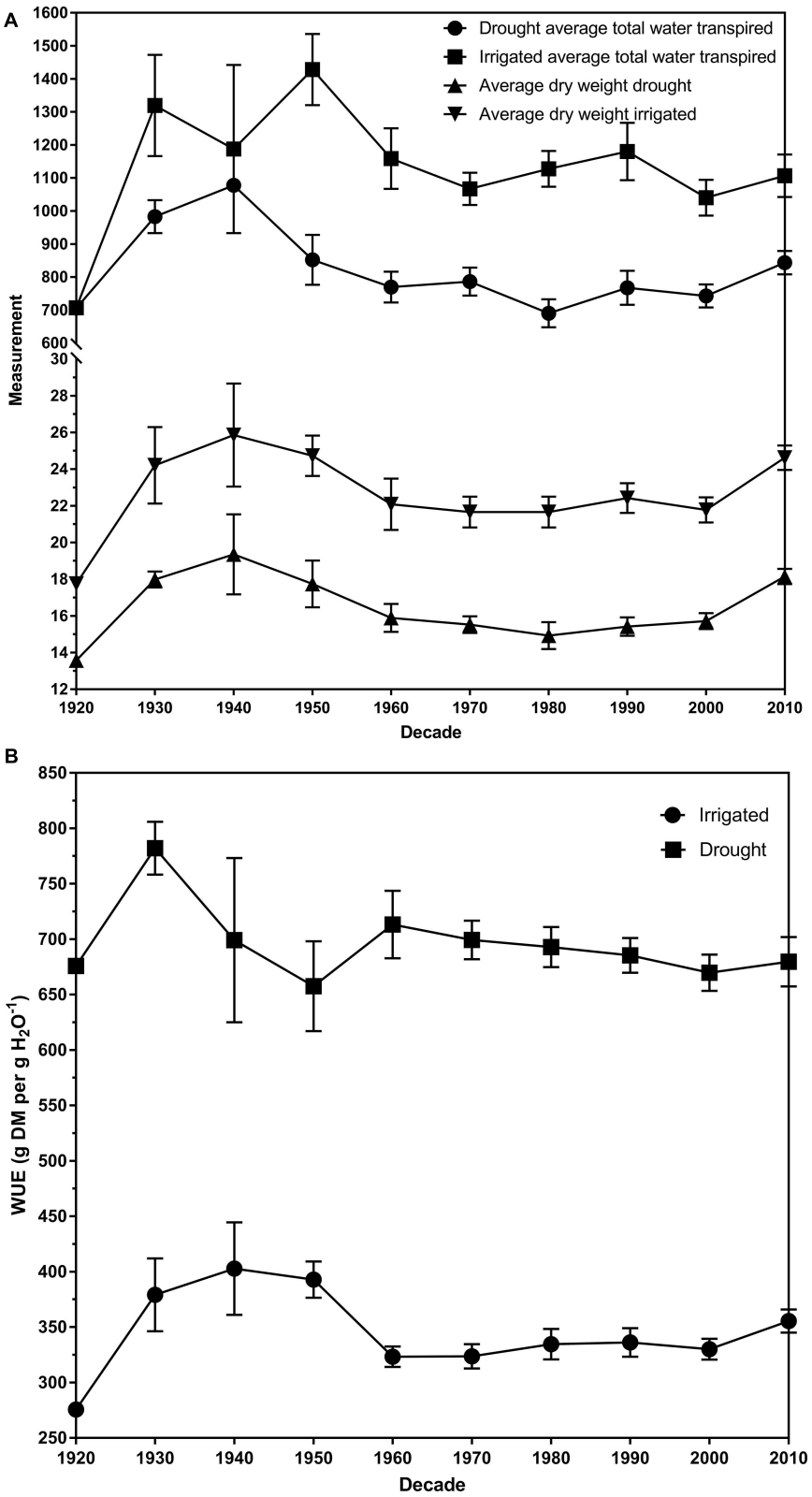

FIGURE 2 | (A) The dry weights and transpiration rates for drought and irrigated plants for eighty white clover cultivars per decade of release. **(B)** The average water use efficiency (WUE) of drought and irrigated plants for eighty white clover cultivars per decade of release expressed as gram of dry matter per gram of water (g DM per g H_20^{-1}). The error bars are the standard error of the means. All data was averaged across the two biological replicates.

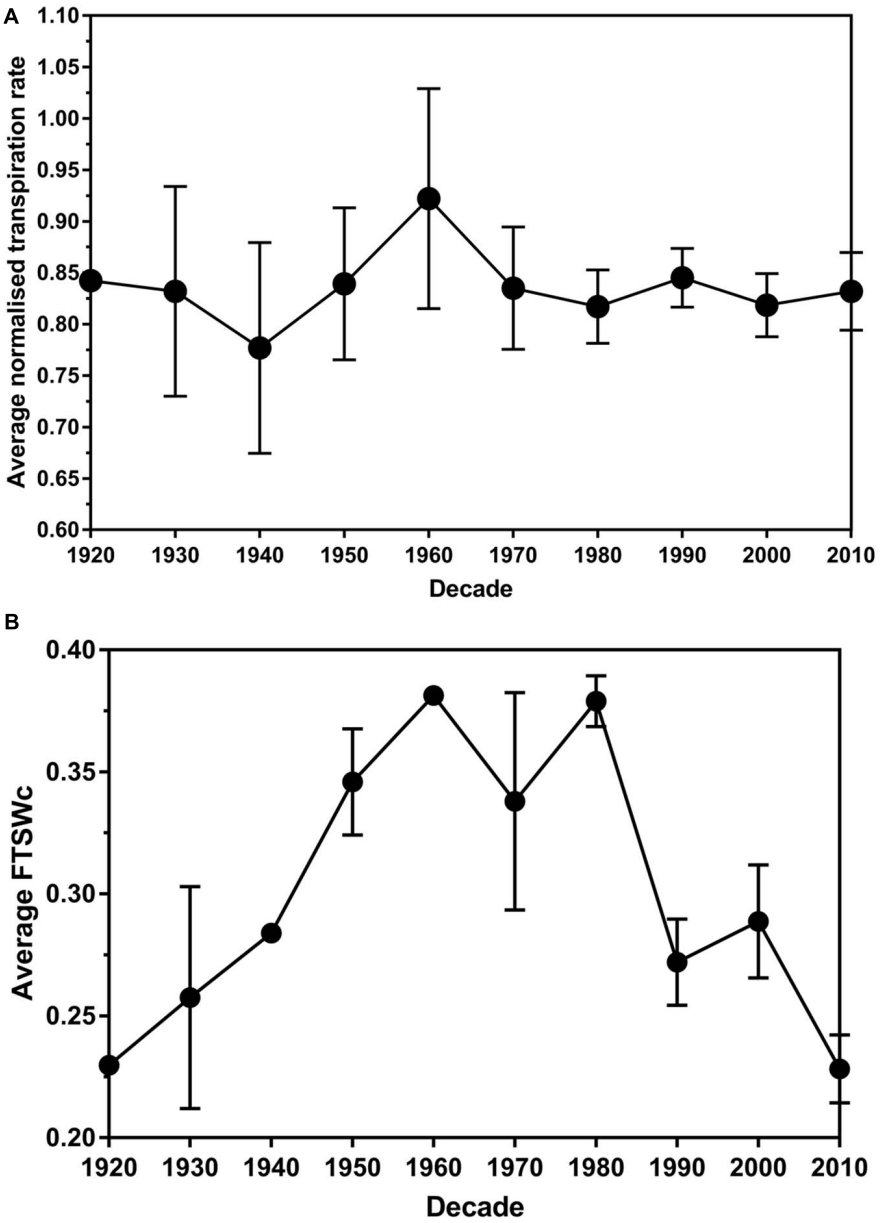

FIGURE 3 | The average normalized transpiration rate **(A)** and critical fraction of transpirable soil water threshold (FTSWc) **(B)** per decade of release for eighty white clover cultivars. The error bars are the standard error of the means.

Meyer and Green, 1981; Sinclair and Ludlow, 1986; Rosenthal et al., 1987; Lecoeur and Sinclair, 1996; Ray and Sinclair, 1997, 1998; Miller, 2000; Gholipoor et al., 2013). The dependency of NTR and FTSW is shown through similar patterns of the NTR-FTSW relationship. The fact that the average FTSW in 1920 was similar to the average FTSW in 2010 suggests that breeding efforts have not implicated the relationship. Regardless of the decade of the release of the cultivar, the response to drought is similar.

White clover breeding in the 1900–1950s is documented most thoroughly in New Zealand compared to Europe and the United States (Zeven, 1991). The large majority of the understanding of white clover genetics and diversity and the effect of selection techniques began in the mid-1960s and onwards (Williams, 1987; Williams et al., 2007). Hoyos-Villegas et al. (2019) showed that breeding progress of white clover cultivars could be divided into two eras; pre- and post-1965. There were significant increases in white clover sward content and dry matter yield after 1965, but not pre-1965. The results in this study were consistent with the results found by Hoyos-Villegas et al. (2019) as the significant increase and decrease of FTSWc could be divided into the same two eras; pre- and-post 1965.

Prior to 1965, the breeding decisions for white clover breeding programs were based on increasing the performance of ecotypes

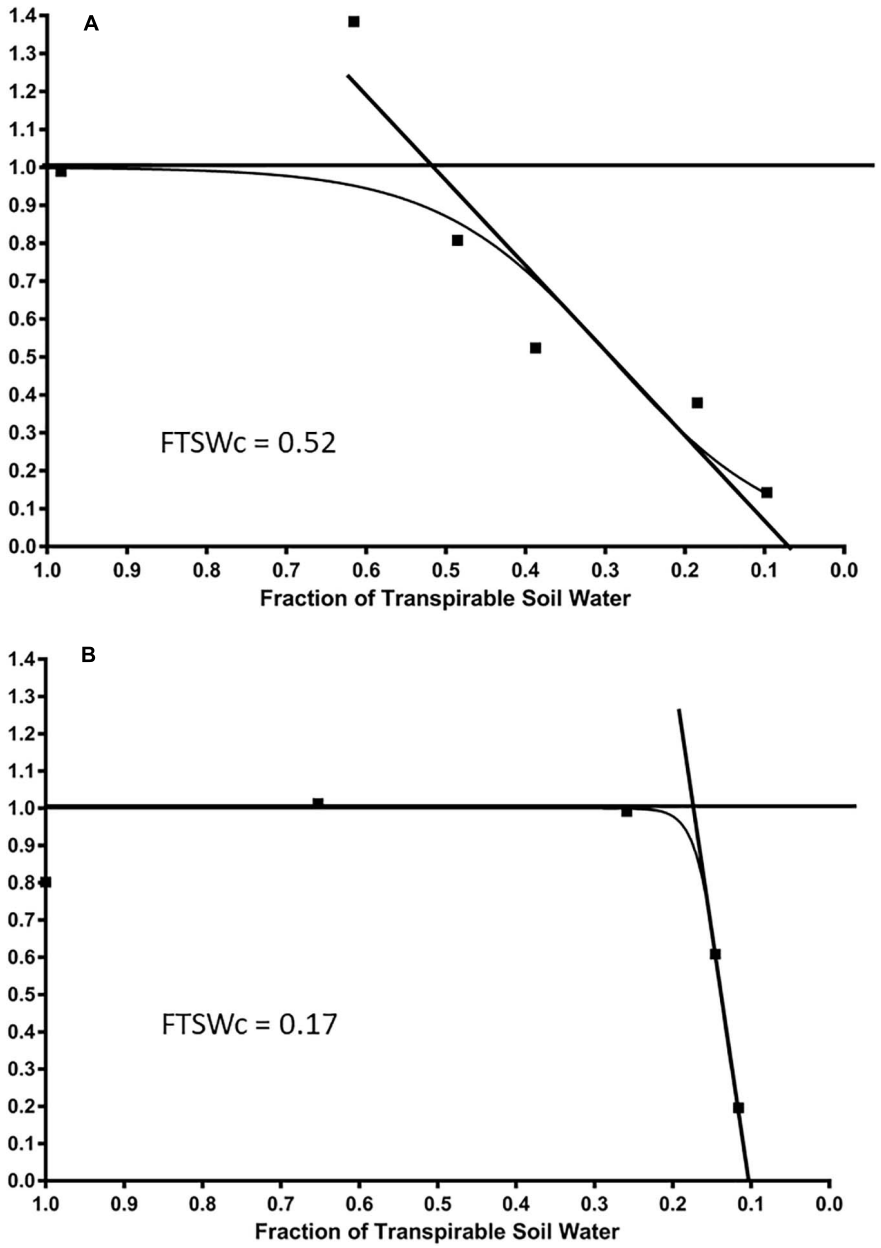

FIGURE 4 | The average daily normalized transpiration rate (NTR) response to the fraction of transpirable soil water (FTSW) of two white clover cultivars, **(A)** Tribute, released in 2000, and **(B)** Chieftain, released in 2000, that show contrasting FTSWc. The FTSWc where NTR begins to decrease are shown.

and existing cultivars, and simple phenotypic selection. The breeding programs and trials were performed across multiple regions and trial sites, and populations were selected for broad adaptation across a range of farming systems (Williams et al., 2007). The breeding programs relied on the variation that was present within countries and local environments, as there was little germplasm exchange between countries. Cultivars bred post-1965 utilized foreign germplasm and selection techniques such as recurrent phenotypic selection and wide hybridization (Ellis and Young, 1967; Williams, 2014). In the 1980s in New Zealand, a large and stable clover seed export market had been established. The cultivars that were exported were bred through a variety of techniques. Local ecotypes and local populations were utilized for adaptation to the target environment, and elite breeding populations were incorporated for a range of desirable traits. The populations were combined and evaluated through phenotypic selection methods (Caradus and Christie, 1998). The introduction of mixed swards to evaluate populations and grazing animals as a selection pressure occurred after 1965 (Woodfield and Caradus, 1994). It is possible that the breeding objectives of production-based traits took priority and tied with the intensification of agriculture, reduced the

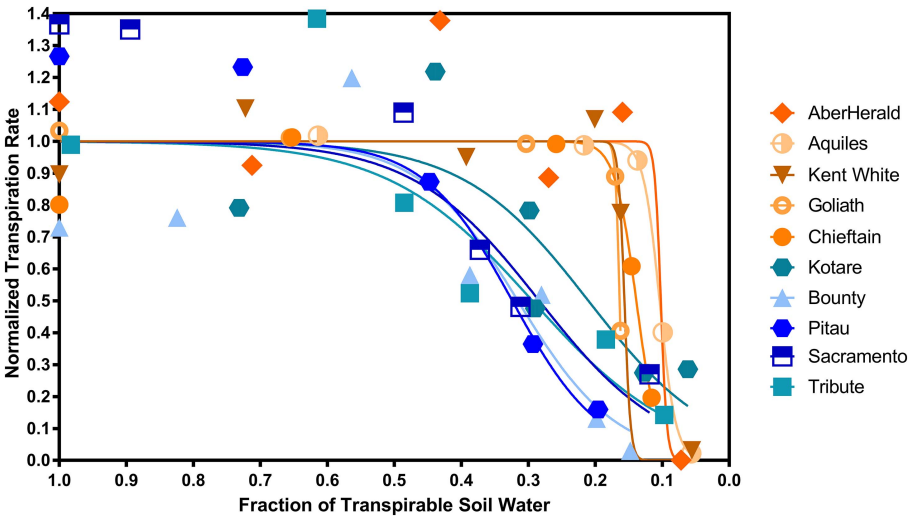

FIGURE 5 | The five highest and five lowest fraction of transpirable soil water thresholds (FTSWc) for eighty white clover cultivars. The cultivars with the highest FTSWc (Kotare, Bounty, Pitau, Sacramento, and Tribute) are denoted in blue, while the cultivars with the lowest FTSW threshold (AberHerald, Aquiles, Kent White, Goliath, and Chieftain) are denoted in orange.

drought tolerance of germplasm. Understanding the history of white clover breeding will inform future breeding decisions and increase efficiency of germplasm utilization.

Globally, germplasm exchange increased to widen the genetic base of populations in the later 1900s. Egan et al. (2019a,b) showed that in white and red clover, the introduction of foreign germplasm into the MFGC peaked in the 1970s and 1980s. By the 1980s, large-scale multi-country breeding programs were established (Williams et al., 2007). It is estimated that exotic germplasm used since the mid-1960s has contributed ~$1 billion annually to the pastoral agricultural exports (Lancashire, 2006). The characterization of the germplasm and new methods of utilizing the foreign germplasm could be expected to increase the performance of white clover germplasm (Williams et al., 2007; Egan et al., 2019a).

However, although foreign germplasm has been utilized effectively worldwide (Rumball and Armstrong, 1974), the world checklists of white clover cultivars show that the large majority of the cultivars with good tolerance to drought and heat were released before 1965 (Caradus, 1986; Caradus and Woodfield, 1997). The rankings could suggest that locally adapted germplasm has outperformed foreign germplasm for drought tolerance. Conversely, germplasm collected from the Mediterranean has been used in breeding programs to produce cultivars with increased winter-growth activity (Cooper et al., 1997; Woodfield et al., 2001; Ayres et al., 2007).

Throughout the decades of breeding, different breeding goals have been the focus of breeding programs. Caradus et al. (1989) summarized the breeding goals for each decade of white clover breeding in New Zealand. The early programs focussed on advancing ecotypes and existing cultivars. In comparison, the later breeding programs focussed on whole plant production and the integration of different farm and grazing management practices. The only decade to focus specifically on physiological and morphological responses to environmental changes was the 1950s, where it is likely that drought tolerance was integrated into cultivars released. A focal breeding target in the 1970s was on the productivity. The lack of statistical significance difference between the average FTSW and the leaf size of cultivars suggests that all cultivars perform similarly under drought conditions. However, these results suggest that certain cultivars may be better utilized in certain environments and farming systems, i.e., short- and long-term droughts. Although the differences between the cultivars are not deemed statistically significant, the implications of a small difference in the NTR-FTSW relationship and FTSWc can be important knowledge for field conditions. Similarly, Barbour et al. (1996) assessed the water use efficiency of ten white clover cultivars under moisture stress and found that there was there were no significant differences between the cultivars. Although statistical significance was not found, the results are biologically relevant and could be utilized in different farming environments.

Understanding the relationship between drought tolerance and persistence will be beneficial for further development of cultivars (Sanderson et al., 2003). Persistence is defined as the maintenance of long-term agronomic yield and is a function of stolon growth and density (Williams, 1987; Annicchiarico and Piano, 2004). Drought is one of the main persistence-limiting traits (Bouton, 2012). Drought conditions limit white clover stolon branching and rooting (Chapman, 1983), and higher stolon density is often associated with superior water conservation (Collins, 1998). The success of a forage cultivar is largely dependent on the ability to survive summer droughts and retain productivity (Annicchiarico et al., 2011; Pecetti et al., 2011). Drought tolerance and stolon density can increase persistence. Hutchinson et al. (1995) carried out a 30 year study of environmental factors affecting the persistence of white clover and found that drought stress in late summer was

the most critical limiting factor. Belaygue et al. (1996) saw an 80% decrease in stolon density when rainfall decreased by 30%. In orchardgrass, Saeidnia et al. (2018) noted that drought-tolerant genotypes had high persistence and Saeidnia et al. (2016) showed that drought conditions reduced forage yield and persistence.

Traditional breeding methods, such as phenotypic selection, have been the most common in white clover breeding programs (Hoyos-Villegas et al., 2018). Selecting for deeper and more extensive rooting systems is a common breeding strategy. However, the correlation between root depth and drought tolerance remains unclear. The results from studies which analyzed the association of rooting depth and drought tolerance are mixed. Caradus (1981) reported that germplasm with larger leaf size and rooting system outperformed germplasm with smaller root systems. Large-leaved cultivars are often characterized by low stolon density, compared to small-leaved cultivars which have high stolon density (Widdup and Barrett, 2011). However, Barbour et al. (1996) found no significant difference between the market class of the cultivar and the performance under drought conditions. Selecting for a deeper root system is convoluted by the rooting pattern of white clover. A taproot is present for the early life of the plant (12–18 months) and afterward is replaced with a shallow nodal root system (Pederson, 1989). Caradus and Woodfield (1986) found that the cultivar with the highest proportion of root to total plant weight did not have a large proportion of taproot to total root weight, suggesting that some nodal roots were more "tap rooted." Annicchiarico and Piano (2004) proposed an alternative in selecting for greater rooting systems by selecting for thicker stolons and found that the plants with thicker stolons had increased root dry weight.

Drought Tolerance in White Clover

Photosynthesis is the critical process that influencing plant performance. Under drought stress, plants close stomata to conserve water, reducing photosynthesis. Stomatal conductance can be influenced by plant anatomy in long term drought (Xu and Zhou, 2008). Plant cultivars with smaller stomata have been reported to have a higher rate of gas exchange and faster stomatal response times. Faster stomatal response times can reduce the impact of drought to plants (Drake et al., 2013). This experiment gives an objective measurement of white clover cultivar transpiration rates and the critical FTSW threshold at which each cultivar begins to have permanent stomatal closure. This deepens the understanding of the expected response of cultivars to drought-like conditions.

A low FTSWc suggests that the cultivar can sustain normal transpiration for a longer period in soils with less available water implying that it would perform advantageously under short-period drought conditions, compared to cultivars with a high FTSW (Ray and Sinclair, 1997). However, He and Dijkstra (2014) found that drought stress had a stronger negative effect on plant nitrogen and phosphorus concentrations in short-term droughts compared to long-term droughts. AberHerald had the lowest FTSWc of the eighty cultivars. AberHerald is a medium leaved cultivar originating from Wales, United Kingdom. It performs well in cold environments, ensuring good stolon survival over winter. Helgadóttir et al. (2001) showed that AberHerald showed morphological adaptation to more marginal climates. AberHerald has good stolon survival and rapid stolon recovery after grazing (Rhodes and Webb, 1993). Other cultivars with a low FTSWc have high persistence under grazing (Charlton and Giddens, 1983; Widdup et al., 2006).

A high FTSWc proposes that the cultivar can perform better in long-period drought conditions as they conserve water stores by closing their stomata early (Ray and Sinclair, 1997). Tribute had the highest FTSWc value (0.52) of the eighty cultivars. Tribute is a medium-leaved cultivar bred from germplasm from New Zealand and Europe and was initially bred through a breeding program for increased drought tolerance in Australia. Woodfield et al. (2003) noted that Tribute had good drought performance in the third year of a grazing trial in Canterbury. Whilst Widdup and Barrett (2011) found that Tribute produced a greater number of stolons and stolon density than other cultivars of medium leaf size.

Generally, the cultivars released pre-1965 have a higher FTSWc than the cultivars post-1965. A high FTSWc could imply an increase in persistence in the cultivar. **Figures 2A,B** illustrate the relationship between average total water transpired and the average dry weights of drought and irrigated exposed plants. All three measurements follow the same trend; a peak in 1940 and decreasing to 1980, before increasing to 2010. The increase in transpiration and dry weights is supported by the study by Hoyos-Villegas et al. (2019). They found that in the same panel of 80 white clover cultivars, dry matter increased more than clover content post-1965, implying that persistence had decreased in post-1965 cultivars. Clover content, the amount of clover present in a sward, is a measurement often used to infer persistence. We could conclude that the stomatal behavior of white clover cultivars has shifted the major agronomic of persistence.

Canopy Wilting

The underlying mechanisms of drought-tolerant phenotypes are vast. Canopy wilting is one of the first signs of drought stress caused by soil water deficits (Kunert and Vorster, 2020). In soybean, the slow-wilting phenotype was first reported in a Japanese landrace (Sloane et al., 1990) and the development of slow-wilting genotypes has enabled selection for breeding (Sinclair et al., 2010). The development of genotypes with delayed canopy wilting phenotypes have been studied thoroughly in soybean and in several plant introductions, and could lead to increased yield stability in drought conditions (Steketee et al., 2020). Simulations have suggested if the phenotype was bred into populations, yield in drought conditions could improve by >80% (Sinclair et al., 2010). However, the physiological mechanisms controlling the slow-wilting phenotype remain uncertain. Failure to understand the mechanisms will constrain breeding efforts.

Recent studies have shown some understanding of the underlying genetic architecture of the slow-wilting phenotype. Quantitative trait loci (QTLs) have been identified for canopy wilting (Abdel-Haleem et al., 2012; Ye et al., 2020) and it has been concluded that it is a polygenic trait (Charlson et al., 2009).

A recent study by Kaler et al. (2017) has identified SNPs associated with canopy-wilting that are located within or close to genes with connections to transpiration or water transport. Devi et al. (2015) analyzed gene expression in the leaves of two slow-wilting accessions and showed that 944 genes were differentially expressed in one accession compared to the other. More recently, Steketee et al. (2020) used a GWAS to identify 45 marker-trait associations with canopy wilting and as a result, several new accessions were identified with the slow-wilting phenotype. Although the research into the slow-wilting phenotype has primarily been performed in soybean, other crops, such as cowpea [*Vigna unguiculata* (L.) Walp], have utilized the phenotype to identify accessions with increased drought tolerance (Pungulani, 2014).

The utilization of a slow-wilting phenotype in white clover could increase the performance under drought conditions. Although the cultivars in this study have been characterized by FTSWc under drought conditions, germplasm exploration to identify accessions with a slow-wilting phenotype is needed to accelerate breeding efforts (Barbour et al., 1996).

CONCLUSION

The results from this study highlight the variable rates of stomatal closure for eighty white clover cultivars. The relationship between NTR and FTSW is consistent for all cultivars, regardless of the decade of release. Cultivars that have a significantly higher or lower FTSWc have been identified and have deepened the knowledge of the cultivar response to drought conditions, follow up studies focusing on stomatal characteristics of contrasting genotypes would be a natural next step. The white clover ISH program shows promise for increasing drought tolerance but further replicated trials are needed to assess performance. The increasing demand for cultivars to perform under extreme conditions in response to climate change requires more research into the genetic and phenotypic basis of drought traits and how these can be incorporated into breeding programs.

DATA AVAILABILITY STATEMENT

The raw data supporting the conclusions of this article will be made available by the authors, without undue reservation.

AUTHOR CONTRIBUTIONS

VH-V conceived the project and designed the experiments. LE and JH analyzed the data, prepared figures, and manuscript. RH and SN contributed with revisions, comments, and writing. All authors contributed to the article and approved the submitted version.

FUNDING

Funding was provided by the AgResearch internal investment funds.

ACKNOWLEDGMENTS

We thank Chikako van Koten (AgResearch) for help provided with the statistical analyses and Portia Crabtree for conducting the glasshouse work.

SUPPLEMENTARY MATERIAL

The Supplementary Material for this article can be found online at: https://www.frontiersin.org/articles/10.3389/fpls.2021.595030/full#supplementary-material

REFERENCES

Abdel-Haleem, H., Carter, T. E., Purcell, L. C., King, C. A., Ries, L. L., Chen, P., et al. (2012). Mapping of quantitative trait loci for canopy-wilting trait in soybean (*Glycine max* L. Merr). *Theor. Appl. Genet.* 125, 837–846. doi: 10.1007/s00122-012-1876-9

Annicchiarico, P., Pecetti, L., Bouzerzour, H., Kallida, R., Khedim, A., Porqueddu, C., et al. (2011). Adaptation of contrasting cocksfoot plant types to agricultural environments across the Mediterranean basin. *Environ. Exp. Bot.* 74, 82–89. doi: 10.1016/j.envexpbot.2011.05.002

Annicchiarico, P., and Piano, E. (2004). Indirect selection for root development of white clover and implications for drought tolerance. *J. Agron. Crop Sci.* 190, 28–34. doi: 10.1046/j.0931-2250.2003.00070.x

Ayres, J., Caradus, J., Murison, R. D., Lane, L., and Woodfield, D. (2007). Grasslands Trophy - a new white clover (*Trifolium repens* L.) cultivar with tolerance of summer moisture stress. *Aust. J. Exp. Agric.* 47, 110–115. doi: 10.1071/EA04029

Barbour, M., Caradus, J., Woodfield, D., and Silvester, W. (1996). "Water stress and water use efficiency of ten white clover cultivars," in *'White Clover: New Zealand's Competitive Edge'*, ed. D. R. Woodfield (Palmerston North: Special Publication - Agronomy Society of New Zealand), 159–162.

Belaygue, C., Wery, J., Cowan, A., and Tardieu, F. (1996). Contribution of leaf expansion, rate of leaf appearance, and stolon branching to growth of plant leaf area under water deficit in white clover. *Crop Sci.* 36, 1240–1246. doi: 10.2135/cropsci1996.0011183X003600050028x

Bermejo, R., Irigoyen, J. J., and Santamaría, J. M. (2006). Short—term drought response of two white clover clones, sensitive and tolerant to O_3. *Physiol. Plant.* 127, 658–669. doi: 10.1111/j.1399-3054.2006.00695.x

Bouton, J. (2012). Breeding lucerne for persistence. *Crop Pasture Sci.* 63, 95–106. doi: 10.1071/CP12009

Brock, J. (1988). Evaluation of New Zealand bred white clover cultivars under rotational grazing and set stocking with sheep. *Proc. N. Z. Grassl. Assoc.* 49, 203–206. doi: 10.33584/jnzg.1988.49.1819

Caradus, J. (1986). World checklist of white clover varieties. *N. Z. J. Exp. Agric.* 14, 119–164. doi: 10.1080/03015521.1986.10426137

Caradus, J., Brock, J., and Hay, M. (1989). Fifty years of white clover research in New Zealand. *Proc. N. Z. Grassl. Assoc.* 50, 25–39. doi: 10.33584/jnzg.1989.50.1868

Caradus, J., and Christie, B. (1998). Winter hardiness and artificial frost tolerance of white clover ecotypes and selected breeding lines. *Can. J. Plant Sci.* 78, 251–255. doi: 10.4141/P96-147

Caradus, J., and Woodfield, D. (1986). "Evaluation of root type in white clover genotypes and populations," in *Proceedings of the DSIR Plant Breeding Symposium 1986. Agronomy Society of New Zealand Special Publication no 5*, Lincoln, OR, 322–325.

Caradus, J., and Woodfield, D. (1997). World checklist of white clover varieties II. *N. Z. J. Agric. Res.* 40, 115–206. doi: 10.1080/00288233.1997.9513239

Caradus, J. R. (1981). Root growth of white clover (*Trifolium repens* L.) lines in glass–fronted containers. *N. Z. J. Agric. Res.* 24, 43–54. doi: 10.1080/00288233.1981.10420870

Caradus, J. R., Woodfield, D. R., and Stewart, A. V. (1996). "Overview and vision for white clover," in *White Clover: New Zealand's Competitive Edge. Spec. Publ. 11. Agron. Soc. New Zealand*, ed. D. R. Woodfield (Palmerston North: New Zealand Grassland Association), 1–6.

Chapman, D. F. (1983). Growth and demography of *Trifolium repens* stolons in grazed hill pastures. *J. Appl. Ecol.* 20, 597–608. doi: 10.2307/2403529

Charlson, D. V., Bhatnagar, S., King, C. A., Ray, J. D., Sneller, C. H., Carter, T. E., et al. (2009). Polygenic inheritance of canopy wilting in soybean [*Glycine max* (L.) Merr.]. *Theor. Appl. Genet.* 119, 587–594. doi: 10.1007/s00122-009-1068-4

Charlton, J., and Giddens, N. (1983). Establishment of hill country white clover selections from oversowing. *Proc. N. Z. Grassl. Assoc.* 44, 149–155.

Collins, R. P. (1998). "The effect of drought stress and winter stress on the persistence of white clover," in *Proceedings of FAO/CIHEAM Lowland Grasslands Sub-Network Meeting*, Eds G. Fisher and B. E. Frankow-Lindberg (La Coruña: FAO).

Conaty, W. C., Mahan, J. R., Neilsen, J. E., and Constable, G. A. (2014). Vapour pressure deficit aids the interpretation of cotton canopy temperature response to water deficit. *Funct. Plant Biol.* 41, 535–546. doi: 10.1071/FP13223

Cooper, B., Clifford, P., and Williams, W. (1997). Development of white clover (Trifolium repens L.) cultivar Grasslands challenge (G23). *Proc. Conf. N. Z. Grassl. Assoc.* 59, 99–102. doi: 10.33584/jnzg.1997.59.2272

Devi, M. J., Sinclair, T. R., and Taliercio, E. (2015). Comparisons of the effects of elevated vapor pressure deficit on gene expression in leaves among two fast-wilting and a slow-wilting soybean. *PLoS One* 10:e0139134. doi: 10.1371/journal.pone.0139134

Drake, P. L., Froend, R. H., and Franks, P. J. (2013). Smaller, faster stomata: scaling of stomatal size, rate of response, and stomatal conductance. *J. Exp. Bot.* 64, 495–505. doi: 10.1093/jxb/ers347

Duncan, D. B. (1955). Multiple range and multiple F tests. *Biometrics* 11, 1–42. doi: 10.2307/3001478

Dziegielewski, B. (2003). "Long-term and short-term measures for coping with drought," in *Tools for Drought Mitigation in Mediterranean Regions. Water Science and Technology Library*, eds G. Rossi, A. Cancelliere, L. S. Pereira, T. Oweis, M. Shatanawi, and A. Zairi (Dordrecht: Springer), 319–339.

Egan, L. M., Hofmann, R. W., Barrett, B. A., Ghamkhar, K., and Hoyos-Villegas, V. (2019a). Identification of founding accessions and patterns of relatedness and inbreeding derived from historical pedigree data in a white clover germplasm collection in New Zealand. *Crop Sci.* 59, 2087–2099. doi: 10.2135/cropsci2018.11.0688

Egan, L. M., Hofmann, R. W., Ghamkhar, K., and Hoyos-Villegas, V. (2019b). Identification of founding accessions and patterns of relatedness and inbreeding derived from historical pedigree data in a red clover germplasm collection in New Zealand. *Crop Sci.* 59, 2100–2108. doi: 10.2135/cropsci2019.01.0045

Ellis, W., and Young, N. R. (1967). The characteristics of European, Mediterranean and other populations of white clover (*Trifolium repens* L.). *Euphytica* 16, 330–340. doi: 10.1007/BF00028939

Fanourakis, D., Giday, H., Milla, R., Pieruschka, R., Kjaer, K. H., Bolger, M., et al. (2015). Pore size regulates operating stomatal conductance, while stomatal densities drive the partitioning of conductance between leaf sides. *Ann. Bot.* 115, 555–565. doi: 10.1093/aob/mcu247

Fischlin, A., Midgley, G. F., Price, J. T., Leemans, R., Gopal, B., Turley, C. M., et al. (2007). "Ecosystems, their properties goods and services," in *Climate Change 2007: Impacts, Adaptation and vulnerability. Contribution of Working Group II to the Fourth Assessment Report of the Intergovernmental Panel on Climate Change*, eds M. L. Parry, J. P. Canziani, J. P. Palutikof, P. J. van der Linden, and C. E. Hanson (Cambridge: Cambridge University Press), 211–272.

Gholipoor, M., Sinclair, T., Raza, M., Löffler, C., Cooper, M., and Messina, C. (2013). Maize hybrid variability for transpiration decrease with progressive soil drying. *J. Agron. Crop Sci.* 199, 23–29. doi: 10.1111/j.1439-037X.2012.00530.x

Giday, H., Kjaer, K. H., Fanourakis, D., and Ottosen, C.-O. (2013). Smaller stomata require less severe leaf drying to close: a case study in *Rosa hydrida*. *J. Plant Physiol.* 170, 1309–1316. doi: 10.1016/j.jplph.2013.04.007

Hampton, J., Rolston, M., Pyke, N. B., and Green, W. (2012). Ensuring the long term viability of the New Zealand seed industry. *Agron. Soc. N. Z.* 42, 129–140.

He, M., and Dijkstra, F. A. (2014). Drought effect on plant nitrogen and phosphorus: a meta−analysis. *New Phytol.* 204, 924–931. doi: 10.1111/nph.12952

Helgadóttir, Á, Dalmannsdóttir, S., and Collins, R. P. (2001). Adaptational changes in white clover populations selected under marginal conditions. *Ann. Bot.* 88, 771–780. doi: 10.1006/anbo.2001.1438

Hoyos-Villegas, V., Arief, V., Yang, W.-H., Sun, M., DeLacy, I., Barrett, B., et al. (2018). QuLinePlus: extending plant breed-ing strategy and genetic model simulation to cross-polli-nated populations: case studies in forage breeding. *Heredity* 122, 684–695. doi: 10.1038/s41437-018-0156-0

Hoyos-Villegas, V., O'Connor, J., Heslop, A., Hilditch, A., Jahufer, M., and Barrett, B. (2019). Rate of genetic gain for persistence to grazing and dry matter yield in white clover across 90 years of cultivar development. *Crop Sci.* 59, 537–552. doi: 10.2135/cropsci2018.07.0471

Hutchinson, K., King, K., and Wilkinson, D. (1995). Effects of rainfall, moisture stress, and stocking rate on the persistence of white clover over 30 years. *Aust. J. Exp. Agric.* 35, 1039–1047. doi: 10.1071/EA9951039

IPCC (2013). "Climate change 2013: the physical science basis," in *Contribution of Working Group I to the Fifth Assessment Report of the Intergovernmental Panel on Climate Change*, eds T. F. Stocker, D. Qin, G.-K. Plattner, M. Tignor, S. K. Allen, J. Boschung, et al. (Cambridge: Cambridge University Press).

Jahufer, M. Z. Z., Ford, J. L., Widdup, K. H., Harris, C., Cousins, G., Ayres, J. F., et al. (2013). Improving white clover for Australasia. *Crop Pasture Sci.* 63, 739–745. doi: 10.1071/CP12142

Kaler, A. S., Ray, J. D., Schapaugh, W. T., King, C. A., and Purcell, L. C. (2017). Genome-wide association mapping of canopy wilting in diverse soybean genotypes. *Theor. Appl. Genet.* 130, 2203–2217. doi: 10.1007/s00122-017-2951-z

Kunert, K., and Vorster, B. J. (2020). In search for drought-tolerant soybean: is the slow-wilting phenotype more than just a curiosity? *J. Exp. Bot.* 71:457. doi: 10.1093/jxb/erz235

Lancashire, J. (2006). "The importance of exotic germplasm to the NZ livestock industry. Breeding for success: diversity in action," in *Proceedings of the 13th Australasian Plant Breeding Conference*, Christchurch, 1034–1041.

Lecoeur, J., and Sinclair, T. R. (1996). Field pea transpiration and leaf growth in response to soil water deficits. *Crop Sci.* 36, 331–335. doi: 10.2135/cropsci1996.0011183X003600020020x

Li, Z., Peng, Y., and Ma, X. (2013). Different response on drought tolerance and post-drought recovery between the small-leafed and the large-leafed white clover (*Trifolium repens* L.) associated with antioxidative enzyme protection and lignin metabolism. *Acta Physiol. Plant.* 35, 213–222. doi: 10.1007/s11738-012-1066-z

Meyer, W., and Green, G. (1981). Plant indicators of wheat and soybean crop water stress. *Irrig. Sci.* 2, 167–176. doi: 10.1007/BF00257978

Miller, G. L. (2000). Physiological response of bermudagrass grown in soil amendments during drought stress. *HortScience* 35, 213–216. doi: 10.21273/HORTSCI.35.2.213

Muchow, R., and Sinclair, T. (1991). Water deficit effects on maize yields modeled under current and "greenhouse" climates. *Agron. J.* 83, 1052–1059. doi: 10.2134/agronj1991.00021962008300060023x

Nas, M. (2003). "A global perspective on future trends and opportunities in herbage seed markets," in *Proceedings of the 5th International Herbage Seed Conference*, Gatton, 1–9.

Nixon, C. (2016). *How Valuable is that Plant Species? Application of a Method for Enumerating the Contribution of Selected Plant Species to New Zealand's GDP*. Wellington: Ministry for Primary Industries.

Pecetti, L., Annicchiarico, P., Abdelguerfi, A., Kallida, R., Mefti, M., Porqueddu, C., et al. (2011). Response of Mediterranean tall fescue cultivars to contrasting agricultural environments and implications for selection. *J. Agron. Crop Sci.* 197, 12–20. doi: 10.1111/j.1439-037X.2010.00443.x

Pederson, G. (1989). Taproot and adventitious root growth of white clover as influenced by nitrogen nutrition. *Crop Sci.* 29, 764–768. doi: 10.2135/cropsci1989.0011183X002900030045x

Pungulani, L. L. M. (2014). *Exploring the Genetic Potential of Locally Adapted Germplasm for Drought Tolerance: A Case for Cowpea (Vigna unguiculata* (L.)) Walp) from Malawi. Doctoral thesis, Massey University, Palmerston North.

Pyke, N., Rolston, P., and Woodfield, D. R. (2004). National and export trends in herbage seed production. *Proc. N. Z. Grassl. Assoc.* 66, 95–102.

Rattray, P. V. (2005). in *Clover Management, Research, Development & Extension in the New Zealand Pastoral Industries*, ed. M. o. P. Industry Wellington: M. o. P. Industry.

Ray, J. D., and Sinclair, T. R. (1997). Stomatal closure of maize hybrids in response to drying soil. *Crop Sci.* 37, 803–807. doi: 10.2135/cropsci1997.0011183X003700030018x

Ray, J. D., and Sinclair, T. R. (1998). The effect of pot size on growth and transpiration of maize and soybean during water deficit stress. *J. Exp. Bot.* 49, 1381–1386. doi: 10.1093/jxb/49.325.1381

Rhodes, I., and Webb, K. J. (1993). Improvement of white clover. *Outlook Agric.* 22, 189–194. doi: 10.1177/003072709302200310

Ritchie, J. T. (1973). Influence of soil water status and meteorological conditions on evaporation from a corn canopy. *Agron. J.* 65, 893–897. doi: 10.2134/agronj1973.00021962006500060014x

Rosenthal, W., Arkin, G., Shouse, P., and Jordan, W. (1987). Water deficit effects on transpiration and leaf growth. *Agron. J.* 79, 1019–1026. doi: 10.2134/agronj1987.00021962007900060014x

Rumball, W., and Armstrong, C. (1974). The performance of overseas ryegrass cultivars in New Zealand. *Proc. N. Z. Grassl. Assoc.* 36, 97–104.

Saeidnia, F., Majidi, M. M., Mirlohi, A., and Ahmadi, B. (2018). Physiological responses of drought tolerance in orchardgrass (*Dactylis glomerata*) in association with persistence and summer dormancy. *Crop Pasture Sci.* 69, 515–526. doi: 10.1071/CP17314

Saeidnia, F., Majidi, M. M., Mirlohi, A., and Shahidaval, S. (2016). Selection for productivity, persistence and drought tolerance in orchardgrass. *Euphytica* 212, 111–130. doi: 10.1007/s10681-016-1776-1

Sanderson, M., Byers, R., Skinner, R., and Elwinger, G. (2003). Growth and complexity of white clover stolons in response to biotic and abiotic stress. *Crop Sci.* 43, 2197–2205. doi: 10.2135/cropsci2003.2197

Sinclair, T., and Ludlow, M. (1986). Influence of soil water supply on the plant water balance of four tropical grain legumes. *Funct. Plant Biol.* 13, 329–341. doi: 10.1071/PP9860329

Sinclair, T. R., Messina, C. D., Beatty, A., and Samples, M. (2010). Assessment across the United States of the benefits of altered soybean drought traits. *Agron. J.* 102, 475–482. doi: 10.2134/agronj2009.0195

Sloane, R. J., Patterson, R. P., and Carter, T. E. Jr. (1990). Field drought tolerance of a soybean plant introduction. *Crop Sci.* 30, 118–123. doi: 10.2135/cropsci1990.0011183X003000010027x

Steketee, C. J., Schapaugh, W. T., Carter, T. E., and Li, Z. (2020). Genome-wide association analyses reveal genomic regions controlling canopy wilting in soybean. *G3 Genes Genomes Genetics* 10, 1413–1425. doi: 10.1534/g3.119.401016

Thomas, H. (1984). Effects of drought on growth and competitive ability of perennial ryegrass and white clover. *J. Appl. Ecol.* 21, 591–602. doi: 10.2307/2403431

Tuberosa, R. (2012). Phenotyping for drought tolerance of crops in the genomics era. *Front. Physiol.* 3:347. doi: 10.3389/fphys.2012.00347

van den Bosch, J., Black, I., Cousins, G., and Woodfield, D. (1993). Enhanced drought tolerance in white clover. *Proc. N. Z. Grassl. Assoc.* 55, 97–101.

VSN-International (2019). *Genstat for Windows*, 20th Edn. Hemel Hempstead: VSN International Ltd.

Weisz, R., Kaminski, J., and Smilowitz, Z. (1994). Water deficit effects on potato leaf growth and transpiration: utilizing fraction extractable soil water for comparison with other crops. *Am. Potato J.* 71, 829–840. doi: 10.1007/BF02849378

Widdup, K., and Barrett, B. (2011). "Achieving persistence and productivity in white clover," in *Pasture Persistence Symposium.* Grassland Research and Practice Series No. 15, ed. C. F. Mercer (Dunedin: New Zealand Grassland Association), 173–180.

Widdup, K., Garcia, J., Amadeo, J., Guillen, R., and Real, D. (2006). "White clover cultivars developed for temperate regions of South America," in *Proceedings of the 13th Australasian Plant Breeding Conference*, Christchurch, 18–21.

Williams, W. (1987). "Genetics and breeding," in *White Clover*, eds M. J. Baker and W. M. Williams (Wallingford: CAB Int), 343–420.

Williams, W. (2014). *Trifolium* interspecific hybridisation: widening the white clover gene pool. *Crop Pasture Sci.* 65, 1091–1106. doi: 10.1071/CP13294

Williams, W., Easton, H., and Jones, C. (2007). Future options and targets for pasture plant breeding in New Zealand. *N. Z. J. Agric. Res.* 50, 223–248. doi: 10.1080/00288230709510292

Woodfield, D., Clifford, P., Baird, I., Cousins, G., Miller, J., Widdup, K., et al. (2003). Grasslands Tribute: a multi-purpose white clover for Australasia. *Proc. N. Z. Grassl. Assoc.* 65, 157–162.

Woodfield, D., Clifford, P., Cousins, G., Ford, J., Baird, I., Miller, J., et al. (2001). Grasslands Kopu II and Crusader: new generation white clovers. *Proc. N. Z. Grassl. Assoc.* 63, 103–108.

Woodfield, D. R., and Caradus, J. R. (1994). Genetic improvement in white clover representing six decades of plant breeding. *Crop Sci.* 34, 1205–1213. doi: 10.2135/cropsci1994.0011183X003400050011x

Xu, Z., and Zhou, G. (2008). Responses of leaf stomatal density to water status and its relationship with photosynthesis in a grass. *J. Exp. Bot.* 59, 3317–3325. doi: 10.1093/jxb/ern185

Ye, H., Song, L., Schapaugh, W. T., Ali, M. L., Sinclair, T. R., Riar, M. K., et al. (2020). The importance of slow canopy wilting in drought tolerance in soybean. *J. Exp. Bot.* 71, 642–652. doi: 10.1093/jxb/erz150

Zeven, A. (1991). Four hundred years of cultivation of Dutch white clover landraces. *Euphytica* 54, 93–99. doi: 10.1007/BF00145635

Conflict of Interest: The authors declare that the research was conducted in the absence of any commercial or financial relationships that could be construed as a potential conflict of interest.

frontiers in Plant Science

ORIGINAL RESEARCH
published: 14 June 2021
doi: 10.3389/fpls.2021.616975

Heterotic Patterns of Temperate and Tropical Maize by Ear Photometry

*Seth A. Tolley[1], Amritpal Singh[1,2] and Mitchell R. Tuinstra[1]**

[1] Department of Agronomy, Purdue University, West Lafayette, IN, United States, [2] Advanta Seeds, College Station, TX, United States

As the plant variety protection (PVP) of commercial inbred lines expire, public breeding programs gain a wealth of genetic materials that have undergone many years of intense selection; however, the value of these inbred lines is only fully realized when they have been well characterized and are used in hybrid combinations. Additionally, while yield is the primary trait by which hybrids are evaluated, new phenotyping technologies, such as ear photometry (EP), may provide an assessment of yield components that can be scaled to breeding programs. The objective of this experiment was to use EP to describe the testcross performance of inbred lines from temperate and tropical origins. We evaluated the performance of 298 public and ex-PVP inbred lines and 274 Drought Tolerant Maize for Africa (DTMA) inbred lines when crossed to Iodent (PHP02) and/or Stiff Stalk (2FACC) testers for 25 yield-related traits. Kernel weight, kernels per ear, and grain yield predicted by EP were correlated with their reference traits with r = 0.49, r = 0.88, and r = 0.75, respectively. The testcross performance of each maize inbred line was tester dependent. When lines were crossed to a tester within the heterotic group, many yield components related to ear size and kernels per ear were significantly reduced, but kernel size was rarely impacted. Thus, the effect of heterosis was more noticeable on traits that increased kernels per ear rather than kernel size. Hybrids of DTMA inbred lines crossed to PHP02 exhibited phenotypes similar to testcrosses of Stiff Stalk and Non-Stiff Stalk heterotic groups for yield due to significant increases in kernel size to compensate for a reduction in kernels per ear. Kernels per ear and ear length were correlated (r = 0.89 and r = 0.84, respectively) with and more heritable than yield, suggesting these traits could be useful for inbred selection.

Keywords: ear photometry, heterotic groups, hybrid breeding, multivariate analysis, tropical maize, high-throughput phenotyping

OPEN ACCESS

Edited by:
Ankush Prashar, Newcastle University, United Kingdom

Reviewed by:
Bernardo Ordas, Consejo Superior de Investigaciones Científicas, Spanish National Research Council, Spain
Glenn Bryan, The James Hutton Institute, United Kingdom

***Correspondence:**
Mitchell R. Tuinstra
mtuinstr@purdue.edu

Specialty section:
This article was submitted to Plant Breeding, a section of the journal Frontiers in Plant Science

Received: *13 October 2020*
Accepted: *17 May 2021*
Published: *14 June 2021*

Citation:
Tolley SA, Singh A and Tuinstra MR (2021) Heterotic Patterns of Temperate and Tropical Maize by Ear Photometry. Front. Plant Sci. 12:616975. doi: 10.3389/fpls.2021.616975

INTRODUCTION

Maize production in the United States totaled 363.2 billion kg on 33.5 million hectares with an average yield of 10,860 kg ha^{-1} in the five growing seasons from 2015 to 2019; an incredible feat considering the nationwide average yield of 2,950 kg ha^{-1} in 1956, which was the beginning of the single-cross hybrid maize era (USDA NASS). In the early 20th century, maize was commonly grown as an open-pollinated variety and yield improvement was stagnant. Since the implementation of double-cross and subsequently single-cross hybrids, maize yields have increased at a rate of 48 and 119 kg ha^{-1}, respectively (USDA NASS). Duvick (2005) attributes about 50% of the increases in maize yields to hybrid maize breeding and the development of superior genetics, while optimized genotype placement and management practices are other key factors.

In 1970, the Plant Variety Protection Act (PVP) allowed commercial breeding programs to register varieties and inbred lines as intellectual property restricting the use, sale, and importation of this material for 20 years (Beckett et al., 2017). Inbred lines selected in commercial breeding programs are highly advanced and have undergone many rounds of intense selection. As PVPs expire, public breeding programs have access to these highly advanced inbred lines that can be used to quickly incorporate useful alleles into breeding programs. Many studies have used genomic and pedigree information to characterize ex-PVP and founder temperate inbred lines (Mikel, 2006, 2008, 2011; Mikel and Dudley, 2006; Nelson et al., 2008; White et al., 2020); however, phenotypic information describing these temperate inbred lines is less common.

Commercial maize is grown as a hybrid F_1 cross of inbred lines from divergent heterotic groups to leverage heterosis (Shull, 1908, 1909a,b, 1911, 1914; East, 1909, 1936). In the United States, maize germplasm is largely classified into three predominant heterotic groups: Stiff Stalk (SS), Non-Stiff Stalk (NS), and Iodent (IO) (Nelson et al., 2008; Beckett et al., 2017; White et al., 2020). Maize breeders exploit the heterotic pattern between these complementary heterotic groups to form hybrids with greater yield potential than their inbred parents. Inbred lines within heterotic groups have been characterized and selected for their combining ability with inbred lines from other heterotic groups. They are evaluated for their testcross rather than *per se* performance (Bernardo, 2014). To conserve the genetic diversity between heterotic groups, germplasm improvement within heterotic groups is typically limited to recycling and recombining the best inbred lines in a population through reciprocal recurrent selection (Duvick et al., 2004; Mikel, 2008). While the founding germplasm for the United States Corn Belt Dent population was large and diverse (Duvick et al., 2004), Mikel and Dudley (2006) stated that much of the current commercial germplasm can be traced back to seven progenitor inbred lines: B73, LH82, LH123, PH207, PH595, PHG39, and Mo17. Yield stagnation due to limited genetic diversity has not been evident, though researchers question whether this bottleneck could restrict future genetic gains (Holland and Goodman, 1995; Goodman, 2005; Nelson and Goodman, 2008). Incorporation of tropical germplasm is one solution to broadening genetic diversity and is a goal of many breeding programs (Uhr and Goodman, 1995a,b; Duvick et al., 2004; Henry et al., 2014). Thus, understanding the combining ability of temperate inbred lines with tropical germplasm could be an important consideration for public and private breeding programs to sustain genetic improvement of maize in the 21st century.

The International Maize and Wheat Improvement Center, CIMMYT, hybrid maize breeding program began in 1985 (Vasal et al., 1992). As a large collection of germplasm was available, the first goal of the program was to assess combining ability and empirically determine heterotic groups. Heterotic groups explored included Tuxpeño, Cuban flints, Coastal tropical flints, ETO, Tuson, Chandelle, Haitian yellow, and Perla (Vasal et al., 1999). However, concurrent development of several heterotic groups for their combining ability was difficult and was further simplified as Tuxpeño, heterotic group A (dent kernel type), and non-Tuxpeño, heterotic group B (flint kernel type) (Vasal et al., 1999; Wu et al., 2016; Cupertino-Rodrigues et al., 2020). Nevertheless, due to the relatively short-term selection of the heterotic groups, tester dependent heterotic group classification of a given line, and diversity in the base population, heterotic groups A and B can often be difficult to classify (Wu et al., 2016).

The recent emergence of high-throughput phenotyping is an important tool with the potential to relieve the bottleneck of testing programs (Furbank and Tester, 2011; Araus and Cairns, 2014; Araus et al., 2018). High-throughput phenotyping can increase the genetic gain by increasing selection intensity, phenotype repeatability, and trait heritability (Araus et al., 2018). Selection intensity is a function of the number of lines selected compared to the number of lines evaluated. With high-throughput phenotyping, larger populations can be evaluated and more stringent selection intensities can be imposed. Response to selection can be increased by minimizing the non-genetic variance by increasing phenotype repeatability and trait heritability (Bernardo, 2014). Minimizing non-genetic variance is often the case of appropriate experiment design and statistics involving blocking, randomization, and replication. High-throughput phenotyping allows for greater replication and reduced between-measurement error by removing the human-element of phenotyping. Limitations of low-throughput phenotyping methods such as its time-consuming and laborious nature, often force breeding programs to limit selection to yield evaluated in multi-environment, multi-year trials; even though the heritability of yield is among the lowest of commonly evaluated traits (Furbank and Tester, 2011). Selection based on yield components that are highly related to and more heritable than yield could be beneficial.

Phenotyping of maize yield components such as ear and kernel properties has been one of the interests for breeding programs and research geneticists. Typical yield components include kernel number, kernel weight, and ears per plant. Previous studies have used manual methods to record ear and kernel traits to dissect the genetic basis of these traits (Flint-Garcia et al., 2005; Ross et al., 2006). However, the process is time-consuming, labor-intensive and difficult to scale to large breeding programs (Cooper et al., 2014). Using a high-throughput phenotyping method known as ear photometry (EP), yield components, such as ear and kernel characteristics, can be measured or predicted (Grift et al., 2017; Miller et al., 2017; Makanza et al., 2018). These studies reported great prediction accuracies for many yield-related traits, giving credibility to the idea that EP could be valuable in assessing large breeding populations.

In 2017 and 2018, testcross hybrids of ex-PVP inbred lines from the United States and tropical inbred lines from the drought tolerant maize for Africa (DTMA) panel from CIMMYT were assessed for 25 yield-related traits when crossed to SS and/or IO testers. Representative ears were hand harvested from each plot for EP studies. The objectives of this experiment were to (1) validate the use of ear photometry on a diverse set of hybrids representing temperate and tropical maize, (2) characterize the relationships among and heritability of ear photometry traits,

and (3) describe the heterotic patterns of temperate and tropical inbred lines in testcross hybrids using ear photometry.

MATERIALS AND METHODS

Experimental Design and Germplasm

This experiment was grown in the summer of 2017 and 2018 at the Purdue University Agronomy Center for Research and Education (40°48′ N, 86°99′ W). The soil type at this location is a Chalmers silty clay loam (Fine-silty, mixed, superactive, mesic Typic Endoaquolls) (Purdue Agriculture Data Engine). Experimental plots followed a maize-soybean crop rotation with planting dates of June 1, 2017 and April 30, 2018. In both years, the fields were cultivated prior to planting. Fertilizer was applied in the fall of 2016 as 168 kg ha^{-1} of mono-ammonium phosphate (11-52-0) and 224 kg ha^{-1} of potash (0-0-60), and in the spring of 2017, 180 kg ha^{-1} of pre-plant ammonium nitrate was applied. Weed control [Bicep II (Atrazine + S-metolachlor), Syngenta] was applied pre-plant at a rate of 3.7 kg ha^{-1}. In 2018, nitrogen was applied in mid-March at a rate of 224 kg ha^{-1} of ammonium nitrate. Weed control [Bicep II (Atrazine + S-metolachlor), Syngenta], was applied pre-plant at a rate of 4.7 kg ha^{-1}. Additionally, [Laudis (Tembotrione), Bayer], was applied after planting at a rate of 210 g ha^{-1}. Prior to silk emergence in 2018, insecticide [Sevin (Carbaryl), Bayer] was applied due to a Japanese Beetle infestation.

Experimental plots were two rows 4.5 m long by 1.5 m wide with a spacing of 76 cm in 2017 and 3 m long by 1.5 m wide with a spacing of 76 cm in 2018 planted to a population of 74,000 seeds ha^{-1} in each year. The hybrids were blocked by temperate or tropical origin and tester to promote pollination among hybrid types and evaluated in a randomized complete block design with two replications.

Germplasm consisted of temperate inbred lines from public breeding programs and available ex-PVP inbred lines and DTMA inbred lines from CIMMYT. Testcross performance of 286 temperate inbred lines and the 274 DTMA inbred lines were evaluated in combination with PHP02 (IO). The choice of a commercial IO tester for the tropical germplasm differentiates this study from previous work which tested *per se* performance (Uhr and Goodman, 1995b) and combining ability to B73/Mo17 (Uhr and Goodman, 1995a). Additionally, 298 temperate inbred lines were evaluated for testcross performance to 2FACC (SS). Heterotic group assignment (SS, IO, or NS) of temperate inbred lines used in this study were previously described by Beckett et al. (2017). CIMMYT provided the heterotic group classification (A, B, or AB) of the DTMA inbred lines.

Ear Photometry Pipeline

Prior to machine harvest, 10 representative ears were selected from the plots in 2017 and 5 representative ears were selected from the plots in 2018 and dried to about 15% moisture followed by red-green-blue (RGB) imaging. These ears were imaged from a single angle using a Canon EOS Rebel T6i camera and an imaging system from Corteva Agriscience formerly DuPont Pioneer (Hausmann et al., 2009). Before imaging, the ears were thoroughly cleaned to remove silks and other debris. In total, more than 4,200 RGB images were acquired and processed to determine the phenotypes of more than 21,000 ears.

Common image processing techniques such as filtering, thresholding, edge finding, edge enhancement, color selection, spectral filtering, and water shedding were used to process images in a semi-automated process (Hausmann et al., 2009). Using a supervised classification method, ears (with kernels) and cobs (without kernels) were extracted from the background. As a template, a representative image with variation in kernel color was selected from each year to define the pixel attributes associated with the cob and kernels. Length measurements were calibrated using a reference image of a ruler.

EP was used to measure or predict 25 traits to provide unique insight into the characteristics of an ear. Traits measured or predicted in EP include, but are not limited to, grain yield (PHTYLD), kernels per ear (PHTKPE), average single kernel weight (KERWGT), and ear length (EARLGT). For a full description and heritability of the 25 EP traits, please refer to **Table 1**: Ear Photometry.

Reference Trait Measurements

Reference traits were measured either to provide additional in-season information related to a hybrid or to validate the EP platform. Reference traits were measured throughout the growing season. The description and heritability of the reference traits are provided in **Table 1**: Reference Physiology. Anthesis date (AD) and silking date (SD) were recorded as date when 50% of the plot reached anthesis or silking, respectively. Growing degree days (GDD) (C°) was calculated for each day from planting to AD and SD and summed to determine accumulated GDD. GDD for each day was calculated using the formula, $GDD = [(T_{max} + T_{min})/2] - 10$. When the maximum and minimum temperatures were greater than 30°C or less than 10°C, then T_{max} and T_{min} were set to 30 and 10°C, respectively (Gilmore and Rogers, 1958). Anthesis-to-silking interval (ASI) was the duration between AD to SD and was measured in GDD and days. In 2017, plant height (PH) was measured from the ground to the top collared leaf, and ear height (EH) was measured from the ground to the node of the primary ear.

The accuracy of EP predicted traits PHTYLD, PHTKPE, and KERWGT was assessed through manual measurements of the reference traits. The abbreviations for reference traits start with *REF* and the heritabilities and descriptions of these traits are provided in **Table 1**: Reference Yield Components. In 2017, the 10 ears per plot used in EP were shelled (Agriculex Single Ear Corn Sheller). The kernels of the 10 ears were combined and a seed counter (VMek Sorting Technology) was used to measure the number of kernels. The total weight of the kernels was measured using an Ohaus (NVT10001/1, Ohaus Corporation, Parsippany, NJ, United States) balance. Kernel number and total weight were subsequently divided by 10 to get measurements on a per ear basis. Kernel number per ear (REFKPE) manually measured was the reference trait for PHTKPE. Total weight per ear (REFYLD) manually measured was the reference trait for PHTYLD. Reference kernel weight (REFKW) was the quotient of REFYLD (g ear^{-1}) divided by REFKPE (count ear^{-1}) and

TABLE 1 | Description of the phenotypes evaluated in this study.

Trait Sections	Traits	Units	Heritability		Definition
			Entry-Mean	Plot-Mean	
Reference Physiology	AD	GDD*	0.91	0.75	Growing degree days to reach anthesis
	SD	GDD	0.92	0.78	Growing degree days to reach silking
	ASI	GDD	0.51	0.22	Anthesis-silking interval measured in growing degree days
	ASI	Days	0.60	0.31	Anthesis-silking interval measured in days
	PH†	Cm	0.91	0.83	Height from ground level to the top collared leaf
	EH†	Cm	0.86	0.76	Height from ground level to the node of the primary ear
Reference Yield Components	REFKW†	g kernel^{-1}	0.79	0.66	Reference average kernel weight manually measured
	REFKPE†	count ear^{-1}	0.84	0.73	Reference kernels per ear manually measured
	REFYLD†	g ear^{-1}	0.82	0.70	Reference grain yield manually measured
	REFYLD18‡	kg ha^{-1}	0.69	0.52	Reference grain yield at 15% moisture measured by combine
	MOISTURE‡	%	0.80	0.66	% moisture at harvest measured by combine
Ear Photometry	PHTYLD	g ear^{-1}	0.52	0.25	Grain yield
	PHTKPE	count ear^{-1}	0.60	0.30	Total number of kernels per ear
	KERWGT	g kernel^{-1}	0.51	0.25	Average kernel weight
	EARAREA	cm^2 ear^{-1}	0.61	0.32	Ear area
	EARBOX	–	0.49	0.22	Ear boxiness
	EARCW	–	0.65	0.38	Ear central width
	EARLGT	cm ear^{-1}	0.71	0.41	Total length of cob
	EARPER	cm ear^{-1}	0.70	0.40	Ear perimeter
	EARTR	cm^2 ear^{-1}	0.46	0.19	Ear tip ratio
	EARVOL	cm^2 ear^{-1}	0.56	0.28	Ear volume
	EARWTH	cm ear^{-1}	0.63	0.35	Width of ear including kernels and cob
	ETB	–	0.50	0.22	Ear tip boxiness
	KERARE	cm^2 kernel^{-1}	0.67	0.39	Average area per kernel
	KERCC	–	0.54	0.25	Kernel central count
	KERFIL	cm^2 (cm^2)$^{-1}$	0.50	0.25	Percent of total ear area with filled kernels
	KERLEN	cm kernel^{-1}	0.58	0.30	Average kernel length
	KERMAXD	cm kernel^{-1}	0.59	0.30	Kernel maximum diameter
	KERMEAND	cm kernel^{-1}	0.71	0.44	Kernel mean diameter
	KERMIND	cm kernel^{-1}	0.74	0.46	Kernel minimum diameter
	KERPER	cm kernel^{-1}	0.75	0.47	Kernel perimeter
	KERWTH	cm kernel^{-1}	0.73	0.45	Average kernel width
	PHTKR	count ear^{-1}	0.63	0.32	Kernel row number
	PHTKPR	count ear^{-1}	0.64	0.34	Total number of kernels per row
	SCTTER	cm^2 (cm^2)$^{-1}$	0.51	0.26	Percent of ear area lost due to scatter grain
	TKERAB	cm cm^{-1}	0.42	0.17	Percent of ear length affected by kernel abortion

*Trait heritability on an entry-mean and plot-mean basis using Equations 2, 3. Traits in the reference section refer to traits measured manually or by combine, while traits in the ear photometry section were measured using the ear photometry platform. *Daily Growing Degree Days (C°) = $\frac{T_{max}\ C - T_{min}\ C}{2} - 10C$ If Max Temp > 30°C, then Max Temp = 30°C. If Max Temp < 10°C, then Max Temp = 10°C. If Min Temp > 30°C, then Min Temp = 30°C. If Min Temp < 10°C, then Min Temp = 10°C. †Only measured in 2017. For these traits, the effect of Year was removed from the model. ‡Only measured in 2018. For these traits, the effect of Year was removed from the model.*

was used as the reference trait for KERWGT. The average EP predicted PHTYLD, PHTKPE, and KERWGT was correlated to their corresponding reference measurement. Subsequently, this validation dataset was split into temperate (n = 989) and tropical (n = 424) origin to verify the use of EP in these perspective backgrounds and are shown in **Supplementary Figure 1**.

In addition to using reference yield (g ear^{-1}) to validate the EP platform, reference yield (REFYLD18) (kg ha^{-1}) was measured on a per plot basis (n = 1,568) in 2018 using a plot combine (Kincaid 8-XP, Haven, KS, United States) with grain weights standardized to 15% moisture. Stand count was used as a covariate in the linear model between REFYLD18 and PHTYLD to limit the variability in yield due to differences in stand. Moisture was measured as the percent moisture in the grain at harvest with the plot combine. This validation dataset was split into temperate (n = 1,120) and tropical (n = 448) origin to verify the use of EP in these perspective backgrounds (**Supplementary Figure 1**).

Genotypic Data

Genotypic data for the temperate ex-PVP and public breeding lines was provided by the Rocheford Lab of Purdue University

and previously described in Beckett et al. (2017). Briefly, the genotypic information of 291 temperate lines was aligned and merged with 58 additional ex-PVP inbred lines. In total, there were 1,281,671 Single Nucleotide Polymorphisms (SNPs) in the merged genotype file for the 349 temperate inbred lines.

Genotypic data for the DTMA germplasm was sourced by CIMMYT from an online repository[1]. This dataset consisted 955,690 SNPs for 282 inbred lines and have been previously described by Guo et al. (2020), Yuan et al. (2019), and Wu et al. (2016). Once aligned and merged, the dataset of temperate and tropical germplasm consisted of 533 inbred lines phenotyped in this project with 755,339 common SNPs.

Statistical Analysis

Data analyses were performed in R (R Core Team, 2019). Best linear unbiased predictions (BLUPs) were predicted using lme4::lmer (Bates et al., 2015) according to equation 1. While the Hybrid × Year interaction was significant for most traits, the amount of variation explained by the Hybrid was typically far greater than the interaction. As such, BLUPs were predicted over the 2 years rather than BLUPs for each year using the following equation.

$$Y_{\text{ijkl}} = \mu + H_i + Yr_j + HYr_{ij} + R(Yr)_{jk} + \varepsilon_{\text{ijkl}} \quad (1)$$

Where Y_{ijkl} is the phenotypic measurement of the i^{th} hybrid, in the j^{th} year, in the k^{th} rep. μ represents the grand mean; H_{i} is the random effect of the i^{th} hybrid; Yr_{j} is the fixed effect of the j^{th} year; HYr_{ij} is the random interaction effect of the i^{th} hybrid in the j^{th} year; $R(Yr)_{jk}$ is the fixed effect of the k^{th} rep nested in the j^{th} year. ε is the random residual error term associated with each phenotypic measurement. Significant differences of heterotic groups were determined using analysis of variance (ANOVA) of the BLUPs. When ANOVA was significant, Tukey test was performed to distinguish between the heterotic groups in R library agricolae::HSD.test.

Broad-sense heritability (Nyquist and Baker, 1991; Piepho and Möhring, 2007) using variance components estimated through restricted maximum likelihood (REML) in Equation 1 was determined on an entry-mean and plot-mean basis as shown in Equations 2, 3, respectively, and are given in **Table 1**.

$$H^2 = \frac{\sigma_H^2}{\sigma_H^2 + \frac{\sigma_{HY}^2}{y} + \frac{\sigma_\varepsilon^2}{yr}} \quad (2)$$

$$H^2 = \frac{\sigma_H^2}{\sigma_H^2 + \sigma_{HY}^2 + \sigma_\varepsilon^2} \quad (3)$$

Where H^2 represents broad-sense heritability of a given trait. Hybrid, hybrid × year interaction, and error variance components are denoted by σ_{H}^2, σ_{HY}^2, and σ_ε^2, respectively. Number of years ($y = 2$) and number of reps per year ($r = 2$) were y and r in equation 2. Phenotypic correlations were computed using R function *cor* and visualized using corrplot::corrplot. Hierarchical clustering of the EP traits was performed through stats::hclust using Ward's Minimum Variance (ward.D2). The Ball-Hall Index was used to determine the appropriate number of clusters among the traits. To visualize the dendrogram, the R function *plot* was used with stats::cutree for colorization and ape::as.phylo to convert our object to class *phylo*. Principal component analysis (PCA) was performed in PLINK v1.9 (Purcell et al., 2007) for SNP data and R function *prcomp* for the EP traits. Data visualization was performed with R libraries ggplot2::ggplot, plot3d::text3d, and scatterplot3d::scatterplot3d.

[1]http://hdl.handle.net/11529/10548156

RESULTS

Weather Conditions

Weather conditions for 2017 and 2018 as well as the 30-year average from 1988 to 2018 are shown in **Supplementary Figure 2**. Maximum and minimum air temperature generally follow the 30-year average. Precipitation was found to be more variable across the 30-year average than temperature. In 2017, temperature was characterized by average monthly minimum and maximum typically falling within one standard deviation of the 30-year average. Precipitation was above average throughout much of the growing season. In 2018, average minimum temperatures were below the 30-year average in March and April. Elevated average minimum temperatures began in May. Average monthly maximum temperature was similar to the 30-year average. Precipitation was greater than one standard deviation of the 30-year average for May, June, August, October, and November, and below one standard deviation of the 30-year average for July.

Validation of Ear Photometry Traits

Ear photometry traits that were validated with this dataset include KERWGT, PHTKPE, and PHTYLD. The correlation between KERWGT, PHTKPE, and PHTYLD to their respective reference measurements (REFKW, REFKPE, REFYLD) were $r = 0.49$, $r = 0.88$, and $r = 0.75$, respectively (**Figure 1**). When the dataset was split based on the background origin, the correlation among KERWGT, PHTKPE, and PHTYLD to their respective reference measurements in temperate germplasm was $r = 0.51$, $r = 0.89$, and $r = 0.86$. In the tropical germplasm these correlations were $r = 0.38$, $r = 0.89$, and $r = 0.49$ (**Supplementary Figure 1**). PHTYLD was further validated on a per plot basis in 2018. The correlation between PHTYLD and REFYLD18 was $r = 0.39$. Nevertheless, unaccounted variation in the stand count for each plot limited the correlation between these two yield measures. When using stand count as a covariate in the model the correlation between adjusted PHTYLD and REFYLD18 increased to $r = 0.47$ ($r = 0.54$ and $r = 0.29$, in temperate and tropical germplasm, respectively) (**Figure 1D**).

Analysis of Ear Photometry Traits

Multivariate analyses were used to assess the relationship among EP traits including PCA (**Figure 2A**), hierarchical clustering (**Figure 2B**), and correlation analysis (**Supplementary Figure 3**). The Ball-Hall index distinguished five groups in the hierarchical clustering. Traits clustered with PHTYLD were those related

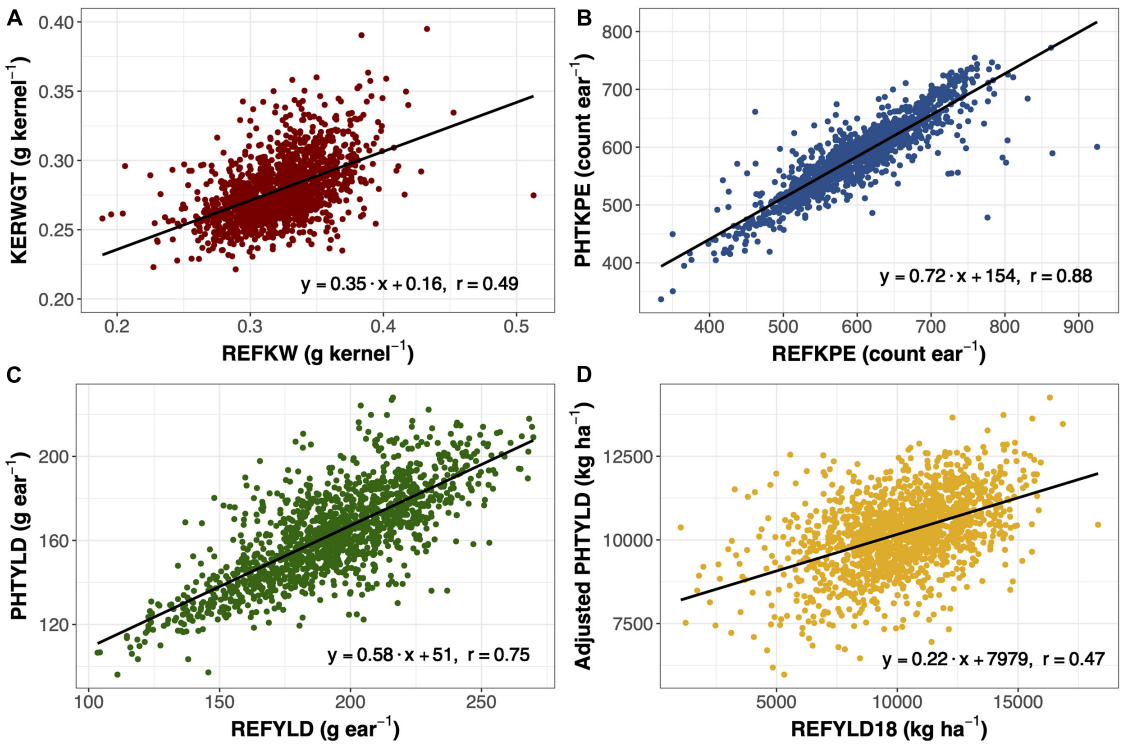

FIGURE 1 | Linear regression and Pearson correlation between reference kernel weight (REFKW) (x-axis) to photometry-estimated kernel weight (KERWGT) (y-axis) in 2017 (*n* = 1,413) **(A)**. Linear regression and Pearson correlation between reference kernels per ear (REFKPE) (x-axis) to photometry-estimated kernels per ear (PHTKPE) (y-axis) in 2017 (*n* = 1,413) **(B)**. Linear regression and Pearson correlation between reference yield (REFYLD) (x-axis) to photometry-estimated yield (PHTYLD) (y-axis) in 2017 (*n* = 1,413) **(C)**. Linear regression and Pearson correlation between reference yield on a plot basis (REFYLD18) and the fitted values for PHTYLD adjusted for stand count in modeling REFYLD18 (REFYLD18 = PHTYLD + Stand Count) in 2018 (*n* = 1,568) **(D)**.

to ear size and kernels per ear (EARVOL, EARAREA, EARPER, EARLGT, EARCW, EARWTH, KERCC, PHTKPE, and PHTKPR). Traits regarding the size, shape, and weight of the individual kernels were less correlated with PHTYLD, nevertheless, they were correlated amongst themselves. The remaining clusters relate to the boxiness of the ear, percent of ear filled with kernels, and kernel rows.

PCA was employed on the EP traits to gain a greater understanding of their relationships (**Figure 2A**). The first three PCs explained 36.5% of the total variance and our interpretations were checked for their orthogonality; beyond PC3, loading factors of the EP traits could not be biologically interpreted. PC1 explained 15.6% of the variation among the traits and was found to separate the traits based on their correlation to yield. PC2 explained 13.7% of the variation and was a contrast between traits involved with increased kernel size and traits that increase kernel number. PC3 explained 7.2% of the variation and was a contrast between the traits that indicated the percent of the ear with kernels and overall ear size.

Broad-sense heritability was estimated for the 25 traits evaluated in this study on an entry-mean and plot-mean basis (**Table 1**). Among EP traits, entry-mean heritability estimates ranged from 0.42 to 0.75. PHTYLD was among the traits with the lowest entry-mean heritability of 0.52. PHTKPE was marginally more heritable than PHTYLD with a heritability of 0.60. EP traits with an entry-mean heritability greater than or equal to 0.70 include EARLGT, EARPER, KERWTH, KERMEAND, KERMIND, and KERPER. Heritability of the physiology traits measured throughout the growing season and reference yield components ranged from 0.51 to 0.92.

Population Structure of Germplasm

Through visual assessment using the elbow method, four PCs were found to sufficiently explain the population structure among these inbred lines with 55.5% of the total variation explained in the PCA of SNP data. PC1 explained 20.2% of the total variance and visually separated the temperate and tropical inbred lines (**Figure 3**). PC2 explained 16.6% of the genomic variation and distinguished the SS from the NS and IO temperate heterotic groups. In PC3, 11.6% of the variance was explained from which the NS and IO heterotic groups could be discriminated (**Supplementary Figure 4**). 6.5% of the total variance in population structure was explained by PC4 which largely differentiated inbred lines in the NS heterotic group. Within these four PC the heterotic groups of the DTMA inbred lines were never visually separated. When performing PCA on the SNPs from DTMA inbred lines without the temperate material, CIMMYT designated heterotic groups remain difficult to separate (**Supplementary Figure 5**). Thus, our

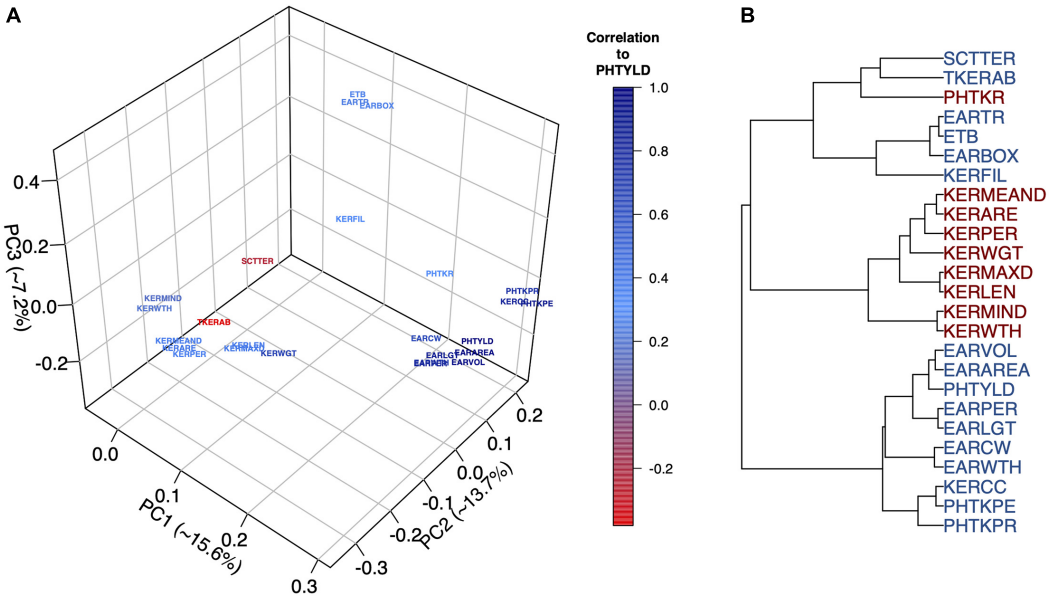

FIGURE 2 | Principal Component Analysis (PCA) to visualize the ear photometry (EP) traits and their correlation to photometry-estimated yield (PHTYLD) **(A)**. Dendrogram displaying the hierarchical clustering of EP traits using Ward's Minimum Variance. The Ball-Hall index was used to determine the correct number of groups (5) among the EP traits **(B)**.

analysis does not separate the DTMA inbred lines into known heterotic groups.

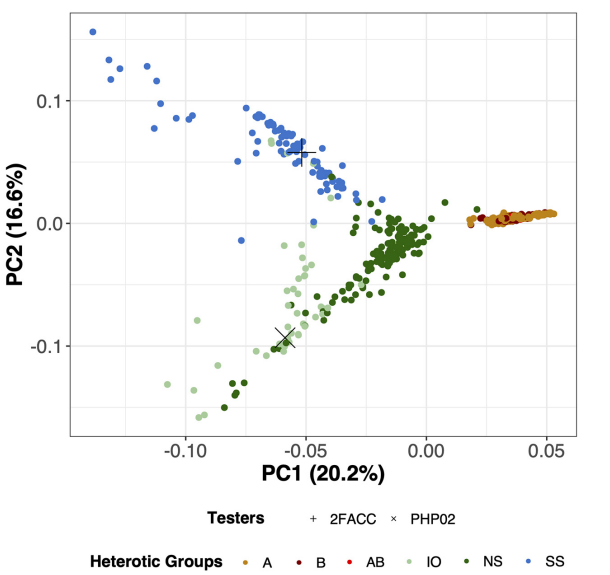

FIGURE 3 | Principal component analysis (PCA) for 533 inbred lines in this study using 755,339 Single Nucleotide Polymorphisms (SNPs). PC1 (x-axis) explains 20.2% of the variation of the SNP data while PC2 (y-axis) explains 16.6% of the variation of the SNP data. Testers in this experiment (2FACC and PHP02) are individually labeled with distinct shapes while heterotic groups are differentiated based on color. A, B, and AB are DTMA heterotic groups, while Iodent (IO), Non-Stiff Stalk (NS), and Stiff Stalk (SS) are temperate heterotic groups.

Analysis of Heterotic Patterns Through Ear Photometry

The heterotic patterns of the temperate and tropical inbred lines were evaluated for their testcross performance with 2FACC (**Table 2**) and PHP02 (**Table 3**). In these tables, the heterotic groups were presented as the mean and range for each trait. Considerable differences were found within and among the heterotic groups based on the means and ranges of the phenotypic traits.

A decrease in testcross performance was seen when 2FACC was crossed within the SS heterotic group compared to NS and IO (**Table 2** and **Figure 4**). Traits significantly (p value < 0.05) reduced included PHTYLD, PHTKPE, EARAREA, EARBOX, EARLGT, EARPER, EARVOL, PHTKPR, REFKPE, and REFYLD. There was also a significant (p value < 0.05) reduction in heterotic potential of the IO heterotic group as compared to NS in testcrosses to 2FACC for PHTYLD, PHTKPE, EARAREA, EARCW, EARVOL, EARWTH, ETB, KERCC, PHTKR, PHTKPR, SCTTER, REFKW, REFKPE, REFYLD, REFYLD18, MOISTURE, AD, SD, and PH. Traits KERWTH, KERMIND, AD, SD, and ASI (GDD) were the only traits significantly greater in the SS as compared to NS heterotic group with IO material as an intermediate not significantly different from either SS or NS for KERMIND, KERWTH, and ASI. In testcross performance with 2FACC, kernel attributes were generally not significantly improved as a result of heterosis.

Many agronomic and EP traits were significantly reduced when PHP02 was crossed within the IO heterotic group as compared to SS and NS heterotic groups. Traits significantly (p value < 0.05) reduced were PHTYLD,

TABLE 2 | Best linear unbiased predictions (BLUPs) of all traits measured in this study for inbred lines crossed to 2FACC based on heterotic group, NS (Non-Stiff Stalk), SS (Stiff Stalk), and IO (Iodent).

Trait Sections	Trait	Units	Significance	NS (*n* = 146)		IO (*n* = 48)		SS (*n* = 104)	
Reference Physiology	AD	GDD*	***	709.9 (656.1–760.1)	b	699.3 (676.1–750.4)	c	719.9 (666.3–757.9)	a
	SD	GDD	***	720.3 (659.2–774.7)	b	711.7 (689.2–763.9)	c	732.5 (673–779.5)	a
	ASI	GDD	*	68.7 (52.3–93.9)	b	70.3 (58.7–93.7)	ab	71.5 (53.3–107.3)	a
	ASI	Days	ns	1.2 (−0.4–2.3)		1.3 (0.8–2.3)		1.3 (0–2.9)	
	PH†	Cm	**	223.9 (189.7–250)	a	217.8 (193.5–235.3)	b	219.9 (187.3–244.8)	b
	EH†	Cm	ns	93.7 (71.6–124.4)		93.6 (77.4–109.1)		95 (71.4–122.1)	
Reference Yield Components	REFKW†	g kernel^{-1}	*	0.324 (0.262–0.45)	a	0.318 (0.277–0.342)	b	0.318 (0.252–0.356)	b
	REFKPE†	count ear^{-1}	***	626.7 (422.7–792.6)	a	596 (476.7–706.9)	b	562.8 (396.6–735.1)	c
	REFYLD†	g ear^{-1}	***	201.5 (151.2–234.8)	a	188.9 (153.5–227.7)	b	179 (138.1–209.1)	c
	REFYLD18‡	kg ha^{-1}	***	10,334.8 (7,155–12,484.8)	a	9,567.8 (7,718.4–11,224.3)	b	9,556 (6,727.2–14,118.8)	b
	MOISTURE‡	%	*	15 (14.5–16.4)	a	14.9 (14.5–16.5)	b	15 (14.6–16.4)	ab
Ear Photometry	PHTYLD	g ear^{-1}	***	162.2 (141.3–193.7)	a	156.4 (142.7–175)	b	151.7 (129–173.9)	c
	PHTKPE	count ear^{-1}	***	597 (480.4–681.7)	a	575.1 (524.5–635.6)	b	556.5 (438.9–648)	c
	KERWGT	g kernel^{-1}	ns	0.272 (0.252–0.315)		0.271 (0.254–0.287)		0.27 (0.249–0.291)	
	EARAREA	cm^2 ear^{-1}	***	88.8 (76.5–100.9)	a	85.4 (77–96.7)	b	82.4 (69.2–92.7)	c
	EARBOX	–	***	0.846 (0.829–0.864)	a	0.843 (0.819–0.855)	a	0.84 (0.817–0.857)	b
	EARCW	–	***	5.12 (4.61–5.76)	a	4.96 (4.77–5.19)	b	5.02 (4.67–5.37)	b
	EARLGT	cm ear^{-1}	***	19.6 (17.3–22.8)	a	19.4 (17.3–21.8)	a	18.5 (15.5–20.3)	b
	EARPER	cm ear^{-1}	***	49.7 (44.8–55.7)	a	48.9 (44.1–54.6)	a	46.8 (40.2–51.2)	b
	EARTR	cm^2 ear^{-1}	***	81.9 (77.4–85.7)	a	81.1 (75.8–83.8)	b	81.1 (75.5–84.6)	b
	EARVOL	cm^2 ear^{-1}	***	373.3 (313–435.7)	a	352.4 (322.6–406.6)	b	343.9 (292.9–394.2)	c
	EARWTH	cm ear^{-1}	***	5.34 (4.96–5.9)	a	5.2 (5–5.43)	b	5.25 (4.91–5.58)	b
	ETB	–	***	69.3 (64.1–74.2)	a	68.4 (62.1–71.6)	b	68.1 (61.6–72.5)	b
	KERARE	cm^2 kernel^{-1}	ns	0.337 (0.305–0.427)		0.339 (0.311–0.362)		0.339 (0.306–0.377)	
	KERCC	–	***	153 (121.5–176)	a	146.5 (134.7–162.9)	b	143.9 (111.2–163.3)	b
	KERFIL	cm^2 (cm^2)$^{-1}$	***	86.5 (78.3–89.2)	b	86.9 (84.7–89.9)	b	87.6 (83.2–90.4)	a
	KERLEN	cm kernel^{-1}	ns	0.867 (0.793–0.939)		0.866 (0.81–0.908)		0.861 (0.81–0.908)	
	KERMAXD	cm kernel^{-1}	ns	0.893 (0.822–0.962)		0.892 (0.837–0.933)		0.887 (0.837–0.933)	
	KERMEAND	cm kernel^{-1}	ns	0.639 (0.603–0.734)		0.641 (0.615–0.662)		0.641 (0.608–0.68)	
	KERMIND	cm kernel^{-1}	*	0.435 (0.394–0.572)	b	0.438 (0.419–0.462)	ab	0.441 (0.404–0.483)	a
	KERPER	cm kernel^{-1}	ns	2.41 (2.24–2.73)		2.4 (2.25–2.5)		2.4 (2.25–2.55)	
	KERWTH	cm kernel^{-1}	*	0.454 (0.416–0.605)	b	0.455 (0.438–0.478)	ab	0.459 (0.423–0.506)	a
	PHTKR	count ear^{-1}	***	17.3 (15.5–19.6)	a	16.9 (15.5–18.5)	b	17.1 (15.8–18.4)	ab
	PHTKPR	count ear^{-1}	***	40.4 (32.4–47)	a	39.5 (34.9–45.4)	b	37.6 (29.1–42.3)	c
	SCTTER	cm^2 (cm^2)$^{-1}$	***	11.5 (8.7–18.6)	a	10.8 (8–13.1)	b	10.3 (7.7–15)	b
	TKERAB	cm cm^{-1}	**	6.5 (4.5–9.6)	b	7.1 (5–10.4)	a	6.7 (4.9–10.3)	ab

*Given in terms of mean for the heterotic group with the range in parenthesis. Letters following the BLUPs indicate significant differences between heterotic groups at p value < 0.05. The same letters signify no significant differences between groups. *Daily Growing Degree Days (C°) = $\frac{T_{max}\ C - T_{min}\ C}{2} - 10C$ If Max Temp > 30°C, then Max Temp = 30°C. If Max Temp < 10°C, then Max Temp = 10°C. If Min Temp > 30°C, then Min Temp = 30°C. If Min Temp < 10°C, then Min Temp = 10°C. †Only measured in 2017. For these traits, the effect of Year was removed from the model. ‡Only measured in 2018. For these traits, the effect of Year was removed from the model.*

PHTKPE, KERWGT, EARAREA, EARCW, EARLGT, EARPER, EARVOL, EARWTH, KERCC, KERLEN, PHTKPR, PH, and EH (**Table 3**). SS and NS heterotic groups were only significantly (p value < 0.05) different for EARBOX, EARTR, ETB, PHTKR, TKERAB, and REFYLD18 when crossed to PHP02.

In testcross performance with PHP02, the DTMA inbred lines exhibited similar performance to SS and NS heterotic backgrounds (**Figure 5**). PHTYLD, EARAREA, EARCW, EARLGT, EARVOL, EARWTH, REFKW, and REFYLD were not significantly different from the SS and NS heterotic groups; however, PHTKPE, EARBOX, EARTR, ETB, KERCC, KERFIL, PHTKPR, REFKPE, and REFYLD18 were significantly (p value < 0.05) reduced. The reduction in kernel number attributes was present due to a significant (p value < 0.05) increase in SCTTER compared to NS and SS heterotic groups and TKERAB compared to NS. PHTYLD was not significantly different between SS, NS, and DTMA heterotic groups though due to a significant (p value < 0.05) increase in KERWGT, EARPER, KERARE, KERLEN, KERMAXD, KERMEAND, KERMIND, KERPER, and KERWTH in DTMA compared to NS and SS inbred lines. In addition to EP traits, hybrids from DTMA inbred lines exhibited significantly (p value < 0.05) greater AD, SD,

TABLE 3 | Best linear unbiased predictions (BLUPs) of all traits measured in this study for inbreds crossed to PHP02 based on heterotic group, NS (Non-Stiff Stalk), SS (Stiff Stalk), IO (Iodent), and DTMA (Drought Tolerant Maize for Africa).

Trait Sections	Trait	Units	Significance	NS (*n* = 151)		IO (*n* = 46)		SS (*n* = 89)		DTMA (*n* = 247)	
Reference Physiology	AD	GDD*	***	704.4 (704.4–761.3)	b	702.4 (670.1–747.9)	b	696.7 (652.9–751.7)	b	774.7 (699.6–856.9)	a
	SD	GDD	***	720.8 (720.6–770.7)	b	727.5 (678.1–846.8)	b	714.5 (676.1–754.3)	b	804.9 (713.4–956)	a
	ASI	GDD	***	74.4 (72.5–107.5)	c	80 (62.2–111.2)	b	76.5 (56.9–104.5)	bc	85.5 (58.2–124.4)	a
	ASI	Days	***	1.5 (1.4–3.2)	c	1.9 (0.9–9.7)	b	1.5 (0.6–2.9)	bc	2.3 (0.7–6.9)	a
	PH†	Cm	***	221.1 (221.3–258.3)	b	205.9 (171.6–250.3)	c	223.5 (183.5–255.5)	b	254.9 (216.5–312.3)	a
	EH†	Cm	***	101.6 (101.7–130.7)	b	93.9 (66.1–120.2)	c	103.1 (79–125.3)	b	133.3 (100.8–175.1)	a
Reference Yield Components	REFKW†	g kernel^{-1}	***	0.334 (0.247–0.383)	a	0.318 (0.268–0.364)	b	0.335 (0.297–0.377)	a	0.338 (0.273–0.41)	a
	REFKPE†	count ear^{-1}	***	618.9 (472.4–799.4)	a	562.4 (451.5–714.8)	c	620.9 (503.3–737.4)	a	597.5 (399.1–730.9)	b
	REFYLD†	g ear^{-1}	***	206.6 (133.8–252.3)	a	180.5 (132.8–241.5)	b	207.3 (153–257.3)	a	201.4 (141.2–240.7)	a
	REFYLD18‡	kg ha^{-1}	***	10,054.1 (4828.2–16,128.4)	b	8,885.1 (5,717.2–13,035.7)	c	10,529.2 (8,342.4–13,726.5)	a	8,598.6 (5,174.6–12,161.3)	c
	MOISTURE‡	%	***	14.9 (10.2–16)	b	14.8 (14.2–15.4)	b	14.9 (10.3–16.1)	b	16.6 (14.9–20.5)	a
Ear Photometry	PHTYLD	g ear^{-1}	***	167.1 (132.9–192)	a	154 (131.1–195.2)	b	166.7 (140.3–185.7)	a	165.6 (128.7–194)	a
	PHTKPE	count ear^{-1}	***	601.9 (505.6–688.9)	a	562.2 (473–718.7)	c	604.8 (530.6–686.5)	a	582.8 (423.5–682.3)	b
	KERWGT	g kernel^{-1}	***	0.278 (0.251–0.312)	b	0.272 (0.256–0.287)	c	0.277 (0.26–0.299)	b	0.284 (0.255–0.327)	a
	EARAREA	cm^2 ear^{-1}	***	91.4 (72–104.7)	a	83.7 (70.5–102)	b	91.5 (76.5–99.6)	a	92 (71.3–104.7)	a
	EARBOX	–	***	0.854 (0.832–0.871)	a	0.85 (0.83–0.864)	ab	0.85 (0.838–0.866)	b	0.845 (0.803–0.869)	c
	EARCW	–	***	5 (4.56–5.56)	a	4.84 (4.53–5.25)	b	5.04 (4.65–5.41)	a	5.02 (4.6–5.41)	a
	EARLGT	cm ear^{-1}	***	20.4 (17–23.8)	a	19.2 (16.8–22.2)	b	20.4 (17.8–22.3)	a	20.6 (16.9–25)	a
	EARPER	cm ear^{-1}	***	51.5 (43.1–57.9)	b	48.3 (42.7–55.7)	c	51.3 (45.1–56.6)	b	52.5 (44.6–67.6)	a
	EARTR	cm^2 ear^{-1}	***	83.9 (80.3–86.7)	a	83.4 (78.8–85.9)	ab	82.8 (80.2–86)	b	82.1 (75.9–86.7)	c
	EARVOL	cm^2 ear^{-1}	***	378 (284.4–453.1)	a	341 (278.8–435.4)	b	380.6 (304.6–424.3)	a	383.3 (296.8–451.4)	a
	EARWTH	cm ear^{-1}	***	5.24 (4.75–5.81)	a	5.08 (4.75–5.52)	b	5.29 (4.88–5.57)	a	5.28 (4.85–5.67)	a
	ETB	–	***	71.7 (67.1–75.6)	a	71.1 (65.3–74.3)	ab	70.5 (67.3–74.6)	b	69.4 (61.7–75.6)	c
	KERARE	cm^2 kernel^{-1}	***	0.352 (0.315–0.398)	b	0.346 (0.318–0.369)	b	0.349 (0.316–0.391)	b	0.365 (0.307–0.443)	a
	KERCC	–	***	155.3 (125.5–185.1)	a	144.6 (119.5–184.5)	c	157.1 (136.7–178.5)	a	152.2 (111.5–179.6)	b
	KERFIL	cm^2 (cm^2) $^{-1}$	***	86.5 (75.8–89.3)	a	87.3 (83.3–89.9)	a	86.5 (79.5–88.8)	a	85.1 (76.5–90.6)	b
	KERLEN	cm kernel^{-1}	***	0.872 (0.8–0.949)	b	0.854 (0.794–0.909)	c	0.866 (0.832–0.934)	b	0.882 (0.817–0.966)	a
	KERMAXD	cm kernel^{-1}	***	0.898 (0.83–0.974)	b	0.881 (0.823–0.934)	c	0.893 (0.857–0.96)	bc	0.91 (0.849–0.989)	a
	KERMEAND	cm kernel^{-1}	***	0.655 (0.619–0.703)	b	0.651 (0.624–0.675)	b	0.653 (0.619–0.696)	b	0.67 (0.61–0.746)	a
	KERMIND	cm kernel^{-1}	***	0.454 (0.408–0.507)	b	0.458 (0.426–0.487)	b	0.453 (0.42–0.51)	b	0.47 (0.41–0.56)	a
	KERPER	cm kernel^{-1}	***	2.44 (2.28–2.72)	b	2.4 (2.26–2.5)	c	2.42 (2.29–2.58)	bc	2.54 (2.36–2.97)	a
	KERWTH	cm kernel^{-1}	***	0.471 (0.424–0.524)	b	0.473 (0.442–0.507)	b	0.468 (0.434–0.523)	b	0.49 (0.429–0.592)	a
	PHTKR	count ear^{-1}	***	16.9 (15.3–19)	b	16.6 (15.4–18.3)	b	17.2 (15.6–18.4)	a	16.8 (15.2–19.6)	b
	PHTKPR	count ear^{-1}	***	41.3 (34–48.2)	a	38.5 (32.4–45.8)	c	40.9 (37–45.1)	a	39.9 (28.2–45)	b
	SCTTER	cm^2 (cm^2) $^{-1}$	***	11.8 (9.1–22.9)	b	10.9 (8.3–15.2)	b	11.7 (9.3–19)	b	12.9 (7.4–21.7)	a
	TKERAB	cm cm^{-1}	***	5.2 (3.5–8.2)	c	5.5 (3.8–7.4)	bc	5.9 (3.5–8)	ab	6.1 (3.2–10.8)	a

*Given in terms of mean for the heterotic group with the range in parenthesis. Letters following the BLUPs indicate significant differences between heterotic groups at p value < 0.05. The same letters signify no significant differences between groups. *Daily Growing Degree Days (C°) = $\frac{T_{max}\ C - T_{min}\ C}{2} - 10C$ If Max Temp > 30°C, then Max Temp = 30°C. If Max Temp < 10°C, then Max Temp = 10°C. If Min Temp > 30°C, then Min Temp = 30°C. If Min Temp < 10°C, then Min Temp = 10°C. †Only measured in 2017. For these traits, the effect of Year was removed from the model. ‡Only measured in 2018. For these traits, the effect of Year was removed from the model.*

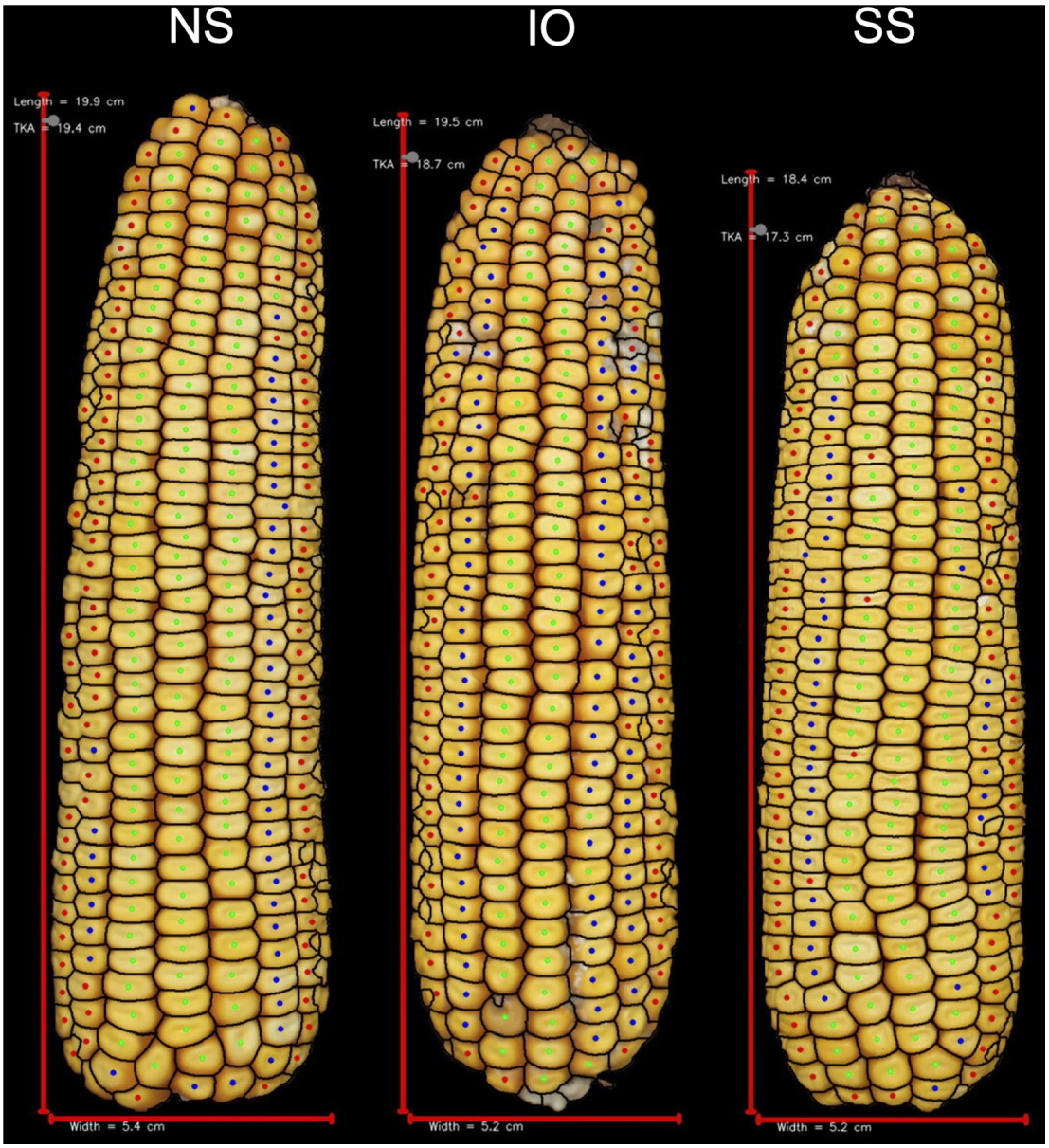

FIGURE 4 | Representative ears for each of the heterotic groups in hybrid combination with 2FACC. Selected ears had an average yield and yield components for their heterotic group combination. Abbreviations for heterotic groups include: NS (Non-Stiff Stalk), IO (Iodent), and SS (Stiff Stalk).

ASI (GDD and Days), PH, and EH as expected due to their tropical origin.

Variance of PHTYLD was estimated on a per plot basis from 10 ears in 2017 and five ears in 2018. Due to the differences in number of ears sampled per plot, analysis was not combined between years. In 2017, mean within-plot variance per plot was 427.5. DTMA testcrosses had significantly greater (p value < 0.001) within-plot variance than plots of temperate descent (510.2 and 392, respectively). In 2018, mean within-plot variance per plot was 316.3. DTMA testcrosses had significantly greater (p value < 0.05) within-plot variance than temperate testcrosses (351.6 and 302.5, respectively).

DISCUSSION

Ear Photometry

Grain yield as measured on a per plot basis has been the primary trait selected upon in commercial breeding programs. As a complex trait, grain yield is a composite of many yield-related traits known as yield components. While yield components generally are found to be more heritable (**Table 1**), phenotyping these traits has historically been time-consuming, labor-intensive, prone to error, and difficult to scale in a large breeding program (Bernardo, 2014; Cooper et al., 2014). Ear photometry removes many of these barriers

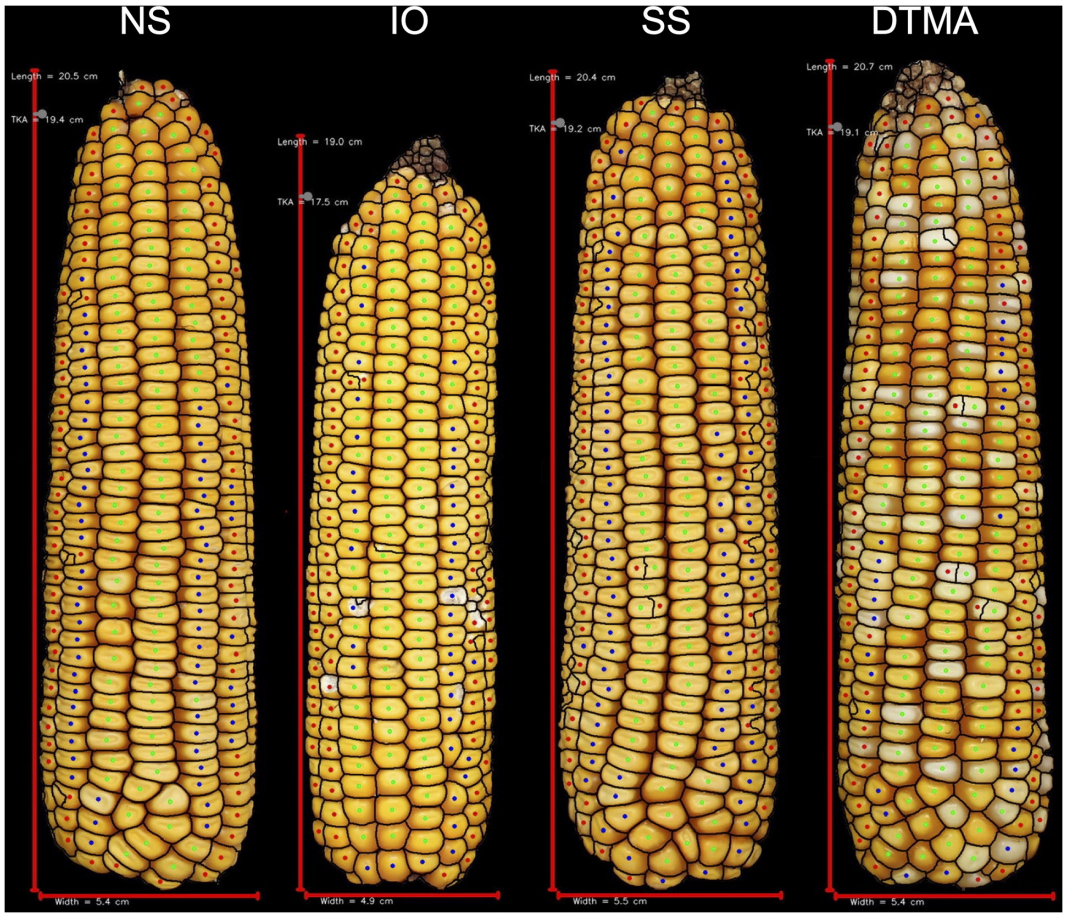

FIGURE 5 | Representative ears for each of the heterotic groups in hybrid combination with PHP02. Selected ears had an average yield and yield components for their heterotic group combination. Abbreviations for heterotic groups include: NS (Non-Stiff Stalk), IO (Iodent), SS (Stiff Stalk), and DTMA (Drought Tolerant Maize for Africa).

while providing a more in-depth understanding of yield and yield components.

Photometry-estimated yield was validated in this study with regards to reference yield measured from a combine in 2018 (n = 1,568) and on a per ear basis in 2017 (n = 1,413). The correlation between photometry-estimated yield and reference yield in 2018 was r = 0.39. When stand count was used as a covariate in the model, the correlation increased to r = 0.47 (**Figure 1D**). On a per ear basis, yield is the product of kernel number and average kernel size. The correlation between photometry-estimated yield per ear and reference yield per ear was r = 0.75 (**Figure 1C**).

Yield components, kernels per ear and kernel weight, were other traits that were validated in 2017 (n = 1413) (**Figure 1**). Kernel number per ear was taken at the plot level and divided by 10, the number of ears taken per plot. Kernel weight was determined by dividing the total kernel weight by the total kernel number. Photometry-estimated kernels per ear was correlated with reference kernels per ear (r = 0.88) (**Figure 1B**). Photometry-estimated kernel weight was correlated with reference kernel weight (r = 0.49) (**Figure 1A**). The correlation between photometry-estimated kernels per ear and reference kernels per ear was unaffected by the background of the germplasm, while the correlation between photometry-estimated kernel weight and reference kernel weight was reduced in the tropical (r = 0.38) compared to the temperate germplasm (r = 0.51) (**Supplementary Figure 1**). As such, the correlation of photometry-estimated yield to reference yield fell in the tropical germplasm (r = 0.49) as compared to the temperate germplasm (r = 0.86). Pioneer Hi-Bred International also validated many of the traits in this platform including kernels per ear (R^2 = 0.87; n = 287) and yield (R^2 = 0.97; n = 1,500) in temperate germplasm (Hausmann et al., 2009). This study shows that EP can be extended to quantify variation in ear traits in tropical germplasm.

Grift et al. (2017), Miller et al. (2017), and Makanza et al. (2018) previously evaluated high-throughput methods for yield component assessment in maize. Grift et al. (2017) used machine learning to evaluate kernel number per year on 23 maize ears. Using the full ear, they found errors ranging from −7.67 to 8.60% which indicated under- and over-counting, respectively, and a coefficient of determination of R^2 = 0.7. Miller et al. (2017) evaluated the yield components of 445 diverse inbred lines. In

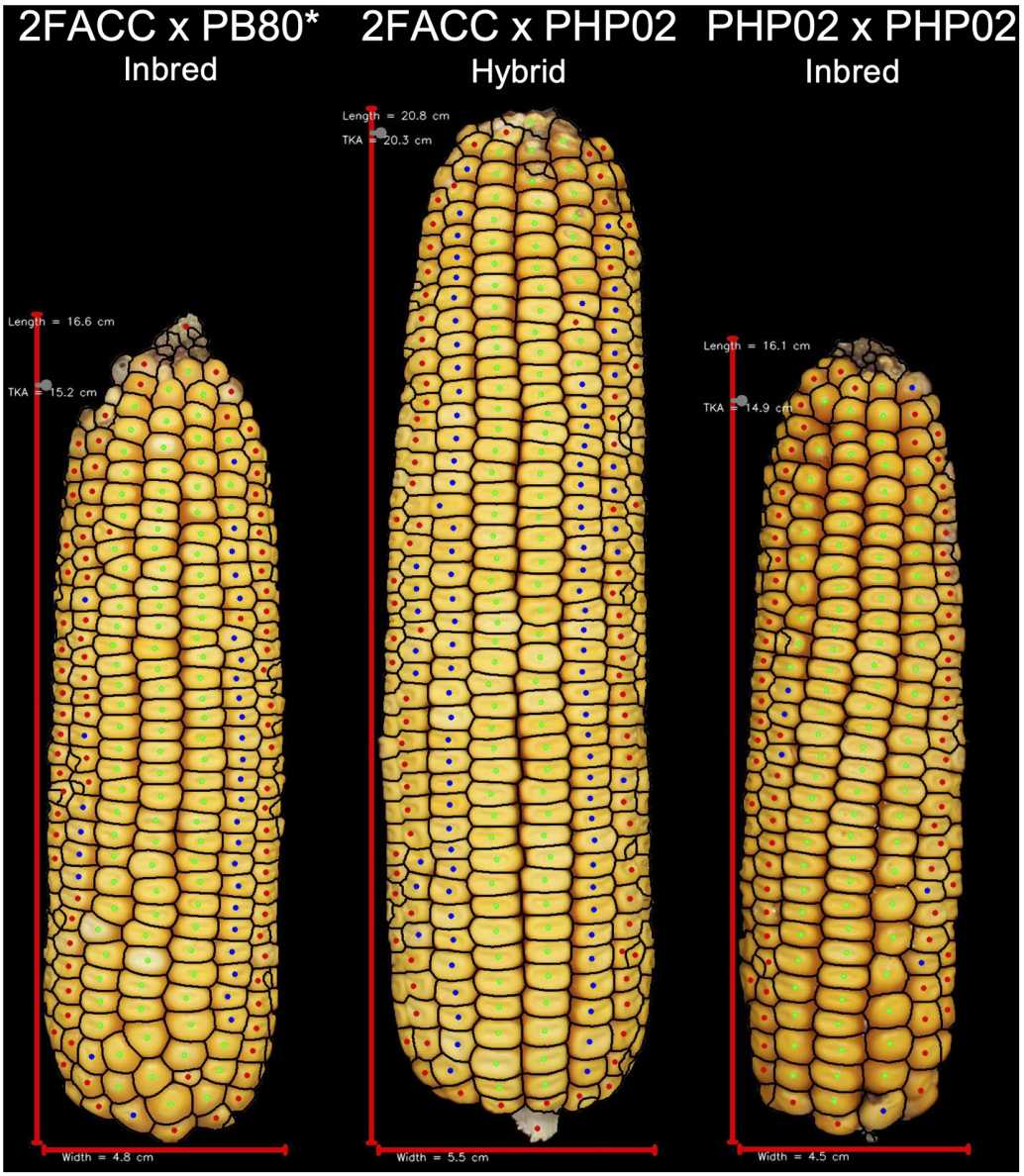

FIGURE 6 | Visual description of hybrid breeding. Inbred line 2FACC, on the left, from the Stiff Stalk heterotic group and inbred line PHP02, on the right, from the Iodent heterotic group show reduced vigor due to inbreeding depression. The hybrid of these inbred lines displays greater yield potential than either inbred parent due to hybrid vigor. *2FACC inbred was not produced in this study. As the progenitor of 2FACC, PB80 produced a highly inbred line when crossed to 2FACC.

their platform, three types of images were obtained. First, each genotype had three ears imaged from two angles where the second angle was a 90-degree rotation of the ear. After being shelled, these cobs were again imaged. Finally, the kernels were imaged when spread out on a black sheet. Using this platform, these authors found high correlations between ear length and kernel length to their reference phenotypes with coefficients of determination of $R^2 = 0.99$ and 0.74, respectively. Makanza et al. (2018) evaluated 10 hybrids from an experiment performed in Zimbabwe. Ears were collected from these field trials, arranged on a black cloth, and were photographed from a mounted camera tripod stand. Shelled kernels were imaged on a black background. Yield components related to the ears (i.e., ear length and ear width) were accurately correlated to reference measurements ($r = 0.99$ and 0.97, respectively). Yield components such as kernel count and kernel weight were also correlated to their reference measurements ($r = 0.99$ and 0.94, respectively).

The phenotyping platform described in this paper presents a potential improvement over the previously mentioned phenotyping strategies as the kernels do not need to be shelled from the ears and the ears are only imaged from one angle. The ease of using this platform enables it to be scaled to the level needed in a breeding program; however, the accuracy of kernel weight assessment was reduced in this study from the platform

described in Makanza et al. (2018) as the kernels were not shelled prior to imaging.

Heritability of a given trait is a function of the germplasm under evaluation and the effect of the environment (Bernardo, 2014). In our study, heritability of photometry-estimated yield was among the lowest traits evaluated (H^2 = 0.52). Lian et al. (2014) evaluated the heritability of multiple traits in 969 maize biparental crosses. They found that heritability of grain yield ranged from 0.17 to 0.92 with a mean of 0.46. In our study, the heritability of many yield components was increased in comparison to photometry-estimated yield (**Table 1**). Photometry-estimated traits such as kernels per ear (H^2 = 0.60), ear length (H^2 = 0.71), and kernel perimeter (H^2 = 0.75) are a subset of yield components with an increased heritability. Ross et al. (2006) evaluated heritability of yield components and found that ear length and kernel row number were more heritable than grain yield. In their study which used a biparental population, kernel attributes such as kernel length, kernel width, kernel thickness, and 100-kernel weight had heritabilities ranging from 0.65 to 0.79. Selection based on these traits with increased heritability could improve genetic gain and selection accuracy (Araus et al., 2018).

Variation between plots is the foundation of plant breeding, indicating sources of genetic variation from which breeders make selections. Variation within plots is measured relatively less often as grain yield is often estimated at a plot level. Nevertheless, within-plot variability has been suggested to be an indicator for yield stability in varying environments (Hausmann et al., 2009). In both of these years, testcrosses to DTMA inbred lines resulted in a significant (p value < 0.001, 2017; p-value < 0.05, 2018) increase in within-plot variance compared to temperate testcrosses. Many of the temperate inbred lines used in this study were the result of intensive selection where inbred lines were evaluated in multi-environment trials within commercial breeding programs where yield stability was an important consideration (Cooper et al., 2014). Additionally, the unadapted nature of the DTMA inbred lines to the United States Corn Belt could have been an extra source of the within-plot variation. However, the range in variability in the DTMA material was 23–2,866 in 2017 and 12–3,166 in 2018 suggesting variability in the yield stability of these testcrosses.

Description of Heterotic Groups

Principal component analysis is commonly employed to assess population structure in genomic studies (**Figure 3**). The heterotic groups of the temperate inbred lines were classified in accordance with Beckett et al. (2017). From canonical axes 2 and 3 (16.6 and 11.6% of the total variation explained, respectively) of the principal component analysis, Stiff Stalk, Non-Stiff Stalk, and Iodent heterotic groups were visually separated (**Supplementary Figure 4**). The Stiff Stalk heterotic group was first separated from the Non-Stiff Stalk and Iodent inbred lines suggesting that the Non-Stiff Stalk and Iodent heterotic groups are more closely related than inbred lines of Stiff Stalk origin as previously reported (Mikel, 2008; Nelson et al., 2008; Beckett et al., 2017).

Mikel (2008) evaluated the genetic diversity of 55 inbred parents used in Holden's Foundation Seeds and Pioneer Hi-Bred International. They classified two major heterotic groups among temperate germplasm: Stiff Stalk and Non-Stiff Stalk. Through pedigree-based records, Mikel and Dudley (2006) and Mikel (2008) trace the lineage of the Stiff Stalk heterotic group to public inbred line B73 and conclude there is less genetic diversity within Stiff Stalk material than Non-Stiff Stalk material. In evaluating the Non-Stiff Stalk material, subgroups included germplasm derivatives from Lancaster Sure Crop, Minnesota 13, Leaming Corn, Northwestern Dent, and Iodent (Troyer, 1999; Mikel, 2008). The role of Iodent germplasm has increased in commercial programs and hybrids composed of Iodent and Non-Stiff Stalk inbred parents are commercially viable (Mikel, 2011) leading to its own designation in this study as has previously been done (Nelson et al., 2008; Beckett et al., 2017; White et al., 2020).

The temperate and tropical inbred lines could be visually separated along principal component 1 (20.2%) (**Figure 3**). Multiple heterotic groups are represented within the CIMMYT breeding program (personal communication), but their classification was difficult to distinguish in PCA with (**Figure 3**) and without the temperate material (**Supplementary Figure 5**) as has previously been reported by Wu et al. (2016). Additionally, inclusion into United States breeding programs did not appear to be dependent on their tropical heterotic group classification. Based on the variation in the genotypic information, we believe that the DTMA germplasm could have potential in hybrid combination with all temperate heterotic groups. Holland and Goodman (1995) report similar findings of broad utility of several exotic families to temperate heterotic groups.

Phenotypic Characteristics of Heterotic Groups

Since maize in the United States is commercially grown as a hybrid crop, inbred lines are normally selected based on testcross rather than *per se* performance (Bernardo, 2014). In this study, inbred testers PHP02 (Iodent) and 2FACC (Stiff Stalk) were used to characterize the heterotic patterns and ear phenotypes of available inbred lines. The implications of heterosis were evident when inter- and intra-heterotic group crosses were compared (**Tables 2**, **3** and **Figures 4**, **5**). Within the crosses to PHP02, Iodent inbred lines were significantly reduced as compared to Stiff Stalk and Non-Stiff Stalk material with regards to traits pertaining to yield, ear size, kernels per ear, and kernel size (**Table 3**). Within crosses to 2FACC, Stiff Stalk inbred lines were significantly reduced for yield, ear size, and kernels per ear; however, many kernel size traits were not significantly reduced (**Table 2**). The effects of heterosis were more noticeable in traits related to yield, ear size, and kernel number than kernel size. Stiff Stalk and Non-Stiff Stalk groups were found to have similar heterotic potential when crossed with Iodent tester PHP02 (**Table 3** and **Figure 5**), while Stiff Stalk tester 2FACC was found to combine best with Non-Stiff Stalk inbred lines with the Iodent heterotic group being an intermittent improvement to the Stiff Stalk heterotic group

(**Table 2** and **Figure 4**). As Plant Variety Protection expires on inbred lines, ear photometry can provide valuable information about these inbred lines which are considered as sources of new germplasm in breeding programs without previous access to the proprietary material.

Heterosis and hybrid vigor are the foundations for the success of modern maize breeding in the United States (**Figure 6**). Hauck et al. (2014) found that the effects of heterosis were apparent in many yield components including kernel row number, kernel weight, and kernels per row. Additionally, in evaluating midparent heterosis, Tollenaar et al. (2004) found the heterotic effect of kernels per area to be greater than kernel weight. While primarily measured at harvest, these yield components are determined throughout the growing season. Maximum kernel number per ear is determined in the vegetative growth stages with optimum growth conditions maximizing this yield component. Subsequently, kernel weight is a function of the number of kernels on a given ear and the amount of resources that are allocated to the reproductive organs in their critical period of grain filling following pollination (Nielsen, 2002). Average kernel weight is the more elastic yield component in comparison with kernel number per ear which leads to its heritability (**Table 1**) and midparent heterosis (Tollenaar et al., 2004) being reduced. The effect of heterosis and genetic gain in physiological processes of maize development is the foundation for greater grain yield (Tollenaar and Lee, 2006).

In hybrid combination with PHP02, the tropical germplasm performed well for many ear traits including yield, kernels per ear, and ear length in this study. Tropical germplasm was previously considered for inclusion into commercial germplasm pools (Holland and Goodman, 1995; Mikel, 2011). Holland and Goodman (1995) found that several semiexotic topcrosses were comparable in yields compared to B73Ht × Mo17Ht F_1 hybrids. These results indicate the potential of these lines to simultaneous increase genetic diversity and grain yield upon intensive plant breeding efforts. Exotic germplasm was previously used in commercial breeding programs. For example, inbred PHG39, a main contributor of the contemporary Pioneer Hi-bred International Stiff Stalk heterotic group, is comprized of 25% exotic germplasm (Maize Amargo) (Mikel and Dudley, 2006; Mikel, 2011). Pre-breeding efforts are needed on traits such as plant height, ear height, and growing degree days to flowering to adapt these inbred lines to production in the United States Corn Belt.

CONCLUSION

Ear photometry methods can be used to identify and quantify traits that were previously difficult to measure at scale in a breeding program. In this study, kernels per ear (r = 0.88) and kernel weight (r = 0.49) were both correlated with their reference measurements. Grain yield on per ear basis and plot basis were also correlated with reference measurements with correlations of r = 0.75 and r = 0.47, respectively. Twenty-five ear traits were assessed. Traits related to ear size and kernels per ear were found to be more related to yield than kernel attributes. Similarly, traits related to ear size and kernels per ear were found to be affected by heterosis to a greater degree than kernel size when evaluating inter-heterotic group crosses compared to intra-heterotic group crosses. Yield components were generally found to be more heritable than grain yield indicating their potential in inbred selection. Temperate, commercial United States heterotic groups had a wide range of phenotypes when inter- and intra-heterotic group testcrosses were evaluated. DTMA inbred lines, when evaluated using an Iodent tester, were found to have comparable yields to temperate material due to an increase in kernel weight that overcame the decrease in kernels per ear. Detailed phenotypic description of inbred lines is instrumental in the use of ex-PVP inbreds in public breeding programs and the incorporation of diverse germplasm to sustain long-term genetic gain in the commercial United States maize industry.

DATA AVAILABILITY STATEMENT

The datasets presented in this study can be found in online repositories. The names of the repository/repositories and accession number(s) can be found below: Best linear unbiased predictions (BLUPs) for the 25 yield-related traits measured by ear photometry for the 831 testcross hybrids evaluated in this study can be found in the Purdue University Research Repository, https://purr.purdue.edu/publications/3623/1.

AUTHOR CONTRIBUTIONS

MT initiated, conceived, and coordinated all the experiments. ST and AS performed most of the experiments. ST wrote the manuscript with contributions of all the authors. All authors contributed to the article and approved the submitted version.

FUNDING

This project was partially funded by a grant (Grant no. 15100072) from the Heat Tolerant Maize for Asia project supported by the Feed the Future Initiative of USAID organized by the International Maize and Wheat Improvement Center (CIMMYT).

ACKNOWLEDGMENTS

Purdue University was granted access to DuPont Pioneer's proprietary phenotyping and ear photometry technology as part of an innovative research collaboration to support plant sciences research.

SUPPLEMENTARY MATERIAL

The Supplementary Material for this article can be found online at: https://www.frontiersin.org/articles/10.3389/fpls.2021.616975/full#supplementary-material

REFERENCES

Araus, J., and Cairns, J. (2014). Field high-throughput phenotyping: the new crop breeding frontier. *Trends Plant Sci.* 19, 52–61. doi: 10.1016/j.tplants.2013.09.008

Araus, J., Kefauver, S., Zaman-Allah, M., Olsen, M., and Cairns, J. (2018). Translating high-throughput phenotyping into genetic gain. *Trends Plant Sci.* 23, 451–466. doi: 10.1016/j.tplants.2018.02.001

Bates, D., Mächler, M., Bolker, B., and Walker, S. (2015). Fitting linear mixed-effects models using lme4. *J. Stat. Softw.* 67, 1–48. doi: 10.18637/jss.v067.i01

Beckett, T., Morales, A., Koehler, K., and Rocheford, T. (2017). Genetic relatedness of previously Plant-Variety-Protected commercial maize inbreds. *Plos One* 12:e0189277. doi: 10.1371/journal.pone.0189277

Bernardo, R. (2014). *Essentials of Plant Breeding*. Woodbury, MN: Stemma Press.

Cooper, M., Gho, C., Leafgren, R., Tang, T., and Messina, C. (2014). Breeding drought-tolerant maize hybrids for the US corn-belt: discovery to product. *J. Exp. Bot.* 65, 6191–6204. doi: 10.1093/jxb/eru064

Cupertino-Rodrigues, M., Dhliwayo, T., Trachsel, S., Guo, R., and San Vicente, F. (2020). Evaluation of U.S. inbred lines with expired plant variety protection for mid-altitude tropical maize breeding. *Euphytica* 216:44. doi: 10.1007/s10681-020-02584-z

Duvick, D. (2005). The contribution of breeding to yield advances in maize (*Zea mays* L.). *Adv. Agron.* 86, 83–145. doi: 10.1016/S0065-2113(05)86002-X

Duvick, D., Smith, J., and Cooper, M. (2004). "Long-term selection in a commercial hybrid maize breeding program," in *Plant Breeding Reviews*, Vol. 24, Part 2, ed. J. Janick (Hoboken, NJ: John Wiley & Sons, Ltd), 109–151. doi: 10.1002/9780470650288.ch4

East, E. (1909). The distinction between development and heredity in inbreeding. *Am. Nat.* 43, 173–181. doi: 10.1086/279042

East, E. (1936). Heterosis. *Genetics* 21, 375–397.

Flint-Garcia, S., Thuillet, A., Yu, J., Pressoir, G., Romero, S., Mitchell, S., et al. (2005). Maize association population: a high-resolution platform for quantitative trait locus dissection. *Plant J.* 44, 1054–1064. doi: 10.1111/j.1365-313X.2005.02591.x

Furbank, R., and Tester, M. (2011). Phenomics – technologies to relieve the phenotyping bottleneck. *Trends Plant Sci.* 16, 635–644. doi: 10.1016/j.tplants.2011.09.005

Gilmore, E., and Rogers, J. (1958). Heat units as a method of measuing maturity in corn. *Agron. J.* 50, 62–81. doi: 10.2134/agronj1958.00021962005000100014x

Goodman, M. (2005). Broadening the U.S. maize germplasm base. *Maydica.* 50, 203–214.

Grift, T., Zhao, W., Momin, M., Zhang, Y., and Bohn, M. (2017). Semi-automated, machine vision based maize kernel counting on the ear. *Biosyst. Eng.* 164, 171–180. doi: 10.1016/j.biosystemseng.2017.10.010

Guo, R., Dhliwayo, T., Mageto, E., Palacios-Rojas, N., Lee, M., Yu, D., et al. (2020). Genomic prediction of kernel zinc concentration in multiple maize populations using genotype-by-sequencing and repeat amplification sequencing markers. *Front. Plant Sci.* 11:534. doi: 10.3389/fpls.2020.00534

Hauck, A., Johnson, G., Mikel, M., Mahone, G., Morales, A., Rocheford, T., et al. (2014). Generation means analysis of elite ex-plant variety protection commercial inbreds: a new public maize genetics resource. *Crop Sci.* 54, 174–189. doi: 10.2135/cropsci2013.03.0172

Hausmann, N., Abadie, T., Cooper, M., Lafitte, H., and Schussler, J. (2009). *Method and System for Digital Image Analysis of ear Traits.* U.S. Patent No US2009/0046890 A1. Washington, DC: U.S. Patent and Trademark Office.

Henry, W., Blanco, M., Rowe, D., Windham, G., Murray, S., and Williams, W. (2014). Diallel analysis of diverse maize germplasm lines for agronomic characteristics. *Crop Sci.* 54, 2547–2556. doi: 10.2135/cropsci2014.01.0078

Holland, J., and Goodman, M. (1995). Combining ability of tropical maize accessions with U.S. germplasm. *Crop Sci.* 35, 767–773. doi: 10.2135/cropsci1995.0011183X003500030022x

Lian, L., Jacobson, A., Zhong, S., and Bernardo, R. (2014). Genomewide prediction accuracy within 969 maize biparental populations. *Crop Sci.* 54, 1514–1522. doi: 10.2135/cropsci2013.12.0856

Makanza, R., Zaman-Allah, M., Cairns, J., Eyre, J., Burgueño, J., Pacheco, Á, et al. (2018). High-throughput method for ear phenotyping and kernel weight estimation in maize using ear digital imaging. *Plant Methods* 14, 1–13. doi: 10.1186/s13007-018-0317-4

Mikel, M. (2006). Availability and analysis of proprietary dent corn inbred lines with expired U.S. plant variety protection. *Crop Sci.* 46, 2555–2560. doi: 10.2135/cropsci2006.05.0358

Mikel, M. (2008). Genetic diversity and improvement of contemporary proprietary north American dent corn. *Crop Sci.* 48, 1686–1695. doi: 10.2135/cropsci2008.01.0039

Mikel, M., and Dudley, J. (2006). Evolution of North American dent corn from public to proprietary germplasm. *Crop Sci.* 46, 1193–1205. doi: 10.2135/cropsci2005.10-0371

Mikel, M. A. (2011). Genetic composition of contemporary U.S. commercial dent corn germplasm. *Crop Sci.* 51, 592–599. doi: 10.2135/cropsci2010.06.0332

Miller, N., Haase, N., Lee, J., Kaeppler, S., de Leon, N., and Spalding, E. (2017). A robust, high-throughput method for computing maize ear, cob, and kernel attributes automatically from images. *Plant J.* 89, 169–178. doi: 10.1111/tpj.13320

Nelson, P., Coles, N., Holland, J., Bubeck, D., Smith, S., and Goodman, M. (2008). Molecular characterization of maize inbreds with expired U.S. plant variety protection. *Crop Sci.* 48, 1673–1685. doi: 10.2135/cropsci2008.02.0092

Nelson, P., and Goodman, M. (2008). Evaluation of elite exotic maize inbreds for use in temperate breeding. *Crop Sci.* 48, 85–92. doi: 10.2135/cropsci2007.05.0287

Nielsen, R. (2002). *Corn Growth and Development: What Goes on From Planting to Harvest*. West Lafayette, IN: Purdue University.

Nyquist, W., and Baker, R. (1991). Estimation of heritability and prediction of selection response in plant populations. *Crit. Rev. Plant Sci.* 10, 235–322. doi: 10.1080/07352689109382313

Piepho, H. P., and Möhring, J. (2007). Computing heritability and selection response from unbalanced plant breeding trials. *Genetics* 177, 1881–1888. doi: 10.1534/genetics.107.074229

Purcell, S., Neale, B., Todd-Brown, K., Thomas, L., Ferreira, M. A. R., Bender, D., et al. (2007). PLINK: a toolset for whole-genome association population-based linkage analysis. *Am. J. Hum. Genet.* 81, 559–575. doi: 10.1086/519795

R Core Team (2019). *R: A Language and Environment for Statistical Computing*. Available online at: http://www.r-project.org/ (accessed August 20, 2019).

Ross, A., Hallauer, A., and Lee, M. (2006). Genetic analysis of traits correlated with maize ear length. *Maydica* 51, 301–313.

Shull, G. (1908). The composition of a field of maize. *J. Hered.* 4, 296–301. doi: 10.1093/jhered/os-4.1.296

Shull, G. (1909a). A pure-line method in corn breeding. *J. Hered.* 5, 51–59. doi: 10.1093/jhered/os-5.1.51

Shull, G. (1909b). Hybridization methods in corn breeding. *J. Hered.* 1, 63–72. doi: 10.1093/jhered/1.2.98

Shull, G. H. (1911). The genotypes of maize. *Am. Soc. Nat.* 45, 234–252.

Shull, G. H. (1914). Duplicate genes for capsule-form in Bursa bursa-pastoris. *Z. Indukt. Abstamm. Vererbungsl.* 12, 97–149. doi: 10.1007/BF01837282

Tollenaar, M., Ahmadzadeh, A., and Lee, E. (2004). Crop physiology and metabolism. *Crop Sci.* 44, 2086–2094. doi: 10.2135/cropsci2004.2086

Tollenaar, M., and Lee, E. (2006). Dissection of physiological processes underlying grain yield in maize by examining genetic improvement and heterosis. *Maydica.* 51, 399–408.

Troyer, A. (1999). Background of U.S. hybrid corn. *Crop Sci.* 39, 601–626.

Uhr, D., and Goodman, M. (1995a). Temperate maize inbreds derived from tropical germplasm: I. Testcross yield trials. *Crop Sci.* 35, 779–784. doi: 10.2135/cropsci1995.0011183x003500030024x

Uhr, D., and Goodman, M. (1995b). Temperate maize inbreds derived from tropical germplasm: II. Inbred yield trials. *Crop Sci.* 35, 785–790. doi: 10.2135/cropsci1995.0011183x003500030025x

Vasal, S., Cordova, H., Pandey, S., and Srinivasan, G. (1999). "Tropical maize and heterosis," in *The Genetics and Exploitation of Heterosis in Crops*, eds J. Coors and S. Pandey (Madison, WI: American Society of Agronomy,

Inc., Crop Science Socieity of Agronomy Inc), 363–373. doi: 10.2134/1999.geneticsandexploitation.c34

Vasal, S., Srinivasan, G., Gonzalez, F., Han, G., Pandey, S., Beck, D., et al. (1992). Heterosis and combining ability of CIMMYT's tropical x subtropical maize germplasm. *Crop Sci.* 32, 1483–1489. doi: 10.2135/cropsci1992.0011183x003200060036x

White, M., Mikel, M., de Leon, N., and Kaeppler, S. (2020). Diversity and heterotic patterns in North American proprietary dent maize germplasm. *Crop Sci.* 60, 100–114. doi: 10.1002/csc2.20050

Wu, Y., San Vicente, F., Huang, K., Dhliwayo, T., Costich, D., Semagn, K., et al. (2016). Molecular characterization of CIMMYT maize inbred lines with genotype-by-sequencing SNPs. *Theor. Appl. Genet.* 129, 753–765. doi: 10.1007/s00122-016-2664-8

Yuan, Y., Cairns, J., Babu, R., Gowda, M., Makumbi, D., Magorokosho, C., et al. (2019). Genome-wide association mapping and genomic prediction analyses reveal the genetic architecture of grain yield and flowering time under drought and heat stess conditions in maize. *Front. Plant Sci.* 9:1919. doi: 10.3389/fpls.2018.01919

Conflict of Interest: AS was employed by the company Advanta Seeds.

The remaining authors declare that the research was conducted in the absence of any commercial or financial relationships that could be construed as a potential conflict of interest.

frontiers in Plant Science

REVIEW
published: 25 June 2021
doi: 10.3389/fpls.2021.611940

Robotic Technologies for High-Throughput Plant Phenotyping: Contemporary Reviews and Future Perspectives

Abbas Atefi[1], Yufeng Ge[1], Santosh Pitla[1] and James Schnable[2]*

[1] Department of Biological Systems Engineering, University of Nebraska–Lincoln, Lincoln, NE, United States, [2] Department of Agronomy and Horticulture, University of Nebraska–Lincoln, Lincoln, NE, United States

Phenotyping plants is an essential component of any effort to develop new crop varieties. As plant breeders seek to increase crop productivity and produce more food for the future, the amount of phenotype information they require will also increase. Traditional plant phenotyping relying on manual measurement is laborious, time-consuming, error-prone, and costly. Plant phenotyping robots have emerged as a high-throughput technology to measure morphological, chemical and physiological properties of large number of plants. Several robotic systems have been developed to fulfill different phenotyping missions. In particular, robotic phenotyping has the potential to enable efficient monitoring of changes in plant traits over time in both controlled environments and in the field. The operation of these robots can be challenging as a result of the dynamic nature of plants and the agricultural environments. Here we discuss developments in phenotyping robots, and the challenges which have been overcome and others which remain outstanding. In addition, some perspective applications of the phenotyping robots are also presented. We optimistically anticipate that autonomous and robotic systems will make great leaps forward in the next 10 years to advance the plant phenotyping research into a new era.

Keywords: autonomous robotic technology, agricultural robotics, phenotyping robot, high-throughput plant phenotyping, computer vision

OPEN ACCESS

Edited by:
Ankush Prashar, Newcastle University, United Kingdom

Reviewed by:
Simon Pearson, University of Lincoln, United Kingdom
Katja Herzog, Institut für Rebenzüchtung, Julius Kühn-Institut, Germany
Rui Xu, University of Georgia, Georgia

***Correspondence:**
Yufeng Ge
yge2@unl.edu

Specialty section:
This article was submitted to Technical Advances in Plant Science, a section of the journal Frontiers in Plant Science

Received: *29 September 2020*
Accepted: *14 May 2021*
Published: *25 June 2021*

Citation:
Atefi A, Ge Y, Pitla S and Schnable J (2021) Robotic Technologies for High-Throughput Plant Phenotyping: Contemporary Reviews and Future Perspectives. Front. Plant Sci. 12:611940. doi: 10.3389/fpls.2021.611940

INTRODUCTION: ROBOTIC TECHNOLOGY IS VITAL FOR HIGH-THROUGHPUT PLANT PHENOTYPING

Agriculture must produce enough food, feed, fiber, fuel, and fine chemicals in next century to meet the needs of a growing population worldwide. Agriculture will face multiple challenges to satisfy these growing human needs while at the same time dealing with the climate change, increased risk for drought and high temperatures, heavy rains, and degradation of arable land and depleting water resources. Plant breeders seek to address these challenges by developing high yielding and stress-tolerance crop varieties adapted to future climate conditions and resistant to new pests and diseases (Fischer, 2009; Furbank and Tester, 2011; Rahaman et al., 2015). However, the rate of crop productivity needs to be increased to meet projected future demands. Advances in DNA sequencing and genotyping technologies have relieved a major bottleneck in both marker assisted selection and

genomic prediction assisted plant breeding, the determination of genetic information for newly developed plant varieties. Dense genetic marker information can aid in the efficiency and speed of the breeding process (Wang et al., 2018; Happ et al., 2019; Moeinizade et al., 2019). However, large and high quality plant phenotypic datasets are also necessary to dissect the genetic basis of quantitative traits which are related to growth, yield and adaptation to stresses (McMullen et al., 2009; Jannink et al., 2010; Phillips, 2010; Fahlgren et al., 2015; Tripodi et al., 2018; Chawade et al., 2019).

Plant phenotyping is the quantitative and qualitative assessment of the traits of a given plant or plant variety in a given environment. These traits include the biochemistry, physiology, morphology, structure, and performance of the plants at various organizational scales. Plant traits are determined by both genetic and environmental factors as well as non-additive interactions between the two. In addition, variation in one phenotypic trait (e.g., leaf characteristics) can result in variation in other plant traits (e.g., plant biomass or yield). Therefore, phenotyping large numbers of plant varieties for multiple traits across multiple environments is an essential task for plant breeders as they work to select desirable genotypes and identify genetic variants which provide optimal performance in diverse and changing target environments (Granier and Tardieu, 2009; Dhondt et al., 2013; Li et al., 2014; Foix et al., 2015; Walter et al., 2015; Costa et al., 2019; Pieruschka and Schurr, 2019).

Traditionally plant traits are quantified using manual and destructive sampling methods. These methods are usually labor-intensive, time-consuming, and costly. In addition, manual sampling and analysis protocols generally involve many steps requiring human intervention, with each step increasing the chances of introducing mistakes. Often the plant and its organ is cut at fixed time points or at particular phenological stages in order to measure its phenotypic traits. This method destroys or damages the plant at one time point, disallowing the temporal examination of the traits for individual plants during the growing season. For example, yield measurement (such as plant biomass and grain weight) is invasive and more labor intensive compare to the measurement of plant height and leaf chlorophyll content (measured by a handheld sensor). As a result of the labor and resource intensive nature of plant phenotyping, many plant breeders rely solely on a single measurement most critical to their efforts: yield. However, yield is considered as one of the most weakly inherited phenotypes in crop breeding (Richards et al., 2010; Furbank and Tester, 2011). The measurement of other traits in addition to yield can increase the accuracy with which yield can be predicted across diverse environments. Enabling high-throughput and non-destructive measurements of plant traits from large numbers of plants in multiple environments would therefore lead to increases in breeding efficiency (McMullen et al., 2009; Andrade-Sanchez et al., 2013; Fahlgren et al., 2015; Foix et al., 2018; Vijayarangan et al., 2018; Ge et al., 2019; Hassanijalilian et al., 2020a).

In recent years, high-throughput systems and workflows have been developed to monitor and measure large populations of plants rapidly in both greenhouse and field environments. These systems combine modern sensing and imaging modalities with the sensor deployment technologies (including conveyor belts, ground and aerial vehicles, and field gantries) to enable fast measurement and wide area coverage (Busemeyer et al., 2013; Ge et al., 2016; Virlet et al., 2017; Hassan et al., 2019). Although not fully autonomous, these systems represent the state of the art in modern plant phenotyping with several advantages over the traditional, manually collected phenotypic traits.

Robotic systems have been playing a more significant role in modern agriculture and considered as an integral part of precision agriculture or digital farming (Wolfert et al., 2017; Chlingaryan et al., 2018; Zhang et al., 2019; Hassanijalilian et al., 2020b; Jin et al., 2020; Pandey et al., 2021). The robots are fully autonomous and do not need experienced operators to accomplish farming tasks. This is the biggest advantage of the robots compared to tractor-based systems (White et al., 2012). Autonomous robots have taken over a wide range of farming operations including harvesting [Arad et al., 2020 (sweet pepper); Hemming et al., 2014 (sweet pepper); Lili et al., 2017 (tomato); van Henten et al., 2002 (cucumber); Hayashi et al., 2010; Xiong et al., 2020 (strawberry); Silwal et al., 2017 (apple)], pest and weed control [Raja et al., 2020 (tomato and lettuce); Oberti et al., 2016 (grape); Åstrand and Baerveldt, 2002 (sugar beet); Blasco et al., 2002 (lettuce)], spraying [Hejazipoor et al., 2021 (Anthurium); Gonzalez-de-Soto et al., 2016 (wheat); Adamides et al., 2017 (grape)], and pruning [Zahid et al., 2020 (apple); Chonnaparamutt et al., 2009; Ishigure et al., 2013 (cedar and hinko trees)]. Together with imaging and sensing, autonomous robotic systems are also deemed essential and integral parts for high-throughput plant phenotyping, as they will enhance substantially the capacity, speed, coverage, repeatability, and cost-effectiveness of plant trait measurements.

In this paper, we reviewed the latest development of robotic technologies in high-throughput plant phenotyping. We define the robotic technologies as a system having three components: (1) a sensing module that senses the target (plants or crops) and its environment, (2) a computational module to interpret the sensed information and form adaptive (or context-specific) decisions, and (3) an actuation module to complete certain desired operations (e.g., robotic probing, trait measurements, and navigation). For example, the robot makes decision based on the existing status of environment, obstacles, and plant geometry to manipulate a robotic arm to locate an imaging system with less occlusion and collision free close to plant organs, find appropriate target point on the leaf and control the end-effector based on the leaf angle for effective grasping, or accurately navigate the ground-based vehicles between crop rows. With this definition, systems like LemnaTec's conveyor-based phenotyping platform (Fahlgren et al., 2015; Ge et al., 2016) was not considered in the review, because the plant movement usually follows a pre-defined schedule and no adaptive decision is made during phenotyping. Also not considered in this review are self-propelled ground vehicles or unmanned aerial vehicles (Bai et al., 2016; Han et al., 2018) that are merely used as a sensor deployment platform with no automated path planning or navigation.

Different artificial intelligence (AI) technologies such as deep learning, fuzzy logic, and genetic algorithms are actively used for control of the phenotyping robots. In recent years, deep

learning techniques has gained increased interest to guide robotic manipulators and mobile platforms. In this regard, deep neural networks (DNNs) are commonly used to detect different objects in images such as crop rows, plant organs, soil, and obstacles. DNNs are typically operate directly on raw images and actively learn a variety of filter parameters during the training of a model (Pound et al., 2017; Irshat et al., 2018). Aguiar et al. (2020) presented a DNN models to detect the vine trunks as reliable features and landmarks to navigate a mobile robot in a vineyard. Parhar et al. (2018) used variation of Generative Adversarial Network (GAN) to detect the stalk of sorghum in the field and grasp it by a robotic manipulator.

There are three motivations behind writing this review paper. Firstly, robotic technologies in agriculture have seen rapid advancement recently with many emerging applications in plant phenotyping. A timely review of the literature is warranted to summarize the newest development in the field. Secondly, there is large and growing interest from the plant breeding and plant science communities in how these new technologies can be integrated into research and breeding programs to improve phenotyping throughput and capacity (Furbank and Tester, 2011; Fiorani and Schurr, 2013; Araus and Cairns, 2014). Thirdly, robotic phenotyping has advanced through cross-disciplinary collaborations between engineers and plant scientists. Outlining capabilities, goals and interests across these two very different disciplines may help readers to identify research gaps and challenges as well as provide insight into the future directions of the plant phenotyping robotic technologies.

REVIEW: MANY INDOOR AND OUTDOOR ROBOTS WERE DEVELOPED TO MEASURE A WIDE RANGE OF PLANT TRAITS

Phenotyping robotic systems have emerged to automate the phenotyping process in different aspects. The robotic manipulators and ground-based vehicles are used as platforms to attach different sensors to collect data rapidly and with higher repeatability. Robotic systems are deployed to collect and measure the human-defined phenotypic traits (such as plant height, and leaf area). Additionally, in some cases it is needed to collect repeated measurements of plant traits within large populations at several time points during a growing season. Robotic systems are highly desirable in this scenario as they provide the necessary speed and accuracy for this kind of phenotyping tasks.

Robotic platforms for plant phenotyping applications can be divided into two categories: those developed for indoor or controlled environments (greenhouse or laboratory), and those for outdoor environments (field) (Shafiekhani et al., 2017). In controlled environment, plants are either placed in a fixed position and the robot moves around the facility to interact with the plants, or the plants are moved by conveyor belts or other automated systems to a fixed location where the robot operates. Often the robotic system does not need to touch the plants. The robotic arm is equipped with RGB cameras or depth sensors [Time of Flight (TOF) cameras or 3D laser scanners] to acquire visible images or point cloud data. The morphological traits of the plants are then estimated from the reconstructed 3D model of the plants. Stem height and leaf length of corn seedlings were measured using a robotic arm at a fixed position and a TOF camera (Lu et al., 2017). Chaudhury et al. (2017) developed a gantry robot system consisted of a 3D laser scanner installed on the end-effector of a seven Degree of Freedom (DOF) robotic arm to compute the surface area and volume of *Arabidopsis* and barley. The settings of both robotic systems were unable to position the vision system to capture images from the leaves hidden by other leaves or the stem. This occlusion problem is common in image-based phenotyping (Das Choudhury et al., 2019). Even with imaging from multiple views (e.g., enabled by rotating plants during image acquisition), occlusion can still be substantial. The use of imaging systems carried by a robotic manipulator can provide viable solution to this issue, due to the flexibility of the robotic manipulator to position and orient cameras at the best intended viewpoints. Wu et al. (2019) proposed an automated multi-robot system, which comprised of three robotic arms each equipped with a depth camera to obtain the point cloud data of the plant (**Figure 1A**). Deep learning based next-best view (NBV) planning pipeline was presented to evaluate and select the next-best viewpoints to maximize the information gain from the plant in data acquisition process. The robotic arms then were manipulated based on the determined optimal viewpoints. Their system was more efficient and flexible compared to other robotic systems to address the occlusion issue. The ability of the system to find the optimal viewpoints, however, can be challenging, because its performance depends upon the predictions produced by the trained deep networks. This means that the best view-points may not be determined by the system if the deep networks can not generate accurate predictions.

A second group of indoor plant phenotyping robots sought to touch or probe plants or plant organs, in order to extend the ability of robotic phenotyping from plant's outward morphological traits to innate physiological and biochemical traits (Schulz and Baranska, 2007; Biskup et al., 2009). In this sense, the phenotyping robot was designed to mimic humans to manipulate plants and measure certain traits from targeted plant organs (**Figure 2**). This type of the robotic systems usually included a robotic gripper designed to attach specialized plant sensors, and a vision module to segment the plant from the background and find an appropriate point on the organs for probing [Alenyà et al., 2011; Shah et al., 2016; Bao et al., 2017 (Ficus plant)] or grasping process [Alenya et al., 2013; Ahlin et al., 2016 (Anthurium, Pothos, and Dieffenbachia)]. A sensor-equipped robot was presented to measure physiological parameters of the plant (Bao et al., 2019c). The sensor unit including RGB, hyperspectral, thermal, and TOF cameras, and a fluorometer were attached to a robotic arm. The robot measured the reflectance spectra, temperature, and fluorescence by imaging the leaf or placing probes with millimeter distance from the leaf surface (**Figure 1B**). Two different plant phenotyping robotic systems were introduced to measure leaf and stem properties of maize and sorghum plants (Atefi et al., 2019, 2020). The

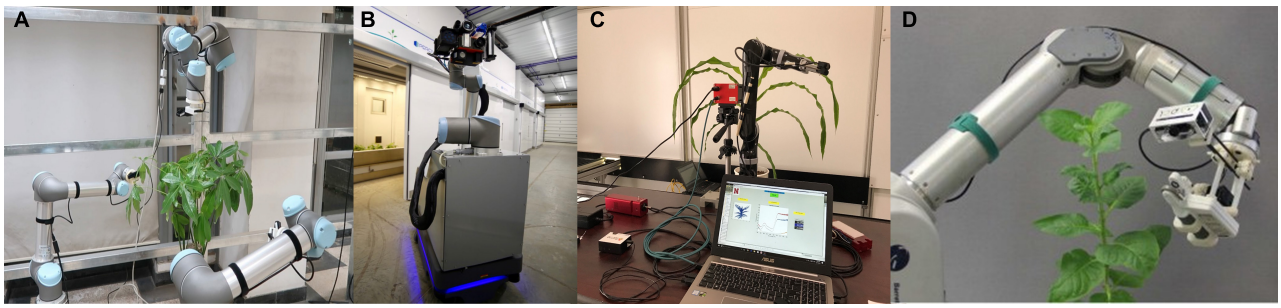

FIGURE 1 | Plant phenotyping robotic systems for indoor environment: **(A)** A multi-robot system equipped with deep learning technique to determine optimal viewpoints for 3D model reconstruction (Wu et al., 2019), **(B)** Sensor-equipped robot to measure the reflectance spectra, temperature, and fluorescence of leaf (Bao et al., 2019c), **(C)** Robotic system to measure leaf reflectance and leaf temperate (Atefi et al., 2019), and **(D)** Robotic system for direct measurement of leaf chlorophyll concentrations (Alenyá et al., 2014).

systems consisted of a TOF camera, a four DOF robotic manipulator, and custom-designed grippers to integrate the sensors to the robotic manipulator. Image-processing and deep-learning based algorithms were presented to find the grasping point on leaves and stem. An optical fiber cable (attached to a spectrometer) and a thermistor were used to collect leaf hyperspectral reflectance and leaf temperature simultaneously. The stem diameter was measured by a linear potentiometer sensor. Leaf hyperspectral reflectance was used to build predictive models for leaf chlorophyll content, water content, N (nitrogen), P (phosphorus), and K (potassium) concentrations (**Figure 1C**). Alenyà Ribas et al. (2012) mounted a SPAD meter to a robotic arm to directly measure leaf chlorophyll concentrations of Anthurium White, Anthurium Red, and Pothus (**Figure 1D**). Quadratic surface models were applied to segment leaves from infrared-intensity images and depth maps captured by a TOF camera. The estimation issues of probing point caused by poor leaf-fitting model reduced the probing success rate of the robotic system (82%).

Although controlled environments can make it easier to grow plants and quantify their phenotypic traits, because environment plays a large role in determining plant traits, plants grown in controlled environments show many differences from plants grown in field conditions. Therefore, with the exception of a growing range of horticultural crops where production occurs in control environments, for many crops the assessment of phenotypic responses in field conditions provides more directly actionable information for crop improvement. A wide range of platforms have been developed for field-based high-throughput plant phenotyping [Montes et al., 2007; White et al., 2012; Gao et al., 2018 (soybean); Weiss and Biber, 2011 (detection and mapping of maize plants); Jenkins and Kantor, 2017 (stalk detection of sorghum); Iqbal et al., 2020 (plant volume and height); Smitt et al., 2020 (fruit counting of sweet pepper and tomato)]. These robotic systems are guided between crop rows and moved toward plants. This creates several new challenges for both navigation and data collection which are absent when robotic phenotyping is conducted in control conditions. Factors like temperature, sunlight, wind, and unevenness of soil surface, can negatively impact the performance of the system. Therefore, the hardware and software of the robotic system must be designed to be resilient to the unique challenges of operating in field conditions. In the field plants are always stationary, necessitating that (1) phenotyping robots move to the plants rather than vice versa, (2) all components of the phenotyping robot including the vision system, robotic arm, and sensors as well as power supplies be carried by a robotic mobile platform, and (3) this platform be capable of navigation whether through global positioning system (GPS) data and/or employing sensors to perceive its local environment to guide navigation.

Unmanned ground vehicle (UGV) robotic systems employ a range of sensor types including light detection and ranging (LIDAR) and cameras [RGB, TOF, near infrared (NIR), and stereo vision] for data collection. They can be installed on a fixed stand within the overall mobile platform, or affixed a robotic arm to increase the number of diversity of positions from which sensor data can be collected. Different techniques such as 3D reconstruction, image processing, and machine learning are used for data analysis and quantify morphological traits. Existing UGV robotic systems have been employed to measure plant height, plant orientation, leaf angle, leaf area, leaf length, leaf and stem width, and stalk count of various species such as maize, and sorghum, sunflower, savoy cabbage, cauliflower, and Brussels sprout (Jay et al., 2015; Fernandez et al., 2017; Baweja et al., 2018; Choudhuri and Chowdhary, 2018; Vázquez-Arellano et al., 2018; Vijayarangan et al., 2018; Bao et al., 2019b; Breitzman et al., 2019; Qiu et al., 2019; Young et al., 2019; Zhang et al., 2020), count the cotton bolls (Xu et al., 2018), architectural traits and density of peanut canopy (Yuan et al., 2018), berry size and color of grape (Kicherer et al., 2015), and shape, volume, and yield estimation of vineyard (Lopes et al., 2016; Vidoni et al., 2017). A compact and autonomous TerraSentia rover equipped with three RGB cameras and a LIDAR was demonstrated to acquire in-field LIDAR scans of maize plants to extract their Latent Space Phenotypes (LSPs) (Gage et al., 2019). They were inferred from the images using machine learning methods (Ubbens et al., 2020) and contained information about plant architecture and biomass distribution. Shafiekhani et al. (2017) introduced a robotic system

FIGURE 2 | Manual measurements of leaf reflectance **(left)**, leaf temperature **(middle)**, and chlorophyll content **(right)** (Atefi et al., 2019).

(Vinobot) including a six DOF robotic arm with a 3D imaging sensor mounted on a mobile platform. The Vinobot collected data in order to measure plant height and leaf area index (LAI) of maize and sorghum (**Figure 3A**). The authors reported that the use of a semi-autonomous approach created most of challenges for navigation of the system. In this approach, the alignment of the robot with the crop rows was required before autonomously moving between the rows and collecting data from the plants.

Measurements of some biochemical and physiological properties require a direct contact between sensors and plants. Measuring these properties therefore requires a robot capable of grasping or touching plant organs. Grasping plant organs in turn requires a dexterous robotic arm as well as onboard sensors and algorithms capable of reconstructing the 3D geometry of the target plant. Robotanist, a UGV equipped with a custom stereo camera, was established to measure stalk strength of sorghum (Mueller-Sim et al., 2017; **Figure 3B**). A three DOF robotic arm along with a special end-effector was mounted on Robotanist. The end-effector consisted of a rind penetrometer that was modified by attaching a force gauge and a needle. When the stalk was grasped by the end-effector, the needle and force gauge were pushed into the stalk to accomplish the measurement. The authors suggested to develop algorithms using laser scan and navigation camera data to improve the performance of the navigation system to reliably work under taller sorghum canopy and throughout the entire growing season. Abel (2018) attached a spectrometer to the robotic manipulator of Robotanist to capture spectral reflectance measurements of leaves and stems of sorghum. Random sample consensus (RANSAC) method was used for leaf and stem detection. A machine learning approach was applied to estimate the chlorophyll content of leaves, and moisture and starch contents of stems from reflectance spectra. Two factors reduced the grasping success rate of leaves (68%). First, the grasping process was failed because the wind moved the leaves and changed the position of the grasping point. Second, the occlusion and overlapping affected the performance of the segmentation algorithms to detect more leaves in the images. Chen et al. (2021) developed a robotic system including LeafSpec (invented at Purdue University) attached to a robotic manipulator to collect hyperspectral images of maize leaves in the field (**Figure 3C**). The robot slid the LeafSpec across the leaf from the beginning to tip to acquire hyperspectral images of entire leaf. The system predicted leaf nitrogen content with $R^2 = 0.73$.

Other autonomous ground-based systems were presented to measure both morphological and biochemical/physiological attributes. A visible and near infrared (VIS/NIR) multispectral camera was mounted on a mobile robot called "Thorvald I" to measure the normalized difference vegetation index (NDVI) of wheat from multispectral images (Burud et al., 2017). The robot then modified to a new version called "Thorvald II" to have better performance for phenotyping tasks (Grimstad and From, 2017; **Figure 3D**). BoniRob was proposed as an autonomous robot platform including spectral imaging and 3D TOF cameras which can be used to measure plant parameters such as plant height, stem thickness, biomass, and spectral reflection (Ruckelshausen et al., 2009; Biber et al., 2012; **Figure 3E**). Underwood et al. (2017) introduced a ground-based system (Ladybird) for row phenotyping of grain and legume crops (wheat, faba bean, lentil, barley, chickpea, and field pea) (**Figure 3F**). Crop height, crop closure, and NDVI were determined after processing the data from the LIDAR and the hyperspectral camera. Flex-Ro, a multi-purpose field robotic platform was used for high-throughput plant phenotyping to measure phenotyping traits of soybean (Murman, 2019; **Figure 3G**). Three sets of sensors were installed on Flex-Ro to collect data from crop rows. For each set, a passive fiber optic cable, a RGB camera, an ultrasonic distance sensor, and an infrared radiometer were used to measure NDVI, canopy coverage, canopy temperature, and height.

Table 1 summarizes the indoor and outdoor robotic systems which could successfully measure plant traits for different crops.

Figure 4 gives summary statistics regarding the plant phenotyping robotic systems that is discussed in this section. It can be seen that the robotic phenotyping research targeted maize and sorghum more than other species (soybean, wheat, barley, chickpea, pea, faba bean, lentil, cabbage, cauliflower, cotton, peanut, sunflower, grape, tomato, sweet pepper, and Arabidopsis) (**Figure 4A**). Maize and sorghum are two of the most economically important and highly diverse cereal crops with vast numbers of accessions (Zhao et al., 2016; Bao et al., 2019b). Therefore, more attention was devoted to breed Maize and sorghum to produce food, animal fodder, and biofuel. Moreover, the available genetic resources for these crops required the phenotyping data to map their genotypes to phenotypes and

FIGURE 3 | Plant phenotyping systems for outdoor environment: **(A)** Vinobot: robotic system including six DOF robotic manipulator and a 3D imaging sensor mounting on a mobile platform to measure plant height and LAI (Shafiekhani et al., 2017), **(B)** Robotanist: UGV-based robotic system equipped with a three DOF robotic manipulator and a force gauge for stalk strength measurement (Mueller-Sim et al., 2017), **(C)** A robotic system to slide LeafSpec across entire leaf to collect its hyperspectral images (Chen et al., 2021), **(D)** Thorvald II: VIS/NIR multispectral camera mounted on a mobile robot to measure NDVI (Grimstad and From, 2017), **(E)** BoniRob: autonomous robot platform using spectral imaging and 3D TOF cameras to measure plant height, stem thickness, biomass, and spectral reflection (Biber et al., 2012), **(F)** Ladybird: ground-based system consisted of a hyperspectral camera, a stereo camera, a thermal camera, and LIDAR to measure crop height, crop closure, and NDVI (Underwood et al., 2017), and **(G)** Flex-Ro: high-throughput plant phenotyping system equipped with a passive fiber optic, a RGB camera, an ultrasonic distance sensor, and an infrared radiometer for the measurement of NDVI, canopy coverage, and canopy height (Murman, 2019).

thus crop yield improvement. Accordingly, there has been an emerging need for phenotyping robots to automatically measure the phenotypic traits. Regarding the plant structure, maize, and sorghum have similar morphology. Their leaves are arranged alternately on each side of the stem that has cylindrical/elliptic-cylinder shape and is positioned in the middle part of the plant. This plant structure provides less complexity for the robotic system to distinguish between the stem and leaves and extract their features. **Figure 4B** shows that the height, width, and volume of plant/canopy are three main (morphological) traits that more frequently measured by the robotic systems than other traits, each of them being $\leq 5\%$ (leaf length, leaf width, leaf angle, leaf area, leaf reflectance, leaf chlorophyll content, leaf/canopy temperature, LAI, plant/canopy NDVI, stem reflectance, stalk strength, stalk count, berry size, and fruit count). Two reasons can be considered for the frequent measurements of these phenotypic traits. Firstly, the plant architectural traits (such as plant height) are the most common and important parameters for field plant phenotyping since they have significant effects on light interception for photosynthesis, nitrogen availability, and yield (Barbieri et al., 2000; Andrade et al., 2002; Tsubo and Walker, 2002). Consequently, by studying and then manipulation of the plant architecture, the crop productivity will be increased. Secondly, as it was discussed in this section, the robot just needs non-contact based sensors (RGB camera or depth sensor) to collect data from the plants. Then, by analyzing the 2D images or creating plant 3D models, the aforementioned plant traits can be estimated in either ways: (1) the correlation between the pixel counts in the images and the ground truth measurements, or (2) extracting the distance/volume in real world from the depth sensor data. Hence, the measurement of these morphological properties is less challenging for the phenotyping robots using simple sensors and algorithms. In addition to the more frequent measurements of stem height and width (of maize and sorghum), these properties were also measured more accurately by the robotic systems because they are less affected by the plant morphology (**Figure 4C**). The first step to extract the stem height and width is to detect the stem and segment it from other plant organs. The morphology of maize and sorghum (alternately arranged leaves, and cylindrical-shaped stem in the middle) provides more hints for stem detection and segmentation. Moreover, the height and width can be measured as linear measurements. Accordingly, these two stem properties can be measured with less complexity and higher accuracy. **Figure 4D** illustrates that non-contact based sensing systems (such as RGB, stereo vision, and multispectral cameras, and LIDAR) were

TABLE 1 | Summary of indoor and outdoor robotic systems that successfully measured plant properties for different crops.

Robot type	References	Species	Plant trait	Performance	Measurement method	Software system
Indoor	Alenyà Ribas et al., 2012	Anthurium Andreanum (White), Anthurium andreanum (Red), Epipremnum aureum (Pothos)	Leaf chlorophyll content	SR = 90%, 85%, 70%	Contact based	ROS
	Lu et al., 2017	Maize	Stem height, leaf length	ER = 13.7%, 13.1%	Non-contact based	Qt development environment (C++)
	Atefi et al., 2019	Maize, Sorghum	Leaf chlorophyll content, leaf potassium content, leaf water content, leaf temperature	R^2 = 0.52, 0.52, 0.61 R^2 = 0.58, 0.63	Contact based	MATLAB
	Atefi et al., 2020	Maize, Sorghum	Stem diameter	R^2 = 0.98, 0.99	Contact based	MATLAB
Outdoor	Jay et al., 2015	Sunflower, Savoy cabbage, cauliflower, Brussels sprout	Plant height, leaf area	R^2 = 0.99, 0.94	Non-contact based	Not reported
	Shafiekhani et al., 2017 (Vinobot)	Maize, sorghum	Plant height	R^2 = 0.99	Non-contact based	ROS
	Abel, 2018 (Robotanist)	Sorghum	Stem starch content, stem moisture content, leaf chlorophyll content	R = 0.81, 0.72, 0.92	Contact based	ROS
	Baweja et al., 2018 (Robotanist)	Sorghum	Stalk count, stalk width	R^2 = 0.88, MAE = 2.77 mm	Non-contact based	ROS
	Choudhuri and Chowdhary, 2018	Sorghum	Stem width	Accuracy = 98.2%	Non-contact based	Python
	Vázquez-Arellano et al., 2018	Maize	Plant height	AME = 8.7 mm SD = 35 mm	Non-contact based	Not reported
	Vijayarangan et al., 2018	Sorghum	Leaf area, leaf length, leaf width	Relative RMSE = 26.15%, 26.67%, 25.15%	Non-contact based	ROS
	Bao et al., 2019b	Maize	Plant height, leaf angle	R^2 = 0.96, 0.83	Non-contact based	Not reported
	Qiu et al., 2019	Maize	Plant height	RMSE = 0.058 m	Non-contact based	ROS
	Young et al., 2019	Sorghum	Plant height, stem width	AE = 15%, 13%	Non-contact based	Not reported
	Zhang et al., 2020	Maize	Stand counting	R = 0.96 SD = 6.76%	Non-contact based	Not reported

ER, error ratio; SR, success rate, MAE, mean absolute error; RMSE, root mean square error; AME, absolute mean error; AE, absolute error; SD, standard deviation; ROS, robot operating system.

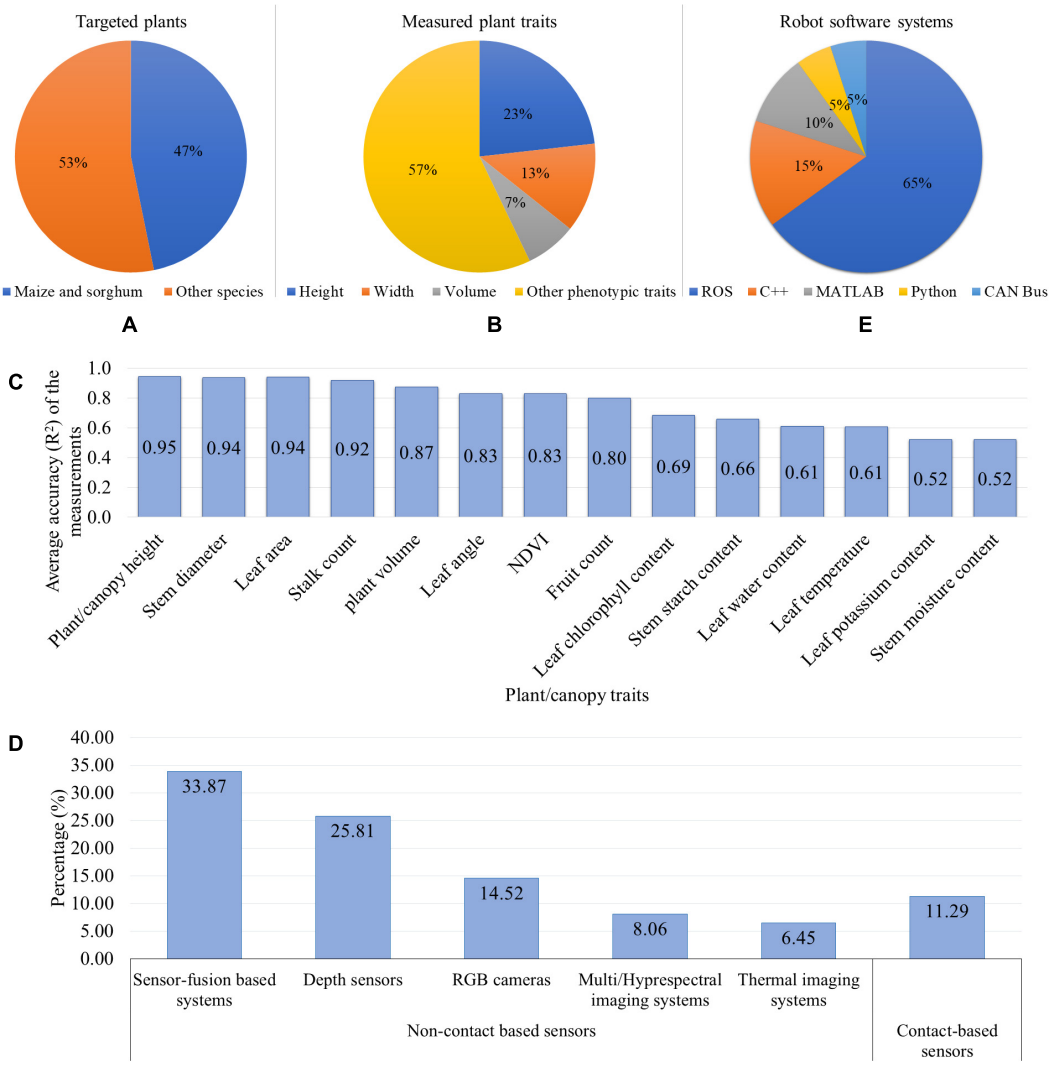

FIGURE 4 | Summary statistics of the phenotyping robotic systems: **(A)** Targeted plants, **(B)** Plant/canopy traits measured by the robots, **(C)** Average accuracy (R^2) to measure the phenotypic traits, **(D)** Robot vision/sensing systems, and **(E)** Robot software systems.

used more in phenotyping robots compared to contact-based sensors (chlorophyll meters, spectrometers, thermistors, and linear potentiometers). This can be explained by the fact that the majority of the robotic systems were developed to measure the morphological traits or some physiological properties. To achieve these goals, the phenotyping robots are required to use the 2D images/3D models of plants using non-contact based sensors. Among the non-contact sensors, the sensor-fusion based systems (including RGBD/stereo vision cameras, RGB camera + LIDAR, RGB + TOF cameras, spectral imaging + TOF camera) and depth sensors (TOF camera, LIDAR, laser scanner, and ultrasonic sensor) were commonly used as vision/sensing systems for the phenotyping robots. The key is to acquire depth information as a vital parameter to manipulate a robotic arm to grasp the plant organs, navigate a mobile robot between crop rows, and measure plant properties (such as height, width, and volume). Sensor-fusion based systems were employed by phenotyping robots more often than depth sensors. The reason would be that these sensors prepare the plant color/spectral information along with the depth information. Consequently, by acquiring more information, the plant can be effectively segmented from the background and the plant properties can be effectively measured. Regarding the robot software system, it can be found that Robot Operating System (ROS) is one the most popular systems to develop the software of the phenotyping robots (**Figure 4E**). ROS is an open source system that provides services, libraries, and tools for sensors-actuators interface, software components communication, and navigation and path planning[1]. Different manufacturers of robot's hardware provide ROS drivers for their products such as imagery systems, sensors, actuators, robotic manipulators, and mobile platforms. This allows the researchers to develop the phenotyping robotic systems more efficiently.

[1]https://www.ros.org/

Regarding the platform of the mobile phenotyping robots, most of the mobile platforms were developed by researchers (86%) and few off-the-shelf robots were used (14%). The custom-designed platform offers potential to meet specific conditions regarding soil, weather, and plant which vary with experimental site and phenotyping task. Moreover, the researcher has more control on modifying the hardware and software. Based on the reviewed papers, most of the mobile platforms used four wheels/legged-wheels (88%) as their driving system compared with tracked mechanism (12%). In the wheeled-vehicles, the wheels can be independently steered (good maneuverability) which provides high flexibility with respect to control and navigation (desired orientation angle and rotation speed) of the vehicles between the crop rows in the field. Moreover, the vehicle can move faster using (legged) wheels and has high ground adaptability (crop height, and irregular and sloped terrain) using legged-wheels. However, the tracked-vehicles create more traction and less pressure on soil (work better in wet soil and less soil compaction), and can drive over rough terrain and obstacles easier than the wheeled-vehicles (Bruzzone and Quaglia, 2012). Accordingly, a hybrid locomotion system can be developed with the combination of legged-wheels and tracked systems. Therefore, this platform can use the advantages of the both driving systems to accomplish phenotyping tasks more effectively and efficiently.

PHENOTYPING ROBOTS FACE SEVERAL CHALLENGES

There are several outstanding challenges in the development of robotic systems for plant phenotyping. Some of these challenges related to segmentation (vision systems) and grasping (robotic manipulators) are shared or at least similar for both indoor and outdoor phenotyping robots. Other challenges, particularly those related to navigation are specific to outdoor robotic phenotypic applications.

Complex and Deformable Nature of Plants Represents a Major Issue for Robot's Vision and Sensing System

The UGV or robotic manipulator equipped with contact/non-contact based sensing systems offer a great potential to measure plant phenotypic data compare to non-autonomous robotic sensing systems. For example, the UGV equipped with stereo vision camera can move between crop rows and collect images from the canopy or individual plant. The image data can be analyzed immediately or can be processed later to extract plant properties. The long-term measurement of the plant traits can provide useful knowledge for crop modeling purposes over time (Duckett et al., 2018). Another example would be the robotic manipulator equipped with a hyperspectral imaging system. The robotic arm can move around the plant to locate the sensor close to the plant organs. With this proximal sensing, more phenotyping information can be acquired about the organs. However, the robotic vision/sensing technologies for the phenotyping task encounter different challenges.

Various imaging technologies are utilized as vision systems of the robots. Visible imaging/RGBD camera are commonly used technologies that rely on the color/texture information of an object. Images are processed to segment plant organs and identify desirable targets for grasping. The identification and localization of different plant organs (such as leaves, stems, flowers, and fruits) is one of the major problems in computer vision, due to complex structure and deformable nature of plants. The overlap between the adjacent leaves or leaf-stem causes occlusion; even though leaf and stem have different architecture, they share similarities in color and texture. Accordingly, it is difficult to distinguish occluded leaves or stem in the image. The morphology of plants (shape and size) varies dramatically across different plant species and even within a single species different varieties or the same variety grown in different conditions may exhibit radically different morphology. In this regard, the software of the robotic system should cover a wide range of scenarios and possibilities to be able to respond and adapt appropriately to day-to-day changes in the same plant or differences between plants within the same experiment. Additionally, non-uniform imaging conditions (lighting and background) make it more complex to find an appropriate color space and optimal approach for the segmentation purposes (Zhang et al., 2016; Narvaez et al., 2017; Qiu et al., 2018; Bao et al., 2019a).

Multispectral/hyperspectral and thermal imaging systems are sensitive to illumination since the reflectance from the plant organ is depend on its distance and orientation toward the light source/incident radiation and camera. Moreover, multiple reflectance and also shade will occur due to the curvature nature and complex geometry of plant (Li et al., 2014; Mishra et al., 2017; Qiu et al., 2018). To deal with these issues, researchers introduced different technical solutions. Behmann et al. (2016) combined the hyperspectral image with 3D point cloud (using a laser scanner) of sugar beet to create hyperspectral 3D model. Then, it was used to quantify and model the effects of plant geometry and sensor configuration. Finally, the geometry effects in hyperspectral images were weakened or removed using reflectance models. Shahrimie et al. (2016) used inverse square law and Lambert's cosine law along with Standard Normal Variate (SNV) for maize plants to remove the distance and orientation effects.

Robotic Control System Needs to Deal With Dynamic and Unstructured Environment

The size and orientation of the plant organs are constantly changing across their growth stages. Therefore, the lack of needed DOF or enough workspace of the robotic manipulator are the limitations for the robots to grasp the plant organs and sense their properties successfully. The robotic arm cannot reach the organs if they are out of its workspace. In addition, a robot arm with less flexibility (DOF) might not able to properly adjust the angle of its end-effector in grasping process.

Field-based robots need to navigate between crop rows and then turned to the next row safely and autonomously. To achieve

this task, the crop rows and obstacles should be detected to build a map of the surrounding area. Then, their position and orientation relative to the vehicle will be found to compute an optimal path and avoid unexpected obstacles. Finally, adequate action will be determined to steer the wheels and guide the system around the field. However, the uncontrolled and unstructured field environment creates challenges for accurate navigation and control of the robot (De Baerdemaeker et al., 2001; Nof, 2009; Bechar and Vigneault, 2016; Shamshiri et al., 2018). GPS is a common method for robot navigation. However, the tall plant canopy affects on the accuracy of GPS for navigation purposes as the canopy blocks the satellite signals to the GPS receiver. Hence, the information provided from other sensors along with GPS is also required to detect the obstacles, precisely guide the phenotyping robot, and minimize the damage to the robot and plants. The UGV based phenotyping robots can facilitate the data fusion of GPS and other sensors since the robot can equipped with various sensors (such as LIDAR, RGB/stereo vision cameras) and also precisely control their location (Duckett et al., 2018). Nonetheless, varying ambient light conditions, changing crop growth stages (size, shape, and color), and similar appearance between crops and weeds are common factors that fail visual navigation. In these situations, RGB sensor-based systems usually cannot find a stable color-space or plant features to detect different objects. Incomplete rows and missing plants can cause errors to compute distance between the robot and plants using range sensors. Different soil properties (soil types and moisture) and terrain variation (even, uneven, flat, slope) are other factors that influence robot dexterous manipulation, wheel-terrain interaction, wheel slip, and steering control algorithms (Åstrand and Baerveldt, 2005; Grift et al., 2008; Li et al., 2009; Shalal et al., 2013).

After navigating the robot between the rows, a suitable path should be selected for the robotic manipulator with minimum collisions inside a plant or canopy to reach and grasp the targets delicately. However, robots operate in extremely complex, dynamic, uncertain, and heterogenous real world condition. In this situation, visual occlusion of a plant by others caused by high plant density should be taken into account for target identification and segmentation. In addition, the target information will be affected by sunlight and wind. For instance, TOF/RGBD cameras use infrared light to measure distance. Since the sunlight has infrared wavelengths and wind moves the targets, the location of the target in 3-dimensional space might not be accurately measured (Andújar et al., 2017; Narvaez et al., 2017; Qiu et al., 2018; Li et al., 2020a). Consequently, the obstacle-avoidance path-planning algorithm cannot be determined correctly. Another example would be when the targets are seen shinier or darker because of specular reflection or shade.

Issues With Robot Software for Phenotyping Robotic System Development

Two main drawbacks present in many robot software are: (1) the lack of support for certain functional packages (of open source software) and (2) real-time constraints (Barth et al., 2014; Park et al., 2020). For the first issue, it can be supposed that a phenotyping robot is developed by researchers to accomplish a phenotyping task. They create the robot library and share their codes with the (open source) software community. However, by ending the project, there is no guarantee to fix the bugs and update the codes. In the case of other researchers might start similar research using the shared codes, it might be problematic to make the research forward because of the lack of support for the robot library. The second challenge is the real-time constraints that causes system malfunction due to latency. One example would be when a UGV moves between crop rows to measure plant traits. If the robot cannot satisfy the real-time constraints, the robot will have delay to identify the obstacles or adjust its position relative to the crop rows. Accordingly, the robot could hit the obstacles and the plants and this causes the physical damage to the robot or plants. Regarding ROS, although ROS1 has real-time constraints, however the community is actively working on software improvement. For example, RT-ROS supports the real-time communication that leads to performance enhancement of ROS1 (Wei et al., 2016). It is obvious that by growing the ROS community, sophisticated libraries and packages will be developed for more plant phenotyping applications.

Other Challenges: Managing Big Data, Reliable Power Source, Durability Under Harsh Environment, and High Cost

The phenotyping robot collects massive volumes and various types of data (such as images, multi/hyperspectral data) taken by different sensors from large population of plants. The robot needs to analyze large quantities of data in real-time for suitable action/decision-making process. In addition, the large-scale phenotypic data could be stored properly for the benefit of future research. Therefore, managing and analyzing the big data as a result of high-throughput, robotically collected plant traits is an emerging issue for the phenotyping robot.

The field-based mobile robots need to be equipped with reliable power sources to provide energy for the vehicle carriage weight, distance traveled, and different electrical components such as sensors for data collection. Batteries are commonly used for this purpose. The problems with batteries are: (1) limited operating time that prevents the robots to work for long time and accomplish large-scale missions, and (2) need to recharge which typically takes a long time.

Another challenge is the durability and stability of these robotic systems under harsh outside environment caused by extreme temperature, high humidity, strong sunlight, and dust. These harsh conditions can cause damages for the components of the robotic system and accordingly will have negative effects on the robot's performance.

The cost of phenotyping robots (in general agricultural robots) is still high and this makes limitations for wide-spread use of the robots. In most cases the phenotyping robotic systems are developed for research purposes and the robots are not commercially available yet. Both the hardware and software

systems were restricted to a very specific condition and could not be transferred to a different scenario. This leads to high R&D (research and development) cost that can not be spread over multiple units. However, more general purpose phenotyping robots can be developed and commercialized in the future and their cost will be reduced substantially. Moreover, with the consistent trend of price reduction of electronics, sensors, and computers, the robotic systems will become cost-effective enough to be more widely used for phenotyping tasks.

POTENTIAL IMPROVEMENTS OF PHENOTYPING ROBOTS

Sensors and Controllers Fusion Technique Can Improve the Performance of Robot

Sensing-reasoning, and task planning-execution are two essential functions for autonomous phenotyping robots. They sense the environment, apply an appropriate control algorithms, make decision, and act in real-time to perform the phenotyping tasks (Grift et al., 2008; Bechar and Vigneault, 2016). The design of the phenotyping robot and its control algorithm needs to be optimized to achieve successful operation in continuously changing environment. To reach this purpose, the phenotyping robots need to employ advanced technology to cope with the dynamic and unstructured environment. The emerging sensor technologies such as sensor fusion increase the robot capabilities and yield better results (Grift et al., 2008). Sensor fusion allows the robot to combine information from a variety of sensing modules to form better decision for navigation and path planning, as well as increase the capacity of sensing to gather more information from the plants. For example, Choudhuri and Chowdhary (2018) measured the stem width of sorghum with 92.5% accuracy using RGB data. However, they achieved higher accuracy (98.2%) after combining RGB + LIDAR data. Kim et al. (2012) could successfully navigate an unmanned weeding robot using sensor fusion of a laser range finder (LRF) and an inertial measurement unit (IMU). The robot also needs more sophisticated and intelligent algorithms to accomplish different subtasks such as sensing, navigation, path-planning, and control. Different control strategies such as genetic algorithm (GA), fuzzy logic (FL), neural network (NN), reinforcement learning (RL), and transfer learning (TL) can be integrated to develop such robot algorithms (Shalal et al., 2013). Therefore, a robust controller will be provided for the phenotyping robot since the robot control system can use the merits of both technologies (combining two control strategies). Batti et al. (2020) studied the performance of fuzzy logic and neuro-fuzzy (NN + FL) approaches to guide a mobile robot moving between the static obstacles. The authors found that neuro-fuzzy controller provide better results for robot navigation compare to fuzzy logic controller. Although several different autonomous phenotyping robots were developed, more research is needed to adapt and improve the advanced technologies to overcome the robot limitations to accomplish the phenotyping tasks, and also increase the autonomy level of the phenotyping robots.

Internet of Robotic Things (IoRT): Technology to Manage Big Data for Phenotyping Robots

Internet of Things (IoT) technologies are helpful to send lots of data collected by different sensors over Internet in a real-time manner. The Internet-of-Robotic-Things (IoRT) is the confluence of autonomous robotic systems with IoT which is an emerging paradigm that can be employed for phenotyping robots (Grieco et al., 2014; Ray, 2016; Batth et al., 2018; Saravanan et al., 2018; Afanasyev et al., 2019). Mobile robots can use IoT to transfer and store a large amount of phenotypic datasets to a central server. By sending the data via IoT, the robots do not need to frequently move to a place and physically upload the collected data to a local server/computer. Moreover, plant breeders/scientists can visualize the data using a mobile device (a tablet or a smartphone) or an office computer and therefore the performance of plants and changes in crop growth and development can be remotely inspected in different regions of the field in a real-time fashion. Another attractive aspect of using IoRT is to send commands to robots to accomplish phenotyping tasks. For instance, an operator can remotely control the greenhouse robotic manipulator systems via Internet any time from his home/office to collect phenotypic data. Another example is when the close inspection of an area in a field is necessary after analyzing the drone-based image data; therefore, commands can be sent via Internet to deploy mobile robots in this regard. Several mobile robots can work together to operate more efficiently to achieve a specific task.

Solar Panels and Hydrogen Fuel Cell: Renewable Power Sources for Phenotyping Robots

Solar panels and hydrogen fuel cell are two technologies that produce clean, renewable, and sustainable energy. A solar panel consists of many small units called photovoltaic cells which convert sunlight into electricity. The maintenance cost of the solar panel is low since it does not have moving parts (no wear) and it just need to clean the cells. The hydrogen fuel cell comprised a pressurized container to store hydrogen. The fuel cell is an electrochemical device that takes oxygen from the air and combines hydrogen with oxygen to produce electricity. Re-fueling time of a hydrogen fuel cell is very short (5 min or less) and its cells are fairly durable.

Based on the advantages of solar panels and hydrogen fuel cell, both technologies can be used as renewable power sources for different components of the phenotyping robots (Underwood et al., 2017; Quaglia et al., 2020). However, there is not a wide range of application of these technologies for the phenotyping robots. The cost of both technologies is high. For solar panels, the efficiency of the system drops in cloudy and rainy days. In addition, more solar panels are needed to produce more electricity

which requires a lot of space. For hydrogen fuel cell, there are relatively few places to re-fuel the cell. Nevertheless, both technologies are constantly developing which can be assumed to reduce their cost and improve their efficiency to produce electricity.

PERSPECTIVE APPLICATIONS OF ROBOTIC PHENOTYPING

Phenotyping Robots Has Great Potential to Measure Other Plant Properties

Section "Review: Many Indoor and Outdoor Robots Were Developed to Measure a Wide Range of Plant Traits" introduced the robotic systems for indoor and outdoor applications to measure several different plant traits. However, other leaf/stem characteristics are also reliable indicators to detect the symptoms of biotic/abiotic stresses and monitor the plant health during a growing season. Stomatal conductance, gas exchange, and chlorophyll fluorescence of leaves are indicative of their water status, photosynthesis, and chlorophyll content (Castrillo et al., 2001; Ohashi et al., 2006; Li et al., 2020b). Stem sap flow and lodging resistance can provide useful information about plant water use and stem strength (Cohen et al., 1990; Kong et al., 2013). These aforementioned phenotypic traits are still measured manually. On the other hand, new clip-on sensor system can be presented to measure them automatically. The system includes a custom-designed gripper/clip combined with novel sensor(s) (Afzal et al., 2017; Palazzari et al., 2017). The design of these sensing systems is important since the accuracy and robustness of trait prediction models depend on the phenotypic data quality (Würschum, 2019). The design of the gripper and DOF of the robotic manipulator should allow a good and gentle contact between the sensing unit and the leaf/stem. Sometimes a vacuum mechanism attached to a soft gripper can hold the leaf/stem and help the sensing unit for effective contact and collect accurate data with less damage to the plant organs (Hayashi et al., 2010; Hughes et al., 2016; Zhang et al., 2020). Moreover, autonomous robots should gather data with minimum error (high signal to noise ratio). Therefore, sensors with high signal to noise ratio should be selected and accurately calibrated. In addition to the accuracy, the robots should rapidly (short execution time) accomplish their missions. Deep reinforcement learning (DRL) technique is an accurate and reliable method to find an optimal path with nearest and collision avoidance route. This technique can be adopted by phenotyping robots to manipulate a robotic arm for grasping process or to navigate a mobile robot between crop rows (Zhang et al., 2015; Zhang et al., 2019; Duguleana and Mogan, 2016; Franceschetti et al., 2018; Taghavifar et al., 2019). Although the robotic phenotyping is mainly focusing on leaf and stem, it can be utilized for other plant organs such as inflorescences (spike, panicle, and tassel), flowers, fruits, and roots.

The morphometric parameters of inflorescence are highly correlated with yield and grain quality (Leilah and Al-Khateeb, 2005; Gegas et al., 2010). Several studies discussed about using image-based techniques (2D images/3D reconstruction) to extract architectural traits such as length and width of inflorescence, inflorescence volume (weight), grain shape and size, grain angle, and number of grains, and number of flowers (Faroq et al., 2013; Crowell et al., 2014; Gage et al., 2017; Rudolph et al., 2019; Sandhu et al., 2019; Xiong et al., 2019; Zhou et al., 2019). In such applications to measure the morphological traits, a robot with LIDAR/camera can be useful to automatically take images/point cloud data from different views of the inflorescence. The physiological traits are indicator for stress or disease. For instance, the temperature of the spikes was used for detecting the plant under the water stress (Panozzo et al., 1999). Conceivably, a robotic arm equipped with a temperature sensor can grasp the spike and insert the sensor into spikelets to record their temperature.

Several properties of fruits such as water content, sugar content, chlorophyll, carotenoid, soluble solid, acidity, and firmness are measured for fruit quality assessment. The spectroscopy/spectral imagery are non-destructive and high-throughput methods to estimate these qualitative parameters (Berardo et al., 2004; ElMasry et al., 2007; Shao and He, 2008; Wu et al., 2008; Nishizawa et al., 2009; Penchaiya et al., 2009; Ecarnot et al., 2013; Guo et al., 2013; Dykes et al., 2014; Wang et al., 2015; Mancini et al., 2020). However, a robotic system can be presented to monitor the dynamics of these attributes for hundreds of growing fruits per day. For example, a portable spectrometer can be attached to the robot's end-effector. After detecting the fruit on the plant, the robot can grasp the fruit and gather its spectral data to further infer its quality parameters.

Since the root has functional roles in resource acquisition, the characteristics of root provide valuable information about plant physiological and ecosystem functioning (Mishra et al., 2016). In traditional root phenotyping, two different methods are used to acquire images from root (in the soil or soil-free or transparent media). In first method, a camera is mounted on a tripod and moved by a human around the root, and in the second method camera(s)/sensor(s) are set in fixed point(s) and root (plant) is rotated (Atkinson et al., 2019). This is a tedious task and some root information (such as fine branches) might be lost due to less flexibility of the system to take up close images from the complex architecture of root. Consequently, automated root phenotyping systems can facilitate and improve the traditional root phenotyping in terms of efficiency and effectiveness with acquiring fast and precise measurements (Wu et al., 2019). Here, the "plant to sensor" system can be used to examine vast number of roots (or plants) without the need of huge space of greenhouse facility. In this system, the root (or plant) is moved toward a robotic manipulator (equipped with camera/sensor) and located on a rotation table. In each step angle of the table, the root is rotated and stopped in front of the robotic system. Then, the robotic manipulator moves the camera around the root and gather close proximity data from different views (positions and angles). Therefore, more detailed information of root can be captured due to high resolution sensing offered by the robotic system.

FIGURE 5 | (A) Mobile Agricultural Robot Swarms (MARS) for seeding process (The European Coordination Mobile Agricultural Robot Swarms (MARS). PDF file. November 11, 2016. http://echord.eu/public/wp-content/uploads/2018/01/Final-Report-MARS.pdf), **(B)** UAV-UGV cooperative system to measure environmental variables in greenhouse (Roldán et al., 2016).

Robots in Greenhouses Complement the Image-Based Phenotyping

Automatic greenhouses such as LemnaTec (LemnaTec GmbH, Aachen, Germany) monitor plants using image-based technique. While it has shown great potential to measure and predict the plant traits, many hurdles cannot be handled by this technology. It needs to efficiently manage "big data" problems and also postprocess images to characterize the plant traits. Moreover, this approach is not sufficient for early detection of stress/disease with internal symptoms. Furthermore, this method requires direct measurements using sensors to calibrate and validate of its models to extract the phenotypic traits from images (Madden, 2012; Mutka and Bart, 2015; Singh et al., 2016; Lee et al., 2018). Hence, several robotic arms with different sensors can be integrated to the greenhouse for real-time and direct measurement of the chemical/physiological traits. Basically, plants are transported by an automatic conveyor belt and stopped in front of each robotic system. Then, the system uses "sensor-to-plant" concept (Lee et al., 2018) in which the robot moves toward the plant to take measurements before sending it through the imaging chambers. These stationary robotic systems are designed to operate in indoor environment. Moreover, several robots can be presented to collect data from a specific plant. It is difficult to develop a general prototype that are broadly applicable for different conditions (Mutka and Bart, 2015; Wu et al., 2019). However, the software and hardware of the robots should be adapted to other species and field-phenotyping applications. The challenge for both type of robots (indoor/outdoor) would be continuously collect and save large amount of data.

Swarm Robot Is a New Frontier to Efficiently Accomplish Complex Phenotyping Tasks

Swarm robotics is a new frontier technology which has potential application for proximal sensing of plants, and data/sample collection in a large field. A swarm robotics system composed of large numbers of autonomous robots that are coordinated with local sensing and communication, and a decentralized control system (Brambilla et al., 2013; Bayındır, 2016; Blender et al., 2016; Chamanbaz et al., 2017; **Figure 5A**). The application of swarm robots has some advantages which is suitable for large scale tasks. Since swarm robotics has large population size, the tasks can be decomposed using parallelism and can be completed efficiently and consequently it would save time significantly. Moreover, the swarm robots can achieve the distributed sensing that means they can have a wide range of sensing in different places at the same time (Navarro and Matía, 2012; Tan and Zheng, 2013).

Both UAV and UGV by itself have been successfully employed in plant phenotyping tasks. The coordination between UAV and UGV enables a new breakthrough application of UAV/UGV cooperative systems to achieve a common goal more effectively and efficiently (Arbanas et al., 2018; Vu et al., 2018). Both vehicles in this cooperative team share complementarities according to their capabilities that allow them to operate in the same field and work together to fulfill phenotyping missions. In this manner, the UAV can fly to quickly obtain overview of the fields beyond the obstacles; whereas the UGV can continuously patrols in the field with large payload capabilities of different sensors and robotic arms (Chen et al., 2016; Roldán et al., 2016; **Figure 5B**). In the context of UAV-UGV cooperation, an obstacle map of the field will be provided by the UAV for UGV path planning. Based on their communication and the map, the UGV can move rapidly between the crop rows for up-close plant investigation.

CONCLUDING REMARKS

Autonomous robotic technologies have the potential to substantially increase the speed, capacity, repeatability, and accuracy of data collection in plant phenotyping tasks. Many robotic systems are successfully developed and deployed in both greenhouse and field environments, tested on a variety of plant species (row crops, specialty crops, and vineyards), and capable of measuring many traits related to morphology, structure, development, and physiology. Many technical challenges remain to be addressed regarding sensing, localization, path planning,

object detection, and obstacle avoidance. Intensive research is needed to overcome these limitations of phenotyping robots and improve their speed, accuracy, safety, and reliability. Collaborations among different disciplines (such as plant science, agricultural engineering, mechanical and electrical engineering, and computer science) are imperative. With this transdisciplinary research, more efficient and robust sensing and control systems will be developed for intelligent plant phenotyping robots. Sophisticated sensor modules can be developed using sensor-fusion techniques. Regarding the control systems, multiple intelligent algorithms (such as different AI algorithms) can be combined to design more powerful controllers. These developments can potentially overcome the issues caused by changing environmental parameters, and complex structure of plants. Moreover, the suitable sensing and control systems yield better performance for accurate object detection (mainly for plants and crops, but also for humans, animals and other obstacles coexisting in the environments), path planning, and navigation. Sufficient funding from the public and private sources is the key to fuel the high-risk research in intelligent phenotyping robots in a sustainable way. We are optimistic that, in the next 10 years, we will see great leaps forward in autonomous and robotic technologies in plant phenotyping, enabled by the confluence of the rapid advancements in sensing, controllers, and intelligent algorithms (AIs).

AUTHOR CONTRIBUTIONS

AA and YG provided the conceptualization of the manuscript. AA drafted the manuscript. YG, SP, and JS substantially edited the manuscript. All the authors contributed to the article and approved the submitted version.

FUNDING

The funding for this work was provided by USDA-NIFA under Grant No. 2017-67007-25941 and National Science Foundation under Grant No. OIA-1557417.

REFERENCES

Abel, J. (2018). *In-Field Robotic Leaf Grasping and Automated Crop Spectroscopy*. Pittsburgh, PA: Carnegie Mellon University.

Adamides, G., Katsanos, C., Parmet, Y., Christou, G., Xenos, M., Hadzilacos, T., et al. (2017). HRI usability evaluation of interaction modes for a teleoperated agricultural robotic sprayer. *Appl. Ergon.* 62, 237–246. doi: 10.1016/j.apergo.2017.03.008

Afanasyev, I., Mazzara, M., Chakraborty, S., Zhuchkov, N., Maksatbek, A., Kassab, M., et al. (2019). Towards the internet of robotic things: analysis, architecture, components and challenges. *arXiv* [Preprint]. Avaliable online at: https://arxiv.org/abs/1907.03817 (accessed April 23, 2020).

Afzal, A., Duiker, S. W., Watson, J. E., and Luthe, D. (2017). Leaf thickness and electrical capacitance as measures of plant water status. *Trans. ASABE* 60, 1063–1074.

Aguiar, A. S., Dos Santos, F. N., De Sousa, A. J. M., Oliveira, P. M., and Santos, L. C. (2020). Visual trunk detection using transfer learning and a deep learning-based coprocessor. *IEEE Access* 8, 77308–77320.

Ahlin, K., Joffe, B., Hu, A.-P., McMurray, G., and Sadegh, N. (2016). Autonomous leaf picking using deep learning and visual-servoing. *IFAC PapersOnLine* 49, 177–183. doi: 10.1016/j.ifacol.2016.10.033

Alenya, G., Dellen, B., Foix, S., and Torras, C. (2013). Robotized plant probing: leaf segmentation utilizing time-of-flight data. *IEEE Robot. Autom. Mag.* 20, 50–59. doi: 10.1109/MRA.2012.2230118

Alenyà, G., Dellen, B., and Torras, C. (2011). "3D modelling of leaves from color and ToF data for robotized plant measuring," in *2011 IEEE International Conference on Robotics and Automation*, Shanghai, 3408–3414. doi: 10.1109/ICRA.2011.5980092

Alenyà Ribas, G., Dellen, B., Foix Salmerón, S., and Torras, C. (2012). "Robotic leaf probing via segmentation of range data into surface patches," in *Proceedings of the 2012 IROS Workshop on Agricultural Robotics: Enabling Safe, Efficient, Affordable Robots for Food Production*, Vilamoura, 1–6.

Alenyá, G., Foix, S., and Torras, C. (2014). ToF cameras for active vision in robotics. *Sensors Actuators A Phys.* 218, 10–22. doi: 10.1016/j.sna.2014.07.014

Andrade, F. H., Calvino, P., Cirilo, A., and Barbieri, P. (2002). Yield responses to narrow rows depend on increased radiation interception. *Agron. J.* 94, 975–980.

Andrade-Sanchez, P., Gore, M. A., Heun, J. T., Thorp, K. R., Carmo-Silva, A. E., French, A. N., et al. (2013). Development and evaluation of a field-based high-throughput phenotyping platform. *Funct. Plant Biol.* 41, 68–79. doi: 10.1071/FP13126

Andújar, D., Dorado, J., Bengochea-Guevara, J. M., Conesa-Muñoz, J., Fernández-Quintanilla, C., and Ribeiro, Á (2017). Influence of wind speed on RGB-D images in tree plantations. *Sensors* 17:914. doi: 10.3390/s17040914

Arad, B., Balendonck, J., Barth, R., Ben-Shahar, O., Edan, Y., Hellström, T., et al. (2020). Development of a sweet pepper harvesting robot. *J. F. Robot.* 37, 1027–1039. doi: 10.3390/s16081222

Araus, J. L., and Cairns, J. E. (2014). Field high-throughput phenotyping: the new crop breeding frontier. *Trends Plant Sci.* 19, 52–61. doi: 10.1016/j.tplants.2013.09.008

Arbanas, B., Ivanovic, A., Car, M., Orsag, M., Petrovic, T., and Bogdan, S. (2018). Decentralized planning and control for UAV–UGV cooperative teams. *Auton. Robots* 42, 1601–1618.

Åstrand, B., and Baerveldt, A.-J. (2002). An agricultural mobile robot with vision-based perception for mechanical weed control. *Auton. Robots* 13, 21–35. doi: 10.1023/A:1015674004201

Åstrand, B., and Baerveldt, A.-J. (2005). A vision based row-following system for agricultural field machinery. *Mechatronics* 15, 251–269. doi: 10.1016/j.mechatronics.2004.05.005

Atefi, A., Ge, Y., Pitla, S., and Schnable, J. (2019). *In vivo* human-like robotic phenotyping of leaf traits in maize and sorghum in greenhouse. *Comput. Electron. Agric.* 163:104854. doi: 10.1016/j.compag.2019.104854

Atefi, A., Ge, Y., Pitla, S., and Schnable, J. (2020). Robotic detection and grasp of maize and sorghum: stem measurement with contact. *Robotics* 9:58.

Atkinson, J. A., Pound, M. P., Bennett, M. J., and Wells, D. M. (2019). Uncovering the hidden half of plants using new advances in root phenotyping. *Curr. Opin. Biotechnol.* 55, 1–8. doi: 10.1016/j.copbio.2018.06.002

Bai, G., Ge, Y., Hussain, W., Baenziger, P. S., and Graef, G. (2016). A multi-sensor system for high throughput field phenotyping in soybean and wheat breeding. *Comput. Electron. Agric.* 128, 181–192. doi: 10.1016/j.compag.2016.08.021

Bao, Y., Tang, L., Breitzman, M. W., Salas Fernandez, M. G., and Schnable, P. S. (2019a). Field-based robotic phenotyping of sorghum plant architecture using stereo vision. *J. F. Robot.* 36, 397–415.

Bao, Y., Tang, L., Srinivasan, S., and Schnable, P. S. (2019b). Field-based architectural traits characterisation of maize plant using time-of-flight 3D imaging. *Biosyst. Eng.* 178, 86–101. doi: 10.1016/j.biosystemseng.2018.11.005

Bao, Y., Zarecor, S., Shah, D., Tuel, T., Campbell, D. A., Chapman, A. V. E., et al. (2019c). Assessing plant performance in the Enviratron. *Plant Methods* 15, 1–14. doi: 10.1186/s13007-019-0504-y

Bao, Y., Tang, L., and Shah, D. (2017). "Robotic 3D plant perception and leaf probing with collision-free motion planning for automated indoor plant phenotyping," in *2017 ASABE Annual International Meeting*, Spokane, WA, 1. doi: 10.13031/aim.201700369

Barbieri, P. A., Rozas, H. n. R. S., Andrade, F. H., and Echeverria, H. n. E. (2000). Row spacing effects at different levels of nitrogen availability in maize. *Agron. J.* 92, 283–288.

Barth, R., Baur, J., Buschmann, T., Edan, Y., Hellström, T., Nguyen, T., et al. (2014). "Using ROS for agricultural robotics-design considerations and experiences," in *Proceedings of the Second International Conference on Robotics and Associated High-Technologies and Equipment for Agriculture and Forestry*, 509–518.

Batth, R. S., Nayyar, A., and Nagpal, A. (2018). "Internet of robotic things: driving intelligent robotics of future-concept, architecture, applications and technologies," in *2018 4th International Conference on Computing Sciences (ICCS)*, Jalandhar: IEEE, 151–160.

Batti, H., Ben Jabeur, C., and Seddik, H. (2020). Autonomous smart robot for path predicting and finding in maze based on fuzzy and neuro-Fuzzy approaches. *Asian J. Control* 23:2345.

Baweja, H. S., Parhar, T., Mirbod, O., and Nuske, S. (2018). in *StalkNet: A Deep Learning Pipeline for High-Throughput Measurement of Plant Stalk Count and Stalk Width BT - Field and Service Robotics*, eds M. Hutter and R. Siegwart (Cham: Springer International Publishing), 271–284.

Bayındır, L. (2016). A review of swarm robotics tasks. *Neurocomputing* 172, 292–321. doi: 10.1016/j.neucom.2015.05.116

Bechar, A., and Vigneault, C. (2016). Agricultural robots for field operations: concepts and components. *Biosyst. Eng.* 149, 94–111. doi: 10.1016/j.biosystemseng.2016.06.014

Behmann, J., Mahlein, A.-K., Paulus, S., Dupuis, J., Kuhlmann, H., Oerke, E.-C., et al. (2016). Generation and application of hyperspectral 3D plant models: methods and challenges. *Mach. Vis. Appl.* 27, 611–624.

Berardo, N., Brenna, O. V., Amato, A., Valoti, P., Pisacane, V., and Motto, M. (2004). Carotenoids concentration among maize genotypes measured by near infrared reflectance spectroscopy (NIRS). *Innov. food Sci. Emerg. Technol.* 5, 393–398.

Biber, P., Weiss, U., Dorna, M., and Albert, A. (2012). "Navigation system of the autonomous agricultural robot Bonirob," in *in Workshop on Agricultural Robotics: Enabling Safe, Efficient, and Affordable Robots for Food Production (Collocated with IROS 2012)*, Vilamoura.

Biskup, B., Scharr, H., Fischbach, A., Wiese-Klinkenberg, A., Schurr, U., and Walter, A. (2009). diel growth cycle of isolated leaf discs analyzed with a novel, high-throughput three-dimensional imaging method is identical to that of intact leaves. *Plant Physiol.* 149, 1452–1461. doi: 10.1104/pp.108.134486

Blasco, J., Aleixos, N., Roger, J. M., Rabatel, G., and Moltó, E. (2002). AE—Automation and emerging technologies: robotic weed control using machine vision. *Biosyst. Eng.* 83, 149–157. doi: 10.1006/bioe.2002.0109

Blender, T., Buchner, T., Fernandez, B., Pichlmaier, B., and Schlegel, C. (2016). "Managing a Mobile Agricultural Robot Swarm for a seeding task," in *IECON 2016 - 42nd Annual Conference of the IEEE Industrial Electronics Society*, Florence, 6879–6886. doi: 10.1109/IECON.2016.7793638

Brambilla, M., Ferrante, E., Birattari, M., and Dorigo, M. (2013). Swarm robotics: a review from the swarm engineering perspective. *Swarm Intell.* 7, 1–41.

Breitzman, M. W., Bao, Y., Tang, L., Schnable, P. S., and Salas-Fernandez, M. G. (2019). Linkage disequilibrium mapping of high-throughput image-derived descriptors of plant architecture traits under field conditions. *F. Crop. Res.* 244:107619. doi: 10.1016/j.fcr.2019.107619

Bruzzone, L., and Quaglia, G. (2012). Locomotion systems for ground mobile robots in unstructured environments. *Mech. Sci.* 3, 49–62.

Burud, I., Lange, G., Lillemo, M., Bleken, E., Grimstad, L., and Johan From, P. (2017). Exploring robots and UAVs as phenotyping tools in plant breeding. *IFAC-PapersOnLine* 50, 11479–11484. doi: 10.1016/j.ifacol.2017.08.1591

Busemeyer, L., Mentrup, D., Möller, K., Wunder, E., Alheit, K., Hahn, V., et al. (2013). BreedVision — A multi-sensor platform for non-destructive field-based phenotyping in plant breeding. *Sensors* 13, 2830–2847. doi: 10.3390/s130302830

Castrillo, M., Fernandez, D., Calcagno, A. M., Trujillo, I., and Guenni, L. (2001). Responses of ribulose-1, 5-bisphosphate carboxylase, protein content, and stomatal conductance to water deficit in maize, tomato, and bean. *Photosynthetica* 39, 221–226.

Chamanbaz, M., Mateo, D., Zoss, B. M., Tokić, G., Wilhelm, E., Bouffanais, R., et al. (2017). Swarm-enabling technology for multi-robot systems. *Front. Robot. AI* 4:12. doi: 10.3389/frobt.2017.00012

Chaudhury, A., Ward, C., Talasaz, A., Ivanov, A. G., Brophy, M., Grodzinski, B., et al. (2017). Machine vision system for 3D plant phenotyping. *arXiv* [Preprint]. arXiv1705.00540.

Chawade, A., van Ham, J., Blomquist, H., Bagge, O., Alexandersson, E., and Ortiz, R. (2019). High-throughput field-phenotyping tools for plant breeding and precision agriculture. *Agronomy* 9:258.

Chen, J., Zhang, X., Xin, B., and Fang, H. (2016). Coordination between unmanned aerial and ground vehicles: a taxonomy and optimization perspective. *IEEE Trans. Cybern.* 46, 959–972. doi: 10.1109/TCYB.2015.2418337

Chen, Z., Wang, J., Wang, T., Song, Z., Li, Y., Huang, Y., et al. (2021). Automated in-field leaf-level hyperspectral imaging of corn plants using a Cartesian robotic platform. *Comput. Electron. Agric.* 183:105996.

Chlingaryan, A., Sukkarieh, S., and Whelan, B. (2018). Machine learning approaches for crop yield prediction and nitrogen status estimation in precision agriculture: a review. *Comput. Electron. Agric.* 151, 61–69. doi: 10.1016/j.compag.2018.05.012

Chonnaparamutt, W., Kawasaki, H., Ueki, S., Murakami, S., and Koganemaru, K. (2009). "Development of a timberjack-like pruning robot: climbing experiment and fuzzy velocity control," in *2009 ICCAS-SICE*, Fukuoka, 1195–1199.

Choudhuri, A., and Chowdhary, G. (2018). "Crop stem width estimation in highly cluttered field environment," in *Proc. Comput. Vis. Probl. Plant Phenotyping (CVPPP 2018)*, Newcastle, 6–13.

Cohen, Y., Huck, M. G., Hesketh, J. D., and Frederick, J. R. (1990). Sap flow in the stem of water stressed soybean and maize plants. *Irrig. Sci.* 11, 45–50.

Costa, C., Schurr, U., Loreto, F., Menesatti, P., and Carpentier, S. (2019). Plant phenotyping research trends, a science mapping approach. *Front. Plant Sci.* 9:1933.

Crowell, S., Falcão, A. X., Shah, A., Wilson, Z., Greenberg, A. J., and McCouch, S. R. (2014). High-resolution inflorescence phenotyping using a novel image-analysis pipeline, PANorama. *Plant Physiol.* 165, 479–495. doi: 10.1104/pp.114.238626

Das Choudhury, S., Samal, A., and Awada, T. (2019). Leveraging image analysis for high-throughput plant phenotyping. *Front. Plant Sci.* 10:508. doi: 10.3389/fpls.2019.00508

De Baerdemaeker, J., Munack, A., Ramon, H., and Speckmann, H. (2001). Mechatronic systems, communication, and control in precision agriculture. *IEEE Control Syst. Mag.* 21, 48–70. doi: 10.1016/j.aca.2020.11.008

Dhondt, S., Wuyts, N., and Inzé, D. (2013). Cell to whole-plant phenotyping: the best is yet to come. *Trends Plant Sci.* 18, 428–439. doi: 10.1016/j.tplants.2013.04.008

Duckett, T., Pearson, S., Blackmore, S., Grieve, B., Chen, W. H., Cielniak, G., et al. (2018). Agricultural robotics: The future of robotic agriculture. *arXiv* [Preprint]. arXiv1806.06762.

Duguleana, M., and Mogan, G. (2016). Neural networks based reinforcement learning for mobile robots obstacle avoidance. *Exp. Syst. Appl.* 62, 104–115. doi: 10.1016/j.eswa.2016.06.021

Dykes, L., Hoffmann, L. Jr., Portillo-Rodriguez, O., Rooney, W. L., and Rooney, L. W. (2014). Prediction of total phenols, condensed tannins, and 3-deoxyanthocyanidins in sorghum grain using near-infrared (NIR) spectroscopy. *J. Cereal Sci.* 60, 138–142.

Ecarnot, M., Bączyk, P., Tessarotto, L., and Chervin, C. (2013). Rapid phenotyping of the tomato fruit model, Micro-Tom, with a portable VIS–NIR spectrometer. *Plant Physiol. Biochem.* 70, 159–163. doi: 10.1016/j.plaphy.2013.05.019

ElMasry, G., Wang, N., ElSayed, A., and Ngadi, M. (2007). Hyperspectral imaging for nondestructive determination of some quality attributes for strawberry. *J. Food Eng.* 81, 98–107.

Fahlgren, N., Feldman, M., Gehan, M. A., Wilson, M. S., Shyu, C., Bryant, D. W., et al. (2015). A versatile phenotyping system and analytics platform reveals diverse temporal responses to water availability in setaria. *Mol. Plant* 8, 1520–1535. doi: 10.1016/j.molp.2015.06.005

Faroq, A.-T., Adam, H., Dos Anjos, A., Lorieux, M., Larmande, P., Ghesquière, A., et al. (2013). P-TRAP: a panicle trait phenotyping tool. *BMC Plant Biol.* 13:122. doi: 10.1186/1471-2229-13-122

Fernandez, M. G. S., Bao, Y., Tang, L., and Schnable, P. S. (2017). A high-throughput, field-based phenotyping technology for tall biomass crops. *Plant Physiol.* 174, 2008–2022. doi: 10.1104/pp.17.00707

Fiorani, F., and Schurr, U. (2013). Future scenarios for plant phenotyping. *Annu. Rev. Plant Biol.* 64, 267–291. doi: 10.1146/annurev-arplant-050312-120137

Fischer, G. (2009). "World food and agriculture to 2030/50," in *Technical Paper From the Expert Meeting on How to Feed the World in*, Rome, 24–26.

Foix, S., Alenyà, G., and Torras, C. (2015). "3D Sensor planning framework for leaf probing," in *2015 IEEE/RSJ International Conference on Intelligent Robots and Systems (IROS)*, Hamburg, 6501–6506. doi: 10.1109/IROS.2015.7354306

Foix, S., Alenyà, G., and Torras, C. (2018). Task-driven active sensing framework applied to leaf probing. *Comput. Electron. Agric.* 147, 166–175. doi: 10.1016/j.compag.2018.01.020

Franceschetti, A., Tosello, E., Castaman, N., and Ghidoni, S. (2018). *Robotic Arm Control and Task Training through Deep Reinforcement Learning.*

Furbank, R. T., and Tester, M. (2011). Phenomics – technologies to relieve the phenotyping bottleneck. *Trends Plant Sci.* 16, 635–644. doi: 10.1016/j.tplants.2011.09.005

Gage, J. L., Miller, N. D., Spalding, E. P., Kaeppler, S. M., and de Leon, N. (2017). TIPS: a system for automated image-based phenotyping of maize tassels. *Plant Methods* 13:21. doi: 10.1186/s13007-017-0172-8

Gage, J. L., Richards, E., Lepak, N., Kaczmar, N., Soman, C., Chowdhary, G., et al. (2019). In-field whole plant maize architecture characterized by latent space phenotyping. *bioRxiv* [Preprint]. doi: 10.1101/763342

Gao, T., Emadi, H., Saha, H., Zhang, J., Lofquist, A., Singh, A., et al. (2018). A novel multirobot system for plant phenotyping. *Robotics* 7:61. doi: 10.3390/robotics7040061

Ge, Y., Atefi, A., Zhang, H., Miao, C., Ramamurthy, R. K., Sigmon, B., et al. (2019). High-throughput analysis of leaf physiological and chemical traits with VIS–NIR–SWIR spectroscopy: a case study with a maize diversity panel. *Plant Methods* 15:66. doi: 10.1186/s13007-019-0450-8

Ge, Y., Bai, G., Stoerger, V., and Schnable, J. C. (2016). Temporal dynamics of maize plant growth, water use, and leaf water content using automated high throughput RGB and hyperspectral imaging. *Comput. Electron. Agric.* 127, 625–632. doi: 10.1016/j.compag.2016.07.028

Gegas, V. C., Nazari, A., Griffiths, S., Simmonds, J., Fish, L., Orford, S., et al. (2010). A genetic framework for grain size and shape variation in wheat. *Plant Cell* 22, 1046–1056. doi: 10.1105/tpc.110.074153

Gonzalez-de-Soto, M., Emmi, L., Perez-Ruiz, M., Aguera, J., and Gonzalez-de-Santos, P. (2016). Autonomous systems for precise spraying – Evaluation of a robotised patch sprayer. *Biosyst. Eng.* 146, 165–182. doi: 10.1016/j.biosystemseng.2015.12.018

Granier, C., and Tardieu, F. (2009). Multi-scale phenotyping of leaf expansion in response to environmental changes: the whole is more than the sum of parts. *Plant. Cell Environ.* 32, 1175–1184. doi: 10.1111/j.1365-3040.2009.01955.x

Grieco, L. A., Rizzo, A., Colucci, S., Sicari, S., Piro, G., Di Paola, D., et al. (2014). IoT-aided robotics applications: technological implications, target domains and open issues. *Comput. Commun.* 54, 32–47.

Grift, T., Zhang, Q., Kondo, N., and Ting, K. C. (2008). A review of automation and robotics for the bio-industry. *J. Biomechatronics Eng.* 1, 37–54.

Grimstad, L., and From, P. J. (2017). Thorvald II - a modular and re-configurable agricultural robot. *IFAC PapersOnLine* 50, 4588–4593. doi: 10.1016/j.ifacol.2017.08.1005

Guo, Z., Huang, W., Chen, L., Wang, X., and Peng, Y. (2013). "Nondestructive evaluation of soluble solid content in strawberry by near infrared spectroscopy," in *Piageng 2013: Image Processing and Photonics for Agricultural Engineering*, (Bellingham: International Society for Optics and Photonics), 87610O.

Han, L., Yang, G., Yang, H., Xu, B., Li, Z., and Yang, X. (2018). Clustering field-based maize phenotyping of plant-height growth and canopy spectral dynamics using a UAV remote-sensing approach. *Front. Plant Sci.* 9:1638. doi: 10.3389/fpls.2018.01638

Happ, M. M., Wang, H., Graef, G. L., and Hyten, D. L. (2019). Generating high density, low cost genotype data in soybean [Glycine max (L.) Merr.]. *G3 Genes Genomes Genet.* 9, 2153–2160. doi: 10.1534/g3.119.400093

Hassan, M. A., Yang, M., Rasheed, A., Yang, G., Reynolds, M., Xia, X., et al. (2019). A rapid monitoring of NDVI across the wheat growth cycle for grain yield prediction using a multi-spectral UAV platform. *Plant Sci.* 282, 95–103. doi: 10.1016/j.plantsci.2018.10.022

Hassanijalilian, O., Igathinathane, C., Bajwa, S., and Nowatzki, J. (2020a). Rating iron deficiency in soybean using image processing and decision-tree based models. *Remote Sens.* 12:4143.

Hassanijalilian, O., Igathinathane, C., Doetkott, C., Bajwa, S., Nowatzki, J., and Haji Esmaeili, S. A. (2020b). Chlorophyll estimation in soybean leaves infield with smartphone digital imaging and machine learning. *Comput. Electron. Agric.* 174:105433. doi: 10.1016/j.compag.2020.10543

Hayashi, S., Shigematsu, K., Yamamoto, S., Kobayashi, K., Kohno, Y., Kamata, J., et al. (2010). Evaluation of a strawberry-harvesting robot in a field test. *Biosyst. Eng.* 105, 160–171. doi: 10.1016/j.biosystemseng.2009.09.011

Hejazipoor, H., Massah, J., Soryani, M., Vakilian, K. A., and Chegini, G. (2021). An intelligent spraying robot based on plant bulk volume. *Comput. Electron. Agric.* 180:105859.

Hemming, J., Bac, C. W., van Tuijl, B. A. J., Barth, R., Bontsema, J., Pekkeriet, E. J., et al. (2014). "A robot for harvesting sweet-pepper in greenhouses," in *Paper Presented at AgEng 2014*, Zurich.

Hughes, J., Culha, U., Giardina, F., Guenther, F., Rosendo, A., and Iida, F. (2016). Soft manipulators and grippers: a review. *Front. Robot. AI* 3:69.

Iqbal, J., Xu, R., Halloran, H., and Li, C. (2020). Development of a Multi-Purpose Autonomous Differential Drive Mobile Robot for Plant Phenotyping and Soil Sensing. *Electronics* 9:1550.

Irshat, K., Petr, R., and Irina, R. (2018). "The selecting of artificial intelligence technology for control of mobile robots," in *2018 International Multi-Conference on Industrial Engineering and Modern Technologies (FarEastCon)*, Vladivostok: IEEE, 1–4.

Ishigure, Y., Hirai, K., and Kawasaki, H. (2013). "A pruning robot with a power-saving chainsaw drive," in *2013 IEEE International Conference on Mechatronics and Automation*, Takamatsu, 1223–1228. doi: 10.1109/ICMA.2013.6618088

Jannink, J.-L., Lorenz, A. J., and Iwata, H. (2010). Genomic selection in plant breeding: from theory to practice. *Brief. Funct. Genomics* 9, 166–177. doi: 10.1093/bfgp/elq001

Jay, S., Rabatel, G., Hadoux, X., Moura, D., and Gorretta, N. (2015). In-field crop row phenotyping from 3D modeling performed using structure from Motion. *Comput. Electron. Agric.* 110, 70–77. doi: 10.1016/j.compag.2014.09.021

Jenkins, M., and Kantor, G. (2017). "Online detection of occluded plant stalks for manipulation," in *Proceedings of the 2017 IEEE/RSJ International Conference on Intelligent Robots and Systems (IROS)*, 5162–5167. doi: 10.1109/IROS.2017.8206404

Jin, X., Zarco-Tejada, P., Schmidhalter, U., Reynolds, M. P., Hawkesford, M. J., Varshney, R. K., et al. (2020). High-throughput estimation of crop traits: a review of ground and aerial phenotyping platforms. *IEEE Geosci. Remote Sens. Mag.* 2, 1–33.

Kicherer, A., Herzog, K., Pflanz, M., Wieland, M., Rüger, P., Kecke, S., et al. (2015). An automated field phenotyping pipeline for application in grapevine research. *Sensors* 15, 4823–4836. doi: 10.3390/s150304823

Kim, G.-H., Kim, S.-C., Hong, Y.-K., Han, K.-S., and Lee, S.-G. (2012). "A robot platform for unmanned weeding in a paddy field using sensor fusion," in *Proceedings of the 2012 IEEE International Conference on Automation Science and Engineering (CASE)*, (Piscataway, NJ: IEEE), 904–907.

Kong, E., Liu, D., Guo, X., Yang, W., Sun, J., Li, X., et al. (2013). Anatomical and chemical characteristics associated with lodging resistance in wheat. *Crop J.* 1, 43–49. doi: 10.1016/j.cj.2013.07.012

Lee, U., Chang, S., Putra, G. A., Kim, H., and Kim, D. H. (2018). An automated, high-throughput plant phenotyping system using machine learning-based plant segmentation and image analysis. *PLoS One* 13:e0196615. doi: 10.1371/journal.pone.0196615

Leilah, A. A., and Al-Khateeb, S. A. (2005). Statistical analysis of wheat yield under drought conditions. *J. Arid Environ.* 61, 483–496. doi: 10.1016/j.jaridenv.2004.10.011

Li, L., Zhang, Q., and Huang, D. (2014). A review of imaging techniques for plant phenotyping. *Sensors* 14, 20078–20111. doi: 10.3390/s141120078

Li, M., Imou, K., Wakabayashi, K., and Yokoyama, S. (2009). Review of research on agricultural vehicle autonomous guidance. *Int. J. Agric. Biol. Eng.* 2, 1–16.

Li, Z., Guo, R., Li, M., Chen, Y., and Li, G. (2020a). A review of computer vision technologies for plant phenotyping. *Comput. Electron. Agric.* 176:105672.

Li, Z., Zhang, Q., Li, J., Yang, X., Wu, Y., Zhang, Z., et al. (2020b). Solar-induced chlorophyll fluorescence and its link to canopy photosynthesis in maize from continuous ground measurements. *Remote Sens. Environ.* 236:111420. doi: 10.1016/j.rse.2019.111420

Lili, W., Bo, Z., Jinwei, F., Xiaoan, H., Shu, W., Yashuo, L., et al. (2017). Development of a tomato harvesting robot used in greenhouse. *Int. J. Agric. Biol. Eng.* 10, 140–149.

Lopes, C. M., Graça, J., Sastre, J., Reyes, M., Guzmán, R., Braga, R., et al. (2016). "Vineyard yeld estimation by VINBOT robot-preliminary results with the white variety Viosinho," in *Proceedings 11th Int. Terroir Congress*, eds G. Jones and N. Doran (Ashland, USA: Southern Oregon University), 458–463.

Lu, H., Tang, L., Whitham, A. S., and Mei, Y. (2017). A robotic platform for corn seedling morphological traits characterization. *Sensors* 17:2082. doi: 10.3390/s17092082

Madden, S. (2012). From databases to big data. *IEEE Internet Comput.* 16, 4–6.

Mancini, M., Mazzoni, L., Gagliardi, F., Balducci, F., Duca, D., Toscano, G., et al. (2020). Application of the non-destructive NIR technique for the evaluation of strawberry fruits quality parameters. *Foods* 9:441. doi: 10.3390/foods9040441

McMullen, M. D., Kresovich, S., Villeda, H. S., Bradbury, P., Li, H., Sun, Q., et al. (2009). Genetic properties of the maize nested association mapping population. *Science* 325, 737–740. doi: 10.1126/science.1174320

Mishra, K. B., Mishra, A., Klem, K., and Govindjee. (2016). Plant phenotyping: a perspective. *Indian J. Plant Physiol.* 21, 514–527. doi: 10.1007/s40502-016-0271-y

Mishra, P., Asaari, M. S. M., Herrero-Langreo, A., Lohumi, S., Diezma, B., and Scheunders, P. (2017). Close range hyperspectral imaging of plants: a review. *Biosyst. Eng.* 164, 49–67.

Moeinizade, S., Hu, G., Wang, L., and Schnable, P. S. (2019). Optimizing selection and mating in genomic selection with a look-ahead approach: an operations research framework. *G3 Genes, Genomes, Genet.* 9, 2123–2133.

Montes, J. M., Melchinger, A. E., and Reif, J. C. (2007). Novel throughput phenotyping platforms in plant genetic studies. *Trends Plant Sci.* 12, 433–436. doi: 10.1016/j.tplants.2007.08.006

Mueller-Sim, T., Jenkins, M., Abel, J., and Kantor, G. (2017). "The robotanist: a ground-based agricultural robot for high-throughput crop phenotyping," in *2017 IEEE International Conference on Robotics and Automation (ICRA)*, Singapore, 3634–3639. doi: 10.1109/ICRA.2017.7989418

Murman, J. N. (2019). *Flex-Ro: A Robotic High Throughput Field Phenotyping System*.

Mutka, A. M., and Bart, R. S. (2015). Image-based phenotyping of plant disease symptoms. *Front. Plant Sci.* 5:734. doi: 10.3389/fpls.2014.00734

Narvaez, F. Y., Reina, G., Torres-Torriti, M., Kantor, G., and Cheein, F. A. (2017). A survey of ranging and imaging techniques for precision agriculture phenotyping. *IEEE ASME Trans. Mechatronics* 22, 2428–2439.

Navarro, I., and Matía, F. (2012). An introduction to swarm robotics. *Isrn Robot.* 2013:608164.

Nishizawa, T., Mori, Y., Fukushima, S., Natsuga, M., and Maruyama, Y. (2009). Non-destructive analysis of soluble sugar components in strawberry fruits using near-infrared spectroscopy. *Nippon Shokuhin Kagaku Kogaku KaishiJ. Japanese Soc. Food Sci. Technol.* 56, 229–235.

Nof, S. Y. (2009). *Springer Handbook of Automation*. Berlin: Springer Science & Business Media.

Oberti, R., Marchi, M., Tirelli, P., Calcante, A., Iriti, M., Tona, E., et al. (2016). Selective spraying of grapevines for disease control using a modular agricultural robot. *Biosyst. Eng.* 146, 203–215. doi: 10.1016/j.biosystemseng.2015.12.004

Ohashi, Y., Nakayama, N., Saneoka, H., and Fujita, K. (2006). Effects of drought stress on photosynthetic gas exchange, chlorophyll fluorescence and stem diameter of soybean plants. *Biol. Plant.* 50, 138–141.

Palazzari, V., Mezzanotte, P., Alimenti, F., Fratini, F., Orecchini, G., and Roselli, L. (2017). Leaf compatible "eco-friendly" temperature sensor clip for high density monitoring wireless networks. *Wirel. Power Transf.* 4, 55–60.

Pandey, P., Dakshinamurthy, H. N., and Young, S. N. (2021). Autonomy in detection, actuation, and planning for robotic weeding systems. *Trans. ASABE.*

Panozzo, J. F., Eagles, H. A., Cawood, R. J., and Wootton, M. (1999). Wheat spike temperatures in relation to varying environmental conditions. *Aust. J. Agric. Res.* 50, 997–1006. doi: 10.1371/journal.pone.0189594

Park, J., Delgado, R., and Choi, B. W. (2020). Real-time characteristics of ROS 2.0 in multiagent robot systems: an empirical study. *IEEE Access* 8, 154637–154651.

Parhar, T., Baweja, H., Jenkins, M., and Kantor, G. (2018). "A deep learning-based stalk grasping pipeline," in *2018 IEEE International Conference on Robotics and Automation (ICRA)*, Brisbane, QLD: IEEE, 6161–6167.

Penchaiya, P., Bobelyn, E., Verlinden, B. E., Nicolaï, B. M., and Saeys, W. (2009). Non-destructive measurement of firmness and soluble solids content in bell pepper using NIR spectroscopy. *J. Food Eng.* 94, 267–273.

Pieruschka, R., and Schurr, U. (2019). Plant phenotyping: past, present, and future. *Plant Phenomics* 2019, 1–6.

Phillips, R. L. (2010). Mobilizing science to break yield barriers. *Crop Sci.* 50, S–99.

Pound, M. P., Atkinson, J. A., Townsend, A. J., Wilson, M. H., Griffiths, M., Jackson, A. S., et al. (2017). Deep machine learning provides state-of-the-art performance in image-based plant phenotyping. *Gigascience* 6:gix083.

Qiu, Q., Sun, N., Bai, H., Wang, N., Fan, Z., Wang, Y., et al. (2019). Field-based high-throughput phenotyping for maize plant using 3D LiDAR point cloud generated with a "Phenomobile.". *Front. Plant Sci.* 10:554. doi: 10.3389/fpls.2019.00554

Qiu, R., Wei, S., Zhang, M., Li, H., Sun, H., Liu, G., et al. (2018). Sensors for measuring plant phenotyping: a review. *Int. J. Agric. Biol. Eng.* 11, 1–17.

Quaglia, G., Visconte, C., Scimmi, L. S., Melchiorre, M., Cavallone, P., and Pastorelli, S. (2020). Design of a UGV powered by solar energy for precision agriculture. *Robotics* 9:13.

Raja, R., Nguyen, T. T., Slaughter, D. C., and Fennimore, S. A. (2020). Real-time robotic weed knife control system for tomato and lettuce based on geometric appearance of plant labels. *Biosyst. Eng.* 194, 152–164.

Rahaman, M. M., Chen, D., Gillani, Z., Klukas, C., and Chen, M. (2015). Advanced phenotyping and phenotype data analysis for the study of plant growth and development. *Front. Plant Sci.* 6:619. doi: 10.3389/fpls.2015.00619

Ray, P. P. (2016). Internet of robotic things: concept, technologies, and challenges. *IEEE Access* 4, 9489–9500.

Richards, R. A., Rebetzke, G. J., Watt, M., Condon, A. G., Spielmeyer, W., and Dolferus, R. (2010). Breeding for improved water productivity in temperate cereals: phenotyping, quantitative trait loci, markers and the selection environment. *Funct. Plant Biol.* 37, 85–97. doi: 10.1071/FP09219 (Tony),

Roldán, J. J., Garcia-Aunon, P., Garzón, M., De León, J., Del Cerro, J., and Barrientos, A. (2016). Heterogeneous multi-robot system for mapping environmental variables of greenhouses. *Sensors* 16:1018. doi: 10.3390/s16071018

Ruckelshausen, A., Biber, P., Dorna, M., Gremmes, H., Klose, R., Linz, A., et al. (2009). BoniRob–an autonomous field robot platform for individual plant phenotyping. *Precis. Agric.* 9, 841–847. doi: 10.3390/s17010214

Rudolph, R., Herzog, K., Töpfer, R., and Steinhage, V. (2019). Efficient identification, localization and quantification of grapevine inflorescences and flowers in unprepared field images using Fully Convolutional Networks. *Vitis* 58, 95–104.

Sandhu, J., Zhu, F., Paul, P., Gao, T., Dhatt, B. K., Ge, Y., et al. (2019). PI-Plat: a high-resolution image-based 3D reconstruction method to estimate growth dynamics of rice inflorescence traits. *Plant Methods* 15:162. doi: 10.1186/s13007-019-0545-2

Saravanan, M., Perepu, S. K., and Sharma, A. (2018). "Exploring collective behavior of internet of robotic things for indoor plant health monitoring," in *2018 IEEE International Conference on Internet of Things and Intelligence System (IOTAIS)*, Bali: IEEE, 148–154.

Schulz, H., and Baranska, M. (2007). Identification and quantification of valuable plant substances by IR and Raman spectroscopy. *Vib. Spectrosc.* 43, 13–25. doi: 10.1016/j.vibspec.2006.06.001

Shafiekhani, A., Kadam, S., Fritschi, B. F., and DeSouza, N. G. (2017). Vinobot and vinoculer: two robotic platforms for high-throughput field phenotyping. *Sensors* 17:214. doi: 10.3390/s17010214

Shah, D., Tang, L., Gai, J., and Putta-Venkata, R. (2016). Development of a mobile robotic phenotyping system for growth chamber-based studies of genotype x environment interactions. *IFAC PapersOnLine* 49, 248–253. doi: 10.1016/j.ifacol.2016.10.046

Shahrimie, M. A. M., Mishra, P., Mertens, S., Dhondt, S., Wuyts, N., and Scheunders, P. (2016). "Modeling effects of illumination and plant geometry on leaf reflectance spectra in close-range hyperspectral imaging," in *2016 8th Workshop on Hyperspectral Image and Signal Processing: Evolution in Remote Sensing (WHISPERS)*, Los Angeles, CA: IEEE, 1–4.

Shalal, N., Low, T., McCarthy, C., and Hancock, N. (2013). *A Review of Autonomous Navigation Systems in Agricultural Environments*.

Shamshiri, R. R., Weltzien, C., Hameed, I. A., Yule, I. J., Grift, T. E., Balasundram, S. K., et al. (2018). Research and development in agricultural robotics: a perspective of digital farming. *Int. J. Agric. Biol. Eng.* 11, 1–14.

Shao, Y., and He, Y. (2008). Nondestructive measurement of acidity of strawberry using Vis/NIR spectroscopy. *Int. J. Food Prop.* 11, 102–111.

Silwal, A., Davidson, J. R., Karkee, M., Mo, C., Zhang, Q., and Lewis, K. (2017). Design, integration, and field evaluation of a robotic apple harvester. *J. F. Robot.* 34, 1140–1159. doi: 10.1002/rob.21715

Singh, A., Ganapathysubramanian, B., Singh, A. K., and Sarkar, S. (2016). Machine learning for high-throughput stress phenotyping in plants. *Trends Plant Sci.* 21, 110–124.

Smitt, C., Halstead, M., Zaenker, T., Bennewitz, M., and McCool, C. (2020). PATHoBot: A Robot for Glasshouse Crop Phenotyping and Intervention. *arXiv* [Preprint]. arXiv2010.16272.

Taghavifar, H., Xu, B., Taghavifar, L., and Qin, Y. (2019). Optimal path-planning of nonholonomic terrain robots for dynamic obstacle avoidance using single-time velocity estimator and reinforcement learning approach. *IEEE Access* 7, 159347–159356.

Tan, Y., and Zheng, Z. (2013). Research advance in swarm robotics. *Def. Technol.* 9, 18–39. doi: 10.1016/j.dt.2013.03.001

Tripodi, P., Massa, D., Venezia, A., and Cardi, T. (2018). Sensing technologies for precision phenotyping in vegetable crops: current status and future challenges. *Agronomy* 8:57.

Tsubo, M., and Walker, S. (2002). A model of radiation interception and use by a maize–bean intercrop canopy. *Agric. For. Meteorol.* 110, 203–215.

Ubbens, J., Cieslak, M., Prusinkiewicz, P., Parkin, I., Ebersbach, J., and Stavness, I. (2020). Latent space phenotyping: automatic image-based phenotyping for treatment studies. *Plant Phenomics* 2020:5801869. doi: 10.34133/2020/5801869

Underwood, J., Wendel, A., Schofield, B., McMurray, L., and Kimber, R. (2017). Efficient in-field plant phenomics for row-crops with an autonomous ground vehicle. *J. F. Robot.* 34, 1061–1083.

van Henten, E. J., Hemming, J., van Tuijl, B. A. J., Kornet, J. G., Meuleman, J., Bontsema, J., et al. (2002). An autonomous robot for harvesting cucumbers in greenhouses. *Auton. Robots* 13, 241–258. doi: 10.1023/A:1020568125418

Vázquez-Arellano, M., Paraforos, D. S., Reiser, D., Garrido-Izard, M., and Griepentrog, H. W. (2018). Determination of stem position and height of reconstructed maize plants using a time-of-flight camera. *Comput. Electron. Agric.* 154, 276–288.

Vidoni, R., Gallo, R., Ristorto, G., Carabin, G., Mazzetto, F., Scalera, L., et al. (2017). "ByeLab: An agricultural mobile robot prototype for proximal sensing and precision farming," in *ASME International Mechanical Engineering Congress and Exposition*, (New York, NY: American Society of Mechanical Engineers), V04AT05A057.

Vijayarangan, S., Sodhi, P., Kini, P., Bourne, J., Du, S., Sun, H., et al. (2018). in *High-Throughput Robotic Phenotyping of Energy Sorghum Crops BT - Field and Service Robotics*, eds M. Hutter and R. Siegwart (Cham: Springer International Publishing), 99–113.

Virlet, N., Sabermanesh, K., Sadeghi-Tehran, P., and Hawkesford, M. J. (2017). Field scanalyzer: an automated robotic field phenotyping platform for detailed crop monitoring. *Funct. Plant Biol.* 44, 143–153. doi: 10.1071/FP16163

Vu, Q., Raković, M., Delic, V., and Ronzhin, A. (2018). "Trends in development of UAV-UGV cooperation approaches," in *Precision Agriculture BT - Interactive Collaborative Robotics*, eds A. Ronzhin, G. Rigoll, and R. Meshcheryakov (Cham: Springer International Publishing), 213–221.

Walter, A., Liebisch, F., and Hund, A. (2015). Plant phenotyping: from bean weighing to image analysis. *Plant Methods* 11:14. doi: 10.1186/s13007-015-0056-8

Wang, H., Peng, J., Xie, C., Bao, Y., and He, Y. (2015). Fruit quality evaluation using spectroscopy technology: a review. *Sensors* 15, 11889–11927.

Wang, L., Zhu, G., Johnson, W., and Kher, M. (2018). Three new approaches to genomic selection. *Plant Breed.* 137, 673–681.

Wei, H., Shao, Z., Huang, Z., Chen, R., Guan, Y., Tan, J., et al. (2016). RT-ROS: a real-time ROS architecture on multi-core processors. *Futur. Gener. Comput. Syst.* 56, 171–178. doi: 10.1016/j.future.2015.05.008

Weiss, U., and Biber, P. (2011). Plant detection and mapping for agricultural robots using a 3D LIDAR sensor. *Rob. Auton. Syst.* 59, 265–273. doi: 10.1016/j.robot.2011.02.011

White, J. W., Andrade-Sanchez, P., Gore, M. A., Bronson, K. F., Coffelt, T. A., Conley, M. M., et al. (2012). Field-based phenomics for plant genetics research. *F. Crop. Res.* 133, 101–112. doi: 10.1016/j.fcr.2012.04.003

Wolfert, S., Ge, L., Verdouw, C., and Bogaardt, M.-J. (2017). Big data in smart farming – a review. *Agric. Syst.* 153, 69–80. doi: 10.1016/j.agsy.2017.01.023

Wu, C., Zeng, R., Pan, J., Wang, C. C. L., and Liu, Y. (2019). Plant phenotyping by deep-learning-based planner for multi-robots. *IEEE Robot. Autom. Lett.* 4, 3113–3120. doi: 10.1109/LRA.2019.2924125

Wu, G. F., Huang, L. X., and He, Y. (2008). Research on the sugar content measurement of grape and berries by using Vis/NIR spectroscopy technique. *Guang pu xue yu Guang pu fen xiGuang pu* 28, 2090–2093.

Würschum, T. (2019). "Modern field phenotyping opens new avenues for selection," in *Applications of Genetic and Genomic Research in Cereals*, eds T. Miedaner and V. Korzun (Amsterdam: Elsevier), 233–250.

Xiong, Y., Ge, Y., Grimstad, L., and From, P. J. (2020). An autonomous strawberry-harvesting robot: Design, development, integration, and field evaluation. *J. F. Robot.* 37, 202–224.

Xiong, B., Wang, B., Xiong, S., Lin, C., and Yuan, X. (2019). 3D morphological processing for wheat spike phenotypes using computed tomography images. *Remote Sens.* 11:1110.

Xu, R., Li, C., and Mohammadpour Velni, J. (2018). Development of an autonomous ground robot for field high throughput phenotyping. *IFAC-PapersOnLine* 51, 70–74. doi: 10.1016/j.ifacol.2018.08.063

Young, S. N., Kayacan, E., and Peschel, J. M. (2019). Design and field evaluation of a ground robot for high-throughput phenotyping of energy sorghum. *Precis. Agric.* 20, 697–722. doi: 10.1007/s11119-018-9601-6

Yuan, H., Wang, N., Bennett, R., Burditt, D., Cannon, A., and Chamberlin, K. (2018). Development of a ground-based peanut canopy phenotyping system. *IFAC PapersOnLine* 51, 162–165. doi: 10.1016/j.ifacol.2018.08.081

Zahid, A., Mahmud, M. S., He, L., Choi, D., Heinemann, P., and Schupp, J. (2020). Development of an integrated 3R end-effector with a cartesian manipulator for pruning apple trees. *Comput. Electron. Agric.* 179:105837.

Zhang, F., Leitner, J., Milford, M., Upcroft, B., and Corke, P. (2015). Towards vision-based deep reinforcement learning for robotic motion control. *arXiv* [Preprint]. arXiv1511.03791.

Zhang, J., Gong, L., Liu, C., Huang, Y., Zhang, D., and Yuan, Z. (2016). Field phenotyping robot design and validation for the crop breeding. *IFAC PapersOnLine* 49, 281–286. doi: 10.1016/j.ifacol.2016.10.052

Zhang, Q., Karkee, M., and Tabb, A. (2019). The use of agricultural robots in orchard management. *arXiv* [Preprint]. arXiv1907.13114.

Zhang, Z., Kayacan, E., Thompson, B., and Chowdhary, G. (2020). High precision control and deep learning-based corn stand counting algorithms for agricultural robot. *Auton. Robots* 44, 1289–1302.

Zhao, J., Mantilla Perez, M. B., Hu, J., and Salas Fernandez, M. G. (2016). Genome-wide association study for nine plant architecture traits in sorghum. *Plant Genome* 9, 1–14. doi: 10.3835/plantgenome2015.06.0044

Zhou, Y., Srinivasan, S., Mirnezami, S. V., Kusmec, A., Fu, Q., Attigala, L., et al. (2019). Semiautomated feature extraction from RGB images for sorghum panicle architecture GWAS. *Plant Physiol.* 179, 24–37. doi: 10.1104/pp.18.00974

Conflict of Interest: The authors declare that the research was conducted in the absence of any commercial or financial relationships that could be construed as a potential conflict of interest.

frontiers in Plant Science

METHODS
published: 12 July 2021
doi: 10.3389/fpls.2021.621711

Raman Spectroscopy as a Robust New Tool for Rapid and Accurate Evaluation of Drought Tolerance Levels in Both Genetically Diverse and Near-Isogenic Maize Lines

Narangerel Altangerel[1,2], *Pei-Cheng Huang*[3], *Michael V. Kolomiets*[3]*, *Marlan O. Scully*[1,2,4] *and Philip R. Hemmer*[5]

[1] *Institute of Quantum Science and Engineering, Texas A&M University, College Station, TX, United States,* [2] *Physics Department, Baylor University, Waco, TX, United States,* [3] *Plant Pathology and Microbiology Department, Texas A&M University, College Station, TX, United States,* [4] *Mechanical and Aerospace Engineering, Princeton University, Princeton, NJ, United States,* [5] *Electrical and Computer Engineering Department, Texas A&M University, College Station, TX, United States*

OPEN ACCESS

Edited by:
Lindsey Compton, University of Birmingham, United Kingdom

Reviewed by:
Ankush Prashar, Newcastle University, United Kingdom
Rajeev Ram, Massachusetts Institute of Technology, United States

****Correspondence:***
Michael V. Kolomiets
kolomiets@tamu.edu

Specialty section:
This article was submitted to Technical Advances in Plant Science, a section of the journal Frontiers in Plant Science

Received: *26 October 2020*
Accepted: *07 May 2021*
Published: *12 July 2021*

Citation:
Altangerel N, Huang P-C, Kolomiets MV, Scully MO and Hemmer PR (2021) Raman Spectroscopy as a Robust New Tool for Rapid and Accurate Evaluation of Drought Tolerance Levels in Both Genetically Diverse and Near-Isogenic Maize Lines. Front. Plant Sci. 12:621711. doi: 10.3389/fpls.2021.621711

Improving drought tolerance of crops has become crucial due to the current scenario of rapid climate change. In particular, development of new maize germplasm with increased drought tolerance is viewed as a major breeding goal to ensure sustainable food and feed production. Therefore, accurate rapid phenotyping techniques for selection of superior maize genotypes are required. The objectives of this study were to determine whether Raman microscopy technique can be applied for accurate assessment of drought-tolerance levels in both genetically diverse and near-isogenic maize lines that differ in their levels of drought-tolerance. Carotenoid degradation is known to be a direct stress response initiated by reactive oxygen species during osmotic stress such as drought. Using Raman mapping, we observed real-time changes in the rate of carotenoid degradation in chloroplasts that was dependent on the strength of osmotic stress. In addition, we showed that the rate of carotenoid degradation as measured by Raman spectroscopy correlates directly with drought tolerance levels of diverse maize genotypes. We conclude that Raman technique is a robust, biochemically selective and non-invasive phenotyping technique that accurately distinguishes drought tolerance levels in both genetically diverse and near-isogenic maize genotypes. We conclude that this technique can be further developed to render it suitable for field-based early assessment of breeding materials with superior drought-tolerance traits.

Keywords: lipoxygenase, Raman spectroscopy, carotenoid degradation, osmotic stress, drought stress, maize inbred lines

INTRODUCTION

Due to rapidly increasing human population, there is a crucial need to meet global food security needs and satisfy the increasing demand for food, feed, and fuel. To do so, it is necessary to provide improved plant phenotyping techniques to breeding programs to aid in the development of germplasm of crops that have increased drought tolerance levels, and can thus help adapt to future

climate changes (Borlaug, 2000; De La Fuente et al., 2014). Improving drought tolerance of crops has become one of the significant challenges in global agricultural production and food security (Tilman et al., 2001; Chaves et al., 2003; De La Fuente et al., 2014).

Maize (*Zea mays*) is the world's most important production crop: its starch, protein, and oil are essential for supplying adequate food and nutrition to both human and animals (Ranum et al., 2014). In addition, maize starch has recently become an important feedstock for ethanol production (Ranum et al., 2014). A major objective in most breeding programs is to develop superior germplasm that tolerate water stress yet produce a higher yield. This is achieved by employing vastly improved breeding strategies through years of genetic research, including marker assisted selection and hybrid seed production (Fiorani and Schurr, 2013). The phenotype of a plant is defined by both differences in genome and their interactions with the environment. Therefore, genotypes that correlate with improved yield or other agronomic traits must be considered in the contexts of various environments to determine optimum phenotypic responses (Fiorani and Schurr, 2013).

The majority of phenotypic traits of genotypes consist of various morphological, physiological, and biotic stress traits; however, the current breeding program also includes the evaluation of germplasm performance under drought conditions. One of the major drawbacks of conventional phenotyping techniques is the long period of time it takes to measure the effect of stress on plants. Current *in vivo* spectroscopic techniques such as reflectance spectroscopy (Gutelson and Merziyak, 1996), IR thermal imaging (Zia et al., 2013), hyperspectral imaging (Behmann et al., 2014), and chlorophyll fluorescence spectroscopy (Kalaji et al., 2011) are limited by the time required for sensing a drought stress response and the level of the stress. Chemical extraction techniques are more relevant but are destructive and labor-intensive.

Because of unpredictable weather patterns, drought tolerance screening of breeding populations during the entire growing session over many months is difficult to perform as drought stress is difficult to control. To speed up this research, there is an urgent need to develop more robust phenotyping techniques for non-destructive, accurate and rapid assessment of breeding populations for drought related responses, especially at early seedling stages and with short periods of withholding water.

Here, we investigated whether Raman spectroscopic techniques can overcome these limitations of traditional phenotyping by achieving the necessary biochemical sensitivity *in vivo*. For this demonstration, we chose to analyze drought stress tolerance among 5 genotypes of maize. Specifically, we measured drought tolerance levels by assessing the level of transpirational water loss among the young seedlings during a week in which water was withheld. Measuring drought tolerance in seedlings is of interest because it shortens the time needed to evaluate different genotypes. Previously, we demonstrated the use of Raman spectroscopy for early *in vivo* detection of plant stress in mature plants, where we found that plants exposed to multiple abiotic stresses such as cold, excess light, saline and drought stress conditions display rapid degradation of carotenoids and accumulation of anthocyanins (Altangerel et al., 2017a). In that study, we used 5 months old genetically identical *Coleus* plants belonging to a single variety. Here, we used two-week old seedlings of genetically diverse maize and near-isogenic inbred lines that differ in their responses to drought stress in an attempt to evaluate whether differences in phenotypic responses to drought stress can be accurately assessed by Raman spectroscopy. Because young seedlings produce anthocyanins for purposes unrelated to drought stress (Karageorgou and Manetas, 2006), we have decided not to assess the level of anthocyanins to study stress in these plants. Instead, we monitored the rate of carotenoid degradation during drought stress for each genotype.

Plants undergo highly intricate physiological, biochemical, and molecular changes when they are exposed to drought (De La Fuente et al., 2014). Notably, highly toxic reactive oxygen species (ROS) accumulate in plants during drought conditions. Carotenoids play irreplaceable roles during abiotic stress such as drought by quenching chlorophyll-excited states, scavenging ROS, and dissipating excess energy to heat (Krinsky, 1989; Muller et al., 2001; Davison et al., 2002; Krieger-Liszkay et al., 2008; Shan and Li, 2008; Yoshikazu et al., 2008; Ramel et al., 2012). They are considered to be the first line of defense against ROS, serving as the main $^1O_2$ quencher in chloroplasts (Krinsky, 1989; Davison et al., 2002; Shan and Li, 2008; Ramel et al., 2012). The oxidative degradation of carotenoids, like the accessory photosynthetic pigment β-carotene, causes accretion of several volatile β-carotene derivatives such as β-cyclocitral. Beta-cyclocitral is a molecular signal responsible for induction of $^1O_2$-responsive genes (Davison et al., 2002; Ramel et al., 2012). Therefore, rapid conversion of β-carotene to β-cyclocitral during oxidative stress is an important line of defense against osmotic stress (Davison et al., 2002; Ramel et al., 2012).

At the same time, β-carotene, along with other carotenoids, absorbs well in the high energy blue spectrum of visible light and are used as accessory pigments in light harvesting complexes (Krieger-Liszkay et al., 2008; Yoshikazu et al., 2008). These are not core elements of the light-harvesting complex but instead are used to saturate energy transfer into the reaction center after excitation at wavelengths varying from those of the more abundant chlorophyll. Degradation of carotenoids reduces saturation, protecting the photosystem core pigments in the reaction center and membrane tissues from the effects of photooxidation (Muller et al., 2001).

Here we demonstrated real-time carotenoid degradation in chloroplasts during drought stress using the combination of our newly developed immediate osmotic stress technique and Raman mapping. Then, we demonstrated Raman technique's ability to sense different rates of carotenoid degradation under various strengths of osmotic stress. At last, we showed that the degradation rate of the carotenoids, as measured by the Raman microscopy technique, can be used to accurately distinguish drought tolerance levels in both genetically diverse and near-isogenic maize genotypes within a short period from several days to a week of withholding water.

MATERIALS AND METHODS

Plant Material and Growth Conditions

Three maize inbred lines differing in their levels of drought responses, B73, CML176, and OH28, were used in this study. In addition, lipoxygenase mutants with contrasting drought tolerance phenotypes, *lox2* and *lox4* mutants, were back-crossed seven times to the recurrent parent B73 to generate near-isogenic mutants which share ∼99.3% genome identity (Huang, 2017). Maize seedlings were grown in conical pots (15 by 3 cm) in the same amount (dry weight) of sieved sterile (autoclaved) commercial potting mix (Metro-Mix 366; Scotts-Sierra Horticultural products, Marysville, OH, U. S. A.) at 22°C under a 14-h day length, 50% humidity, 200 μmol m^2/s of light in the laboratory.

Specifically, two replications of six B73 maize plants per replication were used for the *in-situ* Raman study of immediate osmotic stress in plant tissues. We grew these plants under two different lighting conditions such as normal and completely dark conditions. The normal lighting condition was a 14-h length of 200 μmol m^2/ s of light and a 10-h length of darkness. The completely dark condition was 24-h darkness for a day.

Three of the plants in each replication grew under normal growth conditions and had normal photosynthesis activities and chlorophyll contents. The other three plants in each replication grew under complete darkness which resulted in lower photosynthetic activities due to extremely low content of chlorophyll.

Three replications of 10 plants per replication per genotype were used for the *in-vivo* Raman study. Before withholding water, all experimental plants were soaked in deionized water until reaching 100% water content in their soil. Then, five plants of each genotype were well watered every day and served as a control group in this study. The other five plants of each genotypes were kept withholding water for a week, and served as drought stressed group in this study. After a week of *in-vivo* Raman measurements, all experimental plants were harvested, and root and shoot tissues were separated for dry weight measurement.

Transpirational Water Loss Measurement

Transpirational water loss measurements were performed with slight modifications following the protocol from (Ruggiero et al., 2004). Fourteen days after sowing, pots with seedlings which have two leaves with visible leaf collars (V2 stage) were soaked in deionized water for more than 30 min to reach 100% water content in the soil before withholding water. After the seedlings were soaked in deionized water, each pot was covered with a para-film to avoid water loss from soil surface. Three plants were then placed into a bigger pot as one sample and the pot weight was measured every day and the difference of pot weight represents the amount of water lost via transpiration. Water loss through transpiration was normalized by plant dry weight taken at the end of the experiment.

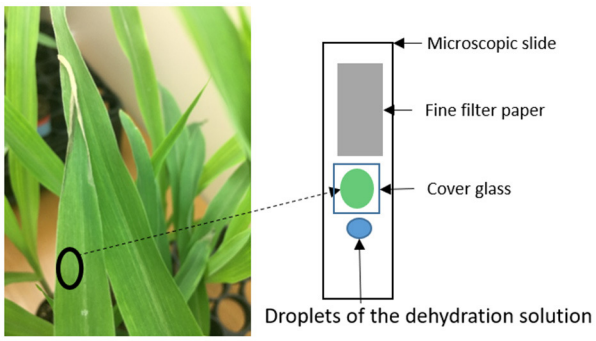

FIGURE 1 | Illustration of the immediate osmotic stress technique.

In situ Raman Studies: Simulating Immediate Osmotic Stress in Plant Tissue and Raman Microscopic Mapping

To simulate immediate drought stress in leaf tissue, we developed a rapid drought stressing technique that uses a dehydrating chemical, mannitol. Watering plants with mannitol solutions chemically induces osmotic stress (Fritz and Ehwald, 2011). Osmotic stress occurs in plants during drought or high salinity conditions. First, we cut about a 1 cm^2 leaf disk from our experimental subjects of two-week old B73 plants. We then wet-mounted it on a microscopic slide in a manner that allowed the leaf tissue to be suspended inside deionized water between the microscopic slide and cover glass. We introduced the dehydration solution to the plant tissue using the capillary effect (**Figure 1**). In order to do so, we dropped 2 drops of mannitol solution near the left edge of the cover glass, holding a filter paper (Whatman, filter 1) near the right edge of the cover glass. Once the solution started to enter between the cover and microscope glasses, the same amount of water was absorbed by the filter paper. Meanwhile, we made sure the location and height of the Raman sampling area stayed the same during this process by observing it with a camera. When mannitol solution enters the tissue area, it creates immediate osmotic stress on the tissue. Here, we used 100, 150, and 250 mM of mannitol solutions to imitate different strengths of osmotic stresses. We took Raman maps before and after introducing mannitol solutions to the wet-mounted plant tissues. Raman mapping was done by a Raman confocal microscope system with an excitation laser of 532 nm laser. The laser sampling size was 2 microns with 2 mW power and 0.5 s acquisition time. Each XY map size was 180 by 140 microns with 80 sampling points, and each XZ map was 160 microns by 15 microns with 30 sampling points. All Raman images are based on the heights of carotenoids' 1,157 cm^{-1} peak.

In vivo Raman Study: Raman Microscopic Measurements, Data Processing, and Statistical Analysis

We used a Raman confocal microscopic system with a 532 nm CW laser for microscopic measurements (Horiba, LabRam HR Revolution), placing plant leaves directly onto the sample holder without physical detachment from the plant. Thus, we used *in vivo*, or non-invasive detection. Air-cooled CCD cameras efficiently detected the laser induced scattered radiation (signal). The laser powers were adjusted to be low enough to not affect the live cells in plant tissue. The laser sampling spot size was 2 microns, and the laser power was 0.5 mW with 1 second acquisition time for microscopic measurements. Twelve Raman spectra were collected from 3rd and 4th leaves of each plant because 1st and 2nd leaves had signs of senescence on drought stressed plants. We took the Raman spectral data of the plants (leaves) every 24 h for 7 days between 8 a.m. and 12 p.m. during the on-set and development of stress. Because plant leaf is a complex system, we used the mean spectra, averaged over different regions, for further analysis. Since the greatest contributor of noise to Raman spectra is the intrinsic fluorescence of molecules in plant tissues, we removed the fluorescence background in order to extract accurate Raman signals from the raw spectra. The baselines of Raman raw spectral data were corrected by fitting the background with high order polynomials with multiple iterations (Lieber and Mahadevan-Jansen, 2003). The spectra were then smoothed by the Savitzky-Golay algorithm with 15 adjacent points and normalized by the unit vector method, a common normalization method for Raman spectra of biological samples. All data processing programs were written in MATLAB R2013a (The Mathworks, Natick, MA, USA). Results are reported as means ±SE, from 3 different experiments. Data were evaluated using one-way analysis (ANOVA) using the Origin Labs 8.1 and $P < 0.05$ were considered to indicate statistical significance.

RESULTS AND DISCUSSION

In situ Raman Studies: Real-Time Carotenoid Degradations During Osmotic Stress

Since the major objective of this study was to determine whether Raman spectroscopy can be utilized to distinguish maize genotypes that display diverse levels of drought tolerance, we first aimed to establish whether carotenoid degradation is proportional to the levels of osmotic stress that leaf tissue experiences by using different concentrations of mannitol treatments of leaf disks. Carotenoids are yellow to orange accessory photosynthetic pigments that have nutritional relevance as an antioxidant and are well-studied for their relevance to plant stress responses (Krinsky, 1989; Muller et al., 2001; Davison et al., 2002; Krieger-Liszkay et al., 2008; Shan and Li, 2008; Yoshikazu et al., 2008; Ramel et al., 2012). Degradation of carotenoids is one of the plant's direct responses to stress, and in our previous study, using Raman microscopy, we observed this degradation in response to multiple stress conditions in genetically identical *Coleus* plants (Altangerel et al., 2017a).

In plants, degradation of carotenoids happens slowly, within days. We reasoned that if degradation of carotenoids could be expedited in plant tissue from days to minutes using our newly developed immediate stress technique, then we would be able to observe this process more closely. One of the important advantages of Raman mapping is the ability to monitor distributions of molecules in real-time (Kann et al., 2015). In addition, we addressed the question of which plastids display carotenoid degradation during an osmotic stress such as drought. Carotenoid contents vary in different types of plastids, for example chlorophyll containing chloroplasts or chlorophyll-less leucoplasts such as etioplasts (Sun et al., 2018). To separately investigate etioplasts and chloroplasts, we grew individual seedlings simultaneously; one in complete darkness and the other under normal light. The plants that grew in darkness did not produce mature chloroplasts and thus could not perform photosynthetic functions (Alberts et al., 2002), whereas the green plants contained photosynthetically active chloroplasts (**Figure 2A**). To understand the subcellular origin of carotenoids being degraded under osmotic stress, we compared the responses of leaf disks from the chlorophyll-less plants that grew under complete darkness that had few if any mature chloroplasts to those that contain normal levels of fully mature chloroplasts. For this, the excised leaf disks were subjected to osmotic stress conditions while taking Raman measurements.

For Raman spectroscopy, a single frequency laser light is used to excite molecules. The excited molecules emit light with new optical frequencies that are downshifted from the incident laser frequency by the amount equal to the molecule vibrational frequencies. This new optical frequency of light (referred to as Stokes radiation) is then measured by a spectrometer. For example, the average Raman spectra of the white and green tissue of live plants are shown in **Figure 2B**, with different intensities of carotenoid's Raman peaks at 1,157 and 1,007 cm^{-1}. Note that normally, carotenoids have the strongest Raman peak at 1,524 cm^{-1}, but we couldn't use it here because it overlaps with the anthocyanin Raman peak that also exists in plant tissue (Altangerel et al., 2017b). Since Raman peak intensity directly correlates with the concentration of molecule, we observed that the chlorophyll-less plants had less carotenoids compared to the chlorophyll containing plants in **Figure 2B**. Indeed, etioplasts are known to accumulate only limited amounts of carotenoids (Lintig et al., 1997; Welsch et al., 2000).

Next, we simulated osmotic stress in the chlorophyll containing (green) and chlorophyll-less (white) leaf disks using our newly developed osmotic stress protocol (**Figure 1**). The leaf disks from each plant were exposed to 150 mM Mannitol solution and we took Raman XZ and XY maps before and after the stress at specific time points. According to Raman maps in **Figure 2C**, one can see clearly that carotenoids emitting at the 1,157 cm^{-1} Raman line did not degrade in white plant tissue during the osmotic stress, yet they did in green plant tissue. This selective degradation seen in the green plants demonstrates that carotenoids in chloroplasts preferentially degraded during osmotic stress compared to carotenoids in etioplasts (**Figure 2D**).

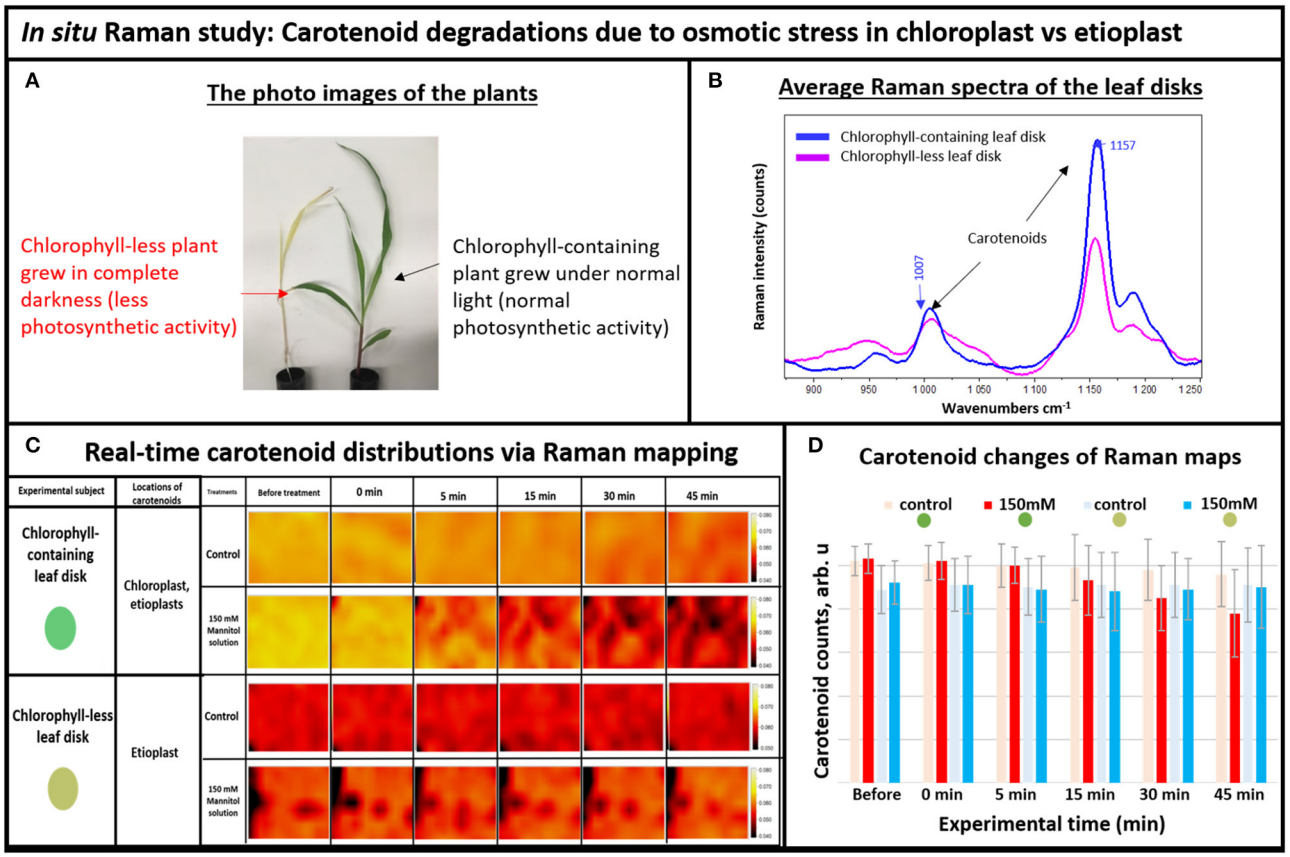

FIGURE 2 | (A) The photo images of the experimental plants: chlorophyll-containing (green) vs. chlorophyll-less (white), **(B)** Average Raman spectra of the chlorophyll-containing and chlorophyll-less leaf disks, **(C)** Real-time carotenoid distribution changes due to the 150 mM mannitol solution vs. pure deionized water, green and white leaf disks (areas of 170 × 140 μm): before treatments and 0, 5, 15, 30, and 45 min after the treatments. **(D)** Histogram of carotenoid changes of Raman maps. Each bar represents mean +SD ($n = 80 \times 3 \times 2$).

Furthermore, we investigated whether Raman technique can sense shifts of carotenoid degradation rate during different levels of the osmotic stress in the chlorophyll containing leaf disks. In general, higher concentrations of mannitol solution should result in faster dehydration rate, which linearly correlates with faster carotenoid degradation. As shown in **Figure 3**, the Raman images for carotenoid distributions in plant tissues (intensities at 1,157 cm^{-1} Raman line) show different strengths of stress for different concentrations of mannitol solutions. One can see that carotenoids are distributed evenly before stressing, suggesting that they exist in similar concentrations throughout the plant tissue under normal conditions. After the dehydration solution was introduced into plant tissue, the pattern of carotenoid distribution changed in minutes in response to different concentrations of mannitol solutions. For example, significant carotenoid degradation was seen throughout the mapped area after 5 min exposure to 250 mM mannitol solution, whereas similar level of degradation took 15 min with 100 mM solution.

Overall, when we increased the mannitol concentration from 100 to 250 mM, the Raman XZ (tissue depth) maps (**Figure 3C**) show that the carotenoid, due to re-distribution or degradation, changed rapidly between 5 and 15 min after the stress. Similarly, the XY Raman images (**Figure 3A**) show that carotenoid degradation also intensifies in response to treatment with mannitol especially between 5 and 15 min after the stress. These results confirm that this new osmotic stress protocol indeed imitates osmotic stress in tissue as reported in our previous study (Altangerel et al., 2017a), and that Raman mapping is able to accurately sense the degradation rate in carotenoid levels caused by different strengths of osmotic stresses.

In vivo Raman Study: Carotenoid Degradation in Maize Inbreds Due to Drought Stress

Next, we investigated whether Raman technique can distinguish drought tolerance levels in response to withholding water for seven days in genetically diverse maize inbred lines including B73, CML176, and OH28 by comparing their carotenoid degradation rates. In **Figure 4A**, we compared the average Raman spectra of OH28 inbred line before and after 72 h of stress, focusing on the intensities of the carotenoid Raman peaks at

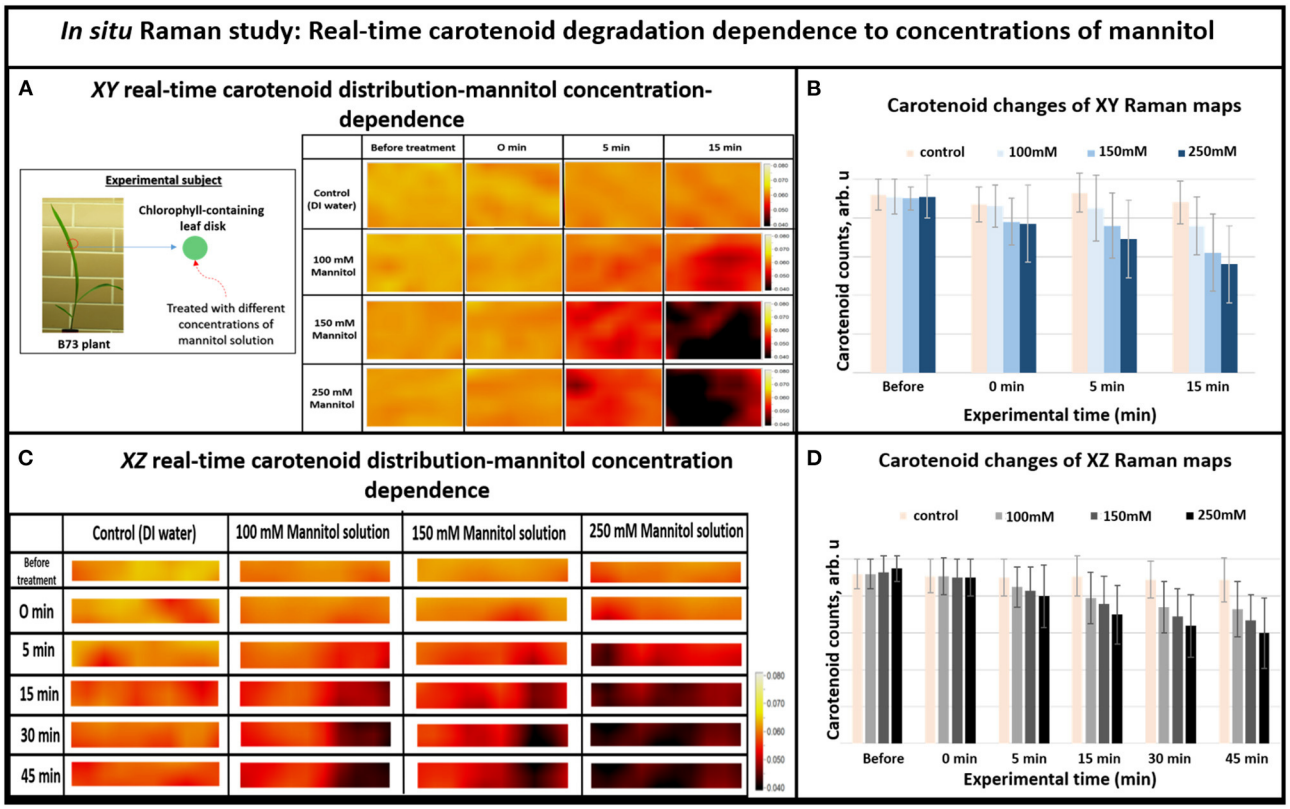

FIGURE 3 | (A) XY Real-time carotenoid distribution changes depend on the mannitol concentrations of 0, 100, 150, and 250 mM, before the treatments and 0, 5, and 15 min after the treatments (the green leaf disks-areas of 170 ×140 μm), **(B)** Histogram of carotenoid changes of XY Raman maps. Each bar represents mean +SD ($n = 80 \times 3 \times 2$), **(C)** XZ Real-time carotenoid distribution changes depend on the mannitol concentrations of 0, 100, 150, and 250 mM, before treatments and 0, 5, 15, 30, and 45 min after the treatments (the green leaf disks where z is depth inside the tissue-areas 170 × 2 μm), **(D)** Histogram of carotenoid changes of XZ Raman maps. Each bar represents mean +SD ($n = 30 \times 3 \times 2$).

1,157 and 1,007 cm^{-1}. The observed decrease allows us to conclude that carotenoids are degraded during these 2 days. **Figure 4B** shows the mean amplitudes of the carotenoid peak at 1,157 cm^{-1} of each genotype from the onset of the experiment to day 7. The rate of carotenoid degradation serves as a proxy how plants respond to drought stress. The faster the carotenoids degrade under drought stress, the less carotenoids left in the plant tissue to scavenge damaging ROS resulting in increased sensitivity to drought stress. Therefore, the germplasm that exhibits greater degradation rate will likely be less drought tolerant. According to our Raman measurements (**Figure 4B**), carotenoids were degraded less in B73 and more in CML176. In particular, the relative carotenoid degradation rates (from day 0 to day 7) were 22, 20, and 6%, respectively for CML176, OH28, and B73 inbreds. At the 0.05 level, the population variances showed no significant difference between 3 replicate experiments. These results, therefore, suggest that B73 is the most drought-tolerant maize inbred and CML176 is the least tolerant.

To measure relative drought tolerance levels in these inbred lines directly, we measured how much water was lost transpirationally in response to withholding water (**Figure 4C**). The results show that CML176 and OH28 plants had the highest transpirational water loss rate, indicating that they are more drought sensitive. In contrast, B73 displayed the lowest level of water loss through transpiration and therefore is the most drought tolerant among these inbreds. The normalized dry weight loss for control vs. stressed plants (**Figure 4D**) agrees with the water loss data. In particular, CML176 had the biggest differences in weight between the control and stressed plants for both above ground and root tissues during the week-long water deprivation. In contrast, B73 had the least differences between control and stressed plants for both tissues. Overall, these results agreed with our inbred line behavior as expected from the carotenoid degradation rates determined by Raman measurements.

In vivo Raman Study: Carotenoid Degradation in Maize Near Isogenic Genotypes Due to Drought Stress

Having demonstrated Raman microscopic technique's ability to distinguish the levels of drought tolerance in the genetically diverse maize genotypes, we shifted the focus to using this technique in the analyses of maize genotypes that are near-isogenic to each other at the genome level but display contrasting drought tolerance responses. For this, we chose

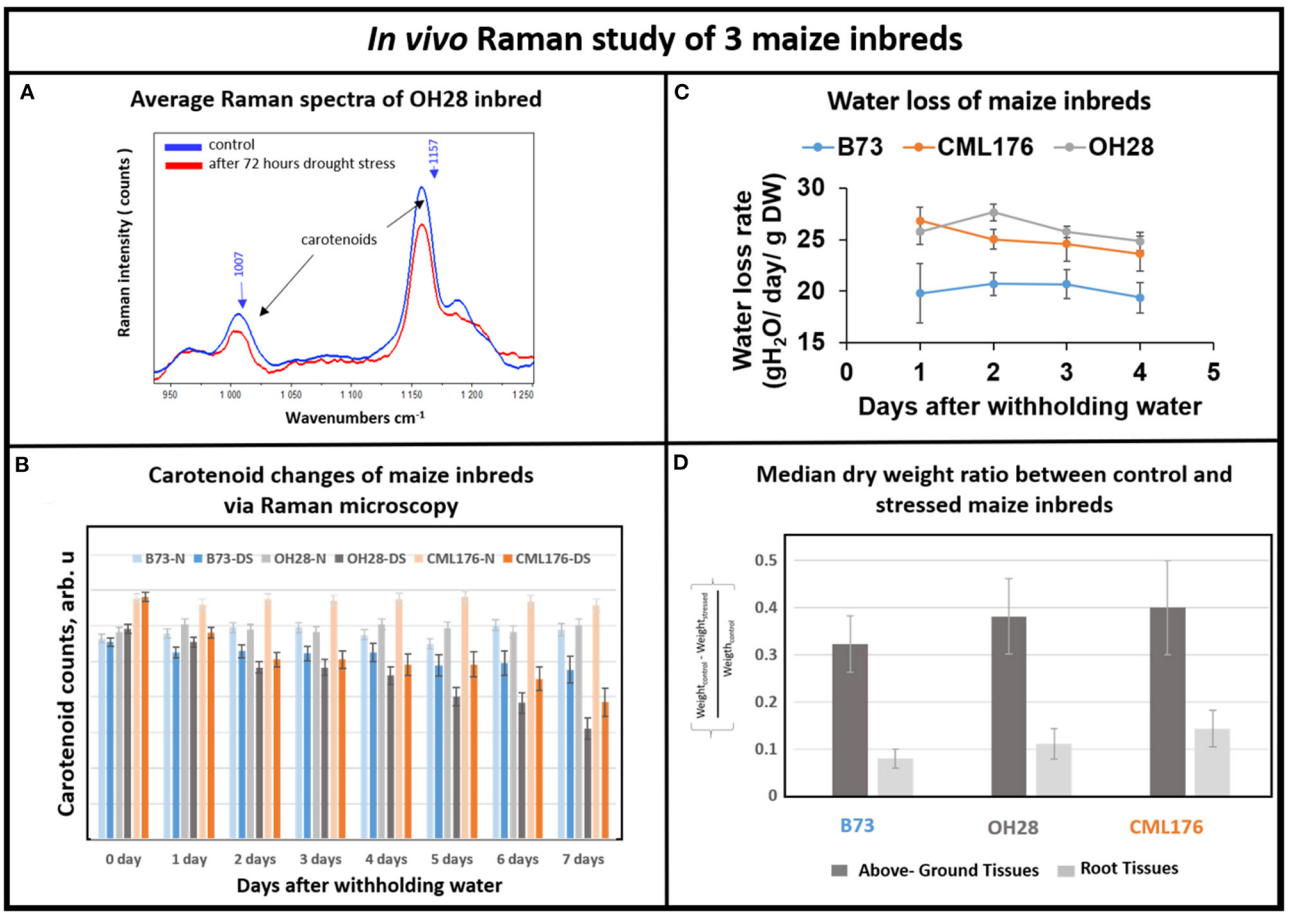

FIGURE 4 | (A) Average Raman spectra of OH28 inbred: control vs. 72 h after drought stress. **(B)** Histogram of a change in the carotenoid content of plants at B73-N (control), B73-DS (drought stressed) CML176-N (control), CML176-DS (drought stressed), OH28-N (control) and OH28-DS (drought stressed). Each bar represents the mean +SE (n = 3x5). **(C)** Transpirational water loss rate of the inbreds. **(D)** Histogram of dry weight ratio between the control and the stressed plants at B73, CML176, and OH28. The higher the value the more weight of tissue is lost and the more sensitive the plants are to drought stress.

B73 inbred and two of its near-isogenic lipoxygenase mutants, *lox2* and *lox4*, that were generated by backcrossing 7 times to recurrent parent B73 inbred line, which resulted in their genome being more than 99.2% identical to the parental B73 inbred line. Transpirational water loss experiments with these three near-isogenic lines (NILs) showed that *lox2* is the most drought sensitive line with the highest transpirational water loss compared to B73, and was unable to recover from a prolonged drought stress period after re-watering (Huang, 2017). In sharp contrast, *lox4* is the most drought tolerant genotype displaying lower water loss through transpiration and better survival after 14 days of withholding water followed by re-watering (Huang, 2017). **Figure 5** shows that relative average carotenoid degradation rates (from day 0 to day 7) were 10, 6, and 3% for the *lox2, B73* and *lox4* genotypes, respectively. These Raman microscopy results mirror the transpirational water loss experimental results in Huang (2017) and confirm that *lox4* is the most drought-tolerant and *lox2* is the most drought-sensitive line among these three genotypes.

It is important to note that Raman spectra for the near isogenic genotypes in **Figure 5** start at nearly the same signal strength for carotenoid levels at the beginning of the experiment, in contrast to **Figure 4B** for the inbreds. This is because the near-isogenic lines, B73, *lox2* and *lox4*, have almost identical genome sequences and presumably contain near-identical levels of carotenoids, whereas the genetically diverse inbreds (B73, CML 176, and OH28) are quite different. Significantly, Raman technique provides the tool to clearly separate the responses of the near-isogenic genotypes after a week-long drought by monitoring degradation of carotenoids. The existing techniques for measuring carotenoids in plants such as reflectance and fluorescence spectroscopies offer low cost but their sensing time is not as fast as Raman. In our previous study with *Coleus* plants (Altangerel et al., 2017a), we collected reflectance and fluorescence spectra from the experimental plants in addition to Raman measurements. The average reflectance, fluorescence and Raman spectra of the experimental plants on the onset of the experiment and 60 h after the drought stress are shown in the

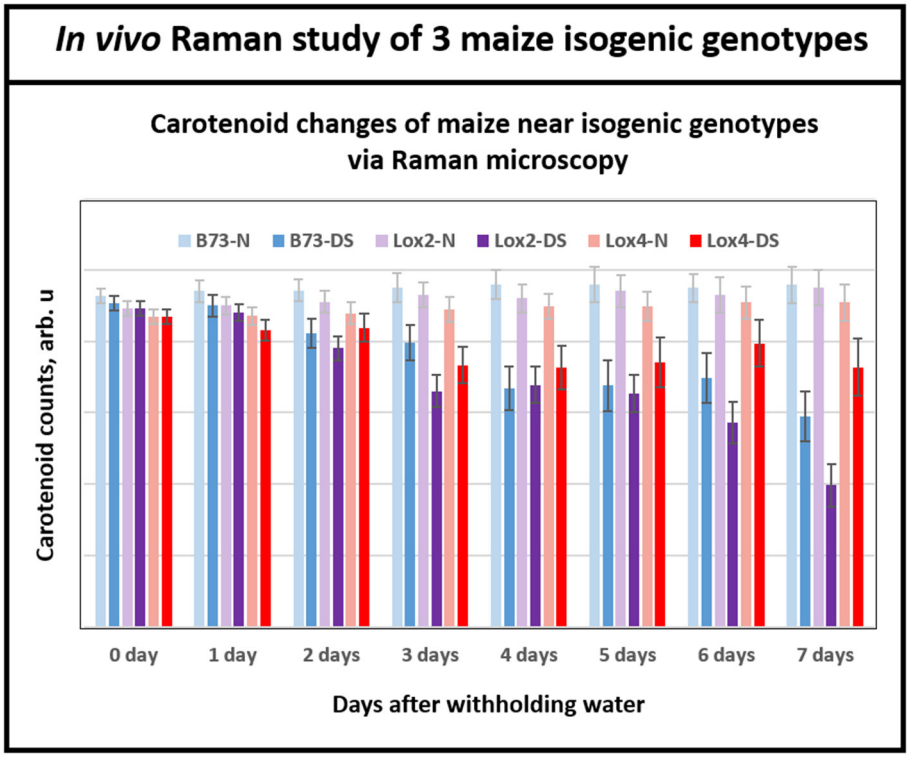

FIGURE 5 | Histogram of a change in the carotenoid content of plants in B73 and near-isogenic lox 2 and lox 4 mutants. While at the beginning of withholding water, all three genotypes showed similar levels of carotenoids, by day 6 and 7 all three genotypes displayed clear separations of carotenoid level between control and drought stressed plants. Each bar represents the mean +SE ($n = 3 \times 5$).

Supplementary Figure 1. The Raman spectra showed significant changes, whereas no changes were observed in the reflectance and fluorescence spectra.

CONCLUSIONS

Carotenoid degradation in plant tissues is one of the plant's first defense against ROS. Since we are detecting these carotenoid molecules in response to drought stress, rather than detecting other physiological changes, we were able to rapidly correlate the dynamics of these biomolecules to the plant tolerance levels. The high accuracy of Raman technique shows that the degradation rate of carotenoids is a reliable indicator of the drought tolerance levels in the genotypes of maize with different levels of drought tolerance.

Raman mapping technique enabled us to observe the real-time dynamics of the changes of carotenoid content in the plant leaf tissue during osmotic stress. In this *in-vitro* study, we found that the distribution of carotenoids in dark-grown (white) tissue didn't change during osmotic stress, and that chlorophyll-less plastids had lower content of carotenoids compared to chrophyll-containing chloroplasts found in the green tissue. The results also showed that only carotenoids in the chloroplast were degraded during osmotic stress.

Most importantly, we demonstrated that Raman technique is a robust, non-invasive, and biochemically selective phenotyping technique that could distinguish drought-tolerance levels not only in genetically diverse genotypes (maize inbred lines) but also in near-isogenic genotypes that contrast in their drought tolerance levels. The robustness of this technique is that it can be performed with two-week old seedlings and requires only a weeklong withholding of water. Climate change increases the odds of a short period of drought stress to happen under natural field conditions in most parts of the world. Thus, using this technique can expedite breeding processes carried out in many areas that do not otherwise provide reliable drought stress conditions. Moreover, this *in vivo* phenotyping technique offers a rapid and accurate method to select drought tolerant genotypes.

In summary, the versatility of Raman techniques allows us to monitor degradation of carotenoids within days in live plants and within minutes in plant leaf disks during drought stress. The robustness and accuracy of this technique offers a great opportunity for future development of high-throughput screening for plant phenotyping. Because hand-held Raman devices are commercially available, this technique has the capability to become mobile and automated, allowing for improved-precision agricultural applications for both breeders and commercial producers.

DATA AVAILABILITY STATEMENT

The original contributions presented in the study are included in the article/**Supplementary Material**, further inquiries can be directed to the corresponding author.

AUTHOR CONTRIBUTIONS

NA: investigation, data curation, and methodology. P-CH: investigation and methodology. MS, MK, and PH: methodology, funding acquisition, and supervision. All authors contributed to the article and approved the submitted version.

FUNDING

NA and PH supported by the Army Research Laboratory Cooperative Agreement W911NF-16-2-0094. MO supported by the Air Force Office of Scientific Research Award No. FA9550-20-1-0366 DEF, Office of Naval Research Award No. N00014-20-1-2184, and Robert A. Welch Foundation Grant No. A-1261. MK research was supported by the Agriculture and Food Research Initiative Grant No. 2015-67013-22816 and 2017-67013-26524 from the USDA National Institute of Food and Agriculture.

ACKNOWLEDGMENTS

We acknowledge Connor Gorman for fruitful discussion.

SUPPLEMENTARY MATERIAL

The Supplementary Material for this article can be found online at: https://www.frontiersin.org/articles/10.3389/fpls.2021.621711/full#supplementary-material

REFERENCES

Alberts, B., Johnson, A., and Lewis, J. (2002). *Molecular Biology of the Cell. 4th Edn*. New York, NY: Garland Science.

Altangerel, N., Ariunbold, G. O., Gorman, C., Alkahtani, M., Borrego, E. J., Bohlmeyer, D., et al. (2017a). *In vivo* diagnostics of early abiotic plant stress response via Raman spectroscopy. *PNAS* 114, 3393–3396. doi: 10.1073/pnas.1701328114

Altangerel, N., Ariunbold, G. O., Gorman, C., Alkahtani, M., Borrego, E. J., Bohlmeyer, D., et al. (2017b). In reply to Dong and Zhao: plant stress via Raman spectroscopy. *PNAS Lett.* 114, E5488–E5490. doi: 10.1073/pnas.1707722114

Behmann, J., Steinrücken, J., and Plümer, L. (2014). Detection of early plant stress responses in hyperspectral images. *ISPRS J. Photogramm. Rem. Sens.* 93, 98–111. doi: 10.1016/j.isprsjprs.2014.03.016

Borlaug, N. E. (2000). Ending world hunger. The promise of biotechnology and the threat of antiscience zealotry. *Plant Physiol.* 124, 487–490. doi: 10.1104/pp.124.2.487

Chaves, M. M., Pereira, J. S., and Moroco, J. (2003). Understanding plant responses to drought – from genes to whole plant. *Funct. Plant Biol.* 30, 239–264. doi: 10.1071/FP02076

Davison, P. A., Hunter, C. N., and Horton, P. (2002). Overexpression of beta-carotene hydroxylase enhances stress tolerance in Arabidopsis. *Nature* 418, 203–206. doi: 10.1038/nature00861

De La Fuente, G. N., Barrero, I., Murray, S. C., Isakeit, T., and Kolomiets, M. V. (2014). "Improving Maize production under drought stress- traits, screening methods and environments," in *Handbook of Plant and Crop Physiology*, ed M. Pessaraki (Boca Raton, FL: CRC press), 887–912. doi: 10.1201/b16675-50

Fiorani, F., and Schurr, U. (2013). Future scenarios for plant phenotyping. *Annu. Rev. Plant Biol.* 64, 267–291. doi: 10.1146/annurev-arplant-050312-120137

Fritz, M., and Ehwald, R. (2011). Mannitol permeation and radial flow of water in maize root. *New Phytol.* 189, 210–217. doi: 10.1111/j.1469-8137.2010.03452.x

Gutelson, A., and Merziyak, M. (1996). Signature analysis of leaf reflectance spectra: algorithm development for remote sensing of chlorophyll. *J. Plant Physiol*. 148, 494–500. doi: 10.1016/S0176-1617(96)80284-7

Huang, P. C. (2017). *Oxylipin signals govern drought and salt tolerance and resistance to pathogens* (Dissertation). College Station, TX: A&M University.

Kalaji, H. M., Bosa, K., Janusz, K., and Hossain, Z. (2011). Chlorophyll fluorescence – a useful tool for early detection of temperature stress in spring barley. *J. Integ. Biol.* 15, 925–934 doi: 10.1089/omi.2011.0070

Kann, B., Offerhaus, H. L., Windbergs, M., and Otto, C. (2015). Raman microscopy for cellular investigations-from single cell imaging to drug carrier uptake visualization. *Adv. Drug Deliv. Rev.* 89, 71–90. doi: 10.1016/j.addr.2015.02.006

Karageorgou, P., and Manetas, Y. (2006). Importance of being red when young: anthocyanins and the protection of young leaves of *Quercus coccifera* from insect herbivory and excess light. *Tree Physiol.* 5, 613–621. doi: 10.1093/treephys/26.5.613

Krieger-Liszkay, A., Fufezanm, C., and Trebst, A. (2008). Singlet oxygen production in photosystem II and related protection mechanism. *Photosyn. Res.* 98, 551–564. doi: 10.1007/s11120-008-9349-3

Krinsky, N. I. (1989). Antioxidant functions of carotenoids. *Free Radic. Biol. Med.* 7, 617–635. doi: 10.1016/0891-5849(89)90143-3

Lieber, C., and Mahadevan-Jansen, A. (2003). Automated method for subtraction of fluorescence from biological Raman spectra. *Appl. Spectrosc.* 57, 1363–1367. doi: 10.1366/000370203322554518

Lintig, J. V., Welsch, R., Bonk, M., Giuliano, G., Batschauer, A., and Kleinig, H. (1997). Light-dependent regulation of carotenoid biosynthesis occurs at the level of phytoene synthase expression and is mediated by phytochrome in *Sinapis alba* and *Arabidopsis thaliana* seedling. *Plant J.* 12, 625–635. doi: 10.1046/j.1365-313X.1997.00625.x

Muller, P., Li, X., and Niyogi, K. (2001). Non-photochemical quenching. A response to excess light energy. *Plant Physiol.* 125, 1558–1566. doi: 10.1104/pp.125.4.1558

Ramel, F., Birtic, S., Cinies, C., Soubigou-Taconnat, L., Triantaphylides, C., and Havaux, M. (2012). Carotenoid oxidation products are stress signals that mediate gene responses to singlet oxygen in plants. *PNAS* 109, 5535–5540. doi: 10.1073/pnas.1115982109

Ranum, P., Pena-Rosas, J. P., and Garcia-Casai, M. N. (2014). Global maize production, utilization and consumption. *Ann. N. Y. Acad. Sci.* 1312, 105–112. doi: 10.1111/nyas.12396

Ruggiero, B., Koiwa, H., Manabe, Y., Quist, T. M., Saccardo, F., Joly, R. J., et al. (2004). Uncoupling the effects of abscisic acid on plant growth and water relations. Analysis of sto1/nced3, an *Abscisic* acid-deficient but salt stress-tolerant mutant in *Arabidopsis*. *Plant Physiol.* 136, 3134–3147. doi: 10.1104/pp.104.046169

Shan, L., and Li, L. (2008). Carotenoid metabolism: biosynthesis, regulation, and beyond. *J. Integr. Plant Biol.* 50, 778–785. doi: 10.1111/j.1744-7909.2008.00708.x

Sun, T., Yuan, H., Cao, H., Yazdani, M., Tadmor, Y., and Li, L. (2018). Carotenoid metabolism in plants: the role of plastids. *Molecular Plant* 11, 58–74. doi: 10.1016/j.molp.2017.09.010

Tilman, D., Fargione, J., Wolff, B., D'Antonio, C., Dobson, A., Howarth, R., et al. (2001). Forecasting agriculturally driven global environmental change. *Science* 292, 281–284. doi: 10.1126/science.1057544

Welsch, R., Beyer, P., Hugueney, P., Kleinig, H., and Lintig, J. V. (2000). Regulation and activation of phytoene synthase, a key enzyme in carotenoid biosynthesis, during photomorphogenesis. *Planta* 211, 846–854. doi: 10.1007/s004250000352

Yoshikazu, T., Sasaki, N., and Ohmiya, A. (2008). Biosynthesis of plant pigments: anthocyanins, betalains, and carotenoids. *Plant J.* 54, 733–749 doi: 10.1111/j.1365-313X.2008.03447.x

Zia, S., Romano, G., Spreer, W., Sanchez, C., Cairns, J., Araus, J. L., et al. (2013). Infrared thermal imaging as a rapid tool for identifying water-stress tolerant maize genotypes of different phenology. *J. Agron. Crop Sci:* 199, 75–84. doi: 10.1111/j.1439-037X.2012.00537.x

Conflict of Interest: The authors declare that the research was conducted in the absence of any commercial or financial relationships that could be construed as a potential conflict of interest.

Advantages of publishing in Frontiers

OPEN ACCESS
Articles are free to read for greatest visibility and readership

FAST PUBLICATION
Around 90 days from submission to decision

HIGH QUALITY PEER-REVIEW
Rigorous, collaborative, and constructive peer-review

TRANSPARENT PEER-REVIEW
Editors and reviewers acknowledged by name on published articles

Frontiers
Avenue du Tribunal-Fédéral 34
1005 Lausanne | Switzerland

Visit us: www.frontiersin.org
Contact us: frontiersin.org/about/contact

REPRODUCIBILITY OF RESEARCH
Support open data and methods to enhance research reproducibility

DIGITAL PUBLISHING
Articles designed for optimal readership across devices

FOLLOW US
@frontiersin

IMPACT METRICS
Advanced article metrics track visibility across digital media

EXTENSIVE PROMOTION
Marketing and promotion of impactful research

LOOP RESEARCH NETWORK
Our network increases your article's readership